IMAGING TECHNOLOGY IN ONCOLOGY PHARMACOLOGICAL RESEARCH

EDITED BY: Jinchao Feng, Xueli Chen, Xu Cao, Hong Shan and Qi Zeng
PUBLISHED IN: Frontiers in Pharmacology and Frontiers in Oncology

frontiers Research Topics

ISSN 1664-8714
ISBN 978-2-88971-395-0
DOI 10.3389/978-2-88971-395-0

About Frontiers

Frontiers is more than just an open-access publisher of scholarly articles: it is a pioneering approach to the world of academia, radically improving the way scholarly research is managed. The grand vision of Frontiers is a world where all people have an equal opportunity to seek, share and generate knowledge. Frontiers provides immediate and permanent online open access to all its publications, but this alone is not enough to realize our grand goals.

Frontiers Journal Series

The Frontiers Journal Series is a multi-tier and interdisciplinary set of open-access, online journals, promising a paradigm shift from the current review, selection and dissemination processes in academic publishing. All Frontiers journals are driven by researchers for researchers; therefore, they constitute a service to the scholarly community. At the same time, the Frontiers Journal Series operates on a revolutionary invention, the tiered publishing system, initially addressing specific communities of scholars, and gradually climbing up to broader public understanding, thus serving the interests of the lay society, too.

Dedication to Quality

Each Frontiers article is a landmark of the highest quality, thanks to genuinely collaborative interactions between authors and review editors, who include some of the world's best academicians. Research must be certified by peers before entering a stream of knowledge that may eventually reach the public - and shape society; therefore, Frontiers only applies the most rigorous and unbiased reviews.
Frontiers revolutionizes research publishing by freely delivering the most outstanding research, evaluated with no bias from both the academic and social point of view. By applying the most advanced information technologies, Frontiers is catapulting scholarly publishing into a new generation.

What are Frontiers Research Topics?

Frontiers Research Topics are very popular trademarks of the Frontiers Journals Series: they are collections of at least ten articles, all centered on a particular subject. With their unique mix of varied contributions from Original Research to Review Articles, Frontiers Research Topics unify the most influential researchers, the latest key findings and historical advances in a hot research area! Find out more on how to host your own Frontiers Research Topic or contribute to one as an author by contacting the Frontiers Editorial Office: frontiersin.org/about/contact

IMAGING TECHNOLOGY IN ONCOLOGY PHARMACOLOGICAL RESEARCH

Topic Editors:
Jinchao Feng, Beijing University of Technology, China
Xueli Chen, Xidian University, China
Xu Cao, Dartmouth College, United States
Hong Shan, Sun Yat-sen University, China
Qi Zeng, Xidian University, China

Citation: Feng, J., Chen, X., Cao, X., Shan, H., Zeng, Q., eds. (2021). Imaging Technology in Oncology Pharmacological Research. Lausanne: Frontiers Media SA. doi: 10.3389/978-2-88971-395-0

Table of Contents

frontiers in Pharmacology

EDITORIAL
published: 23 July 2021
doi: 10.3389/fphar.2021.711387

Editorial: Imaging Technology in Oncology Pharmacological Research

Qi Zeng[1], *Xu Cao*[2], *Jinchao Feng*[3], *Hong Shan*[4] *and Xueli Chen*[1]*

[1]Engineering Research Center of Molecular and Neuro Imaging of the Ministry of Education, School of Life Science and Technology, Xidian University, Xi'an, China, [2]Thayer School of Engineering, Dartmouth College, Hanover, NH, United States, [3]Faculty of Information Technology, Beijing University of Technology, Beijing, China, [4]Department of Interventional Medicine, Guangdong Provincial Engineering Research Center of Molecular Imaging, The Fifth Affiliated Hospital of Sun Yat-Sen University, Zhuhai, China

Keywords: imaging technology, oncology, pharmacological research, cancer therapy, small molecule drugs

Editorial on the Research Topic

Imaging Technology in Oncology Pharmacological Research

Imaging technology is being recognized as an important tool for breaking through the bottleneck of drug development as it is able to provide great insights into the morphology or functionality of pharmacological models, including cell, tissue, and animal. Imaging has several advantages compared to traditional evaluation methods, which include high spatiotemporal resolution, imaging sensitivity, and tissue specificity. In addition, imaging can be utilized to determine the gene expression, metabolism of various substances, cancer detection, drug development, as well as other fields.

Imaging technology includes both microscopic and macroscopic imaging scales, and encompasses fluorescence-based microscopy (Weissleder and Pittet, 2008), Raman-based microscopy (Chen et al., 2017), targeted ultrasound imaging (Frangioni, 2008), photoacoustic imaging (Wang and Hu, 2012), SPECT, PET (Rahmim and Zaidi, 2008), and molecular MRI (Pichler et al., 2008), among others. These technologies can be utilized for imaging or analysis of living systems at various levels. Hence, imaging strategies are commonly applied across several research projects to evaluate the pharmacokinetics, activity, and mechanisms of cancer therapy through the use of small molecule drugs or prodrugs (Gillies, 2002; Wang et al., 2008; Gurny and Mader, 2010; Janib et al., 2010). In parallel, more specific imaging-based evaluation methods have been developed that can help improve the pharmacological studies of chemotherapy. Thus, in this special issue, we further emphasize and describe the research that has provided creative research ideas in this domain.

Two review articles demonstrated the role of one imaging technology in the treatment of cancer. Fang et al. systemically summarized the recent advances that have been made in the development of noninvasive imaging and radiotherapy agents for the different molecular subtypes of breast cancer in preclinical studies in their study, "Theranostics for the different molecular subtypes of breast cancer." The researchers provided a conceptual examination of recent or current original articles that were published within the last decade in the field of preclinical breast cancer nuclear imaging. Data were extracted from the PubMed database and filtered according to the key words "breast cancer," "preclinical," "PET/SPECT," and "targeted imaging." In order to help guide future investigations of novel theranostic agents, they listed different imaging agents and cell lines that were tested in preclinical studies. They think molecular imaging can help with diagnosis, staging, guiding treatment, and predicting response to corresponding targeted therapy. The review of Zeng et al. which was titled "Treatment coherent Raman scattering microscopy in oncology pharmacokinetic research" highlighted coherent Raman scattering (CRS) microscopy as a novel emerging platform to facilitate oncology pharmacokinetic research. It would be of great importance to develop label-free

OPEN ACCESS

Edited and reviewed by:
Olivier Feron,
Université catholique de Louvain, Belgium

***Correspondence:**
Xueli Chen
xlchen@xidian.edu.cn

Specialty section:
This article was submitted to Pharmacology of Anti-Cancer Drugs, a section of the journal Frontiers in Pharmacology

Received: *18 May 2021*
Accepted: *24 June 2021*
Published: *23 July 2021*

Citation:
Zeng Q, Cao X, Feng J, Shan H and Chen X (2021) Editorial: Imaging Technology in Oncology Pharmacological Research. Front. Pharmacol. 12:711387. doi: 10.3389/fphar.2021.711387

optical microscopy that is able to assess stability and dissolution of drugs in the solid state, and uptake, distribution, interaction, and excretion of anticancer drug nanocarriers in a biological environment. Therefore, they summarized the recent technical advances and applications of CRS microscopy in the field of anticancer drug pharmacokinetics at the single cell level, drug stability and dissolution in the solid state, as well as the activities of anticancer drug nanocarriers in single cells. According to their review, there are several reasons to believe that CRS microscopy with label-free, chemically selective, high temporospatial resolution, and highly sensitive imaging can offer novel opportunities for investigation of anticancer drugs.

In order to explore a novel strategy of cancer treatment, imaging technology can be applied across several *in vitro* studies. Zhang et al. in the article "Metabolic reprogramming of sulfur in hepatocellular carcinoma and sulfane sulfur-triggered anti-cancer strategy" uncovered reprogramming of sulfur metabolism in hepatocellular carcinoma (HCC) and were able to provide a potential therapeutic strategy for HCC by donating sulfane sulfurs. Herein, the cell imaging assay was carried out to support their hypothesis. Their findings suggest that application of sulfane sulfurs may be an effective therapeutic strategy, particularly for HCC tumor cells that have reprogrammed the sulfur metabolism. Jin et al. in their article "Hirsutella sinensis fungus regulates CD8 + T cell exhaustion through involvement of T-Bet/Eomes in the tumor microenvironment" have provided insights into the application of Hirsutella sinensis fungus (HSF) in a tumor immune treatment. Their study demonstrated that HSF exerts antitumor effects mainly by reducing the expression of immune checkpoints by inhibiting T-bet in T cells, which lowers Tex cell production in the tumor microenvironment. Additionally, HSF could promote the Eomes expression in order to enhance T cell function. *In vivo* imaging technology was utilized to evaluate the effects of HSF on various tumor mouse models. Their findings were able to provide novel insights into the effect of HSF on tumor immune responses.

Imaging technology was a powerful tool for the *in vivo* evaluation of drugs. Xu et al. in their article "Bioluminescence imaging-based assessment of the anti-triple-negative breast cancer and NF-Kappa B pathway inhibition activity of britanin" were able to evaluate the anti–breast cancer activity of britanin. Their results demonstrated that britanin induces apoptosis *via* inhibition of the NF-κB pathways. The bioluminescence imaging screening system is useful for accelerating application of britanin in the antitumor field, which provides a useful tool for evaluating the efficacy of phytochemicals in inhibiting cancer cell proliferation in animal models. Zhan et al. in their article "Construction of biocompatible dual-drug loaded complicated nanoparticles for *in vivo* improvement of synergistic chemotherapy in esophageal cancer" developed a doxorubicin and *β*-elemene–loaded mesoporous silica nanoparticle system to exert inhibitory effects in esophageal cancer treatment. Fluorescence images were applied in order to validate efficacy of the combination therapy *in vivo*. Zhang et al. in their article "Terphenyllin suppresses orthotopic pancreatic tumor growth and prevents metastasis in mice" reported a novel marine-derived natural product terphenyllin with potent anti-pancreatic cancer (PC) activity. Herein, terphenyllin was found to significantly suppress PC cell growth and metastasis *in vitro* and *in vivo*. Terphenyllin induced PC cell apoptosis by increasing the expression of proapoptotic proteins and decreasing the expression of antiapoptotic proteins. The Panc1-Luc cell lines were utilized to develop an orthotopic mouse model, which may be able to closely mimic the original situation in human PC patients and may be better able to predict the therapeutic efficacy of the test compound. The *in vivo* imaging technique demonstrated significant inhibitory effects of terphenyllin on tumor growth. Their results reveal the therapeutic potential of terphenyllin in PC, which can help provide a basis for further developing this natural compound as an anticancer therapeutic agent.

The integrated diagnosis and treatment of nanoparticles will provide precise information for a cancer treatment strategy. In Li et al.'s "Manganese-based targeted nanoparticles for postoperative gastric cancer monitoring via magnetic resonance imaging," an Mn-based contrast agent for MRI was synthesized to provide accurate evaluation of therapeutic effects and guide treatment strategy adjustment over time. A series of *in vitro* and *in vivo* imaging experiments were employed to assess the characters of Mn_3O_4@PEG-RGD NPs. Their results indicated that Mn_3O_4@PEG-RGD NPs likely have a great potential for the MRI postoperative monitoring of gastric cancer and give an appropriate strategy for following chemotherapy. Xu et al. in their research "Synthesis, characterization, cellular uptake, and *in vitro* anticancer activity of fullerenol-foxorubicin conjugates alpha 3 function by colchicines" designed and synthesized the fuller enol (FU)-DOX conjugates and folic acid (FA)-grafted FU-DOX conjugates in order to improve the selectivity and activity of DOX in cancer cells. They synthesized DOX and FU conjugates (FU-DOX) through the use of the acid-sensitive hydrazone bond and were further modified by FA in order to obtain FA-FU-DOX conjugates for improving tumor-targeting effects. In their study, fluorescent microscopy was utilized to monitor cellular uptake. Indeed, FA-FU-DOX conjugates may optimize the safety and efficacy profile of DOX. Zhou et al. also wrote another review article "pH-Sensitive and long-circulation nanoparticles for near-infrared fluorescence imaging-monitored and chemo-photothermal synergistic treatment against gastric cancer" which reported photothermal–chemotherapy combined nanoparticles (PCC NPs) that have functions of chemo-photothermal synergistic therapy and continuous imaging for gastric cancer. The PCC NPs consisted of dopamine, poloxamer, DOX, and IR-820 *via* π–π stacking and demonstrated good biocompatibility both *in vitro* and *in vivo*. Their study can offer a novel postoperative treatment for gastric cancer.

Moreover, imaging technology also plays a significant role in a clinical anticancer medication strategy. Zhao et al. in their article "Accuracy of endoscopic diagnosis of helicobacter pylori based on the Kyoto classification of gastritis: a multicenter study" provided evidence of clinical accuracy and robustness of the Kyoto classification of gastritis in the Chinese population. Furthermore, they discovered that the reappearance of two

indicators (unclear atrophy boundary and unclear atrophy boundary) in atrophic mucosa could help sufficiently determine the presence of *Helicobacter pylori* (*H. pylori*) infection on an endoscopic basis. Their prospective and multicenter study was based on 650 Chinese patients. In order to prevent the occurrence and development of gastric cancer (GC) early on, their study offered an important novel finding for screening of early GC based on the close relationship between *H. pylori* and GC.

In conclusion, a collection of 11 articles contributed to this research topic, which covers two reviews and nine research articles. It is important to note that these published articles cover a wide spectrum of applications of imaging technology in oncology pharmacological research, which includes exploring a novel anticancer chemotherapy strategy *in vitro*, evaluating *in vivo* anticancer effects, and benefiting the clinical diagnosis. These articles provide deep insights into methodology and applications of imaging technology. We believe that imaging technology would be increasingly welcome in oncology pharmacological research.

AUTHOR CONTRIBUTIONS

QZ and XLC have collectively conceived and wrote the text. All authors contributed to the article and approved the submitted version.

FUNDING

This work was supported in part by the National Key R&D Program of China under grant no. 2018YFC0910600, Key Research and Development Program of Shaanxi (Program No. 2021ZDLSF04-05).

ACKNOWLEDGMENTS

We thanks Wangting Zhou (Xidian University) for writing this editorial. We are grateful to Dan Li (the Fifth Affiliated Hospital of Sun Yat-Sen University) for helping in organization of the special issue.

REFERENCES

Chen, X. L., Zhang, C., Lin, P., Huang, K. C., Liang, J. M., Tian, J., et al. (2017). Volumetric Chemical Imaging by Stimulated Raman Projection Microscopy and Tomography. *Nat. Commun.* 8. doi:10.1038/ncomms15117

Frangioni, J. V. (2008). New Technologies for Human Cancer Imaging. *Jco* 26 (24), 4012–4021. doi:10.1200/Jco.2007.14.3065

Gillies, R. J. (2002). *In Vivo* molecular Imaging. *J. Cell. Biochem.* 87, 231–238. doi:10.1002/jcb.10450

Gurny, R., and Mäder, K. (2010). Imaging Tools for Pharmaceutical Development. *Eur. J. Pharmaceutics Biopharmaceutics* 74 (1), 1. doi:10.1016/j.ejpb.2009.11.006

Janib, S. M., Moses, A. S., and MacKay, J. A. (2010). Imaging and Drug Delivery Using Theranostic Nanoparticles. *Adv. Drug Deliv. Rev.* 62 (11), 1052–1063. doi:10.1016/j.addr.2010.08.004

Pichler, B. J., Wehrl, H. F., and Judenhofer, M. S. (2008). Latest Advances in Molecular Imaging Instrumentation. *J. Nucl. Med.* 49, 5S–23S. doi:10.2967/jnumed.108.045880

Rahmim, A., and Zaidi, H. (2008). PET versus SPECT: Strengths, Limitations and Challenges. *Nucl. Med. Commun.* 29 (3), 193–207. doi:10.1097/Mnm.0b013e3282f3a515

Wang, L. V., and Hu, S. (2012). Photoacoustic Tomography: *In Vivo* Imaging from Organelles to Organs. *Science* 335 (6075), 1458–1462. doi:10.1126/science.1216210

Wang, X., Yang, L., Chen, Z., and Shin, D. M. (2008). Application of Nanotechnology in Cancer Therapy and Imaging. *CA: A Cancer J. Clinicians* 58 (2), 97–110. doi:10.3322/Ca.2007.0003

Weissleder, R., and Pittet, M. J. (2008). Imaging in the Era of Molecular Oncology. *Nature* 452 (7187), 580–589. doi:10.1038/nature06917

Conflict of Interest: The authors declare that the research was conducted in the absence of any commercial or financial relationships that could be construed as a potential conflict of interest.

Publisher's Note: All claims expressed in this article are solely those of the authors and do not necessarily represent those of their affiliated organizations, or those of the publisher, the editors and the reviewers. Any product that may be evaluated in this article, or claim that may be made by its manufacturer, is not guaranteed or endorsed by the publisher.

frontiers in Pharmacology

ORIGINAL RESEARCH
published: 08 April 2020
doi: 10.3389/fphar.2020.00457

Terphenyllin Suppresses Orthotopic Pancreatic Tumor Growth and Prevents Metastasis in Mice

Jia Zhang[1,2†], Weiyi Wang[3†], Yuan Zhou[2†], Jing Yang[2†], Jingli Xu[4], Zhiyuan Xu[5,6,7], Beihua Xu[2], Li Yan[8], Xiang-Dong Cheng[5,6,7], Minghua Li[1*] and Jiang-Jiang Qin[2,5,6,7*]*

[1] Shanxi Province Academy of Traditional Chinese Medicine, Taiyuan, China, [2] College of Pharmaceutical Sciences, Zhejiang Chinese Medical University, Hangzhou, China, [3] Key Laboratory of Marine Biogenetic Resources, Third Institute of Oceanography, Ministry of Natural Resources, Xiamen, China, [4] First Clinical Medical College, Zhejiang Chinese Medical University, Hangzhou, China, [5] Institute of Cancer and Basic Medicine, Chinese Academy of Sciences, Hangzhou, China, [6] Cancer Hospital of the University of Chinese Academy of Sciences, Hangzhou, China, [7] Zhejiang Cancer Hospital, Hangzhou, China, [8] School of Pharmacy, Naval Medical University, Shanghai, China

OPEN ACCESS

Edited by:
Qi Zeng,
Xidian University, China

Reviewed by:
Ke Li,
Xi'an Medical University, China
Hui Xie,
Xidian University, China

***Correspondence:**
Weiyi Wang
wywang@tio.org.cn
Minghua Li
1035448060@qq.com
Jiang-Jiang Qin
jqin@zcmu.edu.cn;
zylysjtu@hotmail.com

[†]These authors have contributed equally to this work

Specialty section:
This article was submitted to Pharmacology of Anti-Cancer Drugs, a section of the journal Frontiers in Pharmacology

Received: 24 February 2020
Accepted: 24 March 2020
Published: 08 April 2020

Citation:
Zhang J, Wang W, Zhou Y, Yang J, Xu J, Xu Z, Xu B, Yan L, Cheng X-D, Li M and Qin J-J (2020) Terphenyllin Suppresses Orthotopic Pancreatic Tumor Growth and Prevents Metastasis in Mice. Front. Pharmacol. 11:457. doi: 10.3389/fphar.2020.00457

Pancreatic cancer (PC) is an aggressive and fatal disease with high incidences of metastasis and recurrence. However, there are no effective treatment options for the majority of PC patients, especially for those with locally advanced tumors and metastatic diseases. Therefore, it is urgently needed to develop safe and effective anti-PC therapeutic agents. We have recently identified a novel marine-derived natural product terphenyllin with potent anti-PC activity. The present study was designed to investigate the efficacy and mechanisms of action of terphenyllin in several human PC cell lines and an orthotopic PC mouse model. The results showed that terphenyllin significantly inhibited the viability of all PC cell lines with minimal effects on a normal human pancreatic cell line (HPNE). We next demonstrated the effects of terphenyllin on colony formation, apoptosis, migration, and invasion in both Panc1 and HPAC cell lines in a concentration-dependent manner. Terphenyllin also suppressed the tumor growth and metastasis in the Panc1 orthotopic mouse model. We further showed the profound effects of terphenyllin on the expression of apoptosis-associated proteins, including Bax, Bad, Puma, Bim_L, Bcl-2, phos-Bcl-2 (Ser70), Bcl-xL, caspase 7, and PARP, which contributed to its anti-PC activity. In summary, terphenyllin suppressed the PC cell growth and metastasis *in vitro* and *in vivo* and may be developed as an anti-PC therapeutic agent in the future.

Keywords: terphenyllin, pancreatic cancer, metastasis, Bax, Bcl-2, Puma

INTRODUCTION

Pancreatic cancer (PC) is one of the most aggressive and fatal types of cancer and ranks the fourth leading cause of cancer-associated death worldwide with a dismal 5-year survival rate of 9% (Siegel et al., 2020). Despite the advancement in the development of new treatments, the therapeutic options for PC patients remain limited (Strobel et al., 2019). Surgical resection combined with chemotherapy provides PC patients with the only hope of long-term survival and cure (Kleeff et al., 2016). However, the majority of patients with early-stage PC are clinically silent, and only about 10% of patients are diagnosed at the

resectable stage (Hartwig et al., 2013). Among the remaining 90% of PC patients, about 30% of them are diagnosed with locally advanced tumors and 60% even have metastatic diseases and poor performance status, which are generally recalcitrant to all forms of cancer treatment (Strobel et al., 2019). Therefore, there is an unmet need to develop novel therapies for improving the survival outcomes of PC patients as well as the quality of life.

Over the last few decades, chemotherapy with gemcitabine or 5-fluorouracil only demonstrates modest clinical benefit for PC patients (Burris et al., 1997; Kleeff et al., 2016). Chemotherapy combinations, such as FOLFIRINOX and gemcitabine plus nab-paclitaxel have significantly increased the overall survival of PC patients with advanced diseases (Mcbride et al., 2017; Nguyen et al., 2017). However, FOLFIRINOX has recently been associated with increased toxicity, mainly febrile neutropenia and diarrhea (Lambert et al., 2017). Numerous studies have unraveled the common molecular alterations occurring in PC, such as mutations in Kras, p53, and BRCA1 (Nag et al., 2013; Cicenas et al., 2017; Waters and Der, 2018), aberrant activation of wnt/β-catenin signaling and keap1/Nrf2 signaling (Qin et al., 2018; Kuo et al., 2019; Qin et al., 2019), and amplification and overexpression of MDM2, cyclin D1, USP7, and MDR1 (Qie and Diehl, 2016; Robey et al., 2018; Wang et al., 2019b; Dong et al., 2020; Qi et al., 2020), which play critical roles in the initiation, progression, metastasis, and chemoresistance of PC. Many targeted agents have been developed and evaluated in the preclinical and clinical settings (Karandish and Mallik, 2016). While several preclinical studies showed positive results (Wang et al., 2014b; Leal et al., 2017; Wang et al., 2018b), only a few of them, *e.g.* erlotinib have proved successful in PC clinical trials (Mosquera et al., 2016). Herein, safe and effective therapeutics are still urgently needed for PC therapy.

Natural products remain one of the most important sources for drug discovery and development (Qin et al., 2017a; Davison and Brimble, 2019). We have initiated an ongoing project aiming at identifying novel anticancer natural products from medicinal plants and marine-derived fungi and characterized several natural compounds with promising efficacy and safety profiles (Wang et al., 2012; Chen et al., 2013; Qin et al., 2015; Wang et al., 2018a). In a recent cancer cell-based screen, we have identified a cytotoxic natural product terphenyllin from a coral-derived fungus (Wang et al., 2017). Terphenyllin and its analogs have shown potent apoptosis-inducing ability in cancer cells (Wang et al., 2017; Wang et al., 2020). However, their *in vivo* efficacy and the molecular mechanisms are yet to be determined. The present study was designed to evaluate the anticancer efficacy of terphenyllin and its underlying mechanisms of action *in vitro* and *in vivo*. Our results demonstrate the therapeutic potential of terphenyllin in PC, which would provide a basis for further developing this natural compound as an anticancer therapeutic agent.

MATERIALS AND METHODS

Cell Lines and Cell Culture

Human pancreatic cancer Panc1, HPAC, and SW1990 cell lines were obtained from the Cell Bank of the Chinese Academy of Science (Shanghai, China). The immortalized normal human pancreas cell line (HPNE) and human pancreatic cancer AsPC1 and CFPAC1 cell lines were kind gifts from Dr. Zhi-Gang Zhang (School of Medicine, Shanghai Jiao Tong University, Shanghai, China). The Panc1-Luc cell line was purchased from Meixuan Biological Science and Technology LTD (Shanghai, China). Panc1, SW1990, and HPNE cells were cultured in the DMEM medium. AsPC1 and CFPAC1 cells were maintained in the RPMI 1640 medium. HPAC cells were cultured in the DMEM/F12 (1:1) medium supplemented with 2 mg/L insulin, 5 mg/L transferrin, 40 ng/ml hydrocortisone, and 10 ng/ml epidermal growth factor. All media were supplemented with 10% fetal bovine serum (FBS) and 1% penicillin/streptomycin.

Chemicals, Antibodies, and Other Reagents

The test compound terphenyllin (**Figure 1A**) was prepared in Dr. Weiyi Wang's laboratory (Third Institute of Oceanography, Ministry of Natural Resources, Xiamen, China), and the structure was confirmed by NMR, MS, UV, and IR spectroscopy. The purity of terphenyllin was greater than 98%. All chemicals and solvents used were of the highest analytical grade available. The anti-rabbit Bax (D2E11), Bad (D24A9), Puma (D30C10), Bim (C34C5), Bcl-2 (D55G8), phos-Bcl-2 (p-Ser70) (5H2), Bcl-xl (54H6), caspase7 (D2Q3L), PARP (9542), and GAPDH (D16H11) antibodies were obtained from Cell Signaling Technology (Boston, USA). The goat anti-mouse IgG (H+L) and goat anti-rabbit IgG (H+L) antibodies were obtained from Bio-Rad (Hercules, CA, USA).

Cell Viability Assay

The effects of terphenyllin on the cell viability were determined by Cell Counting Kit 8 (Nuoyang Biotech, Hangzhou, China). Briefly, HPNE, Panc1, HPAC, SW1990, AsPC1, and CFPAC1 cells were cultured in 96-well plates ($2–3 \times 10^3$ cells/well) overnight and then exposed to terphenyllin (3.125, 6.25, 12.5, 25, 50, 100, or 200 μM) or DMSO for 72 h. The treated cells were further incubated with CCK8 solution and the absorbance was measured at 450 nm by a Multiskan MK3 microplate reader (Thermo Scientific, USA). The cell viability and IC_{50} values were calculated as reported previously (Qin et al., 2016a).

Colony Formation Assay

The colony formation assay was performed as described previously (Qin et al., 2017b; Wang et al., 2019a). Briefly, Panc1 and HPAC cells were seeded in 6-well plates (500 cells/well) overnight and treated with terphenyllin (20, 50, or 200 μM) or DMSO. After 24 h of exposure, the terphenyllin-containing medium was replaced with fresh medium without the test compound. The cells were grown for another 10 days, followed by fixation and crystal violet (Solarbio, China) staining.

Apoptosis Assay

The effects of terphenyllin on cell apoptosis were performed as reported previously (Voruganti et al., 2015b). Briefly, 3×10^5 Panc1 and HPAC cells in 6-well plates were exposed to terphenyllin (20, 50, or 200 μM) or DMSO for 48 h. The

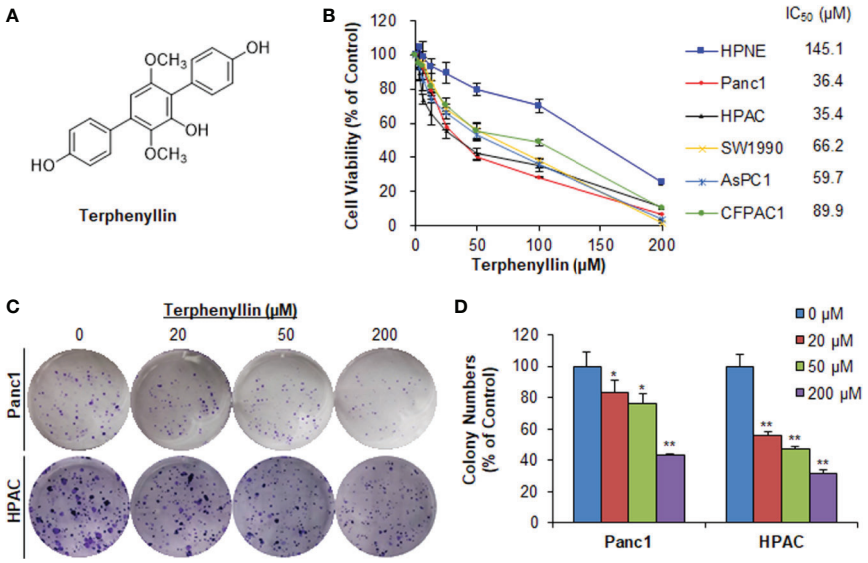

FIGURE 1 | Terphenyllin inhibits pancreatic cancer cell viability and colony formation *in vitro*. **(A)** The chemical structure of terphenyllin. **(B)** HPNE, Panc1, HPAC, SW1990, AsPC1, and CFPAC1 cells were treated with terphenyllin at the indicated concentrations for 72 h, followed by CCK8 assays. **(C)** Panc1 and HPAC cells were treated with terphenyllin at the indicated concentrations for 24 h, followed by 10-day colony formation assays. **(D)** Quantitative analysis of colony formation. Data are representative of at least three experiments. (*$p < 0.05$, **$p < 0.01$).

treated cells were harvested, washed with pre-cooling PBS, and then re-suspended in the mixture of binding buffer and staining reagents from FITC Annexin V Apoptosis Detection Kit I (BD Pharmingen, USA). The effects of terphenyllin on cell apoptosis were analyzed on a BD Accuri™ C6 flow cytometer (BD, Ann Arbor, MI, USA).

Transwell Migration and Invasion Assays

The effects of terphenyllin on cell migration and invasion were determined using the transwell migration and invasion assays according to the manufacturers' protocols (Wang et al., 2019a). For the migration assay, 5×10^4 Panc1 and HPAC were suspended in 200 μl of serum-free medium, seeded in the upper compartment of the transwell chamber (Corning, USA), and incubated with terphenyllin (25 μM) or DMSO. Besides, 700 μl of complete medium with 20% FBS was added into the lower chamber. After 24 h of incubation, the cells on the upper surface of the membrane in the chambers were removed using cotton swabs whereas the cells migrated through the membrane were washed with PBS, stained with crystal violet (Solarbio, China), and analyzed under a microscope (Axio Observer A1, Zeiss, Germany). For the invasion assay, the upper surface of the membrane was covered with a layer of Matrigel (BD Biosciences, USA). The other procedures were similar to the migration assay.

Western Blotting

Panc1 and HPAC cells were seeded in 6-cm dishes ($3–5 \times 10^5$ cells/well) overnight and exposed to terphenyllin (20, 50, or 200 μM) or DMSO for 24 h. The treated cells were then lysed with RIPA buffer (Absin Bioscience Inc, Shanghai, China) containing protease inhibitors (Solarbio Science & Technology Co., Ltd., Beijing, China) and phosphatase inhibitors (Roche, Switzerland). The cell lysates were centrifuged and the supernatants were collected, quantified, separated by an SDS-PAGE gel, and transferred to a PVDF blotting membrane (GE Healthcare, USA) for Western blot analysis following the manufacturer's protocol (Xue et al., 2017; Qin et al., 2018). After blocking with 5% nonfat milk and incubation with primary and second antibodies, the blotting membranes were examined using ECL luminescence reagent (Absin, Shanghai, China), and the images were acquired on a FluorChem Q System (Alpha Innotech, Cell Bioscienes, USA).

Panc1 Orthotopic Pancreatic Cancer Model

The orthotopic pancreatic cancer mouse model was developed as reported previously (Wang et al., 2014b; Wang et al., 2018b). Female 4–5-week-old SCID mice were purchased from the Shanghai Laboratory Animal Center (Shanghai, China). The experimental animal protocols were approved by the Board of Animal Study of Zhejiang Chinese Medical University. Briefly, 50 μl of Panc1-Luc cell solution (1×10^6 cells in a 1:1 mixture of Matrigel and serum-free medium) was slowly injected into the head of the pancreas. Terphenyllin was dissolved in PEG400: ethanol:saline (57.1:14.3:28.6, v/v/v) and administered to mice by intraperitoneal injection at a dose of 20 mg/kg/day, 7 days/week for five weeks. For *in vivo* imaging, mice were administered intraperitoneally with fluorescein substrate (150 mg/kg) and anesthetized with isoflurane using an anesthesia machine (Summit Anesthesia, USA). The *in vivo* images for detecting

the orthotopic tumor growth and metastasis were acquired on a Xenogen IVIS 200 imaging system (Caliper Life Sciences, USA). All the data analyses were performed using LT Living Image 4.3 Software. At the end of the experiments, all mice were examined for tumor metastasis to various organs.

Hematoxylin and Eosin (H&E) Staining

The hematoxylin and eosin (H&E) staining was performed as described previously (Voruganti et al., 2015a; Qin et al., 2016b). At the termination of the *in vivo* experiments using the Panc1 orthotopic model, various tissues (liver, lungs, kidneys, spleen, heart, and brain) were removed from the tumor-bearing mice, fixed in 10% formalin, and embedded in paraffin. These tissue blocks were processed and sectioned at a thickness of 5 μm. The tissue sections were deparaffinized in xylenes, rehydrated, washed with PBS, stained in Mayer's Hematoxylin for 10 min, and then stained with eosin for less than 1 min. After staining, the slides were dehydrated, mounted, and analyzed using an inverted microscope (Axio Observer A1, Zeiss, Germany).

Statistical Analysis

All quantitative data were analyzed using the Prism software version 6 (Graph Pad Software Inc., San Diego, CA, USA) and are presented as means ± SEM derived from three or more independent experiments. The significance of differences for comparisons between two groups was analyzed using Student's t-test. $p < 0.05$ was considered to be statistically significant.

RESULTS

Terphenyllin Exerts Cytotoxicity in Human Pancreatic Cancer Cell Lines With Minimal Effects on Normal Pancreatic Cells

Terphenyllin (**Figure 1A**) was first tested for its cytotoxicity in five human PC cell lines (Panc1, HPAC, SW1990, AsPC1, and CFPAC1) and one normal human pancreatic cell line (HPNE) at various concentrations (0 to 200 μM) for 72 h. As shown in **Figure 1B**, terphenyllin significantly inhibited the growth of all the PC cell lines, with the IC_{50} values ranging from 35.4 to 89.9 μM. Among them, Panc1 and HPAC were the most sensitive cell lines with IC_{50} values of 36.4 and 35.4 μM, respectively. Of note, terphenyllin had minimal effects on the growth of the normal cell line HPNE, indicating the selective cytotoxicity of the compound against PC cells.

Terphenyllin Inhibits the Colony Formation of Pancreatic Cancer Cells *In Vitro*

Terphenyllin was further evaluated for its *in vitro* anticancer activity in the most sensitive cell lines Panc1 and HPAC. As shown in **Figure 1C**, terphenyllin inhibited the cell colony formation in both cell lines in a concentration-dependent manner. At a high concentration of 200 μM, terphenyllin markedly decreased the numbers of colonies by 56.5% ($p < 0.01$) and 68.5% ($p < 0.01$) in Panc1 and HPAC cells, respectively (**Figure 1D**).

Terphenyllin Induces Pancreatic Cancer Cell Apoptosis *In Vitro*

Terphenyllin was examined for its effects on cell apoptosis in Panc1 and HPAC cell lines. As shown in **Figure 2A**, terphenyllin induced significant apoptosis in both cell lines in a concentration-dependent manner. Panc1 cells were less sensitive to terphenyllin treatment than HPAC cells at lower concentrations (20 and 50 μM) but more sensitive at the higher concentration (200 μM). After exposure to 200 μM of terphenyllin for 48 h, 44.5% ($p < 0.01$) of Panc1 cells and 35.4% ($p < 0.01$) of HPAC cells underwent apoptosis, which were significantly higher than that of control cells (**Figure 2B**).

Terphenyllin Modulates the Expression of Apoptosis-Related Proteins

To explore the mechanisms of action for the anticancer activity of terphenyllin, we examined its effects on the expression of key proteins involved in regulating cell apoptosis. As shown in **Figures 2C, D**, terphenyllin markedly increased the levels of pro-apoptotic proteins Bax, Bad, Puma, and Bim_L in both Panc1 and HPAC cell lines. The compound also decreased the levels of anti-apoptotic proteins Bcl-2 and Bcl-xL in both cell lines. It has been reported that the phosphorylation of Bcl-2 at Ser70 increases the anti-apoptotic activity of Bcl-2 by enhancing the dimerization with Bax (Deng et al., 2000; Deng et al., 2009). Terphenyllin reduced the expression of phosphorylated Bcl-2 (phos-Bcl-2) at Ser70, which may contribute to terphenyllin-induced apoptosis. The compound also cleaved and activated caspase 7 and PARP in both cell lines.

Terphenyllin Suppresses Tumor Growth in an Orthotopic Pancreatic Cancer Model

We further assessed the *in vivo* efficacy of terphenyllin in the Panc1 orthotopic mouse model. As shown in **Figure 3A**, SCID mice bearing orthotopic Panc1 tumors were treated with vehicle or terphenyllin at 20 mg/kg/day, 7 days/week for five weeks, resulting in 75.5% inhibition of tumor growth compared with the vehicle-treated mice (**Figure 3B**). Importantly, terphenyllin treatment did not affect the average body weight of the mice in comparison to that of vehicle-treated mice, suggesting that the compound did not cause significant host toxicity during the treatment period (**Figure 3C**). At the end of the experiments, the kidneys, spleen, heart, and brain were carefully dissected from all mice for histological examinations. No abnormalities were observed in the organs from both vehicle- and terphenyllin-treated mice, indicating the absence of host toxicity (**Figure 3D**).

Terphenyllin Prevents Pancreatic Cancer Cell Metastasis *In Vitro* and *In Vivo*

We investigated the effects of terphenyllin on PC cell metastasis *in vitro*. As shown in **Figure 4A**, in a 24-h treatment period, terphenyllin at a sub-lethal concentration of 25 μM significantly reduced the migration of Panc1 and HPAC cells in the transwell migration assay by 24.3% ($p < 0.05$) and 37.0% ($p < 0.01$), respectively (**Figure 4B**). In the transwell Matrigel invasion assay, terphenyllin at 25 μM exerted similar preventive efficacy

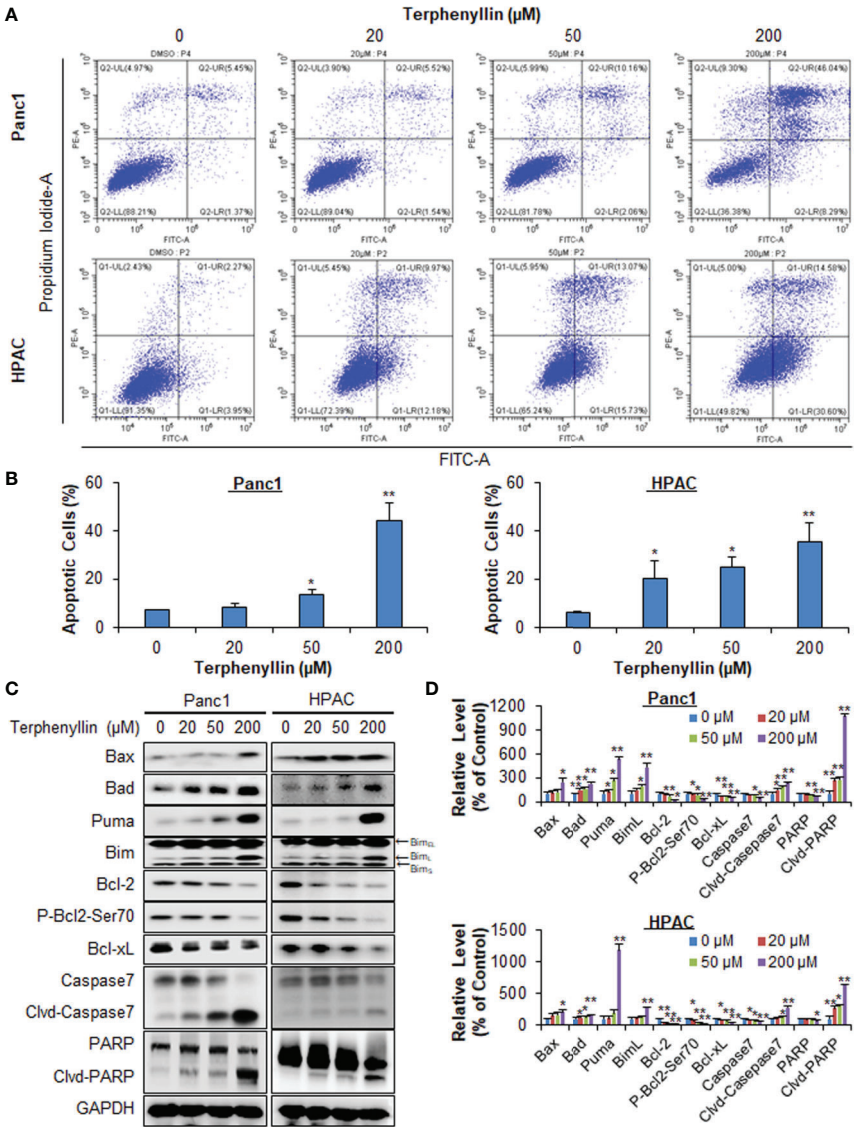

FIGURE 2 | Terphenyllin induces the apoptosis of pancreatic cancer cells *in vitro*. **(A)** Panc1 and HPAC cells were treated with terphenyllin at the indicated concentrations for 48 h, followed by the detection of apoptosis by FITC-Annexin V assay. **(B)** The percentages of apoptotic cells. **(C)** Panc1 and HPAC cells were treated with terphenyllin at the indicated concentrations for 24 h, and the levels of various proteins were detected using specific antibodies by Western blotting analysis. **(D)** Relative band densities of various proteins. The densities of the protein bands were analyzed using ImageJ and normalized to GAPDH. Data are representative of at least three experiments. (*$p < 0.05$, **$p < 0.01$).

(**Figure 4C**) and decreased the numbers of invaded Panc1 and HPAC cells by 24.6% ($p < 0.01$) and 31.6% ($p < 0.01$), respectively (**Figure 4D**). At the end of the *in vivo* studies of the Panc1 orthotopic model, we examined the metastatic lesions in the liver and lungs from all mice (**Figure 5A**). The results showed that 5 and 4 out of 6 vehicle-treated mice developed metastatic lesions in the liver and lungs, respectively, whereas the incidence of liver and lung metastasis in terphenyllin-treated mice was decreased to 2/6 and 1/6, respectively. The histological examinations further confirmed the inhibition of liver and lung metastasis by the compound *in vivo* (**Figure 5B**).

DISCUSSION

Pancreatic cancer is a highly lethal and devastating disease with early metastasis and poor prognosis. Although the extensive molecular analyses of PC have indicated the strong genetic heterogeneity of this disease, some common molecular alterations have been characterized and validated as potential molecular targets for developing anti-PC therapeutic agents (Qie and Diehl, 2016; Cicenas et al., 2017; Waters and Der, 2018; Kuo et al., 2019; Qin et al., 2019). Despite the improvements in chemotherapy and targeted therapy and the considerable progress in increasing overall survival, there are very

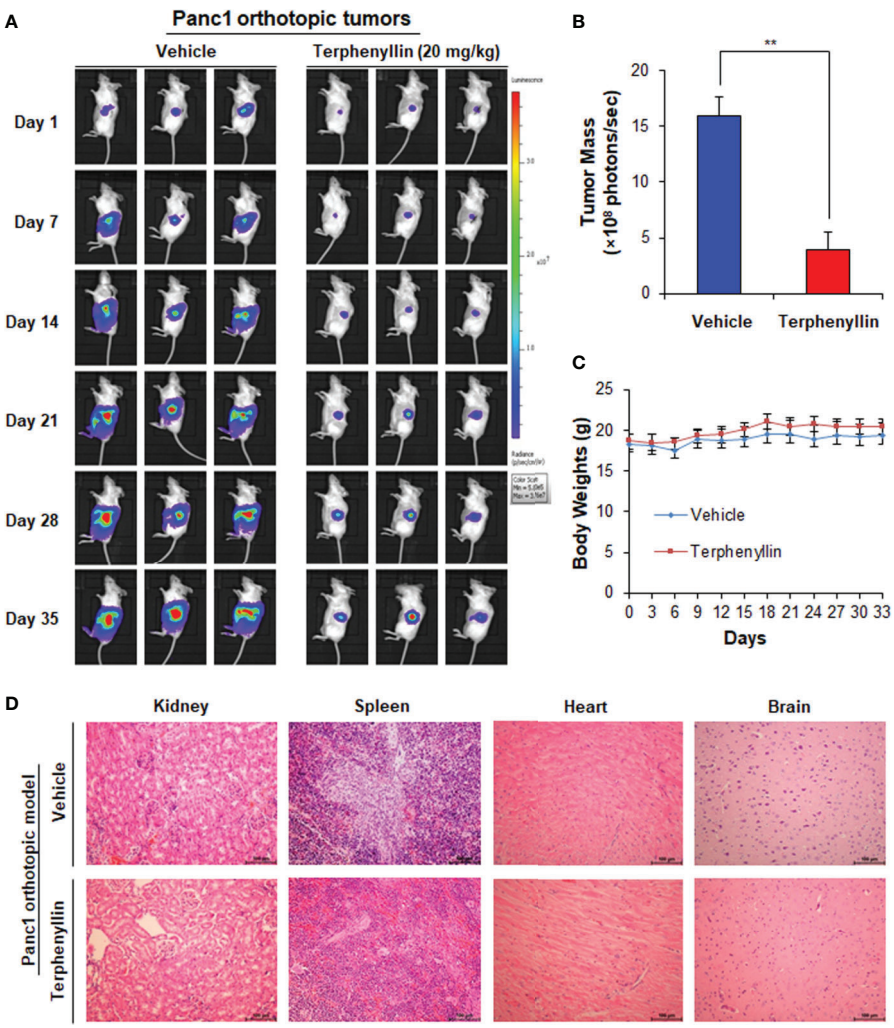

FIGURE 3 | Terphenyllin suppresses the growth of Panc1 orthotopic tumors without causing any host toxicity. Panc1-Luc cells were implanted orthotopically into the pancreas of SCID mice. Mice were treated with terphenyllin by i.p. injection at doses of 20 mg/kg/d, 7 days/week for 5 weeks. **(A)** The luciferase signals in the mice bearing Panc1 orthotopic tumors were detected and images were obtained using an IVIS *in vivo* imaging system. **(B)** At the termination of the experiments, the average tumor mass (determined by the detected photons/sec) of the terphenyllin-treated mice was compared with that of the control mice. **(C)** The mice were monitored for changes in body weight as a surrogate marker for toxicity. **(D)** At the end of the experiments, the kidneys, spleen, heart, and brain were carefully removed from the mice bearing Panc1 orthotopic tumors, and H&E staining was performed on the paraffin sections of these tissues (all images represent serial sections; scale bar, 100 μm). (**$p < 0.01$).

limited treatment options for PC patients, especially for those with locally advanced disease or metastasis (Werner et al., 2013; Rebelo et al., 2017; Neoptolemos et al., 2018).

Natural products provide a rich source of bioactive compounds with unique structures and diverse biological activities and play a crucial role in the discovery and development of anticancer therapeutics (Nag et al., 2012; Qian et al., 2013; Wang et al., 2014a; Kotecha et al., 2016; Kashyap et al., 2019). With a long-term goal of developing safe and effective anticancer agents, our laboratories have carried out cancer cell-based screenings of natural product libraries and identified several compounds with promising efficacy (Cheng et al., 2013; Li et al., 2013; Yao et al., 2017). The present study was designed to examine the anticancer efficacy of a novel marine-derived natural product terphenyllin and explore its molecular mechanisms in clinically relevant PC models *in vitro* and *in vivo*.

In the present study, we found that terphenyllin displayed significant cytotoxicity against human PC cell lines, while Panc1 and HPAC were the most sensitive cell lines. More importantly, we also observed that the normal HPNE cells were much less sensitive to the treatment of terphenyllin, suggesting the selective cytotoxicity toward cancer cells. Indeed, many natural products have potent cancer cell-killing properties; however, they also non-selectively kill normal cells, which largely limits their therapeutic value. In comparison to normal HPNE cells, terphenyllin displayed a selective growth inhibition of PC cancer cell lines,

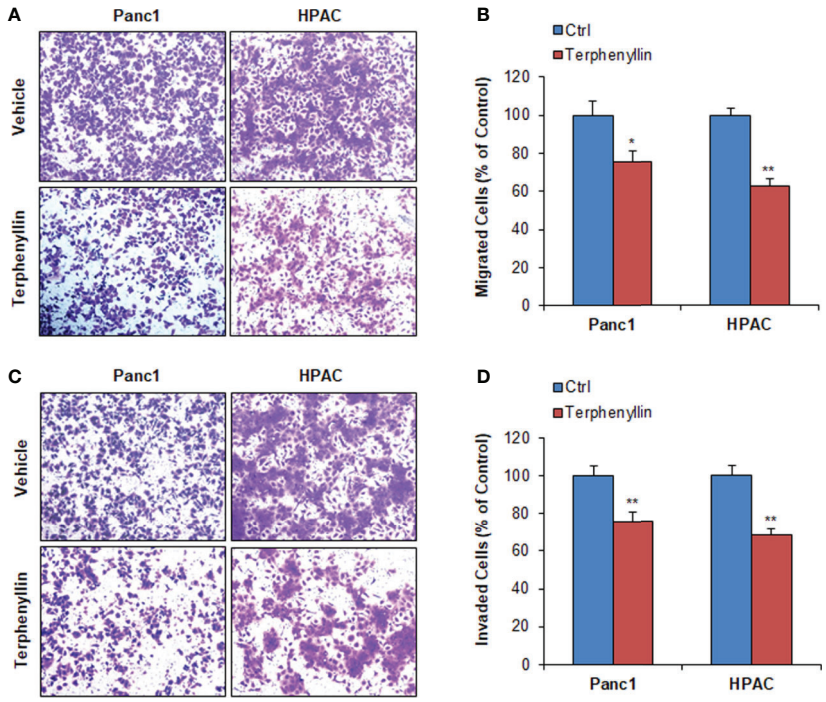

FIGURE 4 | Terphenyllin inhibits pancreatic cancer cell migration and invasion *in vitro*. **(A)** Transwell migration assay was performed in Panc1 and HPAC cells with or without terphenyllin treatment. Representative microscopic images of cells that migrated through the transwell. **(B)** The quantitation of cells that migrated through the transwell in the migration assay. **(C)** Transwell Matrigel invasion assay was performed in Panc1 and HPAC cells with or without terphenyllin treatment. Representative microscopic images of cells that invaded through the transwell. **(D)** Quantitation of cells that invaded through the transwell in the Matrigel invasion assay. Data are representative of at least three experiments. (*$p < 0.05$, **$p < 0.01$).

especially Panc1 and HPAC cell lines, which would be of great importance in the further development of this compound as an anticancer agent. In comparison to other PC cell lines, the selectivity indexes of terphenyllin against Panc1 and HPAC cells are relatively high. Therefore, we used Panc1 and HPAC as cell models for further evaluation of the compound. However, it should be noted that the selectivity index of terphenyllin against PC cell lines is still not good enough according to the "selectivity criteria". Structural optimization of terphenyllin should be performed to improve its efficacy and selectivity in the future.

We further demonstrated that terphenyllin inhibited colony formation and induced apoptosis in PC cell lines in a concentration-dependent manner. To elucidate the molecular mechanisms for the anticancer activity of terphenyllin, we investigated its effects on apoptosis-related proteins. We found that terphenyllin induced PC cell apoptosis by increasing the expression levels of pro-apoptotic proteins (Bax, Bad, Puma, and Bim_L) and decreasing the expression levels of anti-apoptotic proteins (Bcl-2 and Bcl-xL). We also observed that the compound reduced the expression of phos-Bcl-2 (Ser70) and cleaved and activated caspase 7 and PARP. However, this compound did not show any significant effects on several other members of the caspase family, including caspase 3 (data not shown). Its molecular target(s) and detailed mechanisms of action should be further investigated.

To confirm the anticancer efficacy of terphenyllin *in vivo*, we developed the Panc1 orthotopic mouse model, which could more closely mimic the original situation in human PC patients and better predict the therapeutic efficacy of the test compound. Our results showed the significant inhibitory effects of terphenyllin on tumor growth, as illustrated by *in vivo* imaging. Besides, the compound exhibited preventive effects on PC cell metastasis *in vitro*, as demonstrated by transwell migration and invasion assays. These preventive effects were further supported by the *in vivo* studies using the Panc1 orthotopic model. Of note, terphenyllin treatment did not cause any significant loss of mouse body weight or organ damage, indicating that the compound was safe at the effective dose. Nevertheless, it is necessary to examine the *in vivo* toxicity of terphenyllin by assessing the pathological sections of various organs from the terphenyllin-treated mice in our future studies. It has been demonstrated that treatment with different compounds may result in different toxicological responses; they may cause specific toxicity in a single organ (e.g., liver or lungs) or affect the entire body systemically (e.g., the immune system). Therefore, the examination of the organ toxicity will provide important information on the toxicological properties of terphenyllin, which is critically needed before we can move this compound into clinical trials. More clinically relevant PC models, such as patient-derived tumor models and transgenic

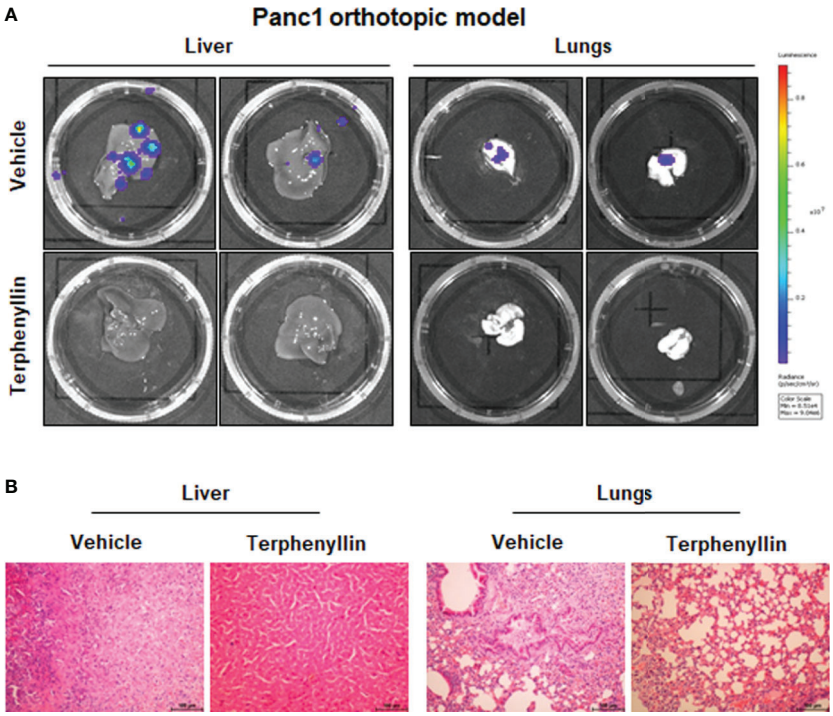

FIGURE 5 | Terphenyllin prevents pancreatic tumor metastasis *in vivo*. **(A)** At the termination of the experiments using the Panc1 orthotopic model, the livers and lungs were carefully removed from the mice and imaged to detect metastatic lesions. **(B)** H&E staining was performed on the paraffin sections of these tissues (all images represent serial sections; scale bar, 100 μm).

mouse models are also expected for the further evaluation of terphenyllin.

In summary, the present study has shown that the marine-derived natural product terphenyllin suppresses PC tumor growth and metastasis *in vitro* and *in vivo* without causing significant toxicity at the effective dose. Although this study has demonstrated its efficacy, safety, and possible molecular mechanisms in PC cell lines *in vitro* and in the Panc1 orthotopic mouse model *in vivo*, future studies are warranted to determine its molecular targets, precise mechanisms of action, efficacy, and pharmacological and toxicological properties.

DATA AVAILABILITY STATEMENT

The datasets generated for this study are available on request to the corresponding authors.

ETHICS STATEMENT

The animal study was reviewed and approved by the Board of Animal Study of Zhejiang Chinese Medical University.

AUTHOR CONTRIBUTIONS

JZ, WW, YZ, JY, JX, BX, and LY designed and conducted experiments, and wrote the manuscript. ZX and X-DC helped study design and interpretation of data. J-JQ and ML organized, conceived, and supervised the study. All authors read and approved the manuscript.

FUNDING

This work was supported by National Natural Science Foundation of China (81903842, 81573953), Program of Zhejiang Provincial TCM Sci-tech Plan (2020ZZ005, 2016ZZ012), Zhejiang Chinese Medical University Startup Funding (111100E014), Medical Science and Technology Project of Zhejiang Province (WKJ-ZJ-1728), Traditional Chinese Medical Science and Technology Major Project of Zhejiang Province (2018ZY006), Science and Technology Projects of Zhejiang Province (2019C03049), Foundation of Third Institute of Oceanography SOA (2017001 and 2018021), Natural Science Foundation of Fujian Province (2018J01064), and COMRA program (DY135-B2-05 and DY135-B2-01).

ACKNOWLEDGMENTS

We thank the specialists from the Academy of Chinese Medical Sciences, Zhejiang Chinese Medical University for their technical supports to this work.

SUPPLEMENTARY MATERIAL

The Supplementary Material for this article can be found online at: https://www.frontiersin.org/articles/10.3389/fphar.2020.00457/full#supplementary-material

REFERENCES

Burris, H., Moore, M. J., Andersen, J., Green, M. R., Rothenberg, M. L., Modiano, M. R., et al. (1997). Improvements in survival and clinical benefit with gemcitabine as first-line therapy for patients with advanced pancreas cancer: a randomized trial. *J. Clin. Oncol.* 15, 2403–2413. doi: 10.1200/JCO.1997.15.6.2403

Chen, D., Wang, W., Qin, J. J., Wang, M. H., Murugesan, S., Nadkarni, D. H., et al. (2013). Identification of the ZAK-MKK4-JNK-TGFbeta signaling pathway as a molecular target for novel synthetic iminoquinone anticancer compound BA-TPQ. *Curr. Cancer Drug Targets* 13, 651–660. doi: 10.2174/15680096113139990040

Cheng, X. R., Zhang, S. D., Wang, C. H., Ren, J., Qin, J. J., Tang, X., et al. (2013). Bioactive eudesmane and germacrane derivatives from Inula wissmanniana Hand.-Mazz. *Phytochemistry* 96, 214–222. doi: 10.1016/j.phytochem.2013.10.006

Cicenas, J., Kvederaviciute, K., Meskinyte, I., Meskinyte-Kausiliene, E., Skeberdyte, A., and Cicenas, J. (2017). KRAS, TP53, CDKN2A, SMAD4, BRCA1, and BRCA2 Mutations in Pancreatic Cancer. *Cancers (Basel)* 9, 42. doi: 10.3390/cancers9050042

Davison, E. K., and Brimble, M. A. (2019). Natural product derived privileged scaffolds in drug discovery. *Curr. Opin. Chem. Biol.* 52, 1–8. doi: 10.1016/j.cbpa.2018.12.007

Deng, X., Ruvolo, P., Carr, B., and May, W. S.Jr. (2000). Survival function of ERK1/2 as IL-3-activated, staurosporine-resistant Bcl2 kinases. *Proc. Natl. Acad. Sci. U. S. A* 97, 1578–1583. doi: 10.1073/pnas.97.4.1578

Deng, X., Gao, F., and May, W. S. (2009). Protein phosphatase 2A inactivates Bcl2's antiapoptotic function by dephosphorylation and up-regulation of Bcl2-p53 binding. *Blood* 113, 422–428. doi: 10.1182/blood-2008-06-165134

Dong, J., Qin, Z., Zhang, W. D., Cheng, G., Yehuda, A. G., Ashby, C. R.Jr., et al. (2020). Medicinal chemistry strategies to discover P-glycoprotein inhibitors: An update. *Drug Resist. Update* 49, 100681. doi: 10.1016/j.drup.2020.100681

Hartwig, W., Werner, J., Jager, D., Debus, J., and Buchler, M. W. (2013). Improvement of surgical results for pancreatic cancer. *Lancet Oncol.* 14, e476–e485. doi: 10.1016/S1470-2045(13)70172-4

Karandish, F., and Mallik, S. (2016). Biomarkers and Targeted Therapy in Pancreatic Cancer. *Biomark Cancer* 8, 27–35. doi: 10.4137/BIC.S34414

Kashyap, D., Tuli, H. S., Yerer, M. B., Sharma, A., Sak, K., Srivastava, S., et al. (2019). Natural product-based nanoformulations for cancer therapy: Opportunities and challenges. *Semin. Cancer Biol.* doi: 10.1016/j.semcancer.2019.08.014

Kleeff, J., Korc, M., Apte, M., La Vecchia, C., Johnson, C. D., Biankin, A. V., et al. (2016). Pancreatic cancer. *Nat. Rev. Dis. Primers* 2, 16022. doi: 10.1038/nrdp.2016.22

Kotecha, R., Takami, A., and Espinoza, J. L. (2016). Dietary phytochemicals and cancer chemoprevention: a review of the clinical evidence. *Oncotarget* 7, 52517–52529. doi: 10.18632/oncotarget.9593

Kuo, T. L., Cheng, K. H., Shan, Y. S., Chen, L. T., and Hung, W. C. (2019). beta-catenin-activated autocrine PDGF/Src signaling is a therapeutic target in pancreatic cancer. *Theranostics* 9, 324–336. doi: 10.7150/thno.28201

Lambert, A., Gavoille, C., and Conroy, T. (2017). Current status on the place of FOLFIRINOX in metastatic pancreatic cancer and future directions. *Therap. Adv. Gastroenterol.* 10, 631–645. doi: 10.1177/1756283X17713879

Leal, A. S., Williams, C. R., Royce, D. B., Pioli, P. A., Sporn, M. B., and Liby, K. T. (2017). Bromodomain inhibitors, JQ1 and I-BET 762, as potential therapies for pancreatic cancer. *Cancer Lett.* 394, 76–87. doi: 10.1016/j.canlet.2017.02.021

Li, X., Yang, X., Liu, Y., Gong, N., Yao, W., Chen, P., et al. (2013). Japonicone A suppresses growth of Burkitt lymphoma cells through its effect on NF-kappaB. *Clin. Cancer Res.* 19, 2917–2928. doi: 10.1158/1078-0432.CCR-12-3258

Mcbride, A., Bonafede, M., Cai, Q., Princic, N., Tran, O., Pelletier, C., et al. (2017). Comparison of treatment patterns and economic outcomes among metastatic pancreatic cancer patients initiated on nab-paclitaxel plus gemcitabine versus FOLFIRINOX. *Expert Rev. Clin. Pharmacol.* 10, 1153–1160. doi: 10.1080/17512433.2017.1365598

Mosquera, C., Maglic, D., and Zervos, E. E. (2016). Molecular targeted therapy for pancreatic adenocarcinoma: A review of completed and ongoing late phase clinical trials. *Cancer Genet.* 209, 567–581. doi: 10.1016/j.cancergen.2016.07.003

Nag, S. A., Qin, J. J., Wang, W., Wang, M. H., Wang, H., and Zhang, R. (2012). Ginsenosides as Anticancer Agents: In vitro and in vivo Activities, Structure-Activity Relationships, and Molecular Mechanisms of Action. *Front. Pharmacol.* 3, 25. doi: 10.3389/fphar.2012.00025

Nag, S., Qin, J., Srivenugopal, K. S., Wang, M., and Zhang, R. (2013). The MDM2-p53 pathway revisited. *J. BioMed. Res.* 27, 254–271. doi: 10.7555/JBR.27.20130030

Neoptolemos, J. P., Kleeff, J., Michl, P., Costello, E., Greenhalf, W., and Palmer, D. H. (2018). Therapeutic developments in pancreatic cancer: current and future perspectives. *Nat. Rev. Gastroenterol. Hepatol.* 15, 333–348. doi: 10.1038/s41575-018-0005-x

Nguyen, K. T., Kalyan, A., Beasley, H. S., Singhi, A. D., Sun, W., Zeh, H. J., et al. (2017). Gemcitabine/nab-paclitaxel as second-line therapy following FOLFIRINOX in metastatic/advanced pancreatic cancer-retrospective analysis of response. *J. Gastrointest Oncol.* 8, 556–565. doi: 10.21037/jgo.2017.01.23

Qi, S. M., Cheng, G., Cheng, X. D., Xu, Z., Xu, B., Zhang, W. D., et al. (2020). Targeting USP7-mediated deubiquitination of MDM2/MDMX-p53 pathway for cancer therapy: Are we there yet? *Front. Cell Dev. Biol.* 8, 233. doi: 10.3389/fcell.2020.00233

Qian, B., Nag, S. A., Su, Y., Voruganti, S., Qin, J. J., Zhang, R., et al. (2013). miRNAs in cancer prevention and treatment and as molecular targets for natural product anticancer agents. *Curr. Cancer Drug Targets* 13, 519–541. doi: 10.2174/15680096113139990031

Qie, S., and Diehl, J. A. (2016). Cyclin D1, cancer progression, and opportunities in cancer treatment. *J. Mol. Med. (Berl.)* 94, 1313–1326. doi: 10.1007/s00109-016-1475-3

Qin, J. J., Wang, W., Voruganti, S., Wang, H., Zhang, W. D., and Zhang, R. (2015). Identification of a new class of natural product MDM2 inhibitor: In vitro and in vivo anti-breast cancer activities and target validation. *Oncotarget* 6, 2623–2640. doi: 10.18632/oncotarget.3098

Qin, J. J., Sarkar, S., Voruganti, S., Agarwal, R., Wang, W., and Zhang, R. (2016a). Identification of linearifolianoid A as a novel dual NFAT1 and MDM2 inhibitor for human cancer therapy. *J. BioMed. Res.* 30, 322–333. doi: 10.7555/JBR.30.20160018

Qin, J. J., Wang, W., Sarkar, S., Voruganti, S., Agarwal, R., and Zhang, R. (2016b). Inulanolide A as a new dual inhibitor of NFAT1-MDM2 pathway for breast cancer therapy. *Oncotarget* 7, 32566–32578. doi: 10.18632/oncotarget.8873

Qin, J., Wang, W., and Zhang, R. (2017a). Novel natural product therapeutics targeting both inflammation and cancer. *Chin. J. Nat. Med.* 15, 401–416. doi: 10.1016/S1875-5364(17)30062-6

Qin, J. J., Li, X., Wang, W., Zi, X., and Zhang, R. (2017b). Targeting the NFAT1-MDM2-MDMX Network Inhibits the Proliferation and Invasion of Prostate Cancer Cells, Independent of p53 and Androgen. *Front. Pharmacol.* 8, 917. doi: 10.3389/fphar.2017.00917

Qin, J. J., Wang, W., Li, X., Deokar, H., Buolamwini, J. K., and Zhang, R. (2018). Inhibiting beta-Catenin by beta-Carboline-Type MDM2 Inhibitor for Pancreatic Cancer Therapy. *Front. Pharmacol.* 9, 5. doi: 10.3389/fphar.2018.00005

Qin, J. J., Cheng, X. D., Zhang, J., and Zhang, W. D. (2019). Dual roles and therapeutic potential of Keap1-Nrf2 pathway in pancreatic cancer: a systematic review. *Cell Commun. Signal* 17, 121. doi: 10.1186/s12964-019-0435-2

Rebelo, A., Molpeceres, J., Rijo, P., and Reis, C. P. (2017). Pancreatic Cancer Therapy Review: From Classic Therapeutic Agents to Modern Nanotechnologies. *Curr. Drug Metab.* 18, 346–359. doi: 10.2174/1389200218666170201151135

Robey, R. W., Pluchino, K. M., Hall, M. D., Fojo, A. T., Bates, S. E., and Gottesman, M. M. (2018). Revisiting the role of ABC transporters in multidrug-resistant cancer. *Nat. Rev. Cancer* 18, 452–464. doi: 10.1038/s41568-018-0005-8

Siegel, R. L., Miller, K. D., and Jemal, A. (2020). Cancer statistics 2020. *CA Cancer J. Clin.* 70, 7–30. doi: 10.3322/caac.21590

Strobel, O., Neoptolemos, J., Jager, D., and Buchler, M. W. (2019). Optimizing the outcomes of pancreatic cancer surgery. *Nat. Rev. Clin. Oncol.* 16, 11–26. doi: 10.1038/s41571-018-0112-1

Voruganti, S., Qin, J. J., Sarkar, S., Nag, S., Walbi, I. A., Wang, S., et al. (2015a). Oral nano-delivery of anticancer ginsenoside 25-OCH3-PPD, a natural inhibitor of the MDM2 oncogene: Nanoparticle preparation, characterization, in vitro and in vivo anti-prostate cancer activity, and mechanisms of action. *Oncotarget* 6, 21379–21394. doi: 10.18632/oncotarget.4091

Voruganti, S., Xu, F., Qin, J. J., Guo, Y., Sarkar, S., Gao, M., et al. (2015b). RYBP predicts survival of patients with non-small cell lung cancer and regulates tumor cell growth and the response to chemotherapy. *Cancer Lett.* 369, 386–395. doi: 10.1016/j.canlet.2015.09.003

Wang, W., Zhang, X., Qin, J. J., Voruganti, S., Nag, S. A., Wang, M. H., et al. (2012). Natural product ginsenoside 25-OCH3-PPD inhibits breast cancer growth and metastasis through down-regulating MDM2. *PloS One* 7, e41586. doi: 10.1371/journal.pone.0041586

Wang, G. W., Qin, J. J., Cheng, X. R., Shen, Y. H., Shan, L., Jin, H. Z., et al. (2014a). Inula sesquiterpenoids: structural diversity, cytotoxicity and anti-tumor activity. *Expert Opin. Invest. Drugs* 23, 317–345. doi: 10.1517/13543784.2014.868882

Wang, W., Qin, J. J., Voruganti, S., Wang, M. H., Sharma, H., Patil, S., et al. (2014b). Identification of a new class of MDM2 inhibitor that inhibits growth of orthotopic pancreatic tumors in mice. *Gastroenterology* 147, 893–902 e892. doi: 10.1053/j.gastro.2014.07.001

Wang, W., Liao, Y., Tang, C., Huang, X., Luo, Z., Chen, J., et al. (2017). Cytotoxic and Antibacterial Compounds from the Coral-Derived Fungus Aspergillus tritici SP2-8-1. *Mar. Drugs* 15, 348. doi: 10.3390/md15110348

Wang, W., Qin, J. J., Li, X., Tao, G., Wang, Q., Wu, X., et al. (2018a). Prevention of prostate cancer by natural product MDM2 inhibitor GS25: in vitro and in vivo activities and molecular mechanisms. *Carcinogenesis* 39, 1026–1036. doi: 10.1093/carcin/bgy063

Wang, W., Qin, J. J., Voruganti, S., Nijampatnam, B., Velu, S. E., Ruan, K. H., et al. (2018b). Discovery and Characterization of Dual Inhibitors of MDM2 and NFAT1 for Pancreatic Cancer Therapy. *Cancer Res.* 78, 5656–5667. doi: 10.1158/0008-5472.CAN-17-3939

Wang, W., Cheng, J. W., Qin, J. J., Hu, B., Li, X., Nijampatnam, B., et al. (2019a). MDM2-NFAT1 dual inhibitor, MA242: Effective against hepatocellular carcinoma, independent of p53. *Cancer Lett.* 459, 156–167. doi: 10.1016/j.canlet.2019.114429

Wang, W., Qin, J. J., Rajaei, M., Li, X., Yu, X., Hunt, C., et al. (2019b). Targeting MDM2 for novel molecular therapy: Beyond oncology. *Med. Res. Rev.* doi: 10.1002/med.21637

Wang, W., Yang, J., Liao, Y. Y., Cheng, G., Chen, J., Cheng, X. D., et al. (2020). Cytotoxic nitrogenated azaphilones from the deep-sea-derived fungus chaetomium globosum MP4-S01-7. *J. Nat. Prod.* 83. doi: 10.1021/acs.jnatprod.9b01165

Waters, A. M., and Der, C. J. (2018). KRAS: The Critical Driver and Therapeutic Target for Pancreatic Cancer. *Cold Spring Harb. Perspect. Med.* 8, a031435. doi: 10.1101/cshperspect.a031435

Werner, J., Combs, S. E., Springfeld, C., Hartwig, W., Hackert, T., and Buchler, M. W. (2013). Advanced-stage pancreatic cancer: therapy options. *Nat. Rev. Clin. Oncol.* 10, 323–333. doi: 10.1038/nrclinonc.2013.66

Xue, B., Wang, W., Qin, J. J., Nijampatnam, B., Murugesan, S., Kozlovskaya, V., et al. (2017). Highly efficient delivery of potent anticancer iminoquinone derivative by multilayer hydrogel cubes. *Acta Biomater.* 58, 386–398. doi: 10.1016/j.actbio.2017.06.004

Yao, W., Ba, Q., Li, X., Li, H., Zhang, S., Yuan, Y., et al. (2017). A Natural CCR2 Antagonist Relieves Tumor-associated Macrophage-mediated Immunosuppression to Produce a Therapeutic Effect for Liver Cancer. *EBioMedicine* 22, 58–67. doi: 10.1016/j.ebiom.2017.07.014

Conflict of Interest: The authors declare that the research was conducted in the absence of any commercial or financial relationships that could be construed as a potential conflict of interest.

frontiers in Pharmacology

ORIGINAL RESEARCH
published: 05 May 2020
doi: 10.3389/fphar.2020.00575

Bioluminescence Imaging-Based Assessment of the Anti-Triple-Negative Breast Cancer and NF-Kappa B Pathway Inhibition Activity of Britanin

Xinyi Xu[1†], Yingying Guo[1†], Getao Du[1], Huifang Liu[1], Lin Wang[2] and Dan Chen[1*]*

[1] Engineering Research Center of Molecular and Neuroimaging, Ministry of Education, School of Life Science and Technology, Xidian University, Xi'an, China, [2] School of Information Sciences and Technology, Northwest University, Xi'an, China

Britanin has been reported to have therapeutic effects on neurodegenerative and inflammation-based diseases. However, whether it is involved in the regulation of triple-negative breast cancer development has not been elucidated. In this study, we investigated the anti-tumor activity against triple-negative breast cancer tumor of Britanin by bioluminescence imaging *in vivo* using athymic (nu/nu) mice implanted with MDA-MB-231 and SUM-159 cells expressing a luciferase reporter gene, and explored the anti-tumor mechanism of Britanin. The results showed that Britanin treatment inhibited triple-negative breast cancer cell proliferation *in vivo,* and Cell Counting Kit-8 (IC_{50} values are 4.27 and 5.05 μM) and colony formation tests ($P < 0.001$) confirmed this result. Transwell assays were conducted to verify that Britanin treatment inhibited cell migration and invasion ($P < 0.001$). Apoptosis was determined by TdT-mediated dUTP nick-end labeling method. Western blot and qRT-PCR analysis showed that Britanin treatment caused a decrease in the member expression of NF-kappa B signaling pathway. Computational modeling showed that Britanin could directly bind to a p-65 core region composed of Cys38, Cys120, and Gln128 residues. The results showed that the inhibitory mechanisms of Britanin on cancer cells may be by ways of inhibiting the NF-kappa B pathway. In addition, bioluminescence imaging screening system is useful for accelerating the application of Britanin in the antitumor field, and provides a useful tool for evaluating the phytochemicals efficacy in inhibiting cancer cell proliferation in animal models.

Keywords: bioluminescence imaging, Britanin, triple-negative breast cancer, phytochemical, nuclear factor-kappa B pathway

OPEN ACCESS

Edited by:
Jinchao Feng,
Beijing University of Technology, China

Reviewed by:
Xiu-An Yang,
Chengde Medical College, China

Xiaopeng Ma,
Shandong University, China

****Correspondence:***
Lin Wang
wanglinmig@gmail.com
Dan Chen
dchen@xidian.edu.cn

[†]These authors have contributed equally to this work

Specialty section:
This article was submitted to Pharmacology of Anti-Cancer Drugs, a section of the journal Frontiers in Pharmacology

Received: *18 February 2020*
Accepted: *15 April 2020*
Published: *05 May 2020*

Citation:
Xu X, Guo Y, Du G, Liu H, Wang L and Chen D (2020) Bioluminescence Imaging-Based Assessment of the Anti-Triple-Negative Breast Cancer and NF-Kappa B Pathway Inhibition Activity of Britanin. Front. Pharmacol. 11:575. doi: 10.3389/fphar.2020.00575

INTRODUCTION

In 2018 approximately 2.1 million newly diagnosed female breast cancer cases accounted for almost one in four cancer cases among women (Bray et al., 2018). There are many therapeutic approaches to treat breast cancer including chemotherapy to inhibit the growth of cancer cells. Most of the current chemotherapeutic agents, including anthracyclines, hormone drugs, aromatase inhibitors, and biological drugs, are antimetabolites or target specific hormone receptors (Carels et al., 2016). Researchers have found that sequential single-drug chemotherapy has an indefinite effect on progression-free survival, while combined chemotherapy has an increased the efficacy of chemotherapy (Dear et al., 2013). Experiments results proved that the application of natural product-based agents in combination with chemotherapeutic drugs is a productive approach to the treatment of breast cancer (Israel et al., 2018). Phytochemicals, such as isoflavones (Shao et al., 1998), epigallocatechin gallate (Sen and Chatterjee, 2011), resveratrol (Gomez et al., 2013), curcumin (Cheng et al., 2001), lignans (Saarinen et al., 2007), and carotenoids (Dorjgochoo et al., 2009), have proven effective at inhibiting tumorigenesis, suppressing breast cancer cell growth, and even increasing the apoptosis of breast cancer cells. The above experiments have shown that combining chemotherapeutic agents with phytochemicals is a plausible novel strategy for treating breast cancer patients. Some works suggest that in 50% of tumors, the nuclear factor-kappa B (NF-κB) pathway is constitutively activated in a variety of cancer types, including breast cancer. It is very meaningful to develop a new anti-cancer drug for the NF-κB pathway. Britanin is a guaiacyl-type sesquiterpene lactone extracted from *Inula britannica*. Previous studies have shown that Britanin inhibits the NF-κB pathway by inhibiting the degradation of IκB-α, nuclear translocation of NF-κB, and NF-κB/DNA binding activity (Park et al., 2014).

The pharmacological activity of phytochemicals has mainly been studied by cell-level methods or histopathological methods *in vitro*, but the traditional methods mentioned above still have some limitations. First, the amount of animal samples that the experiment needed is huge, the statistical results of the data are complicated and the workload is great (Johnson et al., 2001). Second, histopathological sections provide quantitative information on the section, and the measurement of the volume of the tumor cannot achieve the accuracy of three-dimensional analyses (Dear et al., 2013). Third, as traditional methods are invasive, which cannot allow for continuous studies in a single animal and cannot provide important information on the optimal timing and dosing of drugs (Rudin and Weissleder, 2003). In order to find more effective tumor inhibition natural phytochemicals, a range of imaging techniques for discovering new drug have been used. Optical imaging techniques, such as fluorescence imaging and bioluminescence imaging (BLI), are inexpensive, which have high-throughput capabilities, do not require the steps of radionuclides labeling and enable semiquantitative analyses *via* the measurement of fluorescence intensity per unit area, have been used to monitor tumor tissue growth and metastasis. It is also used to monitor the release and diffusion of trace drugs *in vivo*. Jenkins et al. (2003) injected human prostate cancer cells expressing the luciferase gene into mice and used an *in vivo* bio-optical imaging system to monitor the recurrence and metastasis of prostate cancer cells after chemotherapy in real-time and *in vivo*. Due to the subcellular resolution of optical imaging systems, cellular heterogeneity within organs can be quantified and monitored in drug screens (Walsh et al., 2014). These studies have identified that optical imaging techniques have the potential to increase the efficiency of drug screening, assess the pharmacokinetics of new drugs, and evaluate drug effects *in vivo*.

In this paper, the BLI method was used to assess whether Britanin has anti-breast cancer activity *in vivo*. To investigate the mechanism of the anticancer action of this compound, CCK-8 method and colony forming test were used to evaluate the effect of Britanin on inhibiting tumor cell proliferation. The effects of Britanin on cell migration and invasion were estimated by Transwell assays. The effect of Britanin on tumor cell apoptosis was evaluated by the TdT-mediated dUTP nick-end labeling (TUNEL) method. And the western blot and qRT-PCR method were performed to detect the expression of the proteins of related signaling pathways. A molecular docking simulation was performed to identify whether Britanin could bind to the NF-κB pathway protein p-65 *via* possible covalent binding sites.

MATERIALS AND METHODS

Cell Lines and Reagents

Human breast cancer cells included MDA-MB-231 cells, MDA-MB-231 luc cells, SUM-159 cells, and SUM-159 luc cells (provided by Xi'an Medical University) were incubated at 37°C with 5% CO_2 in RPMI-1640 (GIBCO) supplemented with 10% fetal bovine serum (FBS, HyClone, Thermo Scientific), penicillin (100 IU/ml), and streptomycin (100 mg/ml). Cells were passaged three times a week. The Britanin working solutions (10 mM Britanin dissolved in DMSO) provided by Shanghai Jiaotong University were prepared by dilution of the stock solution in fresh culture medium on the day of use. Britanin, as a natural product, was purified by high-performance liquid chromatography and characterized by nuclear magnetic resonance (NMR) spectroscopy. The purity of Britanin was greater than 95% (**Figure S1**). A Cell Counting Kit-8 (Dojindo), Hoechst staining kit (Beyotime), TUNEL Apoptosis Detection kit (Beyotime), D-Luciferin potassium salt (Sciencelight), and antibodies (Abcam) were used in this study. Total RNA RNA extraction and CDNA synthesis used RNAiso Plus and the Reverse Transcription System (TaKaRa, Tokyo, Japan). Quantitative RT-PCR (qRT-PCR) analysis was performed in a 7300 Real-Time System (ABI, New York, America) using the SYBR Green RealMasterMix (TIANGEN, Beijing, China).

Cell Viability Assay

Measurements of cell viability at different drug concentrations were performed. MDA-MB-231 cells, MDA-MB-231 luc cells,

SUM-159 cells, and SUM-159 luc cells (1×10^4 cells/ml) were seeded in 96-well plates (100 µl) at 37°C overnight with 5% CO_2 and then incubated with various concentrations of Britanin (0.33, 1, 3, 9, 27, and 81 µM) at 37°C for 72 h. Four wells containing only complete medium were used as blank control group, and four wells containing tumor cells suspended in the complete medium which were used as control group. Thiazolyl blue tetrazolium bromide (0.5 mg/ml, 10 µl) was added to each well. After incubation for 4 h, using a Multiskan Ascent microplate photometer, the absorbance was measured at 492 nm wavelength. The control group cells were regarded as having a 100% survival rate. And the percentage of growth inhibition was calculated as cell growth inhibition (%) = (treated OD-blank OD)/(control OD-blank OD) × 100%. The concentration required for a 50% inhibition of viability (IC_{50}) was then determined.

Colony Formation Assay

MDA-MB-231 luc and SUM-159 luc cells (500 cells/well) were seeded in 12-well flat-bottomed plates and incubated for 24 h. Using the complete medium as the control group and different concentrations of Britanin as the experimental group, MDA-MB-231 luc cells and SUM-159 luc cells were tested. Cells were pretreated with different concentrations (2, 4, or 8 µM) of Britanin for 48 h. The treatment medium was replaced with normal growth medium and was replaced with normal growth medium every 3 d; After 2 weeks of incubation, formed colonies were fixed with 4% paraformaldehyde for 10 min, stained with 0.5% crystal violet for 10 min, washed again with PBS and photographed. The results were quantified with Adobe Photoshop Software.

Transwell Migration Assay

For the Transwell migration experiment, cells were seeded into the upper Matrigel filled chamber of a 24-well Transwell plate with 200 µl of serum-free medium. The MDA-MB-231 and SUM-159 cells density were adjusted to 2×10^5 cells/ml. Then, Britanin with different concentrations (2, 4, 6 µM) were added to the cells. Four wells containing the solution served as the control group. Simultaneously, 500 µl of 10% FBS-supplemented medium was added to the lower chamber. Cells were removed from the upper Matrigel chamber membrane using a cotton swab after 24 h of incubation and were attached to a glass slide, fixed with methanol and stained with Giemsa. Three fields per chamber were analyzed by light microscopy for migrated cell quantification. The experiment was repeated three times.

Animal Studies

All animal studies carried out in compliance with the Guide for the Care and Use of Laboratory Animal Resources and approved by the University of Xi'an Jiaotong Animal Care and Use Committee (number XY-AUC-2017-213). Two weeks after the implantation of cancer cells (5×10^6 cells/site), Britanin was intraperitoneally injected. Model mice were randomly divided into two or three groups (control group [0 mg/kg] and test group [5 mg/kg], or high dose group [10 mg/kg], low dose group [5 mg/kg] and control group [0 mg/kg]). Britanin dissolved in PBS. Mice were treated once every other day. The size of the tumor *in vivo* and the weight of mice were measured and compared with that of the xenograft tumors in mice of the placebo control. BLI was recorded during the experiment. D-luciferin (30 mg/ml^{-1}, 100 µl) was injected with the mice 10 min before BLI. The animals were then anesthetized with 2% isoflurane and 0.3 L/min of oxygen. The area of regions of interest (ROIs) image processing and analysis visualized using Live Image 4.5 software. To quantitative analysis, the ROIs of the tumor were evaluated with a white light image, and muscle regions of similar size (opposite positioning with the tumor) were selected as muscle ROI. The background value is subtracted from each of the luminescence images. The average of the fluorescence signal within each ROI is then calculated. Simultaneously, tumor volume was also calculated *in vitro* using calipers. After the mice were sacrificed, tumor volume was calculated with calipers, tumors and organs were fixed with 10% formalin solution.

Histological Analysis

The *in vivo* toxicity of Britanin was analyzed through H&E histological staining of the major organs. The tumors, liver, hearts and kidneys were embedded in tissue freezing medium, frozen to −80°C and then cut into slices with a thickness of approximately 8 µm. These cell tissue slices were then stained using DAPI and imaged using confocal laser scanning microscopy.

TdT-Mediated dUTP Nick End Labeling Assay

The paraffin-embedded tumor tissue sections were treated with fresh xylene and a gradient ethanol solution several times for dewaxing and rehydration at room temperature. The slides were incubated with protease K (20 µg/ml) in PBS for 30 min and then immersed in 4% paraformaldehyde for 5 min at room temperature. The slides were rinsed twice with PBS for 5 min per rinse. Then, the slides were equilibrated with 100 µl of equilibration buffer at room temperature for 5 min, and the slides were incubated with 100 µl of rTdT reaction mix per slide at 37°C in a humidified chamber for 1 h. Next, the slides were immersed in 2×SSC at room temperature for 15 min. Each slide was incubated with 100 µl of streptavidin HRP solution for 30 min and washed twice in PBS for 5 min per wash at room temperature. The slides were washed twice again with PBS for 5 min per wash at room temperature. At the last step, diaminobenzidine peroxidase substrate was added, and the slides were analyzed by light microscopy. The excised tumors were also stained with hematoxylin-eosin (H&E).

Western Blot and Quantitative RT-PCR Analysis

The cells were cultured at 0 and 5 mg Britanin for 24 h respectively. The cells were subsequently lysed using buffer with protease inhibitors. Total protein (30 µg) were separated by sodium dodecyl sulfate-polyacrylamide gel electrophoresis (10%) and transferred to polyvinylidenedifluoride membranes. Membranes were blocked with 5% fat-free milk/TBST and incubated with primary antibodies and secondary antibodies. Antibodies against

p-65, p150/p50, p-p65, and housekeeping gene, GAPDH were obtained from Abcam. Secondary antibodies were HRP-conjugated antibodies and visualized by a chemiluminescent reagent (The original data of Western Blot in **Data Sheet 1**).

The cells were cultured in 0 or 5 mg Britanin for 24 h respectively, homogenized and suspended with buffer for the RNA isolation and cDNA synthesis according to the manufacturer's instruction. The PCR parameters were same as manufacturer's instruction. Oligonucleotide primers for p-65, p-50, and GAPDH were as follows: oligonucleotide sequence of p-50 (217 bp), p50F: 5′-AGTAGCTGAGAGGCACATGG-3′, p50R: 5′-AGCGCACTCCAACCTTCTCA-3′, oligonucleotide sequence of p65 (256 bp), p65F: 5′-GCACTTACGGATTCTGGTGG-3′, p65R: 5′-GCACTTACGGATTCTGGTGG-3′, oligonucleotide sequence of GAPDH (252 bp), GAPDHF: 5′-CACTGGCATGGCCTTCCGTG-3′, GAPDHR: 5′-GAAATGAGCTTGACAAAGTG-3′. The quantification of each sample of cDNA was performed in triplicate, each PCR was replicated three times for verification, and the $2^{-\Delta\Delta CT}$ method was used to analyze the relative changes in gene expression from the qPCR experiments.

Molecular Docking Simulation Method

In this study, the monomer in the p-65 was used as the initial structure and receptor protein (PDB coded: 1IKN) (Huxford et al., 1998). Cys38 of p-65 was set as the center of the docking box, and the size of the box was set to 40 Å × 40 Å ×40 Å. Using the Tripos standard force field and Powell energy gradient method, the low energy stable conformation of the small molecule was obtained after 100 optimization iterations. All docking simulations were performed using AutoDock Vina software (Sanner, 1999).

Statistical Analysis

Data are presented as the mean values ± SD of independently repeated experiments, with values of $P < 0.05$ considered to represent a statistically significant difference between compared data.

RESULTS

Cell Viability Assay

As indicated in **Figure S2**, Britanin had apparent antigrowth activity in the four cell lines in a concentration-dependent manner. At a 9 μM Britanin treatment concentration, the cell survival rates of MDA-MB-231 luc cells, MDA-MB-231 cells, SUM 159 luc cells, and SUM 159 cells were approximately 8.9%, 9.0%, 16.4%, and 22.0% after 72 h. The half-maximal inhibitory concentrations (IC_{50}) of Britanin in MDA-MB-231 luc, MDA-MB-231, SUM 159 luc, and SUM 159 cell lines were 4.27, 4.41, 5.05, and 5.33 μM, respectively. Luc-labeled cells and non-Luc-labeled cells showed the same reactions to Britanin, so Luc-labeled cells were used in subsequent experiments.

The Antiproliferation Effect of Britanin

As shown in **Figure 1**, Britanin treatment significantly inhibited colony formation in two cell lines. The number of MDA-MB-231 luc and SUM-159 luc cell colonies decreased by more than 50% when cells were pretreated with 4 μM Britanin. Britanin pretreatment at 8 μM eliminated more than 90% of the colony formation in MDA-MB-231 luc cells and SUM-159 luc cells. The differences in numbers of cell colonies in the two groups were significant. Therefore, the results of the above test suggest that Britanin inhibits breast cancer cell proliferation in a dose-dependent manner *in vitro*.

Effect of Britanin on Migration and Invasion in Transwell Assays

As shown in **Figure 2**, the data revealed that Britanin treatment notably restrained MDA-MB-231 luc cell (48% inhibition at 2 μM, 83% inhibition at 4 μM) migration and markedly abated SUM-159 luc cell migration and invasion (41% inhibition at 2 μM, 80% inhibition at 4 μM). The differences in numbers of cell in the test group and control group were significant. Therefore,

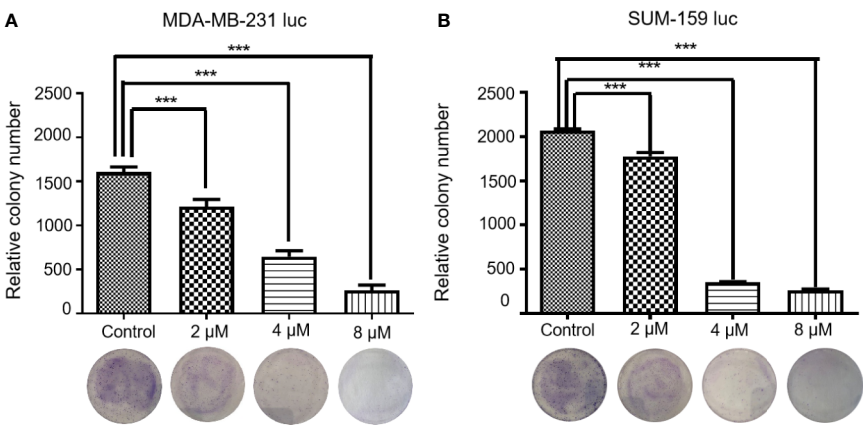

FIGURE 1 | Representative images of MDA-MB-231 luc cells **(A)** and SUM-159 luc cells **(B)** treated with Britanin (2, 4, and 8 μM) or complete medium as the control group for 48 h and were stained with crystal violet. Data are expressed as the mean ± S.D. of three independent experiments. ***P < 0.001 vs. untreated cells.

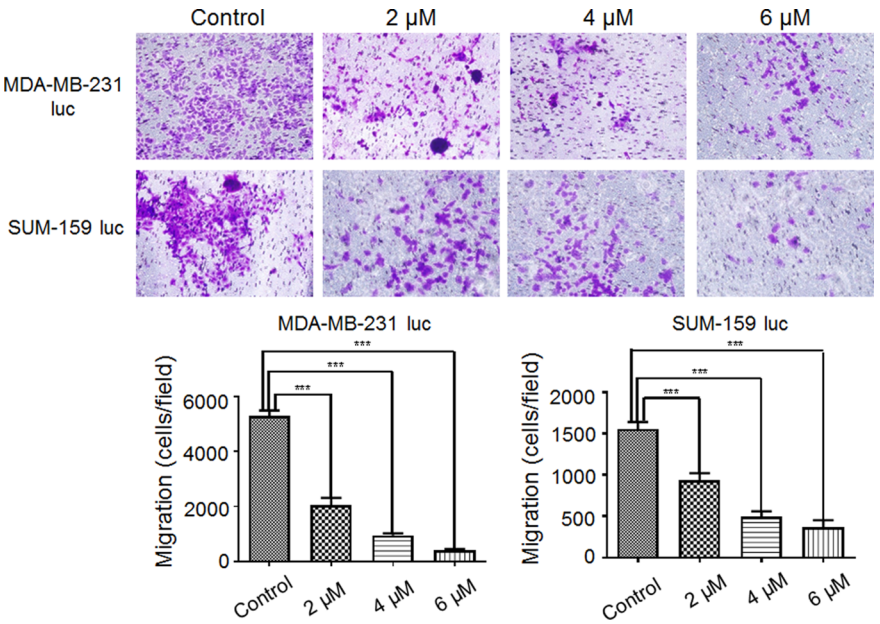

FIGURE 2 | Effect of Britanin on the migration of MDA-MB-231 luc cells and SUM-159 luc cells. Transwell chambers were used to detect the ability of cells to migrate (×100, magnification). Cells were treated with 0, 2, 4, or 6 μM Britanin for 24 h. The percent cell migration is shown. The error bars represent three independent experiments and each experiment was repeated three times. ***P < 0.001 vs. untreated cells.

these data support the hypothesis that Britanin inhibits the migration of breast cancer cells.

Britanin-Mediated Reduction of Tumor Growth *In Vivo*

The tumor tissues growth inhibition activity of Britanin on MDA-MB-231 luc cells transplanted in mice (n=6, two groups) was studied by BLI continuously *in vivo*. Initially, 1×10^5 cells were implanted into the bilateral legs of mice. At 2 weeks post-implantation, when the luminescence signal of cells reached 2×10^5 p/s/cm^2/sr, the mice were injected with Britanin once every 2 d or the placebo. By the 14th day post-treatment, the growth of the luminescence signal of MDA-MB-231 luc cells implanted in mice treated with Britanin (the average was 2.02×10^5 p/s/cm^2/sr, **Figure 3C**) was lower than that in mice of the placebo control group (2.27×10^5 p/s/cm^2/sr, **Figure 3A**). By the 27th day post-treatment, the growth of the luminescence signal of MDA-MB-231 luc cells implanted in mice treated with Britanin (2.81×10^5 p/s/cm^2/sr, **Figure 3D**) was significantly lower than that in mice of the placebo control group (5.31×10^5 p/s/cm^2/sr, **Figure 3B**). The mice in the Britanin treatment group lost an average of 5.8% in weight during the treatment (**Figure 3E**). Another experiment was carried out at the same time. On the 27 day post-treatment, using the calipers to calculate with the tumor volume, the average volume of the MDA-MB-231 luc xenograft tumors in athymic nu/nu mice treated with Britanin (843.2 ± 34.2 mm^3) was smaller than that of MDA-MB-231 luc tumors in the mice of the placebo control (1253.6 ± 48.0 mm^3, **Figure 3F**). The differences in volume of tumors in the test group and control group were significant. The resulting showed that an average increasing in tumor volume of test group approximately 5.2 times and an average increasing in tumor volume of test group approximately 8.0 times, relative to the baseline volume. At the end of the 27th day, the excised tumors were weighed after euthanasia, and the average tumor volume of the Britanin-treated group was decreased by 53% compared to that of the control group (**Figure 3G**). By the measurement of the micrometer caliper *in vitro*, the differences in volume of tumors in the test group and control group were significant.

We performed the same experiments with a mouse xenotransplant model of SUM-159 luc cells. The results showed that the *in vivo* bioluminescence signal of the test group tumor was significantly lower than that of the placebo control group and suggested that the growth rate of tumors was inhibited by Britanin (**Figure S3A**). The daily bioluminescence signals were plotted to show that the bioluminescence signals in the high-dose group increased slowly over time, while those in the placebo control group showed an increased growth trend from 13th day (**Figure S3B**). The mice in the Britanin treatment group gained weight normally and showed no signs of discomfort during the treatment (**Figure S3E**). The tumors in athymic nu/nu mice treated with Britanin were significantly smaller than those in the mice of the placebo control group ($P < 0.001$, **Figures S3D–F**).

Histology

After 27 d of continuous treatment, involving the intraperitoneal injection of Britanin (5 mg/kg) into BALB/c mice xenotransplant model of SUM-159 luc cells or MDA-MB-231 luc cells, the major organs (heart, liver, and kidneys) were harvested for

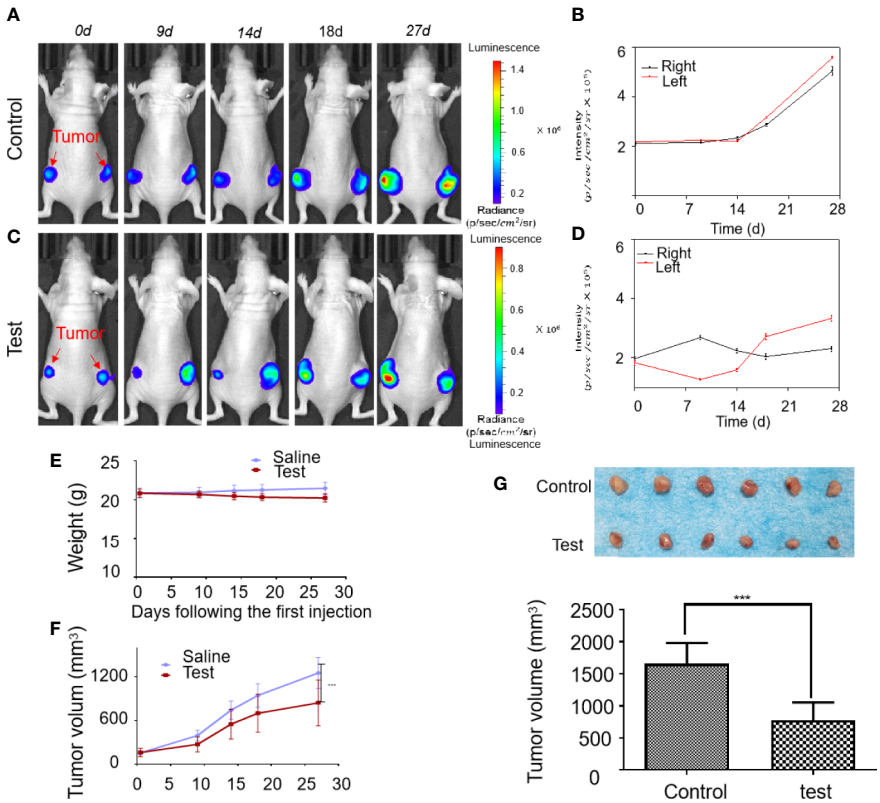

FIGURE 3 | The activity evaluation of Britanin on breast cancer model mouse *in vivo*. **(A)** Representative bioluminescence images in an untreated control group of MDA-MB-231 luc inoculated mice tumor model. **(B)** Quantification of bioluminescence intensity by ROIs that encompass the tumor. Data represent as the means ± S.D. **(C)** Representative bioluminescence images recorded before and after injection Britanin of 5 mg/kg every 2 d for 27 d by intraperitoneal injection in MDA-MB-231 luc inoculated mice tumor models as the test group. **(D)** Quantification of the tumor bioluminescence ROIs. Data represent as the means ± S.D. **(E)** The mouse was weighed before and after Britanin injections, and there was no significant difference with an untreated control group. **(F)** Tumor volume was calculated before and after Britanin injections. **(G)** Photograph of excised tumors from the control, test treatment group. The graph represents the average volume of the tumor. ***P < 0.001.

histopathological analysis. No noticeable tissue or cellular damage was observed in the H&E-stained organ slices from Britanin-treated mice compared to those from nude mice treated with saline as control, except for some binuclear nucleolar cells in the liver (**Figure 4**).

TUNEL Assay, Immunohistochemical, and qRT-PCR Results

Five mg/kg of Britanin was injected into the tail veins of BALB/c mice in the low dose test group, 10 mg/kg of Britanin was injected into the mice in the high dose test group, and an equal volume of saline was injected into the tail veins of mice in the control group. Then, the tumor tissue was harvested for histopathological analysis after 72 h (**Figures 5A, D**). The TUNEL experiment results showed that Britanin treatment induced apoptosis in human breast cancer cells, and apoptosis was induced to a greater extent in the MDA-MB-231 cells than the SUM-159 cells (**Figures 5B–F**). The number of apoptotic cells tumors in athymic nu/nu mice treated with Britanin were significantly more than those in the mice of the placebo control group ($P < 0.001$). Furthermore, we used western blot and qRT-PCR to determine the effect of Britanin on the p-65, p105/p-50, and p-p65 in MDA-MB-231 luc cells and SUM-159 luc cells treated for 24 h. The p-50 protein expression concentrations decreased 24 h after the Britanin interventions when compared to non-treated group values (18.2% in MDA-MB-231 luc cells; 40.7% in SUM 159 luc cells, **Figures 6A, B**), although p-50 mRNA concentration levels increased 86.3% in MDA-MB-231 luc cells and 90.7% in SUM 159 luc cells by qRT-PCR analysis (**Figures 6C, D**). The p-p-50 protein expression levels decreased 24 h after the Britanin interventions when compared to non-treated group values (32.6% in MDA-MB-231 luc cells, 16.5% in SUM 159 luc cells) (**Figures 6A, B**). No significant differences in p-65 protein expression were observed after the Britanin intervention by western blot analyses (**Figures 6A, B**), although p-65 mRNA concentration levels increased 11.9% in MDA-MB-231 luc cells and 16.5% in SUM 159 luc cells by qRT-PCR analysis (**Figure 6C**).

Molecular Docking for Binding Mode Prediction

Britanin docked into the binding pocket of p-65 (PDB coded: 1IKN), and the optimal energy conformation was selected by

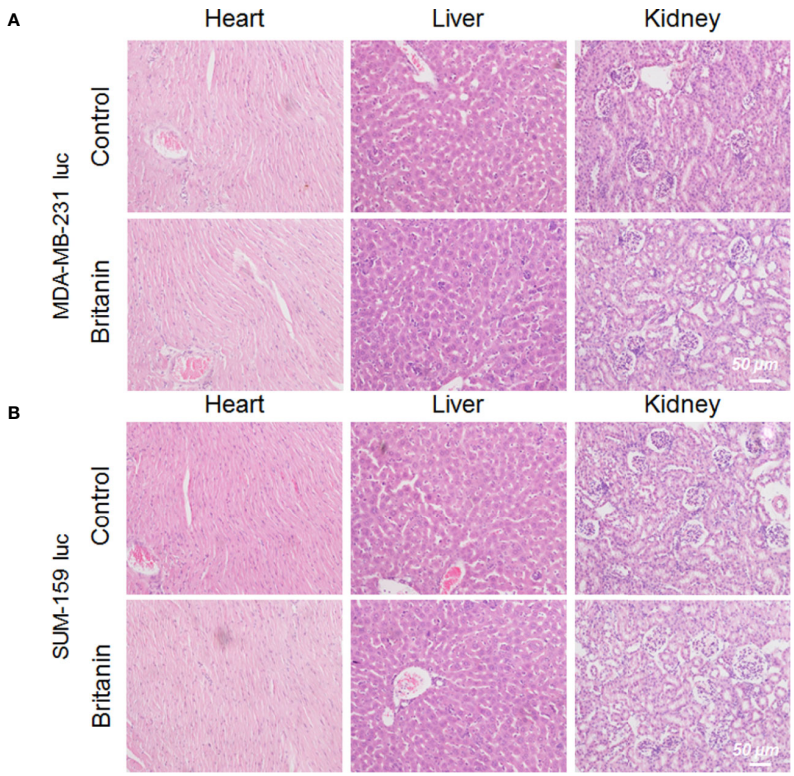

FIGURE 4 | Histological analysis of organs from mice in the control group and Britanin treatment group. **(A)** Histological analysis of major organs (including heart, liver and kidneys) from mice xenotransplant model of MDA-MB-231 luc cells in the control group (with saline as control) and Britanin treatment (5 mg/kg) group. **(B)** Histological analysis of major organs (including heart, liver and kidneys) from mice xenotransplant model of SUM-159 luc cells in the control group (with saline as control) and Britanin treatment (5 mg/kg) group.

analyzing the results of 100 docking iterations. Ligands enter the target protein active sites mainly through hydrophobic and van der Waals chemical forces and interact with amino acid residues, including Lys37, Cys38, Gln89, Gln119, Cys120, Val121, Lys122, Asp125, Gln128, and Ala129. The docking energy is −6.07, and the binding activity of the ligand to the target protein is noncovalent. Oxygen atoms in the five-membered ring of the ligand form hydrogen bonds with Gln128, and the hydrogen bond length is 3.1 Å. The formation of hydrogen bonds is beneficial to small molecule-targeting proteins, thus inhibiting p-65 activity (**Figure 7**).

DISCUSSION

Triple-negative breast cancer (TNBC) is defined as a subtype of breast cancer and has the features of aggressive behavior, poor prognosis and no standard chemotherapy protocols. A comparison of TNBC with normal breast tissue showed substantial changes in the NF-κB signaling pathway that controls angiogenesis and tumorigenesis. Thus, NF-κB p-65 is a common and effective therapeutic drug target. Many plant-derived compounds inhibit the NF-κB pathway in breast cancer, such as triptolide parthenolide, hirsutine, and andrographolide. Britanin is a guaiacyl-type sesquiterpene lactone and an inhibitor of the NF-κB pathway that controls inflammatory responses. Therefore, we evaluated the anti-TNBC activity of Britanin using athymic nu/nu mice implanted with MDA-MB-231 luc and SUM-159 luc cells expressing a luciferase reporter gene *in vivo* by BLI and by measurement of tumor size *in vitro*. The results obtained from the BLI and measurement of the size of the tumors showed that Britanin inhibited the proliferation of tumor cells. Furthermore, the tumors in athymic nu/nu mice treated with Britanin were smaller than those in the mice treated with the placebo control. Thus, Britanin inhibited the proliferation of tumor cells effectively. Then, the mechanism of the anti-tumor activity of Britanin was studied by colony formation, Transwell migration. Britanin inhibited the proliferation of tumor cells. By western blot and qRT-PCR analysis, Britanin treatment inhibited the NF-κB pathway and reduced the metastatic and proliferative potential of TNBC cells. The anticancer mechanism was analyzed. The molecular docking results revealed that Britanin could covalently bind to the p-65 protein. These results of this study strongly support the investigation of Britanin as a promising new natural anticancer phytochemical for the treatment of TNBC refractory to currently available anticancer drugs.

In our study, the MDA-MB-231 cells derived from the pleural effusions of a Caucasian breast cancer patient and SUM-159 cells derived from a noninflammatory metaplastic patient selected for

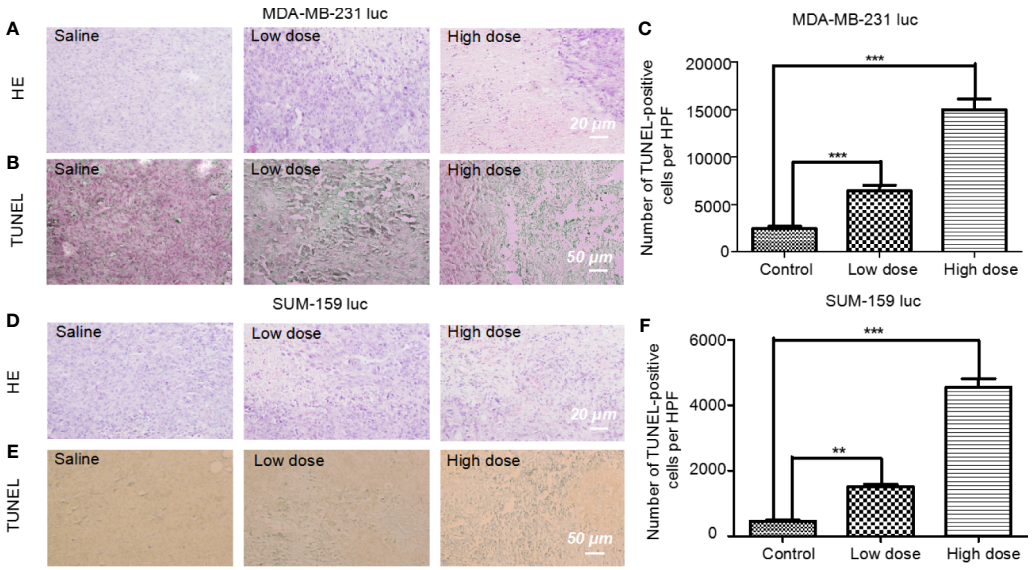

FIGURE 5 | Pathological analysis of tumor tissue treated with or without Britanin using H&E staining and apoptosis assay with the TUNEL stain. **(A)** Histological analysis of tumor tissue from mice xenotransplant model of MDA-MB-231 luc cells in the control group, low dose (5 mg/kg), and high dose (10 mg/kg) Britanin treatment group. **(B)** TUNEL assay on the tissue-sample sections from mice xenotransplant model of MDA-MB-231 luc cells, where the apoptotic cells are stained brown. **(C)** TUNEL assay on the tissue-sample from mice xenotransplant model of SUM-159 luc cells in the control group, low dose (5 mg/kg), and high dose (10 mg/kg) Britanin treatment group. The graph represents the number of apoptotic cells on a high-power field (n = 6), data represent as the means ± S.D., ***P < 0.001. **(D)** Histological analysis of tumor tissue from mice xenotransplant model of SUM-159 luc cells in the control group, low dose (5 mg/kg), and high dose (10 mg/kg) Britanin treatment group. **(E)** TUNEL assay on the tissue-sample sections from mice xenotransplant model of SUM-159 luc cells, where the apoptotic cells are stained brown. **(F)** TUNEL assay on the tissue-sample from mice xenotransplant model of SUM-159 luc cells in the control group, low dose (5 mg/kg), and high dose (10 mg/kg) Britanin treatment group. The graph represents the number of apoptotic cells on a high-power field (n = 6), data represent as the means ± S.D., **p < 0.01, ***p < 0.001.

this screen were used to elucidate whether Britanin inhibits cell growth. In the *in vivo* BLI process, the luciferase report gene was transfected and used to label both of the above cell types. Cell lines stably expressing luciferase were established. The BLI *in vivo* results showed that there were no cell-specific effects by this method. The luminescence intensities of ROIs after treatment with Britanin were examined from the bioluminescence images continuously. And the trend in these results were similar with the trend in the tumor volume growth values. The experimental results show that there is a difference between tumor volume measured *in vivo* and tumor volume dissected. Because the tumor sizes of the experimental group and control group are different, their accurate measurement may be easily influenced by subjective factors. It is worth noting that by the traditional method the difference in tumor size between the test group and control group of mice was not evident on the 9th day and could not be observed until after the 14th day. However, from the first observation point (4th day or 9th day), the ROI value of the experimental group increased less than that of the control group. Meanwhile, real-time monitoring of BLI adds information to the effects of different Britanin concentrations and enables consecutive observation. Noninvasive examination *in vivo* combined with conventional and classical methods. The metabolically active cells in the BLI response, especially in small tumors, can be accurately detected, avoiding the impact of factors such as peritumoral edema for the traditional tumor volume measurement. Thus, Bioluminescence assays are more sensitive than traditional methods for detecting tumor size *in vivo* and *vitro*.

The TUNEL analysis revealed that compared to the control treatment, Britanin treatment markedly induced apoptosis in MDA-MB-231 and SUM-159 cells. The results herein indicate that Britanin markedly inhibits cell proliferation in MDA-MB-231 and SUM-159 human TNCB cancer cells in a dose- and time-dependent manner. The western blot and qRT-PCR analysis results showed that the expression of p-p65 of the test group cells was lower than that of the control group, and the total expression of p-65 has no difference between the test group and the control group. And NF-κB p-65 and p-50 mRNA levels had less than 10% increase. NF-κB is a dimeric form of transcription factor family ubiquitous in eukaryotes. In the cytoplasm, the NF-κB subunits p-65 and p-50 exist as heterodimers and form a complex with its inhibitory protein IκB. This complex in the cytoplasm covered the nuclear localization signal of the p-65, so the complex was in an inactive state. The p-65 was phosphorylated to exert its transcriptional effect. In addition, Britanin contains sesquiterpenoid lactones with α-methylene-γ-butyrolactone moiety. The binding mode prediction is that Michael-type thiols bind to cysteine sulfhydryl groups of p-65.

In conclusion, the results of the present study show a novel use of Britanin in mitigating human TNBC proliferation and

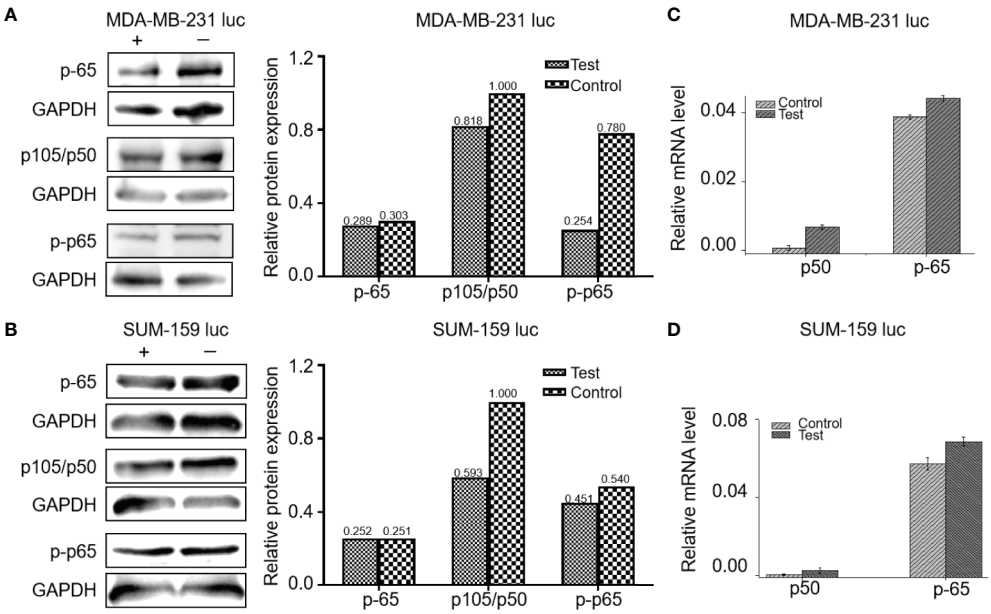

FIGURE 6 | Britanin regulates the proteins levels of NF-κB p-65, p105/50, p-p-65, and regulates the mRNA levels of NF-κB p-65, p105/50 from cells treated with or without Britanin for 24 h. **(A)** Western blots of proteins extracted from MDA-MB-231 luc cells treated with or without Britanin with the indicated antibodies: NF-κB p-65, p105/50 and p-p-65, GAPDH was used as a control. The data of relative protein expression of NF-κB pathway presented in bar charts. **(B)** Western blots of proteins extracted from SUM-159 luc cells treated with or without Britanin with the indicated antibodies: NF-κB p-65, p105/50, p-p-65, GAPDH was used as a control. The data of relative protein expression of NF-κB pathway presented in bar charts. **(C)** Relative mRNA concentrations of NF-κB p-65, p105/50 in MDA-MB-231 luc cells. Data represent as the means ± S.D. of three independent experiments (n=3). **(D)** Relative mRNA concentrations of NF-κB p-65, p105/50 in SUM-159 luc cells. Data represent as the means ± S.D. of three independent experiments (n=3).

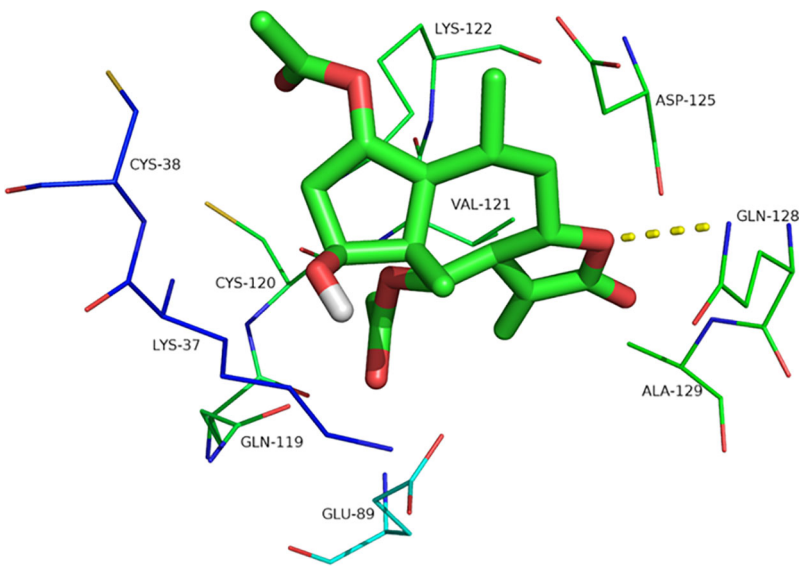

FIGURE 7 | The interaction site of Britanin with p-65 by docking simulations. The p-65 is represented in the stick model and compound Britanin is drawn in green bold stick model.

inducing apoptosis *via* the inhibition of the NF-κB pathways. Another conclusion is that this bioluminescence evaluation method allows the simultaneous visualization of changes in tumor volume and could be applied to new types of drug screening, discovery, and development.

DATA AVAILABILITY STATEMENT

The raw data supporting the conclusions of this article will be made available by the authors, without undue reservation, to any qualified researcher.

ETHICS STATEMENT

All animal studies carried out in compliance with the Guide for the Care and Use of Laboratory Animal Resources and approved by the University of Xi'an Jiaotong Animal Care and Use Committee (number XY-AUC-2017-213).

AUTHOR CONTRIBUTIONS

XX carried out biological experiments. YG carried out animal experiments. GD and HL analyzed data and review the manuscript. LW and DC wrote the paper and led the research.

FUNDING

This work was supported, in part, by the National Key R&D Program of China under Grant No. 2018YFC0910600 and the Natural Science Basic Research Plan in Shaanxi Province of China under Grant No. 2019JQ-519 and 2018JM7072.

SUPPLEMENTARY MATERIAL

The Supplementary Material for this article can be found online at: https://www.frontiersin.org/articles/10.3389/fphar.2020.00575/full#supplementary-material.

REFERENCES

Bray, F., Ferlay, J., Soerjomataram, I., Siegel, R. L., Torre, L. A., and Jemal, A. (2018). Global cancer statistics 2018: GLOBOCAN estimates of incidence and mortality worldwide for 36 cancers in 185 countries. *CA Cancer J. Clin.* 68 (6), 394–424. doi: 10.3322/caac.21492

Carels, N., Spinasse, L. B., Tilli, T. M., and Tuszynski, J. A. (2016). Toward precision medicine of breast cancer. *Theor. Biol. Med. Model* 13, 7. doi: 10.1186/s12976-016-0035-4

Cheng, A. L., Hsu, C. H., Lin, J. K., Hsu, M. M., Ho, Y. F., Shen, T. S., et al. (2001). Phase I clinical trial of curcumin, a chemopreventive agent, in patients with high-risk or pre-malignant lesions. *Anticancer Res.* 21 (4B), 2895–2900. doi: 10.1110/ps.0212902

Dear, R. F., McGeechan, K., Jenkins, M. C., Barratt, A., Tattersall, M. H., and Wilcken, N. (2013). Combination versus sequential single agent chemotherapy for metastatic breast cancer. *Cochrane Database Syst. Rev.* 18 (12), CD008792. doi: 10.1002/14651858.CD008792.pub2

Dorjgochoo, T., Gao, Y. T., Chow, W. H., Shu, X. O., Li, H., Yang, G., et al. (2009). Plasma carotenoids, tocopherols, retinol and breast cancer risk: results from the Shanghai Women Health Study (SWHS). *Breast Cancer Res. Treat* 117 (2), 381–389. doi: 10.1007/s10549-008-0270-4

Gomez, L. S., Zancan, P., Marcondes, M. C., Ramos-Santos, L., Meyer-Fernandes, J. R., Sola-Penna, M., et al. (2013). Resveratrol decreases breast cancer cell viability and glucose metabolism by inhibiting 6-phosphofructo-1-kinase. *Biochimie* 95 (6), 1336–1343. doi: 10.1016/j.biochi.2013.02.013

Huxford, T., Huang, D. B., Malek, S., and Ghosh, G. (1998). The crystal structure of the IkappaBalpha/NF-kappaB complex reveals mechanisms of NF-kappaB inactivation. *Cell* 95 (6), 759–770. doi: 10.1016/s0092-8674(00)81699-2

Israel, B. B., Tilghman, S. L., Parker-Lemieux, K., and Payton-Stewart, F. (2018). Phytochemicals: current strategies for treating breast cancer. *Oncol. Lett.* 15 (5), 7471–7478. doi: 10.3892/ol.2018.8304

Jenkins, D. E., Yu, S. F., Hornig, Y. S., Purchio, T., and Contag, P. R. (2003). *In vivo* monitoring of tumor relapse and metastasis using bioluminescent PC-3M-luc-C6 cells in murine models of human prostate cancer. *Clin. Exp. Metastasis* 20 (8), 745–756. doi: 10.1023/B:Clin.0000006817.25962.87

Johnson, J. I., Decker, S., Zaharevitz, D., Rubinstein, L. V., Venditti, J., Schepartz, S., et al. (2001). Relationships between drug activity in NCI preclinical *in vitro* and *in vivo* models and early clinical trials. *Br. J. Cancer* 84 (10), 1424–1431. doi: 10.1054/bjoc.2001.1796

Park, H. H., Kim, S. G., Park, Y. N., Lee, J., Lee, Y. J., Park, N. Y., et al. (2014). Suppressive effects of britanin, a sesquiterpene compound isolated from Inulae flos, on mast cell-mediated inflammatory responses. *Am. J. Chin Med.* 42 (4), 935–947. doi: 10.1142/S0192415X14500591

Rudin, M., and Weissleder, R. (2003). Molecular imaging in drug discovery and development. *Nat. Rev. Drug Discovery* 2 (2), 123–131. doi: 10.1038/nrd1007

Saarinen, N. M., Warri, A., Airio, M., Smeds, A., and Makela, S. (2007). Role of dietary lignans in the reduction of breast cancer risk. *Mol. Nutr. Food Res.* 51 (7), 857–866. doi: 10.1002/mnfr.200600240

Sanner, M. F. (1999). Python: a programming language for software integration and development. *J. Mol. Graphics Model.* 17 (1), 57–61. doi: 10.1016/S1093-3263(99)00019-4

Sen, T., and Chatterjee, A. (2011). Epigallocatechin-3-gallate (EGCG) downregulates EGF-induced MMP-9 in breast cancer cells: involvement of integrin receptor alpha5beta1 in the process. *Eur. J. Nutr.* 50 (6), 465–478. doi: 10.1007/s00394-010-0158-z

Shao, Z. M., Wu, J., Shen, Z. Z., and Barsky, S. H. (1998). Genistein exerts multiple suppressive effects on human breast carcinoma cells. *Cancer Res.* 58 (21), 4851–4857.

Walsh, A. J., Cook, R. S., Sanders, M. E., Aurisicchio, L., Ciliberto, G., Arteaga, C. L., et al. (2014). Quantitative optical imaging of primary tumor organoid metabolism predicts drug response in breast cancer. *Cancer Res.* 74 (18), 5184–5194. doi: 10.1158/0008-5472.Can-14-0663

Conflict of Interest: The authors declare that the research was conducted in the absence of any commercial or financial relationships that could be construed as a potential conflict of interest.

frontiers in Oncology

ORIGINAL RESEARCH
published: 05 May 2020
doi: 10.3389/fonc.2020.00622

Construction of Biocompatible Dual-Drug Loaded Complicated Nanoparticles for *in vivo* Improvement of Synergistic Chemotherapy in Esophageal Cancer

Wenhua Zhan[1,2†], *Hanrui Li*[3†], *Yingying Guo*[3], *Getao Du*[3], *Yayan Wu*[1] *and Dexin Zhang*[4*]

[1] *Key Laboratory of Biomedical Information Engineering of Education Ministry, School of Life Science and Technology, Xi'an Jiaotong University, Xi'an, China,* [2] *Department of Radiation Oncology, General Hospital of Ningxia Medical University, Yinchuan, China,* [3] *Engineering Research Center of Molecular & Neuro Imaging of the Ministry of Education, School of Life Science and Technology, Xidian University, Xi'an, China,* [4] *Department of Respiratory Medicine, Second Affiliated Hospital of Medical College, Xi'an Jiaotong University, Xi'an, China*

OPEN ACCESS

Edited by:
Jinchao Feng,
Beijing University of Technology, China

Reviewed by:
Haiming Luo,
Huazhong University of Science and Technology, China
Sixiang Shi,
University of Texas MD Anderson Cancer Center, United States

***Correspondence:**
Dexin Zhang
dexin1994@mail.xjtu.edu.cn

†These authors have contributed equally to this work

Specialty section:
This article was submitted to Pharmacology of Anti-Cancer Drugs, a section of the journal Frontiers in Oncology

Received: *06 March 2020*
Accepted: *03 April 2020*
Published: *05 May 2020*

Citation:
Zhan W, Li H, Guo Y, Du G, Wu Y and Zhang D (2020) Construction of Biocompatible Dual-Drug Loaded Complicated Nanoparticles for in vivo Improvement of Synergistic Chemotherapy in Esophageal Cancer. Front. Oncol. 10:622. doi: 10.3389/fonc.2020.00622

Combination chemotherapy is a routine treatment for esophageal cancer, but some shortcomings, such as drug toxicity and side effects, greatly limit the clinical application of combination therapy. To overcome these shortcomings, we have developed a mesoporous silica nanoparticle system that was used to load doxorubicin and β-elemene. β-elemene was encapsulated in the pore of mesoporous silica nanoparticle and doxorubicin was electrostatically adsorbed on the surface of mesoporous silica nanoparticle by hyaluronic acid to construct dual drugs synergistic nanoparticles (bMED NPs, ~77.15 nm). *In vitro* studies demonstrated that bMED NPs had a good treatment effect in esophageal cancer cell lines. *In vivo* fluorescence imaging results demonstrated that bMED NPs could accumulate in tumor sites and achieve *in vivo* long-term circulation and continuous drug release. In addition, bMED NPs exhibited significant antitumor effects in the esophageal cancer mouse model, which may provide a great platform for esophageal cancer chemotherapy.

Keywords: esophageal cancer, combination chemotherapy, doxorubicin, β-elemene, mesoporous silica nanoparticles

INTRODUCTION

Esophageal cancer is the sixth leading cause of cancer deaths in the world (1). The incidence is higher in East Asia, southeastern Africa and northwestern Europe. In China, esophageal cancer is also one of the four major cancers (2). Most cases of esophageal cancer are diagnosed at an advanced stage and the 5-year survival rate is very poor (3). Surgery has a certain therapeutic effect in the clinic, however, surgery-caused damage is irreversible, and the patient quality of life is greatly reduced. Meanwhile, surgery may be followed by cancer recurrence and tumor metastasis (4, 5). Combination chemotherapy is a common method for the treatment of esophageal cancer and when compared with single drug treatment, this approach has an obvious superiority (6).

By using several drugs, the possibility of a significant increase in single drug toxicity caused by drug overdosing can be avoided (7, 8). In addition, the long-term and repeated use of the same drug is one of the factors that lead to tumor resistance. Combination chemotherapy can prevent resistance factors, thereby reducing the possibility of cancer resistance (9).

The choice of drugs is critical for combination chemotherapy. In previous studies, many chemotherapeutic drugs were used in esophageal cancer therapy. Among them, cetuximab is one of the FDA-approved chemotherapeutic drugs that has a certain therapeutic effect on esophageal cancer (10). However, in previous reports, cetuximab has a marked increase of toxicity on 75 years of age or older patients and in 2011, DMC and NCI approved an amendment to limit cetuximab treatment to the under 75 years of age (11). Doxorubicin (DOX) is a commonly used chemotherapy drug for cancer (12, 13) and DOX is also widely used in the treatment of esophageal cancer (14, 15). However, DOX has an inevitable cardiotoxicity and severe side effects, resulting in a poor prognosis (16). There are many studies on the combination of DOX and other anticancer drugs for esophageal cancer that aim at improving the antitumor effect (17, 18). However, due to the differences in the metabolic timing, pathways and patterns of the two drugs, it was difficult to determine the optimal dose and ratio of the drug to exert optimal therapeutic effects at the tumor sites. Therefore, the drugs optimal ratio is critical for combination chemotherapy, and a more effective combination is essential. β-elemene is a natural drug that was shown to exert antitumor effects in a variety of tumors (19–23). It is mainly used as an adjuvant in cancer treatment to improve the efficacy of chemotherapy, reduce its toxicity and prevent drug resistance (24). In previous studies, it has been shown that DOX and β-elemene can be used in combination therapy for tumors (25). In addition, previous studies showed that the insertion of DOX into duplex DNA is the main reason for its anti-cancer activity through the inhibition of DNA replication (26), while, β-elemene may exert its antitumor effect by mediating via a mitochondrial cytochrome c release-dependent apoptotic pathway and downregulating the expression of Bcl-2 (27). Therefore, DOX and β-elemene may be able to cause apoptosis through different signaling pathways, which is of great significance for tumor combination chemotherapy.

Our previous studies demonstrated that DOX and β-elemene had synergistic effects. However, the physical and chemical properties of DOX and β-elemene are different, with *in vivo* differences in pharmacokinetics, which lead to decreased in accumulation, in an optimal ratio and with a certain concentration *in vivo*. Nanocarriers can load two or more chemotherapeutic drugs in an optimal ratio and achieve better therapeutic effects. In previous studies, a variety of nanocarriers have been reported as an option for combination therapy, such as micelle (28), nanoparticle (29, 30) and vesicular nanocarriers (31). Among these, the mesoporous silica nanoparticle has a large specific surface area and pore size, low toxicity and a surface which can be easily modified for common use as a nanocarrier (32).

To study the combination therapeutic effects of β-elemene and DOX on tumors, we synthesized biodegradable mesoporous silica nanoparticles (bMSN NPs) as nanocarrier for the dual-drug combination therapy and according to the previously described method (33). β-elemene is adsorbed in bMSN pores and the DOX surface is covered with hyaluronic acid (HA) using electrostatic adsorption. Both β-elemene and DOX are loaded on the bMSN NPs in an optimal ratio (bMED NPs) to improve the efficacy of the dual-drug nanoparticles. The bMED NPs based on the combination chemotherapy effects of β-elemene and DOX, can enhance their pharmacokinetic characteristics and promote their passive targeting via enhanced permeability and retention (EPR) effects, thereby, reducing their toxicity. The bMED NPs have been proven to have low toxicity, good biocompatibility and good targeting capabilities through a series of *in vitro* experiments. Furthermore, to verify the antitumor effect of bMED NPs *in vivo*, a subcutaneous tumor model of esophageal cancer was established, and the mice body weight and tumors size were monitored for 22 days. The results indicated that the synthesized bMED NPs exert excellent antitumor effects *in vitro* and *in vivo* and provide a novel drug choice for the treatment of esophageal cancer.

MATERIALS AND METHODS

Materials

β-elemene were purchased from Sigma. DOX (98%), HA, hyaluronidase (HAase), coumarin 6, crystal violet, Giemsa stain, 4′,6-diamidino-2-phenylindole (DAPI), propidium iodide (PI), annexin V-100 and triton X-100 were purchased from Aladdin (Shanghai, China). IR780 iodide (95%) were purchased from Sigma-Aldrich. Fetal Bovine Serum (FBS) was purchased from Biological Industries (Israel). Dulbecco's modified eagle medium (DMEM) was purchased from Hyclone. Cell Counting Kit-8 (CCK-8) was purchased from Dojindo (Shanghai, China). Terminal deoxynucleotidyl transferase-mediated dUTP-biotin nick-end labeling (TUNEL) Apoptosis Detection Kit were purchased from Beyotime (Shanghai, China). The primary anti-Bcl-2, anti β-actin and anti-Bax antibody were purchased from Abcam (Shanghai, China). Goat anti-rabbit IgG (H+L), HRP-conjugated was purchased from Beijing TDY Biotech (Beijing, China).

Cell Lines and Esophageal Cancer Animal Model

Three esophageal cancer cells lines (K510, K30, K150) were provided by Procell Life Science & Technology Co., Ltd. (Wuhan, China). All cells lines were cultured in 10% (w/w) FBS medium and incubated in incubator under 5% CO_2 at 37°C. Male nude mice (4 weeks, approximately 16 g) were purchased from the Experimental Center of Xi'an Jiaotong University. Mice were acclimatized for 1 week under SPF conditions. Approximately 100 μL DMEM medium, containing 5×10^5 K30 cells, was subcutaneously injected. The tumor-bearing mouse model was used in further experiments when the tumor grew to the appropriate volume. All animal experiments were carried out in compliance with the Guidelines for Use and Care of Animals at Xi'an Jiaotong University (Number XJTULAC 2016-412).

Determination of Drugs Combination Optimal Synergy

Three esophageal cancer cells (K510, K30, and K150) were cultured in DMEM with 10% (w/w) FBS and incubated at 37°C with 5% CO_2. The cells were treated with DOX and β-elemene at different dilution ratios (1:5; 1:10 and 1:15) for 72 h. Cell growth inhibition was measured by the CCK-8 method. During the plating, all samples had 3 duplicated wells. A 100 μL of leuco medium was added to each well, containing 10% (v/v) CCK-8. After incubation for 2 h, the absorbance for each well (at 450 mm) was obtained using a microplate reader. The drug concentration was determined by IC50, calculated using the GraphPad Prism 5 software. The combination index (CI) value reflects the combinable effect of the drugs. CalcuSyn program was used to calculate the CI according to the previous research (34). When the CI value was <0.9, the two drugs were considered to have a synergistic effect. When the CI value was >0.9 and <1.1, it was considered as a superposition effect, and when >1.1, it was considered as an antagonistic effect.

Preparation and Characterizations of bMED NPs

β-elemene is adsorbed in the positively charged bMSN NPs to form bMSN@β-elemene and DOX forms a hybrid DOX@HA with the HA negatively charged surface. bMSN@β-elemene and DOX@HA are combined to form bMED NPs by electrostatic adsorption, which is negatively charged. The method for synthesizing bMED NPs was as follows: 9 mg of amino-modified bMSN NPs were dispersed in 5 mL of water, 1 mg β-elemene was slowly added and continuously stirred to prevent flocculent precipitation. React overnight. 0.1 mg of DOX was slowly added to the HA aqueous solution, and stirred for 10 min. Slowly added the synthesized bMSN@β-elemene to DOX@HA, and reacted for 2 h to obtain bMED NPs. All reactions were performed at room temperature. The size and potential of the bMED NPs were measured using a Malvern instrument and their morphology was measured by a transmission electron microscope (TEM). The encapsulation efficiency (EE) of β-elemene in bMED NPs was determined by high performance liquid chromatography and the drug loading (DL) of DOX was determined by fluorescence spectrophotometry. These values were calculated using the following formulas:

$$\textbf{Encapsulation efficiency} = \frac{\mathbf{C_{drug\ remain}}}{\mathbf{C_{drug\ input}}} \times \mathbf{100\%}$$

$$\textbf{Drug loading} = \frac{\mathbf{C_{drug\ remain}}}{\mathbf{C_{bMED\ NPs\ input}}} \times \mathbf{100\%}$$

In vitro Drug Release of bMED NPs

DOX drug release by bMED NPs was studied using dialysis. β-elemene is insoluble in water and therefore cannot be detected in the experiment to determine whether bMED NPs released it. Thus, DOX is mainly used for this test as it is water-soluble and fluorescent. The same concentration of bMED NPs, with 10 U mL^{-1} HAase and free DOX, was dialyzed as a control and with same conditions.

In vitro Stability of bMED NPs

bMED NPs were dissolved in PBS (4 and 37°C), medium (37°C) and serum (37°C), to determine whether they were stable. This property was achieved by detecting the size of bMED NPs using a Malvern particle size analyzer.

In vitro Cytotoxicity of bMED NPs

K510, K30, and K150 cells (1×10^4) were seeded into 96-well sterile flat-bottomed culture plates (100 μL per well) and incubated for 24 h under a 5% CO_2 atmosphere at 37°C. Then, bMSN NPs, bMED NPs and dual drugs solution was added to each well (DOX: 15 μg mL^{-1}; β-elemene: 150 μg mL^{-1}). The plates were incubated in an incubator for 48 h at 37°C with 5% CO_2. Ten microliters of CCK-8 reagent was added to each well, and the plates were incubated for further 3 h. The optical density (OD) was measured at 450 nm using an ELISA plate reader (Infinite® 200 Pro, Tecan, Switzerland). The cell viability was calculated by the following formula:

$$\textbf{Cell viability} = \frac{\mathbf{OD_{bMED\ NPs} - OD_{blank}}}{\mathbf{OD_{control} - OD_{blank}}} \times \mathbf{100\%}$$

Colony Formation and Transwell Migration Assays

Colony formation assay: the ability of K30 cells to proliferate, under different drug treatments, was examined by the cell colony formation assay. The cells were uniformly dispersed, equal numbered and cultured into 5 culture dishes. After incubation at 37°C with 5% CO_2 for 24 h, the medium was replaced and a new one was added with DOX, β-elemene, dual drug and bMED NPs (C_{DOX}: 30 μg mL^{-1} and $C_{\beta-elemene}$: 300 μg mL^{-1}). DMSO was used as a control. The cell cultures were terminated when visible clones appeared in the culture dishes. The supernatants were discarded, and the cells carefully washed twice with PBS and fixed in 4% paraformaldehyde for 15 min. After fixative removal, the cells were stained with an appropriate amount of crystal violet for 10–30 min. Finally, the staining solution was washed away with PBS and photographed to calculate the number of clones using Image J.

Transwell migration assay: the amount of K30 migrating cells was used to evaluate the anti-migration ability of the drugs. The cells were treated with DOX, β-elemene, dual drugs, and bMED NPs (C_{DOX}: 6 μg mL^{-1} and $C_{\beta-elemene}$: 60 μg mL^{-1}) with DMSO treated cells used as a control. The cells were suspended in serum-free medium and their number was adjusted to 4×10^4 cells. The medium with 10% serum was added in the lower chamber and at the bottom of the 24-well plate, and the cell suspension was added to the upper chamber. After 24 h incubation, the chamber was removed with forceps, the upper chamber fluid blotted, and transferred to a well containing 800 μL of Giemsa stain and incubated for 10–30 min at room temperature. Five visually selected fields were randomly determined, under the microscope, for statistical analysis.

Cell Uptake of bMED NPs

In order to detect the cell uptake behavior of bMED NPs, coumarin 6 replaced β-elemene in the pore of bMSN NPs

(bMCD NPs) and HA was used as blocker. The samples were added and incubated with the cells for 48 h. The cells were fixed for 10 min with paraformaldehyde (4%) and the nuclei labeled with DAPI. The cell internalization of bMCD NPs was observed by confocal microscopy (TCS SP5 II, Leica, Germany).

Western Blot

After treating K30 cells with saline, DOX, β-elemene, dual drugs, bMED NPs for 48 h, the cells were collected by centrifugation and lysed with radio immunoprecipitation assay (RIPA, Beyotime) lysis buffer supplemented with 1% phenylmethylsulfonyl fluoride (PMSF). The proteins were separated by SDS-PAGE gel and semi-dry transferred to a nitrocellulose membrane. After washing the membrane with TBS-Tween-20 (TBST), to block proteins non-specific, the membrane was soaked in a 5% skimmed milk blocking solution at 4°C overnight. The membrane was washed and incubated with the primary antibody (in blocking solution) for 1 h with shaking. This step was followed by membrane washing and incubation with the secondary antibody was incubated (on a shaker) for 1 h. Finally, the reaction band was observed with an enhanced chemiluminescence reagent (Pierce).

Flow Cytometry Analysis

Apoptosis was detected using flow cytometry. The quantitative detection of phosphatidylserine on the surface of apoptotic cells was performed using Annexin-V-FITC and PI staining. The cells were incubated with DOX, β-elemene, dual drugs and bMED NPs for 48 h and the cells were treated with saline as control (C_{DOX}: 3 μg mL^{-1} and $C_{\beta-elemene}$: 30 μg mL^{-1}), and the cells were harvested by centrifugation at 800 rpm for 5 min, washed with PBS, centrifuged again and resuspended in PBS. The cells were stained with Annexin-V-FITC for 1 h, stained with PI for 30 min and analyzed by a FACScan system.

Hemolysis Test

Mice whole blood were taken and the blood samples were divided into triton X-100 (1% v/v), bMSN NPs, bMED NPs, dual drug and DMSO (0.5% v/v) groups. After incubating for 2 h at 37°C, the blood samples were centrifuged at 13,000 rpm for 15 min and the supernatants were dissolved and measured by a UV-Vis spectrophotometer (UV 2900, Shanghai) at a wavelength of 394 nm. All animal experiments were approved by the Experimental Animal Management Committee of Xi'an Medical University.

In vivo Toxicity of bMED NPs

20 mice (10 males and 10 females) were randomly divided into two groups. After 3 days of feeding under SPF conditions, bMED NPs and dual drugs were intravenously injected (contained drug concentration: DOX: 15 mg kg^{-1}, β-elemene: 150 mg kg^{-1}). Two days after the administration, mice vital signs were observed. Mice weights and deaths were continuously recorded, and mortality was calculated within 14 days. Heart, liver and kidney tissues were collected for histopathology analysis.

In vivo Distribution of bMED NPs

The animal models were injected in the tail vein with IR780-loaded bMSN NPs (10 mg mL^{-1}, 200 μL) and with the same amount of free IR780 for the control group. IR780 was adsorbed in the mesopores of bMSN NPs, which was achieved by hydrophobic adsorption, according to the synthesis method of bMSN@β-elemene. DOX was still adsorbed on the surface of bMSN NPs, through the electrostatic adsorption. The fluorescence distribution in mice was observed at different time points using the IVIS Imaging System with the excitation wavelength is 780 nm and the emission wavelength is 845 nm. At the end of imaging, all the mice were euthanized and the hearts, livers, spleens, lungs, kidneys and tumors were collected. The fluorescent signals in the tissues were detected under the same conditions.

In vivo Antitumor Effects of bMED NPs

The *in vivo* tumor inhibition effects of bMED NPs were studied using 30 tumor-bearing mice. Mice were randomly divided into 5 groups of 6 animals each. Mice treatments started when the tumor volume reached the appropriate level. Each group of mice was intravenously injected with the same dose of saline, β-elemene, DOX, dual drugs and bMED NPs twice a week for 3 weeks. During this period, body weight and tumors size were continuously recorded. After 3 weeks, removed all the tumor tissues from mice in each group and measured the tumor size and weight. The tumor tissues were embedded in paraffin and cut into 5 μm thick slices. Hematoxylin-eosin (H&E) staining and TUNEL staining were used to detect tumor cell morphology and apoptosis. TUNEL staining was conducted with a TUNEL apoptosis assay kit (Beyotime Biotechnology, Shanghai, China), and the experiment was performed according to the instructions. The paraffin sections were dewaxed and then 20 μg mL^{-1} of proteinase k was added and took effect at 37°C for 15 min. The excess proteinase k was washed away with PBS, and the sections were incubated in 3% hydrogen peroxide at room temperature for 20 min, and washed with PBS for three times. Fluorescence microscopy was used to analyze the results.

Statistical Analysis

Data are expressed as the mean ± SD of three independent replicates, which was calculated with the Graphpad Prism 5.0 software. When the P-value < 0.05, it was considered to represent a statistically significant difference between comparative data. And the statistical differences between the means were analyzed by the Student's t-test. The significance was set to 5%.

RESULTS

Synergistic Effect of DOX and β-Elemene

The combination of DOX and β-elemene were incubated with the cells (K 510, K30, and K 150) at the proportion of 1:5, 1:10, and 1:15, and the cytotoxicity of all three cell lines was increased. The CI was calculated by the CompuSyn software. As shown in **Table 1**, the CI values of the three treated cell lines were <0.9, indicating that DOX and β-elemene have excellent synergistic effects. When DOX with β-elemene were mixed in proportion of 1:10, the CI value was the smallest, indicating that this concentration has the greatest cytotoxicity for the three cell

TABLE 1 | CI and dose reduction values for inhibition on K510, K30, and K150 by combining doxorubicin with β-elemene in proportion of 1:10.

% Inhibition	CI	Doxorubicin			β-elemene		
		Conc.:(μM)		Dose reduction	Conc.:(μM)		Dose reduction
		Alone	Mix		Alone	Mix	
K510							
50	0.6463	27.87	5.881	4.739	355.5	57.32	6.202
75	0.7332	49.43	9.537	5.183	835.1	94.77	8.812
95	0.7643	99.87	18.53	5.390	1334	179.2	7.444
K30							
50	0.6354	38.14	9.222	4.136	478.9	93.24	5.136
75	0.6112	71.31	20.36	3.502	992.7	200.7	4.946
95	0.5895	110.3	32.63	3.380	1413	331.4	4.264
K150							
50	0.6432	31.46	7.321	4.297	297.4	77.32	3.846
75	0.6752	65.82	15.24	4.319	584.2	154.4	3.784
95	0.7743	104.5	20.57	5.080	1067	201.6	5.293

lines. Therefore, when DOX and β-elemene were combined at a ratio of 1:10, the optimal synergistic ratio was achieved. The highest sensitivity was observed in the K30 cell line. The drugs CI values and concentrations for K510, K30, and K150 inhibition using the combinations DOX and β-elemene at the proportions of 1:5 and 1:15, are shown in **Tables S1, S2**.

Preparation and Characterization of bMED NPs

The bMED NPs were prepared according to the protocol described in **Figure 1**. First, DOX@HA and bMSN@β-elemene were synthesized. Next, we assembled bMED NPs by electrostatic adsorption, in which β-elemene in the pore of bMSN NPs and DOX@HA was adsorbed around bMSN@β-elemene. As shown in **Figure 2A**, the shapes of bMSN NPs and bMED NPs were spherical and their particle sizes were 56.05 $\pm$ 5.78 and 77.15 $\pm$ 8.61 nm, respectively. And average hydrodynamic diameter were 59.19 $\pm$ 8.66 and 91.94 $\pm$ 13.46 nm, respectively. The nanocarriers showed uniform particle size distributions, as expected. The change of zeta potential proved to be a packaging process. The results showed that the zeta potentials of bMSN NPs and bMED NPs are 34.2 $\pm$ 1.06 and$-$17.1 $\pm$ 0.5 mV.

The bMED NPs EE and DL were measured and calculated using high performance liquid chromatography (HPLC). The maximum EE and DL of β-elemene were 96.7 $\pm$ 2.7% and 9.9 $\pm$ 1.4%; while, the EE and DL of DOX were 85.2 $\pm$ 6.2% and 1.1 $\pm$ 0.3%. **Figure 2B** showed the release curve of DOX in bMED NPs. The bMED NPs with HAase and free DOX were used as control. As shown, the free DOX group has a burst release with a rate of up to 92% at 12 h. The DOX release in the bMED NPs group was slower with only 46.89% of the DOX released at 72 h. Significantly, HAase could increase the ability of bMED NPs to release DOX. When HAase was added, DOX in bMED NPs was rapidly released, and at 24 h, the release rate increased to 88.79%.

As shown in **Figure 2C**, the stability studies were performed by measuring changes in the hydrodynamic diameters of bMED NPs at different times. The bMED NPs remained stable in PBS at 4 and 37°C, and the size did not change. The nanoparticles also remained stable in complete medium and FBS at 37 °C.

Colony Formation and Transwell Migration Assays

We obtained images of the colony formation (**Figure 3A**) and counted the number of colonies (**Figure 3B**). As shown, the control cells had the highest colonies number. The β-elemene and DOX groups were relatively reduced, with fewer in dual drug groups and minimal bMED NPs groups. Moreover, the drug treated group was significantly different from the DMSO treated group. When treated with bMED NPs, the proliferative capacity of K30 cells was almost completely inhibited. As shown in **Figures 3C**,**D**, the migration ability of K30 cells, after treatment with the different samples, was significantly attenuated. The migration ability of cells became very low when treated with bMED NPs.

In vitro Cytotoxicity and Cellular Uptake of bMED NPs

The cytotoxicity of bMED NPs for K510, K30, and K150 cells was detected by the CCK-8 method. As shown in **Figure S1**, bMSN NPs has no obvious cytotoxicity and there was no significant difference in cytotoxicity between bMED NPs and dual drugs. In the cellular uptake experiment, coumarin 6 was used to replace β-elemene, and was loaded in the pore of bMSN NPs to form bMCD NPs with double fluorescence (DOX has red fluorescence). **Figure 4** showed bMCD NPs internalization in the K30 cells. As shown in **Figure 4A**, the dynamic distribution of coumarin 6 and DOX, during the internalization process, was significantly different. In the first hour, the DOX and coumarin 6 mainly distributed in the cytoplasm. In the whole internalization process, the fluorescence of coumarin 6 was basically distributed in the cytoplasm and the fluorescence intensity gradually increased. However, the fluorescence signal distribution of DOX changed after 3 and 6 h. After 3 h, the DOX signal gradually spread from the cytoplasm to the whole cell. Six hours later, the fluorescence of DOX accumulated in the nucleus. **Figure 4B** showed the nucleus/cytoplasm fluorescence intensity ratio of DOX. With time, the ratio gradually increased, indicating that the DOX signal gradually accumulated and strengthened into the nucleus. **Figure 4C** showed a quantitative analysis of the fluorescence intensity of the coumarin 6 in the cytoplasm, which corresponded to the result of the confocal images shown in **Figure 4A**. **Figure 5** showed an overall picture of cell uptake, with or without HA blocking. During the experiment, 1% HA was added to the medium before incubation with bMCD NPs and after 1 h of incubation, a distinct fluorescence was observed in the cytoplasm. On the contrary, only weak fluorescence was observed in the blocking group.

Western Blot and Flow Cytometry Analysis

As shown in **Figure S2A**, K30 cells that were treated with the bMED NPs had an upregulation of Bax protein expression and

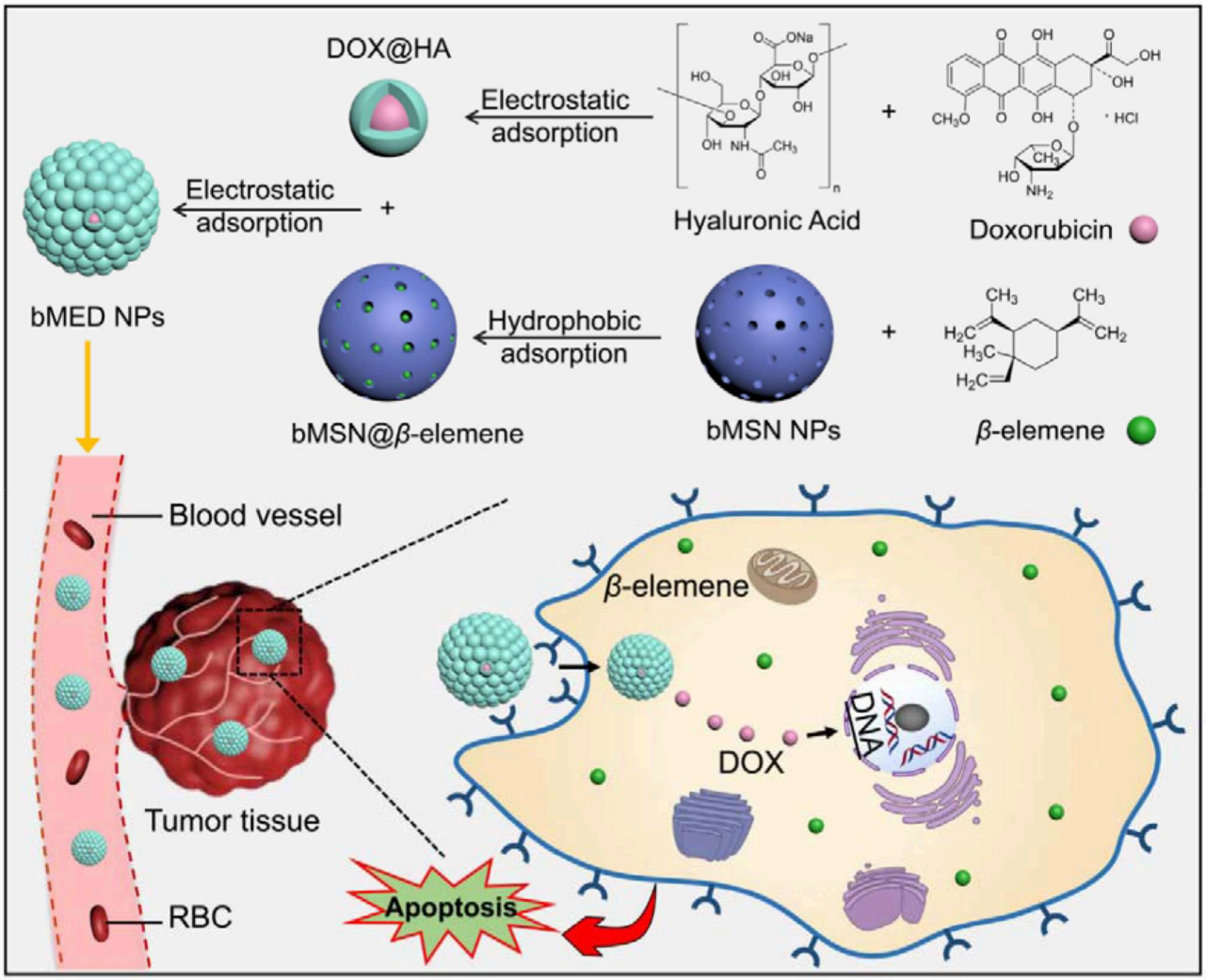

FIGURE 1 | Synthesis of bMED NPs.

a downregulation of Bcl-2 protein expression. **Figures S2B–D** showed quantitative analyses of Bax and Bcl-2 proteins expression, with the gradual decrease of Bcl-2 protein expression and increase of Bax protein expression in the bMED NPs groups. The results of flow cytometry (**Figure S2E**) showed a greater apoptosis in the dual drugs group compared to DOX and *β*-elemene groups. In the bMED NPs group, apoptosis was also greater than that in the dual drugs group.

In vivo Toxicity of bMED NPs

A major advantage of anti-tumor nanocarriers is their ability to reduce non-specific toxicity for normal organs and tissues. **Figure 6A** showed the acute toxicity results of bMED NPs and dual drugs. After 14 days, the survival rate of mice was 80% in the bMED NPs treatment group; while, the survival rate was only 40% in the dual drugs group. The acute toxicity of bMED NPs was significantly lower than that with dual drugs. Fourteen days later, the mice were euthanized and the hearts, kidneys and livers collected, sectioned and stained. As shown in **Figure 6B**, the organs of mice that were treated with bMED NPs had less damage compared to the dual drugs group. The result of the hemolysis test showed that bMED NPs had lower hemolytic toxicity relative to triton-X and the dual drugs treatment group (**Figure 6C**).

In vivo Distribution and Antitumor Effects of bMED NPs

IR780 was attached to the surface of the bMED NPs. The esophageal cancer animal model was used to detect the *in vivo* distribution of bMED NPs. **Figure 7A** showed fluorescence images of mice at different time points after their injection with same amounts of IR780-loaded bMED NPs and free IR780. The arrow pointed to the tumors. At 6 h, the fluorescence was accumulated in the livers and tumors of the IR780-loaded bMED NPs mice group, and the fluorescence in the tumors was much stronger than in the livers. At 12 h, the fluorescence continued to

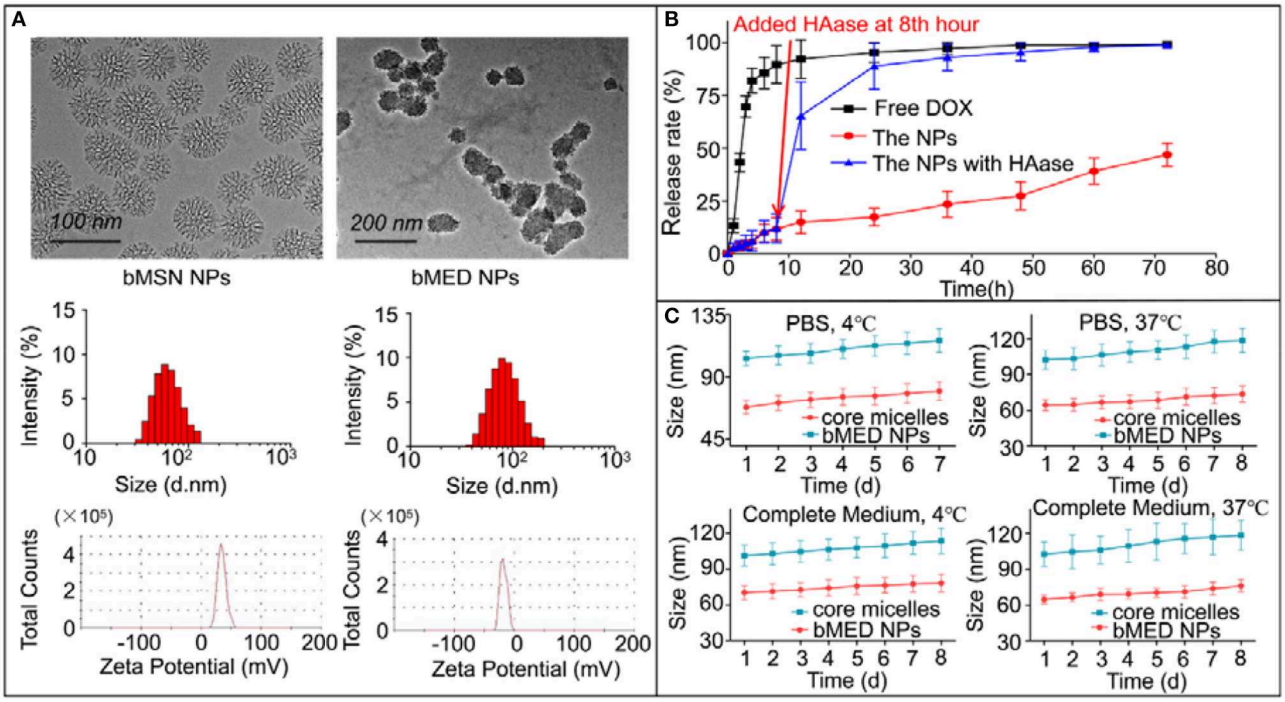

FIGURE 2 | Characterization of bMED NPs: **(A)** Morphology, size and zeta potential of bMSN NPs and bMED NPs; **(B)** *In vitro* DOX releasing of free DOX, bMED NPs, and bMED NPs with HAase; **(C)** *In vitro* stability of bMED NPs in different temperature and different solvent. The data reported are the mean ± SD for triplicate samples.

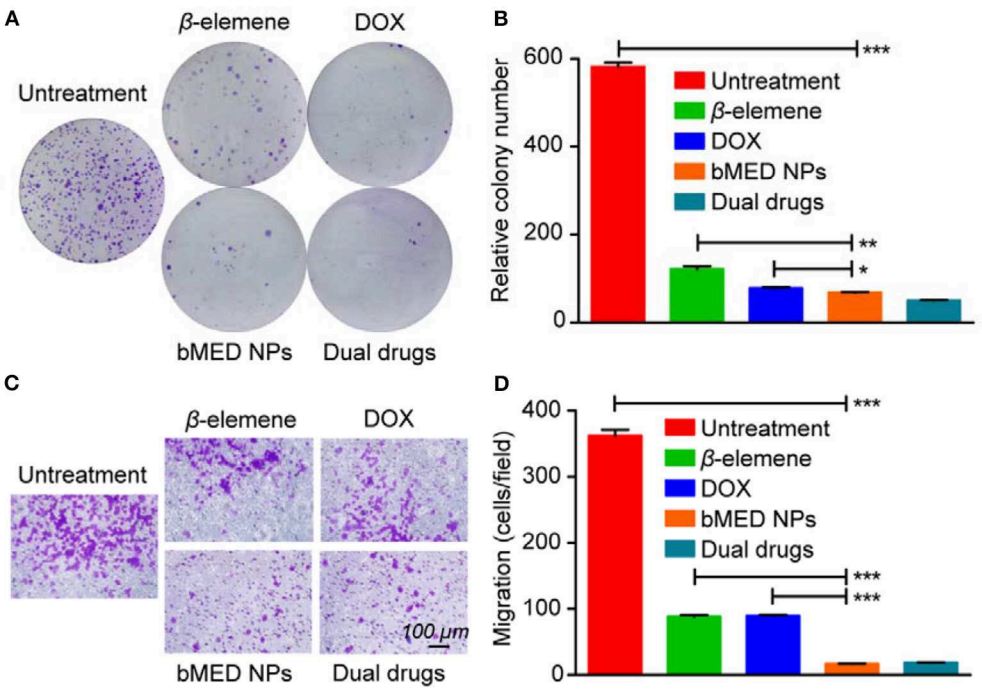

FIGURE 3 | The anti-proliferation and anti-migration effect assay in K30 cells when treated with β-elemene, DOX, dual drugs and bMED NPs: **(A)** Clony images of cells; **(B)** Quantitative data on the relative colony number; **(C)** The images of cells in transwell migration assay; **(D)** Quantitative data on transwell migration. Error bars represent the SD of the mean. $^{*}p < 0.05$, $^{**}p < 0.01$, $^{***}p < 0.001$.

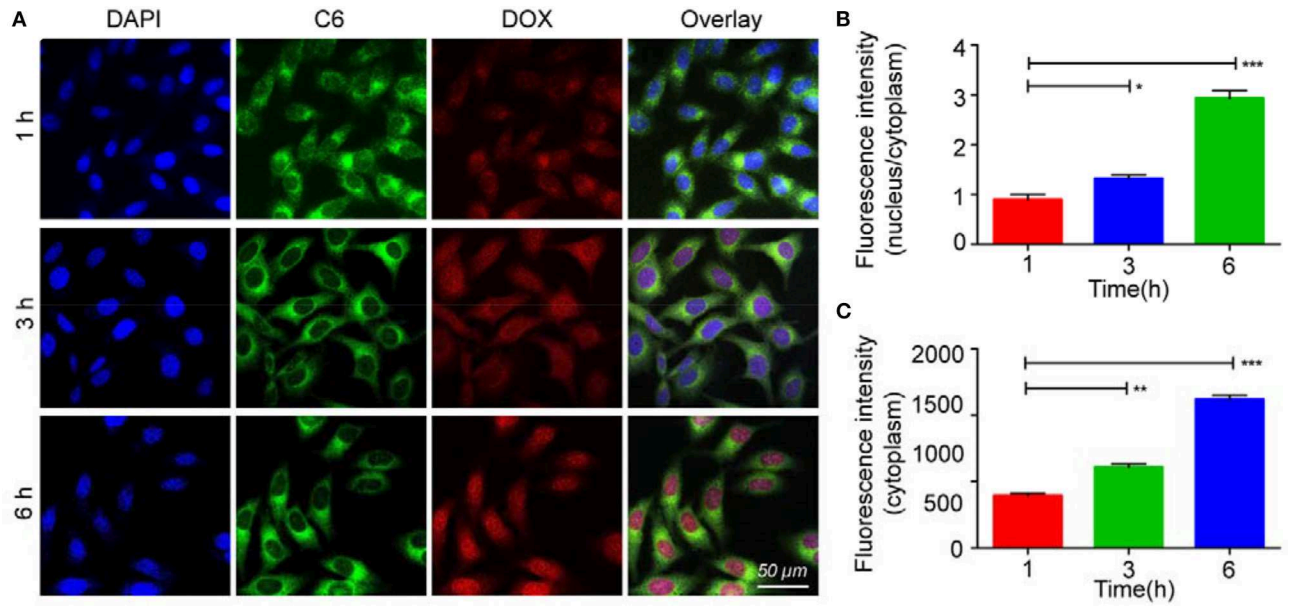

FIGURE 4 | *In vitro* internalization of bMCD NPs: **(A)** The K30 cells were incubated with dual-fluorescence bMCD NPs for 1 h, 3 h and 6 h; **(B)** The ratio of the fluorescence intensity of the nucleus to the cytoplasm represents that DOX is released and enters the nucleus from the cytoplasm; **(C)** Changes in the fluorescence intensity of coumarin 6 in the cytoplasm over time. Error bars represent the SD of the mean. $^{*}p < 0.05$, $^{**}p < 0.01$, $^{***}p < 0.001$.

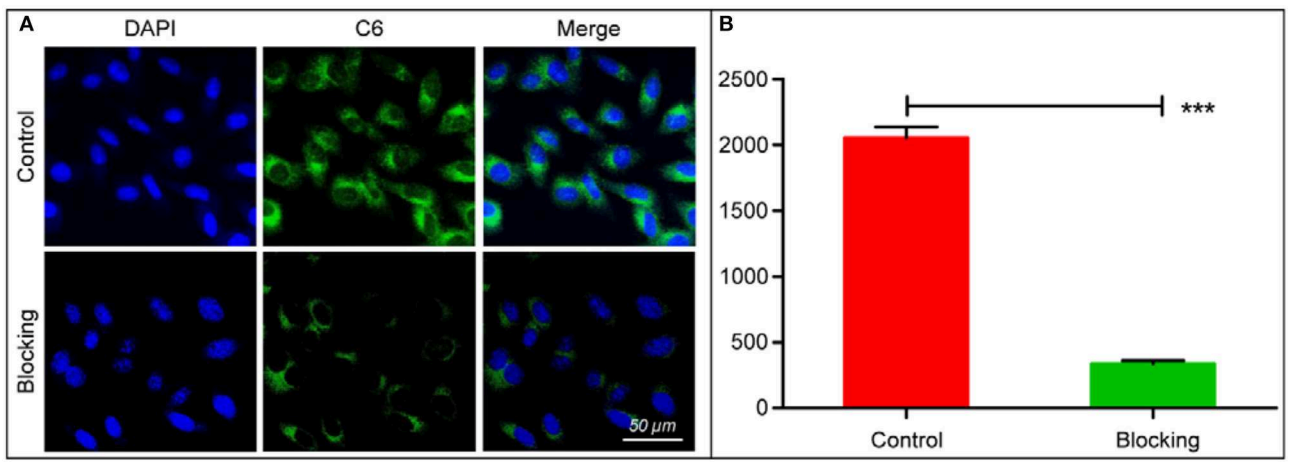

FIGURE 5 | *In vitro* cell affinity of bMCD NPs: **(A)** Fluorescent images of cells before and after blocking with HA. Cell nucleus stained with DAPI. **(B)** Histogram showed cell fluorescence integrated density of bMCD NPs and bMCD NPs with HA blocking. The data reported are the mean ± SD for triplicate samples; $^{***}p < 0.001$.

accumulate in the tumor sites, and the fluorescence intensity of the livers gradually increased. The strongest fluorescence was at 12 h. In the free-IR780 group, no significant signal accumulation was observed in the tumors. **Figure 7B** showed that the bMED NPs significantly prolonged the *in vivo* circulation time of IR780. At the end of the imaging period, all mice were sacrificed and the hearts, livers, spleens, lungs, kidneys and tumors were taken. The fluorescence in the tissues was detected under the same conditions. As shown in **Figure 7C**, the fluorescence mainly accumulated in the tumors and there were few fluorescence signals in other organs, which could be ignored. **Figure 7D** showed the fluorescence intensity of the major organs, which is consistent with the *in vivo* imaging results.

The tumor volume is intuitively a response to the *in vivo* antitumor effects. Therefore, tumors size and body weight of tumor-bearing mice were measured after injection. The tumor growth curve was shown in **Figure 8C**. The tumors were the smallest in the bMED NPs group. The tumor size of the dual drugs group was smaller than those in the single drug group. The mean tumor volume was the largest in the saline group. As shown in **Figure 8D**, the body weight of mice in the DOX treatment group was less than that in the β-elemene treatment

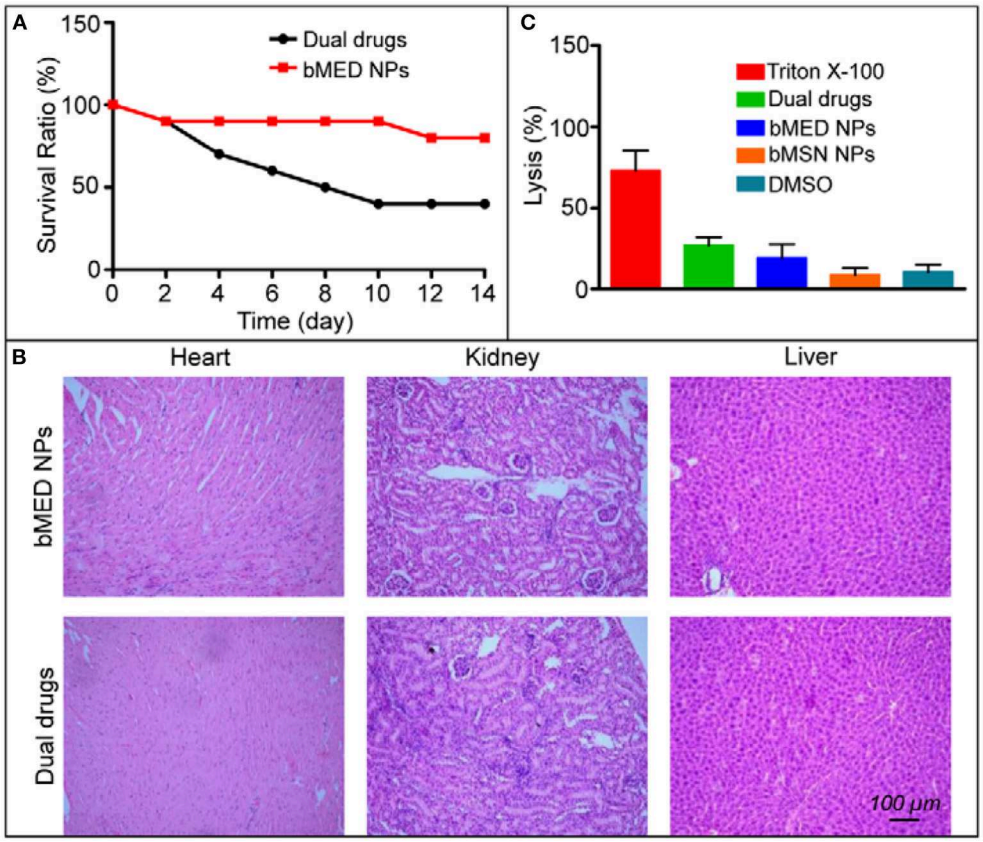

FIGURE 6 | *In vivo* toxicity results of bMED NPs: **(A)** Survival rate of free dual drugs and bMED NPs; **(B)** The H&E staining results of pathological examination of the heart, kidney and liver treated with dual drugs and bMED NPs; **(C)** The results of hemolysis analysis.

group, due to DOX high toxicity; while, β-elemene was less toxic. There was no significant decrease in body weight and saline in the bMED NPs group, indicating that bMED NPs can reduce drug toxicity. **Figure 8B** showed the weight of the tumors corresponding to **Figure 8A**. Statistically, bMED NPs group was significantly different from saline group ($^{***}p < 0.001$), the bMED NPs group showed a significant anti-tumor effect than in the dual drugs group and the dual drugs group was more effective than the DOX and β-elemene groups.

Pathological Section

To test the potential *in vivo* toxicity of bMED NPs, the mice were sacrificed and tumor tissues were taken and stained with H&E for histological analysis. As shown in **Figure S3A**, there was no significant damage in the saline group. The tissue necrotic area of the β-elemene, DOX and dual drugs groups increased. The organs in the bMED NPs treatment group were healthier than those in the dual drugs group. TUNEL staining was used to detect apoptosis and the results showed that treatment with bMED NPs could significantly induce apoptosis and inhibit tumor growth (**Figure S3B**). Quantification of TUNEL staining also showed the consistent results (**Figure S4**).

DISCUSSION

Esophageal cancer is one of the four major cancers in China that has high incidence and low five-year survival rate (2). Combination therapy is a very important tool in cancer treatment (35–37). Our previous studies have shown that β-elemene and DOX have a combination therapeutic effect. However, due to the difference in pharmacokinetics between the β-elemene and DOX, it is difficult to determine the optimal dose and drug ratio to exert optimal therapeutic effects at the tumor site. The combination of multiple drugs may produce better antitumor effects and the assessment of drug-drug interactions are critical (38). CI analysis is a common method for assessing the drugs interactions in combination therapy. The synergistic effect of DOX and β-elemene, as a dual drug delivery system, was verified by measuring CI. The CI value was <0.9 when the ratio of DOX to β-elemene was 1:10, which indicated that DOX and β-elemene had good synergistic effect and can be used as drugs of choice for combination therapy of esophageal cancer.

The bMSN NPs have larger pores size and specific surface areas, which make them good carriers for combination therapy (39). They can also be loaded with DOX and β-elemene in a determined ratio. Among bMSN NPs, the HA shell encapsulates DOX by electrostatic adsorption (DOX@HA). β-elemene is

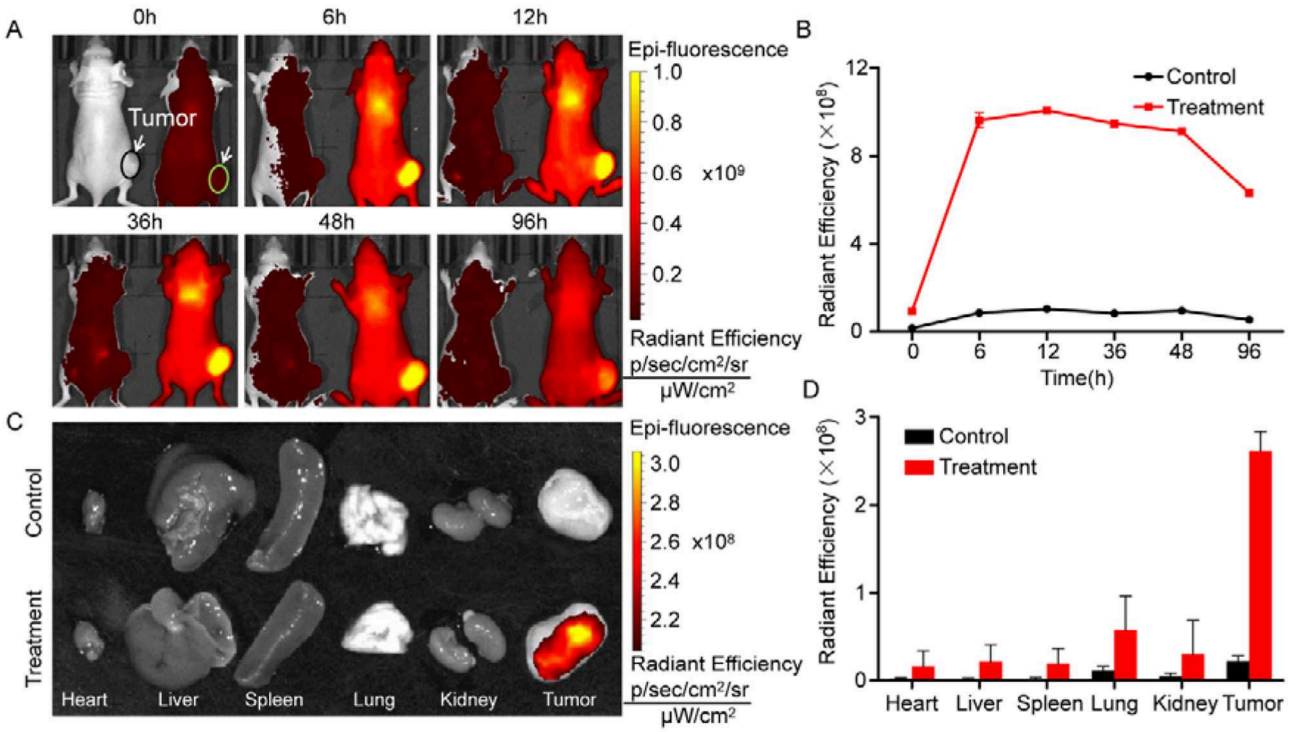

FIGURE 7 | *In vivo* distribution of bMED NPs. **(A)** Fluorescent images of mice within 96 hours. The right mouse was injected IR780-loaded bMSN NPs, meanwhile, the left mouse was injected free IR780 dye. The arrows were pointed to tumors; **(B)** Line graph of fluorescence intensity at tumor sites; **(C)** Fluorescent images of major organs and tumor tissues; **(D)** Quantification of fluorescence intensity in major organs and tumor tissues.

loaded into bMSN NPs pores by hydrophobic interaction. DOX@HA is then loaded onto the surface of the bMSN NPs by electrostatic adsorption. The synthesized bMED NPs have a particle size of 77 nm, which guaranteed an improved accumulation at the tumor sites through the EPR effect. The negative potential of bMED NPs also provides a better stability in the circulatory system *in vivo*. The drug loading of the nanocarriers is very important for a targeted delivery of the drug. The larger pore size and superficial area of the bMSN NPs allow the maximization of DOX and β-elemene loading, which leads to an efficient drug delivery *in vivo*, their larger particle size can also extend the time of *in vivo* drug delivery. To assess the drug delivery capacity of bMED NPs at the cellular level, cell uptake and affinity experiments were performed. To observe the cellular uptake of bMED NPs, the hydrophobic green fluorescent dye coumarin 6 was encapsulated into the pore of bMSN NPs. Coumarin 6 has a strong fluorescence and affinity to cell membranes (40) and can be used for dual fluorescence under a confocal microscope when used with DOX red fluorescence. The dual fluorescence signal of the coumarin 6 and DOX-loaded bMSN nanoparticles (bMCD NPs) can show cell uptake of the dual drug nanoparticles. Over time (0–6 h), bMCD NPs entered the cytoplasm by endocytosis, which was consistent with previous research results (41). As bMCD NPs decomposed, DOX was released and gradually entered into the nucleus. Since DOX binds mainly to the nuclear DNA, it could be observed that the fluorescent signal gradually shifts from the cytoplasm to the nucleus. After bMCD NPs decomposition, the coumarin 6 in the pore of bMSN NPs is gradually released, through the cell membrane and into the cytoplasm. Therefore, a gradual increase in the green fluorescence of coumarin 6 can be observed. These results indicated that bMED NPs could achieve efficient delivery of β-elemene and DOX based on their synergistic effect. The results of the affinity experiment showed that the green fluorescence of coumarin 6 was very weak compared with the control group after HA addition. The group without HA showed a strong fluorescent signal 1 h after bMED NPs treatment. These results indicated that bMED NPs had a good ability to target esophageal cancer cells and indicated that its targeting was caused by HA. This can be explained by HA function as CD44 protein receptor, which is highly expressed in various cancers, including esophageal cancer (42, 43). In addition, the release efficiency of DOX in bMED NPs has also been studied to assess the drug delivery capacity of bMED NPs. The addition of HAase mimics the *in vivo* environment and significantly increase the efficiency of DOX release; thereby, demonstrating that the presence of HA provides bMED NPs with good targeting and drug delivery capabilities. To verify the distribution and targeting ability of bMED NPs *in vivo*, the changes in fluorescent signals, provided by surface modified IR780, were monitored in a subcutaneous tumor model of esophageal cancer for 96 h. The results showed that bMED NPs were well-targeted to tumors and effectively prolonged the circulating time *in vivo* compared to small molecule drugs alone, which

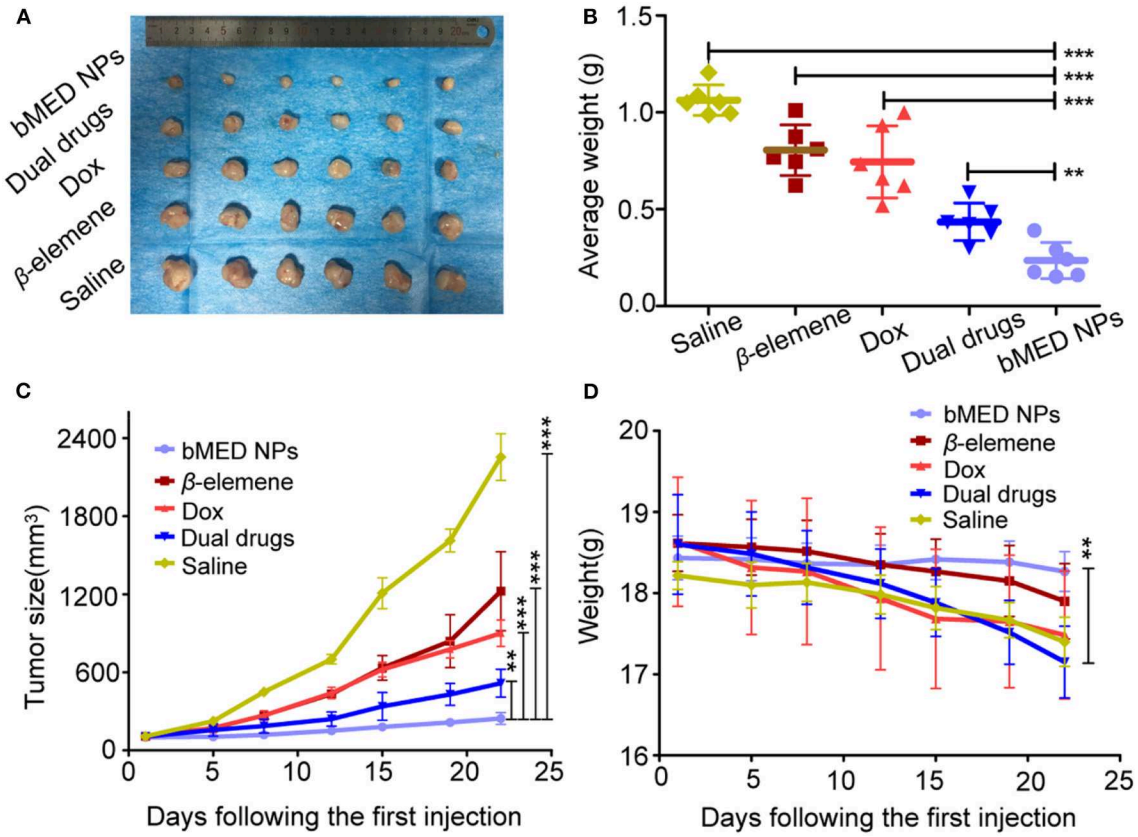

FIGURE 8 | *In vivo* tumor inhibition of bMED NPs: **(A)** The tumors images in different groups; **(B)** The tumor weight curves of mice in each group; **(C)** Tumor size curves in each treatment groups; **(D)** The body weight curves of mice in each group. Error bars represent the SD of the mean. $^{**}p < 0.01$, $^{***}p < 0.001$.

was demonstrated from the efficiency of bMSN nanocarriers. Up to 96 h, the tumor site showed a strong fluorescence intensity, demonstrating targeting by bMED NPs and an *in vivo* long-term circulation, which were also due to the effects of HA and the stability of bMED NPs. The results *in vivo* were consistent with those *in vitro*.

To further verify the antitumor effects of bMED NPs, three esophageal cancer cell lines were selected (K510, K30, and K150) and the cytotoxicity of bMED NPs was detected by CCK-8 analysis. For the three cell lines, there was almost no cytotoxicity detected; however, approximatively 50% of the cells died after administration of the dual drug and bMED NPs, suggesting that the cytotoxicity is due to the cytotoxicity of the dual drugs. To assess bMED NPs antitumor effects, it was necessary to detect the *in vivo* toxicity of bMED NPs. The results of *in vivo* acute toxicity did not show significant toxicity, demonstrating that bMSN nanocarriers were effective in reducing the non-specific toxicity of DOX and β-elemene to normal tissues and organs. Tissue sections staining also showed no significant tissue damage compared to the dual drugs treatment group. These results further indicated that bMED NPs could be used for tumors combined treatment.

To study the *in vivo* antitumor effects of bMED NPs, changes in mice body weight were monitored within 22 days, and the results showed that the mice in the bMED treatment group had substantially no change in body weight compared with the dual drugs treatment and the single drug treatment groups. This may be due to the cardiotoxicity of DOX and the liver metabolism of the hydrophobic β-elemene. In addition, from the tumor size of each group of mice dissected after 22 days, the tumors of the bMED treatment group were the smallest and the therapeutic effects were the best. The dual drug treatment group also showed good antitumor effects by inhibiting tumor growth. However, due to the rapid metabolism rate of small molecule drugs, it was difficult for the dual drugs therapy to continue exerting antitumor effects; thereby, a weaker tumor suppressing effect was observed compared with the bMED NPs treatment group. Tumor weighing and volume calculation also showed similar results. The *in vivo* efficient antitumor effect was also attributed to the targeted drug delivery of bMED NPs, whose sustained and effective drug delivery may help deliver the drugs to the tumor site for better antitumor effects. These results indicated that bMED NPs had good antitumor effects *in vivo*. The results of the studies on the antitumor mechanism of bMED NPs showed that bMED can downregulate the expression

of Bcl-2, increase the ratio of Bcl-2/Bax and cause apoptosis. This is consistent with the results of previous studies. H&E and TUNEL staining of tumor tissues also showed that bMED NPs had the best therapeutic effects. The above results indicated that bMED NPs had good antitumor effects *in vitro* and *in vivo* and could provide a good nanodrug platform for the treatment of esophageal cancer.

DATA AVAILABILITY STATEMENT

The raw data supporting the conclusions of this article will be made available by the authors, without undue reservation, to any qualified researcher.

ETHICS STATEMENT

The animal study was reviewed and approved by Xian Jiaotong University Animal Care and Use Committee.

AUTHOR CONTRIBUTIONS

WZ and HL designed the experiments. WZ, HL, and YG performed the experiments. YG and GD analyzed the data. HL and YG wrote the manuscript. YW and DZ provided guidance of the project. All authors have read and agreed to the published version of the manuscript.

FUNDING

This work was supported, in part, by the National Natural Science Foundation of China under Grant No. 81660505.

SUPPLEMENTARY MATERIAL

The Supplementary Material for this article can be found online at: https://www.frontiersin.org/articles/10.3389/fonc.2020.00622/full#supplementary-material

REFERENCES

1. Arnal MJD, Arenas AF, Arbeloa AL. Esophageal cancer: risk factors, screening and endoscopic treatment in Western and Eastern countries. *World J Gastroentero*. (2015) 21:7933–43. doi: 10.3748/wjg.v21.i26.7933
2. Bray F, Ferlay J, Soerjomataram I, Siegel RL, Torre LA, Jemal A. Global cancer statistics 2018: GLOBOCAN estimates of incidence and mortality worldwide for 36 cancers in 185 countries. *Ca-Cancer J Clin*. (2018) 68:394–424. doi: 10.3322/caac.21492
3. Kano M, Seki N, Kikkawa N, Fujimura L, Hoshino I, Akutsu Y, et al. miR-145, miR-133a and miR-133b: tumor-suppressive miRNAs target FSCN1 in esophageal squamous cell carcinoma. *Int J Cancer*. (2010) 127:2804–14. doi: 10.1002/ijc.25284
4. Lin JL. T1 esophageal cancer, request an endoscopic mucosal resection (EMR) for in-depth review. *J Thorac Dis*. (2013) 5:353–6. doi: 10.3978/j.issn.2072-1439.2013.06.03
5. Gockel I, Sgourakis G, Lyros O, Polotzek U, Schimanski CC, Lang H, et al. Risk of lymph node metastasis in submucosal esophageal cancer: a review of surgically resected patients. *Expert Rev Gastroent*. (2011) 5:371–84. doi: 10.1586/egh.11.33
6. Mohri J, Katada C, Ueda M, Sugawara M, Yamashita K, Moriya H, et al. Predisposing factors for chemotherapy-induced nephrotoxicity in patients with advanced esophageal cancer who received combination chemotherapy with docetaxel, cisplatin, and 5-fluorouracil. *J Trans Int Med*. (2018) 6:32–7. doi: 10.2478/jtim-2018-0007
7. Larkin J, Chiarion-Sileni V, Gonzalez R, Grob JJ, Cowey CL, Lao CD, et al. Combined nivolumab and ipilimumab or monotherapy in untreated melanoma. *New Engl J Med*. (2015) 373:23–34. doi: 10.1056/NEJMoa1504030
8. Douillard JY, Cunningham D, Roth AD, Navarro M, James RD, Karasek P, et al. Irinotecan combined with fluorouracil compared with fluorouracil alone as first-line treatment for metastatic colorectal cancer: a multicentre randomised trial. *Lancet*. (2000) 355:1041–7. doi: 10.1016/S0140-6736(00)02034-1
9. Greco F, Vicent MJ. Combination therapy: opportunities and challenges for polymer-drug conjugates as anticancer nanomedicines. *Adv Drug Deliver Rev*. (2009) 61:1203–13. doi: 10.1016/j.addr.2009.05.006
10. Enzinger PC, Burtness BA, Niedzwiecki D, Ye X, Douglas K, Ilson DH, et al. CALGB 80403 (Alliance)/E1206: a randomized phase II study of three chemotherapy regimens plus cetuximab in metastatic esophageal and gastroesophageal junction cancers. *J Clin Oncol*. (2016) 34:2736–42. doi: 10.1200/JCO.2015.65.5092
11. Suntharalingam M, Winter K, Ilson D, Dicker AP, Kachnic L, Konski A, et al. Effect of the addition of cetuximab to paclitaxel, cisplatin, and radiation therapy for patients with esophageal cancer the NRG oncology RTOG 0436 Phase 3 randomized clinical trial. *JAMA Oncol*. (2017) 3:1520–8. doi: 10.1001/jamaoncol.2017.1598
12. Gewirtz DA. A critical evaluation of the mechanisms of action proposed for the antitumor effects of the anthracycline antibiotics adriamycin and daunorubicin. *Biochem Pharmacol*. (1999) 57:727–41. doi: 10.1016/S0006-2952(98)00307-4
13. Xiong XB, Ma ZS, Lai R, Lavasanifar A. The therapeutic response to multifunctional polymeric nano-conjugates in the targeted cellular and subcellular delivery of doxorubicin. *Biomaterials*. (2010) 31:757–68. doi: 10.1016/j.biomaterials.2009.09.080
14. Ross P, Nicolson M, Cunningham D, Valle J, Seymour M, Harper P, et al. Prospective randomized trial comparing mitomycin, cisplatin, and protracted venous-infusion fluorouracil (PV1 5-FU) with epirubicin, cisplatin, and PV15-FU in advanced esophagogastric cancer. *J Clin Oncol*. (2002) 20:1996–2004. doi: 10.1200/JCO.2002.08.105
15. Zhang L, Yao MC, Yan W, Liu XN, Jiang BF, Qian ZY, et al. Delivery of a chemotherapeutic drug using novel hollow carbon spheres for esophageal cancer treatment. *Int J Nanomed*. (2017) 12:6759–69. doi: 10.2147/IJN.S142916
16. Singal PK, Iliskovic N. Doxorubicin-induced cardiomyopathy. *New Engl J Med*. (1998) 339:900–5. doi: 10.1056/NEJM199809243391307
17. Honda M, Miura A, Izumi Y, Kato T, Ryotokuji T, Monma K, et al. Doxorubicin, cisplatin, and fluorouracil combination therapy for metastatic esophageal squamous cell carcinoma. *Dis Esophagus*. (2010) 23:641–5. doi: 10.1111/j.1442-2050.2010.01070.x
18. Lee HH, Ye S, Li XJ, Lee KB, Park MH, Kim SM. Combination treatment with paclitaxel and doxorubicin inhibits growth of human esophageal squamous cancer cells by inactivation of Akt. *Oncol Rep*. (2014) 31:183–8. doi: 10.3892/or.2013.2851
19. Chen WX, Lu Y, Wu JM, Gao M, Wang AY, Xu B. β-elemene inhibits melanoma growth and metastasis via suppressing vascular endothelial growth factor-mediated angiogenesis. *Cancer Chemoth Pharm*. (2011) 67:799–808. doi: 10.1007/s00280-010-1378-x
20. Li QQ, Wang GD, Huang FR, Banda M, Reed E. Antineoplastic effect of beta-elemene on prostate cancer cells and other types of solid tumour cells. *J Pharm Pharmacol*. (2010) 62:1018–27. doi: 10.1111/j.2042-7158.2010.01135.x
21. Liu J, Zhang Y, Qu JL, Xu L, Hou KZ, Zhang JD, et al. β-Elemene-induced autophagy protects human gastric cancer cells from undergoing apoptosis. *Bmc Cancer*. (2011) 11:1–10. doi: 10.1186/1471-2407-11-183
22. Zhan YH, Liu J, Qu XJ, Hou KZ, Wang KF, Liu YP, et al. β-elemene induces apoptosis in human renal-cell carcinoma 786-0 cells through inhibition of MAPK/ERK and PI3K/Akt/mTOR signalling pathways. *Asian Pac J Cancer P*. (2012) 13:2739–44. doi: 10.7314/APJCP.2012.13.6.2739

23. Chang ZW, Gao M, Zhang WJ, Song LJ, Jia YX, Qin YR. β-elemene treatment is associated with improved outcomes of patients with esophageal squamous cell carcinoma. *Surg Oncol*. (2017) 26:333–7. doi: 10.1016/j.suronc.2017.07.002
24. Zhai BT, Zeng YY, Zeng ZW, Zhang NN, Li CX, Zeng YJ, et al. Drug delivery systems for elemene, its main active ingredient beta-elemene, and its derivatives in cancer therapy. *Int J Nanomed*. (2018) 13:6279–96. doi: 10.2147/IJN.S174527
25. Cao C, Wang Q, Liu Y. Lung cancer combination therapy: doxorubicin and beta-elemene co-loaded, pH-sensitive nanostructured lipid carriers. *Drug Des Dev Ther*. (2019) 13:1087–98. doi: 10.2147/DDDT.S198003
26. Agudelo D, Bourassa P, Berube G, Tajmir-Riahi HA. Review on the binding of anticancer drug doxorubicin with DNA and tRNA: structural models and antitumor activity. *J Photoch Photobio B*. (2016) 158:274–9. doi: 10.1016/j.jphotobiol.2016.02.032
27. Li CL, Chang L, Guo L, Zhao D, Liu HB, Wang QS, et al. β-elemene induces caspase-dependent apoptosis in human glioma cells in vitro through the upregulation of bax and Fas/FasL and downregulation of Bcl-2. *Asian Pac J Cancer P*. (2014) 15:10407–12. doi: 10.7314/APJCP.2014.15.23.10407
28. Dai SJ, Ye ZM, Wang FZ, Yan FQ, Wang L, Fang J, et al. Doxorubicin-loaded poly(epsilon-caprolactone)-Pluronic micelle for targeted therapy of esophageal cancer. *J Cell Biochem*. (2018) 119:9017–27. doi: 10.1002/jcb.27159
29. Kolishetti N, Dhar S, Valencia PM, Lin LQ, Karnik R, Lippard SJ, et al. Engineering of self-assembled nanoparticle platform for precisely controlled combination drug therapy. *Proc Natl Acad Sci USA*. (2010) 107:17939–44. doi: 10.1073/pnas.1011368107
30. Hu CMJ, Zhang LF. Nanoparticle-based combination therapy toward overcoming drug resistance in cancer. *Biochem Pharmacol*. (2012) 83:1104–11. doi: 10.1016/j.bcp.2012.01.008
31. Estanqueiro M, Amaral MH, Conceicao J, Lobo JMS. Nanotechnological carriers for cancer chemotherapy: the state of the art. *Colloid Surface B*. (2015) 126:631–48. doi: 10.1016/j.colsurfb.2014.12.041
32. He QJ, Shi JL. Mesoporous silica nanoparticle based nano drug delivery systems: synthesis, controlled drug release and delivery, pharmacokinetics and biocompatibility. *J Mater Chem*. (2011) 21:5845–55. doi: 10.1039/c0jm03851b
33. Li HR, Li K, Dai YP, Xu XY, Cao X, Zeng Q, et al. *In vivo* near infrared fluorescence imaging and dynamic quantification of pancreatic metastatic tumors using folic acid conjugated biodegradable mesoporous silica nanoparticles. *Nanomed-Nanotechnol*. (2018) 14:1867–77. doi: 10.1016/j.nano.2018.04.018
34. Liu SW, Lu H, Neurath AR, Jiang SB. Combination of candidate microbicides cellulose acetate 1,2-benzenedicarboxylate and UC781 has synergistic and complementary effects against human immunodeficiency virus type 1 infection. *Antimicrob Agents Chemother*. (2005) 49:1830–6. doi: 10.1128/AAC.49.5.1830-1836.2005
35. Alderson D, Cunningham D, Nankivell M, Blazeby JM, Griffin SM, Crellin A, et al. Neoadjuvant cisplatin and fluorouracil versus epirubicin, cisplatin, and capecitabine followed by resection in patients with oesophageal adenocarcinoma (UK MRC OE05): an open-label, randomised phase 3 trial. *Lancet Oncol*. (2017) 18:1249–60. doi: 10.1016/S1470-2045(17)30447-3
36. Catenacci DVT, Tebbutt NC, Davidenko I, Murad AM, Al-Batran SE, Ilson DH, et al. Rilotumumab plus epirubicin, cisplatin, and capecitabine as first-line therapy in advanced MET-positive gastric or gastro-oesophageal junction cancer (RILOMET-1): a randomised, double-blind, placebo-controlled, phase 3 trial. *Lancet Oncol*. (2017) 18:1467–82. doi: 10.1016/S1470-2045(17)30566-1
37. Lorenzen S, Knorrenschild JR, Haag GM, Pohl M, Thuss-Patience P, Bassermann F, et al. Lapatinib versus lapatinib plus capecitabine as second-line treatment in human epidermal growth factor receptor 2-amplified metastatic gastro-oesophageal cancer: a randomised phase II trial of the arbeitsgemeinschaft internistische onkologie. *Eur J Cancer*. (2015) 51:569–76. doi: 10.1016/j.ejca.2015.01.059
38. Liu J, Cheng H, Han L, Qiang Z, Zhang XW, Gao W, et al. Synergistic combination therapy of lung cancer using paclitaxel- and triptolide-coloaded lipid-polymer hybrid nanopartices. *Drug Des Dev Ther*. (2018) 12:3199–209. doi: 10.2147/DDDT.S172199
39. Xu C, Chen F, Valdovinos HF, Jiang DW, Goel S, Yu B, et al. Bacteria-like mesoporous silica-coated gold nanorods for positron emission tomography and photoacoustic imaging-guided chemo-photothermal combined therapy. *Biomaterials*. (2018) 165:56–65. doi: 10.1016/j.biomaterials.2018.02.043
40. Rivolta I, Panariti A, Lettiero B, Sesana S, Gasco P, Gasco MR, et al. Cellular uptake of coumarin-6 as a model drug loaded in solid lipid nanoparticles. *J Physiol Pharmacol*. (2011) 62:45–53. doi: 10.0000/PMID21451209
41. Zhu DW, Tao W, Zhang HL, Liu G, Wang T, Zhang LH, et al. Docetaxel (DTX)-loaded polydopamine-modified TPGS-PLA nanoparticles as a targeted drug delivery system for the treatment of liver cancer. *Acta Biomater*. (2016) 30:144–54. doi: 10.1016/j.actbio.2015.11.031
42. Goodison S, Urquidi V, Tarin D. CD44 cell adhesion molecules. *Mol Pathol*. (1999) 52:189–96. doi: 10.1136/mp.52.4.189
43. Almeida PV, Shahbazi MA, Makila E, Kaasalainen M, Salonen J, Hirvonen J, et al. Amine-modified hyaluronic acid-functionalized porous silicon nanoparticles for targeting breast cancer tumors. *Nanoscale*. (2014) 6:10377–87. doi: 10.1039/C4NR02187H

Conflict of Interest: The authors declare that the research was conducted in the absence of any commercial or financial relationships that could be construed as a potential conflict of interest.

frontiers in Oncology

ORIGINAL RESEARCH
published: 19 August 2020
doi: 10.3389/fonc.2020.01348

Association of the Trough, Peak/Trough Ratio of Imatinib, Pyridine–N-Oxide Imatinib and ABCG2 SNPs 34 G>A and SLCO1B3 334 T>G With Imatinib Response in Egyptian Chronic Myeloid Leukemia Patients

*Mervat M. Omran[1], Raafat Abdelfattah[2], Heba S. Moussa[3], Nelly Alieldin[4] and Samia A. Shouman[1]**

[1] Pharmacology Unit, Cancer Biology Department, National Cancer Institute, Cairo University, Cairo, Egypt, [2] Medical Oncology Department, National Cancer Institute, Cairo University, Cairo, Egypt, [3] Clinical Pathology Department, National Cancer Institute, Cairo University, Cairo, Egypt, [4] Medical Statistics Department, National Cancer Institute, Cairo University, Cairo, Egypt

OPEN ACCESS

Edited by:
Qi Zeng,
Xidian University, China

Reviewed by:
Sabrina Angelini,
University of Bologna, Italy
Lalit Kumar,
All India Institute of Medical Sciences, India

***Correspondence:**
Samia A. Shouman
uwebmasternderline@nci.cu.edu.eg;
samia.shouman@nci.cu.edu.eg

Specialty section:
This article was submitted to Pharmacology of Anti-Cancer Drugs, a section of the journal Frontiers in Oncology

Received: 11 March 2020
Accepted: 26 June 2020
Published: 19 August 2020

Citation:
Omran MM, Abdelfattah R, Moussa HS, Alieldin N and Shouman SA (2020) Association of the Trough, Peak/Trough Ratio of Imatinib, Pyridine–N-Oxide Imatinib and ABCG2 SNPs 34 G>A and SLCO1B3 334 T>G With Imatinib Response in Egyptian Chronic Myeloid Leukemia Patients. Front. Oncol. 10:1348. doi: 10.3389/fonc.2020.01348

Imatinib mesylate (IM) is highly efficacious in the treatment of chronic myeloid leukemia (CML). Therapeutic drug monitoring and pharmacogenetic screening are affirmed for better management of IM therapy. The goal of this study was to gain a greater mechanistic understanding of the factors controlling variability in IM level and its relation to the response. One hundred and two patients with CML at chronic phase were recruited in this study. Blood samples were withdrawn at least 30 days after drug administration, and trough and peak concentrations of imatinib, N-des-methyl imatinib, and pyridine-N-oxide imatinib were determined by HPLC/MS/MS. Genetic polymorphism of the genes ABCG2 SNPs 34 G>A and 421C >A; ABCB1 SNPs 2677 G>A/T, 1236 C>T, 3435 C>T; SLCO1B3 SNPs 334 T>G and CYP3A5 were studied using PCR-RFLP technique. Our study presented significant higher trough IM (1,281 ± 578 ng/ml), lower Peak/Trough ratio, clearance (Cl), and elimination rate constant, k_e, among patients who achieved favorable responses ($N = 64$) than those for patients who suffered unfavorable response ($N = 37$). The P/T ratio was the only significant independent factor affecting response, as the P/T ratio increased by one, the risk of unfavorable response increased by more than double as compared to favorable response with 95% CI (1.28–3.92, $P = 00.005$). Moreover, like the results of IM, the trough concentration of Pyridine-N-oxide imatinib was significantly higher ($P = 0.01$) and its P/T ratio was significantly lower ($P = 0.008$) in patients achieved favorable response than those without. The wild GG genotype of the ABCG2.34 G>A gene was associated with favorable response ($P = 0.01$), lower Cl, K_e and high plasma IM trough level than both (AA+GA) genotypes. ABCG2.421C >A (CC) genotype had a significantly higher plasma peak of IM, N-des-methyl imatinib and higher C_{ss}. The GG and TG alleles of the SLCO1B3.334 T>G gene were significantly correlated

to favorable response, while the wild allele TT was linked to unfavorable response ($P = 0.03$). In conclusion, the trough and P/ T ratio for both IM and Pyridine-N-oxide imatinib, in addition to Polymorphism of ABCG2 SNPs 34 G>A and SLCO1B3.334 T>G gene, is a good predictor for response of IM in CML Egyptian patients.

Keywords: imatinib, pyridine-N-oxide imatinib, P/T ratio, response, SNP, ABCG2, CML

INTRODUCTION

Chronic myeloid leukemia (CML) is characterized by a chromosomal abnormality, the Philadelphia [Ph] chromosome, which resulted in a unique molecular event, *BCR-ABL1* oncogene, which encodes the chimeric BCR-ABL1 protein with constitutive kinase activity (1, 2). In the absence of treatment, CML is an unavoidable and fatal disease. Imatinib mesylate (IM) is a tyrosine kinase inhibitor that selectively inhibits the BCR-ABL1 oncoprotein and induces effective and safe durable cytogenetic responses in most patients (3). Imatinib has been found effective in the chronic and accelerated phases of CML, as well as in blast crisis (4). The estimated rate of complete cytogenetic response (CCyR) to IM at 18 months was 76%. The 5-year follow-up analysis specified an estimated 87% cumulative CCyR and an estimated overall survival of 89% among 553 patients who received IM as first-line therapy (5).

Imatinib pharmacokinetics (PK) is characterized by rapid and complete oral bioavailability (98%) and a proportional dose-exposure relationship. It is used once daily as its terminal half-life is ∼20 h (6). Despite the significant efficacy and better clinical responses and the favorable pharmacokinetic properties of IM, there are cases of suboptimal responses, developing drug resistance, or undergoing relapse after initial success. Therefore, understanding the key contributors to interpatient variability in imatinib disposition is essential for better treatment outcome. Data indicate the important roles of pharmacokinetic, pharmacogenetic in IM efficacy, as well as the initial therapeutic response, and for the time to progression (7). Imatinib is mostly metabolized by hepatic cytochrome P450 enzymes system, mainly CYP3A4 and CYP3A5, which exhibit widely variable activity among different individuals leading to high interpatient variability during IM exposure in CML patients (8). N-des-methyl imatinib is an active metabolite of IM, which is pharmacologically active but 3–4 times less cytotoxic than IM, and its plasma level in patients represents ∼20% of the parent drug (9). Two N-oxide metabolites of IM, imatinib pyridine-N-oxide, and imatinib piperdine-N-oxide, have also been identified in patient urine 2 h post-dose but were not observed at 24 h after dosing (10).

One of the patient factors that are probable to be relevant for the observed differences in IM pharmacokinetics is the contribution of single nucleotide polymorphisms in genes related to IM absorption, distribution, metabolism, and excretion. Imatinib uptake is mediated by the human organic anionic transporter OATP1B3 (SLCO1B3 gene product) (11). It is a substrate of adenosine triphosphate binding cassette ATP as efflux transporters such as ABCB1 and ABCG2 (12). Imatinib is mostly metabolized by the cytochrome P450 (CYP) proteins CYP3A4 and CYP3A5 (13). This study aimed at investigating the impact of pharmacokinetic and pharmacogenetic in the clinical response of IM in Egyptian patients with CML.

PATIENTS AND METHODS

Design and Sampling

This study was designed as an observational study. A total of 102 patients from the Hematological Outpatient Clinic of the National Cancer Institute, Cairo University, were recruited in this study. The eligible patients were diagnosed with CML, age $\geq$ 18 years, on IM treatment for at least 30 days (to reach the steady state), and not more than 38 days, with mean and standard deviation of the timepoint of sample collection at 32 $\pm$ 2.44 and median (range) 31 (14–22) days. The excluded patients include those with known sensitivity to IM and patients with a severe medical condition that prohibited participation in the study. Plasma level of peak, trough, and peak/trough (P/T) ratio of IM, and its main metabolites, N-des-methyl imatinib, and Pyridine-N-oxide imatinib were determined. Single nucleotide polymorphisms (SNP) of genes involved in IM uptake and efflux transporters and metabolism genes were assessed using restriction fragment length polymorphism (RFLP). In addition, different types of toxicities were monitored. The time of the study was continued for 2 years from the start of sampling time. The study protocol was approved by the Institution Review Board (IRB) of the National Cancer Institute of Cairo University, Egypt, and written informed consent was obtained according to the Declaration of Helsinki from all patients with acceptance number IRB00004025.

Response Assessment

Pretreatment, cytogenetic analyses of bone marrow or peripheral blood for Philadelphia [Ph] chromosome was done. A minimum of 20 metaphases was required to be examined for a patient to be classified as Ph-positive. The response of the patient to the treatment can be tracked by cytogenetic (karyotype and/or Fish) and molecular (by detecting the presence of BCR-ABL1 mRNA metaphases) that identify the optimal and suboptimal response, and treatment failure, based on molecular and cytogenetic response over the course of treatment (23). According to ELN guidelines, the clinical effect was evaluated at 12 months after IM therapy. Patients with favorable responses include those who achieved either complete cytogenetic response (CCyR) or major molecular response (MMR). The CCyR is defined as 0% Ph metaphase cells of 20 examined field and MMR, subjects who achieved CCyR as 3 or more log reduction in BCR-ABL/BCR

ratio by polymerase chain reaction (PCR) assay relative to a standardized baseline derived from the median ratio for 30 untreated patients with chronic-phase CML (24).

Chemicals

Imatinib mesylate (Enzo, NY, USA), N-des methyl imatinib, Pyridine-N-oxide imatinib, palonosetron hydrochloride were purchased from Santa Cruz Biotechnology (TX, USA), methanol for HPLC 99.9%, 2-propanol (Riedel-deHaën, Honeywell, Germany), formic acid for mass spectrometry, 98%, ethanol (Sigma-Aldrich, Steinheim, Germany), Agarose A (Biobasic, Ontario, Canada), Tris-acetate -EDTA(TAE) (Invitrogen Life Technologies, NY, USA). In addition, DNA ladder (Solis BioDyne, Estonia), PCR Master Mix kit (2X) (Thermo Scientific, IL, USA), Restriction enzymes: RsaI, Acl I, Dde I, Mbo I, AluI (Promega, Madison, MI, USA), and Bse3D I, Bsu R I, Bst 4C I, Bse 3D I (SibEnzyme Ltd, Russia) were obtained.

Pharmacokinetic Analysis

Samples Preparation

After approval of IRB and the individual consent, whole blood samples were collected into EDTA-containing tubes just before drug administration (trough sample), and 2 h after IM administration (peak sample). The plasma was separated by centrifugation at 2,500 × g for 10 min, 400 ul of plasma was transferred to a glass tube and was spiked with 40 μL of the internal standard (IS) stock solution (2 ug/ml), then 1,200 ul of methanol was added. The mixture was mixed by vortex and then centrifuged at 10,000 × g at 4°C for 10 min. The clear supernatant was transferred to HPLC autosampler vials and 10 μl was injected onto the LC/MS/MS system following the method of Titier et al. (25).

LC-MS-MS Instrumentation and Operating Conditions

The LC-MS-MS system consisted of a ABSCIEX Q TRAP 3200 mass spectrometer (ABSCIEX, Germany) equipped with an electrospray ionization (ESI) interface coupled to an Agilent 1200 HPLC system (Agilent Technologies, CA, USA) with a quaternary gradient pump (Agilent 1,260 infinity) and an autosampler (Agilent 1,260 infinity). Data acquisition was performed with analyst 4.0 software (ABSCIEX). The separation was performed using Agilent pro shell EC, C18 (5 μm, 50 × 4.6 mm) reversed-phase analytical column (Agilent, CA, USA). The mobile phase consisted of 0.1% formic acid in methanol/water (55:45, v/v) and pumped at a flow rate of 700 μl/min. The overall run time was 6 min. The mass spectrometer was operated in the positive ESI mode at a temperature of 350°C. The calculation is done by the Multiquant software program. Quantification was performed with multiple reaction monitoring (MRM) and the following ion transitions: m/z 494:394, 480: 394, 510:217, and 297:110 for IM, N-des-methyl imatinib, pyridine–N-oxide imatinib and palonosetron (IS), respectively.

Calibration Curve

Stock solutions of IM, N-des-methyl imatinib, pyridine-N-oxide imatinib, and palonosetron as internal standard (IS) were prepared by dissolving 1 mg of each drug in 1 ml methanol/water (50:50). Serial dilutions were prepared at concentrations that ranged from (4.8–5,000) ng/ml for IM, (2.7–700) ng/ml for N-des-methyl imatinib, and (5.4–700) ng/ml for pyridine-N-oxide imatinib in drug-free plasma and spiked with the known concentration of the IS as previously described in sample predation calibration plasma standards of imatinib and its metabolites were constructed and used for sample calculation.

Pharmacogenetic Analysis

Preparation of DNA

For determination of polymorphism, Leukocyte cell pellets were isolated using hemolysis buffer (8.46 g ammonium chloride, 1 g ethylene diamine disodium salt, and 1 g potassium bicarbonate dissolved in 1 L at the pH = 7–7.2). The whole-cell pellet was used for the extraction of genomic DNA using the Gentra Puregene Blood Kit (Qiagen Inc, Minneapolis, MN, USA) following the manufacturer's instructions. The DNA was stored at −80°C until analysis.

Polymerase chain reaction-restriction fragment length polymorphism (PCR-RFLP) method was adopted for the genotyping of ABCG2 SNPs 34 G>A (rs2231137) and 421C >A (rs2231142), ABCB1 SNPs 2677 G>A/T (rs2032582), 2677 G> T/A (rs2032582), 1236 C>T (rs1128503), 3435C>T (rs60023214), the solute carriers OATP1B3 (SLCO1B3) SNPs 334T>G (rs 4149117) and CYP 450 3A5 (rs776746). Thermal cycling was started using a thermocycler (Biometra, Germany) according to parameters described in **Supplement 1**.

Ten μl of each sample was analyzed, along with a suitable DNA size marker, by electrophoresis on 2.5% agarose/ethidium bromide gel. The gel was photographed by (Uvitec, Cambridge, UK) (26, 27).

Assessment of Drug Adherence

MMAS is a validated, self-reported questionnaire that is a commonly used tool to assess a person's medication adherence behavior. The MMAS is a 4–8 question survey that is designed to measure a specific medication-taking behavior. The use of the modified MMAS is common in the biomedical and professional literature and is customized to address circumstances surrounding adherence behavior related to a particular disease state. Scoring is based on yes/no answers that are then scored by an administrator. Score and intent to adhere to a prescribed medication regimen share a direct relationship (28).

Statistical Method

Genotype distribution was tested for Hardy-Weinberg equilibrium (HWE) using Fisher's exact test. Quantitative variables were described by mean ± standard deviation and median with range are used when distribution did not follow normality. Qualitative data was described by number and percentages and Chi-square or Fisher exact tested proportion independence. For comparing mean values of 2 independent groups, a *t*-test was used, and for more than 2 groups, we used a one-way analysis of variance (ANOVA) test followed by Bonferroni test for "pairwise group comparisons." Relation analysis was used to show the strength and significance

of the association between quantitative variables. Logistic regression analysis showed which of the variables that relate to unfavorable response has an independent effect on the response to chemotherapy. *P*-value is always 2 tailed and significant at 0.05 level. Graphs were performed using Prism software program (GraphPad prism software, version 5, CA, USA).

RESULTS

The Demographic Characteristics and Treatment Response of CML Patients

Table 1 shows the demographic characteristics of 102 CML patients, and the study includes 47 males and 55 females with a mean age of 40.6 years with performance status (0 and 1) with normal liver and kidney laboratory functions. Only 7.8% of the patient has Eutos score ≥87 which indicating high risk. When correlating the demographic characteristics with the response, the only significant relation was between blood platelets and the response ($P = 0.047$). During the two years follow-up, 37 (36.6%) patients showed an unfavorable response (includes patients who do not achieve a molecular response and the patients who develop a progressive disease as an accelerated phase or blast crises). While the favorable responses were achieved in 64 (63.6%) patients and include patients who achieved complete molecular response (CMR), major molecular response (MMR) or complete cytogenetic response (CCyR) (**Table 2**).

Drug Level and Pharmacokinetic Data

The IM pharmacokinetic is considered as a one-compartment model. This model considers all body tissues and fluids as a part of this compartment. It assumes that the dose of drug distributes instantaneously to all body areas and a rapid drug equilibrium between the blood and tissue distribution and elimination occurs. In this study we used the formulae to calculate pharmacokinetic

TABLE 1 | Patient characteristics and response to therapy.

Characteristics		Total (*N* = 102)	Favorable response (*N* = 64)	Unfavorable response (*N* = 37)	*P*-value
Gender					0.636
Male	N (%)	47.0 (46.0%)	28 (43.8%)	18 (48.6%)	
Female	N (%)	55.0 (53.9%)	36 (56.3%)	19 (51.4%)	
Age (year)	Mean (SD)	40.6 (11.0)	40.9 (10.0)	40.0 (12.6)	0.629
PS					0.687
0	N (%)	99.0 (97.0%)	63 (98.4%)	35 (94.6%)	
1	N (%)	3.0 (2.9%)	1 (1.6%)	2 (5.4%)	
Smoking					0.093
Current smoker	N (%)	13 (12.7%)	5 (7.8%)	7 (18.9%)	
No smoking	N (%)	89 (87.2%)	59 (92.2%)	30 (81.1%)	
Other diseases other than CML	N (%)	35 (34.3%)	23 (35.9%)	12 (32.4%)	0.723
Hypertension	N (%)	8 (7.8%)			
Diabetes	N (%)	8 (7.8%)			
Others	N (%)	21 (20.5%)			
Administration of concomitant Drug	N (%)	26 (25.5%)	16 (25.0%)	10 (27.0%)	0.823
					0.938
Family history of cancer	N (%)	16 (15.7%)	10 (15.6%)	6 (16.2%)	
Eutos score					0.1
High risk	N (%)	8 (7.8%)	3 (4.7%)	5 (13.5%)	
Low risk	N (%)	94 (92.2%)	61 (95.3%)	32 (86.5%)	
Laboratory data at sampling time					
Hg (g/dl)	Mean (SD)	11.7 (1.9)	11.7 (1.7)	11.5 (2.1)	0.857
WBC (/mm^3)	Mean (SD)	5.7 (2.2–185.0)	5.7 (2.5–15.5)	5.6 (2.2–185.0)	0.413
platlet (/mm^3)	Median (Range)	186.5 (14.0–934.0)	197.5 (100–934)	152.5 (14.0–554)	0.047*
AST (IU)	Median (Range)	22 (11.7–115.4)	22.2 (12.0–68.0)	21 (11.7–115.4)	0.302
ALT (IU)	Median (Range)	18.2 (7.4–117.0)	19.0 (8.0–72.3)	17.6 (7.4–117.0)	0.766
Creatinine(mg/dl)	Median(Range)	0.9 (0.3–1.4)	0.9 (0.49–1.4)	0.8 (0.3–1.3)	0.117
Urea (mg/dl)	Median (Range)	24.0 (12.0–46.0)	23.6 (12.0–46.0)	24.0 (12.0–41.0)	0.884

*Hg, Hemoglobin; WBC, White Blood cell Count; PS, Performance Status; AST, Aspartate, aminotransferase; ALT, Alanine aminotransferase; SD, Standard Deviation; Eutos score: 7*basophils%+4*spleen size (distance from costal margin cm), high risk ≥ 87, low risk ≤ 87.*

TABLE 2 | Drug Doses and Response.

Characteristics		*N* = 102
Imatinib treatment dose		
400 mg	No of patients (%)	94 (92.1%)
300 mg	No of patients (%)	7 (6.8%)
200 mg	No of patients (%)	1 (0.98%)
BCR/ABL at sampling time		
Unfavorable Response	Mean (SD)	0.73 (1.37)
PD	Mean (SD)	1.45 (0.05)
NR	Mean (SD)	0.70 (1.38)
Favorable response	Mean (SD)	0.007 (0.01)
CMR	Mean (SD)	0 (0)
MMR	Mean (SD)	0.002 (0.002)
CCyR	Mean (SD)	0.04 (0.03)
Response after 1 year of follow-up		
Unfavorable Response	No of patients (%)	37 (36.6%)
PD	No of patients (%)	3 (8%)
NR	No of patients (%)	34 (92%)
Favorable response	No of patients (%)	64 (63.4%)
CMR	No of patients (%)	21 (33%)
MMR	No of patients (%)	34 (53%)
CCyR	No of patients (%)	9 (14%)
Response after 2 years of follow-up		
Unfavorable response	No of patients (%)	37 (36.6%)
PD	No of patients (%)	3 (8%)
NR	No of patients (%)	34 (92%)
Favorable response	No of patients (%)	64 (63.4%)
CMR	No of patients (%)	21 (33%)
MMR	No of patients (%)	32 (50%)
CCyR	No of patients (%)	11 (17%)

SD, Standard Deviation; FR, Favorable Response; UF, Unfavorable Response; PD, Progressive Disease; NR, No Response; CMR, Complete Molecular Response; MMR, Major Molecular Response; CCyR, Complete Cytogenetic Response.

parameters using two points, the trough and the peak (29). **Table 3** shows the levels of pharmacokinetic parameters of IM. The plasma IM peak level was 2,423 ± 902 ng/ml (mean ± SD), while the trough plasma level was 1,199 ± 506 ng/ml and peak/trough ratio (P/T) ratio were 2.4 ± 1.5. The peak concentration of the active N-des-methyl imatinib plasma level was 311.1 ± 129.2 ng/ml; the trough concentration was 208.8 ± 98.2 ng/ml. The second metabolite, pyridine -N-oxide imatinib, had a peak concentration of 37.0 ± 22.0 ng/ml and the trough concentration was 16.7 ± 12.6 ng/ml. Following the one-compartment model, the pharmacokinetic parameters of IM were the median (range), 0.034 (0.0005–0.11), the mean concentrations of steady (C_{SS}), volume of distribution (V_d) and clearance (Cl) of IM were 1,769 ± 689 ng/ml, 186 ± 81.7 L and 158 ± 147 L/h., respectively, **Table 3**.

Relation of Pharmacokinetic Parameters and Clinical Response

Logistic regression analysis was done where the favorable or unfavorable response was as the dependent variable and age, sex, IM dose, and trough level P/T ratio of IM and pyridine -N- oxide, K_e, and clearance as prognostic variables. The relation between different pharmacokinetic parameters and the clinical response to IM therapy is presented in **Table 3** and **Figure 1**. There was an insignificant relation between the demographic characteristics and IM dose with the response. The IM trough level among patients who achieved favorable response ($N = 64$) was significantly higher than those for patients who did not achieve favorable response ($N = 37$). The mean values of the trough level were 1,281 ± 578 ng/ml for responders vs. 935 ± 559 ng/ml for non-responders, respectively ($P = 0.006$). The P/T ratio of patients who achieved favorable response was significantly lower (2.06 ± 0.8) than those for patients who had an unfavorable response (2.8 ± 2.1) ($P = 0.001$) (**Table 3** and **Figure 1**). Similarly, the trough concentration of pyridine-N-oxide was significantly higher in patients who had favorable responses ($P = 0.01$). The elimination rate constant and the clearance are significantly higher in patients who achieve unfavorable responses ($P = 0.001$ and 0.004), respectively. After logistic regression analysis, the only significant independent factor affecting the response was the P/T ratio of IM. As the peak/trough ratio increased by one, the risk of bad response increased by more than double as compared to favorable response with 95% CI (1.28–3.92, $P = 0.005$).

Relation Between Genetic Polymorphism and Clinical Response

One hundred and two DNA samples were analyzed using PCR-RFLP displayed in **Supplement 2** and Logistic regression analysis was done where favorable or unfavorable response as was the dependent variable and gene polymorphism were the prognostic variables in the model, **Table 4**; **Figures 2**, **3**. The frequency distribution of the genes and their relation with response is illustrated in **Table 4**. The frequency distribution of the gene variant of the efflux transporter ABCG2.34 G>A among our patients was 81.4% with homozygous wild type GG allele, 16.7% with heterozygous GA allele, and 2% with the variant type AA, **Table 4**. Regarding the relation of the variant ABCG2. 34 G>A gene with response, it was found the patients with the wild allele GG had higher IM trough level ($P = 0.01$) lower Ke ($P = 0.005$) and clearance (Cl) ($P = 0.02$) **Figure 3** and linked to favorable response compared to (GA and AA alleles) (**Table 4**).

On the other hand, the frequencies of ABCG2. 421C >A were 89.2, 9.8, and 1% for the CC wild type, the CA heterozygous, and the AA variant, respectively. Concerning the genotype 421C >A, the homozygous CC had significantly higher peak, and C_{SS} of IM as well as higher peak level of desmethyl imatinib compared to the allele AA and CA ($P = 0.03$, $P = 0.05$, $P = 0.02$, respectively), **Figure 4**.

The frequency distribution of the efflux transporter gene variant of ABCB1. 3435C>T was 37.3% for the homozygous wild type CC, 47.1% for the heterozygous (CT), and 15.7% for the TT

TABLE 3 | Relation of Response with Pharmacokinetic Parameters.

	Unit	Total	Favorable response ($N = 64$)	Unfavorable response ($N = 37$)	*P*-value
		(Mean ± SD)	Mean ± SD	Mean ± SD	
IM level					
Peak	ng/ml	2,423 ± 902	2,378 ± 893	2,433 ± 927	0.45
Trough	ng/ml	1,199 ± 506	1,281 ± 578	935 ± 559	0.006*
P/T ratio		2.4 ± 1.5	2.06 ± 0.8	2.8 ± 2.1	0.001*
N-des-methyl imatinib					
Peak	ng/ml	311.1 ± 129.2	306 ± 131	320 ± 128	0.61
Trough	ng/ml	208.8 ± 98.2	217 ± 94	192 ± 104	0.22
P/T ratio		1.71 ± 1.33	1.51 ± 0.52	2.13 ± 2.09	0.095
Pyridine-N-oxide imatinib					
Peak	ng/ml	37.1 ± 22.0	38.2 ± 24.3	35.5 ± 17.2	0.52
Trough	ng/ml	16.8 ± 12.6	18.8 ± 14.2	13.2 ± 8.1	0.01*
P/T ratio		2.78 ± 2.13	2.06 ± 0.79	3.12 ± 2.09	0.008*
Pharmacokinetic parameters					
K_e		0.034 (0.0005–0.11)	0.029 ± 0.018	0.040 ± 0.021	< 0.001*
C_{SS}	ng/ml	1,769 ± 689	1,840 ± 679	1,684 ± 706	0.22
V_d	L	186 ±81.7	192 ± 89	166 ± 64	0.41
Cl	L/hr	158 ± 147	128 ± 137	175 ± 158	0.004*
Alph-1-acid gp	μg/ml	1.62 ± 0.52	1.62 ± 0.55	1.58 ± 0.44	0.68

**P value is significant ≤ 0.05.*

IM, Imatinib; K_e, elimination constant; C_{SS}, IM Steady State plasma Concentration; V_d, Volume of distribution; Cl, IM Clearance; P/T, Peak/Trough ratio.

variant type. The wild allele CC of ABCB1.3435C>T gene had significantly higher steady-state concentration compared to the two allele TT and CT ($P = 0.038$), **Figure 5A**.

In addition, the distribution of ABCB1. 1,236 C>T was 35.3% for TT allele, 48% CT, and 16.7% for CC allele. The relation of 1,236 C>T gene polymorphism with pharmacokinetic parameters, a significant lower N-des-methyl imatinib trough plasma level in heterozygous CT genotype compared to homozygous CC and TT ($P = 0.004$), **Figure 5B**.

On the other hand, the frequency distribution of homozygous wild type GG of ABCB1.2677 G>A/T was 99%, and the heterozygous frequency GT was 1%, and no patients with the homozygous variant type (AA or TT) were detected, **Table 4**.

The intake transporter SLCO1B3.334 T>G, known as organic anion-transporting polypeptide 1B3 (OATP1B3), had the following distribution: 7.1% TT, 31.3% TG, and 61.6% GG. The alleles GG and TG of the gene variant SLCO1B3. 334 T>G were significantly correlated to favorable response while wild allele TT was linked to unfavorable response ($P = 0.03$), **Figure 2**.

In the genotypes of metabolizing enzyme CYP3A5, the frequency distribution was as follows: the homozygous wild variant (*1) 5.9%, heterozygous (*1/3) 27.5%, and the homozygous variant (*3) 66.7%.

Our results did not detect association of the three variants of ATP-binding cassette, subfamily B1 and ABCG2 421C >A, and metabolizing enzyme CYP3A5 with IM response.

Relation of Adherence and Response

Parametric relation analysis of drug response according to adherence score was illustrated in **Supplement 3**. The median (range) of MMAS knowledge in the patients who achieved favorable response and the patients who suffering unfavorable response was the same 3 (1–3), the MMAS motivation was 3 (1–3), and 2 (1–3), respectively, and the total adherence score was the same 5 (2–6) with no statistical significance.

The Most Recorded Side Effects of IM

The recorded side effects of the administered dose of IM was illustrated in **Supplement 4**. Our result showed 29 (28.4%) patients did not suffer from any side effect; however, the most common side effects were gastrointestinal disorder 24 (23.4%), followed by musculoskeletal disorders 21 (20.5%) and nervous system disorders 21 (20.5%). The gastrointestinal disorders include heartburn 3.0 (2.9%), tooth pain 4.0 (3.9%), visceral pain 15.0 (14.7%), and vomiting 2.0 (1.9%). In addition to fatigue, inflammation disorders, weight were recorded in 7 (6.8%), 4 (3.9%), and 4 (3.9%), respectively.

DISCUSSION

Imatinib is the current treatment standard of care for CML disease; it induces durable responses and prolongs event and progression-free survival (30). The individual variability in IM pharmacokinetics often leads to an unsatisfactory clinical

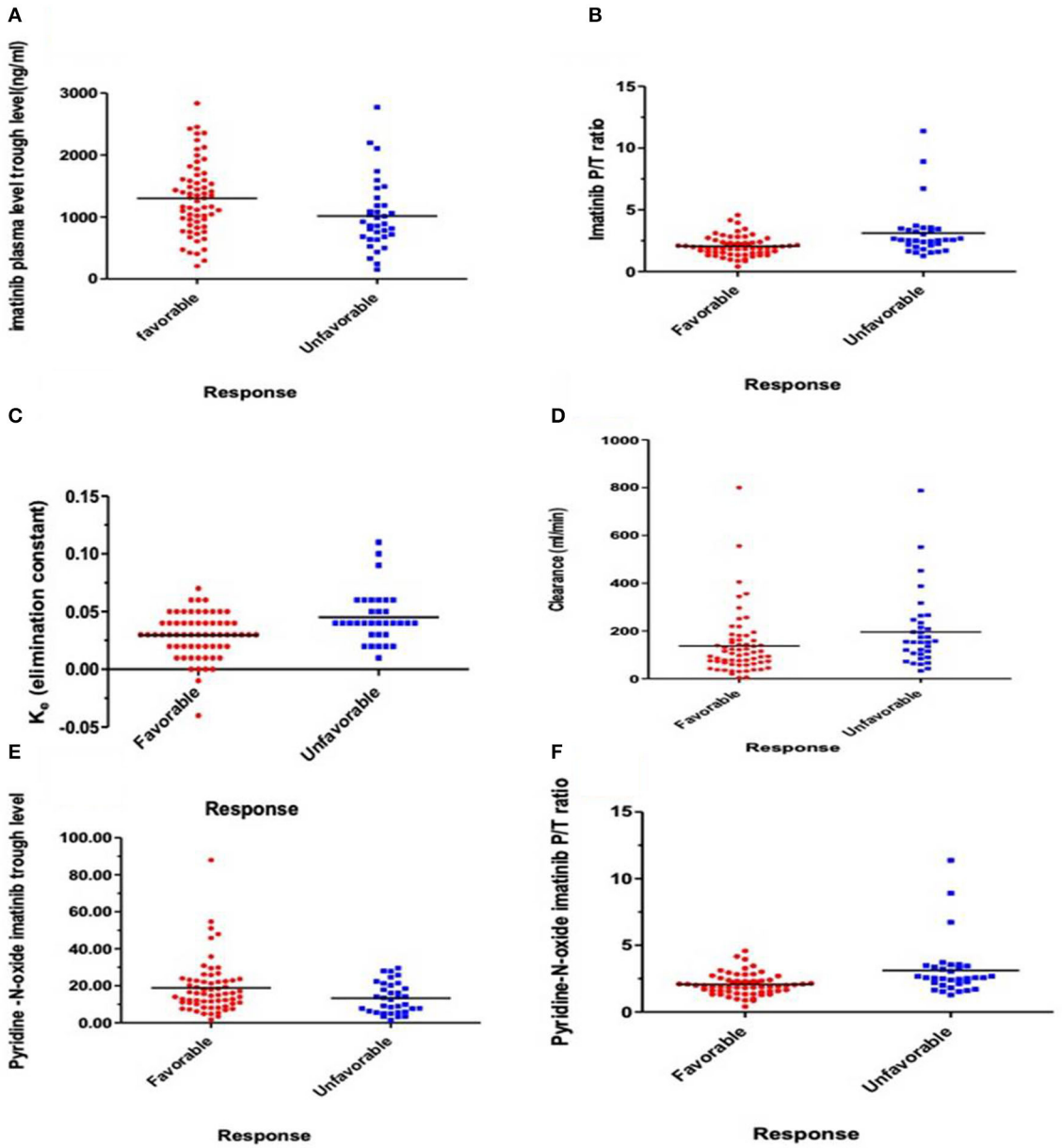

FIGURE 1 | Relations express the relation between response and pharmacokinetic parameters. **(A)** Plasma IM trough concentration (ng/ml) ($P = 0.006$), **(B)** IM peak/trough ratio (P/T) ($P = 0.001$), **(C)** Elimination rate constant (K_e) ($P = 0.001$), **(D)** IM clearance (ml/min) ($P = 0.004$), **(E)** Plasma trough of Pyridine-N-oxide imatinib ($P = 0.01$), and **(F)** Peak/Trough ratio (P/T) Pyridine-N-oxide imatinib ($P = 0.008$).

outcome in patients with CML (31). The results of the present study added a great value to the importance of implementing routine therapeutic drug monitoring (TDM) for better management of CML patients treated with IM for dose adjustment. Data of the present study showed a significant higher trough IM (1281 ng/ml) ($P = 0.006$), lower P/T ratio ($P = 0.001$), lower clearance (Cl) ($P = 0.004$), and elimination rate constant, k_e ($P = 0.001$), among patients who achieved favorable responses ($N = 64$) than those for patients who suffered unfavorable responses (935 ng/ml) ($N = 37$). It was reported that patients with trough concentration over 1,002 ng/ml of IM were good responders and were significantly associated with achieving MMR (32–34). Contrary to the previous studies, IM trough concentration was not significantly associated with the molecular response in Chinese CML patients (35) that was referred to ethnic metabolic distinction of Chinese compared to Caucasian CML patients group (36).

The present study is the first to report an association of Peak/Trough ratio of IM with the response. The P/T ratio was the only significant independent factor affecting

TABLE 4 | Relation between Genetic Polymorphism and Clinical Response.

		The frequency	Response		*P* value
			Favorable N (row %)	Unfavorable N (row %)	
ABCG2.34 G>A	GG	83 (81.4%)	57 (69.5%)	25 (30.5%)	0.01*
	GA	17 (16.7%)	7 (41.2%)	10 (58.8%)	
	AA	2 (2%)		2 (100.0%)	
ABCG2. 421C>A	CC	91 (89.2%)	55 (60.4%)	36 (39.6%)	0.20
	CA	10 (9.8%)	8 (88.9%)	1 (11.1%)	
	AA	1 (1%)	1 (100.0%)		
ABCB1.2677 G>A/T	GG	101(99%)	64 (64.0%)	36 (36.0%)	0.37
	GA	1 (1%)		1 (100.0%)	
	AA	0 (0%)			
	TT	0 (0%)			
ABCB1.1236 C>T	CC	17 (16.7%)	10 (58.8%)	7 (41.2%)	0.47
	CT	49 (48%)	34 (69.4%)	15 (30.6%)	
	TT	36 (35.3%)	20 (57.1%)	15 (42.9%)	
ABCB1.3435C>T	CC	38 (37.3%)	21 (56.8%)	16 (43.2%)	0.51
	CT	48 (47.1%)	33 (68.8%)	15 (31.3%)	
	TT	16 (15.7%)	10 (62.5%)	6 (37.5%)	
SLCO1B3.334 T>G	TT	7 (7.1%)	1 (16.7%)	5 (83.3%)	0.03*
	TG	31 (31.3%)	23 (74.2%)	8 (25.8%)	
	GG	61 (61.6%)	39 (63.9%)	22 (36.1%)	
CYP3A5	*1	6 (5.9%)	3 (50.0%)	3 (50.0%)	0.83
	*1/3	28 (27.5%)	18 (64.3%)	10 (35.7%)	
	*3	68 (66.7%)	43 (64.2%)	24 (35.8%)	

G, guanine; C, cytosine; A, adenine; T, thiamine; ABCB1, multidrug resistant gene; ABCG2, breast cancer resistant gene; SLCO1B3, uptake gene; CYP3A5, cytochrome metabolizing gene.
**p value is significant ≤ 0.05.*

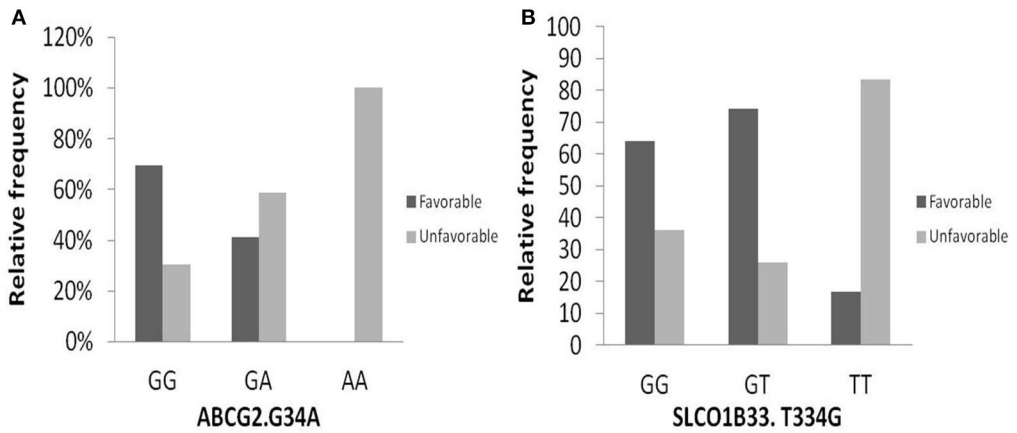

FIGURE 2 | Relation of relative frequency of the gene variant ABCG2. 34 G>A and SLCO1B3. 334 T>G with response. **(A)** ABCG2. 34 G>A gene, **(B)** SLCO1B3. 334 T>G gene.

the response, as the P/T ratio increased by one, the risk of unfavorable response increased by more than double as compared to favorable response with 95% CI (1.28–3.92, $P = 0.005$). Moreover, like our results of IM, the trough concentration of Pyridine-N-oxide imatinib was significantly higher ($P = 0.01$) and its P/T ratio was significantly lower ($P = 0.008$) in patients achieved favorable response than those without. Up until now, we did not find any previous data

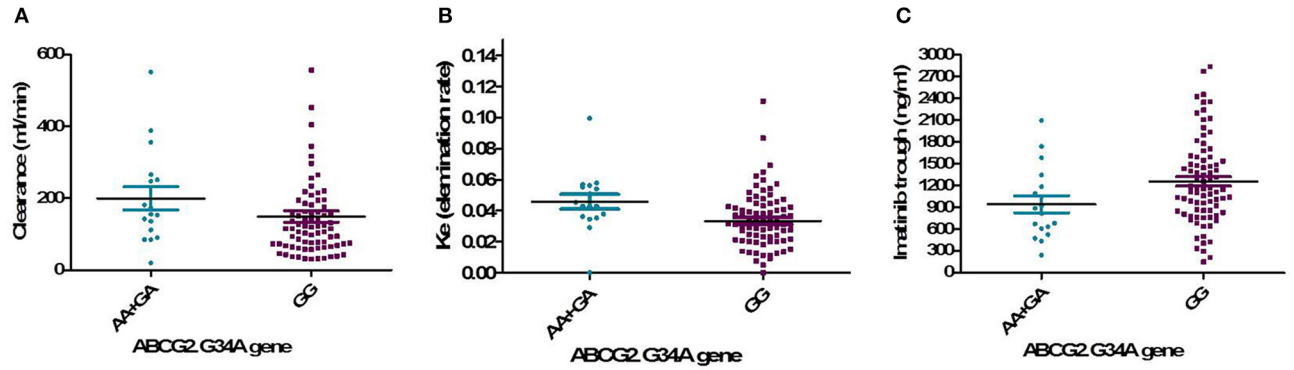

FIGURE 3 | Relation of the genotype variant ABCG2. 34 G>A gene with pharmacokinetic parameters. **(A)** IM clearance ($P = 0.02$), **(B)** K_e, elimination rate constant ($P = 0.005$), **(C)** IM trough plasma concentration ($P = 0.01$).

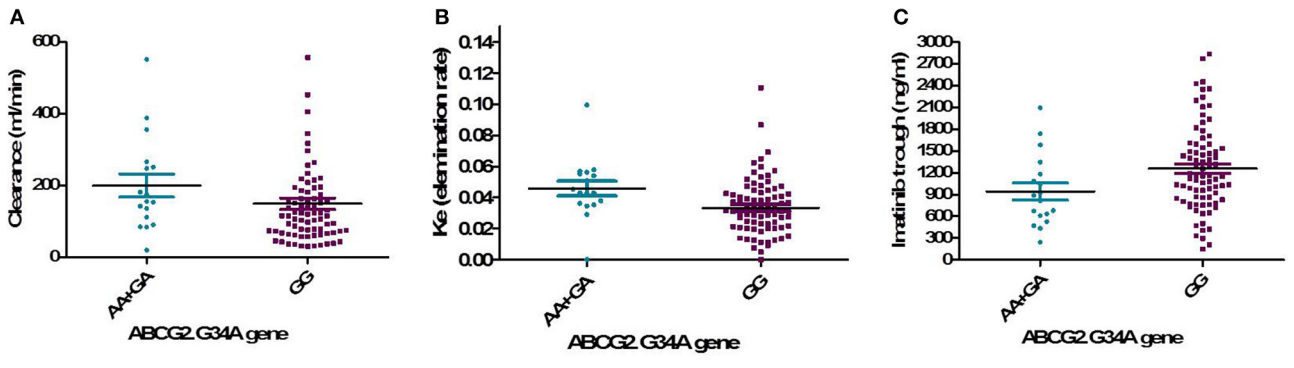

FIGURE 4 | Relation of the genotype variant ABCG2. 421C >A with pharmacokinetic parameters. **(A)** Plasma IM peak concentration (ng/ml) ($P = 0.03$), **(B)** IM steady state concentration (ng/ml) ($P = 0.05$), **(C)** Peak of N-des-methyl IM (ng/ml) ($P = 0.02$).

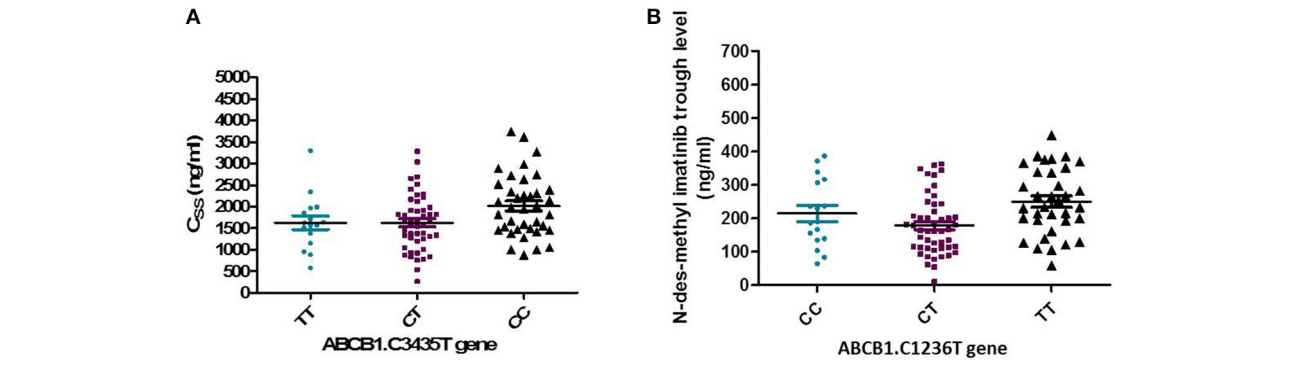

FIGURE 5 | Relation of ABCB1. 3435C>T and 1236 C>T gene with pharmacokinetics of Imatinib. **(A)** Association of ABCB1. 3435C>T with the steady state concentration (ng/ml) ($P = 0.038$). **(B)** Association of ABCB1. 1236 C>T gene with trough concentration of N-des-methyl imatinib (ng/ml) ($P = 0.004$).

about the biological activity or the relation of the level of this metabolite with the response to IM. However, limited information about the biological activity of pyridine-N-oxide metabolite as it has some activity, we suggest that the Pyridine-N-oxide imatinib may be a final product due to the action of other types of cytochromes on IM or it may pass certain pathways that lead to its activation. In addition, great variability in Cl, the volume of distribution, and elimination half-life ($T_{1/2}$) of IM were reported in previous studies as well as in our study. The variability in Cl of IM was ∼73% and the volume of distribution was 63% (37). These differences in pharmacokinetics parameters may be related to demographic covariates as hepatic and renal dysfunction, body weight, age, sex, and disease state (38).

The interindividual Pharmacogenetic variability can affect IM disposition and its metabolism leading to differences in drug responses (7). The ABCG2 gene encodes a membrane-bound protein and acts as a xenobiotic transporter which may have a role in drug resistance to chemotherapeutic agents, including IM (14). In this study, the distribution frequency of ABCG2 the genotype 34 G>A was GG (81.4%), GA (16.7%), and AA (2%), and the GG allele was associated with favorable response ($P = 0.01$), lower Cl, K_e, and higher trough IM than both (AA+GA) alleles. Our result was supported by the study of Delord et al. (15) who reported the GG genotype had favorable response compared to genotypes AA and GA. On the other hand, a Canadian study found that the GG genotype 34 G>A was significantly correlated with unfavorable response to IM especially for CCyR (16). These diversities of findings may be due to ethnic variability.

The current data showed that the wild allele (CC) of the genotype ABCG2 421C >A had significantly higher plasma peak of IM ($P = 0.03$), higher C_{ss} ($P = 0.049$), and higher N-des-methyl imatinib ($P = 0.02$). However, a previous study found that the CC genotype was higher significantly in IM resistant group ($P = 0.004$), and the CA genotype was higher with favorable response ($P = 0.0001$) (26). Moreover, Takahashi et al. (13) found that AA of the genotype had significantly higher IM trough concentration ($P = 0.015$), while Jiang et al. (34) disclosed a relation of patient with AA genotype and higher rate of MMR.

The ABCB1 gene, one of the ABC superfamily, encodes for a transmembrane glycoprotein (P-glycoprotein) capable of pumping IM out of the tumor cell (12). Its overexpression may offer resistance to IM in the cell lines model and at the clinical level (17). In the current work, the distribution frequency of the gene ABCB1.3435C>T among our patients was 37.3% (CC), 47.1% (CT), and 15.7% (TT), and the variant TT and CT had significantly lower C_{ss} IM compared to CC genotype ($P = 0.038$). No significant relation was detected between the ABCB1 3435C>T and response. Similarly, previous studies of Kim et al. (16), Polillo et al. (18), and Jiang et al. (34) did not find a relation of the genotype 3435C>T and response. Contrary to the previous studies and our results, Angelini et al. (19) denoted a significant association of (CC) genotype with CMR in Caucasians patients while the TT genotype was higher in IM resistant CML patients (26). Moreover, patients with the (CC) genotype were found to have significantly higher IM clearance ($P = 0.035$) (20) and had a poor cytogenetic response (21).

Our data revealed the variant ABCB1.1236 C>T had a distribution frequency of 16.7% (CC), 48%CT, 35.3%TT, a significantly higher Css (ng/ml) in CC carriers than those carrying the homozygous TT genotype and the heterozygous CT genotype ($P = 0.038$). The heterozygous CT variant of ABCB1. 1236 C>T, had significantly lower N-des-methyl imatinib trough than CC and TT ($P = 0.004$). On the other hand, a previous study reported an association between 1236 C>T (TT/CT) and higher MMR rates (22). The variations in frequencies are ethnically related (39).

Concerning the frequency distribution of the ABCB1 2677 G>A/T gene, it showed 99% (GG), and 1% (GA). Our result is in agreement with a previous study that revealed a significantly lower frequency of TT genotype in Egyptian CML patients. On the contrary to our results, they reported optimal and suboptimal responses in patients with TT genotype; however, GG genotype had no association with drug response (40). It was suggested that these contradictions may be due to the presence of different amino acids at position 893. The SNP 2677 G>A/T (TT) in exon 21 (893 codon) results in substitution of alanine lipophilic residue to serine/threonine hydrophilic residue resulting higher resistance to various drugs such as Adriamycin and vinblastine (41).

The organic anion transporting polypeptides OATP1B3 was suggested to mediate the uptake of IM into cells. Therefore, it is suggested that *SLCO1B3*.334 T>G genotype may have a clinical importance in IM treatment outcome prediction. Our data showed a significant association of the genotype TT of SLCO1B3 334 T>G with higher risk of unfavorable response ($P = 0.03$), while the patients with (GT/GG) genotypes showed a higher probability of achieving a favorable response ($P = 0.03$). Our finding agrees with the study of Nair et al. (42). Contrary to the previous result, the (TT) genotype was more frequent in the responder group ($P = 0.042$) and carriers of (TG/GG) genotypes were more frequent in the non-responder group (43). Moreover, no association was found between SLCO1B3.334 T>G polymorphism and response to IM therapy ($P = 0.938$) (27).

The genotype frequency fraction of the CYP3A5 gene is different in different ethnic populations. In Japanese it was 23.25% (1*), 76.75% (3*), in Caucasian it was 14.81% (1*), 85.19% (3*). In our study, the genotype distribution of CYP3A5 was 5.9% for (1*) allele, 27.5% for (1/3*) allele, 66.7% for (3*) allele. Our data are supported by previous Egyptian study found that the fraction of (*3) allele was (50%) and the (*1) allele was the least frequent (12.5%). Although the authors found that the CYP3A5*3 gene polymorphism was linked to unfavorable outcome ($P < 0.001$) (27), contrary to our result that did not detect an association between CYP3A5 gene as and pharmacokinetic parameters or response. Similarly, to our data, Takahashi et al. (13) and Ankathil et al. (44) reported insignificant relations between CYP3A5 gene polymorphism and IM trough concentration ($P = 0.645$). Despite the important role of CYP activity in the regulation of IM metabolism, it may be due to its activity and not the rate-limiting step in IM metabolism and excretion (45).

In conclusion, the current study is the first to disclose the novel relations of the high trough, a low P/T ratio of IM and its metabolite, pyridine -N-oxide imatinib to good IM response, as well as to reveal that the only independent prognostic marker IM response is P/T ratio of IM. Moreover, the association of the genotypes ABCG2.34 G>A and SLCO13.334 T>G with IM favorable response in Egyptian CML patients.

Future studies with larger patients' numbers are necessary to validate these findings, including the assessment of patients' compliance with more than one method, confirmation of the different types of genotypes of polymorphism by gene expression, as well as recording the drug toxicity and its relation with IM kinetics and polymorphism.

DATA AVAILABILITY STATEMENT

All datasets generated for this study are included in the article/**Supplementary Material**.

ETHICS STATEMENT

The studies involving human participants were reviewed and approved by the Institution Review Board (IRB) of the National Cancer Institute of Cairo University, Egypt with acceptance number IRB00004025. The patients/participants provided their written informed consent to participate in this study in accordance with the Declaration of Helsinki.

AUTHOR CONTRIBUTIONS

MO performed sample collection, the experimental work, and drafted the paper. RA help in patient follow-up and revised the manuscript. HM helped in experimental work and revised the manuscript. NA performed data statistical analysis. SS designed the experimental work and revised the manuscript. All authors contributed to revising the manuscript and approved it.

FUNDING

The authors thank the National Cancer Institute, Cairo University for funding the research.

ACKNOWLEDGMENTS

The authors of the manuscript acknowledge the National Cancer Institute, Cairo University for providing the facility for carrying this study.

SUPPLEMENTARY MATERIAL

The Supplementary Material for this article can be found online at: https://www.frontiersin.org/articles/10.3389/fonc.2020.01348/full#supplementary-material

REFERENCES

1. Goldman JM, Melo JV. Chronic myeloid leukemia: advances in biology and new approaches to treatment. *N Engl J Med.* (2003) 349:1451–64. doi: 10.1056/NEJMra020777
2. Quintás-Cardama A, Cortes JE. Chronic myeloid leukemia: diagnosis and treatment. *Mayo Clin Proc.* (2006) 81:973–88. doi: 10.4065/81.7.973
3. Hehlmann R, Berger U, Hochhaus A. Chronic myeloid leukemia: a model for oncology. *Ann Hematol.* (2005) 84:487–97. doi: 10.1007/s00277-005-1039-z
4. Kantarjian H, Sawyers C, Hochhaus A, Guilhot, F, Schiffer C, Gambacorti-Passerini C, et al. Hematologic and cytogenetic responses to imatinib mesylate in chronic myelogenous leukemia. *N Engl J Med.* (2002) 346:645–52. doi: 10.1056/NEJMoa011573
5. García-Gutiérrez V, Hernández-Boluda JC. Tyrosine kinase inhibitors available for chronic myeloid leukemia: efficacy and safety. *Front Oncol.* (2019) 9:1–10. doi: 10.3389/fonc.2019.00603
6. Peng B, Loyd P, Schran H. Clinical pharmacokinetics of imatinib. *Clin Pharmacokinet.* (2005) 444:879–94. doi: 10.2165/00003088-200544090-00001
7. Eechoute K, Sparreboom A, Burger H, Franke RM, Schiavon G, Verweij J, et al. Drug transporters and imatinib treatment: implications for clinical practice. *Clin Cancer Res.* (2011) 17:406–15. doi: 10.1158/1078-0432.CCR-10-2250
8. Wojnowski L. Genetics of the variable expression of CYP3A in humans. *Ther Drug Monit.* (2004) 26:192–9. doi: 10.1097/00007691-200404000-00019
9. Mlejnek P, Dolezel P, Faber E, Kosztyu P. Interactions of N-desmethyl imatinib, an active metabolite of imatinib, with P-glycoprotein in human leukemia cells. *Ann Hematol.* (2011) 90:837–42. doi: 10.1007/s00277-010-1142-7
10. Filppula AM, Laitila J, Neuvonen PJ, Backman JT. Potent mechanism-based inhibition of CYP3A4 by imatinib explains its liability to interact with CYP3A4 substrates. *Br J Pharmacol.* (2012) 165:2787–98. doi: 10.1111/j.1476-5381.2011.01732.x
11. Hu S, Franke RM, Filipski KK, Hu C, Orwick SJ, de Bruijn EA, et al. Interaction of imatinib with human organic ion carriers. *Clin Cancer Res.* (2008) 14:3141–9. doi: 10.1158/1078-0432.CCR-07-4913
12. Dohse M, Scharenberg C, Shukla S, Robey RW, Volkmann T, Deeken JF, et al. Comparison of ATP-binding cassette transporter interactions with the tyrosine kinase inhibitors imatinib, nilotinib and dasatinib. *Drug Metab Disposit.* (2010) 38:1371–80. doi: 10.1124/dmd.109.031302
13. Takahashi N, Miura M, Scott SA, Kagaya H, Kameoka Y, Tagawa H, et al. Influence of CYP3A5 and drug transporter polymorphisms on imatinib trough concentration and clinical response among patients with chronic phase chronic myeloid leukemia. *J Human Genet.* (2010) 55:731–7. doi: 10.1038/jhg.2010.98
14. Doyle LA, Ross DD. Multidrug resistance mediated by the breast cancer resistance protein BCRP (ABCG2). *Oncogene.* (2003) 22:7340–58. doi: 10.1038/sj.onc.1206938
15. Delord M, Rousselot P, Cayuela JM, Sigaux F, Guilhot J, Preudhomme C, et al. High imatinib dose overcomes insufficient response associated with ABCG2 haplotype in chronic myelogenous leukemia patients. *Oncotarget.* (2013) 4:1582–91. doi: 10.18632/oncotarget.1050
16. Kim DH, Sriharsha L, Xu W, Kamel-Reid S, Liu X, Siminovitch K, et al. Clinical relevance of a pharmacogenetic approach using multiple candidate genes to predict response and resistance to imatinib therapy in chronic myeloid leukemia. *Clin Cancer Res.* (2009) 15:4750–8. doi: 10.1158/1078-0432.CCR-09-0145
17. Ghallab O, Hamed NAM, El Shafei S, Abo Elwafa R, Sherif S. MDR1 gene polymorphism and outcome in egyptian chronic myeloid leukaemia patients. *J Cancer Biol Res.* (2015) 3:1062–70.
18. Polillo M, Galimberti S, Baratè C, Petrini M, Danesi R, Di Paolo A, et al. Pharmacogenetics of BCR/ABL inhibitors in chronic myeloid leukemia. *Int J Mol Sci.* (2015) 16:22811–29. doi: 10.3390/ijms160922811
19. Angelini S, Soverini S, Ravegnini G, Barnett M, Turrini E, Thornquist M, et al. Association between imatinib transporters and metabolizing enzymes genotype and response in newly diagnosed chronic myeloid leukemia patients receiving imatinib therapy. *Haematologica.* (2013) 98:193–200. doi: 10.3324/haematol.2012.066480
20. Yamakawa Y, Hamada A, Nakashima R, Yuki M, Hirayama C, Kawaguchi T, et al. Association of genetic polymorphisms in the influx transporter SLCO1B3 and the efflux transporter ABCB1 with imatinib pharmacokinetics in patients with chronic myeloid leukemia. *Ther Drug Monit.* (2011) 33:244–50. doi: 10.1097/FTD.0b013e31820beb02
21. Salimizand H, Amini S, Abdi M, Ghaderi B, Azadi NA. Concurrent effects of ABCB1 C3435T, ABCG2 C421A, and XRCC1 Arg194Trp genetic polymorphisms with risk of cancer, clinical output, and response to treatment with imatinib mesylate in patients with chronic myeloid leukemia. *Tumor Biol.* (2016) 37:791–8. doi: 10.1007/s13277-015-3874-4
22. Dulucq S, Bouchet S, Turcq B, Lippert E, Etienne G, Reiffers J, et al. Multidrug resistance gene (MDR1) polymorphisms are associated with major molecular responses to standard-dose imatinib in chronic myeloid leukemia. *Blood.* (2008) 112:2024–31. doi: 10.1182/blood-2008-03-147744
23. Baccarani M, Deininger MW, Rosti G, Hochhaus A, Soverini, S, Apperley JF, et al. European leukemianet recommendations for

the management of chronic myeloid leukemia: 2013. *Blood*. (2013) 122:872–84. doi: 10.1182/blood-2013-05-501569
24. Hughes TP, Kaeda J, Branford S. Frequency of major molecular responses to imatinib or interferon alfa plus cytarabine in newly diagnosed chronic myeloid leukemia. *N Engl J Med*. (2003) 349:1423–32. doi: 10.1056/NEJMoa030513
25. Titier K, Picard S, Ducint D, Teilhet E, Moore N, Berthaud P, et al. Quantification of imatinib in human plasma by high-performance liquid chromatography-tandem mass spectrometry. *Therap Drug Monitor*. (2005) 27:634–40. doi: 10.1097/01.ftd.0000175973.71140.91
26. Anthony A, Ankathil R, Ai-Sim G, Fadilah SA, Baba AA. Influence of ABCB1 C3435T and ABCG2 C421A gene polymorphisms in response to imatinib mesylate in chronic myeloid leukemia patients. *Int J Environ Sci Dev*. (2012) 3:274–8. doi: 10.7763/IJESD.2012.V3.230
27. Bedewy AML, El-Maghraby SM. Do SLCO1B3 (T334G) and CYP3A5*3 polymorphisms affect response in Egyptian chronic myeloid leukemia patients receiving imatinib therapy? *Hematology*. (2013) 18:211–7. doi: 10.1179/1607845412Y.0000000067
28. Morisky DE, Ang A, Krousel-Wood M, Ward HJ. Predictive validity of a medication adherence measure in an outpatient setting. *J Clin Hypertens*. (2008) 10:348–53. doi: 10.1111/j.1751-7176.2008.07572.x
29. Jambhekar SS, Breen P. *Intravenous Bolus Administration (One Compartment Model) in Pharmacokinetics Basic*. 2nd edition. Bradenton, FL: Pharmaceutical press (2012). p. 29–55.
30. Bhamidipati PK, Kantarjian H, Cortes J, Cornelison AM, Jabbour E. Management of imatinib-resistant patients with chronic myeloid leukemia. *Therap Adv Hematol*. (2013) 4:103–17. doi: 10.1177/2040620712468289
31. Levêque D, Maloisel F. Clinical pharmacokinetics of imatinib mesylate. *In Vivo*. (2005) 19:77–84. doi: 10.1200/JCO.2005.05.246
32. Picard S, Titier K, Etienne G, Teilhet E, Ducint D, Bernard MA, et al. Trough imatinib plasma levels are associated with both cytogenetic and molecular responses to standard dose imatinib in chronic myeloid leukemia. *Blood*. (2007) 109:3496–9. doi: 10.1182/blood-2006-07-036012
33. Guilhot F, Hughes TP, Cortes J, Druker BJ, Baccarani M, Gathmann I, et al. Plasma exposure of imatinib and its correlation with clinical response in the tyrosine kinase inhibitor optimization and selectivity trial. *Haematologica*. (2012) 97:731–8. doi: 10.3324/haematol.2011.045666
34. Jiang ZP, Zhao XL, Takahashi N, Angelini S, Dubashi B, Sun L, et al. (2017). Trough concentration and ABCG2 polymorphism are better to predict imatinib response in chronic myeloid leukemia: a meta-analysis. *Pharmacogenomics*. 18:35–56. doi: 10.2217/pgs-2016-0103
35. Li Q, Chen C, Chen Z, Wang H, Wu Y, You Y, et al. Imatinib plasma trough concentration and its correlation with characteristics and response in Chinese CML patients. *Acta Pharmacol Sinica*. (2010) 31:999–1004. doi: 10.1038/aps.2010.79
36. Zhu Y, Qian S. Clinical efficacy and safety of imatinib in the management of Ph+ chronic myeloid or acute lymphoblastic leukemia in Chinese patients. *OncoTargets Therap*. (2014) 7:395–404. doi: 10.2147/OTT.S38846
37. Judson I, Ma P, Peng B, Verweij J, Racine A, di Paola ED, et al. Imatinib pharmacokinetics in patients with gastrointestinal stromal tumour: a retrospective population pharmacokinetic study over time. EORTC soft tissue and bone sarcoma group. *Cancer Chem Therap Pharmacol*. (2005) 55:379–86. doi: 10.1007/s00280-004-0876-0
38. Widmer N, Decosterd LA, Csajka C, Leyvraz S, Duchosal MA, Rosselet A et al. Population pharmacokinetics of imatinib and the role of α1-acid glycoprotein. *Br J Clin Pharmacol*. (2006) 62:97–112. doi: 10.1111/j.1365-2125.2006.02719.x
39. Cropp C, Yee S, Giascomini K. Genetic variation in drug transporters in ethnic populations. *Clin Pharmacol Therap*. (2008) 84:412–6. doi: 10.1038/clpt.2008.98
40. Elghannam DM, Ibrahim L, Ebrahim MA, Azmy E, Hakem H. Association of MDR1 gene polymorphism (G2677T) with imatinib response in Egyptian chronic myeloid leukemia patients. *Hematology*. (2014) 19:123–31. doi: 10.1179/1607845413Y.0000000102
41. Kim RB, Leake BF, Choo EF, Dresser GK, Kubba SV, Schwarz UI, et al. Identification of functionally variant MDR1 alleles among European Americans and African Americans. *Clin Pharmacol Therap*. (2001) 70:189–99 doi: 10.1067/mcp.2001.117412
42. Nair D, Dhangar S, Shanmukhaiah C, Vundinti BR. Association of genetic polymorphisms of the ABCG2, ABCB1, SLCO1B3 genes and the response to Imatinib in chronic myeloid leukemia patients with chronic phase. *Meta Gene*. (2017) 11:14–9. doi: 10.1016/j.mgene.2016.11.002
43. Neul C, Schaeffeler E, Sparreboom A, Laufer S, Schwab M. Impact of membrane drug transporters on resistance to small-molecule tyrosine kinase inhibitors. *Trends Pharmacol Sci*. (2016) 37:904–32. doi: 10.1016/j.tips.2016.08.003
44. Ankathil R, Zian AA, Nizam ZM, Azlan H, Baba AA. P0223 CYP3A4*18 and CYP3A5*3 gene polymorphisms and imatinib resistance in Malaysian patients with chronic myeloid leukaemia. *Eur J Cancer*. (2014) 50:71–2. doi: 10.1016/j.ejca.2014.03.267
45. Skoglund K, Richter J, Olsson-Strömberg U, Bergquist J, Aluthgedara W. *In vivo* cytochrome P450 3A isoenzyme activity and pharmacokinetics of imatinib in relation to therapeutic outcome in patients with chronic myeloid leukemia. *Therap Drug Monitor*. (2016) 38:230–8. doi: 10.1097/FTD.0000000000000268

Conflict of Interest: The authors declare that the research was conducted in the absence of any commercial or financial relationships that could be construed as a potential conflict of interest.

frontiers in Pharmacology

ORIGINAL RESEARCH
published: 25 September 2020
doi: 10.3389/fphar.2020.571143

Metabolic Reprogramming of Sulfur in Hepatocellular Carcinoma and Sulfane Sulfur-Triggered Anti-Cancer Strategy

Ximing Zhang[1], Mianrong Chen[1], Xiang Ni[2], Yingying Wang[3], Xue Zheng[1], Hui Zhang[1], Shi Xu[2] and Chun-tao Yang[1]**

[1] Affiliated Cancer Hospital & Institute of Guangzhou Medical University, Guangzhou Municipal and Guangdong Provincial Key Laboratory of Protein Modification and Degradation, School of Basic Medical Science, Guangzhou Medical University, Guangzhou, China, [2] Department of Chemistry, Brown University, Providence, RI, United States, [3] Department of Chemistry, Washington State University, Pullman, WA, United States

OPEN ACCESS

Edited by:
Qi Zeng,
Xidian University, China

Reviewed by:
Hui Xie,
Xidian University, China
Wen Zhou,
Guangzhou University of Chinese Medicine, China

***Correspondence:**
Chun-tao Yang
cyang@gzhmu.edu.cn
orcid.org/0000-0002-5640-0930
Shi Xu
shi_xu@brown.edu
orcid.org/0000-0002-4325-6503

Specialty section:
This article was submitted to Pharmacology of Anti-Cancer Drugs, a section of the journal Frontiers in Pharmacology

Received: 10 June 2020
Accepted: 01 September 2020
Published: 25 September 2020

Citation:
Zhang X, Chen M, Ni X, Wang Y, Zheng X, Zhang H, Xu S and Yang CT (2020) Metabolic Reprogramming of Sulfur in Hepatocellular Carcinoma and Sulfane Sulfur-Triggered Anti-Cancer Strategy. Front. Pharmacol. 11:571143. doi: 10.3389/fphar.2020.571143

Metabolic reprogramming is a cancer hallmark. Although the reprogramming of central carbon has been well documented, the role of sulfur metabolism has been largely overlooked. Additionally, the effects of sulfur are sometimes contradictory in tumorigenesis. In this study, we aimed to investigate the gene expression profile in hepatocellular carcinoma (HCC) and the effects of reactive sulfur species (RSS) on HCC tumor cells. Furthermore, the cell imaging technology was applied to discover some potential anti-cancer compounds. Gene Set Enrichment Analysis (GSEA) of Gene Expression Omnibus (GEO) dataset (GSE102083) revealed that sulfur amino acid-related metabolism and vitamin B_6 binding activity in HCC tissues were downregulated. Calculation of the interaction network identified nine hub genes, among which eight were validated by differential expression and survival analysis in the TCGA_LIHC cohort, and two (CSE and CBS) had the highest enrichment degree. The metabolomics analysis suggested that the hub genes were associated with RSS metabolism including H_2S, H_2S_2, cystine, cysteine, homocysteine, cystathionine, and methionine. The cell viability assay demonstrated that H_2S_2 had significant anti-cancer effects in HCC SNU398 tumor cells. The cell imaging assay showed that treatment with H_2S_2 remarkably increased intracellular sulfane sulfur content. On this basis, the anti-cancer activity of some other sulfane sulfur compounds, such as DATS and DADS, was further verified. Lastly, according to the fact that HCC tumor cells preferentially take in cystine due to high expression of SLC7A11 (a cystine/glutamate transporter), persulfided cysteine precursor (PSCP) was tested for its sulfane sulfur release capability and found to selectively inhibit HCC tumor cell viability. Collectively, this study uncovered sulfur metabolism in HCC was reprogrammed, and provided a potential therapeutic strategy for HCC by donating sulfane sulfur.

Keywords: bioinformatics, hepatocellular carcinoma, metabolic reprogramming, reactive sulfur species, sulfane sulfur

INTRODUCTION

In liver cancer, hepatocellular carcinoma (HCC) is the most common primary malignancy, which has been the leading cause of cancer-related death globally. Surgical resection was considered to be the standard and first option treatment of HCC, because of its resistance to radiotherapy or chemotherapy (Lohitesh et al., 2018). Unfortunately, many HCC patients may not have the chance of surgical resection because the diagnosis usually occurs at the late stage. Therefore, revealing the altered cell biological behavior with the gene expression profile at the early stage will contribute to the discovery of potential targets that are of therapeutic significance.

It has been known for decades that plants carrying organosulfur-containing compounds, like garlic, have anti-cancer effects (Weisberger and Pensky, 1957). Studies supported that many of garlic's effects are attributed to the generation of sulfane sulfur, a reactive sulfur species (RSS) (Iciek et al., 2001; Iciek et al., 2012). For human beings, persulfide (RSSH), polysulfide (RSS_nR), and thiosulfate ($RSSO_3$) are major forms of sulfane sulfur in the body (Yuan et al., 2017; Akaike et al., 2017; Alvarez et al., 2017; Yang et al., 2019a; Liu H. et al., 2019). Additionally, some endogenous RSS, like cystine, cysteine, homocysteine, methionine, glutathione, and hydrogen sulfide (H_2S), are not sulfane sulfur *per se*, but can be metabolized to produce sulfane sulfur (Jackson et al., 2012). However, the effects of these RSS on cancer therapy including HCC are contradictory, as both anti-cancer (Iciek et al., 2001; Iciek et al., 2012) and pro-cancer (Pan et al., 2014; Zhen et al., 2018; Yang et al., 2019b) activities have been reported, which hinders the sulfur-based HCC therapy.

Metabolic reprogramming is an important cancer hallmark that has been studied over a century but is still of research significance (DeBerardinis et al., 2008; Faubert et al., 2020; Zhou et al., 2020). In tumor cells, a variety of metabolic processes, such as aerobic glycolysis, glutamine catabolism, macromolecular synthesis, and redox homeostasis, are distinctively different from that in normal cells. This metabolic flexibility is believed to fuel tumor fast proliferation (Kim and DeBerardinis, 2019). However, the metabolism of RSS in HCC tissues has often been overlooked. Additionally, it is unclear whether the different therapeutic outcomes of sulfur compounds are associated with the reprogramed RSS metabolism. A recent study showed that the diet restriction of methionine (a sulfur amino acid) was able to inhibit tumor growth in colorectal cancer (Gao et al., 2019). On the other hand, the elevated level of homocysteine (Wu and Wu, 2002), or decreased level of vitamin B_6 (Galluzzi et al., 2013), could promote tumorigenesis. As known, vitamin B_6 (pyridoxal 5'-phosphate) is a cofactor of cystathionine-β-synthase (CBS) or cystathionine-γ-lyase (CSE/CTH) in the generation of RSS including H_2S and H_2S_2 (Renga, 2011; Gregory et al., 2016). These studies inspired us to explore the overall difference between HCC and normal liver tissues in the RSS metabolism, by which some useful therapeutic strategies may be uncovered.

Transcriptomics analysis of high throughput RNA sequencing is a highly efficient means to discover the potential causes of unique HCC phenotype. Gene Set Enrichment Analysis (GSEA) is one of the most popular computational tools for transcriptomics analysis. Therefore, in this work, GSEA was used to demonstrate whether the sulfur metabolism was reprogrammed in HCC tissues. Then, through the bioinformatics analysis, the involved hub genes were revealed, their significance was verified, and the interacted RSS were discovered. With the cell imaging and viability assay, some RSS that have anti-HCC activity were suggested. Lastly, based on the enhanced cystine transport capacity in HCC tumor cells, persulfided cysteine precursor (PSCP) and a series of esterase-triggered sulfane sulfur donors were synthesized and their anti-HCC effects were evaluated.

MATERIALS AND METHODS

Materials

Sodium sulfide (Na_2S), sodium persulfide (Na_2S_2), sodium trisulfide (Na_2S_3), and Cell Counting Kit (CCK)-8 were purchased from Dojindo Lab (Kyushu, Japan). N-acetyl cysteine (NAC), cystine, cystathionine, and GSSG were bought from Thermo Fisher Scientific Co. (Pittsburgh, PA, USA). Gemcell™ fetal bovine serum (FBS) was supplied by Gemini Company (Woodland, CA, USA). SSP4, PSCP, and the controllable sulfane sulfur donors were synthesized following the literature procedure and their characterization matches reported data (Rietman et al., 1994; Chen et al., 2013; Artaud and Galardon, 2014).

Cell Culture and Viability Assay

HCC (SNU387 and SNU398) tumor cells, lung adenocarcinoma A549 cells, prostate cancer PC3 cells, cervical cancer Hela cells, breast MDA-MB-231 cells, raw-blue macrophages, LO2 liver cells, and H9c2 cardiomyocytes were obtained from ATCC. The cells were maintained in DMEM-F12 medium supplemented with 10% FBS at 37°C under an atmosphere of 5% CO_2 and 95% air. They were passaged and harvested with 0.25% trypsin.

Cell viability was measured with the CCK-8 kit. The cells were plated in 96-well plates at a density of 7,000 cells/well. When grown to approximately 60~70% confluence, they were treated correspondingly for 48 h. Then, the plates were washed and 100 μl of CCK-8 solution diluted with FBS-free medium was added. The cells were incubated for a further 2 h at 37°C. The absorbance was measured at 450 nm with a microplate reader (Molecular Devices, USA).

Data Collection

The microarray data of four normal mouse liver tissues and four HCC tumor tissues were downloaded from Gene Expression Omnibus (GEO) (https://www.ncbi.nlm.nih.gov/geo/query/acc.cgi?acc=%20GSE102081) (Chiyonobu et al., 2018). For the Cancer Genome Atlas (TCGA) data, the analysis of differential expression was downloaded from GEPIA2 (http://gepia2.cancer-pku.cn/#analysis), and the survival data were downloaded from the Human Protein Atlas (https://www.proteinatlas.org/).

Gene Set Enrichment Analysis

The expression dataset from GSE102081 was converted as follows: According to the probes of Agilent Sureprint

G3ge8x60k in the first column, a column of gene symbol (mgi_symbol) was added. The subsequent columns were named C1, C2, C3, and C4 for the normal liver tissues, while H1, H2, H3, and H4 for the HCC tumor tissues. The data file was imported into Gene Set Enrichment Analysis (GSEA) 4.0.3 software for further calculation and illustration according to the protocol (Subramanian et al., 2005).

Prediction of Hub Genes

The interaction of the leading-edge genes identified by GSEA was subjected to STRING analysis (https://string-db.org/) by constructing a protein-protein interaction (PPI) network. The disconnected nodes were not involved in this network. The data were downloaded and imported to Cytoscape 3.7 software for further calculation, visual analysis, and hub gene prediction.

Observation of Intracellular Sulfane Sulfur Levels

HCC SNU398 tumor cells were inoculated in 24-well plates and grown to 60∼70% confluence. After treatment with the indicated RSS for 1 h, intracellular sulfane sulfur was measured with SSP4 fluorescent probe (Chen et al., 2013; Bibli et al., 2018). Briefly, the treated cells were incubated with 10 μM SSP4 in the presence of 20 μM cetyl trimethyl ammonium bromide (CTAB) in 1% FBS medium for 20 min in the dark. The cell imaging was carried out after a slight wash with PBS buffer. The intracellular fluorescence signal was visualized under the Nikon E600 Fluorescence microscope (Walpole, MA, US).

Chemical Synthesis and Characterization

PSCP was synthesized following reported procedure (Rietman et al., 1994). NMR matches the reported data. ^{1}H NMR (400 MHz, Methanol-*d4*) 4.24 (m, 1H), 3.93 (s, 3H), 3.44–3.47 (dd, 2H), 3.21–3.27 (m, 2H).

Compounds **1**, **3**, **5**, **7**, and **9** were synthesized by treating protected cysteine/penicillamine **(10)** with the corresponding tosylated para-substituted benzyl mercaptans (**11**). Briefly, to a solution of **10** (2 mM) in dichloromethane (10 ml) was added **11** (1.8 mM) and triethylamine (4 mM). Reaction was stirred under room temperature overnight. The mixture was then purified by column chromatography (**Scheme 1**).

Compounds **2**, **4**, **6**, and **8** were synthesized by (**10**) with the corresponding para-substituted benzyl bromides (**12**). Briefly, under argon, to a solution of **12** (1.9 mM) and triethylamine (5 mM) in dichloromethane (5 ml) was added a solution of **10** (2 mM) in dichloromethane dropwise. Reaction was stirred under argon overnight. The mixture was then purified by column chromatography (**Scheme 1**).

Measurement of Sulfane Sulfur Content

SSP4 and CTAB were dissolved in DMSO and ethanol respectively to make 1 mM and 5 mM stock solutions. To initiate the experiment, 2 mM PSCP was prepared with PBS buffer (pH 7.4, 50 mM, 10 ml). At 5 min, 10 min, 20 min, 1 h, 1.5 h, 2 h, 4 h, 6 h, and 12 h, 80 μl of the above solution was aliquoted into a testing solution containing CTAB stock solution (80 μl), SSP4 stock solution (40 μl) and PBS buffer (pH 7.4, 50 mM, 3,800 μl), making the concentration of PSCP, SSP4, and CTAB 40, 10, and 100 μM, respectively. The resulting solution was incubated under room temperature for 10 min and fluorescence was analyzed by a fluorometer (Cary Eclipse, Agilent, USA).

Statistical Analysis

The experiment data are presented as mean ± standard deviation (SD). Significance between groups was evaluated by one-way analysis of variance (ANOVA) followed by Student-Newman-Keuls Test using GraphPad Prism 8 software (SanDiego, US). A probability <0.05 was considered statistically significant.

RESULT

Sulfur Metabolism Is Reprogrammed in HCC Tissues

To dissect the difference of sulfur metabolism between normal liver and HCC tumor tissues, the gene expression profile was

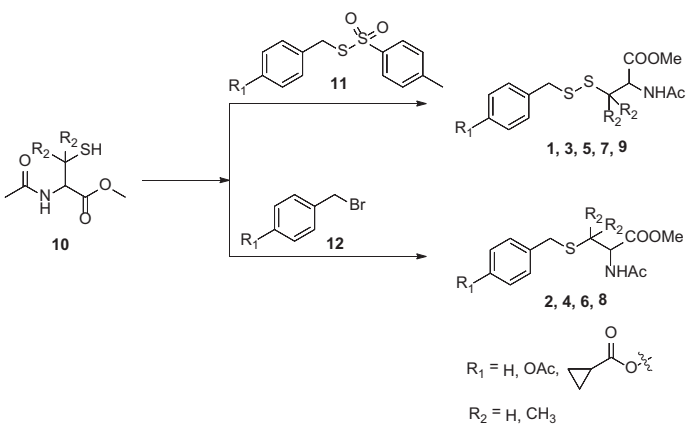

SCHEME 1 | Synthesis of esterase-activated sulfane sulfur donors and their controls.

screened using the GSEA tool. As presented in **Figure 1**, compared with the normal liver tissues, in HCC tumor tissues 12 out of 16 genes were negatively expressed in sulfur amino acid metabolism GO geneset (**Figures 1A, D**), 17 out of 32 genes were negatively expressed in cysteine and methionine metabolism KEGG geneset (**Figures 1B, E**), and 26 out of 48 genes were negatively expressed in vitamin B_6 binding activity GO geneset (**Figures 1C, F**). The result indicates that sulfur-related metabolism is distinctively disturbed in the HCC phenotype.

Prediction of Hub Genes in Leading-Edge Sets

To visualize the inter-relationships between these enriched genesets, a chord diagram was drawn. As shown in **Figure 2A**, 10 mutual genes were found, *i.e.* AHCY, BHMT, GOT2, MAT1A, MPST, NFS1, SDS, TAT, CBS, and CTH, among which CTH and CBS were shared by three genesets. Additionally, after the genes were sorted by expression level, which was displayed as $\log_2$ (Fold of Change), CTH was found to be dramatically downregulated.

In order to reveal the interaction of leading-edge genes, 12 enriched genes in sulfur amino acid metabolism GO set, 17 enriched genes in cysteine and methionine metabolism KEGG set, and 26 enriched genes in vitamin B_6 binding activity GO geneset were subjected to the PPI analysis. As shown in **Figure 2B**, nine genes, *i.e.* CBS, CTH, SHMT1, MAT1A, SDS, BHMT, TAT, GLDC, and GOT2 had significantly high interaction degrees (>15), thereby being considered as hub genes responsible for the unique HCC phenotype.

Expression and Significance of Hub Genes in HCC Patients

To verify whether the hub genes were downregulated in HCC tumor tissues, the TCGA cohort (368 tumor samples *vs.* 50 normal liver samples) and GTEx dataset (110 normal liver samples) were applied for differential expression analysis. As shown in **Figures 3A–H**, all the hub genes except GOT2 (**Figure 3I**) were significantly downregulated in HCC tumor tissues compared with normal tissues ($P < 0.001$). Additionally, importance of the hub genes was evaluated by observing their influence on HCC patient survival in the TCGA cohort. As shown in **Figures 3J–R**, the downregulation of CBS, CTH, SHMT1, MAT1A, SDS, BHMT, TAT, and GOT2 could significantly reduce the survival rate, instead of GLDC (**Figure 3Q**). Therefore, GLDC was not involved in the following investigation.

Identification of RSS That Interact With Hub Genes

To find out which RSS were potentially affected by the aforementioned hub genes, the metabolomics was investigated with the Metscape 3.0 tool, which is used to show the interaction of genes and compounds. As presented in **Figure 4**, the metabolism of methionine, cystine, cysteine, homocysteine, cystathionine, H_2S, and H_2S_2 was found to be closely associated with the above hub genes. Therefore, the imbalance of these compounds is probably responsible for the development of HCC, and their application may affect the growth of HCC tumor cells.

Effects of Identified RSS on Viability in HCC SNU398 Tumor Cells

With the identified RSS compounds that can interact with the hub genes, we investigated their influence on the viability in HCC SNU398 tumor cells. This cell line has relatively low CTH expression among 25 HCC tumor cell lines (**Figure 5A**), which is consistent with the discovery of reprogrammed sulfur metabolism in HCC tissues. Therefore, SNU398 tumor cells were applied in the following experiments. As shown in **Figure 5**, comparing with H_2S (in the form of Na_2S) (**Figure 5B**),

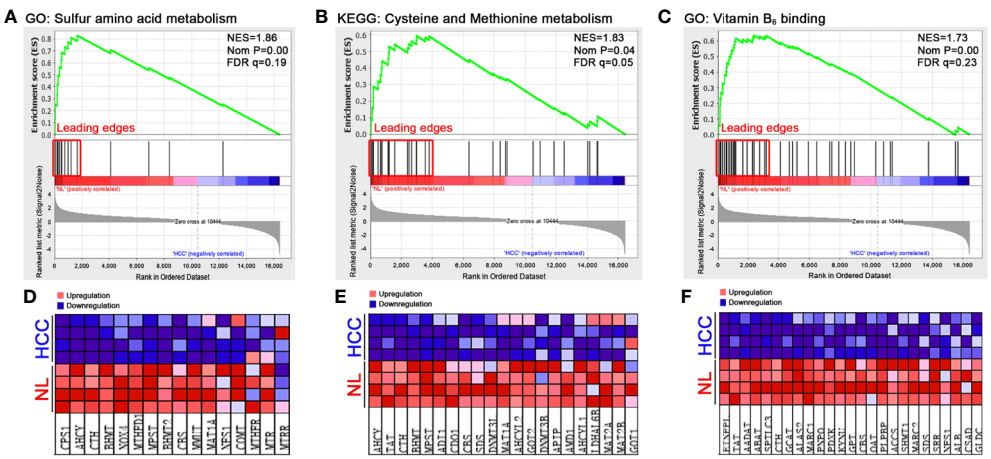

FIGURE 1 | Functional enrichment analysis of genesets in HCC tumor tissues. A microarray dataset (GSE102081) of HCC tumor tissues and normal liver (NL) tissues was analyzed using the GSEA tool. **(A–C)** The enrichment indexes of three genesets are shown in **(A)** (sulfur amino acid metabolism), **(B)** (cysteine and methionine metabolism), and **(C)** (vitamin B_6 binding activity), respectively. The genesets were considered to be significantly enriched at NES (normalized enrichment score) >1, Nom *P* (nominal p-value) <0.05, and FDR q-value <0.25. **(D–F)** Heatmaps of the enriched genes in **(A–C)** were created to display their relative expression.

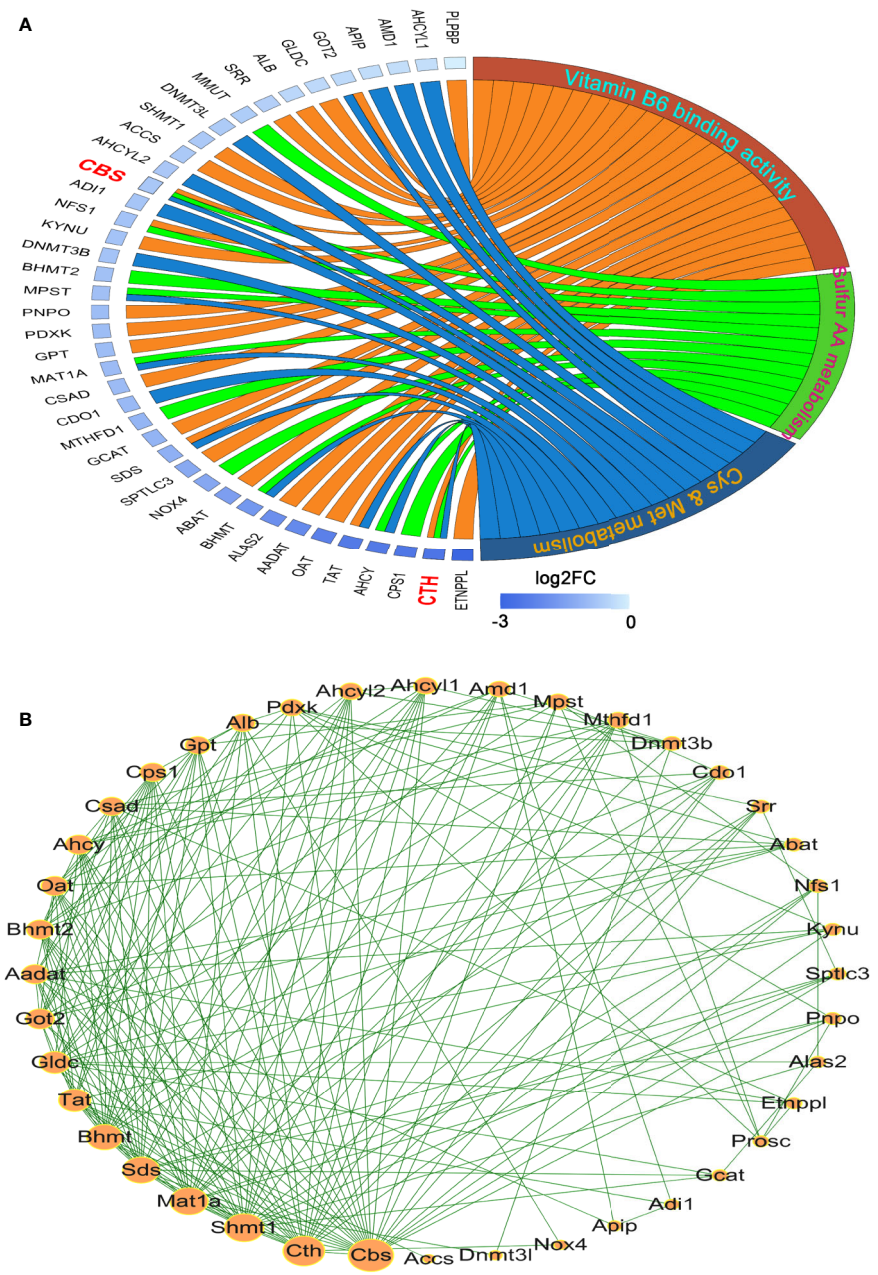

FIGURE 2 | Analysis of the interaction among the leading-edge genes. **(A)** The ownership and relative expression of the leading-edge genes from three genesets (sulfur amino acid metabolism GO set, cysteine and methionine metabolism KEGG set, and vitamin B_6 binding activity GO set) were presented through a chord diagram, which was drawn using the GOPlot R package. **(B)** The interaction of the genes was analyzed with the STRING online tool. The PPI network was constructed and the interaction degrees were calculated with Cytoscape 3.7 software.

treatment of the cells with H_2S_2 (in the form of Na_2S_2) (**Figure 5C**) or H_2S_3 (in the form of Na_2S_3) (**Figure 5D**) for 48 h remarkably decreased SNU398 cell viability, and the effect of H_2S_3 was much stronger. On the contrary, treatment with 200 μM H_2S increased cell viability (**Figure 5B**). Additionally, RSS, such as sulfur-containing amino acids (NAC, homocysteine, and cystine), as well as derived peptide (cystathionine and GSSG), did not show inhibitory effects on the cell viability (**Figures 5E–I**).

To examine whether the effects of H_2S_2 and H_2S_3 were associated with reactive sulfane sulfur, the cell imaging technology was applied to observe intracellular sulfane sulfur content. As shown in **Figure 6**, the treatment with H_2S_2 or H_2S_3 could clearly enhance the intracellular sulfane sulfur content, while other RSS compounds did not show significant effects (**Figure 6**). Moreover, scavenging sulfane sulfur with excess GSH remarkably attenuated Na_2S_3-induced anti-HCC effects

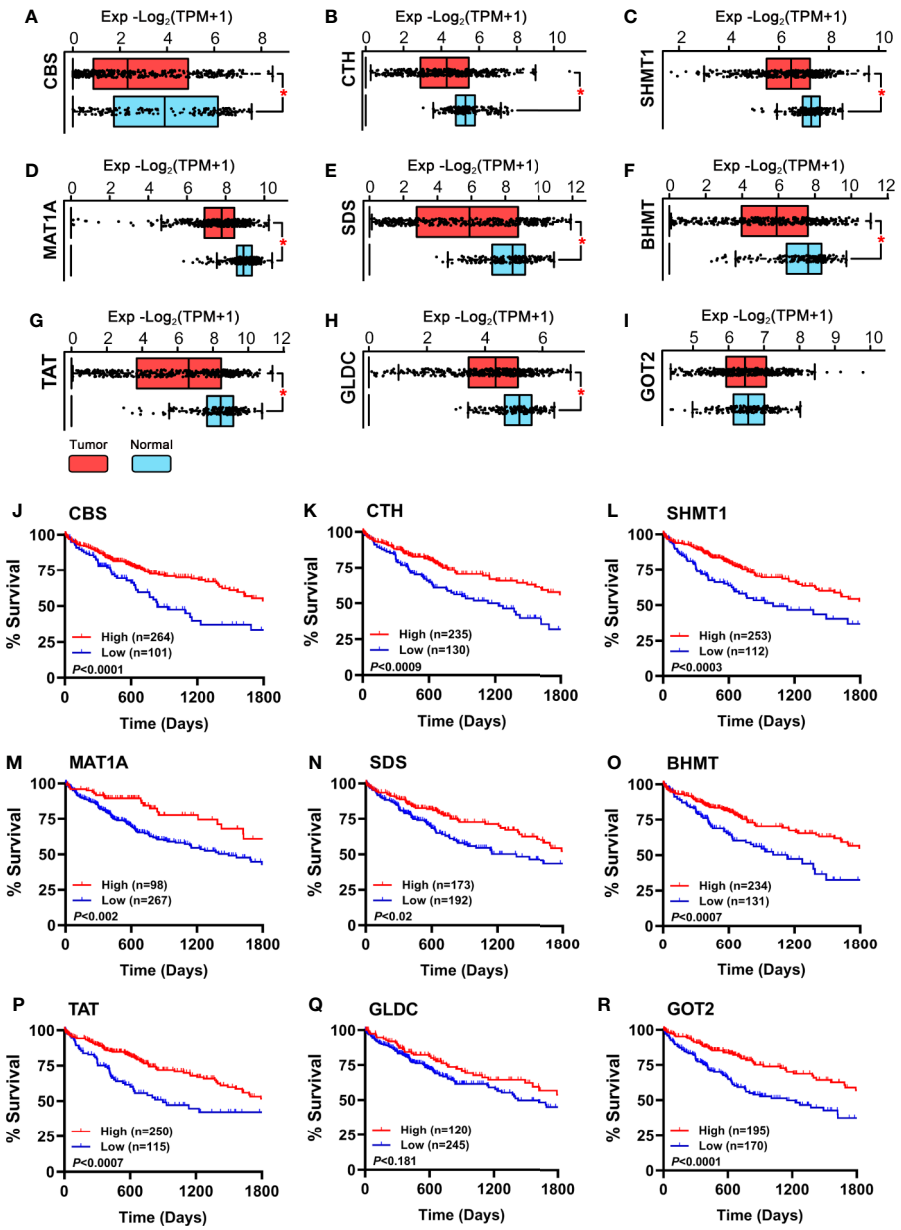

FIGURE 3 | **(A–I)** Expression of the hub genes between 160 normal liver tissues (50 samples of TCGA_LIHC cohort and 110 samples in GTEx dataset) and 368 HCC tumor tissues of TCGA_LIHC cohort were observed. Data are shown as median ± quartile, *$P < 0.001$ *vs.* Normal liver tissues. **(J–R)** Analysis of the survival rate of HCC patients in TCGA_LIHC database between high expression (red lines) and low expression (blue lines) of the hub genes. The number of patients in either group and the Log-rank test's *P* are shown in each panel.

(**Supplementary Figure 1**). The data indicate that among RSS, sulfane sulfur may be important for HCC therapy.

Sulfane Sulfur Mediates RSS-Induced Anti-HCC Effects in SNU398 Tumor Cells

Since H_2S_2 and H_2S_3 could reduce SNU398 cell viability and increase intracellular sulfane sulfur content, and scavenging sulfane sulfur could attenuate H_2S_3-induced anti-HCC effects, we further validated this finding by sulfane sulfur-containing compounds. As shown in **Figure 7A**, exposure of SNU398 cells to diallyl trisulfide (DATS) significantly reduced cell viability. Such inhibitory effects were also observed in dimethyl trisulfide (DMTS), although only under high concentrations (**Figure 7B**). Additionally, the treatment with DATS or DMTS could increase intracellular sulfane sulfur contents (**Figure 7C**). The result supports the significance of sulfane sulfur in HCC therapy.

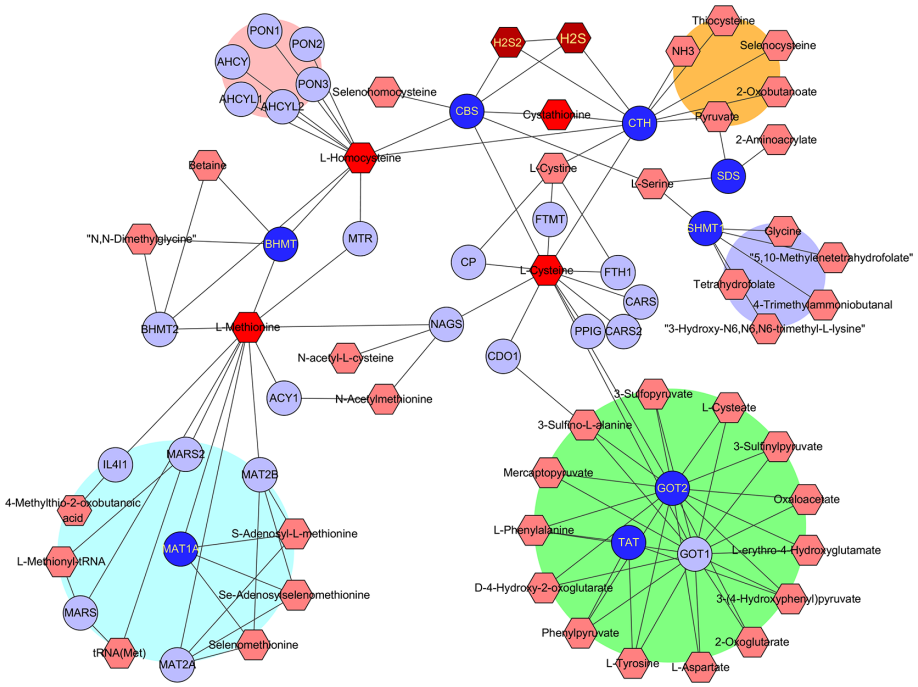

FIGURE 4 | Identification of RSS affected by the hub genes. The hub genes and RSS compounds were imported into Metscape 3.0 software. The construction of network type was set as compound-gene, and the network was created. Hub genes (Dark blue ○), Related genes (Light blue ○), Interacted RSS compounds (Dark red hexagon).

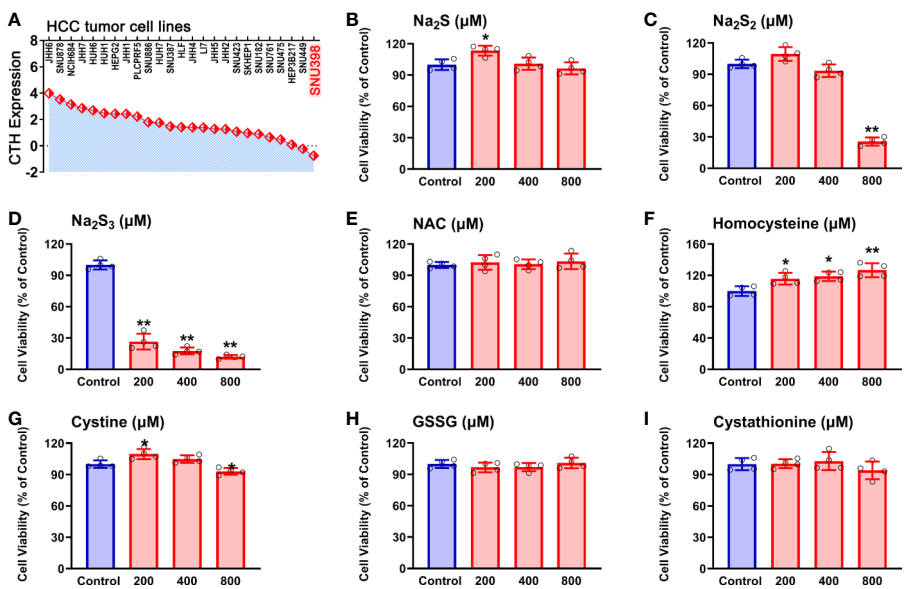

FIGURE 5 | Effects of RSS on viability in HCC SNU398 tumor cells. **(A)** Expression of CTH in various common HCC liver cancer cell lines. **(B–I)** After treatment with increasing concentrations of Na_2S **(B)**, Na_2S_2 **(C)**, Na_2S_3 **(D)**, NAC **(E)**, Homocysteine **(F)**, Cystine **(G)**, GSSG **(H)**, or Cystathionine **(I)** for 48 h, the cell viability was tested with CCK-8 assay. Data are expressed as mean ± SD of four independent experiments. $^*P < 0.05$, $^{**}P < 0.01$ *vs.* Control group.

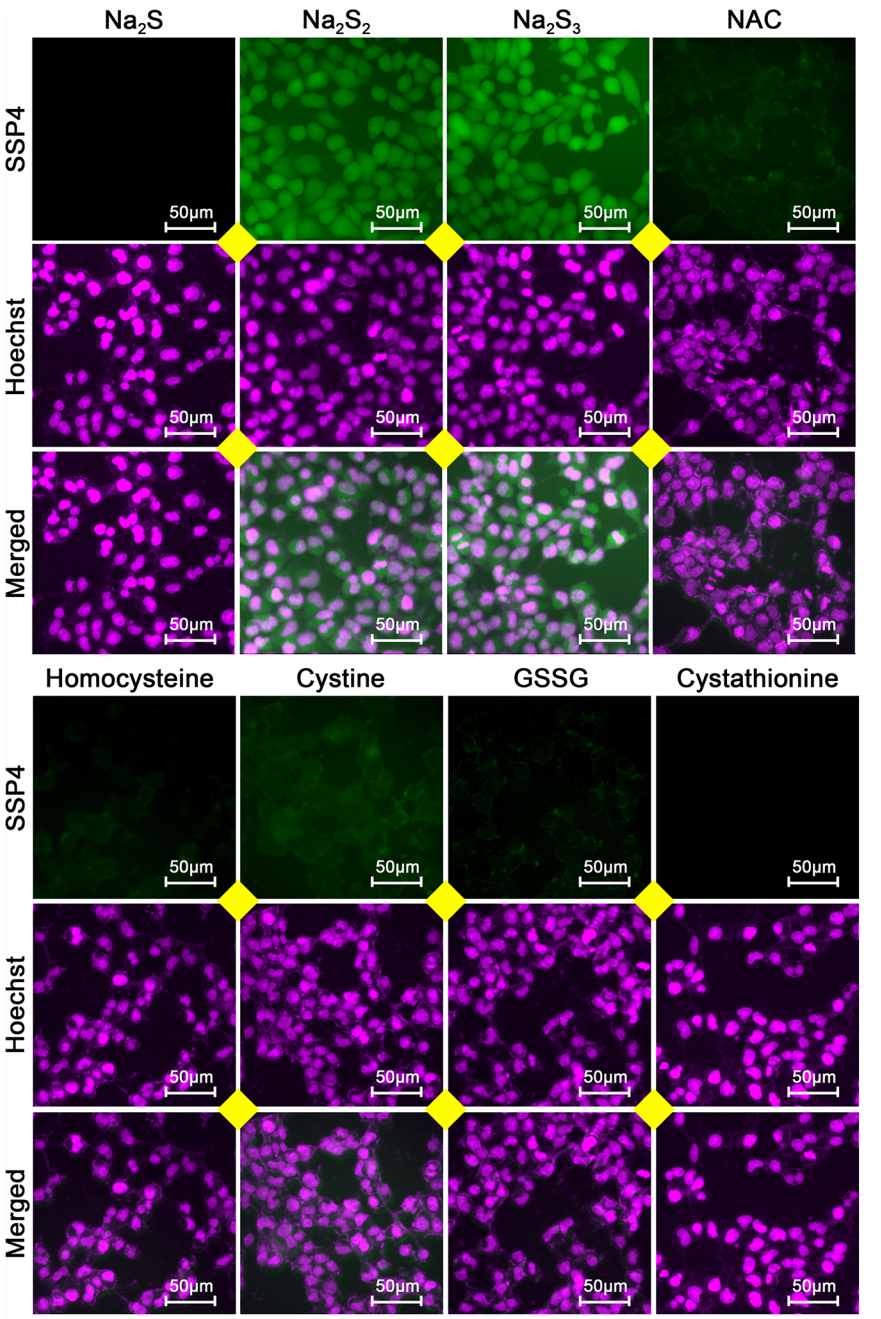

FIGURE 6 | Effects of RSS on intracellular sulfane sulfur content in HCC SNU398 cells. After treatment with 400 μM of Na_2S, Na_2S_2, Na_2S_3, NAC, Homocysteine, Cystine, GSSG, or Cystathionine for 1 h, the intercellular sulfane sulfur was observed with fluorescent probe SSP4 staining followed by photofluorography, and the cell nuclei were labeled through Hoechst 33324 staining.

Design, Synthesis, and Evaluation of Controllable Sulfane Sulfur Donors

Although Na_2S_2 and Na_2S_3 could inhibit the viability of SNU398 cells by producing sulfane sulfur, their usage probably has some problems. First, they are difficult to handle due to fast decomposition. Additionally, they may contain impurities like Na_2S, further complicating the situation. Especially, Na_2S_2 and Na_2S_3 have limited trans-membrane ability. In the TCGA dataset, SLC7A11 was found to be a pivotal risk for the poor survival of HCC patients (**Figure 8A**). This gene is highly expressed in HCC tumor tissues, as well as some tumor cell strains including SNU398 and SNU387 liver cancer cells

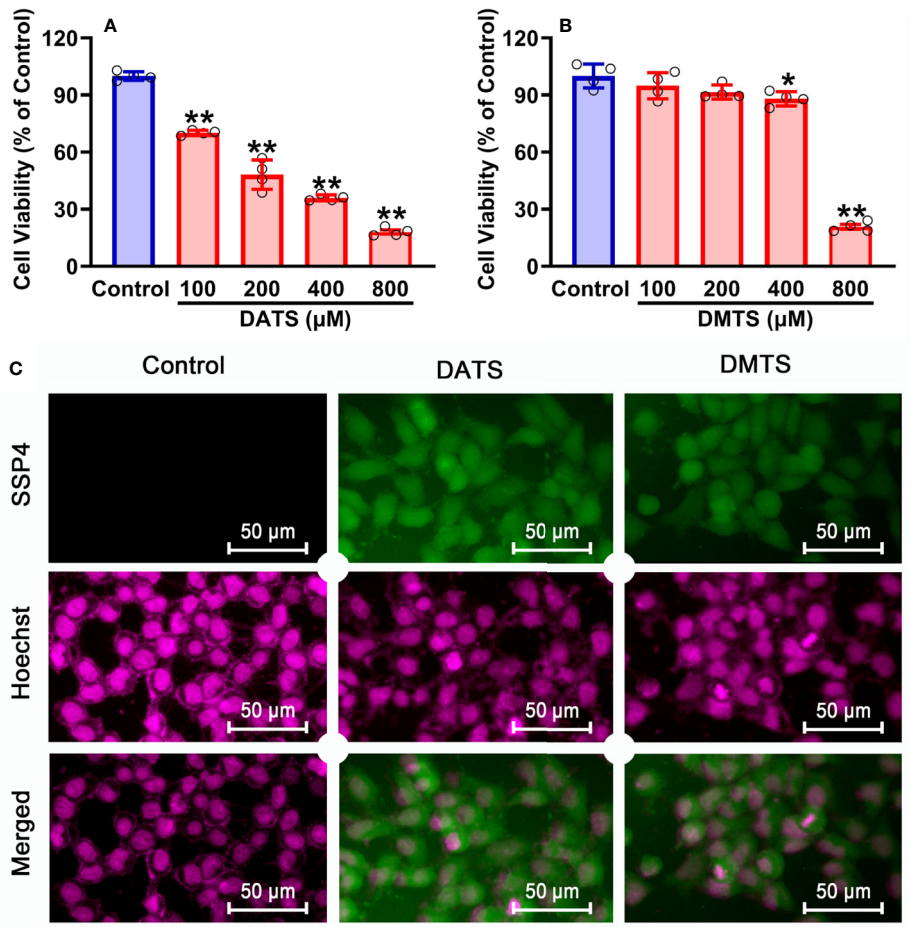

FIGURE 7 | Anti-cancer effects of sulfane sulfurs in HCC SNU398 cells. **(A, B)** The cells were treated with increasing concentrations of DATS or DMTS for 48 h. The cell viability was measured with CCK-8 assay. Data are expressed as mean ± SD of four independent experiments. *$P < 0.05$, **$P < 0.01$ *vs*. Control group. **(C)** After the treatment with 400 μM DATS or DMTS, the intercellular content of sulfane sulfur was observed with SSP4 staining followed by photofluorography, and the cell nuclei were labeled using Hoechst 33324.

(**Figure 8B**). Since SLC7A11 protein is responsible for the transport of cystine or cysteine, we envisioned sulfane sulfur donors with a structure similar to cystine/cysteine might have better efficiency for HCC's therapy. Additionally, they would be more stable and flexible due to the absence of free persulfide (R-SSH). As such, we prepared and tested S-(methoxycarbonylsulfenyl) cysteine hydrochloride, a persulfided cysteine precursor (PSCP). Under physiological pH, PSCP can undergo an intramolecular acyl transfer reaction to release cysteine persulfide (Cys-SSH), which eventually degrades to form polysulfides (**Figure 8C**), similar to a known design (Artaud and Galardon, 2014). Additionally, mass spectroscopy identified cysteine di-, tri-, and tetrasulfide derivatives in the solution (**Supplementary Figure 2**). These compounds are not only evidence of the persulfide formation, but also are sulfane sulfur themselves for tri- and tetrasulfide. Both persulfides and polysulfides belong to sulfane sulfur, so PSCP can be considered as the precursor of cysteine-derived sulfane sulfur. As expected, under physiological pH, sulfane sulfur formed from PSCP (2 mM) reached the maximum concentration in 120 min. Significant amounts of sulfane sulfur were still detectable after 720 min (**Figure 8D**). The cell imaging assay showed that treatment with PSCP was able to increase intracellular sulfane sulfur contents in SNU 398 cells (**Figure 8E**).

However, as found in **Figures 8C, D** and **Supplementary Figure 1**, the generation of sulfane sulfur from PSCP was spontaneous and the effect of sulfane sulfur was dramatically attenuated by GSH, which may impede its future application. Therefore, we have attempted to develop donors triggered by physiological stimuli, like enzymes. As such, four esterase-triggered donors were designed and synthesized (**1**, **3**, **5**, and **7**), which consisted of a cleavable ester trigger, a self-immolative linker, and a sulfane sulfur-releasing moiety. These donors can theoretically release protected cysteine or penicillamine persulfide, a form of sulfane sulfur, upon reaction with intracellular esterase. Meanwhile, four control compounds (**2**, **4**, **6**, and **8**), which should only release protected cysteine/penicillamine, were also prepared. The characterizations of

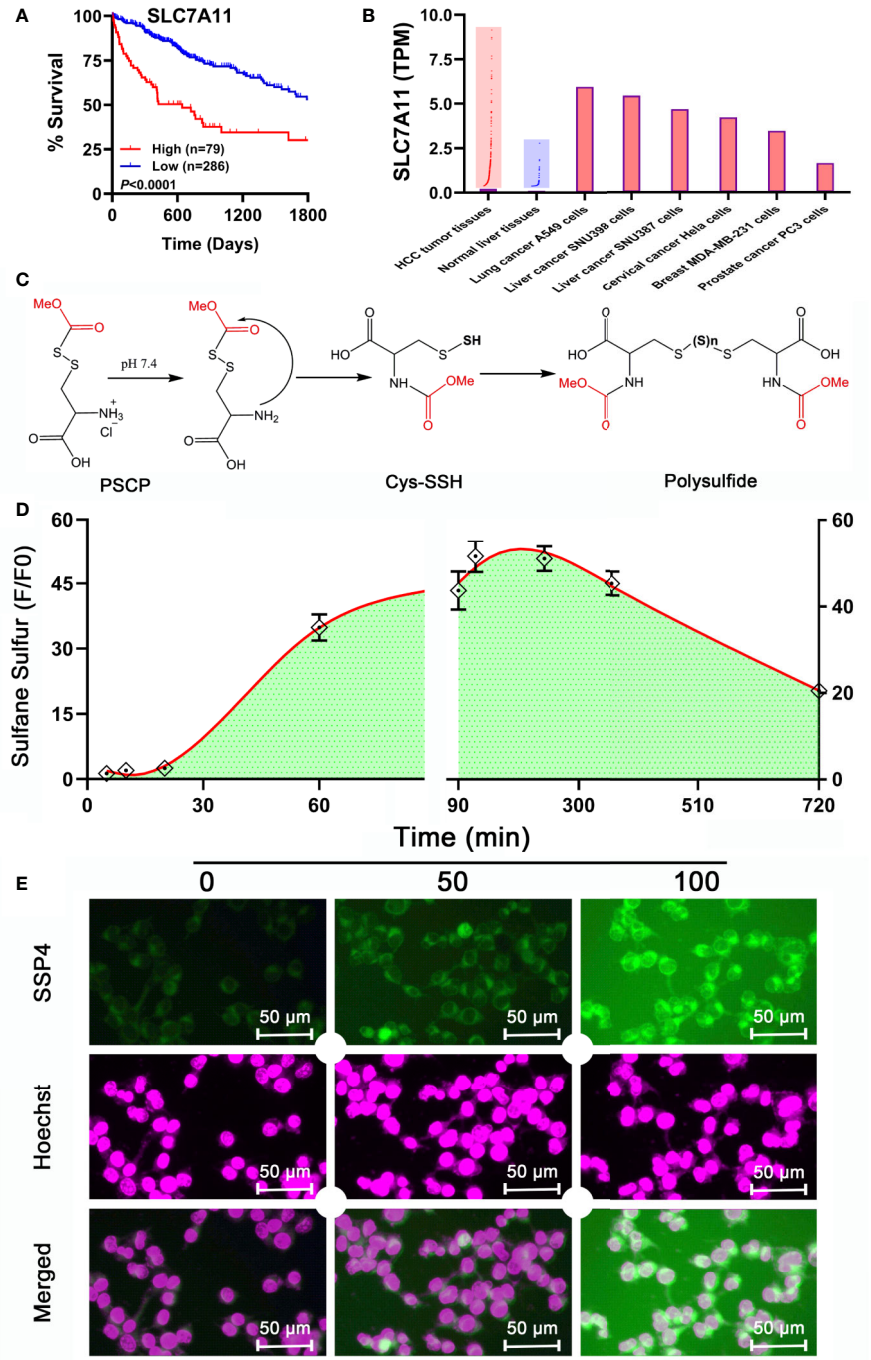

FIGURE 8 | Development of a sulfane sulfur donor-specific to tumor tissues. **(A)** With TCGA cohort, effects of SLC7A11 on HCC patient survival between high (red line) and low (blue line) expression groups were examined using Log-rank test. **(B)** Analysis of TCGA cohort and Cancer Cell Line Encyclopedia for SLC7A11 expression in HCC patient tissues and tumor cell lines, respectively. **(C)** Mechanism underlying sulfane sulfur generation from PSCP. **(D)** The generated sulfane sulfur in PBS buffer was measured with a spectrophotometer. **(E)** After treatment of SNU398 cells with 200 μM PSCP for different times, intracellular sulfane sulfur was observed with SSP4 staining followed by photofluorography, and the cell nuclei were labeled using Hoechst 33324 staining.

Compound 1-8 can be found in **Supplementary Figure 3**. Additionally, we have made a compound, which has no ester trigger and is therefore not able to release persulfide (**9**). As shown in **Figure 9**, treatment with these esterase-triggered donors (**1**, **3**, **5**, and **7**) significantly inhibited SNU398 cell viability (**Figures 9A, C, E, G**), while no obvious inhibitory

effects in the control compounds (**2**, **4**, **6**, and **8)** was found (**Figures 9B, D, F, H**). Although these results are promising, compound **9**, which theoretically cannot generate sulfane sulfur, also reduced cell viability. Additionally, we were not able to detect sulfane sulfur generation from these donors using SSP4. The data suggest that inhibitory effects of (**1**, **3**, **5**, and **7**) may not come from sulfane sulfur. Although it is still not clear how these compounds achieved inhibitor effects, the present design of esterase-triggered sulfane sulfur donor should be improved.

Evaluation of PSCP's Anti-Cancer Effects in Various Cells

As shown in **Figure 10**, in HCC SNU398 cells (**Figure 10A**) and another liver cancer cell line SNU387 (**Figure 10B**), PSCP could exert obvious anti-cancer effects. However, in other tumor cell strains, including lung cancer A549 cells (**Figure 10C**), prostate cancer PC3 cells (**Figure 10D**), cervical cancer Hela cells (**Figure 10E**), and breast MDA-MB-231 cells (**Figure 10F**), remarkable anti-cancer effects were not observed. Notably, in normal cells, such as Raw-blue macrophages, H9c2 cardiomyocytes, as well as normal liver cells, PSCP did not show severe toxicity. The result suggests that sulfane sulfur (PSCP) is able to inhibit tumor cell viability in a liver cancer-specific manner.

DISCUSSION

Metabolic reprogramming is a distinctive hallmark of cancer. The reprogrammed glucose metabolism in tumorigenesis has been studied for many years (Kato et al., 2018; Lin et al., 2019). Additionally, the metabolism of amino acids, such as cysteine, homocysteine, glutamine, and methionine, are attracting increased attention in recent years (Gao et al., 2019; Lieu et al., 2020). Through metabolic reprogramming, tumor cells can generate large amounts of acids, reduced compounds, as well as one-carbon units, to support their rapid growth (Pavlova and Thompson, 2016; Sun et al., 2020).

Sulfur metabolism in HCC tumor tissues is still a novel field of research. In this work, we observed the sulfur metabolism was reprogrammed in HCC through the bioinformatic GSEA screening. The scanning revealed that the gene sets of sulfur amino acid metabolism, cysteine and methionine metabolism, and vitamin B_6 binding activity were remarkably impaired in HCC tissues. The further PPI analysis suggested that CBS, CTH, SHMT1, MAT1A, SDS, BHMT, TAT, and GOT2 were significant hub genes. Importantly, the TCGA analysis validated their significance in HCC patients. Through these data, we believe that the genes related to sulfur metabolism should be dysregulated in HCC tissues, which may be responsible for the low survival of patients. Recently, some studies demonstrated that high levels of methionine and homocysteine were able to promote tumorigenesis (Sun et al., 2002; Gao et al., 2019), while the methionine-restricted diet arrested tumor growth and increased chemotherapy sensitivity (Hoffman, 2019). Moreover, a previous study showed that the content of vitamin B_6 pyridoxal phosphate and the activity of pyridoxine kinase in Morris hepatomas were lower than those in normal liver tissues (Meisler et al., 1982). The antioxidant NAC, a cysteine equivalent, was reported to accelerate lung cancer progression (Sayin et al., 2014). These studies support that the increased methionine, homocysteine, and cysteine, as well as the decreased vitamin B_6 binding activity, are probably important causes for HCC tumor growth, which is consistent with the present analyses. For this reason, metabonomic analysis can bring to light the potential interaction between RSS and the hub genes in HCC tissues. Meanwhile, the findings provide a reasonable explanation that through sulfur metabolic reprogramming, HCC tumor cells can raise the content of methionine, homocysteine, or cysteine to fuel their fast proliferation.

Reprogrammed sulfur metabolism is likely to make HCC tumor cells adapt to a new sulfur environment. Since the metabolism of RSS was impaired, we scanned the effects of RSS on HCC tumor cell viability. It was found that Na_2S_2 and Na_2S_3 remarkably inhibited cell viability, while the other RSS compounds did not exert such effects. It is worth noting that Na_2S_2 and Na_2S_3 are sulfane sulfur donors (Jiang et al., 2019). Also, DATS and DMTS belong to sulfane sulfurs, which could also attenuate HCC tumor cell viability in the present study, consistent with the previous reports (Weisberger and Pensky, 1957; Liu X. et al., 2019). Some researchers considered that anti-cancer effects from garlic-derived compounds were attributed to H_2S generation. However, in this study, we did not observe that H_2S had anti-cancer effects at the same treatment profile. In recent years, the studies of H_2S on HCC tumorigenesis are conflicting, *i.e.* anti-cancer *vs.* pro-cancer (Wu et al., 2017; Yang et al., 2019b; Wu et al., 2019). Those studies on H_2S's anti-HCC activity, we think, are probably due to the generation of sulfane sulfur from Na_2S/NaHS.

To support the above hypothesis, the cell imaging assay was performed and the results demonstrated that the treatment with Na_2S_2 or Na_2S_3 was able to enhance the intracellular sulfane sulfur levels, so did DATS and DMTS. Importantly, their treatment all showed anti-HCC effects. Moreover, scavenging of sulfane sulfur with excess GSH significantly attenuated sulfane sulfur-induced anti-HCC effects. These findings support the notion that the application of sulfane sulfurs may be an effective therapeutic strategy, especially for the HCC tumor cells with reprogrammed sulfur metabolism.

Notably, Na_2S_2 and Na_2S_3 are unstable chemicals, while commercial DATS is highly volatile, which will hinder their applications. Through the TCGA cohort analysis, it was shown that SLC7A11 (xCT) is upregulated in HCC tissues, indicating an increased cystine transportability. We then synthesized PSCP and found it was able to produce cystine sulfane sulfurs including per-, tri-, and tetrasulfide. The continuous monitoring indicated that the content of sulfane sulfur could keep stable for at least ten hours in aqueous solution. Additional cell experiments showed that the treatment with PSCP did not only enhance intracellular sulfane sulfur, but also inhibited cell viability. Furthermore, we tested the effects of PSCP in other cancer cells like lung cancer A549 cells, prostate cancer PC3 cells, cervical cancer Hela cells, and breast MDA-MB-231 cells, and did not find remarkable

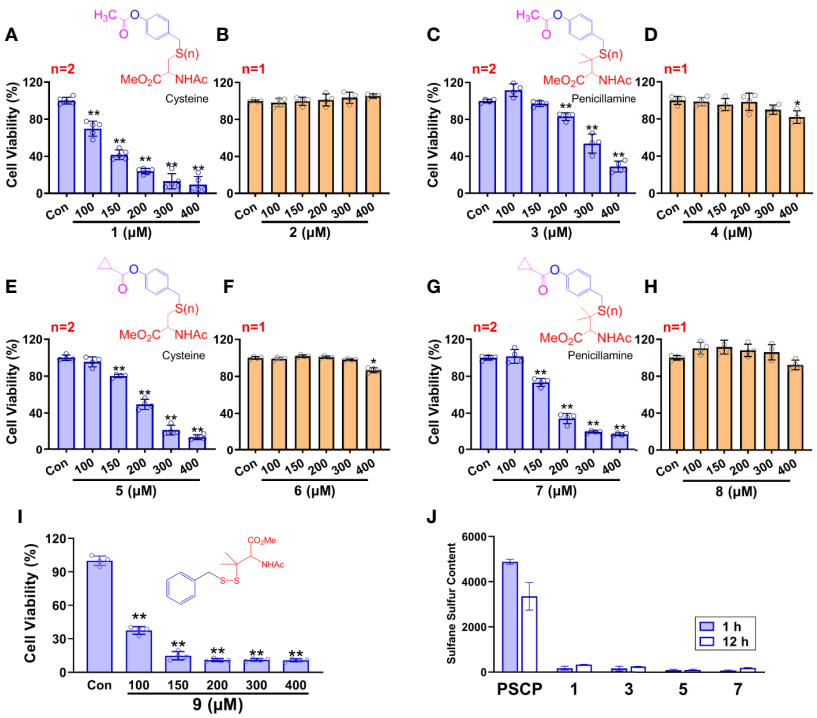

FIGURE 9 | Controllable sulfane sulfur compounds-mediated inhibition of cell viability. HCC SNU398 cells were treated with esterase-triggered sulfane sulfur donor 1 **(A)**, 3 **(C)**, 5 **(E)**, or 7 **(G)**, their control compounds 2 **(B)**, 4 **(D)**, 6 **(F)**, or 8 **(H)**, as well as 9 **(I)**, which does not generate sulfane sulfur. After 48 h, the cell viability was tested with CCK-8 assay. **(J)** Sulfane sulfur generated from the **1**, **3**, **5**, and **7** was measured at 1 and 12 h with a fluorescence probe SSP4. Data are expressed as mean ± SD of four independent experiments. $^{*}P < 0.05$, $^{**}P < 0.01$ *vs*. Control group.

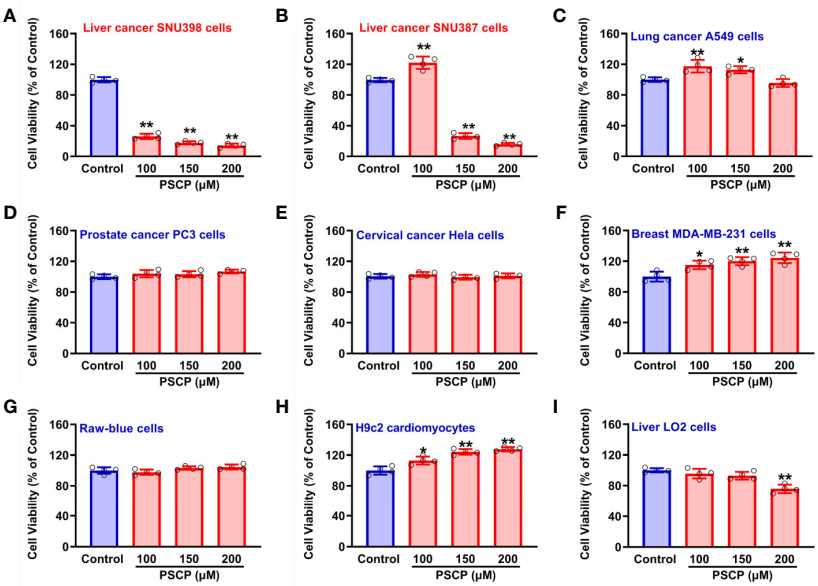

FIGURE 10 | Effects of PSCP on viability in various cell strains. **(A)** Liver cancer SNU398 cells, **(B)** Liver cancer SNU387 cells, **(C)** Lung cancer A549 cells, **(D)** Prostate cancer PC3 cells, **(E)** Cervical cancer Hela cells, **(F)** Breast MDA-MB-231 cells, **(G)** Raw-blue macrophages, **(H)** H9c2 cardiomyocytes, and **(I)** Liver LO2 cells. Different types of cell strains were treated with increasing concentrations of PSCP for 48 h. The cell viability was tested with CCK-8 assay. Data are expressed as mean ± SD of four independent experiments. $^{*}P < 0.05$, $^{**}P < 0.01$ *vs.* Control group.

inhibitory activity. We surmise that the sulfur metabolism may not be reprogrammed, although some of these cells have high cystine transportability, for example the increased SLC7A11 expression in A549 cells. Interestingly, in H9c2 cardiomyocytes and normal liver LO2 cells, the cytotoxicity was not very high, indicating its safety for the future *in vivo* application. Lastly, because of the spontaneous release of sulfane sulfur from PSCP and the influence of GSH, we synthesized esterase-triggered sulfane sulfur donors. Although the donors may produce sulfane sulfur theoretically and showed promising inhibition on cell viability, we were not able to observe the generation of sulfane sulfur from them. Therefore, the present design of enzyme-triggered sulfane sulfur donors should be improved in the future.

In conclusion, we have discovered that sulfur-related metabolism in HCC is reprogrammed. The RSS screening indicates that HCC tumor cells are sensitive to sulfane sulfur. The selective inhibition of HCC cell viability from PSCP, a sulfane sulfur donor, further validates this finding. This study provides a basic evidence for the treatment of HCC that has sulfur metabolic reprogramming.

DATA AVAILABILITY STATEMENT

All datasets presented in this study are included in the article/ **Supplementary Material**.

AUTHOR CONTRIBUTIONS

CY, SX, and XMZ designed the experiments and wrote the manuscript. MC, XN, YW, and HZ performed all the experiments and statistical analyses. All authors contributed to the article and approved the submitted version.

FUNDING

This work was supported by Natural Science Foundation of Guangdong Province (2017A030313892) and Guangzhou Key Medical Discipline Construction Project.

ACKNOWLEDGMENTS

We thank Kaoru Mogushi at Juntendo University for the mRNA expression microarray.

SUPPLEMENTARY MATERIAL

The Supplementary Material for this article can be found online at: https://www.frontiersin.org/articles/10.3389/fphar.2020.571143/full#supplementary-material

REFERENCES

Akaike, T., Ida, T., Wei, F. Y., Nishida, M., Kumagai, Y., Alam, M. M., et al. (2017). Cysteinyl-tRNA synthetase governs cysteine polysulfidation and mitochondrial bioenergetics. *Nat. Commun.* 8, 1177. doi: 10.1038/s41467-017-01311-y

Alvarez, L., Bianco, C. L., Toscano, J. P., Lin, J., Akaike, T., and Fukuto, J. M. (2017). Chemical biology of hydropersulfides and related species: Possible roles in cellular protection and redox signaling. *Antioxid. Redox Signal.* 27, 622–633. doi: 10.1089/ars.2017.7081

Artaud, I., and Galardon, E. (2014). A persulfide analogue of the nitrosothiol SNAP: formation, characterization and reactivity. *Chembiochem* 15, 2361–2364. doi: 10.1002/cbic.201402312

Bibli, S. I., Luck, B., Zukunft, S., Wittig, J., Chen, W., Xian, M., et al. (2018). A selective and sensitive method for quantification of endogenous polysulfide production in biological samples. *Redox Biol.* 18, 295–304. doi: 10.1016/j.redox.2018.07.016

Chen, W., Liu, C., Peng, B., Zhao, Y., Pacheco, A., and Xian, M. (2013). New fluorescent probes for sulfane sulfurs and the application in bioimaging. *Chem. Sci.* 4, 2892–2896. doi: 10.1039/C3SC50754H

Chiyonobu, N., Shimada, S., Akiyama, Y., Mogushi, K., Itoh, M., Akahoshi, K., et al. (2018). Fatty acid binding protein 4 (FABP4) overexpression in intratumoral hepatic stellate cells within hepatocellular carcinoma with metabolic risk factors. *Am. J. Pathol.* 188, 1213–1224. doi: 10.1016/j.ajpath.2018.01.012

DeBerardinis, R. J., Lum, J. J., Hatzivassiliou, G., and Thompson, C. B. (2008). The biology of cancer: metabolic reprogramming fuels cell growth and proliferation. *Cell Metab.* 7, 11–20. doi: 10.1016/j.cmet.2007.10.002

Faubert, B., Solmonson, A., and DeBerardinis, R. J. (2020). Metabolic reprogramming and cancer progression. *Science* 368, eaaw5473. doi: 10.1126/science.aaw5473

Galluzzi, L., Vacchelli, E., Michels, J., Garcia, P., Kepp, O., Senovilla, L., et al. (2013). Effects of vitamin B_6 metabolism on oncogenesis, tumor progression and therapeutic responses. *Oncogene* 32, 4995–5004. doi: 10.1038/onc.2012.623

Gao, X., Sanderson, S. M., Dai, Z., Reid, M. A., Cooper, D. E., Lu, M., et al. (2019). Dietary methionine influences therapy in mouse cancer models and alters human metabolism. *Nature* 572, 397–401. doi: 10.1038/s41586-019-1437-3

Gregory, J. F., DeRatt, B. N., Rios-Avila, L., Ralat, M., and Stacpoole, P. W. (2016). Vitamin B_6 nutritional status and cellular availability of pyridoxal 5'-phosphate govern the function of the transsulfuration pathway's canonical reactions and hydrogen sulfide production via side reactions. *Biochimie* 126, 21–26. doi: 10.1016/j.biochi.2015.12.020

Hoffman, R. M. (2019). Clinical studies of methionine-restricted diets for cancer patients. *Methods Mol. Biol.* 1866, 95–105. doi: 10.1007/978-1-4939-8796-2_9

Iciek, M. B., Rokita, H. B., and Wlodek, L. B. (2001). Effects of diallyl disulfide and other donors of sulfane sulfur on the proliferation of human hepatoma cell line (HepG2). *Neoplasma* 48, 307–312.

Iciek, M., Kwiecien, I., Chwatko, G., Sokolowska-Jezewicz, M., Kowalczyk-Pachel, D., and Rokita, H. (2012). The effects of garlic-derived sulfur compounds on cell proliferation, caspase 3 activity, thiol levels and anaerobic sulfur metabolism in human hepatoblastoma HepG2 cells. *Cell Biochem. Funct.* 30, 198–204. doi: 10.1002/cbf.1835

Jackson, M. R., Melideo, S. L., and Jorns, M. S. (2012). Human sulfide: quinone oxidoreductase catalyzes the first step in hydrogen sulfide metabolism and produces a sulfane sulfur metabolite. *Biochemistry* 51, 6804–6815. doi: 10.1021/bi300778t

Jiang, G., Li, M., Wen, Y., Zeng, W., Zhao, Q., Chen, C., et al. (2019). Visualization of sulfane sulfur in plants with a near-infrared fluorescent probe. *ACS Sens.* 4, 434–440. doi: 10.1021/acssensors.8b01423

Kato, Y., Maeda, T., Suzuki, A., and Baba, Y. (2018). Cancer metabolism: New insights into classic characteristics. *Jpn. Dent. Sci. Rev.* 54, 8–21. doi: 10.1016/j.jdsr.2017.08.003

Kim, J., and DeBerardinis, R. J. (2019). Mechanisms and implications of metabolic heterogeneity in cancer. *Cell Metab.* 30, 434–446. doi: 10.1016/j.cmet.2019.08.013

Lieu, E. L., Nguyen, T., Rhyne, S., and Kim, J. (2020). Amino acids in cancer. *Exp. Mol. Med.* 52, 15–30. doi: 10.1038/s12276-020-0375-3

Lin, J., Xia, L., Liang, J., Han, Y., Wang, H., Oyang, L., et al. (2019). The roles of glucose metabolic reprogramming in chemo- and radio-resistance. *J. Exp. Clin. Cancer Res.* 38, 218. doi: 10.1186/s13046-019-1214-z

Liu, H., Radford, M. N., Yang, C. T., Chen, W., and Xian, M. (2019). Inorganic hydrogen polysulfides: chemistry, chemical biology and detection. *Br. J. Pharmacol.* 176, 616–627. doi: 10.1111/bph.14330

Liu, X., Baecker, A., Wu, M., Zhou, J. Y., Yang, J., Han, R. Q., et al. (2019). Raw garlic consumption and risk of liver cancer: A population-based case-control study in Eastern China. *Nutrients* 11, 2038. doi: 10.3390/nu11092038

Lohitesh, K., Chowdhury, R., and Mukherjee, S. (2018). Resistance a major hindrance to chemotherapy in hepatocellular carcinoma: an insight. *Cancer Cell Int.* 18, 44. doi: 10.1186/s12935-018-0538-7

Meisler, N. T., Nutter, L. M., and Thanassi, J. W. (1982). Vitamin B_6 metabolism in liver and liver-derived tumors. *Cancer Res.* 42, 3538–3543.

Pan, Y., Ye, S., Yuan, D., Zhang, J., Bai, Y., and Shao, C. (2014). Hydrogen sulfide (H_2S)/cystathionine gamma-lyase (CSE) pathway contributes to the proliferation of hepatoma cells. *Mutat. Res.* 763–764, 10–18. doi: 10.1016/j.mrfmmm.2014.03.002

Pavlova, N. N., and Thompson, C. B. (2016). The emerging hallmarks of cancer metabolism. *Cell Metab.* 23, 27–47. doi: 10.1016/j.cmet.2015.12.006

Renga, B. (2011). Hydrogen sulfide generation in mammals: the molecular biology of cystathionine-beta- synthase (CBS) and cystathionine-gamma-lyase (CSE). *Inflamm. Allergy Drug Targets.* 10, 85–91. doi: 10.2174/187152811794776286

Rietman, B. H., Peters, R. F. R., and Tesser, G. I. (1994). A facile method for the preparation of S-(Alkylsulfenyl)cysteines. *Synthetic Commun.* 24, 1323–1332. doi: 10.1080/00397919408011734

Sayin, V. I., Ibrahim, M. X., Larsson, E., Nilsson, J. A., Lindahl, P., and Bergo, M. O. (2014). Antioxidants accelerate lung cancer progression in mice. *Sci. Transl. Med.* 6, 221ra15. doi: 10.1126/scitranslmed.3007653

Subramanian, A., Tamayo, P., Mootha, V. K., Mukherjee, S., Ebert, B. L., Gillette, M. A., et al. (2005). Gene set enrichment analysis: a knowledge-based approach for interpreting genome-wide expression profiles. *Proc. Natl. Acad. Sci. U. S. A.* 102, 15545–15550. doi: 10.1073/pnas.0506580102

Sun, C. F., Haven, T. R., Wu, T. L., Tsao, K. C., and Wu, J. T. (2002). Serum total homocysteine increases with the rapid proliferation rate of tumor cells and decline upon cell death: a potential new tumor marker. *Clin. Chim. Acta* 321, 55–62. doi: 10.1016/s0009-8981(02)00092-x

Sun, H., Zhou, Y., Skaro, M. F., Wu, Y., Qu, Z., Mao, F., et al. (2020). Metabolic reprogramming in cancer is induced to increase proton production. *Cancer Res.* 80, 1143–1155. doi: 10.1158/0008-5472.CAN-19-3392

Weisberger, A. S., and Pensky, J. (1957). Tumor-inhibiting effects derived from an active principle of garlic (Allium sativum). *Science* 126, 1112–1114. doi: 10.1126/science.126.3283.1112-a

Wu, L. L., and Wu, J. T. (2002). Hyperhomocysteinemia is a risk factor for cancer and a new potential tumor marker. *Clin. Chim. Acta* 322, 21–28. doi: 10.1016/s0009-8981(02)00174-2

Wu, D., Li, M., Tian, W., Wang, S., Cui, L., Li, H., et al. (2017). Hydrogen sulfide acts as a double-edged sword in human hepatocellular carcinoma cells through EGFR/ERK/MMP-2 and PTEN/Akt signaling pathways. *Sci. Rep.* 7, 5134. doi: 10.1038/s41598-017-05457-z

Wu, D. D., Wang, D. Y., Li, H. M., Guo, J. C., Duan, S. F., and Ji, X. Y. (2019). Hydrogen sulfide as a novel regulatory factor in liver health and disease. *Oxid. Med. Cell Longev.* 2019, 3831713. doi: 10.1155/2019/3831713

Yang, C. T., Devarie-Baez, N. O., Hamsath, A., Fu, X. D., and Xian, M. (2019a). S-Persulfidation: chemistry, chemical biology, and significance in health and disease. *Antioxid. Redox Signal.* doi: 10.1089/ars.2019.7889

Yang, C. T., Wang, Y., Marutani, E., Ida, T., Ni, X., Xu, S., et al. (2019b). Data-driven identification of hydrogen sulfide scavengers. *Angew. Chem. Int. Ed. Engl.* 58, 10898–10902. doi: 10.1002/anie.201905580

Yuan, S., Shen, X., and Kevil, C. G. (2017). Beyond a gasotransmitter: Hydrogen sulfide and polysulfide in cardiovascular health and immune response. *Antioxid. Redox Signal.* 27, 634–653. doi: 10.1089/ars.2017.7096

Zhen, Y., Wu, Q., Ding, Y., Zhang, W., Zhai, Y., Lin, X., et al. (2018). Exogenous hydrogen sulfide promotes hepatocellular carcinoma cell growth by activating the STAT3-COX-2 signaling pathway. *Oncol. Lett.* 15, 6562–6570. doi: 10.3892/ol.2018.8154

Zhou, Q., Lin, M., Feng, X., Ma, F., Zhu, Y., Liu, X., et al. (2020). Targeting CLK3 inhibits the progression of cholangiocarcinoma by reprogramming nucleotide metabolism. *J. Exp. Med.* 217, e20191779. doi: 10.1084/jem.20191779

Conflict of Interest: The authors declare that the research was conducted in the absence of any commercial or financial relationships that could be construed as a potential conflict of interest.

frontiers in Oncology

ORIGINAL RESEARCH
published: 19 October 2020
doi: 10.3389/fonc.2020.601538

Manganese-Based Targeted Nanoparticles for Postoperative Gastric Cancer Monitoring *via* Magnetic Resonance Imaging

Ke Li[1]*, *Peng Li*[2], *Yang Wang*[3] and *Shuang Han*[4]*

[1] Shaanxi Key Laboratory of Brain Disorders, Institute of Basic and Translational Medicine, Xi'an Medical University, Xi'an, China, [2] Department of Medical Technology, Xi'an Medical University, Xi'an, China, [3] Department of Basic Medical Science, Xi'an Medical University, Xi'an, China, [4] Department of Gastroenterology, HongHui Hospital, Xi'an, China

Postoperative recurrence is a common and severe problem in the treatment of gastric cancer; consequently, a prolonged course of chemotherapy treatment is inevitable. Monitoring by imaging could provide an accurate evaluation of the therapeutic effects, which would be beneficial to guide a treatment strategy adjustment over time. However, current imaging technologies remain insufficient for the continuous postoperative monitoring of gastric cancer. In this case, molecular imaging offers an efficient strategy. Targetable contrast agents are an essential part of molecular imaging, which could greatly enhance the accuracy and quality of monitoring. Herein, we synthesized a Mn-based contrast agent for magnetic resonance imaging (MRI) of gastric cancer monitoring. Initially, small-sized Mn_3O_4 nanoparticles (NPs) were synthesized. Then, a functionalized polyethylene glycol (PEG) lipid was attached to the surface of the Mn_3O_4 NPs, to improve biocompatibility. The targetable MRI contrast agent (Mn_3O_4@PEG-RGD NPs) was further prepared by the conjugation of the arginine-glycine-aspartic acid (RGD) peptides. The completed Mn_3O_4@PEG-RGD NPs had the small size of 7.3 ± 2.7 nm and exhibited superior colloidal stability in different solution environments. In addition, Mn_3O_4@PEG-RGD NPs exhibited reliable biotolerance and low toxicity both *in vitro* and *in vivo*. Imaging experiments amply demonstrated that Mn_3O_4@PEG-RGD NPs could efficiently accumulate in gastric cancer tissues and cells *via* RGD mediation, and immediately significantly increased the MRI effects. Through this study, we can conclude that Mn_3O_4@PEG-RGD NPs have the potential to be a novel MRI contrast agent for the postoperative monitoring of gastric cancer.

Keywords: gastric cancer, contrast agent, magnetic resonance imaging, Mn_3O_4, nanoparticles

OPEN ACCESS

Edited by:
Qi Zeng,
Xidian University, China

Reviewed by:
Xiu-An Yang,
Chengde Medical College, China
Xiangrong Cheng,
Jiangnan University, China

***Correspondence:**
Ke Li
tonyklee08@gmail.com
Shuang Han
shuanghamy@163.com

Specialty section:
This article was submitted to Pharmacology of Anti-Cancer Drugs, a section of the journal Frontiers in Oncology

Received: *01 September 2020*
Accepted: *23 September 2020*
Published: *19 October 2020*

Citation:
Li K, Li P, Wang Y and Han S (2020) Manganese-Based Targeted Nanoparticles for Postoperative Gastric Cancer Monitoring via Magnetic Resonance Imaging. Front. Oncol. 10:601538. doi: 10.3389/fonc.2020.601538

INTRODUCTION

Gastric cancer currently represents one of the highest incidences of malignant gastrointestinal tumors worldwide. Moreover, the mortality of this disease has increased year over year, with more than approximately 980000 new cases and 730,000 mortalities occurring annually (1–3). Complete prevention of gastric cancer is difficult to achieve. A multitude of factors are related to the disease,

such as genetics, dietary habits, environmental elements and bacterial infection (4, 5). The majority of patients with gastric cancer do not exhibit obvious symptoms until the cancer is advanced and cannot be treated effectively. In the clinic, gastrectomy, chemotherapy and radiotherapy are still the main treatments of gastric cancer (6). However, it is important to point out that early diagnosis provides the best opportunity for the effective treatment of gastric cancer because it would provide certain information, such as the location and stage, for initial surgery and radiation treatment. Currently, the methods for the accurate diagnosis of gastric cancer primarily include imaging, detection of biomarkers and tissue biopsy (7, 8). However, postoperative recurrence is very common in mid- and late-stage gastric cancer. This means that a prolonged intense course of chemotherapeutic treatment is necessary. Hence, an accurate assessment of tumor progress is the most significant element to determine the appropriate chemotherapeutic schedule (9, 10). However, some impenetrable limitations and defects in monitoring remain and seriously influence the prognosis (11).

Currently, in the clinical diagnosis of gastric cancer, many imaging technologies, such as endoscopic ultrasonography, computerized tomography (CT), single-photon emission computed tomography (SPECT), positron emission tomography (PET), and MRI, have been demonstrated to be very useful (12, 13). Imaging can reveal the location and border of tumor tissues, which will be used to guide surgery and radiotherapy. However, ionizing radiation, invasive injury, and an expensive cost are inescapable problems during monitoring. Moreover, these defects are more severe in the postoperative monitoring of patients with gastric cancer. Compared with other imaging methods, MRI has certain advantages for the postoperative monitoring of gastric cancer. MRI itself is especially applicable to detection in soft tissues, is a main method in clinical inspection and is characterized by its non-invasiveness, high spatial resolution and radiationless nature (14). This technology could be used to locate and distinguish various tissues for the diagnosis of gastric cancer, but it also has limitations (15). For example, normal MRI lacks the ability to effectively distinguish between food and tumors in the stomach (16). However, molecular imaging provides a novel means to visually access to a tumor at the ultramicro level. This technique has brought significant value gastric cancer monitoring because of its ability to accurately map out tumor tissues in the whole body at the molecular level (17–19). Moreover, molecular imaging not only allows finding the accurate location of the tumors but also possesses the ability to monitor the biological processes of tumor proliferation, metastasis, and response to therapy (20–22). Molecular MRI combines MRI with molecular imaging and has emerged as a novel tool to monitor cancer (23, 24). Functional contrast agents can efficiently enhance the sensitivity of MRI, thereby hopefully solving the present problems (25). Based on the mechanism, the existing MRI contrast agents have broadly been divided into two categories: T1 and T2 contrast agents. T1 contrast agents mainly utilize Gd and Mn. T2 agents are superparamagnetic Fe_3O_4 nanoparticles (NPs) (26). Gd-based contrast agents are widely used in clinical MRI. However, there have been some reports of brain deposition and renal fibrosis after the clinical application of Gd-based contrast agent (27, 28). These defects limit the utility of T1 contrast agent for the postoperative monitoring of gastric cancer. Additionally, superparamagnetic Fe_3O_4 NPs are being evaluated in clinical tests. However, magnetic susceptibility artifacts and dark signals impede the clinical promotion of T2 contrast agents (29, 30). Mn is a necessary trace element that has a high relaxation spin and bright signal; thus, Mn-based contrast agents have attracted considerable attention in recent decades (31). However, Mn is difficult to use in MRI directly. A suitable Mn preparation might help overcome this limitation.

NPs could provide an effective opportunity to address the above-mentioned problem. The NPs could be loaded with a functional agent as an enhanced beacon for imaging. A novel NPs-based contrast agent could improve the MRI effects for the diagnosis of gastric cancer, which allows earlier and more accurate detection of tumor tissues and improves the prognosis of the disease. Mn_3O_4 can be used to synthesize NPs with favorable monodispersity. The synthesis conditions are mild and have high yields (32). Many Mn_3O_4-based contrast agents have been reported for tumor imaging, including MRI, a combination of fluorescence and MR and an MR/PET combination (33–35). Currently, there are researchers who are exploiting more effective Mn_3O_4 NPs contrast agents. In this study, we synthesized small-scale Mn_3O_4 NPs to monitor gastric cancer *in vivo*. However, Mn_3O_4 NPs cannot disperse in the aqueous phase and lack a positive tumor target. In order to overcome these defects, we applied functionalized polyethylene glycol (PEG) lipids to modify the Mn_3O_4 NPs. PEG was modified on the surface of Mn_3O_4, which allowed the NPs to stably disperse in water. The functional groups in PEG also allow for the further conjugation of targeting molecules. The RGD peptide was employed as the targetable component in this case. The RGD peptide possesses ligand-receptor interaction with $\alpha v\beta_3$ integrin, which is a transmembrane protein that mediates interactions between the inside and outside of living cells (36). Integrin $\alpha v\beta_3$ is expressed at low level in normal cells but is usually over-expressed in a wide variety of cancer cells, such as gastric cancer, breast cancer and hepatic cancer (37–40). Thus, RGD-based targeted nanocarriers have been developed for tumor treatment (41). It is crucial for Mn_3O_4 NPs to actively target gastric tumor for MRI. The synthetic process is exhibited in **Figure 1A**, and the final MRI contrast agent was named Mn_3O_4@PEG-RGD NPs. The NPs possess low toxicity, effective biocompatibility and T1-weighted imaging, which could be utilized for the postoperative monitoring of gastric cancer.

MATERIALS AND METHODS

Materials

Manganese (II) acetate (98%), oleic acid, oleylamine, and fluorescein isothiocyanate isomer (FITC) were purchased from Aladdin Inc. (Shanghai, China). DSPE-PEG-NH_2, DSPE-

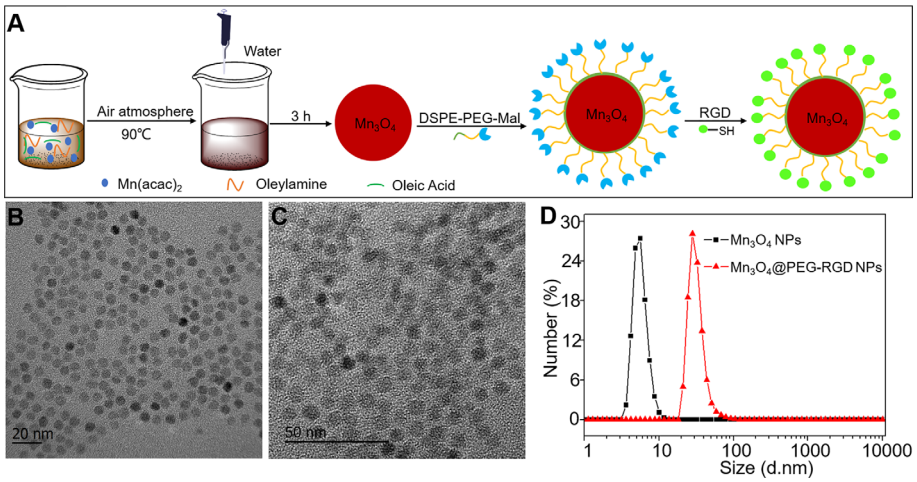

FIGURE 1 | Synthesis and characteristics of Mn_3O_4@PEG-RGD NPs. The preparation scheme of Mn_3O_4@PEG-RGD NPs **(A)**, TEM observations of Mn_3O_4 NPs **(B)**, and Mn_3O_4@PEG-RGD NPs **(C)**; Distributions of hydrodynamic size of Mn_3O_4 NPs and Mn_3O_4@PEG-RGD NPs **(D)**.

PEG-Mal, and SCM-PEG-Mal and supplied by Creative PEGworks (NC, USA). Core molecule was PEG5000. Traut's reagent and RGD antibody were bought from Thermo Fisher Inc. (MA, USA). RGD peptide was purchased from Haode Peptide Co., Ltd. (Wuhan, China). Human umbillical vein endothelial cells (HUVECs), human embryonic lung fibroblast cells (IMR-90), human gastric adenocarcinoma cells (SGC-7901), human gastric carcinoma cells (BGC-823), DMEM high glucose medium, and foetal bovine serum (FBS) were purchased from Procell Inc. (Wuhan, China). The CCK-8 kit, DAPI kit, antibiotics and trypsin (0.25%) were ordered from Beyotime Inc. (Shanghai, China). Other chemical reagents were purchased from Sinopharm Corp. (Beijing, China). BALB/c mice and BALB/c-nu/nu mice were purchased from Peking HFK Biotech Corp. (Beijing, China).

Synthesis of Mn_3O_4 NPs

The synthesis of Mn_3O_4 NPs was described in Yu's report (32). First, 1 mmol of manganese acetate (0.17 g), 640 μl of oleic acid and 3.28 ml of oleylamine were added to 15 ml of xylene, and the mixture was heated to 90°C with stirring. The mixture reacted for 10 min. Then, 1 ml of ultrapure water was added to the mixture, and the reaction continued for another 2.5 h with vigorous stirring. When the reaction was complete, 40 ml of ethyl alcohol was added to the mixture. The powdered Mn_3O_4@PEG-Mal NPs were obtained *via* centrifugation.

Synthesis of Mn_3O_4@PEG-RGD NPs

Ten milligrams of Mn_3O_4 NPs powder were dispersed into 3 ml of chloroform, and 25 mg of DSPE-PEG5000-Mal was added. The mixture stirred for 4 h after which chloroform was removed *via* rotary evaporation. The mixture was eluted with 10 ml of ultrapure water under sonication for 30 min, and excess DSPE-PEG-Mal was removed *via* centrifugation. Thus, Mn_3O_4@PEG-Mal NPs was obtained. In the next step, Traut's reagent and a solution of the peptide RGD (molar ratio of 1:25) were co-incubated at pH 8.0 for 2 h. Then, the Mn_3O_4@PEG-Mal NPs were added to the solution dropwise and the mixture was further incubated with stirring under the same conditions for 1 h. Excess peptide and Traut's reagents were removed by 3 cycles of centrifugation. Thus, complete Mn_3O_4@PEG-RGD NPs were obtained for further experiments.

FITC-labeled Mn_3O_4@PEG-RGD NPs were also synthesized. In the first step, Mn_3O_4@PEG-NH_2 NPs was prepared by the same process of Mn_3O_4@PEG-Mal NPs. Then Mn_3O_4@PEG-NH_2 NPs were conjugated with FITC at pH 8.5 for 3 h. The molar ratio of FITC to Mn_3O_4@PEG-NH_2 NPs was 1:10. The NPs were further conjugated with SCM-PEG-Mal under the same conditions as those of DSPE-PEG-NH_2 conjugation. Finally, FITC-Mn_3O_4@PEG-Mal NPs was obtained. The RGD peptide was then conjugated onto the NPs *via* the same method which mentioned previously.

Characterization of Mn_3O_4@PEG-RGD NPs

The hydrodynamic sizes of the Mn_3O_4 NPs and Mn_3O_4@PEG-RGD NPs were measured with a Malvern Zetasizer Nano ZS (Malvern, UK). Transmission electron microscopy (TEM) was used to investigate the morphologies and sizes of the NPs. The X-ray diffraction (XRD) pattern of the Mn_3O_4 NPs was investigated with Cu Kα radiation (λ = 0.15405) with a Bruker D8 diffractometer (MA, USA). The T1-relaxivities and T1-weighted images of Mn_3O_4 aqueous solution were observed and measured by a 0.5 T mouse MRI scanner (Niumag Corp., Shanghai, China). The conventional spin-echo acquisition sequence was as follows: TE = 18.2 ms, TR = 350 ms, Slice Thickness = 4 mm, and Slice Gap = 0.8 mm. The stability of the NPs was evaluated by measuring their hydrodynamic sizes under different conditions. In order to detect whether the NPs could be

used in further *in vitro* or *in vivo* investigations, the dispersion solutions included PBS, complete medium, and FBS.

Cell and Animal Models

Two normal human cell lines (HUVECs and IMR-90 cells) and two human gastric cancer cell lines (SGC-7901 and BGC-823 cells) were utilized in the study. All cell lines were incubated in DMEM high glucose medium with 10% of FBS, 1% of antibiotics at 37°C under 5% CO_2. Logarithmic phase cells were seeded into dishes or plates for further utilization in *in vitro* experiments.

BALB/c-nu/nu mice were used to establish xenograft animal model. Four-week-old male mice were fed under SPF conditions 5 days for acclimation. If the physiological status of the mice was normal, they could be used for model. First, 100 μl of a SGC-7901 cell suspension containing 1×10^6 cells was subcutaneously injected into the right crotch of each mouse. When the tumor grew to a sufficient size, the animal could be used for *in vivo* experiments. All animal experiments were supervised by the Laboratory Animal Administration Committee of Xi'an Medical University. Animal experimental protocols followed by the Guidelines for the Use and Care of Experimental Animals at Xi'an Medical University.

Cytotoxicity Tests

The *in vitro* cytotoxicity of Mn_3O_4@PEG-RGD NPs was evaluated by CCK-8 assay. Four human cell lines (HUVECs and IMR-90, SGC-7901 and BGC-823 cells) were used for the evaluation of the *in vitro* cytotoxicity. Mn_3O_4@PEG NPs and RGD peptide were used as controls. During the logarithmic growth phase, cells were seeded into 96-well plate at a density of 8×10^4 cells/well. Subsequently, samples at different concentrations were added. After 72 h, when the cells in the untreated wells grew to 90% confluence, the medium was replaced with fresh colorless medium containing 10% CCK-8 agent. The plate was further incubated for 2 h, and the absorbance at 450 nm of each well was measured with a microplate reader (Infinite® 200 Pro, Tecan, Switzerland). The cell viability was calculated.

Cell Internalization and Affinity Assay

FITC-labeled Mn_3O_4@PEG-RGD NPs were prepared for evaluation by internalization and affinity assays. SGC-7901 cells were incubated in confocal dishes for 24 h. Then, the NPs were added to the dishes. Subsequently, the cells were fixed with a 4% paraformaldehyde solution for 0.5 h, 2 h and 4 h, and then the cell nuclei were stained with a DAPI kit. The dishes were observed *via* a confocal microscope (TCS SP5 II, Leica, Germany). The affinity assay was utilized to evaluate targeted delivery *in vitro*. The RGD peptide was the competitive agent of NP endocytosis. Cells were again incubated in confocal dishes for 24 h. Half of the dishes were supplemented with the RGD peptide as a blocking agent. After 1 h, the NPs were added. After incubation, the dishes were fixed with a 4% paraformaldehyde solution, and the cell nuclei were stained with DAPI. The dishes were observed by confocal microscopy. All fluorescent signals were quantified by ImageJ software.

Hemolysis Assay

The primary route of administration of the Mn_3O_4@PEG-RGD NPs is intravenous injection. Therefore, the influence of the NPs on erythrocytes should be evaluated. Whole blood was drawn from the mice, and heparin was immediately added. The red blood cells were collected by centrifugation. The cells were then resuspended in PBS at 2% concentration. The red blood cell suspension was infused into a 6-well plate, and then Mn_3O_4@PEG-RGD NPs, Mn_3O_4@PEG NPs and RGD were added. Trition X-100 (1%, v/v) and saline were the positive and negative controls, respectively. The plates were incubated at 37°C for 2 h. Subsequently, the cell suspensions were centrifuged, and then the supernatant was collected for determination of the absorbance at 394 nm.

In Vivo Acute Toxicity

Thirty of BALB/c mice (15 females and 15 males, with an average weight of 20 g) were fed under SPF conditions for 5 days to acclimatize themselves, and then, they were randomly divided into 3 groups. The three groups were intravenously injected with Mn_3O_4@PEG-RGD NPs, Mn_3O_4@PEG NPs or RGD peptide. The doses of both the Mn_3O_4@PEG-RGD NPs and Mn_3O_4@PEG NPs groups were 100 mg/kg, and the dose of RGD peptide was 2 mg/kg. The survival rate was recorded within 14 d. Subsequently, the remaining mice were euthanized, and their organs were collected for pathological evaluation.

In Vivo MRI Investigation

Three xenograft mice were used for the MRI experiment. Two mice were intravenously injected with either Mn_3O_4@PEG-RGD NPs or Mn_3O_4@PEG NPs. The third mouse was administrated 2 mg of the RGD peptide intratumorally for blocking and then intravenously injected with Mn_3O_4@PEG-RGD NPs. The doses of both the Mn_3O_4@PEG-RGD NPs and Mn_3O_4@PEG NPs groups were 30 mg/kg. T1-MRI was performed with a 0.5 T mouse MRI scanner (Niumag Corp., Shanghai, China). The sequential time points of imaging were 0, 0.5, 1, 2, 4, and 8 h. The MRI system parameters were as follows: TE = 18.2 ms, TR = 350 ms, Slice Thickness = 4 mm, Flip Angle = 90°, FOV = 100, NEX = 2, Matrix: 256 × 256, Axial images.

Histology Assay

A xenograft mouse was intravenously injected with Mn_3O_4@PEG-RGD NPs at a dose of 30 mg/kg. After 4 h, the mouse was euthanized, the liver, kidney, spleen and tumor were collected. All tissues were frozen and immunofluorescent staining for histological assays. The RGD antibody and FITC-labeled second antibody were used to mark the Mn_3O_4@PEG-RGD NPs. The slides were observed with an inverted fluorescence microscope (DP72, Olympus, Tokyo, Japan).

Statistical Analysis

GraphPad Prism 5.0 software was employed to calculate the data. The data of independently repeated experiments are presented as the mean values ± standard deviation (SD). Statistical differences between the groups are indicated $p < 0.05$.

RESULTS

Preparation and Characterization of the Mn_3O_4@PEG-RGD NPs

The process of Mn_3O_4@PEG-RGD NPs preparation is exhibited in **Figure 1A**. The synthesis included three steps: synthesis of the Mn_3O_4 NPs, modification with functional PEG and then conjugation with the RGD peptide. **Figures 1B, C** are TEM images of the Mn_3O_4 NPs and Mn_3O_4@PEG-RGD NPs. Both kinds of NPs were spherical and showed good monodispersity. The diameters of the Mn_3O_4 NPs and Mn_3O_4@PEG-RGD NPs were 5.4 ± 1.4 nm and 7.3 ± 2.7 nm, respectively. The increase in size preliminarily indicated that the surface modification was successful. Further, the hydrodynamic diameters of Mn_3O_4 NPs and Mn_3O_4@PEG-RGD NPs were measured with a Malvern instrument. The average sizes of the NPs are shown in **Figure 1D**. The size of the Mn_3O_4 NPs was 5.9 ± 1.9 nm, showing no obvious differences between the TEM observation. Nevertheless, in the measurement of Mn_3O_4@PEG-RGD NPs, the hydrodynamic size was 28.5 ± 7.4 nm, which was more than 4 times that of the TEM observation. The primary reason for this result is that the hydrated PEG layer of the Mn_3O_4@PEG-RGD NPs evaporated during sample preparation and TEM observation. The Mn_3O_4 NPs were dispersed in cyclohexane since the NPs could not be dispersed in aqueous solution. By comparison, PEG modified NPs could be effectively dispersed in water. The results also indicated that PEG successfully crosslinked onto the surface of the Mn_3O_4 NPs.

The XRD pattern indicates that the Mn_3O_4 NPs were well-crystallized. The Joint Committee on Powder Diffraction Standard (JCPDS) card number 24-0734 was used to contrast the diffraction peaks. The results are shown in **Figure S1**. The Mn_3O_4 NPs peaks coincide with the standard. The stability of the NPs was evaluated by changing the hydrodynamic size under different conditions. Mn_3O_4 NPs were dispersed in cyclohexane as the control. The results are shown in **Figure 2**. Both the Mn_3O_4@PEG NPs and Mn_3O_4@PEG-RGD NPs could be stably dispersed in PBS. Compared with the control, the size distributions of Mn_3O_4@PEG NPs and Mn_3O_4@PEG-RGD NPs at 37°C were significantly broader than those at low temperature. The possible reason for this result is that an increase in temperature promotes PEG to form a thicker hydrated rete. Similarly, the Mn_3O_4@PEG NPs and Mn_3O_4@PEG-RGD NPs, which were dispersed in medium and FBS, also showed broad size distribution curves. Beside temperature factor, proteins in solution appear to have an impact on hydrated retia. Overall, Mn_3O_4@PEG NPs and Mn_3O_4@PEG-RGD NPs could be effectively dispersed in various conditions, indicating good colloidal stability of the NPs.

A 0.5 T MRI scanner was utilized to evaluate magnetic resonance contrast performance of Mn_3O_4@PEG-RGD NPs in aqueous solution. As shown in **Figure 3A**, Mn_3O_4@PEG-RGD

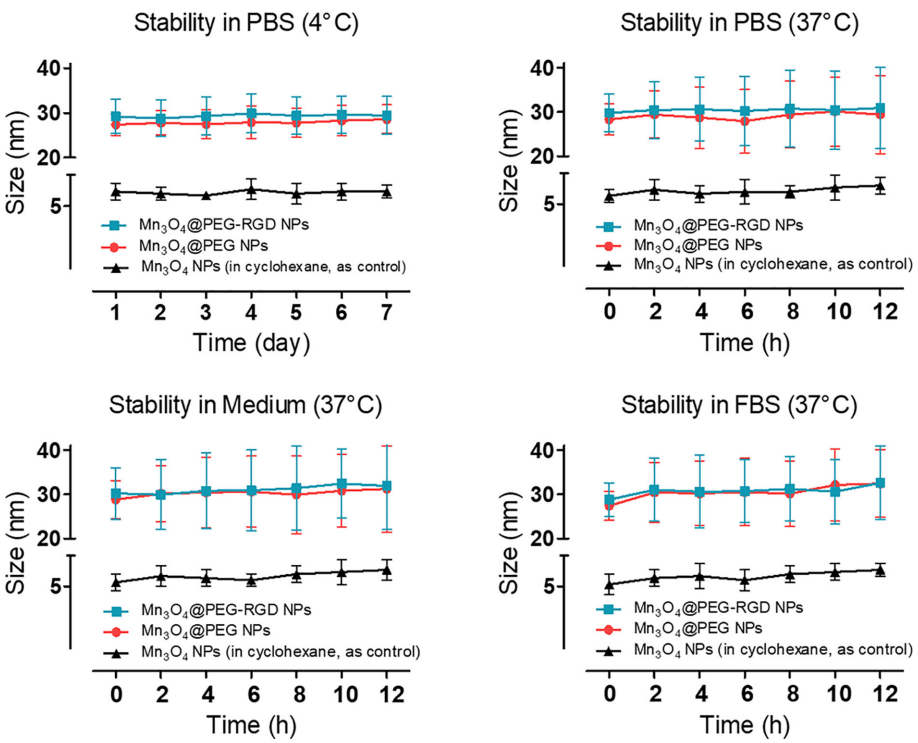

FIGURE 2 | Colloidal stability of Mn_3O_4@PEG-RGD NPs. The NPs were dispersed in PBS, complete medium and FBS, respectively. Mn_3O_4 NPs and Mn_3O_4@PEG NPs were employed as control. Mn_3O_4 NPs was dispersed in cyclohexane.

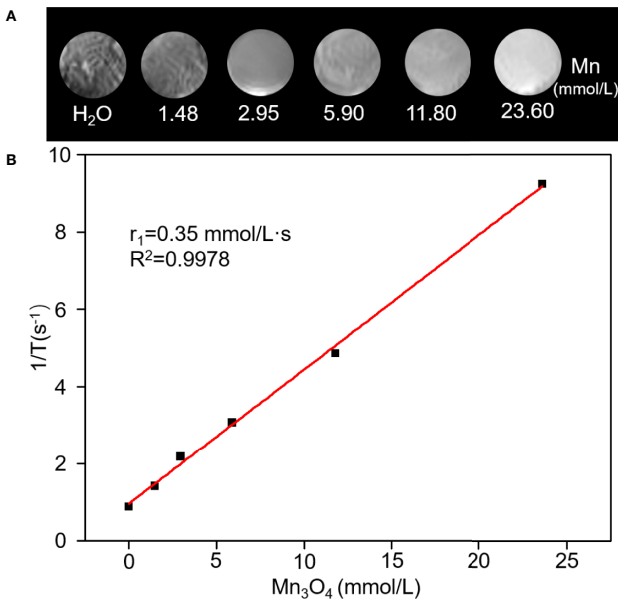

FIGURE 3 | Relaxation performances of Mn_3O_4@PEG-RGD NPs. T1-weighted MRI of the NPs in aqueous phase **(A)**. Calculation of Relaxation rate (r_1) of Mn_3O_4@PEG-RGD NPs **(B)**.

NPs exhibited a significant reinforcement effect on T1-MRI. The concentration-response relationship is remarkable. The relaxation rate (r_1) of the Mn_3O_4@PEG-RGD NPs was calculated by measuring the proton relaxation time. The results are shown in **Figure 3B**. The data also correspond to the concentration of the NPs. The r_1 value was determined to be 0.35 mmol/L·s.

In Vitro Cytotoxicity and Internalization Assay

The cytotoxicity of Mn_3O_4@PEG-RGD NPs was evaluated by CCK-8 assay, which used two normal human cell lines (HUVECs and IMR-90 cells) and two of human gastric cancer cell lines (SGC-7901 and BGC-823 cells). Mn_3O_4@PEG NPs and the RGD peptide were used as the control. Mn_3O_4 NPs were not applicable in this experiment due to their water-insoluble nature. As shown in **Figure 4**, all of those treatments exhibited low cytotoxicity in 4 cell lines. More than 90% of the cells survived at the highest concentration of Mn_3O_4. The cell viabilities did not exhibit significant difference between treatment with the Mn_3O_4@PEG-RGD NPs and Mn_3O_4@PEG NPs. The results preliminarily indicate that Mn_3O_4@PEG-RGD NPs have good biocompatibility *in vitro*.

The internalization process of Mn_3O_4@PEG-RGD NPs is shown in **Figure 5**. The green and blue fluorescence originates from FITC-labeled Mn_3O_4@PEG-RGD NPs and DAPI-labeled cell nuclei respectively. An enhancement in cellular green fluorescence reflects the internalization process. After the initial 0.5 h, the green fluorescent signal appeared in the cytoplasm. Then the fluorescence intensity gradually increased in cells. After 2 h, the cell image appeared completely. At 4 h, the fluorescent signal strength in the cell accumulated to a higher level. The RGD peptide provided the NPs cancer cell targeting function, which was achieved by the interaction with the integrin receptor. In order to verify the effect of targeted delivery, we used the RGD peptide as a competitive inhibitor to block Mn_3O_4@PEG-RGD NPs endocytosis. The results are shown in **Figure 6**. The green fluorescent intensity in blocking group was significantly lower than that in the untreated group, which means the RGD peptide could effectively block the internalization of Mn_3O_4@PEG-RGD NPs. This result indicates that the transmembrane transport of Mn_3O_4@PEG-RGD NPs is mediated by RGD-integrin receptor interactions and preliminarily suggests that Mn_3O_4@PEG-RGD NPs could achieve tumor-targeted delivery.

In Vivo Toxicity Evaluation

The route of administration of Mn_3O_4@PEG-RGD NPs is intravenous injection. Therefore, the erythrocyte impact of the NPs should initially be evaluated. The hemolysis results are shown in **Figure 7C**. Triton X-100 caused severe red blood cell plasmorrhexis, and the lysis rate was over 70%. By comparison, the samples in the Mn_3O_4@PEG-RGD NPs, Mn_3O_4@PEG NPs, and RGD treatment groups exhibited low lysis rates, all of which were less than 5%. The results indicate that Mn_3O_4@PEG-RGD NPs have little impact on erythrocytes. The safety of intravenous injection is guaranteed.

Subsequently, an acute toxicity test was further employed to evaluate the *in vivo* toxicity of the Mn_3O_4@PEG-RGD NPs. As **Figure 7A** shows, no mice died in the RGD peptide treatment group, and most of the mice survived in the Mn_3O_4@PEG-RGD NPs and Mn_3O_4@PEG NPs groups, which did not exhibit prominent toxic effects at a high dose. The pathological sections further demonstrated the results. The NPs treatments did not obviously injure the main organs. Histological evaluation of the heart, liver and kidney did not show pathological injury (**Figure 7B**). These results amply demonstrated that Mn_3O_4@PEG-RGD NPs had excellent biocompatibility.

In Vivo MRI Evaluation

The BALB/c nu/nu mouse xenograft model was utilized to evaluate the T1-weight effect of Mn_3O_4@PEG-RGD NPs in MRI. First, the NPs were intravenously injected into each mouse. The images were then successively captured in sequential time points. The MRI images are shown in **Figure 8A**, and the MR signal intensity was calculated and is exhibited in **Figure 8B**. In the Mn_3O_4@PEG-RGD NPs group, the signal was observed immediately. The reason for this result is that the scanning time of MRI needs approximately 25 min; and at this time, the NPs have accumulated in the tumor tissues. After 1 h, the signal in the Mn_3O_4@PEG-RGD NPs group reached its maximum, and then fell gradually. Mn_3O_4@PEG NPs did not show positive targeted performance, and the accumulation quantity in the tumor was obviously lower than that of the Mn_3O_4@PEG-RGD NPs group. Nevertheless, both NPs treatment groups exhibited similar trends. The curve in the RGD-blocking treatment group showed difference that the peak appeared in 2 h, and the intensity was stronger than that

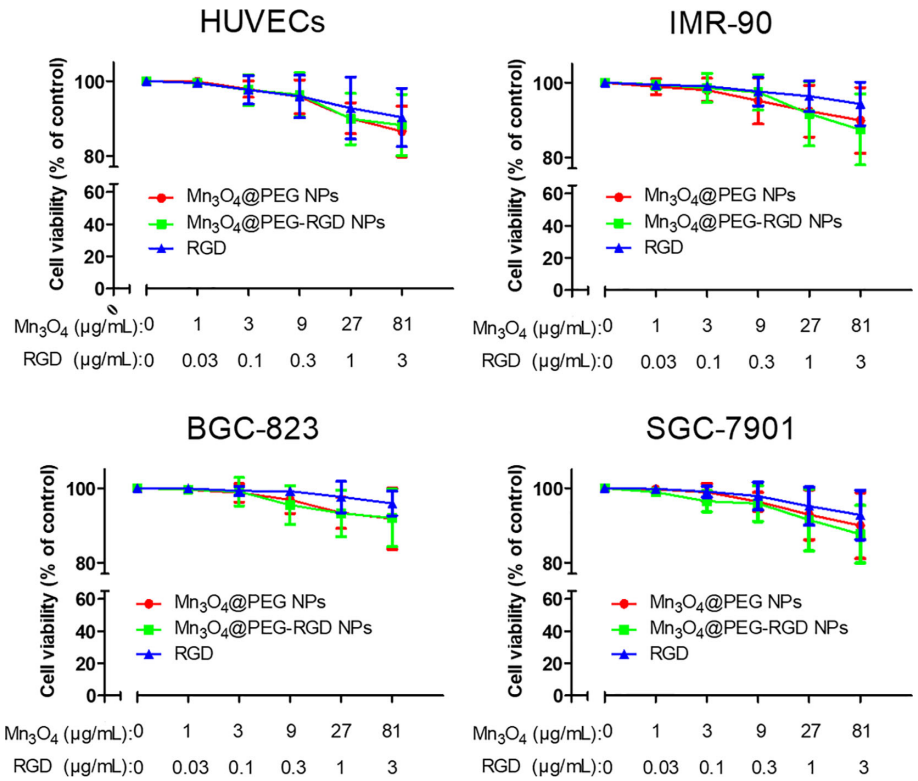

FIGURE 4 | *In vitro* cytotoxicity of Mn_3O_4@PEG-RGD NPs. Cell viabilities of HUVECs, IMR-90, BGC-823, and SGC-7901, which were incubated with different concentrations of the NPs. Mn_3O_4@PEG NPs and RGD peptide were used as control. The concentration of NPs was set by quantity of Mn_3O_4.

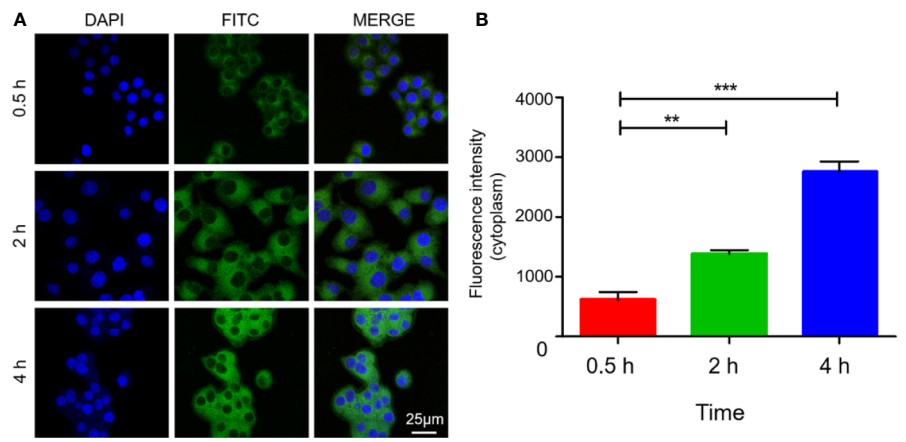

FIGURE 5 | Internalization of Mn_3O_4@PEG-RGD NPs in SGC-7901 cell line. Confocal imaging of cell co-incubation in different time points **(A)**. Quantitation of fluorescent intensity in cell **(B)**. Error bars represent the SD of the mean. The ** indicated $p < 0.01$, *** indicated $p < 0.001$.

in the Mn_3O_4@PEG NPs group in subsequent 6 h. This trend indicates that RGD could initially block the positive tumor target of Mn_3O_4@PEG-RGD NPs. When the RGD peptide is metabolized, the targeted delivery of Mn_3O_4@PEG-RGD NPs is regained.

Immunofluorescence analysis was further employed to verify the targeted delivery of the Mn_3O_4@PEG-RGD NPs. As shown in **Figure 9**, green fluorescent spots were observed in tumor tissues from the Mn_3O_4@PEG-RGD NPs treated mouse obviously. However, the fluorescent spot was almost invisible

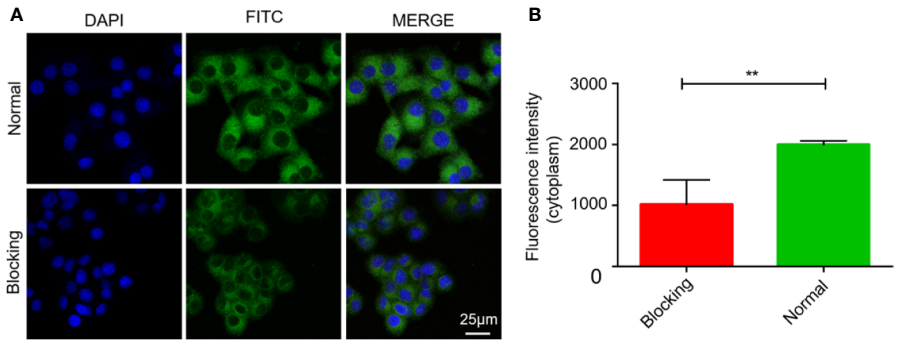

FIGURE 6 | RGD blocking test of Mn_3O_4@PEG-RGD NPs. Confocal imaging of cell in different treatments **(A)**. Quantitation of fluorescent intensity in cell **(B)**. Error bars represent the SD of the mean. The ** indicated $p < 0.01$.

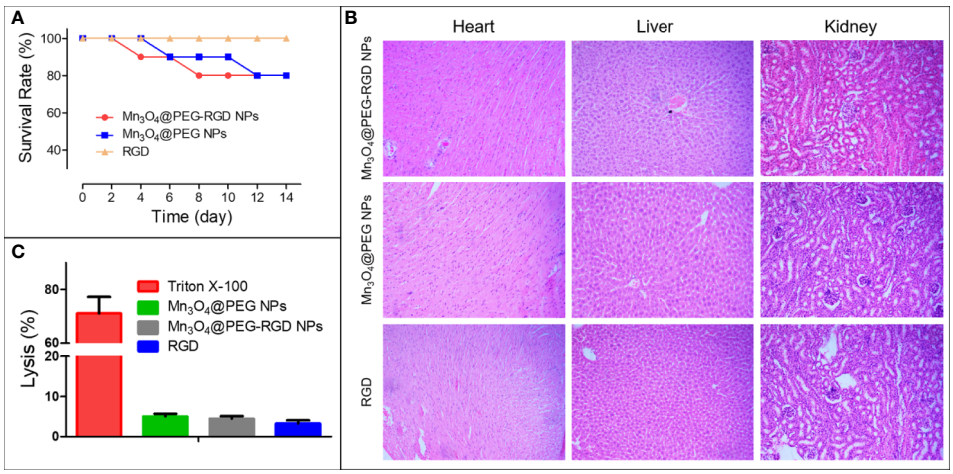

FIGURE 7 | *In vivo* toxicity of Mn_3O_4@PEG-RGD NPs. Survival rate of mice in different treatments **(A)**. Pathological sections of heart, liver and kidney **(B)**. Results of hemolytic assay **(C)**.

in the normal organs after Mn_3O_4@PEG-RGD NPs treatment and in the tumor after Mn_3O_4@PEG NPs treatment. These results further demonstrate that Mn_3O_4@PEG-RGD NPs have an excellent tumor targeting function.

DISCUSSION

Worldwide, gastric cancer has become one of the most common malignant gastrointestinal tumors and displays high mortality (1). In gastric cancer, radical surgery can lead to a positive curative effect. However, postoperative recurrence is an unavoidable problem in the majority of patients. If recurrence occurs, chemotherapy is the primary treatment, and the therapy must be long-term. How effectively patients continue their therapy can also depend on the evaluation of the therapeutic effect, especially the imaging-guided monitoring. To prolong survival in patients with gastric cancer, researchers employed various imaging technologies for diagnosis. Although, gastroscopy, CT, PET, and SPECT exhibit accuracy in the early diagnosis of gastric cancer, radioactivity and invasive injury severely limit their applications in continuous monitoring. By comparison, MIR, a non-invasive and non-radiological imaging method, is an important iconography for gastric cancer diagnosis (14). Contrast agents can be used to further improve clarity in MRI scans of the cancer tissues. However, there are currently still several problems with the administration of contrast agents in clinical MRI. In order to increase the efficiency of the MRI in continuous postoperative monitoring, we prepared Mn_3O_4@PEG-RGD NPs, which could be used for *in vivo* gastric cancer MRI observation. The core of the contrast agent is a Mn_3O_4 NPs. Synthesis of the NPs was based on the thermal decomposition reaction of water and manganese acetate in the presence of oleylamine. During the synthesis, water promoted the nucleation of nanocrystals, and oleylamine was used as catalyst (32). As the results show, Mn_3O_4 NPs were spherical and appeared to be monodispersed in an excellent manner. The average size of the

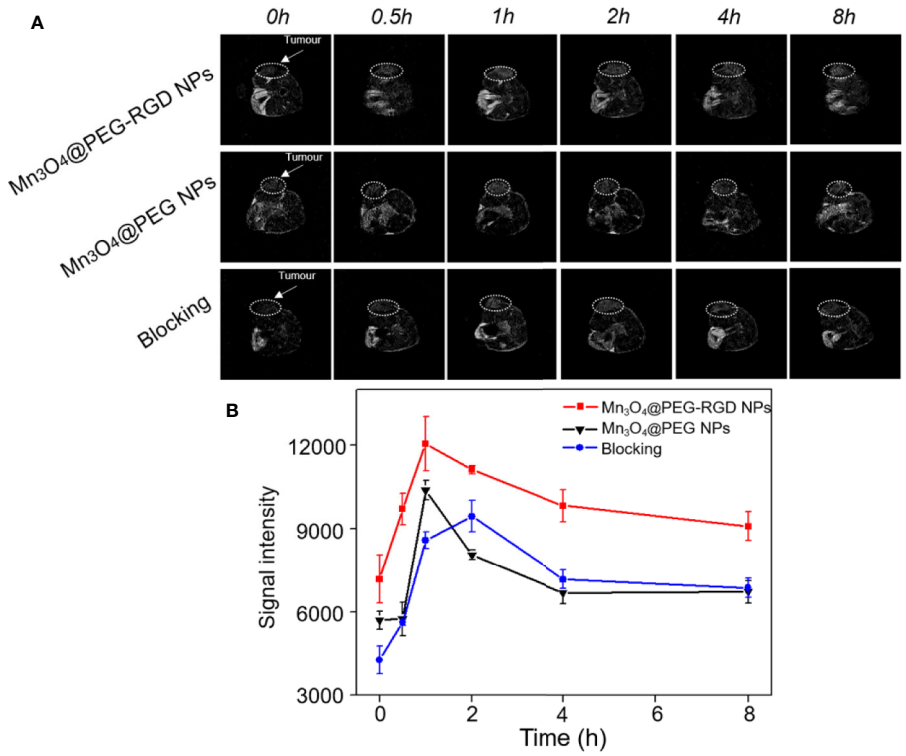

FIGURE 8 | *In vivo* T1-weighted MRI of Mn_3O_4@PEG-RGD NPs at different time points. White circles points location of tumor **(A)**. Quantitation of MR intensity in tumor at different time points **(B)**. Error bars represent the SD of the mean.

NPs was approximately 5 nm. This result was also verified by XRD. However, the relatively low biocompatibility of Mn_3O_4 NPs was a problem. The NPs dispersed in cyclohexane, meaning that they could not be used in the aqueous phase. In order to compensate for this limitation, we employed PEG to modify the Mn_3O_4 NPs (25, 42, 43). Moreover, for further modification, a functionalized PEG lipid was used in the hydrophilization of the Mn_3O_4 NPs. The Mn_3O_4@PEG NPs also exhibited good monodispersity and aqueous stability. Their size in TEM observation increased by approximately 2 nm, which indicated that PEG successfully covered the surface of Mn_3O_4 NPs. In the next step, the RGD peptide was further conjugated to the PEG layer, which provided a tumor-targeting function. The hydrodynamic size of the Mn_3O_4@PEG-RGD NPs also increased nearly quintuple. This phenomenon was due to the expansion of the PEG hydration layer in the DLS measurements (44, 45). Colloidal stability is a critical performance indicator of the NPs (46). Dispersed in PBS, medium and FBS, the sizes of the Mn_3O_4@PEG-RGD NPs or Mn_3O_4@PEG NPs were sequentially measured. The Mn_3O_4@PEG-RGD NPs did not show flocculation and precipitation throughout the experiment. More notably, the data indicated that the hydrodynamic size of the NPs was very stable in different solutions and under various temperature conditions. These results amply demonstrated that the NPs exhibited excellent stability under physiological conditions. Importantly, the manufacturing process and cost of the Mn_3O_4@PEG-RGD NPs are efficient enough for mass production and application. These NPs will be more beneficial for the continuous postoperative monitoring in patients with gastric cancer.

Biotolerance, which ensures safe *in vivo* application, is a necessary feature for MRI agents. In order to evaluate whether the Mn_3O_4@PEG-RGD NPs could be used as an MRI contrast agent, a series of experiments were conducted. Initially, the *in vitro* cytotoxicity of the NPs was evaluated in four cell lines, including HUVECs and IMR-90, SGC-7901 and BGC-823 cells. HUVECs are human umbilical vein endothelial cells and used to evaluated the impact of the NPs on the blood vessel endothelium. Originating from human embryonic lung fibroblast tissues, IMR-90 cells were used to verify the cytotoxicity of Mn_3O_4@PEG-RGD NPs in normal cell. Both SGC-7901 and BGC-823 cells were employed to investigate their influence on gastric cancer cells. The results of the CCK-8 assay indicated that the Mn_3O_4@PEG-RGD NPs did not show obvious cytotoxicity in any of the four cell lines. The cell viabilities were over 90%, even at maximum concentration of the Mn_3O_4@PEG-RGD NPs. A similar result appeared after treatment with Mn_3O_4@PEG NPs. Therefore, the low cytotoxicity of the Mn_3O_4@PEG-RGD NPs was verified. Subsequently, we evaluated *in vivo* toxicity of Mn_3O_4@PEG-RGD NPs. Initially, a hemolysis assay was applied to investigate whether the Mn_3O_4@PEG-RGD NPs could impact red blood cells. The lysis rate after treatment with Mn_3O_4@PEG-RGD NPs was less than 5%. Then, we further evaluated the *in vivo* acute toxicity in animals.

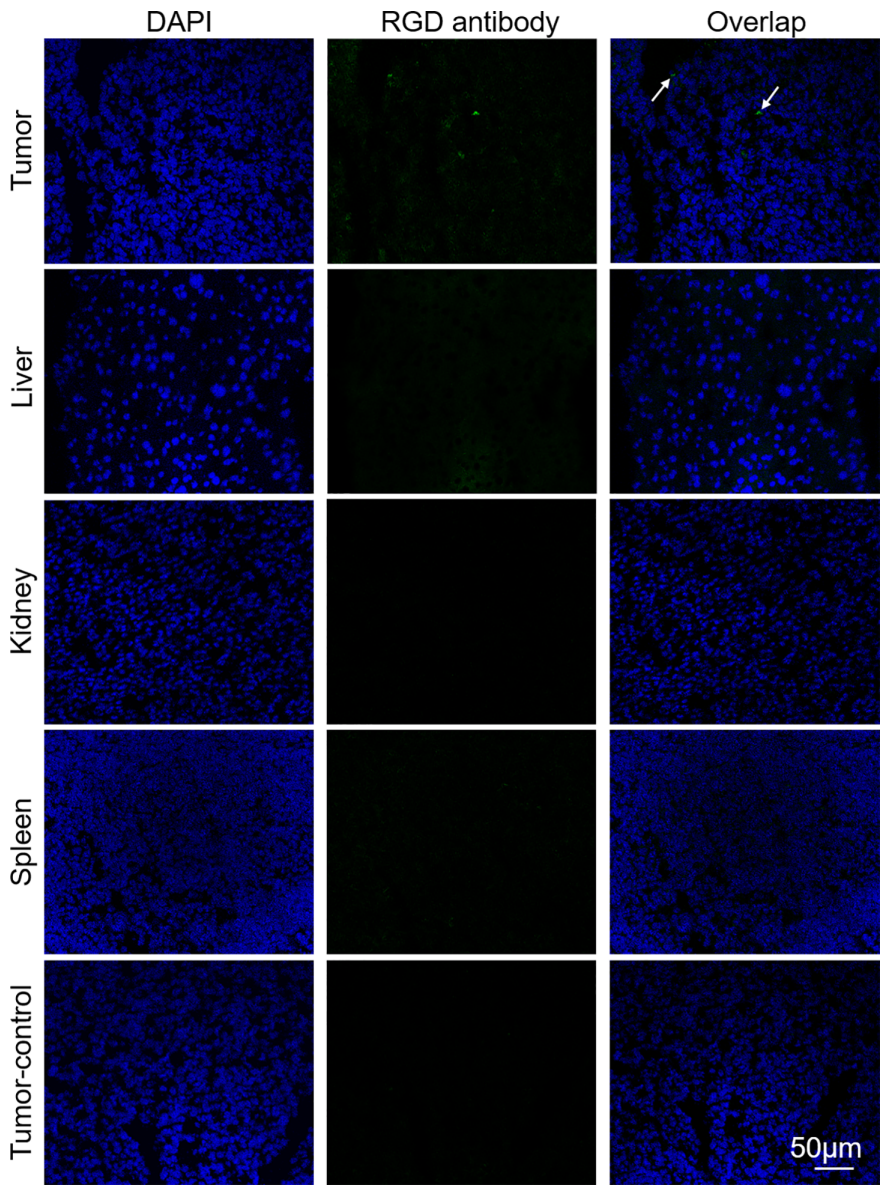

FIGURE 9 | Immunofluorescent assay of Mn_3O_4@PEG-RGD NPs in various tissues *via* RGD antibody. Green fluorescent signal derives Mn_3O_4@PEG-RGD NPs (Pointed by white arrow). Blue fluorescent signal is from DAPI, which indicates nuclei. Scale bar: 50 μm.

Mn_3O_4@PEG-RGD NPs, Mn_3O_4@PEG NPs and RGD peptide were injected into BALB/c mice, respectively. The intravenous injection dose was 100 mg/kg, which is well above the dose for practical imaging applications. After two weeks of observation and recording, 80% of the mice in Mn_3O_4@PEG-RGD NPs treatment groups were survived. By comparison, the survival ratios in the Mn_3O_4@PEG NPs and RGD peptide groups were also impressive. In addition, pathological analysis further verified that there were no obvious injuries to the major organs. Based on these results, the biotolerance of the Mn_3O_4@PEG-RGD NPs was amply demonstrated. And it indicated that the NPs could be safely utilized in long-term for MRI *in vivo*. The excellent performance suggests that Mn_3O_4@PEG-RGD NPs could be used for the continuous postoperative monitoring in gastric cancer patients, without cumulative toxicity.

MR imaging of Mn_3O_4@PEG-RGD NPs is the essential endpoint of this study. A series of *in vitro* and *in vivo* imaging experiments were employed to evaluate whether Mn_3O_4@PEG-RGD NPs could be used as an MRI contrast agent for the postoperative monitoring of gastric cancer. In the evaluation of magnetic resonance contrast performance, Mn_3O_4@PEG-RGD NPs showed a remarkable concentration-response relationship. As the concentration increased, the MRI signal was enhanced. The r_1 value was 0.35 mmol/L·s. The data are much lower than that of Gd-based MR contrast agents. The probable reason for the low r_1 value might be due to the valences of Mn_3O_4. Mn_3O_4 contains two trivalent Mn

atoms and one bivalent Mn. The paramagnetic strength of the ions depends on the number of unpaired electrons in the 3d orbital. Thus, more unpaired electrons will have stronger paramagnetic strength (31). The unpaired electron number of the trivalent Mn is less than that of divalent Mn; therefore, the r_1 value of Mn_3O_4 is relatively low. Besides, PEG modification also probably contributes to this result. PEG provides hydrophilia to the Mn_3O_4 NPs. At the same time, it forms a thick hydrophobic layer, which hinders the chemical exchange between magnetic ions and protons (47, 48). However, Mn_3O_4@PEG-RGD NPs still exhibited obvious T1-weighted effects both *in vitro* and *in vivo*. It can fully meet the demands of the monitoring of gastric cancer. The gastric tumor target of Mn_3O_4@PEG-RGD NPs was mediated by RGD-integrin receptor interaction (36). The integrin receptor is widely expressed on the cytomembrane of various tumor cells, such as in gastric cancer, hepatic cancer, pulmonary cancer and colon cancer (37, 39, 40). In this study, fluorescently labeled NPs were used for the observation of internalization (49, 50). Under normal conditions, FITC-labeled Mn_3O_4@PEG-RGD NPs gradually accumulated in the cytoplasm of SGC-7901 cells. However, competitive suppression with the RGD peptide could block the endocytosis of Mn_3O_4@PEG-RGD NPs. The results preliminarily demonstrated that the NPs possess gastric tumor targeted delivery. Subsequently, the *in vivo* MRI evaluation of Mn_3O_4@PEG-RGD NPs was performed in a gastric cancer xenograft mouse model. In Mn_3O_4@PEG-RGD NPs-treated mouse, the MR signal was rapidly observed in tumor tissues after intravenous injection. After 1 h, the intensity of MR signal reached its peak, and then gradually decreased. The signal in Mn_3O_4@PEG NPs was significantly lower than that in the targeted NPs. Remarkably, intratumoral injection of the RGD peptide could effectively blocking accumulation of Mn_3O_4@PEG-RGD NPs. Thus, Mn_3O_4@PEG-RGD NPs have an excellent *in vivo* gastric tumor-targeting ability and can effectively perform *in vivo* MR imaging. Moreover, immunofluorescence analysis verified that Mn_3O_4@PEG-RGD NPs could accumulate in gastric tumor in the mouse model, meanwhile, barely exhibited accumulation in normal organs and tissues. The results indicate that Mn_3O_4@PEG-RGD NPs can rapidly penetrate into the gastric tumor, and then be gradually metabolized. In principle, the metabolites are safe and non-toxic. The RGD peptide will be hydrolyzed in the same manner as other amino acids. PEG is widely used in medicine and food. Mn is a necessary element in the body that can effectively be metabolized and excreted out of the body. Throughout the whole monitoring process, the Mn_3O_4@PEG-RGD NPs did not cause obvious side effects, which could certify their long-term reliability. All of these results indicated that Mn_3O_4@PEG-RGD NPs may have great potential for the MRI postoperative monitoring of gastric cancer.

CONCLUSION

In the present study, we demonstrated that Mn_3O_4@PEG-RGD NPs could be a reliable MRI contrast agent for monitoring gastric cancer *in vivo*, due to its possession of obvious advantages, such as simple preparation, low cost, effective T1-weighted, rapid metabolism, and low toxic. All of these attributes are suitable for the long-term monitoring of gastric cancer. Initially, Mn_3O_4 NPs were synthesized followed by modification with PEG and conjugation of the RGD peptide to prepare the targeted T1-MRI contrast agent. Within these NPs, the Mn_3O_4 NPs are the core for MRI. An appropriate size and shape make the NPs usable in MRI and suitable for further modification and functionalization. PEG modification makes these NPs to disperse in aqueous solution, thus resolving the problem of biocompatibility. The RGD peptide provides the NPs with a gastric tumor-targeting function, which allows the NPs to rapidly accumulate in gastric tumor tissues *in vivo*. Moreover, a series of evaluations verified that Mn_3O_4@PEG-RGD NPs have excellent biosecurity and colloidal stability. In conclusion, Mn_3O_4@PEG-RGD NPs were amply demonstrated to be a potential nano contrast agent for postoperative monitoring of gastric cancer *via* MRI.

DATA AVAILABILITY STATEMENT

The raw data supporting the conclusions of this article will be made available by the authors, without undue reservation.

ETHICS STATEMENT

The animal study was reviewed and approved by Laboratory Animal Administration Committee of Xi'an Medical University.

AUTHOR CONTRIBUTIONS

KL and SH designed the study. KL and PL performed the experiments. KL, PL, YW, and SH analyzed the results and data. KL and PL prepared the manuscript. YW and SH modified the manuscript. All authors contributed to the article and approved the submitted version.

FUNDING

This study was supported, in part, by the National Natural Science Foundation of China (81801863), the Natural Science Basic Research Program of Shaanxi (2019JQ-485), Innovation Capability Support Program of the Shaanxi Province (2020KJXX-050).

SUPPLEMENTARY MATERIAL

The Supplementary Material for this article can be found online at: https://www.frontiersin.org/articles/10.3389/fonc.2020.601538/full#supplementary-material

SUPPLEMENTARY FIGURE 1 | X-ray diffraction pattern of Mn_3O_4 NPs.

REFERENCES

1. Sigel RL, Miller KD, Jemal A. Cancer statistics, 2020. *CA Cancer J Clin* (2020) 70:7–30. doi: 10.3322/caac.21590
2. Sitarz R, Skierucha M, Mielko J, Offerhaus GJA, Maciejewski R, Polkowski WP. Gastric cancer: epidemiology, prevention, classification, and treatment. *Cancer Manage Res* (2018) 10:239–48. doi: 10.2147/CMAR.S149619
3. Ferlay J, Soerjomataram I, Dikshit R, Eser S, Mathers C, Rebelo M, et al. Cancer incidence and mortality worldwide: sources, methods and major patterns in GLOBOCAN 2012. *Int J Cancer* (2015) 136:E359–86. doi: 10.1002/ijc.29210
4. Abdul Kuddus S. Nanoparticles to deal with gastric cancer. *J Gastrointestinal Cancer Stromal Tumors* (2017) 2:112. doi: 10.4172/2572-4126.1000112
5. Yang W, Ma J, Zhou W, Cao B, Zhou X, Yang Z, et al. Molecular mechanisms and theranostic potential of miRNAs in drug resistance of gastric cancer. *Expert Opin Ther Targ* (2017) 21:1063–75. doi: 10.1080/14728222.2017.1389900
6. Benbrahim Z, Mekkaoui AE, Lahmidani N, Mellas N, Ismali Z. Gastric cancer: an epidemiological overview. *Epidemiology* (2017) 7:1000304. doi: 10.4172/2161-1165.1000304
7. Ried K, Eng P, Sali A. Screening for circulating tumour cells allows early detection of cancer and monitoring of treatment effectiveness: an observational study. *Asian Pac J Cancer Prev* (2020) 18:2275–85. doi: 10.22034/APJCP.2017.18.8.2275
8. Kitabatake S, Niwa Y, Miyahara R, Ohashi A, Matsuura T, Iguchi Y, et al. Confocal endomicroscopy for the diagnosis of gastric cancer in vivo. *Endoscopy* (2006) 38:1110–4. doi: 10.1055/s-2006-944855
9. Dhar DK, Kubota H, Tachibana M, Kotoh T, Tabara H, Watanabe R, et al. Long-term survival of transmural advanced gastric carcinoma following curative resection: Multivariate analysis of prognostic factors. *World J Surg* (2000) 24:588–93. doi: 10.1007/s002689910099
10. Zhang XF, Huang CM, Lu HS, Wu XY, Wang C, Guang GX, et al. Surgical treatment and prognosis of gastric cancer in 2,613 patients. *World J Gastroenterol* (2004) 10:3405–8. doi: 10.3748/wjg.v10.i23.3405
11. Lazar DC, Avram MF, Romosan I, Cornianu M, Tiban S, Goldi A. Prognostic significance of tumor immune microenvironment and immunotherapy: Novel insights and future perspectives in gastric cancer. *World J Gastroenterol* (2018) 24:3583–616. doi: 10.3748/wjg.v24.i32.3583
12. Galante E, Okamura T, Sander K, Kikuchi T, Okada M, Zhang MR, et al. Development of Purine-Derived 18F-Labeled Pro-drug Tracers for Imaging of MRP1 Activity with PET.J. *Med Chem* (2014) 57:1023–32. doi: 10.1021/jm401764a
13. Kurdziel KA, Kiesewetter DO. PET imaging of multidrug resistance in tumors using 18F-fluoropaclitaxel. *Curr Top Med Chem* (2010) 10:1792–8. doi: 10.2174/156802610792928077
14. Sun C, Lee JSH, Zhang MQ. Magnetic nanoparticles in MR imaging and drug delivery. *Adv Drug Deliv Rev* (2008) 60:1252–65. doi: 10.1016/j.addr.2008.03.018
15. de Zwart IM, de Roos A. MRI for the evaluation of gastric physiology. *Eur Radiol* (2010) 20:2609–16. doi: 10.1007/s00330-010-1850-3
16. Kim IY, Kim SW, Shin HC, Lee MS, Jeong DJ, Kim CJ, et al. MRI of gastric carcinoma: results of T and N-staging in an in vitro study. *World J Gastroenterol* (2009) 15:3992–8. doi: 10.3748/wjg.15.3992
17. Na HB, Song IC, Hyeon T. Inorganic nanoparticles for MRI contrast agents. *Adv Mater* (2009) 21:2133–48. doi: 10.1002/adma.200802366
18. Hu H, Dai A, Sun J, Li X, Gao F, Wu L, et al. Aptamer-conjugated Mn3O4@SiO2 core-shell nanoprobes for targeted magnetic resonance imaging. *Nanoscale* (2013) 5:10447–54. doi: 10.1039/c3nr03490a
19. Terreno E, Delli Castelli D, Viale A, Aime S. Challenges for molecular magnetic resonance imaging. *Chem Rev* (2010) 2010(110):3019–42. doi: 10.1021/cr100025t
20. Kim JK, Choi KJ, Lee M, Jo MH, Kim S. Molecular imaging of a cancer-targeting theragnostics probe using a nucleolin aptamer-and microRNA-221 molecular beacon-conjugated nanoparticle. *Biomaterials* (2012) 33:207–17. doi: 10.1016/j.biomaterials.2011.09.023
21. Gong P, Shi BH, Zheng MB, Wang B, Zhang PF, Hu DH, et al. PEI protected aptamer molecular probes for contrast-enhanced in vivo cancer imaging. *Biomaterials* (2012) 33:7810–7. doi: 10.1016/j.biomaterials.2012.07.011
22. Kircher MF, Hricak H, Larson SM. Molecular imaging for personalized cancer care. *Mol Oncol* (2012) 6:182–95. doi: 10.1016/j.molonc.2012.02.005
23. Gossmann A, Okuhata Y, Shames DM, Helbich TH, Roberts TP, Michael MF, et al. Prostate cancer tumor grade differentiation with dynamic contrast-enhanced MR imaging in the rat: comparison of macromolecular and small-molecular contrast media—preliminary experience. *Radiology* (1999) 213:265–72. doi: 10.1148/radiology.213.1.r99oc43265
24. Pinker K, Stadlbauer A, Bogner W, Gruber S, Helbich TH. Molecular imaging of cancer: MR spectroscopy and beyond. *Eur J Radiol* (2012) 81:566–77. doi: 10.1016/j.ejrad.2010.04.028
25. Lei M, Fu C, Cheng X, Fu B, Wu NN, Zhang Q, et al. Activated surface charge-reversal manganese oxide nanocubes with high surface-to-volume ratio for accurate magnetic resonance tumor imaging. *Adv Funct Mater* (2017) 27:1700978. doi: 10.1002/adfm.201700978
26. Zhao ZH, Zhou ZJ, Bao JF, Wang ZY, Hu J, Chi XQ, et al. Octapod iron oxide nanoparticles as high-performance T2 contrast agents for magnetic resonance imaging. *Nat Commun* (2013) 4:2266. doi: 10.1038/ncomms3266
27. Caravan P. Strategies for increasing the sensitivity of gadolinium based MRI contrast agents. *Chem Soc Rev* (2006) 35:512–23. doi: 10.1039/b510982p
28. Idee JM, Port M, Dencausse A, Lancelot E, Corot C. Involvement of gadolinium chelates in the mechanism of nephrogenic systemic fibrosis: an update. *Radiol Clin* (2009) 47:855–69. doi: 10.3109/10408444.2014.955568
29. Zhan YH, Zhan WH, Li HR, Xu XY, Cao X, Zhu SP, et al. In vivo dual-modality fluorescence and magnetic resonance imaging-guided lymph node mapping with good biocompatibility manganese oxide nanoparticles. *Molecules* (2017) 22:2208. doi: 10.3390/molecules22122208
30. Neves HR, Bini RA, Barbosa JHO, Salmon CEG, Varanda LC. Dextran-coated antiferromagnetic MnO nanoparticles for a T1-MRI contrast agent with high colloidal stability. *Part Syst Charact* (2016) 33:167–76. doi: 10.1002/ppsc.201500251
31. Garcia-Hevia L, Banobre-Lopez M, Gallo J. Recent Progress on Manganese-Based Nanostructures as Responsive MRI Contrast Agents. *Chem Eur J* (2019) 25:431–41. doi: 10.1002/chem.201802851
32. Yu T, Moon J, Park J, Park YII, Na HB, Kim BH, et al. Various-shaped uniform Mn3O4 nanocrystals synthesized at low temperature in air atmosphere. *Chem Mater* (2009) 21:2272–9. doi: 10.1021/cm900431b
33. Nikolaou K, Kramer H, Grosse C, Clevert D, Dietrich O, Hartmann M, et al. High-spatial-resolution multistation MR angiography with parallel imaging and blood pool contrast agent: initial experience. *Radiology* (2006) 241:861–72. doi: 10.1148/radiol.2413060053
34. Zhan YH, Ehlerding EB, Shi SX, Graves SA, Goel S, Engle JW, et al. Intrinsically zirconium-89-labeled manganese oxide nanoparticles for in vivo dual-modality positron emission tomography and magnetic resonance imaging. *Nanotechnol* (2018) 14:900–9. doi: 10.1166/jbn.2018.2498
35. Zhan YH, Shi SX, Ehlerding EB, Graves SA, Goel S, Engle JW, et al. Radiolabeled, antibody-conjugated manganese oxide nanoparticles for tumor vasculature targeted positron emission tomography and magnetic resonance imaging. *ACS Appl Mater Interf* (2017) 9:38304–12. doi: 10.1021/acsami.7b12216
36. Wang F, Chen L, Zhang R, Chen Z, Zhu L. RGD peptide conjugated liposomal drug delivery system for enhance therapeutic efficacy in treating bone metastasis from prostate cancer. *J Control Release* (2014) 196:222–33. doi: 10.1016/j.compstruct.2014.06.029
37. Shukla R, Hill E, Shi X, Kim J, Muniz MC, Sun K, et al. Tumor microvasculature targeting with dendrimer-entrapped gold nanoparticles. *Soft Matter* (2008) 4:2160–3. doi: 10.1039/b810885d
38. Rapoport NY, Kennedy AM, Shea JE, Scaife CL, Nam KH. Controlled and targeted tumor chemotherapy by ultrasound-activated nanoemulsions/microbubbles. *J Control Release* (2009) 138:268–76. doi: 10.1016/j.jconrel.2009.05.026
39. Desgrosellier JS, Cheresh DA. Integrins in cancer: biological implications and therapeutic opportunities. *Nat Rev Cancer* (2010) 10:9–22. doi: 10.1038/nrc2748
40. Jin C, Zhang BN, Wei Z, Ma B, Pan Q, Hu P. Effects of WD-3 on tumor growth and the expression of integrin αvβ3 and ERK1/2 in mice bearing human gastric cancer using the 18F-RGD PET/CT imaging system. *Mol Med Rep* (2017) 16:9295–300. doi: 10.3892/mmr.2017.7827

41. Levine RM, Scott CM, Kokkoli E. Peptide functionalized nanoparticles for nonviral gene delivery. *Soft Matter* (2012) 9:985–1004. doi: 10.1039/c2sm26633d
42. Hao R, Xing RJ, Xu ZC, Hou YL, Gao S, Sun SH. Synthesis, functionalization, and biomedical applications of multifunctional magnetic nanoparticles. *Adv Mater* (2010) 22:2729–42. doi: 10.1002/adma.201000260
43. Zhao ZH, Huang DT, Yin ZY, Chi XQ, Wang XM, Gao JH. Magnetite nanoparticles as smart carriers to manipulate the cytotoxicity of anticancer drugs: magnetic control and pH-responsive release. *J Mater Chem* (2012) 2012 (22):15717–25. doi: 10.1039/C2JM31692G
44. Li HR, Li K, Dai YP, Xu XY, Cao X, Zeng Q, et al. In vivo near infrared fluorescence imaging and dynamic quantification of pancreatic metastatic tumors using folic acid conjugated biodegradable mesoporous silica nanoparticles. *Nanomed-Nanotechnol* (2018) 14:1867–77. doi: 10.1016/j.nano.2018.04.018
45. Li JJ, Wu C, Hou PF, Zhang M, Xu K. One-pot preparation of hydrophilic manganese oxide nanoparticles as T1 nano-contrast agent for molecular magnetic resonance imaging of renal carcinoma in vitro and in vivo. *Biosens Bioelectron* (2018) 102:1–8. doi: 10.1016/j.bios.2017.10.047
46. Sun WJ, Zhang JL, Zhang CC, Wang P, Peng C, Shen MW, et al. Construction of hybrid alginate nanogels loaded with manganese oxide nanoparticles for enhanced tumor magnetic resonance imaging. *ACS Macro Lett* (2018) 7:137–42. doi: 10.1021/acsmacrolett.7b00999
47. Dubertret B, Skourides P, Norris DJ, Noireaux V, Brivanlou AH, Libchaber A. In vivo imaging of quantum dots encapsulated in phospholipid micelles. *Science* (2002) 298:1759–62. doi: 10.1126/science.1077194
48. Gao JH, Chen K, Miao Z, Ren G, Chen XY, Gambhir SS, et al. Affibody-based nanoprobes for HER2-expressing cell and tumor imaging. *Biomaterials* (2011) 32:2141–8. doi: 10.1016/j.biomaterials.2010.11.053
49. Eley JG, Pujari VD, Mclane J. Poly (lactide-co-glycolide) nanoparticles containing coumarin-6 for suppository delivery: in vitro release profile and in vivo tissue distribution. *Drug Deliv* (2004) 11:255–61. doi: 10.1080/10717540490467384
50. Rivolta I, Panariti A, Lettiero B, Sesana S, Gasco P, Gasco MR, et al. Cellular uptake of coumarin-6 as a model drug loaded in solid lipid nanoparticles. *J Physiol Pharmacol* (2011) 62:45–53. doi: 10.1152/jn.01060.2010

Conflict of Interest: The authors declare that the research was conducted in the absence of any commercial or financial relationships that could be construed as a potential conflict of interest.

frontiers in Pharmacology

ORIGINAL RESEARCH
published: 26 November 2020
doi: 10.3389/fphar.2020.610883

pH-Sensitive and Long-Circulation Nanoparticles for Near-Infrared Fluorescence Imaging-Monitored and Chemo-Photothermal Synergistic Treatment Against Gastric Cancer

Yun Zhou[1,2], *Xuanzi Sun*[1], *Liansuo Zhou*[2] *and Xiaozhi Zhang*[1]*

[1]Department of Radiation Oncology, The First Affiliated Hospital of Xi'an Jiaotong University, Xi'an Jiaotong University, Xi'an, China, [2]College of Clinical Medicine, Xi'an Medical University, Xi'an, China

Gastrectomy is the primary therapeutic option for gastric cancer. Postoperative treatment also plays a crucial role. The strategy to improve the postoperative prognosis of gastric cancer requires a combined system that includes a more efficient synergistic treatment and real-time monitoring after surgery. In this study, photothermal-chemotherapy combined nanoparticles (PCC NPs) were prepared via π-π stacking to perform chemo-photothermal synergistic therapy and continuous imaging of gastric cancer. PCC NPs had a spherical morphology and good monodispersity under aqueous conditions. The hydrodynamic diameter of PCC NPs was 59.4 ± 3.6 nm. PCC NPs possessed strong encapsulation ability, and the maximum drug loading rate was approximately 37%. The NPs exhibited extraordinary stability and pH-response release profiles. The NPs were rapidly heated under irradiation. The maximum temperature was close to 58°C. PCC NPs showed good biocompatibility both *in vitro* and *in vivo*. Moreover, the NPs could effectively be used for *in vivo* continuous monitoring of gastric cancer. After one injection, the fluorescent signal remained in tumor tissues for nearly a week. The inhibitory effect of PCC NPs was evaluated in a gastric cancer cell line and xenograft mouse model. Both *in vitro* and *in vivo* evaluations demonstrated that PCC NPs could be used for chemo-photothermal synergistic therapy. The suppression effect of PCC NPs was significantly better than that of single chemotherapy or photothermal treatment. This study lays the foundation for the development of novel postoperative treatments for gastric cancer.

Keywords: gastric cancer, photothermal therapy, chemotherapy, synergistic treatment, continuous imaging

OPEN ACCESS

Edited by:
Xu Cao,
Dartmouth College, United States

Reviewed by:
Hui Xie,
Xidian University, China
Guangfeng Jia,
Xi'an Technological University, China

***Correspondence:**
Xiaozhi Zhang
zhangxiaozhi@xjtu.edu.cn

Specialty section:
This article was submitted to Pharmacology of Anti-Cancer Drugs, a section of the journal Frontiers in Pharmacology

Received: *27 September 2020*
Accepted: *23 October 2020*
Published: *26 November 2020*

Citation:
Zhou Y, Sun X, Zhou L and Zhang X (2020) pH-Sensitive and Long-Circulation Nanoparticles for Near-Infrared Fluorescence Imaging-Monitored and Chemo-Photothermal Synergistic Treatment Against Gastric Cancer. Front. Pharmacol. 11:610883. doi: 10.3389/fphar.2020.610883

INTRODUCTION

Gastric cancer has one of the highest incidences of malignant gastrointestinal tumors worldwide. Globally, the morbidity and mortality of gastric cancer rank fifth and third, respectively (Song et al., 2017; Sigel et al., 2020). Effectively early diagnosis of gastric cancer is difficult to achieve. Multiple factors are related to gastric cancer (Yang et al., 2017). The therapeutic strategy for gastric cancer mainly depends on surgical treatment, which includes local excision, partial gastrectomy, and total gastrectomy. Chemotherapy is primary supplementary treatment postoperatively. Currently, surgery combined with postoperative chemotherapy for gastric cancer patients improves prognosis in early

stage gastric cancer; however, the prognosis of intermediate and advanced gastric cancer remains unsatisfactory (Kang et al., 2015; Zuo et al., 2017). The strategy of further improving the comprehensive efficacy of gastric cancer involves a synergistic system that includes more efficient early diagnosis, monitoring, and synergistic treatment after surgery. Local thermotherapy is an adjuvant method to treat cancer. The majority of cancers are heat sensitive, and apoptosis is triggered at temperatures over 43°C (Hildeberandt et al., 2002). Photothermal therapy (PTT) is a novel noninvasive therapeutic technology. Photothermal agents are heated under irradiation and cause ablation of tumor tissues (Shibu et al., 2013). In addition, PTT can be used in combination with other treatments, such as chemotherapy, photodynamic therapy, immunotherapy, and radiotherapy (Sherlock et al., 2011; Sahu et al., 2013; Wang et al., 2013; Guo et al., 2014; Yi et al., 2015). Photothermal therapy combined with chemotherapy is an effective method to achieve synergistic therapy of gastric cancer because heat can promote release and endocytosis and reduce resistance (Shi et al., 2012). Moreover, dynamic monitoring postoperatively is also an important part of the synergistic system and can be used to assess tumor to guide the appropriate treatment schedule (Dhar et al., 2000; Zhang et al., 2004).

The functional agent is the core of the thermal therapy, and various materials are used for thermal therapy (Huang et al., 2006; Abadeer and Murphy, 2016; Liu et al., 2016). However, in recent decades near-infrared (NIR) dyes have been of interest in PTT against cancer, because they have strong photothermal effects, low toxicity, and appropriate excitation wavelengths (Zheng et al., 2011). Furthermore, the fluorescence of the NIR fluorescent dye also allows excellent real-time monitoring of tumor progress. At present, many NIR fluorescent dyes are used in clinical medicine and achieve a certain effect. Among them, indocyanine green (ICG) has been approved by the FDA for clinical application. However, defects ultimately limit the further utilization of ICG, including its poor solubility, low bioavailability, and concentration-related aggregation (Bahmani et al., 2013). Anthocyanin dye has been used as a fluorescent probe for *in vivo* tumor imaging (Wang et al., 2016; Li et al., 2017). IR-820 is a novel anthocyanin with properties similar to those of IGC but exhibits better stability and photothermal effects; thus, IR-820 can be used for tumor photothermal therapy. In addition, IR-820 can emit NIR fluorescence under irradiation, indicating that the dye can be used for tumor monitoring (Li et al., 2016; Zhang et al., 2018; Dong et al., 2019). However, IR-820 is also problematic in clinical applications. When IR-820 is combined with other medicines, such as chemotherapeutic agents, it may have an efficient synergistic antitumor effect. Doxorubicin (DOX) is commonly used in clinical cancer chemotherapy and also in combination with other drugs or agents for synergistic treatment (Bao et al., 2016; Zhao et al., 2016). Mechanistically DOX and IR-820 have great potential and complementarity in the treatment of gastric cancer. First, DOX has severe systemic toxicity and susceptibility to drug resistance (Xiong et al., 2010). IR-820 can be heated under irradiation; the hyperthermy can promote the accumulation of the drug and reduce the occurrence of resistance. Thus, the effective dosage of DOX can be significantly decreased in treatment and its side effects can be reduced. However, DOX and IR-820 possess distinct pharmacokinetic properties that are difficult to achieve simultaneously with good accumulation and performance in tumor tissues and will be an insurmountable limitation in clinical applications. Therefore, *in vivo* codelivery and long-term stability of the two agents are crucial technical issues to be solved in synergistic treatment of gastric cancer.

Developing and applying nanotechnology bring great benefit to medicine. However, the drug loading of common nanocarriers is often less than 10%. This disadvantage limits the further development of nanocarriers (Choi et al., 2011; Chen et al., 2015). Some physical bonding effects have been attempted to strengthen the effect on the construction of nanocarriers (Ke et al., 2014; Zhang et al., 2017). π-π stacking, which is similar to hydrogen bonding, is a noncovalent interaction between aromatic nuclei. Recently, π-π stacking technology has become an attractive method for molecular assembly, especially in the self-assembly of nanoparticles and drug delivery systems. This method does not destroy the properties of drugs and can improve their bioavailability (Shi et al., 2015). The majority of antitumor drugs are known to contain complex aromatic structures, which lead to poor water solubility and low bioavailability. Hence, π-π stacking can be used to assemble drug-loaded complexes for these drugs (Wei et al., 2016; Wang et al., 2017; Zhuang et al., 2019). Hennink and colleagues prepared a polymeric micelle via π-π stacking for paclitaxel delivery; the drug loading rate reached 23%, which is well above that of the clinical paclitaxel medicine Genexol-PM (Shi et al., 2013). He et al. developed a series of micelles via π-π stacking and found that their ability for DOX loading was proportional to the aromatic ring (Liang et al., 2015). Zhang et al. prepared multidrug loading nanocarriers via π-π stacking for combination chemotherapy (Zhang et al., 2015). Both DOX and IR-820 have aromatic nuclei in their molecular structures, which means that these agents can assemble via π-π stacking. For the assembly material, we considered dopamine. Dopamine is a small compound with a benzene ring and possesses excellent biocompatibility and stability. Dopamine can combine with DOX and IR-820 in an alkaline aqueous solution through π-π stacking and form stable drug-loaded NPs. The prepared NPs not only extend the circulation time of the payloads, but also perform tumor targeted delivery through enhanced permeability and retention (EPR) effects (Peer et al., 2007; Jain and Stylianopoulos, 2010).

In the present study, a multifunctional nanocarrier was constructed for chemo-photothermal synergistic therapy and dynamic monitoring in gastric cancer. The materials that were used are dopamine and poloxamer F127, which is a surfactant for hydrotropy. The agents were DOX and IR-820, which have chemotherapeutic effects and can be used for simultaneous photothermal treatment and *in vivo* fluorescent imaging. The morphology, encapsulation, and stability were initially of the PCC NPs evaluated. Subsequently, the toxicity, targeted delivery, and tumor suppression of the PCC NPs were determined in cell lines and a BALB/c mouse model. The results could provide a theoretical foundation for the postoperative treatment of gastric cancer.

MATERIALS AND METHODS

Materials

Dopamine hydrochloride (98%), poloxamer F-127, DOX, and tris(hydroxymethyl)aminomethane (Tris) were purchased from Sigma-Aldrich Corp. (MO, USA). IR-820 was purchased from Aladdin Crop. (Shanghai, China). The antibiotics, trypsin, CCK-8 kit, Annexin V-FITC apoptosis kit, and DAPI kit were purchased from Beyotime Co., Ltd. (Shanghai, China). HL-7702 (human normal liver cells), IMR-90 (human embryonic lung fibroblast cells), and HUVECs (human umbilical vein endothelial cells) were purchased from Tongpai Co., Ltd. (Shanghai, China). Human gastric cancer cell lines (MKN45, BGC-823 and SGC-7901) were purchased from Huiying Co., Ltd. (Shanghai, China). DMEM high glucose medium and fetal bovine serum (FBS) were purchased from Thermo Fisher Inc. (MA, USA). Other reagents were supplied by Sinopharm Crop. (Beijing, China). BALB/c mice and BALB/c-nu/nu mice were purchased from Tengxin Co., Ltd. (Chongqing, China).

Preparation of PCC NPs

Construction of PCC NPs is a self-assembly process that depends on π-π stacking of dopamine, DOX, and IR-820 under alkaline conditions. The methods were reported by Wang et al. (2018). Initially, 18 ml of Tris solution, pH 8.8, was poured into a flask. Subsequently, 18 mg of dopamine and 1 ml of a poloxamer and IR-820 mixed solution (DMSO; poloxamer, 10 mg/ml; IR-820, 20 mg/ml) were dropped into the flask under stirring. The 100 μL of DOX solution (20 mg/ml) was added to the mixture solution, and stirring was maintained for 3 min. The mixture was ultrasonically treated for 10 min. Then, mixture was incubated for 72 h at 28°C in a rotary stirrer, and PCC NPs were obtained. The NPs were further purified by dialysis and centrifugation to remove unreacted materials. The PCC NPs dispersed liquid was concentrated to 10 mg/ml by centrifugation.

Characterization of PCC NPs

The hydrodynamic diameter of PCC NPs was initially measured by dynamic light scattering using a Malvern instrument (Malvern, Ltd., UK). The morphology and size of PCC NPs were observed by TEM (JEOL Corp., Japan). The encapsulation ability of PCC NPs was further evaluated. The total mass of PCC NPs was measured by residue of freeze-drying method. The DOC or IR-820 in residue was redissolved by DMSO and the concentrations were measured via fluorescence spectrometry. The encapsulation rate (ER) and drug loading rate (DL) of DOX and IR-820 were calculated by total mass of PCC NPs and input and remaining mass of agents. The *in vitro* stability of PCC NPs was evaluated according to the changing of hydrodynamic size under various conditions, including PBS, complete medium, and FBS at 4°C or 37°C. *In vitro* drug release was evaluated by dialysis. The PCC NPs dispersion liquid was enclosed in dialysis bags, with a molecular weight cutoff of 2000 Da. Then the dialysis bags were assigned in various experiments. First, the release of PCC NPs was tested in PBS at 4°C and free DOX at the same concentration as the control. The pH-response of PCC NPs was measured in acetate buffered saline at pH 7.4, pH 6.5, and pH 5.2. The effect of temperature on the release of DOX was evaluated in PBS at 4, 37, 45, and 58°C. The release rates were determined and calculated by concentrations of DOX in the outer phase of dialysis.

Photothermal Conversion of PCC NPs

The PCC NPs dispersion liquid (500 μl, 50 μg/ml) was added to a 1.5 ml tube. Then the tube was continuously irradiated with 808 nm laser at a power density of 1 W/cm^2, and the temperature change was measured using an infrared thermometer at 0, 1, 2, and 3 min. The photothermal conversion in different concentrations of PCC NPs was also evaluated in a 1.5 ml tube with the same laser irradiation parameters. The concentrations of PCC NPs were 10, 20, 30, and 40 μg/ml. To evaluate the photothermal effect of PCC NPs under different conditions, the NPs were dispersed in PBS, complete medium, and FBS, and irradiation was performed at a power density of 1 W/cm^2 for 3 min. The temperature changes were also determined using an infrared thermometer. The photothermal effect was further evaluated in mouse. Fifty microliters of the PCC NPs dispersion liquid at a concentration of 40 μg/ml was subcutaneously injected into the right crotch of a BALB/c-nu/nu mouse. Then the injection area was irradiated by the laser at a power density of 1 W/cm^2, and the temperature change was determined at different time points. Moreover, the photothermal conversions of the materials were also measured. The photothermal curve of PCC NPs was plotted according to the temperature values before and after switching off the laser.

Cell Internalization of PCC NPs

DOX emits red fluorescence, which could be used to directly observe internalization and intracellular release of PCC NPs. SGC-7901 cells were seeded into 3.5 cm confocal dishes at a density of 1.5×10^5 cells/dish and incubated at 37°C under 5% CO_2 for 24 h. When cell adherence and growth were good, PCC NPs were added to dishes. Subsequently, the cells were treated with a 4% paraformaldehyde solution for different times, and cell nuclei were stained with a DAPI kit. All samples were observed with a confocal microscope (TCS SP5 II, Leica, Germany). The fluorescent intensities in cells were measured using ImageJ software.

Cytotoxicity of PCC NPs

A CCK-8 assay was employed to evaluate the cytotoxicity of PCC NPs in various cells, including normal human cells (HUVECs, IMR-90, and HL-7702) and human gastric cancer cell lines (BGC-823, SGC-7901, and MKN45). The logarithmic phase cells were seeded into 96-well plates at a density of 8 × 10^3 cells/well. Subsequently, PCC NPs, IR-820, and DOX at different concentrations were added to the wells. The plates were incubated at 37°C under 5% CO_2. The cell densities were continuously observed via microscopy (Nikon, Japan). After 24 h of coincubation, the wells were replaced with a fresh colorless medium containing 10% CCK-8 solution. The incubation was extended for 2 h, and then the wells were measured at 450 nm absorbance with a microplate reader (Varioskan LUX,

ThermoFisher, USA). The cell viabilities were calculated with GraphPad Prism 5.0 software.

In vitro Antitumor Effect of PCC NPs

SGC-7901 cells were seeded into 3.5 cm dishes at a density of 2×10^5 cells/dish. When the cells in the dish grew to over 90% confluence, PCC NPs were added. The dish was then incubated at 37°C under 5% CO_2 overnight. Then stale medium was replaced by fresh colorless medium, and aluminum foil was used to cover half of the dish. Then the dish was exposed to 808 nm laser irradiation at a power density of 1 W/cm^2 for 8 min. The cellular morphology on both sides of the cover line was observed with a microscope (Nikon, Japan). Meanwhile, a CCK-8 assay was also used to evaluate the effects of the photothermal treatment in SGC-7901, BGC-823, and MKN45 cells. Logarithmic phase cells were seeded into 96-well plates at a density of 8×10^3 cells/well. Subsequently, PCC NPs at different concentrations were added to the wells and incubated at 37°C under 5% CO_2 for 24 h. The wells were replaced with fresh colorless medium, and an 808 nm laser was used at a power density of 1 W/cm^2 for 5 min in each well. After incubation for 1 h, the cell viabilities were measured and calculated with the method described above.

A colony formation assay was used to evaluate cell proliferation under photothermal treatment. SGC-7901, BGC-823, or MKN45 cells were seeded into 6 cm dishes at a density of 500 cells/dish. Then PBS, IR-820, DOX, and PCC NPs were added to dishes. The dishes were incubated at 37°C under 5% CO_2 for 48 h. In the photothermally treated group, PCC NPs or IR-820 were added to the cells and incubated for 8 h. Then the cells were suspended at a density of 500 cells/ml. One milliliter of the cell suspension was added to a 1.5 ml tube and 808 nm laser irradiation was performed at a power density of 1 W/cm^2 for 5 min. Then, the cells were seeded into a 6 cm dish and incubated for 48 h. Subsequently, stale medium was replaced with fresh medium containing 20% FBS. Cells were incubated for another 5 d and treated with fix-stain buffer (5% Coomassie brilliant blue in methanol) for 15 min. The stained cell colonies were counted.

Flow cytometry was used to determine the apoptosis of SGC-7901 cells under treatments. The cells were seeded into 24-well plates at a density of 1×10^5 cells/well. PCC NPs were added to the dish and incubated for 8 h. Then the dish was treated with 808 nm laser irradiation for 3 min and further incubated for 4 h. The cells were collected and stained with an Annexin V-FITC apoptosis kit. In the control groups, the dishes were treated with DOX or IR-820. The cells were analyzed using flow cytometry (Accuri C6, BD, USA).

Hemolysis Assay

PCC NPs were administered via intravenous injection. Therefore, toxicity was initially evaluated via a hemolysis assay. Red blood cells of mice were collected for the experiment. The cells were dispersed in PBS at a density of 2% and infused into 1.5 ml tubes. Subsequently, Triton X-100 (10 mg/ml), PCC NPs (30 mg/ml), DOX (1 mg/ml), and IR-820 (10 mg/ml) were added to the tubes. All tubes were placed in a 37°C water bath for 2 h. Then, the cell suspensions were centrifuged. The supernatants were used to measure absorbance at 394 nm and the lysis ratio was calculated.

In vivo Acute Toxicity of PCC NPs

Fifteen female and fifteen male BALB/c mice were utilized to evaluate the acute toxicity of PCC NPs *in vivo*. The mice were fed in a SPF animal room for 1 week to acclimate. Then, the mice were randomly divided into three groups of five females and five males in each group. The PCC NPs, IR-820, and DOX were intravenously injected into respective groups. The dose of PCC NPs was 100 mg/kg, DOX was 3 mg/kg, and IR-820 was 30 mg/kg. The survival rate was recorded during 2 weeks. After euthanasia, the hearts, livers, and kidneys of mice were collected for pathological analysis. All animal experiments in this study were approved by the Laboratory Animal Administration Committee of Xi'an Medical University. The protocols for animal experiments followed the Guidelines for the Use and Care of Experimental Animals at Xi'an Medical University. The Animal Ethics Approved Document Number is XY-AUC-2019-168.

Xenograft Mouse Model

Male BALB/c-nu/nu mice were used for the preparation of the gastric cancer xenograft model. The mice were fed in a SPF animal room for 1 week to acclimate. SGC-7901 cells were digested with 0.25% trypsin and cell suspension was prepared at a density of 5×10^6 cells/ml. One hundred microliters of the cell suspension was subcutaneously injected into the crotch of the mouse. When the tumor grew to an appropriate size, the mice were used as a xenograft model for *in vivo* experiments.

In Vivo Distribution of PCC NPs

IR-820 is a NIR fluorescent dye that can be used to monitor PCC NPs. Two xenograft models were chosen to determine the *in vivo* distribution of PCC NPs. Two hundred microliters of the PCC NPs dispersed liquid with 20 μg/ml IR-820 was intravenously injected into mice. Another mouse was injected with an equal concentration of IR-820 solution as the control. Fluorescent signals were observed with an IVIS instrument (Perkin Elmer, MA, USA) at sequential time points after injection. Mice were euthanized after observation, and their organs and tumors were collected. The tissues were observed using an IVIS instrument with the same parameters.

In Vivo Antitumor Evaluation of PCC NPs

Twenty xenograft models with average tumor volume of approximately 100 mm^3 were utilized to evaluate the *in vivo* antitumor effect of PCC NPs. The mice were randomly divided into four groups. These groups were treated with 1) saline; 2) DOX; 3) IR-820 + laser; and 4) PCC NPs + laser. The dose of DOX was 0.5 mg/kg, IR-820 was 5 mg/kg, and dose of PCC NPs was 15 mg/kg. Laser irradiation was performed at a power density of 1 W/cm^2 for 3 min and the irradiating distance was 5 cm. The irradiation intensity was verified to not cause obvious burns on the mouse skin in experiment. The route of administration of the PCC NPs was intravenous injection. The interval time of laser treatment was based on the results of the *in vivo* distribution. The tumors were photographed and their size was measured every 5 days. After 30 days, the mice were euthanized by CO_2 overdose. Tumor tissues were collected and weighed.

Statistical Analysis

Two-way ANOVA and Student's *t*-test were used in statistical analyses performed using GraphPad Prism 5.0 software. The data are presented as the mean values ± standard deviation (SD) of independently repeated experiments. A p value <5 indicated that the data were significantly different.

RESULTS

Preparation and Characterization of PCC NPs

PCC NPs exhibited a spherical morphology and good monodispersity in TEM observation. The average size of the NPs was approximately 60 nm (**Figure 1A**). The hydrodynamic diameter was 59.4 ± 3.6 nm, which was mutually confirmed by TEM observation. **Figures 1C–F** show the stability of PCC NPs under different conditions. The colloidal stability was evaluated by the change of hydrodynamic diameter. Within 8 weeks, the size of the PCC NPs did not exhibit an obvious change in PBS at 4°C. The results indicated that PCC NPs could be effectively stored in PBS. Subsequently, PCC NPs were evaluated in PBS, complete medium, and FBS at 37°C. The aim was to determine whether the NPs could be used in further *in vitro* and *in vivo* experiments. The hydrodynamic size was extremely stable in all the solution environments. Although the average diameters were not significantly changed, an increase in the size distribution interval was the only matter worthy of attention. This phenomenon indicated that PCC NPs efficiently disperse under physiological conditions and could be utilized in subsequent experiments. The encapsulation ability of PCC NPs was evaluated via ER and DL. The maximum ER and DL of DOX were 96.7 ± 2.4 and 3.6 ± 0.9%, respectively. Meanwhile, the maximum ER and DL of DOX were 97.2 ± 1.8 and 34.1 ± 2.5%,

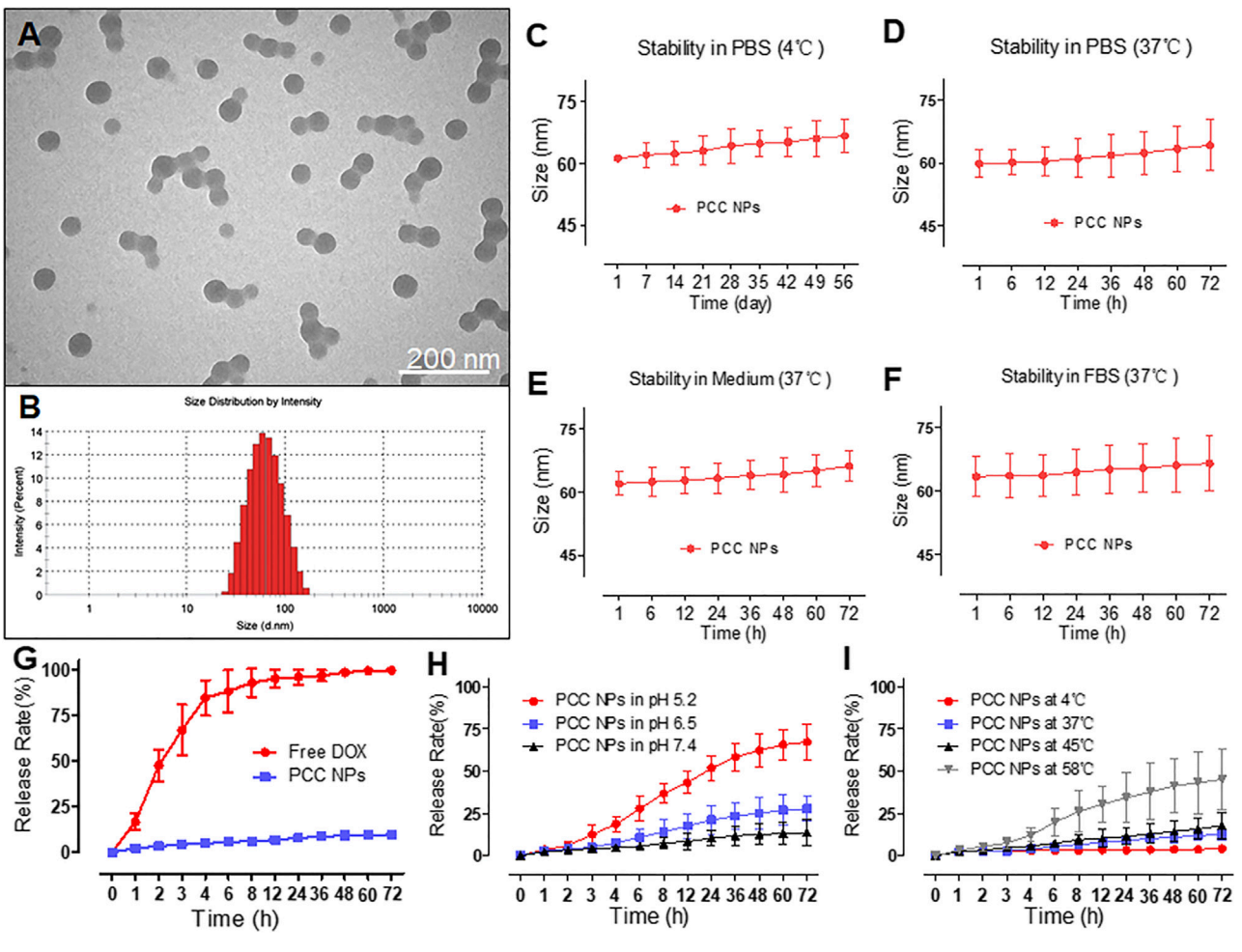

FIGURE 1 | Characterization of PCC NPs. Morphology of PCC NPs under TEM observation **(A)**; hydrodynamic size of PCC NPs **(B)**; *in vitro* stability of PCC NPs in PBS at 4°C **(C)**; *in vitro* stability of PCC NPs in PBS at 37°C **(D)**; *in vitro* stability of PCC NPs in completed medium at 37°C **(E)**; *in vitro* stability of PCC NPs in FBS at 37°C **(F)**; *in vitro* drug release of PCC NPs **(G)**; *in vitro* pH-response drug release of PCC NPs **(H)**; *in vitro* temperature-related drug release of PCC NPs **(I)**. Error bars represent the SD of the mean.

respectively. The mass ratio of DOX and IR-820 in PCC NPs was approximately 1:10. The proportion was consistent with the input of DOX and IR-820, which further demonstrated that the NPs possess a superior encapsulation ability.

In Vitro Release Profile of PCC NPs

To verify control and sustained release of PCC NPs, we determined the release profile. **Figure 1G** shows the normal release process in PBS at room temperature. Free DOX was used as the control and exhibited obvious burst release characteristics, with the majority of DOX released within 8 h. By comparison, DOX in PCC NPs showed a very sustained release profile. Less than 10% of the payloads were released into the outer phase of dialysis. Then, the pH-response release of PCC NPs was evaluated. The results are shown in **Figure 1H**. PCC NPs exhibited a significant distinction of release under different pH conditions. As mentioned above, π-π stacking can only occur under alkaline conditions. When the pH was 7.4, the release of PCC NPs was obviously slower than at pH 6.5 and pH 5.2. These two pH values match the tumor microenvironment and interior of the lysosome. A pH 7.4 is a common physiological condition *in vivo*. The results indicated that PCC NPs undergo a pH-response release. As photothermal NPs, PCC NPs will appear at high temperatures. As shown in **Figure 1I**, the release of PCC NPs at 58°C was much faster than that at 4, 37, and 45°C. Moreover, even at 58°C, the release rate was still lower than 50%. Among the temperatures, 4°C is commonly used in storage, and 37°C is the normal physiological temperature *in vivo*. The temperature of 45°C is usually used for tumor thermotherapy, while 58°C is the maximum photothermal conversion temperature of PCC NPs. The results indicated PCC NPs can be stably released at different temperatures.

Photothermal Conversion of PCC NPs

Photothermal conversion is another core performance of PCC NPs and is combined with chemotherapy for the synergistic treatment of gastric cancer. **Figure 2** shows the *in vitro* photothermal effect of PCC NPs. **Figure 2A** shows the

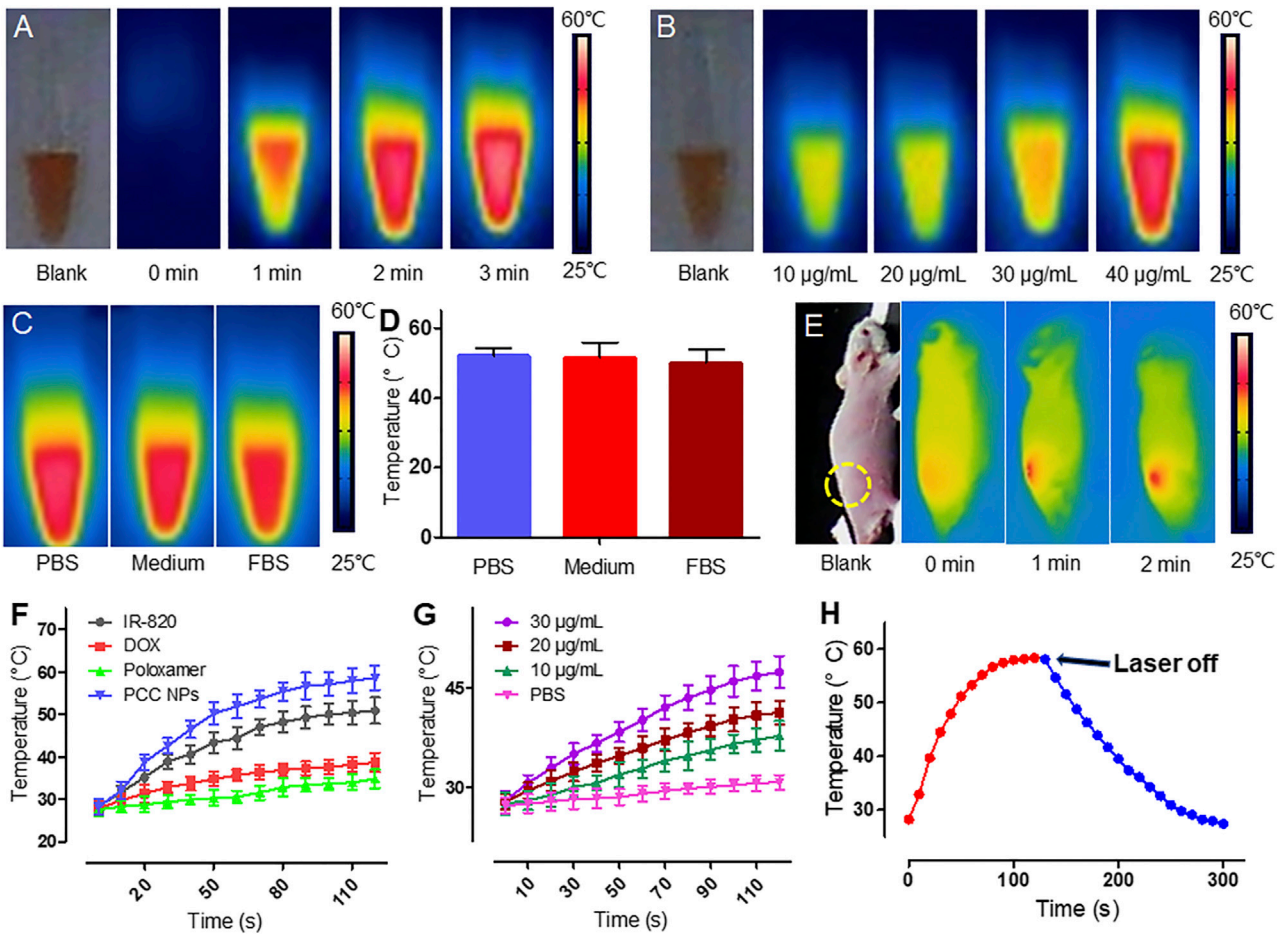

FIGURE 2 | Photothermal conversion of PCC NPs. Infrared thermal imaging of PCC NPs under irradiation at different times **(A)**; infrared thermal imaging of PCC NPs under irradiation at different concentrations **(B)**; photothermal effect of PCC NPs in different solution with irradiation time of 3 min **(C** and **D)**; infrared thermal imaging of mouse that was subcutaneously injected PCC NPs under irradiation **(E)**; photothermal performance of PCC NPs and compositions **(F)**; temperature changing curves of PCC NPs at different concentrations **(G)**; temperature change of PCC NPs before and after switching off the irradiation **(H)**. All of the samples were irradiated with 808 nm laser at a power density of 1 W/cm^2. Error bars represent the SD of the mean.

temperature increase of 50 μg/ml PCC NPs under 808 nm laser irradiation. PCC NPs exhibited a rapid heating effect under irradiation. The maximum temperature reached 58°C over 3 min. The concentration-related photothermal effect is shown in **Figure 2B**. Photothermal effect of PCC NPs exhibited an obvious correlation with concentration. Nevertheless, the increase was not obvious at low concentrations. This phenomenon was further verified in the temperature curve (**Figure 2G**). The increase in temperature only reaches 45°C under 30 μg/ml. The primary reason of this result is that the maximum temperature of PCC NPs was only approximately 58°C. However, the temperature increase is very appropriate, as it fits the requirements for *in vivo* tumor thermotherapy well. PCC NPs were verified to be effectively dispersed in various solutions. The effects of photothermal conversion in the different aqueous conditions were evaluated. The results are shown in **Figures 2C,D**. There was no significant difference between PCC NPs dispersed in PBS, medium, and FBS. All groups could approximately reach the maximum temperature. Subsequently, the temperature increase of transdermal irradiation was determined in a BALB/c-nu/nu mouse. As shown in **Figure 2E**, the temperature in the PCC NPs injection area was obviously increased under irradiation at a power density of 1 W/cm^2 for 2 min. The maximum temperature reached approximately 47°C, which is well suited for *in vivo* tumor thermotherapy. **Figure 2F** shows the difference between PCC NPs and other materials. DOX and poloxamer do not have photothermal effects; thus, there were no obvious temperature increases in either group. The temperature slightly increased in the DOX solution under laser irradiation. The increase in temperature occurred more significantly in PCC NPs than in the IR-820 group. The primary reason for this difference is that polydopamine (PDA) also has a certain effect on photothermal conversion. **Figure 2H** indicates that the temperature increase was caused by irradiation. When the laser irradiation was switched off, the temperature rapidly decreased. The results amply demonstrate that PCC NPs possess excellent photothermal effects, which are appropriate in the treatment of gastric cancer.

In vitro Internalization of PCC NPs

The cell internalization profile is shown in **Figure 3**. The red and blue fluorescence originated from DOX and DAPI-stained cell nuclei, respectively. As shown in **Figure 3A**, the fluorescent signal of DOX was gradually enhanced in cells, especially in nuclei. Initially, after 1 h, there was scarce red fluorescence accumulated in the cell, concentrated mainly in the cytoplasm. After 3 h, the red fluorescent signal was spread all throughout the cell, and more remarkably, some nuclei exhibited higher accumulation than the cytoplasm. At 6 h of treatment, the red fluorescent signal was more obvious and mainly accumulated in cell nuclei. Quantitative analysis of the fluorescent signal further verified this phenomenon. The mean fluorescence intensity gradually increased in the cell (**Figure 3B**). However, a different increase of the signal occurred between the nuclei and cytoplasm. As **Figure 3C** shows, the fluorescence ratio between nuclei and the cytoplasm exhibited a different variation trend compared with the fluorescent signal. The ratio indicated that more DOX accumulated in cell nuclei over time. This phenomenon suggested that PCC NPs could steadily release the payloads in the cell.

In Vitro Cytotoxicity and Suppression Effect of PCC NPs

To evaluate the cytotoxicity of PCC NPs without laser irradiation, a CCK-8 assay was employed in the experiment. Three normal human cell lines: HUVECs, IMR-90, and HL-7702, were initially incubated for determination of cytotoxicity. These cell lines were derived from the vascular endothelium, lung, and liver and were used to evaluate potential toxicity in normal organs and tissues. Meanwhile, three gastric cancer cell lines (BGC-823, SGC-7901, and MKN45) were also utilized in the measurements. The results are shown in **Figure 4**. The concentration ratio of DOX and IR-

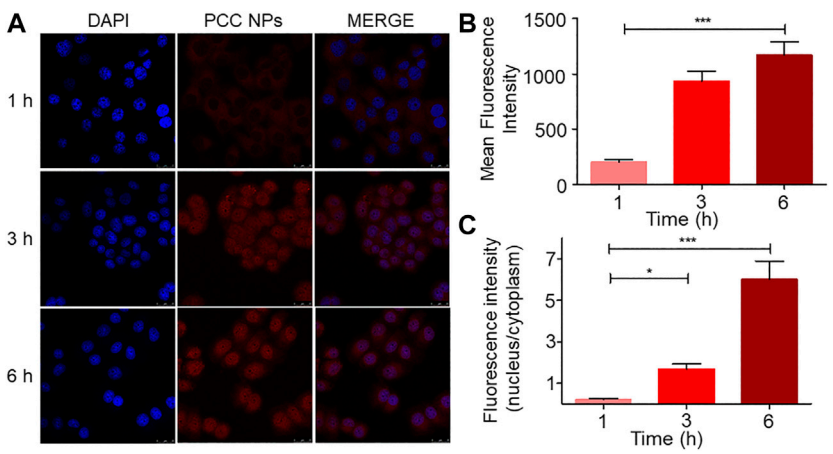

FIGURE 3 | Internalization and intracellular release profile of PCC NPs in SGC-7901 cells. The distribution of fluorescence in cells **(A)**; average fluorescence intensity in cell **(B)**; ratio of the fluorescence intensity between nuclei and cytoplasm **(C)**. Error bars represent the SD of the mean. * indicates $p < 0.05$, *** indicates $p < 0.001$.

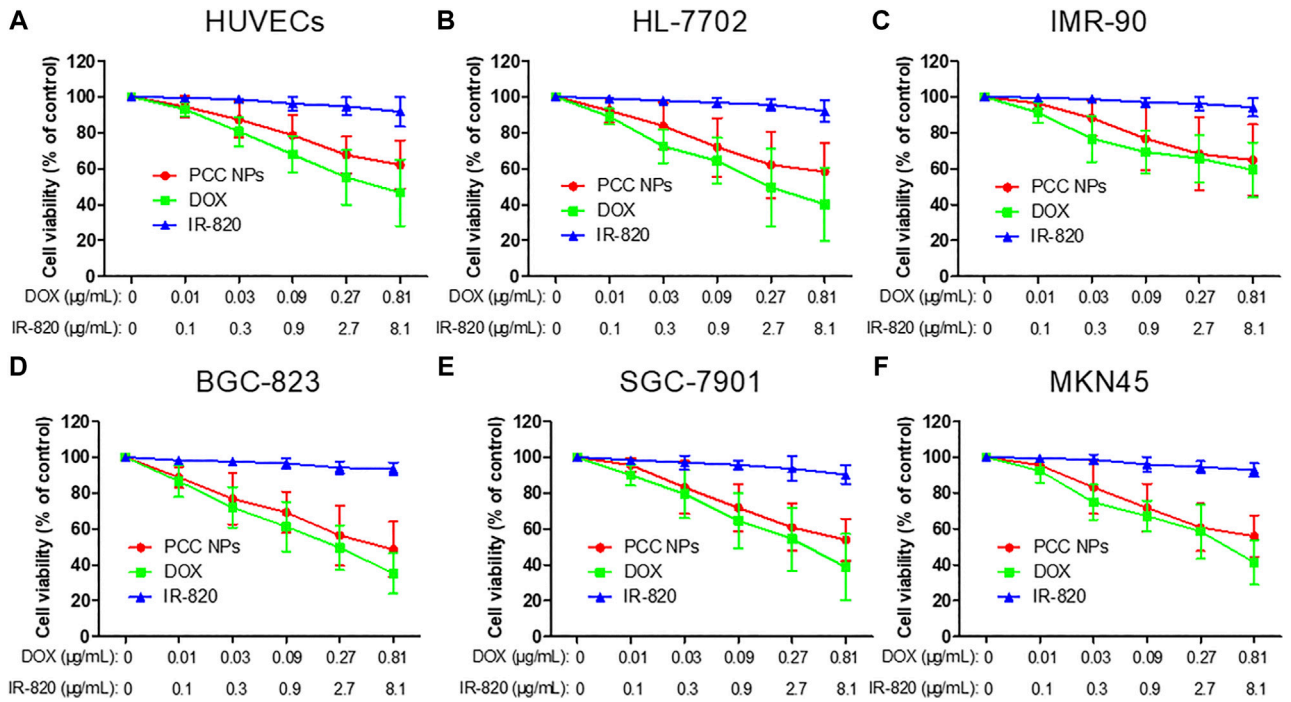

FIGURE 4 | *In vitro* cytotoxicity of PCC NPs. Human umbilical vein endothelial cell, HUVECs **(A)**; human normal liver cell, HL-7702 **(B)**; human embryonic lung fibroblasts cells, IMR-90 **(C)**; human gastric cancer cell, BGC-823, SGC-7901, and MKN45 **(D–F)**. Error bars represent the SD of the mean.

820 was 1:10, meeting the proportion in PCC NPs. All of the cells were insensitive to IR-820 treatment. This result indicated that IR-820 has low cytotoxicity. DOX treatments exhibited more cytotoxicity than the PCC NPs treatment groups. However, there was no significant difference between the two groups. The results suggested that PCC NPs could perform chemotherapeutic effect of DOX. The possible reason for the lower cytotoxicity of PCC NPs than DOX is that DOX in PCC NPs is more slowly released in cells. Their biocompatibility was initially verified by these *in vitro* experiments.

In vitro photothermal treatment was evaluated using the gastric cancer cell lines SGC-7901, BGC-823, and MKN45. **Figure 5A** shows direct SGC-7901 cell damage with PCC NPs under laser irradiation. The morphology of cells in the untreated area showed obvious abnormalities. By comparison, a significant morphological change did not occur in cells in the covered area. Subsequently, the treatment effects under different concentrations of PCC NPs were evaluated by the CCK-8 assay. The results are shown in **Figure 5B** and **Supplementary Figures S1A, C**. There was no obvious cytotoxicity in 40 μg/ml PCC NPs without irradiation. However, once irradiation was applied, cell viability showed a significant negative correlation with the concentration of PCC NPs. A colony formation assay further demonstrated the *in vitro* antitumor effect in three gastric cancer cell lines. The colony number in the treatment of PCC NPs was significantly less than that in photothermal treatment or chemotherapy (**Figures 5C, D** and **Supplementary Figures S1 B, D**). Flow cytometry was used to evaluate the effects of triggering apoptosis under different treatments. **Figure 6E** shows the flow cytometry result for the treatments. The PCC NPs treated group exhibited more significant apoptosis in SGC-7901 cells than the other group. The results indicated that PCC NPs could efficiently exert photothermal-chemotherapeutic synergy in gastric cancer cells.

In Vivo Toxicity Evaluation of PCC NPs

PCC NPs were administrated via intravenous injection. Initially, the impact of PCC NPs in red blood cells was evaluated. The results of the hemolysis assay are shown in **Figure 6A**. Triton X-100 as the positive control caused more than 70% of red blood cells to hemolyze, which indicated that severe plasmorrhexis occurred under the treatment. The lysis rates of DOX and PCC NPs were both lower than 10%. This result suggests that PCC NPs do not cause hemolysis. Lysis in the IR-820 treatment accounted for nearly 20% of the total. One possible reason of this result is that the solvent of IR-820 was DMSO, which caused a degree of lysis. Then, the acute toxicity of PCC NPs was evaluated in BALB/c mice. The survival rate is shown in **Figure 6B**. Although the dose of DOX was only 3 mg/kg, it still exhibited obvious toxicity. Mortality was 60%. Two mice died after IR-820 treatment on day 1, possibly due to the solvent. IR-820 was dispersed in a mixture of DMSO and saline. The injection dose of PCC NPs was 100 mg/kg, but mice in the group still showed the highest survival rate. Pathological sections are displayed in **Figure 6C**. The results further demonstrated the safety of PCC NPs. DOX could cause severe myocarditis. Pathological slides of the heart in the DOX treated group show obvious typical characteristics of myocarditis. In the area where the arrow

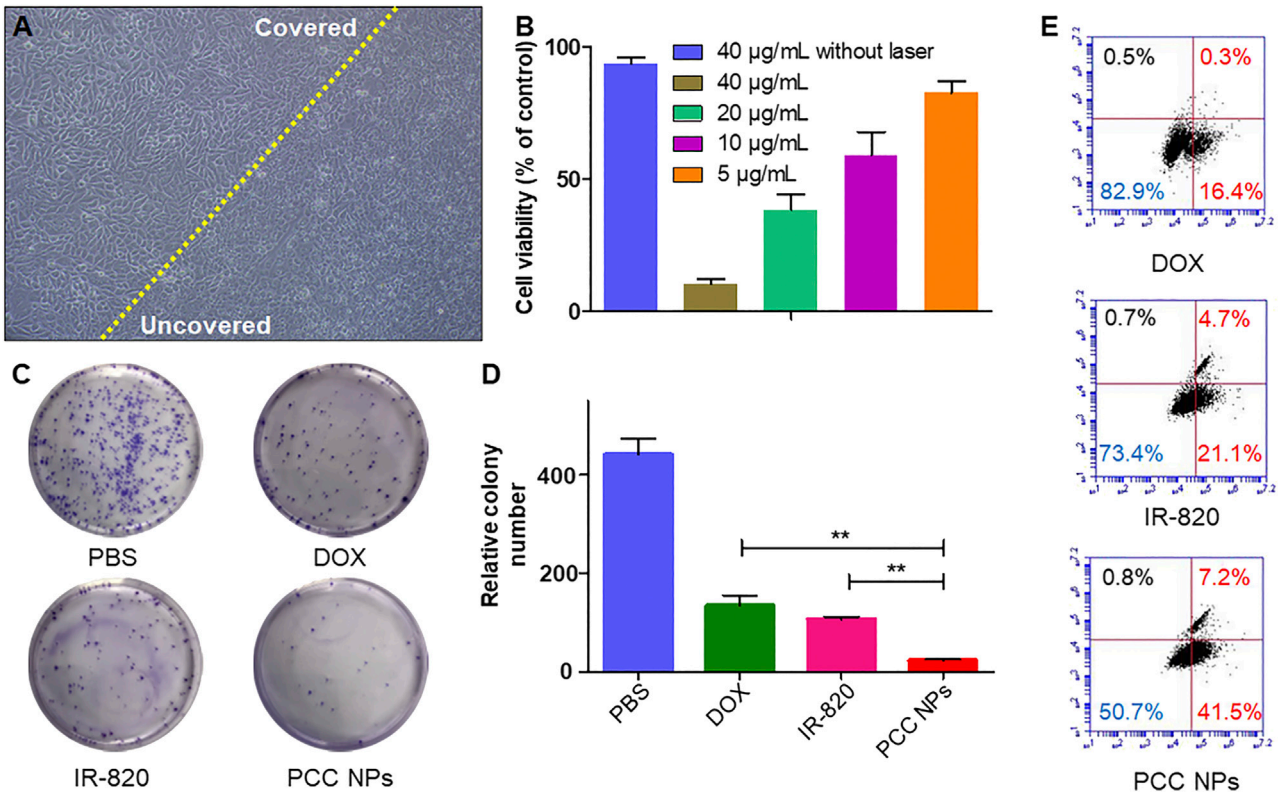

FIGURE 5 | *In vitro* antitumor effect of PCC NPs. Directly damage cells under photothermal treatment, the cells on the left of the yellow line were untreated, and the right side was treated with PCC NPs under irradiation **(A)**; the cell viability at different concentrations of PCC NPs under photothermal treatment **(B)**; the results of colony formation assays. Cells in the PCC NPs and IR-820 treated groups were irradiated after the administration of samples **(C, D)**; flow cytometry assay of cells treated with PCC NPs, IR-820, or DOX **(E)**. Error bars represent the SD of the mean. ** indicated $p < 0.01$.

points, myocardial tissues were filled with lymphocytes. Moreover, hepatic tissue was also damaged by DOX treatment. The PCC NPs treated group also exhibited slight lymphocyte infiltration in cardiac and hepatic tissues. *In vivo* toxicity demonstrated that PCC NPs possess excellent biocompatibility.

In Vivo Distribution of PCC NPs

The *in vivo* distribution of PCC NPs was investigated using the Caliper IVIS Lumina II system (PE, USA). The results are shown in **Figure 7**. The continuous observation is exhibited in **Figure 7A**. The tumors of the control mouse were filled with a low fluorescent signal. In PCC NPs treated mouse, fluorescent signal initially appeared in the thorax and epigastrium and was then observed in the tumor area. Subsequently, the fluorescence continuously increased in the lung, liver, and tumor areas. The cumulative peak of the fluorescent signal in the tumor area appeared at approximately 24 h. Subsequently, fluorescence has declined across the whole body. Remarkably, the fluorescent signal remaining in tumor tissue was much more stable than that in other areas. The signal was continuously monitored in the tumor until 144 h, which means that PCC NPs could extend the circulation time of the payloads. The organs and tumor tissues were collected and observed. All tissues of control mouse had very low fluorescent signals, while the signals in PCC NPs treated mouse were still dense, especially in tumor. The results are shown in **Figures 7C,D**. The results amply demonstrate that PCC NPs could effectively increase accumulation of payload in tumor.

In Vivo Antitumor Evaluation of PCC NPs

To demonstrate the synergistic antitumor effect of PCC NPs, we randomly divided twenty gastric cancer xenograft models into four groups, which included the PCC NPs treated group, chemotherapeutic group, photothermal treatment group, and untreated group. The visual effects and tumor growth curves of the treatments are shown in **Figures 8A**, **B**. The untreated group was injected with saline, and the tumor rapidly grew to a large volume within a month. The average size of tumors increased almost 9-fold. The tumors in the chemotherapeutic group also grew quickly. The suppression effect was hardly discernible. The primary reason was that dose of the DOX in the treatment was low and could not inhibit proliferation. The single photothermal treatment was also ineffective. Although tumor under the skin area exhibited slight injury, the average tumor volume was increased nearly 6-fold. It is worth noting that the PCC NPs treatment greatly suppressed the growth of gastric tumors. As shown in **Figure 8A**, the tumor in the PCC NPs treated group exhibited slight burn after the first treatment, and the burn wound gradually increased until the tumor area was

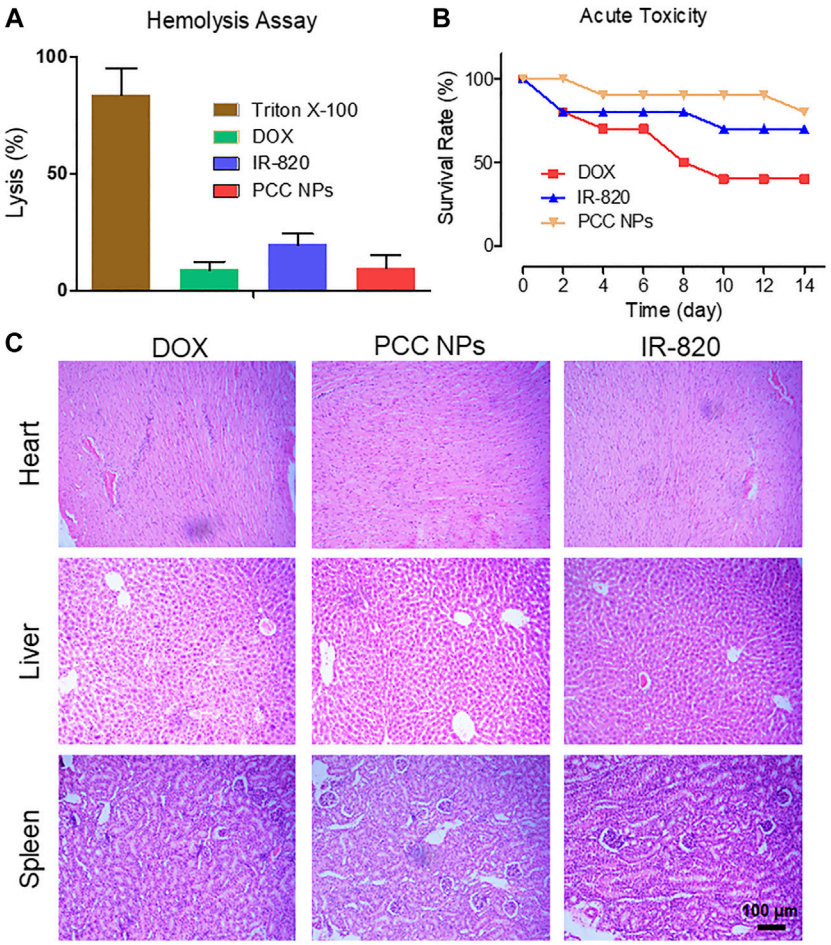

FIGURE 6 | *In vivo* toxicity evaluation of PCC NPs. The hemolysis ratio in the PCC NPs, IR-820, and DOX treated groups **(A)**; survival rate of mice in the different treatment groups **(B)**; pathological characteristics of the heart, liver, and kidney in the different treatment groups **(C)**. Error bars represent the SD of the mean.

completely necrotic. The sizes of the tumors in the PCC NPs group were decreased under treatment and three tumors were eliminated. The suppression effect of PCC NPs was significantly better than that of the DOX or IR-820 treatment (**Figures 8B,D**). The weights of tumors exhibited identical results. The results indicated that PCC NPs could effectively treat gastric cancer *in vivo*.

Moreover, the weights of mice reflect the advantage of PCC NPs. The average weight of mice in the PCC NPs treated group underwent a rebound in the fourth week. By comparison, the mice in the DOX treated and untreated groups suffered constant emaciation. The average weight of mice in the IR-820 treated group increased in the first ten days and then gradually decreased until the experiment was completed. The results further demonstrated that PCC NPs possess superior *in vivo* biosecurity.

DISCUSSION

Early gastric cancer clinically has no obvious characteristic manifestations and diagnosis is difficult; the 5-year survival rate of patients with advanced gastric cancer is lower than 20% (Song et al., 2017). Gastrectomy is a primary mode of therapy for gastric cancer. However, postoperative recurrence is the most common form of problem and the most important cause of death in advanced gastric cancer after radical dissection. Adjuvant chemotherapy is a major part of the comprehensive treatment for gastric cancer; however, insufficient effect still impedes improvements in prognosis (Lazar et al., 2018). Therefore, an effective treatment combined with an accurate assessment of tumor progression is the most beneficial method in continuous therapy of gastric cancer. The combination of chemotherapy, photothermal therapy, and real-time monitoring can enhance curative effects in tumor treatment (Liu et al., 2011; Zheng et al., 2013; Chen et al., 2016; Li et al., 2016). For this purpose, a multifunctional nanoparticle, consisting of DOX and IR-820, was prepared via π-π stacking of PDA. PCC NPs have a distinctly spherical morphology and could be monodispersed under various aqueous conditions, such as PBS, FBS, and medium. The hydrodynamic diameter was 59.4 ± 3.6 nm, which allows tumor targeting via the EPR effect (Iyer et al., 2006). PCC NPs possess a superior encapsulation ability, which

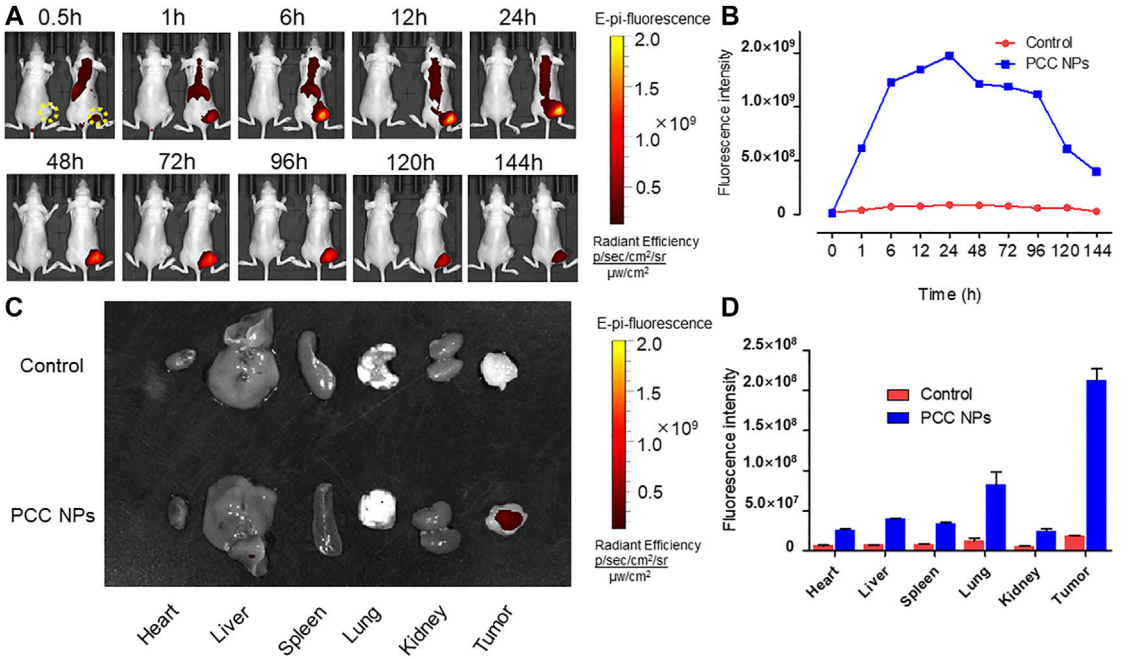

FIGURE 7 | *In vivo* distribution and long-circulation of PCC NPs. The distribution of the NIR fluorescent signal in mouse **(A)**; the fluorescent intensity in tumor at different time **(B)**; the distribution of NIR fluorescent signal in organs and tumor tissues **(C)**; the fluorescent intensity in organs and tumor tissues **(D)**. Error bars represent the SD of the mean.

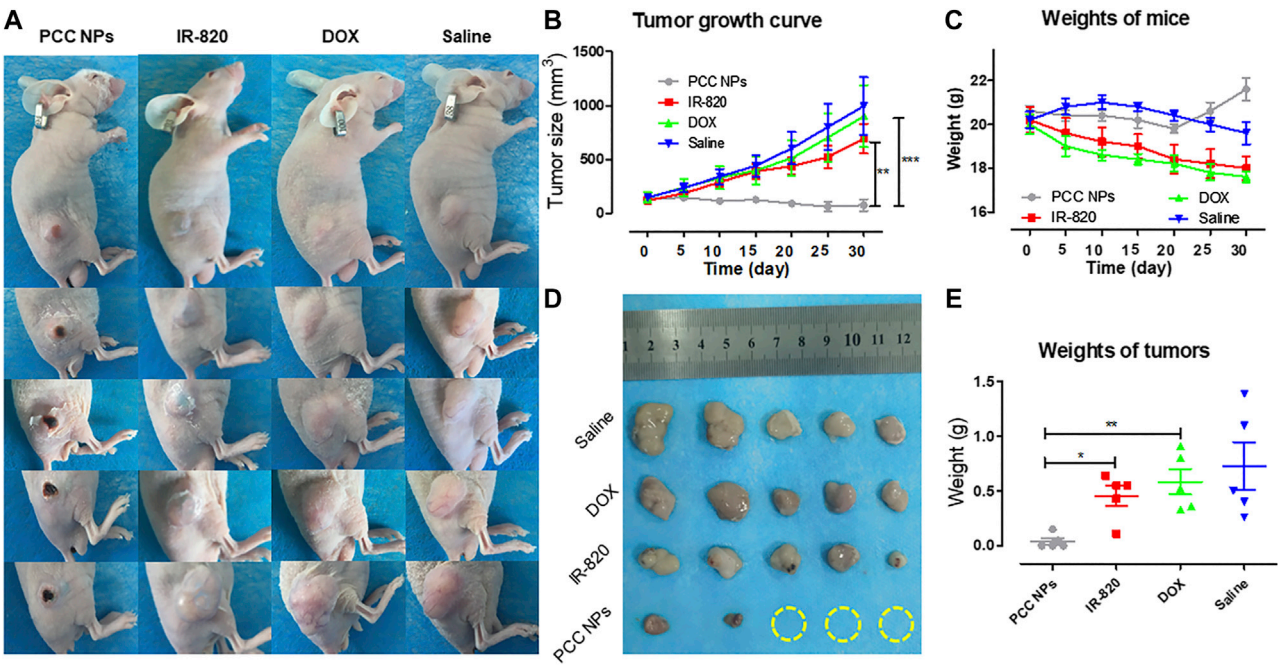

FIGURE 8 | *In vivo* antitumor evaluation of PCC NPs. Mice photos under continuous monitoring **(A)**; the average volume of tumor in different treatment groups during the experiment **(B)**; the average weight of mice in different treatment groups during the experiment **(C)**; the tumor tissues from each treated group **(D)**; the average weight of tumor tissues from each treated group **(E)**. Error bars represent the SD of the mean. * indicates $p < 0.05$, ** indicates $p < 0.01$, and *** indicates $p < 0.001$.

increased the bioavailability of the agents. The maximum ER of DOX and IR-820 were both over 96%, and the total DL was more than 37%. PCC NPs efficiently dispersed under physiological conditions and exhibited extraordinary stability. The release profile is another advantage of PCC NPs. There is a problem in pharmaceutical research, which is the trouble of the initial burst release of drugs. π-π stacking can realize sustained and controlled release of a loaded agent while ensuring better encapsulation and effectively avoiding burst release. The payload in PCC NPs could be stably encapsulated under the neutral conditions. Once the NPs enter an acidic environment, such as tumor tissues or lysosomes, the drugs will be released gradually (Wang et al., 2018). Meanwhile, when photothermy triggered, the payloads are also released from the NPs. The photothermal effect is crucial component of PCC NPs that not only directly injure tumor, but can also improve chemotherapy to meet the synergistic treatment of gastric cancer. In this study, PCC NPs have been proven to have superior photothermal conversion under laser irradiation. The NPs exhibited a rapid heating effect under irradiation. The maximum temperature was approximately 58°C and exhibited an obvious concentration dependence. The photothermal effect of PCC NPs was not impacted by the dispersed conditions. Moreover, the maximum temperature under the skin of the mouse reached approximately 47°C which is well suited for *in vivo* tumor thermotherapy and does not injure normal tissues (Hildebrandt et al., 2002). These results amply verify that PCC NPs possess excellent synergistic effect, which are appropriate in the treatment of gastric cancer.

Toxicity is the overriding factor regarding whether PCC NPs can be used in the treatment of gastric cancer. A series of evaluations were employed to verify the safety of PCC NPs. Initially, the cytotoxicity of the NPs was evaluated in six cell lines. PCC NPs were given as an injection through a vein. Thus, HUVECs, human umbilical vein endothelial cells, were used to initially evaluate injury to blood vessels. HL-7702 and IMR-90 are human normal liver cells and human embryonic lung fibroblast cells, respectively. These cells were employed to preliminarily evaluate whether PCC NPs could injure the liver and lung, which are most common cumulative organs of NPs. Moreover, three gastric cancer cell lines (BGC-823, SGC-7901, and MKN45) were used to determine the essential cytotoxicity of PCC NPs without irradiation. The results indicated that IR-820 has low cytotoxicity and DOX treatments exhibited more cytotoxicity than the PCC NPs treated groups; however there was no significant difference between the two treatments. Sustained release of DOX caused slightly low cytotoxicity of PCC NPs. Thus, biocompatibility was preliminarily verified *in vitro*. Subsequently, *in vivo* toxicity was evaluated using a hemolysis assay and according to acute toxicity. The NPs enter the circulation system first; thus, a hemolysis assay was used to measure the impact of PCC NPs in red blood cells. The lysis rate in the PCC NPs treated group was lower than 10%, suggesting that the NPs do not cause severe hemolysis. After the acute toxicity test, only two mice died in the PCC NPs injected group after 2 weeks. By comparison, the dose of DOX was only 3 mg/kg, but mortality reached 60% in DOX treated mice. Pathological analysis of the main organs further verified the safety of PCC NPs. Moreover, continuous *in vivo* administration also proves that PCC NPs possess superior *in vivo* biosecurity. The weights of the mice increased after PCC NPs treatment for 3 weeks. In contrast to the PCC NPs treated group, the mice in the DOX, IR-820, and saline treated groups suffered varying degrees of emaciation. These results indicated that PCC NPs could decrease systemic toxicity *in vivo* and exhibited excellent biocompatibility.

Continuous monitoring of gastric cancer is one of the main functions of PCC NPs. *In vitro* and *in vivo* imaging experiments were used to demonstrate whether PCC NPs could be used as probes for postoperative monitoring of gastric cancer. The cell internalization process showed that the PCC NPs could stably deliver dyes into the cell and then undergo intracellular release. The *in vivo* monitoring effect of PCC NPs was investigated by live imaging technology. The time-intensity curve, peak time, and tissue accumulation of the mouse were analyzed. At 30 min, the fluorescent signal synchronously appeared in the thorax, epigastrium, and tumor area of PCC NPs treated mouse and then continuously increased in these areas. After 24 h, the fluorescent peak in the tumor area appeared. Subsequently, the fluorescence gradually decreases. It is worth noting that the fluorescent signal was continuously observed in tumor over 6 days, and by comparison, the fluorescent signal remaining in tumor tissue was more stable than that in thorax and epigastrium. Subsequently, the main organs and tumors were observed and measured. The fluorescent signal in PCC NPs treated mouse was still dense, especially in tumor tissue. The results mean that PCC NPs could extend the circulation time of the payloads to large degree. Wang et al. reported ultralong circulating lollipop-like NPs, which are constructed with polydopamine, DOX, and gossypol via π-π stacking. The fluorescent signal remained in tumor tissues for 8 days. And the *in vivo* pharmacokinetic parameters of agents were greatly enhanced by the NPs (Wang et al., 2018). Postoperative continuous monitoring of gastric cancer could be performed by PCC NPs via NIR fluorescent imaging. Therefore, PCC NPs could be used to probe for accurate assessment of tumor progression. The ability will provide reliable information on the dynamic process of treatment, which can be used to determine or modify the appropriate therapeutic schedule against gastric cancer.

Many researchers have focused on chemo-photothermal combinations in cancer therapy (Hauck et al., 2008; Zhang et al., 2014). The suppression of PCC NPs was finally evaluated in a gastric cancer cell line and xenograft mouse model. SGC-7901 cells exhibited obvious damage after treatment with PCC NPs. The cellular morphology rapidly changed under irradiation; the vast majority of cells were abnormal. By comparison, the cells did not exhibit significant morphological changes in the unirradiated area. Meanwhile, the results indicated that cell viability showed a significant negative correlation with the concentration of PCC NPs under irradiation. Both colony formation and flow cytometry assays demonstrated that treatment with PCC NPs was significantly stronger than single photothermal treatment or chemotherapy. The results indicated that PCC NPs could effectively exert synergistic effects of chemotherapy and photothermal therapy against gastric cancer cells. Subsequently, *in vivo* antitumor evaluation

was further employed to determine the synergistic effect of PCC NPs. Satisfyingly, PCC NPs treatment greatly suppressed the growth of gastric cancer in xenograft models. After treatment with PCC NPs, the tumor exhibited a slight burn within a short time; and then the burn wound gradually increased to fill the entire tumor area; finally, the tumor tissues became completely necrotic. Following continuous treatment with PCC NPs, the average volume of the tumors gradually decreased, and three tumors eliminated. The *in vivo* suppression effect of PCC NPs was also significantly better than that of single chemotherapy or photothermal treatment. The results amply demonstrated that PCC NPs could effectively treat gastric cancer.

CONCLUSION

In conclusion, multifunctional NPs consisted of dopamine, poloxamer, DOX, and IR-820 via π-π stacking for the synergistic treatment of gastric cancer. PCC NPs possess a spherical morphology and good monodispersity. Meanwhile, the NPs exhibit a superior encapsulation ability, extraordinary stability, and pH-response release. *In vitro* photothermal conversion indicated that PCC NPs could effectively heat up under irradiation, and the temperature was suited to photothermal therapy. The biosecurity of the NPs was verified on six cell lines and BALB/c mice. The *in vivo* imaging results demonstrate that PCC NPs can perform continuous monitoring of gastric cancer. The fluorescent signal in tumor tissues was maintained for nearly 1 week after one injection. *In vitro* and *in vivo* antitumor experiments finally verified that PCC NPs possess an effective synergistic effect against gastric cancer. The present study can provide a theoretical basis for the development of a novel postoperative treatment method for gastric cancer.

DATA AVAILABILITY STATEMENT

The raw data supporting the conclusions of this article will be made available by the authors, without undue reservation.

ETHICS STATEMENT

The animal study was reviewed and approved by the Laboratory Animal Administration Committee in Xi'an Medical University.

AUTHOR CONTRIBUTIONS

YZ and XZ designed the study. YZ and XS performed the experiments. YZ, XS, LZ, and XZ analyzed the results and data. YZ and XS prepared the manuscript. XZ and LZ modified the manuscript.

FUNDING

This study was supported, in part, by the Youth Program of National Natural Science Foundation of China (81801863) and Innovation Capability Support Program of the Shaanxi Province (2020KJXX-050).

SUPPLEMENTARY MATERIAL

The Supplementary Material for this article can be found online at: https://www.frontiersin.org/articles/10.3389/fphar.2020.610883/full#supplementary-material

REFERENCES

Abadeer, N. S., and Murphy, C. J. (2016). Recent progress in cancer thermal therapy using gold nanoparticles. *J. Phys. Chem. C.* 120, 4691–4716. doi:10.1021/acs.jpcc.5b11232

Bahmani, B., Bacon, D., and Anvari, B. (2013). Erythrocyte-derived phototheranostic agents: hybrid nano-vesicles containing indocyanine green for near infrared imaging and therapeutic applications. *Sci. Rep-Uk.* 3, 2180. doi:10.1038/Srep02180

Bao, Y. L., Yin, M. X., Hu, X. M., Zhuang, X. T., Sun, Y., Guo, Y. Y., et al. (2016). A safe, simple and efficient doxorubicin prodrug hybrid micelle for overcoming tumor multidrug resistance and targeting delivery. *J. Control. Release.* 235, 182–194. doi:10.1016/j.jconrel.2016.06.003

Chen, M. C., Lin, Z. W., and Ling, M. H. (2016). Near-infrared light-activatable microneedle system for treating superficial tumors by combination of chemotherapy and photothermal therapy. *ACS Nano* 10, 93–101. doi:10.1021/acsnano.5b05043

Chen, W., Meng, F. H., Cheng, R., Deng, C., Feijen, J., and Zhong, Z. H. (2015). Facile construction of dual-bioresponsive biodegradable micelles with superior extracellular stability and activated intracellular drug release. *J. Control. Release.* 210, 125–133. doi:10.1016/j.jconrel.2015.05.273

Choi, K. Y., Yoon, H. Y., Kim, J. H., Bae, S. M., Park, R. W., Kang, Y. M., et al. (2011). Smart nanocarrier based on PEGylated hyaluronic acid for cancer therapy. *ACS Nano* 5, 8591–8599. doi:10.1021/nn202070n

Dhar, D. K., Kubota, H., Tachibana, M., Kotoh, T., Tabara, H., Watanabe, R., et al. (2000). Long-term survival of transmural advanced gastric carcinoma following curative resection: multivariate analysis of prognostic factors. *World. J. Surg.* 24, 588–593. doi:10.1007/s002689910099

Dong, X., Liang, J., Yang, A. F., Qian, Z. Y., Kong, D. L., and Lv, F. (2019). Fluorescence imaging guided CpG nanoparticles-loaded IR820-hydrogel for synergistic photothermal immunotherapy. *Biomaterials*. 209, 111–125. doi:10.1016/j.biomaterials.2019.04.024

Guo, L. R., Yan, D. D., Yang, D. F., Li, Y. J., Wang, X. D., and Olivia, Z. (2014). Combinatorial photothermal and immuno cancer therapy using chitosan-coated hollow copper sulfide nanoparticles. *ACS Nano* 8, 5670–5681. doi:10.1021/nn5002112

Hauck, T. S., Jennings, T. L., Yatsenko, T., Kumaradas, J. C., and Chan, W. C. (2008). Enhancing the toxicity of cancer chemotherapeutics with gold nanorod hyperthermia. *Adv. Mater.* 20, 3832–3838. doi:10.1002/adma.200800921

Hildebrandt, B., Wust, P., Ahlers, O., Dieing, A., Sreenivasa, G., Kerner, T., et al. (2002). The cellular and molecular basis of hyperthermia. *Crit. Rev. Oncol. Hemat.* 43, 33–56. doi:10.1016/S1040-8428(01)00179-2

Huang, X. H., El-Sayed, I. H., Qian, W., and El-Sayed, M. A. (2006). Cancer cell imaging and photothermal therapy in the near-infrared region by using gold nanorods. *J. Am. Chem. Soc.* 128, 2115–2120. doi:10.1021/ja057254a

Iyer, A. K., Khaled, G., Fang, J., and Maeda, H. (2006). Exploiting the enhanced permeability and retention effect for tumor targeting. *Drug Discov. Today* 11,812–818. doi:10.1016/j.drudis.2006.07.005

Jain, R. K., and Stylianopoulos, T. (2010). Delivering nanomedicine to solid tumors. *Nat. Rev. Clin. Oncol.* 7, 653–664. doi:10.1038/nrclinonc.2010.139

Kang, W. M., Meng, Q. B., Yu, J. C., Ma, Z. Q., and Li, Z, T. (2015). Factors associated with early recurrence after curative surgery for gastric cancer. *World. J. Gastroenterol.* 21, 5934–5940. doi:10.3748/wjg.v21.i19.5934

Ke, X., Ng, V. W. L., Ono, R. J., Chan, J. M. W., Krishnamurthy, S., Wang, Y., et al. (2014), Role of non-covalent and covalent interactions in cargo loading capacity and stability of polymeric micelles. *J. Control. Release.* 193, 9–26. doi:10.1016/j.jconrel.2014.06.061

Lazar, D. C., Avram, M. F., Romosan, I., Cornianu, M., Tiban, S., and Goldi, A. (2018). Prognostic significance of tumor immune microenvironment and immunotherapy: novel insights and future perspectives in gastric cancer. *World. J. Gastroenterol.* 24, 3583–3616. doi:10.3748/wjg.v24.i32.3583

Li, S., Johnson, J., Peck, A., and Xie, Q. (2017). Near infrared fluorescent imaging of brain tumor with IR780 dye incorporated phospholipid nanoparticles. *J. Trans. Med.* 15, 18. doi:10.1186/s12967-016-1115-2

Li, W. T., Peng, J. R., Tan, L. W., Wu, J., Shi, K., Qu, Y., et al. (2016). Mild photothermal therapy/photodynamic therapy/chemotherapy of breast cancer by Lyp-1 modified Docetaxel/IR820 Co-loaded micelles. *Biomaterials*. 106, 119–133. doi:10.1016/j.biomaterials.2016.08.016

Liang, Y., Deng, X., Zhang, L. G., Peng, X. Y., Gao, W. X., Gao, J., et al. (2015). Terminal modification of polymeric micelles with π-conjugated moieties for efficient anticancer drug delivery. *Biomaterials*. 71, 1–10. doi:10.1016/j.biomaterials.2015.08.032

Liu, H. Y., Chen, D., Li, L. L., Liu, T. L., Tan, L. F., Wu, X. L., et al. (2011). Multifunctional gold nanoshells on silica nanorattles: a platform for the combination of photothermal therapy and chemotherapy with low systemic toxicity. *Angew. Chem. Int. Edit.* 50, 891–895. doi:10.1002/anie.201002820

Liu, M. Y., Zeng, G. J., Wang, K., Wan, Q., Tao, L., Zhang, X. Y., et al. (2016). Recent developments in polydopamine: an emerging soft matter for surface modification and biomedical applications. *Nanoscale*. 8, 16819–16840. doi:10.1039/c5nr09078d

Peer, D., Karp, J. M., Hong, S. P., Farokhzad, O. C., Margalit, R., Langer, R., et al. (2007). Nanocarriers as an emerging platform for cancer therapy. *Nat. Nanotechnol.* 2, 751–760. doi:10.1038/nnano.2007.387

Sahu, A., Choi, W. I., Lee, J. H., and Tae, G. Y. (2013). Graphene oxide mediated delivery of methylene blue for combined photodynamic and photothermal therapy. *Biomaterials*. 34, 6239–6248. doi:10.1016/j.biomaterials.2013.04.066

Sherlock, S. P., Tabakman, S. M., Xie, L. M., and Dai, H. J. (2011). Photothermally enhanced drug delivery by ultrasmall ultifunctional FeCo/graphitic shell nanocrystals. *ACS Nano* 5, 1505–1512. doi:10.1021/nn103415x

Shi, P., Qu, K. G., Wang, J. S., Li, M., Ren, J. S., and Qu, X. G. (2012). pH-responsive NIR enhanced drug release from gold nanocages possesses high potency against cancer cells. *Chem. Commun.* 48, 7640–7642. doi:10.1039/c2cc33543c

Shi, Y., Steenbergen, M. J., Teunissen, E. A., Novo, L., Gradmann, S., Baldus, M., et al. (2013). π–π stacking increases the stability and loading capacity of thermosensitive polymeric micelles for chemotherapeutic drugs. *Biomacromolecules*. 14, 1826–1837. doi:10.1021/bm400234c

Shi, Y., van Der Meel, R., Theek, B., Oude Blenke, E., Pieters, E. H. E., Fens, M. H. A. M., et al. (2015). Complete regression of xenograft tumors upon targeted delivery of paclitaxel via π–π stacking stabilized polymeric micelles. *ACS Nano* 9,3740–3752. doi:10.1021/acsnano.5b00929

Shibu, E. S., Hamada, M., Murase, N., and Biju, V. (2013). Nanomaterials formulations for photothermal and photodynamic therapy of cancer. *J. Photoch. Photobio. C.* 15:53–72. doi:10.1016/j.jphotochemrev.2012.09.004

Sigel, R. L., Miller, K. D., and Jemal, A. (2020). Cancer statistics, 2020. CA. *Cancer. J. Clin.* 70, 7–30. doi:10.3322/caac.21590

Song, Z. Y., Wu, Y. Y., Yang, J. B., Yang, D. Q., and Fang, X. D. (2017). Progress in the treatment of advanced gastric cancer. *Tumor Biol.* 39, 1010428317714626. doi:10.1177/1010428317714626

Wang, H., Chen, J., Xu, C., Shi, L., Tayier, M., Zhou, J., et al. (2017). Cancer nanomedicines stabilized by π-π stacking between heterodimeric prodrugs enable exceptionally high drug loading capacity and safer delivery of drug combinations. *Theranostics*. 15, 3638–3652. doi:10.7150/thno.20028

Wang, K. K., Zhang, Y. F., Wang, J., Yuan, A., Sun, M. J., Wu, J. H., et al. (2016). Self-assembled IR780-loaded transferrin nanoparticles as an imaging, targeting and PDT/PTT agent for cancer therapy. *Sci. Rep-Uk*. 6, 27421. doi:10.1038/srep27421

Wang, Y., Wang, K., Zhao, J., et al. (2013). Multifunctional mesoporous silica-coated graphene nanosheet used for chemo-photothermal synergistic targeted therapy of glioma. *J. Am. Chem. Soc.* 135, 4799–4804. doi:10.1021/ja312221g

Wang, Y., Wu, Y. S., Li, K., Shen, S. H., Liu, Z. Y., and Wu, D. C. (2018). Ultralong circulating lollipop-like nanoparticles assembled with gossypol, doxorubicin, and polydopamine via π–π stacking for synergistic tumor therapy. *Adv. Funct. Mater.* 29, 1805582. doi:10.1002/adfm.201805582

Wei, X., Wang, Y., Xiong, X., Guo, X., Zhang, L., Zhang, X. B., et al. (2016). Codelivery of a π–π stacked dual anticancer drug combination with nanocarriers for overcoming multidrug resistance and tumor metastasis. *Adv. Funct. Mater.* 26, 8266–8280. doi:10.1002/adfm.201603336

Xiong, X. B., Ma, Z. S., Lai, R., and Lavasanifar, A. (2010). The therapeutic response to multifunctional polymeric nano-conjugates in the targeted cellular and subcellular delivery of doxorubicin. *Biomaterials*. 31, 757–768. doi:10.1016/j.biomaterials.2009.09.080

Yang, W., Ma, J., Zhou, W., Cao, B., Zhou, X., Yang, Z., et al. (2017). Molecular mechanisms and theranostic potential of miRNAs in drug resistance of gastric cancer. *Expert Opin. Ther. Targets* 21, 1063–1075. doi:10.1080/14728222.2017.1389900

Yi, X., Yang, K., Liang, C., Zhong, X. Y., Ning, P., Song, G. S., et al. (2015). Imaging-guided combined photothermal and radiotherapy to treat subcutaneous and metastatic tumors using iodine-131-doped copper sulfide nanoparticles. *Adv. Funct. Mater.* 25,4689–4699. doi:10.1002/adfm.201502003

Zhang, D., Zhang, J., Li, Q., Tian, H. L., Zhang, N., Li, Z. H., et al. (2018). pH- and enzyme-sensitive IR820-paclitaxel conjugate self-assembled nanovehicles for near-infrared fluorescence imaging-guided chemo-photothermal therapy. *ACS. Appl. Mater. Inter.* 10, 30092–30102. doi:10.1021/acsami.8b09098

Zhang, J., Li, M., Ghazwani, W., Zhao, Y., Huang, X., Zhang, R., et al. (2015). Effective co-delivery of doxorubicin and dasatinib using a PEG-Fmoc nanocarrier for combination cancer chemotherapy. *Biomaterials*. 67, 104–114. doi:10.1016/j.biomaterials.2015.07.027

Zhang, X. F., Huang, C. M., Lu, H. S., Wu, X. Y., Wang, C., Guang, G. X., et al. (2004). Surgical treatment and prognosis of gastric cancer in 2,613 patients. *World. J. Gastroenterol.* 10, 3405–3408. doi:10.3748/wjg.v10.i23.3405

Zhang, Y., Ren, T., Gou, J., Zhang, L., Tao, X., Tian, B., et al. (2017). Strategies for improving the payload of small molecular drugs in polymeric micelles. *J. Control. Release.* 261, 352–366. doi:10.1016/j.jconrel.2017.01.047

Zhang, Z., Wang, J., Nie, X., Wen, T., Ji, Y. L., Wu, X. C., et al. (2014). Near infrared laser-induced targeted cancer therapy using thermoresponsive polymer encapsulated gold nanorods. *J. Am. Chem. Soc.* 136, 7317–7326. doi:10.1021/ja412735p .

Zhao, Y., Wei, R., Zhong, T., Zhang, S., Huang, D., Guo, Y., et al. (2016). Tumor-specific pH-responsive peptide-modified pH-sensitive liposomes containing doxorubicin for enhancing glioma targeting and anti-tumor activity. *J. Control. Release.* 222, 56–66. doi:10.1016/j.jconrel.2015.12.006

Zheng, M. B., Yue, C. X., Ma, Y. F., Gong, P., Zhao, P. F., Zheng, C. F., et al. (2013). Single-step assembly of DOX/ICG loaded lipid–polymer nanoparticles for highly effective chemo-photothermal combination therapy. *ACS Nano* 7, 2056–2067. doi:10.1021/nn400334y

Zheng, X. H., Xing, D., Zhou, F. F., Wu, B. Y., and Chen, W. R. (2011). Indocyanine green-containing nanostructure as near infrared dual-functional targeting probes for optical imaging and Photothermal Therapy. *Mol. Pharmaceut.* 8, 447–456. doi:10.1021/mp100301t

Zhuang, W. R., Wang, Y., Cui, P. F., Xing, L., Lee, J. W., Kim, D. Y., et al. (2019). Applications of π-π stacking interactions in the design of drug-delivery systems. *J. Control. Release*. 294, 311–326. doi:10.1016/j.jconrel.2018.12.014

Zuo, T. T., Zheng, R. S., Zeng, H. M., Zhang, S., and Chen, W. (2017). Epidemiology of stomach cancer in China. *Chin. Times. J. Clin. Oncol.* 44, 52–58. doi:10.3969/j.issn.1000-8179.2017.01.881

Conflicts of Interest: The authors declare that the research was conducted in the absence of any commercial or financial relationships that could be construed as a potential conflict of interest.

frontiers in Oncology

ORIGINAL RESEARCH
published: 04 December 2020
doi: 10.3389/fonc.2020.599218

Accuracy of Endoscopic Diagnosis of *Helicobacter pylori* Based on the Kyoto Classification of Gastritis: A Multicenter Study

Jing Zhao[1], Shaoxian Xu[2], Yuan Gao[3], Yali Lei[4], Baicang Zou[1], Mimi Zhou[1], Danyan Chang[1], Lei Dong[1] and Bin Qin[1]**

[1] Department of Gastroenterology, The Second Affiliated Hospital of Xi'an Jiaotong University, Xi'an, China, [2] Department of Gastroenterology, Shaanxi Provincial People's Hospital, Xi'an, China, [3] Department of Gastroenterology, Ankang Central Hospital, Ankang, China, [4] Department of Gastroenterology, Weinan Central Hospital, Weinan, China

OPEN ACCESS

Edited by:
Xueli Chen,
Xidian University, China

Reviewed by:
Yanglin Pan,
Air Force Medical University, China
Hao Hu,
Zhongshan Hospital, Fudan University, China
Xiaolan Lu,
Pudong Medical Center Fudan University, China

***Correspondence:**
Lei Dong
Dong556@126.com
Bin Qin
qinbin16@163.com

Specialty section:
This article was submitted to Pharmacology of Anti-Cancer Drugs, a section of the journal Frontiers in Oncology

Received: *26 August 2020*
Accepted: *03 November 2020*
Published: *04 December 2020*

Citation:
Zhao J, Xu S, Gao Y, Lei Y, Zou B, Zhou M, Chang D, Dong L and Qin B (2020) Accuracy of Endoscopic Diagnosis of Helicobacter pylori Based on the Kyoto Classification of Gastritis: A Multicenter Study. Front. Oncol. 10:599218. doi: 10.3389/fonc.2020.599218

Background: There is lack of clinical evidence supporting the value of the Kyoto classification of gastritis for the diagnosis of *Helicobacter pylori* (*H. pylori*) infection in Chinese patients, and there aren't enough specific features for the endoscopic diagnosis of past infections, which is of special significance for the prevention of early gastric cancer (GC).

Methods: This was a prospective and multicenter study with 650 Chinese patients. The *H. pylori* status and gastric mucosal features, including 17 characteristics based on the Kyoto classification and two newly-defined features unclear atrophy boundary (UAB) and RAC reappearance in atrophic mucosa (RAC reappearance) were recorded in a blind fashion. The clinical characteristics of the subjects were analyzed, and the diagnostic odds ratio (DOR), sensitivity, specificity, positive predictive value (PPV), negative predictive value (NPV), area under the receiver operating characteristics curve (ROC/AUC), and 95% confidence intervals were calculated for the different features, individually, and in combination.

Results: For past infection, the DOR of UAB was 7.69 (95%CI:3.11–19.1), second only to map-like redness (7.78 (95%CI: 3.43–17.7)). RAC reappearance showed the highest ROC/AUC (0.583). In cases in which at least one of these three specific features of past infection was considered positive, the ROC/AUC reached 0.643. For current infection, nodularity showed the highest DOR (11.7 (95%CI: 2.65–51.2)), followed by diffuse redness (10.5 (95%CI: 4.87–22.6)). Mucosal swelling showed the highest ROC/AUC (0.726). Regular arrangement of collecting venules (RAC) was specific for no infection.

Conclusions: This study provides evidence of the clinical accuracy and robustness of the Kyoto classification of gastritis for the diagnosis of *H. pylori* in Chinese patients, and confirms UAB and RAC reappearance partly supplement it for the diagnosis of past infections, which is of great benefit to the early prevention of GC.

Keywords: unclear atrophy boundary, RAC reappearance in atrophic mucosa, early gastric cancer, *Helicobacter pylori*, Kyoto classification of gastritis

INTRODUCTION

Gastric cancer (GC) is a highly lethal malignancy, with only one in five patients surviving longer than five years after diagnosis (1). Most gastric adenocarcinomas, particularly those of the intestinal type, are associated with a sequence of phenotypic changes of the native mucosa triggered by long-standing inflammation, induced mostly by *H. pylori* (2). Approximately 89% of all gastric cancers can be attributed to *H. pylori* infection. It has been reported that 14.2% of gastric cancers occur in patients with past *H. pylori* infections, while only 0.42% of gastric cancers occur in uninfected patients (3). Therefore, clarifying the *H. pylori* infection status of patients is of great importance for the detection of early GC.

Different invasive and non-invasive tests are available to detect *H. pylori* infection. Invasive methods are based on gastric biopsy samples and include *H. pylori* culture, histological staining, rapid urease test (RUT) and PCR methods. Non-invasive methods include the urease breath test, *H. pylori* stool antigen test and serum IgG tests (4). The accuracy of the invasive methods is affected by inevitable external factors, like the location, size, and quantity of biopsy samples, the staining method, use of proton pump inhibitors, antibiotic administration, and experience of the examiners (5). Non-invasive examinations are cheap, fast, and easy to perform, but there are also factors that can affect their diagnostic accuracy, such as the use of antibiotics, bismuth agents, some traditional Chinese medicines for the treatment of *H. pylori*, as well as the test reaction time (6).

H. pylori infection triggers inflammation, and its eradication diminishes inflammation, which is manifested histologically as aggregation, infiltration, and disappearance of multinuclear and mononuclear cells, destructing and restoring the microstructure of the gastric mucosa. Increasingly advanced endoscopic techniques have made it possible to visualize minute mucosal structures, such as the patterns of gastric pits and microvascular branching, raising the possibility of diagnosing *H. pylori* infection by endoscopy (7).

Conventional endoscopy, the most widely used endoscopic technique, was thought to be a poor method to diagnose the *H. pylori* status, since *H. pylori* gastritis does not produce specific manifestations detectable under conventional endoscopy, and infection is usually distributed in multiple foci (8, 9). However, this view changed when the Kyoto classification was published in Japan in 2014. This classification permits the diagnosis of *H. pylori* gastritis and an evaluation of gastric cancer risk under endoscopic examination (10). Nevertheless, endoscopic features may differ based on the geographic location and the ethnicity of patients. For example, some features which are typical of GC in Asian patients may not be present in Caucasian patients (11). It has been reported that there are significant differences in gastric mucosa of gastric cancer patients from different countries and regions in Asia. Therefore, endoscopic features associated with the *H. pylori* status may also differ between Chinese and Japanese patients, despite the high incidence of GC in both populations. This indicates that more evidence is needed to conclude that the Kyoto classification-based conventional endoscopic features are clinically effective for determining the *H. pylori* status in different populations. Moreover, there are rare specific signs of past infection in the Kyoto classification, making it difficult to distinguish these cases from uninfected patients. As mentioned earlier, patients with past *H. pylori* infection and uninfected ones have a different risk of GC. Hence, another aim of this study was to clarify the usefulness of two new features, "unclear atrophy boundary (UAB)" and "RAC reappearance in atrophic mucosa (RAC reappearance)", for the diagnosis of past infections. These signs were first noticed in patients with past infections in our clinical practice and have not been studied before.

MATERIALS AND METHODS

Subjects

This was a prospective, multicenter study, in which four facilities (the Second Affiliated Hospital of Xi'an Jiaotong University, Shaanxi Provincial People's Hospital, Ankang Central Hospital and Weinan Central Hospital) participated. A total of 650 patients >18 years old who had undergone upper gastrointestinal endoscopy) were consecutively recruited in the four facilities between July 2018 and December 2019 (202 in the Second Affiliated Hospital of Xi'an Jiaotong University, 120 in the Shaanxi Provincial People's Hospital, 157 in the Ankang Central Hospital and 171 in the Weinan Central Hospital). The exclusion criteria were as follows: severe brain, liver, or cardiopulmonary dysfunction, end-stage renal disease requiring dialysis, schizophrenia, or other mental diseases interfering with patient cooperation, pregnancy, patients with pyloric obstruction or poor preparation (who had to withdraw due to excessive food residue interfering with the endoscopy), treatment with antibiotics or proton pump inhibitors (PPIs) four weeks prior to study initiation, previous diagnosis of early or advanced gastric cancer, gastrectomy, or hemorrhagic tendency.

Assuming 80% sensitivity/specificity, the required sample size was 264 to keep the 95% confidence interval within ±5%. If the prevalence of *H. pylori* is 50% (estimated at 55.8% in China (1)), the total sample size needed to be 528. We finally set the final sample size at 581, taking into consideration the possibility of incomplete or incorrect data in 10% of the subjects.

This study was approved by the ethics committee of The Second Affiliated Hospital of Xi'an Jiaotong University (Ethics approval No.2018076). All participating subjects signed an informed consent.

Procedures

In this study we investigated the association between endoscopic features and a positive diagnosis of *H. pylori* infection made by traditional detection methods (urease breath test and rapid urease test), as well as the patient's past history. Blindness method was used to collect data, and control information bias. The endoscopic examiner was blinded to the *H. pylori* test results and to the past history of patients, which were both accurately recorded by a separate investigator before the endoscopy. The primary endpoint was the diagnostic value of each endoscopic feature for *H. pylori* infection, determined individually. The secondary endpoint was the diagnostic value of endoscopic features for *H. pylori* infection, determined in combination.

Diagnosis of *H. pylori* Infection

A specific interviewer was responsible for recording the patients' responses to an inquiry of past history of *H. pylori* infection at each facility. Every patient was required to undergo at least one of the diagnostic tests [urease breath test (13C-UBT or 14C-UBT) or rapid urease test (RUT)], within two weeks of the gastroscopy, and these results were also recorded by the interviewer.

The following methods and equipment were used to determine the *H. pylori* status of the participants: HY-IREXB *Helicobacter pylori* detector (Guangzhou Huayou Mingkang Photoelectric Technology Co., Ltd.), urea [13C] breath test diagnostic kit (Beijing Huabo Medical Technology Co., Ltd.); YH04F *H. pylori* detector, YH04 series *H. pylori* breath card (Anhui Yanghe Medical Equipment Co., Ltd.), 14C capsule (Shanghai Xinke Pharmaceutical Co., Ltd.); and *Helicobacter pylori* rapid detection test (Guangzhou beisiqi Diagnostic Reagent Co., Ltd.) for rapid urease test.

Based on the above results, the *H. pylori* status of the participants was divided into the following three types: 1) "Past infection" (eradicated): When more than four weeks had elapsed after a single and only *H. pylori* eradication event, subjects who were currently confirmed negative by either RUT or 13C-UBT/14C-UBT tests. 2) "No infection": Subjects without a history of *H. pylori* eradication who were confirmed negative by any of the three testing methods. 3) "Current infection": Subjects without a history of eradication who were confirmed positive by any of the three methods.

The endoscopists were blinded to the *H. pylori* status of each subject before and during the operation.

Endoscopic Assessment of Different Features

Five endoscopists performed endoscopy in the study (two in the Second Affiliated Hospital of Xi'an Jiaotong University and one in each of the other three centers). To improve diagnostic accuracy among participating facilities, all endoscopists were experienced, having performed over 5,000 gastroscopies and were familiar with the Kyoto classification of gastritis after twice pre-study training. In order to obtain uniform endoscopic diagnoses and to avoid inter-operator variability, abstracts summarizing typical images of endoscopic features were distributed to each endoscopist before study initiation.

All procedures were performed by well-trained endoscopists using high-resolution electronic endoscopes (GIF-HQ 260, Olympus Medical Systems) which allowed clear visualization of the collecting venules. Oxybuprocaine hydrochloride gel (30 mg, Shenyang Oasis Pharmaceutical Co., Ltd, China) and dimethylsilicone oil powder (0.5–1%, Jianheng, Zigong Honghe Pharmaceutical Co., Ltd) were used before and during endoscopy.

The following 17 distinctive endoscopic features related to *H. pylori* status (uninfected, infected, or eradicated) were defined based mainly on the Kyoto classification of gastritis (10): 1) sticky mucus, 2) atrophy, 3) diffuse redness, 4) spotty redness, 5) mucosal swelling, 6) hyperplastic polyp, 7) xanthoma, 8) enlarged fold/tortuous fold, 9) nodularity, 10) regular arrangement of collecting venules (RAC), 11) fundic gland polyp (FGP), 12) red streak, 13) hematin, 14) raised erosion, 15) map-like redness, 16) cobblestone-like mucosa, and 17) multiple white and flat elevated lesions. In addition, UAB was defined as atrophy without a clear line of separation between redness and whiteness, but with a spot-like appearance instead. RAC reappearance was defined as reappearance of typical or atypical RAC in atrophic gastric mucosa. Patients with both atrophy (graded C2 or higher), and RAC were defined as positive for "RAC reappearance". These features were divided into three categories (10), as follows: 1–9) are reported to be strongly associated with current infection with *H. pylori*, 10–13) with non-infection and 14–17) plus the new features (UAB and RAC reappearance) with past infection. Because of the multiple diagnostic significance of some features, the diagnostic odds ratios for each feature were calculated in relation to the three *H. pylori* states, as a supplement to the Kyoto classification of gastritis. Based on the results, the features were further classified into categories defined by their highest diagnostic tendency, and on this basis further statistical analyses were carried out. Intestinal metaplasia in the Kyoto classification of gastritis was not included because it itself is difficult to be accurately diagnosed by conventional endoscopy. Hence, it was usually considered as a histological diagnosis rather than an endoscopic diagnosis in clinics in China. Typical endoscopic images are shown in **Figures 1**–**3**. The presence or absence of each feature was evaluated during the endoscopy based on the diagnostic criteria. Immediately after the examination, the endoscopist recorded whether the features were present or not.

Quality Control

To ensure the authenticity and validity of the statistical analyses, we designed the recording form with opposing groups, like "RAC present" and "RAC absent". Forms in which none of the items were selected were considered invalid. In addition, we also included a supplementary group classification, with categories like "atrophy" and "UAB". Forms in which "UAB" was selected but "atrophy" was not were likewise considered invalid.

Statistical Analysis

The diagnostic odds ratios (DORs) and 95% confidence intervals of the endoscopic features for the three *H. pylori* status were calculated. One-way ANOVA was used to distinguish age differences between the three different *H. pylori* status groups. Chi-squared test was used to analyze gender and features differences. $P < 0.05$ was regarded as significant. Sensitivity, specificity, PPV, NPV, ROC/AUC, and 95% confidence intervals were calculated for those features showing significant statistical differences. All statistical analyses were performed using IBM SPSS Statistics 21.

RESULTS

Patient Characteristics

A total of 650 patients were consecutively recruited. Those who didn't have a recent *H. pylori* test result (n = 12) and those with an unclear past history of *H. pylori* infection (n = 36) were excluded. Next, we verified whether there were accurate records of the endoscopic features we defined. A total of 583 patients

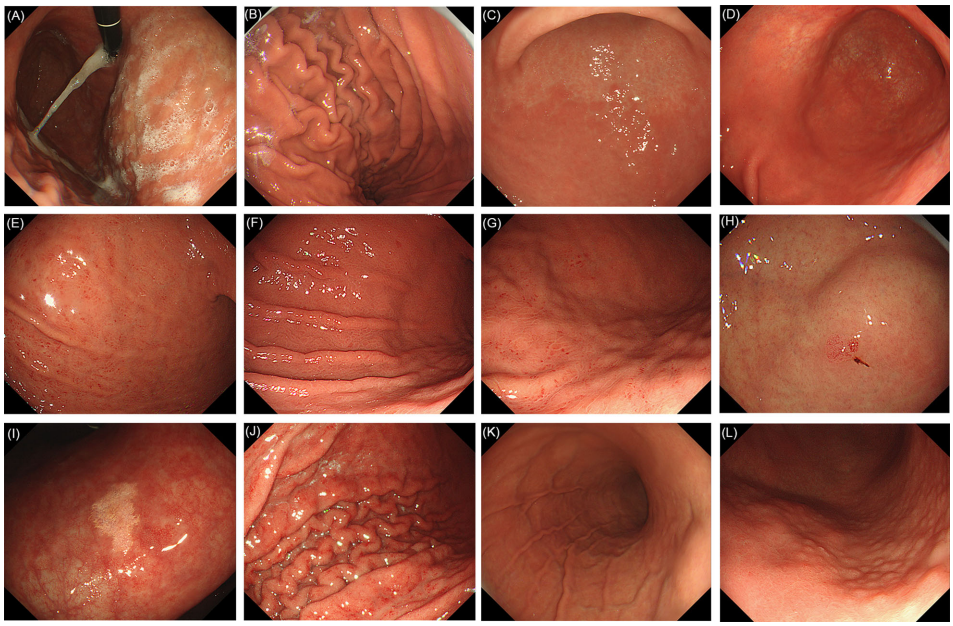

FIGURE 1 | Evaluated endoscopic features for *H. pylori* current infection. **(A)** Sticky mucus: present. **(B)** Sticky mucus: absent. **(C)** Atrophy. **(D)** Diffuse redness. **(E)** Spotty redness. **(F)** Mucosal swelling. **(G)** Spotty redness, along with mucosal swelling. **(H)** Hyperplastic polyp. **(I)** Xanthoma. **(J)** Enlarged fold/tortuous fold: present. **(K)** Enlarged fold/tortuous fold: absent. **(L)** Nodularity.

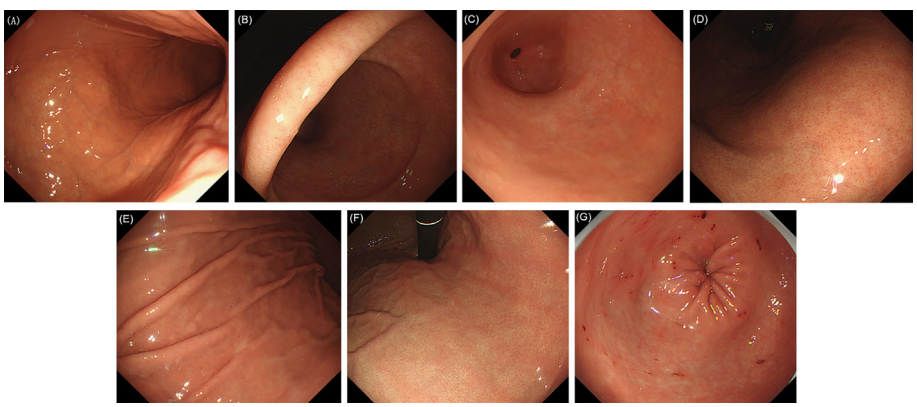

FIGURE 2 | Evaluated endoscopic features for *H. pylori* no infection. **(A)** Normal mucosa of gastric corpus. **(B)** Normal mucosa of gastric gastric angle. **(C)** Normal mucosa of gastric antrum. **(D)** Regular arrangement of collecting venules (RAC). **(E)** Fundic gland polyp (FGP). **(F)** Red streak. **(G)** Hematin.

were finally included in the study, after excluding those with incorrect records based on quality control (n = 8) and those who had other characteristics in addition to the 19 defined features, or other typical lesions such as gastric ulcer, early GC or other (n = 11) (**Figure 4**).

Regarding the baseline characteristics of the patients, 226 (38.8%) were classified as "no infection" patients, 246 (42.2%) as "current infection" patients, and 111 (19.0%) as "past infection" patients. Their mean ages (SD) were: 47.9 (13.4), 45.9 (13.9), and 49.1 (13.6) years, respectively, with no significant difference between groups (P = 0.082). Among 278 (47.7%) male patients, 95 (34.2%) were classified as "no infection", 116 (41.7%) as "current infection" and 67 (24.1%) as "past infection". Among 305 (52.3%) female patients, the corresponding numbers were 131 (43.0%), 130 (42.6%), and 44 (14.4%), respectively. No infection and past infection patients showed significant difference in terms of gender (P = 0.007).

18 features were further analyzed (excluding cobblestone-like mucosa, which was not observed in any of the subjects). The DORs of the individual endoscopic features for the three *H. pylori*

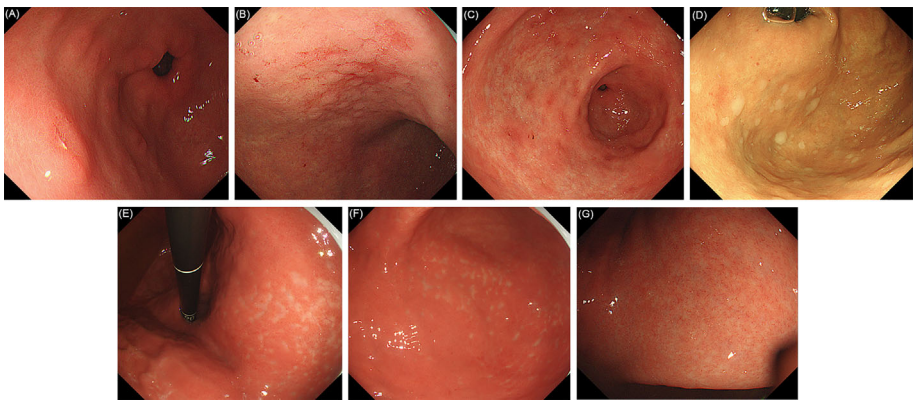

FIGURE 3 | Evaluated endoscopic features for *H. pylori* past infection. **(A)** Raised erosion. **(B)** Map-like redness of gastric corpus. **(C)** Map-like redness of gastric antrum. **(D)** Multiple white and flat elevated lesions. **(E)** Unclear atrophy boundary in lesser curvature of the stomach. **(F)** Unclear atrophy boundary in greater curvature of the stomach. **(G)** RAC reappearance in atrophic mucosa after *H. pylori* eradication.

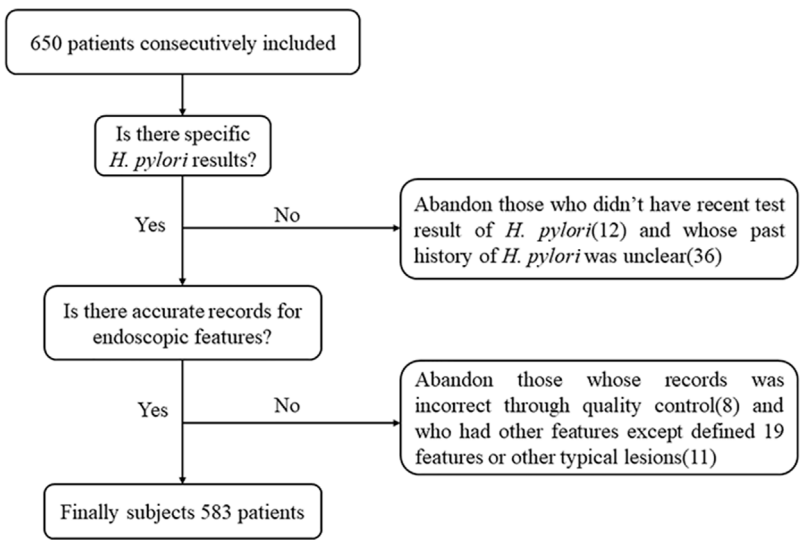

FIGURE 4 | Schematic view of subjects screening.

status are shown in **Table 1** (**Supplementary Material**). In contrast to the overwhelming majority of features which showed the same diagnostic tendency (as expected), atrophy showed the same DOR (1.91) for current infection and past infection. In addition, the DOR of RAC for no infection was 4.64, and for past infection 1.74. As expected, the DOR of UAB for past infection was as high as 7.69, second only to map-like redness (7.78), and its DOR for current infection was 0.137, meaning that it was unlikely to be present in current infection cases. Another newly defined sign, RAC reappearance, showed similar diagnostic efficacy.

Diagnostic Efficacy of Features for Current Infection

Associations between endoscopic features and current *H. pylori* infection are shown in **Table 2** (**Supplementary Material**). Among the nine features which are supposed to suggest "current infection", atrophy, mucosal swelling and spotty redness appeared most frequently, in 266/583 (45.6%), 203/583 (34.8%), and 184/583 (31.6%) of the cases, respectively. The frequency of the other features was less than 10% of the total.

Regarding single features, sticky mucus, atrophy, diffuse redness, spotty redness, mucosal swelling and nodularity showed significant differences between "current infection" and the other two groups ("no infection" and "past infection"). The ROC/AUCs of the first five showed statistical significance, but this was not true in the case of nodularity. Mucosal swelling showed the highest ROC/AUC (0.726), and its sensitivity (61.0%) and NPV (74.7%) were also the highest. On the other hand, nodularity showed the highest specificity (99.4%) and PPV (88.9%).

When the nine individual signs were analyzed together, the ROC/AUC of only one positive feature wasn't statistically significant. The ROC/AUC of two or more positive features showed the highest value (0.723), followed by one or more, in which case the sensitivity and NPV showed the highest values (94.3 and 91.3%, respectively). According to the DOR value, there was a close relationship between nodularity, diffuse redness, mucosal swelling and "current infection" among the single features. When cases testing positive for at least one of the three previously mentioned endoscopic findings were classified as current infection, the sensitivity was 69.1%, the specificity was 82.5%, the PPV was 74.2%, the NPV was 78.5%, and the ROC/AUC was 0.758 (95% CI:0.717–0.799); these were the highest values for all single and combined features. When cases which were positive for at least two of these features were classified as "current infection", the sensitivity was 17.1% and the specificity was 98.8%. When the number reached three, the sensitivity and specificity were 1.63% and 100%, respectively.

Diagnostic Efficacy of Features for No Infection

Among the four features suggestive of "no infection" (**Table 3**, **Supplementary Material**), RAC and hematin were most frequently observed, in 235/583 (40.3%) and 80/583 (13.7%) of the cases, respectively, while the rest were below 10% of the total. RAC, red streak, and hematin showed significant differences between "no infection" and the other two groups ("current infection" and "past infection"), with all three showing statistically significant ROC/AUCs. RAC showed the highest ROC/AUC (0.680), the highest sensitivity (62.4%), and the highest NPV (75.6%), but the lowest specificity (73.7%).

Regarding combined features, one or more positive features showed the highest ROC/AUC (0.701), the highest sensitivity (94.3%), and the highest NPV (91.3%). When cases testing positive for at least three features were classified as "no infection", the specificity and PPV showed the highest values (99.7 and 94.4%, respectively).

Diagnostic Efficacy of Features for Past Infection

Six features for "past infection" were included in the study, including atrophy (**Table 4**, **Supplementary Material**). The frequency of these signs was low, with the exception of atrophy (n = 266). RAC reappearance (n = 58), came after atrophy, representing only 9.95% of the total.

RAC reappearance, atrophy, map-like redness, UAB, and raised erosion showed significant differences between "past infection" and the other two groups ("current infection" and "no-infection"). The ROC/AUCs of the first three features showed statistical significance, but this was not the case for the last two. Among all the single features, RAC reappearance showed the highest ROC/AUC (0.583, 95%CI: 0.520–0.646). UAB showed the highest PPV (61.9%) and the second highest specificity (98.3%). However, it was observed in only 21 patients (3.60%) and its ROC/AUC was low (0.550, 95% CI: 0.488–0.613), making it difficult to evaluate in this study. The sensitivity and NPV of atrophy showed the highest values (58.6 and 85.5%, respectively).

The results of the combined analysis of these six signs are as follows: When the number of combined positive features was increased (from one or more features to three or more), the sensitivity and NPV decreased, while the specificity and PPV increased. In general, when cases testing positive for at least two features were classified as "past infection", the ROC/AUC was the highest (0.617). The distribution and diagnostic performance of atrophy combined with UAB were the same as that of UAB alone, since atrophy necessarily had to be present when UAB was detected. In addition, the ROC/AUC of either map-like redness positive or atrophy positive was 0.597 (95%CI: 0.539–0.655), while its sensitivity and specificity were 62.2 and 57.2%, respectively. When cases testing positive for at least one of the three features (map-like redness, UAB or RAC reappearance) were classified as past infection, the sensitivity was 37.8%, the specificity was 90.7%, the PPV was 48.8%, the NPV was 86.1%, and the ROC/AUC was 0.643 (95%CI: 0.580–0.705); these were the highest values in the analysis for all single and combined features of past infection. Moreover, the ROC/AUC of either UAB positive or RAC reappearance positive was 0.614 (95%CI: 0.551–0.677), higher than any other single feature.

DISCUSSION

H. pylori has been identified as a Group I carcinogen by the International Agency for Research on Cancer. Timely endoscopic identification of current infection and past infection is of great benefit to the monitoring of high risk population of early GC. This was a prospective, multicenter study to evaluate the diagnostic value of endoscopic features for *H. pylori* infection status, mainly based on the Kyoto classification of gastritis. In addition, two new features, "UAB" and "RAC reappearance", were investigated, which were beneficial for the diagnosis of past infection.

We divided the *H. pylori* status of the participants into three categories: *H. pylori* positive ("current infection"), *H. pylori* negative ("no infection") and *H. pylori* negative after eradication ("past infection"). Of note, the risk of GC is far greater in patients who are *H. pylori* negative after successful eradication than in uninfected patients (3). Traditional testing methods such as the urease breath test, rapid urease test, and others cannot make a direct, accurate diagnosis of "past infection". Hence, in cases in which the patient's past history is unknown, it would be clinically important to be able to determine past infection endoscopically. Importantly, the *H. pylori* status and endoscopic features were recorded separately in this study, avoiding subjective influence. Additionally, cooperation between multiple centers improved the comprehensiveness and integrity of the data.

Swelling and redness of the gastric mucosa have been endoscopically confirmed in cases with *H. pylori* -induced inflammation (12, 13). Mucosal swelling has become the most valuable feature for the diagnosis of *H. pylori*-infection of the gastric mucosa, with a ROC of 0.726 in published studies. Nowadays, high-resolution endoscopy permits the detection of mucosal unevenness and swelling of the *areae gastricae*, even without the use of the indigo carmine contrast (IC) method, as in former studies (14). Diffuse redness is considered to be a marker of histologic mucosal

hyperemia, and this feature strongly associates with the hemoglobin index (IHb), an objective index of redness (12). In Kato's study, it was concluded that diffuse redness was a diagnostically useful endoscopic finding in *H. pylori*-infected stomachs (14). Consistent with previous studies, we found diffuse redness to be highly associated with current *H. pylori* infection, with a ROC/AUC of 0.590 (13, 14). Nodularity is the result of lymphofollicular hyperplasia, and it is considered strong evidence in favor of *H. pylori* infection (15–17). Our results are in agreement with these conclusions since nodularity showed the highest DOR (11.7), although its ROC/AUC was low because of its low frequency (only observed in 18 patients). Based on the DORs, we found there was a close relationship between nodularity, diffuse redness, mucosal swelling and "current infection" among the single features. When cases testing positive for at least one of these three endoscopic features were classified as "current infection", the ROC/AUC was 0.758, which was the highest in the study, underscoring the importance of paying attention to these three features during evaluation.

On the other hand, consistent with previous studies, sticky mucus, atrophy, spotty redness, hyperplastic polyp, xanthoma and enlarged/tortuous folds were suggestive of current *H. pylori* infection (14, 18, 19). Considering all nine features, if only one is present, it is insufficient to diagnose a current *H. pylori* infection (see **Table 2**). But when two or more are positive, all these features are useful for evaluation (ROC/AUC 0.723). Early detection of *H. pylori* gastritis and prompt eradication are an effective therapeutic strategy for the prevention of gastric cancer (20, 21). From this point of view, our results are promising, contributing to the early detection of *H. pylori* gastritis.

In contrast, RAC, red streak, hematin, and FGP have been reported to be correlated with an *H. pylori*-negative, normal stomach (14, 18, 19). In accordance with previous studies, RAC showed a good diagnostic value for non-infected patients in this study, with a ROC of 0.680 (22). Consistent with previous studies, the other three features also showed a certain diagnostic value, but their frequency was low, so two or more seldom appeared simultaneously. Cases positive for one or more of these features and diagnosed as "no infection" showed the highest ROC/AUC (0.701). Undoubtedly, the more these features are present simultaneously, the more likely the gastric mucosa will be *H. pylori* negative.

Successful eradication of *H. pylori* improves gastritis and may prevent various diseases associated with *H. pylori* infection (23). The diagnosis of past *H. pylori* infection is especially important for the early monitoring of gastric cancer. It is well documented that *H. pylori* eradication alleviates histologic gastritis (24). In terms of histological parameters, most studies report similar trends, such as disappearance or reduction of inflammatory cells, including both polymorphonuclear cells and mononuclear cells (24). However, due to a lack of specific endoscopic signs, previous studies usually diagnosed *H. pylori* eradication based on an improvement of signs of "current infection". For example, Kato et al. found that regression of spotty redness after eradication suggested past infection (25). Using magnifying endoscopy, Yagi et al. concluded that mucosal swelling disappeared and mucosal redness improved after eradication (26). However, strict and continuous endoscopic monitoring of the gastric mucosa before and after *H. pylori* eradication is too difficult and expensive to achieve in real clinical situations in China. In this regard, map-like redness as well as cobblestone-like mucosa have been reported to be specific for past infection in the Kyoto gastritis classification, and this undoubtedly constitutes a great breakthrough in endoscopic diagnosis (18, 27, 28).

No cobblestone-like mucosa was seen in all cases in this study. However, map-like redness was indeed an effective diagnostic index, with a DOR of 7.78 (which was the highest) and a significant ROC/AUC of 0.561. But more important were the other two specific features investigated in this study, UAB and RAC reappearance. Previous long-term follow-up studies of patients showed that the degree of atrophy of the gastric mucosa can be reduced after *H. pylori* eradication, but whether the atrophic boundary becomes blurred due to the disappearance of inflammation has not been determined (29). We detected and defined this finding as "unclear atrophy border (UAB)". In this study, UAB was highly correlated with past infection (DOR 7.69). Its sensitivity was low (11.7%), but its specificity (98.3%) was very high and its accuracy similar to that of map-like redness (81.8%). However, low frequency prevented an accurate evaluation of its diagnostic efficacy. More samples and renewed focus on this new specific feature are warranted. Moreover, RAC reappearance, which has often been ignored in previous traditional endoscopic studies, also effectively indicated past *H. pylori* infection, a finding that is in agreement with the results of Yagi et al. using magnifying endoscopy (26). *H. pylori*-infected and inflamed gastric mucosa, characterized by the continuous breakdown and regeneration of blood vessels due to severe inflammation, will show remarkable changes in these gastric mucosal patterns if successfully treated (24, 30). The density of fine irregular vessels will decrease, and RAC may reappear, even in atrophic mucosa resulting from persistent inflammation. Although it was observed in only 21 cases in this study, its specificity was 93.2% and its ROC/AUC (0.583) was the highest for a single sign. Hence, this feature will be of great benefit for the diagnosis of past infection. When cases testing positive for at least one of these two features (UAB and RAC reappearance) were classified as past infection, the ROC/AUC was 0.614, suggesting that these two features may be unique indicators of past *H. pylori* infection in Chinese patients. When cases testing positive for at least one of these two features or map-like redness were classified as past infection, the ROC/AUC reached 0.643, which was the highest score, a rare finding, since all of these features of "past infection" are uncommon.

Atrophy, which is caused by *H. pylori* infection, is certainly observed in the gastric mucosa with current infection (31). After eradication, the atrophy improves in degree, but usually still persists, even if the boundary becomes unclear (29). Because it is present in patients in whom *H. pylori* has been eradicated, atrophy is not specific for either current infection or past infection. As in previous studies, raised erosion and multiple white and flat elevated lesions suggested past *H. pylori* infection to some extent (10). When analyzing these six features together, the ROC/AUC was a

significant 0.617, highlighting the importance of paying attention to all these features during evaluation.

For the diagnosis of *H. pylori* status, it is first necessary to assess the presence or absence of atrophy. This was the most common feature in nearly half of the samples. The presence of atrophy is rarely indicative of "no infection". Therefore, if it occurs, further careful observation of whether there is RAC reappearance in the atrophic background or unclear atrophy boundary is the key to determine whether it corresponds to "past infection". With the exception of atrophy, features of past infection like these two usually appear with low frequency but have high specificity; that is, once any appears, the diagnostic accuracy for determining past infection is very high. On the contrary, if there is no such feature, but mucosal swelling, diffuse redness, and other signs appear together with atrophy, then the diagnosis of "current infection" is more likely. In general, a single feature indicative of current infection can achieve relatively ordinary diagnostic value, but the more features, the higher the accuracy. On the other hand, if the patient does not have atrophy, it is very likely that he has never been infected with *H. pylori* ("no infection"). If specific features of no infection such as RAC, red streak, and others can also be observed, "no infection" can be diagnosed. The probability of two or three kinds of correlating features appearing at the same time is small, so judgment is usually made according to the features which appear more frequently. On the other hand, it is also possible to combine the patient's past history to assist in the diagnosis and even return to the traditional methods like urease breath test, rapid urease test and others to diagnose the more difficult cases. After all, the ultimate goal is to reach the best clinical diagnosis.

We acknowledge that our study has some limitations. First of all, although abundant time was devoted to studying the Kyoto classification of gastritis and each feature was defined uniformly and strictly before study initiation, the assessment of these features depended on the endoscopists themselves during examination, so there may have been some inter- and intra-observer variability. Second, natural elimination of *H. pylori* infection or unintentional *H. pylori* eradication may have been underestimated; that is, patients with no history of eradication and negative test results were classified as "no infection" according to the classification, but features like UAB, RAC reappearance and so on may have appeared due to "past infection"; third, traditional detection methods, considered the gold standard in this study, may have produced false negative or false positive results, leading to some degree of error in the actual classification of *H. pylori* status.

In conclusion, this is the first study that provides evidence of the clinical accuracy and robustness of the Kyoto classification of gastritis in the Chinese population and provides two new indicators of past *H. pylori* infection, UAB and RAC reappearance in atrophic mucosa as the supplement, giving the judgment of *H. pylori* sufficient endoscopic basis. We believe that, despite its limitations, our study offers important new findings for screening of early GC based on the close relationship between *H. pylori* and GC.

DATA AVAILABILITY STATEMENT

The raw data supporting the conclusions of this article will be made available by the authors, without undue reservation.

ETHICS STATEMENT

The studies involving human participants were reviewed and approved by the ethics committee of the Second Affiliated Hospital of Xi'an Jiaotong University. The patients/participants provided their written informed consent to participate in this study.

AUTHOR CONTRIBUTIONS

JZ, BQ, and LD designed the study. JZ, BQ, SX, YG, YL, and BZ collected and analyzed the data. JZ drafted the manuscript. LD, MZ, and DC revised the manuscript. All authors contributed to the article and approved the submitted version.

FUNDING

This work was supported by the 2016 Special Fund Project for Local Science and Technology Development Guided by the Central Government of China [2016ZY-HM-01], and the Fundamental Research Funds of Xi'an Jiaotong University.

SUPPLEMENTARY MATERIAL

The Supplementary Material for this article can be found online at: https://www.frontiersin.org/articles/10.3389/fonc.2020.599218/full#supplementary-material

REFERENCES

1. Hooi JKY, Lai WY, Ng WK, Suen MMY, Underwood FE, Tanyingoh D, et al. Global Prevalence of Helicobacter pylori Infection: Systematic Review and Meta-Analysis. *Gastroenterology* (2017) 153:420–9. doi: 10.1053/j.gastro.2017.04.022
2. Colquhoun A, Arnold M, Ferlay J, Goodman KJ, Forman D, Soerjomataram I. Global patterns of cardia and non-cardia gastric cancer incidence in 2012. *Gut* (2015) 64:1881–8. doi: 10.1136/gutjnl-2014-308915
3. Ono S, Kato M, Suzuki M, Ishigaki S, Takahashi M, Haneda M, et al. Frequency of Helicobacter pylori -negative gastric cancer and gastric mucosal atrophy in a Japanese endoscopic submucosal dissection series including histological, endoscopic and serological atrophy. *Digestion* (2012) 86:59–65. doi: 10.1159/000339176
4. Diaconu S, Predescu A, Moldoveanu A, Pop CS, Fierbinteanu-Braticevici C. Helicobacter pylori infection: old and new. *J Med Life* (2017) 10:112–17.
5. Logan RP, Walker MM. ABC of the upper gastrointestinal tract: Epidemiology and diagnosis of Helicobacter pylori infection. *BMJ* (2001) 323:920–2. doi: 10.1136/bmj.323.7318.920

6. Makristathis A, Hirschl AM, Megraud F, Bessede E. Review: Diagnosis of Helicobacter pylori infection. *Helicobacter* (2019) 24(Suppl 1):e12641. doi: 10.1111/hel.12641
7. Ji R, Li YQ. Diagnosing Helicobacter pylori infection in vivo by novel endoscopic techniques. *World J Gastroenterol* (2014) 20:9314–20. doi: 10.3748/wjg.v20.i28.9314
8. Suzuki H, Moayyedi P. Helicobacter pylori infection in functional dyspepsia. *Nat Rev Gastroenterol Hepatol* (2013) 10:168–74. doi: 10.1038/nrgastro.2013.9
9. Ford AC, Forman D, Hunt RH, Yuan Y, Moayyedi P. Helicobacter pylori eradication therapy to prevent gastric cancer in healthy asymptomatic infected individuals: systematic review and meta-analysis of randomised controlled trials. *BMJ* (2014) 348:g3174. doi: 10.1136/bmj.g3174
10. Kamada T, Haruma K, Inoue K, Shiotani A. [Helicobacter pylori infection and endoscopic gastritis -Kyoto classification of gastritis]. *Nihon Shokakibyo Gakkai zasshi = Jpn J gastro-enterol* (2015) 112:982–93. doi: 10.11405/nisshoshi.112.982
11. Redeen S, Petersson F, Jonsson KA, Borch K. Relationship of gastroscopic features to histological findings in gastritis and Helicobacter pylori infection in a general population sample. *Endoscopy* (2003) 35:946–50. doi: 10.1055/s-2003-43479
12. Uchiyama K, Ida K, Okuda J, Asai Y, Ohyama Y, Kuroda M, et al. Correlations of hemoglobin index (IHb) of gastric mucosa with Helicobacter pylori (H-pylori) infection and inflammation of gastric mucosa. *Scand J Gastroenterol* (2004) 39:1054–60. doi: 10.1080/00365520410009645
13. Dohi O, Yagi N, Onozawa Y, Kimura-Tsuchiya R, Majima A, Kitaichi T, et al. Linked color imaging improves endoscopic diagnosis of active Helicobacter pylori infection. *Endosc Int Open* (2016) 4:E800–5. doi: 10.1055/s-0042-109049
14. Kato T, Yagi N, Kamada T, Shimbo T, Watanabe H, Ida K. Diagnosis ofHelicobacter pyloriinfection in gastric mucosa by endoscopic features: A multicenter prospective study. *Dig Endosc* (2013) 25:508–18. doi: 10.1111/den.12031
15. Shiotani A, Kamada T, Kumamoto M, Nakae Y, Nakamura Y, Kakudo K, et al. Nodular gastritis in Japanese young adults: endoscopic and histological observations. *J Gastroenterol* (2007) 42:610–5. doi: 10.1007/s00535-007-2073-5
16. Chen MJ, Wang TE, Chang WH, Liao TC, Lin CC, Shih SC. Nodular gastritis: an endoscopic indicator of Helicobacter Pylori infection. *Dig Dis Sci* (2007) 52:2662–6. doi: 10.1007/s10620-006-9281-3
17. Loffeld RJ. Diagnostic value of endoscopic signs of gastritis: with special emphasis to nodular antritis. *Netherlands J Med* (1999) 54:96–100. doi: 10.1016/s0300-2977(98)00146-6
18. Watanabe K, Nagata N, Nakashima R, Furuhata E, Shimbo T, Kobayakawa M, et al. Predictive findings for Helicobacter pylori-uninfected, -infected and -eradicated gastric mucosa: validation study. *World J Gastroenterol* (2013) 19:4374–9. doi: 10.3748/wjg.v19.i27.4374
19. Watanabe K, Nagata N, Shimbo T, Nakashima R, Furuhata E, Sakurai T, et al. Accuracy of endoscopic diagnosis of Helicobacter pylori infection according to level of endoscopic experience and the effect of training. *BMC Gastroenterol* (2013) 13:128. doi: 10.1186/1471-230X-13-128
20. Malfertheiner P, Megraud F, O'Morain C, Bazzoli F, El-Omar E, Graham D, et al. Current concepts in the management of Helicobacter pylori infection: the Maastricht III Consensus Report. *Gut* (2007) 56:772–81. doi: 10.1136/gut.2006.101634
21. Cheung DY. Helicobacter pylori Eradication Therapy, the Reasonable First Line Therapy for Gastric Mucosa-Associated Lymphoid Tissue Lymphoma Irrespective of Infection Status and Disease Stages. *Gut Liver* (2016) 10:659–60. doi: 10.5009/gnl16359
22. Machado RS, Viriato A, Kawakami E, Patricio FR. The regular arrangement of collecting venules pattern evaluated by standard endoscope and the absence of antrum nodularity are highly indicative of Helicobacter pylori uninfected gastric mucosa. *Dig Liver Dis* (2008) 40:68–72. doi: 10.1016/j.dld.2007.08.003
23. Take S, Mizuno M, Ishiki K, Hamada F, Yoshida T, Yokota K, et al. Seventeen-year effects of eradicating Helicobacter pylori on the prevention of gastric cancer in patients with peptic ulcer; a prospective cohort study. *J Gastroenterol* (2015) 50:638–44. doi: 10.1007/s00535-014-1004-5
24. Hojo M, Miwa H, Ohkusa T, Ohkura R, Kurosawa A, Sato N. Alteration of histological gastritis after cure of Helicobacter pylori infection. *Aliment Pharmacol Ther* (2002) 16:1923–32. doi: 10.1046/j.1365-2036.2002.01346.x
25. Kato M, Terao S, Adachi K, Nakajima S, Ando T, Yoshida N, et al. Changes in endoscopic findings of gastritis after cure of H. pylori infection: multicenter prospective trial. *Dig Endosc* (2013) 25:264–73. doi: 10.1111/j.1443-1661.2012.01385.x
26. Yagi K, Honda H, Yang JM, Nakagawa S. Magnifying endoscopy in gastritis of the corpus. *Endoscopy* (2005) 37:660–6. doi: 10.1055/s-2005-861423
27. Nagata N, Shimbo T, Akiyama J, Nakashima R, Kim HH, Yoshida T, et al. Predictability of Gastric Intestinal Metaplasia by Mottled Patchy Erythema Seen on Endoscopy. *Gastroenterol Res* (2011) 4:203–9. doi: 10.4021/gr357w
28. Takahari K, Haruma K, Ohtani H, Kiyoto S, Watanabe A, Kamada T, et al. Proton Pump Inhibitor Induction of Gastric Cobblestone-like Lesions in the Stomach. *Intern Med* (2017) 56:2699–703. doi: 10.2169/internalmedicine.7964-16
29. Rokkas T, Pistiolas D, Sechopoulos P, Robotis I, Margantinis G. The long-term impact of Helicobacter pylori eradication on gastric histology: a systematic review and meta-analysis. *Helicobacter* (2007) 12(Suppl 2):32–8. doi: 10.1111/j.1523-5378.2007.00563.x
30. Okubo M, Tahara T, Shibata T, Nakamura M, Yoshioka D, Maeda Y, et al. Changes in gastric mucosal patterns seen by magnifying NBI during H. pylori eradication. *J Gastroenterol* (2011) 46:175–82. doi: 10.1007/s00535-010-0335-0
31. Kawaguchi H, Haruma K, Komoto K, Yoshihara M, Sumii K, Kajiyama G. Helicobacter pylori infection is the major risk factor for atrophic gastritis. *Am J Gastroenterol* (1996) 91:959–62. doi: 10.1016/0016-5085(95)23102-1

Conflict of Interest: The authors declare that the research was conducted in the absence of any commercial or financial relationships that could be construed as a potential conflict of interest.

frontiers in Pharmacology

ORIGINAL RESEARCH
published: 08 January 2021
doi: 10.3389/fphar.2020.612620

Hirsutella Sinensis Fungus Regulates CD8$^+$ T Cell Exhaustion Through Involvement of T-Bet/Eomes in the Tumor Microenvironment

Lu Jin[1†], *Lushuai Jin*[1,2†], *Renjie Wu*[3], *Xia Liu*[1], *Xinhai Zhu*[4], *Qiyang Shou*[1,2*] *and Huiying Fu*[1,2*]

[1]*The Second Clinical Medical School, Zhejiang Chinese Medical University, Hangzhou, China,* [2]*School of Pharmacy, Zhejiang Chinese Medical University, Hangzhou, China,* [3]*Department of Medicine, Zhejiang Academy of Traditional Chinese Medicine, Hangzhou, China,* [4]*Department of Thoracic Surgery, Zhejiang Hospital, Hangzhou, China*

OPEN ACCESS

Edited by:
Qi Zeng,
Xidian University, China

Reviewed by:
Yu Cai,
Jinan University, China
Yanjie Huang,
Henan, University of Traditional Chinese Medicine, China

***Correspondence:**
Qiyang Shou
sqy133@126.com
Huiying Fu
fhy131@126.com

†*These authors have contributed equally to this work*

Specialty section:
This article was submitted to Pharmacology of Anti-Cancer Drugs, a section of the journal Frontiers in Pharmacology

Received: *30 September 2020*
Accepted: *01 December 2020*
Published: *08 January 2021*

Citation:
Jin L, Jin L, Wu R, Liu X, Zhu X, Shou Q and Fu H (2021) Hirsutella Sinensis Fungus Regulates CD8$^+$ T Cell Exhaustion Through Involvement of T-Bet/Eomes in the Tumor Microenvironment. Front. Pharmacol. 11:612620. doi: 10.3389/fphar.2020.612620

Background: Targeting exhausted T (Tex) cells is a promising strategy for anti-tumour treatment. Previously, we demonstrated that *Hirsutella sinensis* fungus (HSF) could significantly increase T cell infiltration and the effector T cell ratio in the tumor microenvironment, activating systemic immune responses. However, we do not know how HSF regulates Tex cells in the tumor microenvironment. Here, we explored the mechanism underlying HSF inhibition of Tex cells and tumor growth and metastasis in breast cancer.

Methods: We examined the effects of HSF on various tumor mouse models using *in vivo* imaging technology. Lung metastasis was detected by H&E staining and the T cell subsets in the tumor microenvironment were assayed with flow cytometry. The *in vitro* proliferation, function and apoptosis of CD8$^+$ T cells were measured, as well as the *T-bet* and *PD-1* mRNA expressions.

Results: HSF inhibited tumor growth and lung metastasis in the mice, and had significantly higher CD44^{Low}CD62L^{Hi} and CD44^{Hi}CD62L^{Low}populations in the tumour-infiltrating CD8$^+$ T cells. However, HSF significantly reduced levels of inhibitory receptors, such as PD-1, TIGIT, CTLA-4, and regulatory T cells. *In vitro*, HSF inhibited the CD8$^+$ T cell apoptosis rate, and promoted CD8$^+$ T cell proliferation and secretion of interferon (IFN)-γ and granzyme B. Furthermore, HSF treatment both *in vivo* and *in vitro* significantly increased Eomes expression, while decreasing T-bet expression.

Conclusion: HSF exerted anti-tumour effects mainly through the immune system, by promoting effector/memory T cells and reducing Tex cell production in the tumor microenvironment. The specific mechanisms involved inhibiting T-bet and promoting Eomes to decrease the expression of immune inhibitor receptors and enhance the T cell function, respectively.

Keywords: Cordyceps sinensis, *in vivo* imaging technology, exhausted T cells, Inhibitory receptors, T-bet/Eomes

INTRODUCTION

During acute infection or vaccinations, partly functional effector $CD8^+$ T cells are naturally transformed into memory $CD8^+$ T cells after viral clearance. In contrast, during chronic infections or cancers, the presence of persistent antigens hampers the proper development of $CD8^+$ memory T cells, generating exhausted T (Tex) cells instead (Wherry, 2011; Jiang et al., 2015; Mclane et al., 2019; ; Philip and Schietinger, 2019). Tex cells have a unique differentiation, phenotype, and function, along with stable epigenetic inheritance. The action of the transcription factor Tox partially locks Tex cells during the early stages of infection (Mann and Kaech, 2019). Specific deletion of Tox in tumour-specific T cells eliminates the T cell exhaustion program, as inhibitory receptors (e.g. Pdcd1, Cd244, and Tigit) (Khan et al., 2019; Alfei et al., 2019) can no longer be upregulated. However, tumour-specific T cells lacking Tox fail to persist in the tumor. Therefore, in conditions such as cancer with chronic antigen stimulation, T cell exhaustion appears to be a self-protection measure that prevents excessive stimulation and activation-induced T cell death (Mclane et al., 2019). However, Tex cells restrict pathogen infections and immune responses to tumors, thereby limiting immune-mediated pathological damage to cancers (Mann and Kaech, 2019). This response often leads to continuous disease progression, meaning that Tex cells play a central role in the development of cancer and chronic infections (Khan et al., 2019). Fortunately, this exhaustion can be reversed, at least in part, mainly by blocking inhibitory pathways such as PD-1 (Wherry, 2011). Thus, how to better and reverse the Tex cells is currently a key issue in tumor immunotherapy.

Hirsutella sinensis fungus (HSF) is an artificial fermentation product of *Cordyceps sinensis* and is widely used in China as a substitute for the latter Li et al., 2020 and Zhang et al., 2020. The fermentation product can improve immunity and enhance disease resistance in postoperative or chemoradiotherapy patients (Liu et al., 2017; Yan et al., 2020). Our previous studies proved that HSFs can significantly increase T cell infiltration and effector T cell ratio in tumors and improve the immunosuppressive tumor environment that is considered to be the key factor of immunotherapy tolerance (Fu et al., 2018; Yan et al., 2020). Additionally, HSF can activate systemic immune responses, suggesting it as a useful drug in combination with immunotherapy, as effective cancer immunotherapy requires systemic immunity (Spitzer et al., 2017; Allen et al., 2020). However, we currently have little insight regarding how HSF regulates Tex cells in the tumor microenvironment and its potential active mechanism.

In this study, we investigated whether HSF inhibited tumor growth and metastasis through the immune system using imaging technology *in vivo*. We also analyzed the T cell subsets and the relationship to HSF mechanisms in the tumor microenvironment and *in vitro*. Our results provide insights into the applications of HSF in tumour-immune treatment.

METHODS

Reagents and Chemicals

HSF was provided by Hangzhou KSBIO Science and Technology (BinJiang, Zhejiang, China). Quality control was performed following published methods (Fu et al., 2011).

The anti-mouse antibodies for fluorescence-activated cell sorting (FACS) were as follows: anti-CD45 FITC, anti-CD8 APC-H7, anti-Eomes PE-Cy7, anti-T-bet BV421, anti-PD-1 BV605, anti-CD4 PE, anti-CD44 BV510, and anti-CD62L PE-Cy7 from BD Biosciences.

Cell Culture and $CD8^+$ T Cells Isolation

The 4T1-Luc cells were cultured in IMDM medium supplemented with 10% fetal bovine serum, 50 IU/ml penicillin, and 50 μg/ml streptomycin (Hyclone, Logan, UT, USA) in a 5% CO_2 incubator at 37 °C.

$CD8^+$ T cells were isolated from splenocytes in C57/BL mice. Cells were magnetically labeled with anti-CD8a beads and isolated from spleen cell suspension using an LS Column (Miltenyi Biotec) placed in the magnetic field of a MACS separator. The process retained magnetically labeled $CD8^+$ T cells in the column, and was then rinsed vigorously using 5 ml MACS buffer. $CD8^+$ T cells were used for CFSE proliferation assays.

Animal Experiments

We investigated HSF anti-breast cancer activity using spontaneous, postoperative metastasis and subcutaneous inoculation models. The protocol was approved by the Committee on the Ethics of Animal Experiments of Zhejiang Chinese Medical University (Number of resolution: ZSLL-2017–178). Spontaneous PyMT mice were obtained from Jackson Labs and bred at the Animal Center of Zhejiang University of Traditional Chinese Medicine. Twenty 6–8-week-old female PyMT mice (18–20 g) were randomly divided into two groups: model (distilled water) and HSF (6 g/kg, refer to our previously published article by Fu et al.). Animals were given HSF and water daily for 44 days. On days 0, 7, 15, 22, 29, 37, 44, and 47, tumor measurements were taken with Vernier calipers. Tumor volume was calculated as $V = (\text{length} \times \text{width}^2)/2$. Mice were sacrificed with CO_2 asphyxiation on day 47 for lung collection.

To generate a postoperative metastasis breast cancer model, 20 female BALB/C mice (6–8-week-old, 18–20 g) were obtained from the Shanghai Laboratory Animal Center (Shanghai, China). They were housed under standard conditions. Their bottom-right second mammary fat pad was orthotopically injected with 5×10^5 4T1-luc cells in 100 μL PBS. After 3 weeks, tumors grew to an average volume of 250 mm. The mice were divided into model and HSF groups (n = 10 per group) based on their tumor volume. Tumors *in situ* were then surgically removed. On the following day, distilled water and HSF (6 g/kg) were intragastrically administered to the model and HSF groups, respectively, for four weeks.

To generate the subcutaneous inoculation model, 20 6–8-week-old female nude mice (18–20 g in weight) were injected with 4T1-luc cells (5×10^5) in 100 μL PBS into the left armpit. On the following day, mice were randomly divided into model (distilled water) and HSF (6 g/kg HSF) groups. The mice were imaged on days 0, 4, 7, 11, and 14 for each group. Before imaging, mice were intraperitoneally injected with fluorescein substrate (150 mg/kg). At 8 min after the injection, the mice were anesthetized with isoflurane using an anesthesia machine

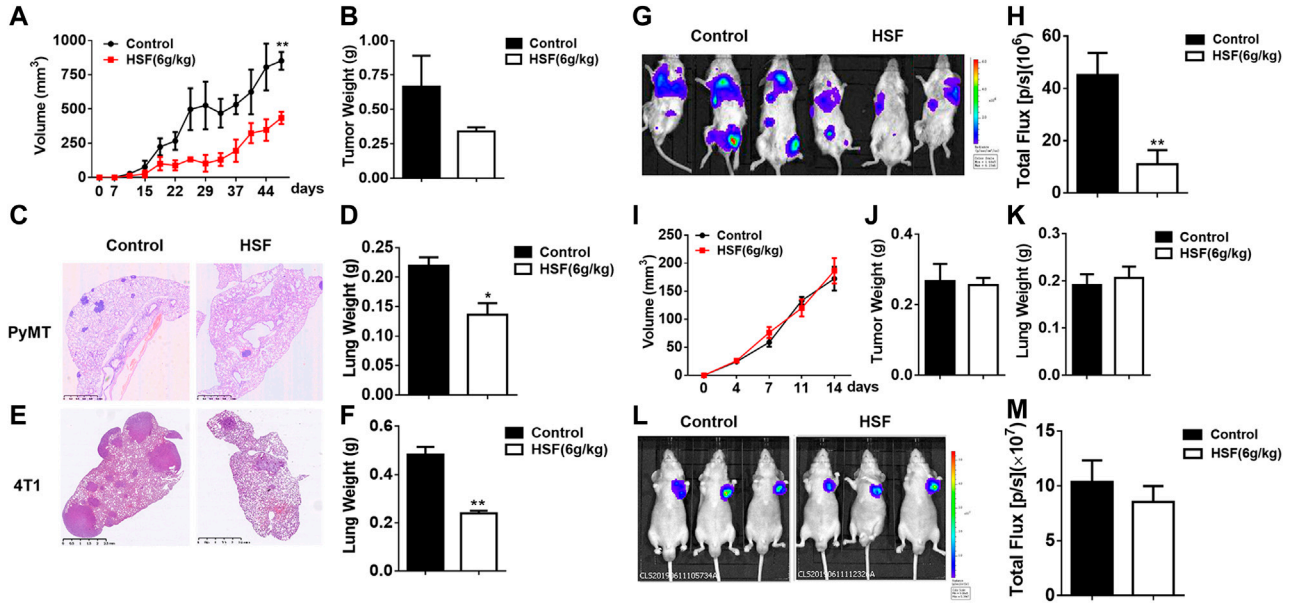

FIGURE 1 | Anti-tumour effects of HSF in different mouse models of breast cancer. **(A)** Tumor volumes in PyMT mice over time. **(B)** Tumor weights in PyMT mice. **(C)** Representative image of pathological H&E staining in the lung tissue of control and HSF-treated PyMT mice. **(D)** Lung weights in PyMT mice. **(E)** Representative image of pathological H&E staining in the lung tissue from the postoperative metastasis mice. **(F)** Lung weights of the postoperative metastasis mice. **(G)** Representative luciferase image of 4T1-Luc tumor cell lung metastasis. **(H)** Quantitative statistics of lung metastasis luciferase imaging. **(I)** Tumor volumes in nude mice over time. **(J)** Tumor weights in nude mice. **(K)** Lung weights in nude mice. **(L)** Representative luciferase image of 4T1-Luc subcutaneous tumor. **(M)** Quantitative statistics of subcutaneous tumor luciferase imaging. Statistical analysis was performed with unpaired t-tests. Values are means ± SEM; n ≥ 6 mice/group; $^{*}p < 0.05$, $^{**}p < 0.01$, $^{***}p < 0.001$.

(Summit Anesthesia, Salt Lake, UT, USA). They were then placed on a Xenogen IVIS 200 imaging system (Caliper Life Sciences, Hopkinton, MA, USA) to acquire *in vivo* images for measuring the primary-breast-cancer tumor size. Data analysis was performed using LT Living Image 4.3.

Apoptosis Assay *in vitro*

Apoptosis experiments were performed using the Annexin V-FITC Apoptosis Detection Kit (BD Biosciences). Briefly, activated $CD8^+$ T cells were cultured *in vitro* for one or 3 days. Cells were washed twice with pre-cooled PBS, then centrifuged at 300 g for 5 min, and 300 µL 1x binding buffer was added to the suspended cells. Cells were stained with 5 µL Annexin V-FITC for 15 min (in darkness, at 25 °C). Next, 5 µL PI stain was added, followed by washing twice with PBS. Before apoptosis detection, 200 µL 1x binding buffer was added to resuspend cells.

CFSE Proliferation Assay *in vitro*

$CD8^+$ T cells were purified and resuspended in PBS, then stained with carboxyfluorescein succinimidyl ester (CFSE; ThermoFisher Scientific) for 10 min at 37 °C. The reaction was stopped with CTL medium (RPMI 1640, 10% heat-inactivated fetal calf serum, 1% penicillin/streptomycin, 1% L-glutamine, 1% nonessential amino acids, 1% sodium pyruvate, and 0.1% β-mercaptoethanol), then resuspended in CTL medium. Cells were seeded (1×10^5 cells/well) in 96-well plates coated with CD3 antibodies, and then HSF (0.2 mg/ml) was added to the medium. After culturing for 3 days, cells were collected for detection by flow cytometry.

Functional Assay of $CD8^+$ T Cell *in vitro*

$CD8^+$ T cells (1×10^5/well) were seeded in 96-well plates coated with CD3/CD28 antibodies and cultured for 3 days. Cells were then treated with PMA (40 ng/ml), ionomycin (2 µmol/L), and monensin (1.4 µL/ml) for 4 h at 37 °C with 5% CO_2. They were then collected and fixed with Cytofix/Cytoperm (BD Bioscience) for 40 min at 4 °C. After washing twice, cells were stained with granzyme B and IFN-γ for 30 min at 4 °C, and resuspend in FACS buffer to assay.

Flow Cytometry Assay

Tumor or spleen samples were placed into a six-well plate containing 2 ml of Harvest medium (RPMI 1640, 2% heat-inactivated fetal calf serum, 1% penicillin/streptomycin), and then ground into a single cell suspension using a grinding rod. After filtering with a 70 mM strainer, cells were placed on ice in FACS buffer (PBS, 2% heat-inactivated fetal calf serum, 1% penicillin/streptomycin, and 0.1% sodium azide) for 30 min of staining with surface antibodies. For intranuclear staining, cells were fixed with Cytofix/Cytoperm (BD Bioscience) for 40 min at 4 °C and then stained with intracellular antibodies (T-bet, Eomes). After washing twice with FACS buffer, samples were detected with FACS Canto II Cytometry (BD, USA), and the data were analyzed in FlowJo.

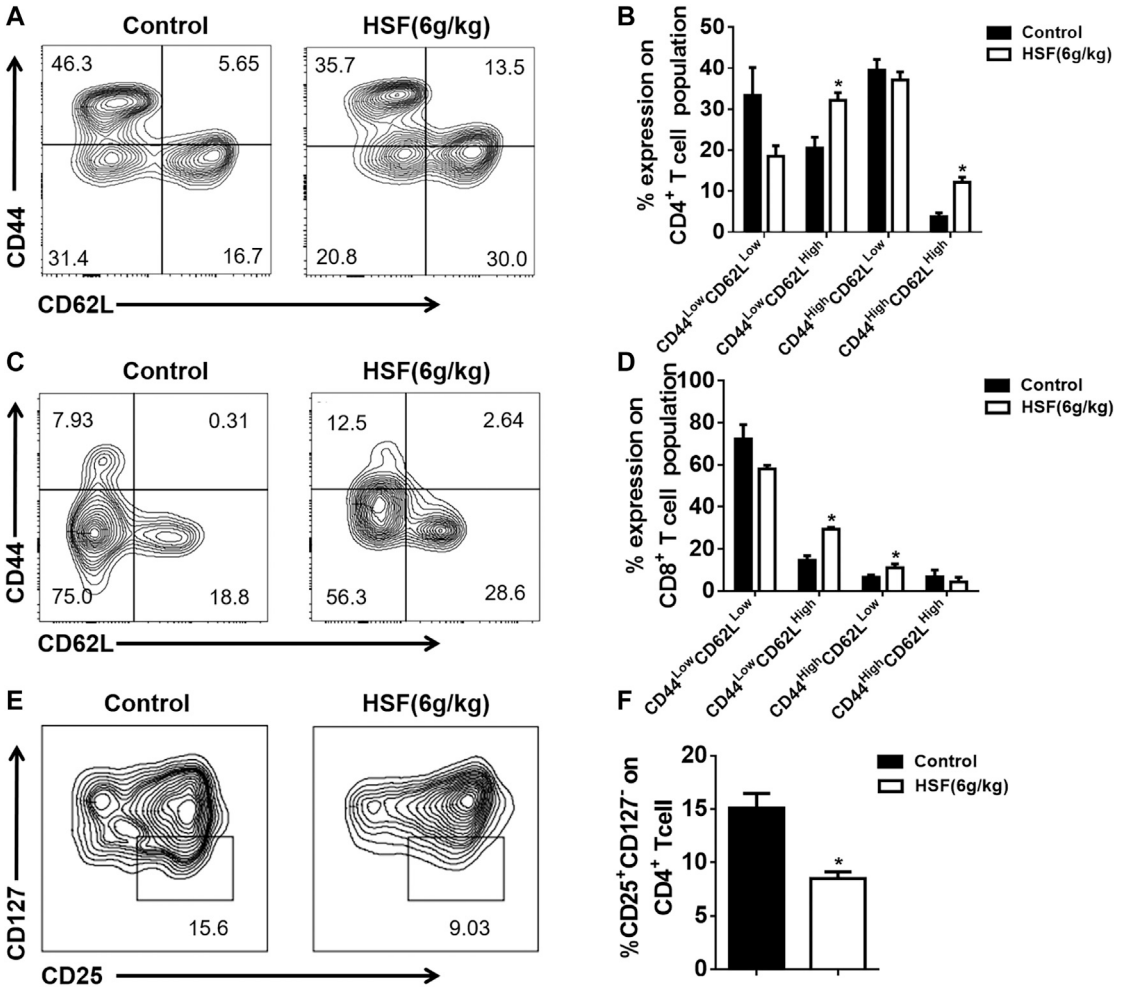

FIGURE 2 | Effect of HSF on $CD4^+$, $CD8^+$, and regulatory T cells in the lung tumor microenvironment of postoperative metastasis mice. **(A)** Representative image of $CD4^+$ $CD44^{Hi}CD62L^{Low}$, $CD4^+$ $CD44^{Hi}CD62L^{Hi}$, $CD4^+$ $CD44^{Low}CD62L^{Hi}$, $CD4^+$ $CD44^{Low}CD62L^{Low}$ population. **(B)** Flow cytometry results of $CD4^+$ $CD44^{Hi}CD62L^{Low}$, $CD4^+$ $CD44^{Hi}CD62L^{Hi}$, $CD4^+$ $CD44^{Low}CD62L^{Hi}$, $CD4^+$ $CD44^{Low}CD62L^{Low}$, expressed as percentage of tumour-infiltrating $CD4^+$ T cells. **(C)** Representative image of $CD8^+$ $CD44^{Hi}CD62L^{Low}$, $CD8^+$ $CD44^{Hi}CD62L^{Hi}$, $CD8^+$ $CD44^{Low}CD62L^{Hi}$, $CD8^+$ $CD44^{Low}CD62L^{Low}$ population. **(D)** Flow cytometric results of $CD8^+$ $CD44^{Hi}CD62L^{Low}$, $CD8^+$ $CD44^{Hi}CD62L^{Hi}$, $CD8^+$ $CD44^{Low}CD62L^{Hi}$, $CD8^+$ $CD44^{Low}CD62L^{Low}$, expressed as percentage of tumour-infiltrating $CD8^+$ T cells. **(E)** Representative image of $CD4^+CD25^+CD127^-$ population. **(F)** Flow cytometric results of $CD25^+CD127^-$, expressed as percentage of tumour-infiltrating $CD4^+$ T cells. Values are means ± SEM; n = 10 mice/group; $^*p < 0.05$, $^{**}p < 0.01$, $^{***}p < 0.001$ (unpaired t-tests).

Hematoxylin-Eosin Staining of Lung Tissues

Lung tissue was dissected and embedded in paraffin, cut into 4 μm sections, and stained with hematoxylin and eosin (H&E). Sections were imaged using a NanoZoomer Digital Slice Scanner (NDP; Nikon, Tokyo, Japan) and analyzed in NDP. view.

RNA Purification and Quantitative PCR

$CD8^+$ cells were treated with HSF (0.2 mg/ml) for 3 days before detection by qPCR. Total RNA was extracted using TRIzol (Invitrogen), then reverse-transcribed to cDNA using the PrimeScript RT Reagent Kit (Takara, USA). Samples were amplified using the TB Green PCR Master Mix kit (Takara) on an ABI 7900HT Fast Real-Time PCR System (Applied Biosystems, USA). Relative mRNA expression was normalized to β-actin and calculated using the $2^{-\Delta\Delta Ct}$ method. The primer sequences were as follows: T-bet Forward: GATCACTCAGCT GAAAATCGAC, T-bet Reverse: AGGCTGTGAGATCATATC CTTG; PD-1 Forward: ATGACTTCCACATGAACATCCT, PD-1 Reverse: CTCCAGGATTCTCTCTGTTACC; β-actin Forward: GTGACGTTGACATCCGTAAAGA; β-actin Reverse: GCCGGA CTCATCGTACTCC.

Statistical Analysis

Data are shown as means ± SEM. Between-group differences were determined using unpaired t-tests in SPSS 18.0. Significance was set at $p < 0.05$.

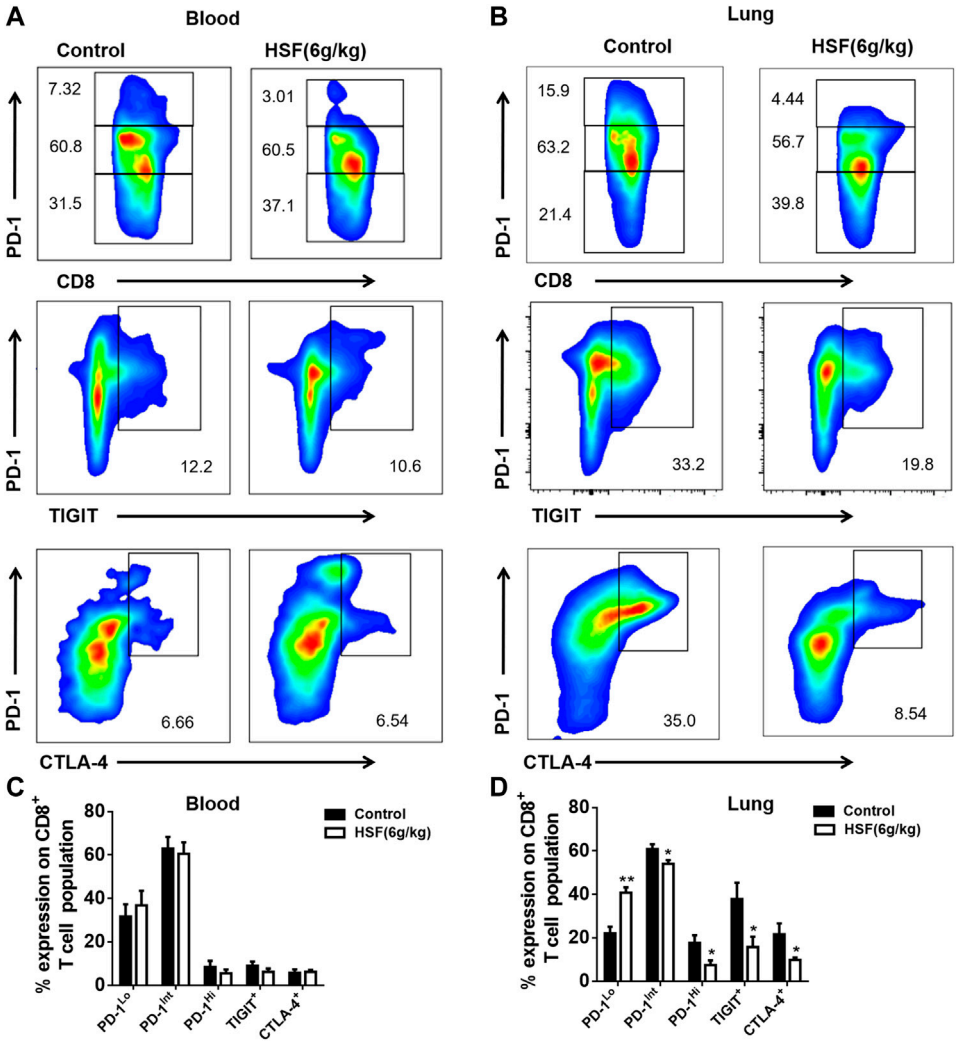

FIGURE 3 | Effect of HSF on PD-1, TIGIT, and CTLA-4 in the blood and lung samples of the breast cancer postoperative metastasis mice. **(A)** Representative image of PD-1, TIGIT, and CTLA-4 population in the blood. **(B)** Flow cytometry of PD-1, TIGIT, and CTLA-4, expressed as percentage of $CD8^+$ T cells in the blood. **(C)** Representative image of PD-1, TIGIT, and CTLA-4 population in the lungs. **(D)** Flow cytometry of PD-1, TIGIT, and CTLA-4, expressed as percentage of tumour-infiltrating $CD8^+$ T cells in the lungs. Values are means ± SEM; n = 10 mice/group; $^*p < 0.05$, $^{**}p < 0.01$, $^{***}p < 0.001$ (unpaired t-tests).

RESULTS

HSF Inhibited Tumor Growth and Lung Metastasis in Mice Through the Immune System

As shown in **Figure 1**, in a breast cancer model of mouse mammary tumor virus-polyomavirus middle T-antigen (MMTV-PyMT), tumor volume were significantly lower in the HSF-treated group than in the control group (**Figures 1A,B**), and tumors had more fluid-like substances in the control group, tumor weight were lower in the HSF-treated group. In addition, lung metastasis was significantly alleviated in the HSF-treated PyMT mice (**Figure 1C**) and postoperative metastasis mice (**Figure 1E**). These results were further confirmed with lung weight (**Figures 1D,F**). These results were consistent with the luciferase assay (**Figures 1G,H**). However, HSF treatment did not alter tumor volume, tumor weight, or lung weight in nude mice (**Figures 1I–K**), which was further confirmed by *in vivo* imaging technology (**Figures 1L,M**).

HSF Increased Effector/Memory T Cells and Decreased Regulatory T Cells in the Tumor Microenvironment

As showed in **Figure 2**, HSF markedly increased the percentage of $CD44^{Low}$ $CD62L^{Hi}$ and $CD44^{Hi}$ $CD62L^{Hi}$ to $CD4^+$ T cell populations in the postoperative metastasis mice (**Figures 2A,B**), and also significantly increased the proportion of $CD44^{Low}$ $CD62L^{Hi}$ and $CD44^{Hi}$ $CD62L^{Low}$ $CD8^+$ T cell populations (**Figures 2C,D**). Additionally, HSF significantly

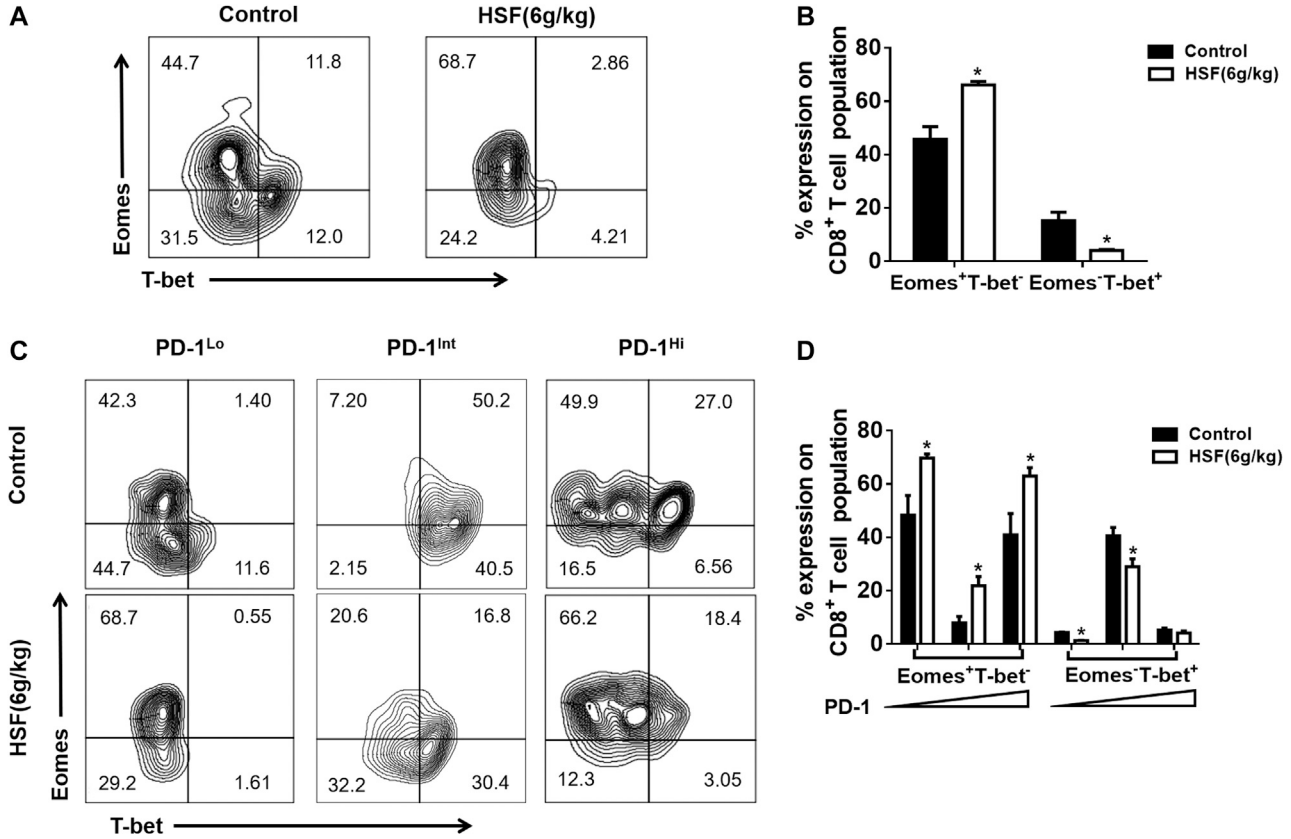

FIGURE 4 | Effect of HSF on Eomes and T-bet expression in exhausted $CD8^+$ T cells. **(A)** Representative image of T-bet and Eomes expression on $CD8^+$T cells. **(B)** Flow cytometry of T-bet and Eomes, expressed as percentage of lung $CD8^+$ T cells. **(C)** Representative image of T-bet and Eomes expression on lung PD-1^{Lo}, PD-1^{Int}, and PD-1^{Hi} cells. **(D)** Flow cytometry of T-bet and Eomes, expressed as percentage of lung PD-1^{Lo}, PD-1^{Int}, and PD-1^{Hi} cells. Values are means ± SEM; n = 10 mice/group; $*p < 0.05$, $**p < 0.01$, $***p < 0.001$ (unpaired t-tests).

decreased the $CD4^+CD25^+CD127^-$ population (regulatory T cells) in the tumor environment (**Figures 2E,F**).

HSF Inhibited $CD8^+$ Tex Cells in the Tumor Microenvironment

As shown in **Figure 3**, the inhibitory receptors of the $CD8^+$ T cells from blood, such as PD-1, TIGIT, and CTLA-4, were not significantly different between the HSF and control groups (**Figures 3A,B**). However, HSF significantly reduced the expression of inhibitor receptors in the $CD8^+$ T cells from the lung tumor microenvironment compared to that of the control (**Figures 3C,D**), and markedly decreased PD-1^{Int} and PD-1^{Hi} $CD8^+$ T cell populations. In addition, the results also showed that the inhibitor receptor expression in $CD8^+$ T cells was enhanced from the blood to tumor microenvironment.

HSF Regulated the Expression of the Transcription Factors T-Bet and Eomes in $CD8^+$ T Cells

T-box transcription factors (T-bet) and Eomesodermin (Eomes) are key to regulating $CD8^+$ T cell differentiation and function. We found a very high proportion of $Eomes^+T\text{-}bet^-$ expression, while there was a decreased proportion of $Eomes^-T\text{-}bet^+$ expression in total $CD8^+$ T cells after HSF administration (**Figures 4A,B**). We further detected Eomes and T-bet expression on PD-1 subpopulations. HSF increased Eomes expression in PD-1^{Low}, PD-1^{Int}, and PD-1^{Hi} three cell populations, whereas decreased the T-bet expression in PD-1^{Low} and PD-1^{Int} cell populations (**Figures 4C,D**).

HSF Inhibited $CD8^+$ T Cell Apoptosis and Promoted Proliferation and Function *in vitro*

The first day after treatment, apoptotic $CD8^+$ T cell rate showed no obvious difference between the control (19.5%) and HSF groups (14.7%). However, after 3 days, the HSF group had a significantly lower rate of apoptotic cells (15.2%) than that of the control group (25.5%) (**Figures 5A,B**). We also found that HSF significantly promoted cell proliferation (**Figures 5C,D**), and secretion of IFN-γ (**Figures 5E,F**) and granzyme B (**Figures 5G,H**) compared to the control.

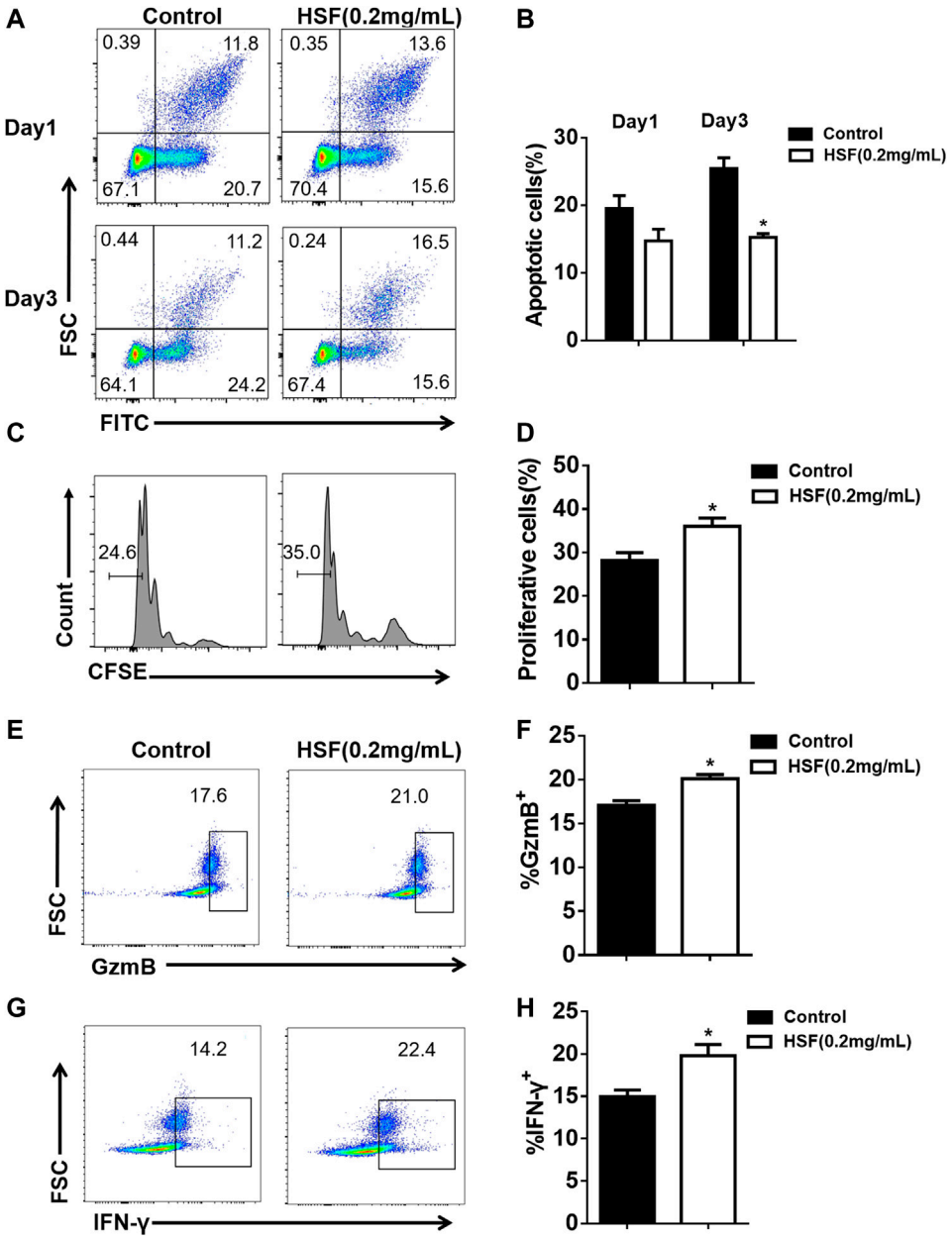

FIGURE 5 | Effect of HSF on the apoptosis, proliferation, and function of $CD8^+$ T cells *in vitro*. **(A)** Representative image of apoptotic cells. **(B)** Flow cytometry showing percentage of apoptotic cells among the $CD8^+$ T cells. **(C)** Representative image of FACS detecting cell proliferation. **(D)** Statistical analysis of the proliferation percentage of $CD8^+$ T cells. **(E)** FACS detection of GzmB production by $CD8^+$T cells after 3 days of HSF treatment. **(F)** Flow cytometry of GzmB, expressed as percentage in $CD8^+$ T cells. **(G)** FACS detection of IFN-γ production by $CD8^+$ T cells after 3 days of HSF treatment. **(H)** Flow cytometry of IFN-γ, expressed as percentage in the $CD8^+$ T cells. Values are means ± SEM; $^*p < 0.05$, $^{**}p < 0.01$, $^{***}p < 0.001$ (unpaired t-tests).

HSF Inhibited the Transcription Factor T-Bet in $CD8^+$ T Cells *in vitro* and *in vivo*

HSF decreased the PD-1^+ levels of $CD8^+$ T cells activated with CD3 for 3 days (**Figures 6A,B**), this result was also confirmed by the mRNA expression assay using qPCR (**Figure 6C**). Additionally, HSF treatment significantly increased the $Eomes^+$T-bet^- cell population in $CD8^+$ T cells, while it decreased $Eomes^-$T-bet^+ cell population and *T-bet* mRNA expression (**Figures 6D–F**).

DISCUSSION

Preventing T cell exhaustion and enhancing $CD8^+$ T cell function has become one of the most urgent issues in immunotherapy (Mclane et al., 2019). Our study found that HSF inhibited tumor growth in mice with spontaneous PyMT breast cancer and reduced orthotopic lung metastasis with *in situ* resection of 4T1-luc tumors. These results are consistent with our previous

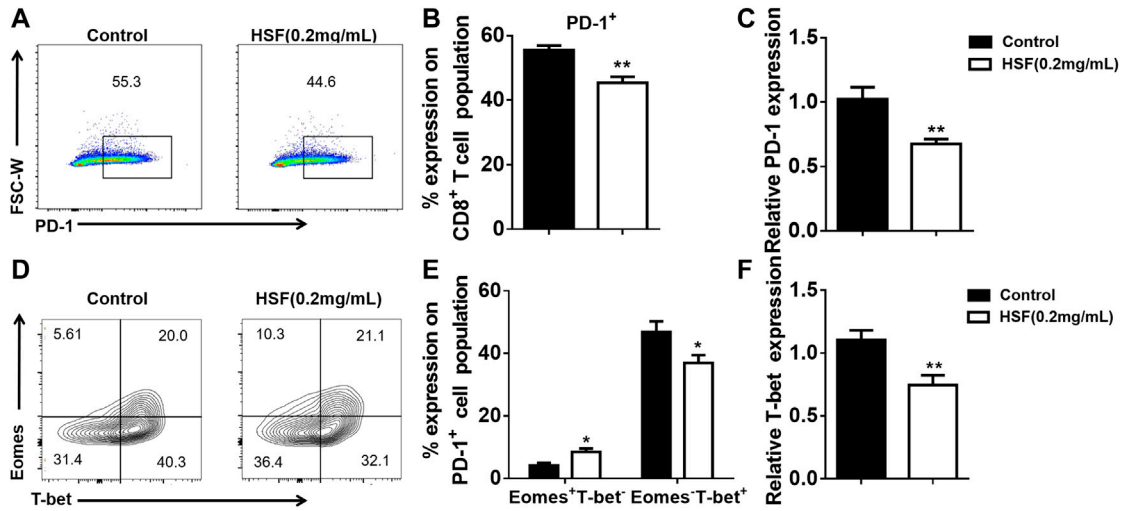

FIGURE 6 | Effect of HSF on *PD-1*, *T-bet*, and *Eomes* expression in CD8$^+$ T cells *in vitro*. **(A)** Representative image of PD-1$^+$ expression. **(B)** Flow cytometry of PD-1$^+$ population, expressed as percentage on the surface of CD8$^+$ T cells. **(C)** qRT-PCR of PD-1 expression on CD8$^+$ T cells. **(D)** Representative image of T-bet and Eomes expression in CD8$^+$ T cells. **(E)** Flow cytometry of Eomes$^+$T-bet$^-$ and Eomes$^-$T-bet$^+$ populations as percentage in CD8$^+$ T cells. **(F)** qRT-PCR of T-bet expression in HSF-treated CD8$^+$ T cells. Values are means ±SEM; $^*p < 0.05$, $^{**}p < 0.01$, $^{***}p < 0.001$ (unpaired t-tests).

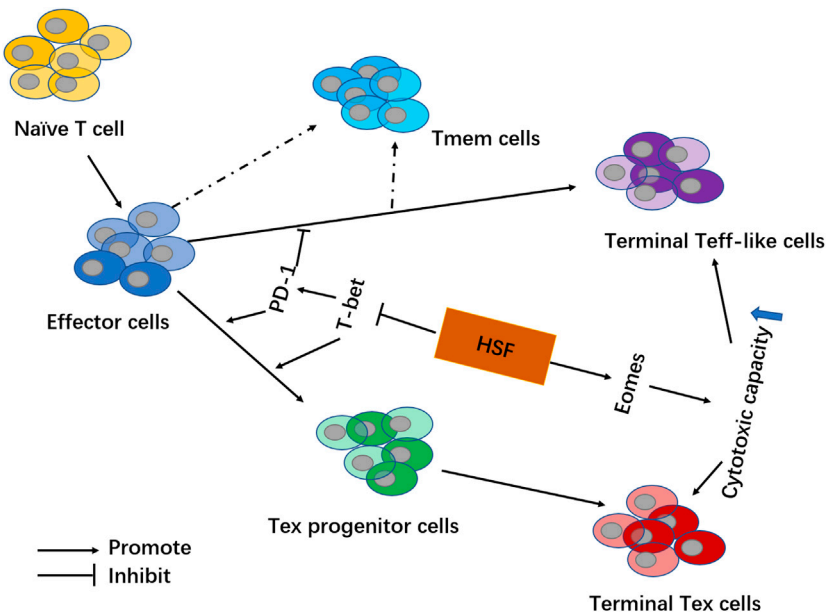

FIGURE 7 | Schematic showing HSF mechanisms involved in regulating exhausted T cells in the tumor microenvironment. By inhibiting transcription factor T-bet, HSF reduces PD-1 expression on T cells and decreases Tex cell formation (including Tex progenitor cells and Terminal Tex cells). Additionally, HSF promotes transcription factor Eomes to increase the secretion of IFN-γ and granzyme B, thereby enhancing the cytotoxic capacity among effector T cells (including Terminal Teff-like cells and Terminal Tex cells).

study showing that HSF has anti-tumour effects on lung cancer (Fu et al., 2018). Notably, we also found that HSF has no effect on immunodeficient nude mice. Our results suggest that HSF exerts an anti-tumour effect mainly through the immune system.

Accordingly, we further analyzed the T cell subgroups in the tumor microenvironment. CD4 and CD8 memory T cells can be divided into different subgroups according to homing characteristics and effector functions. Central Memory cells ($CD44^{Hi}CD62L^{Hi}$, T_{CM}) effectively promote the homing of memory T cells to lymphoid organs and respond to antigen secondary stimulation by proliferating and rapidly differentiating into effector T cells. In contrast, effector memory cells

($CD44^{Hi}$ $CD62L^{Low}$, T_{EM}) lack lymphoid homing receptors and migrate to non-lymphoid tissues to mediate the ultimate effector function, also called Terminal Teff-like cells (**Figure 7**). In addition to T_{CM} and T_{EM}, recent studies have shown the presence of another type of memory cell in both humans and mice: T memory stem cells (T_{SCM}) (Farber et al., 2014; Boudousquié et al., 2014; Chiu et al., 2020). The phenotype of T_{SCM} is $CD44^{Low}$ $CD62L^{Hi}$ $SCA\text{-}1^{Hi}$ $CD122^{Hi}$, with strong self-renewal abilities and potential to transform into T_{CM}, T_{EM} and effector T cells (Boudousquié et al., 2014; Chiu et al., 2020). In our study, it was found that HSF significantly increased the percentages of effector ($CD44^{Low}CD62L^{Hi}$) $CD4^+$ T_{SCM} cells, and central memory ($CD44^{Hi}CD62L^{Hi}$) $CD4^+$ T_{CM} cells, as well as the percentages of ($CD44^{Low}CD62L^{Hi}$) $CD8^+$ T_{SCM} cells and central memory ($CD44^{Hi}$ $CD62L^{Low}$) $CD8^+$ T_{EM} cells, while inhibiting the portion of Tex cells. These effects may be the key mechanism underlying HSF's ability to significantly improve patient immunity after chemotherapy or surgery.

Tex cells gradually lose effector function and memory T cell characteristics due to prolonged exposure to persistent antigens and inflammation. PD-1 overexpression on $CD8^+$ T cells is an important sign of T exhaustion (Pauken and Wherry, 2015a; Wherry and Kurachi, 2015). Tex cells lose their effector function in a progressive and hierarchical manner, depending on antigen levels and disease environment. There is evidence that intermediate PD-1 (PD-1 ^{Int}) is expressed in early Tex cells and further differentiated into terminal Tex cells (PD-1 ^{Hi}) with a high expression of PD-1 under continuous antigen stimulation, and it is believed that only the PD-1 ^{Int} Tex cells can respond to immune checkpoint inhibitors. Our results showed HSF significantly decreased inhibitory receptor molecules, such as PD-1, Tigit, and CTLA-4, and inhibited these two percentages of PD-1 ^{Int} and PD-1 ^{Hi} $CD8^+$ T cell populations. Additionally, our *in vitro* experiments showed HSF promoted T cell expansion, increased IFN-γ and granzyme B secretion, reduced apoptosis, and inhibited PD-1 expression in activated T cells. These results indicate that HSF directly inhibits T cell exhaustion.

Eomes and T-bet are transcription factors that regulate T cell differentiation (Pauken and Wherry, 2015a; Sen et al., 2016). Eomes upregulation is necessary for the formation of long-term memory-like cytotoxic T cells (Pearce et al., 2003). Eomes loss causes defects in memory T cell populations (Chen et al., 2019). In contrast, T-bet induces the production of inhibitory receptor molecules, such as PD-1 and Tigit (Doering et al., 2012). Some evidence has revealed that the Tex cells contain two subpopulations: Tex progenitor cells and terminal Tex cells. Tex progenitor cells highly express T-bet ($T\text{-}bet^{Hi}$ $PD\text{-}1^{Int}$), which regenerates and maintains virus-specificity through splitting. However, they could differentiate into mature terminal Tex cells expressing Eomes ($Eomes^{Hi}PD\text{-}1^{Hi}$). This subgroup is more effective against viruses, but cannot self-replicate (Pauken and Wherry, 2015b; Paley et al., 2012; Beltra et al., 2020). Consistent with available literature, we showed that $PD\text{-}1^{Int}$ $CD8^+$ T cell populations highly expressed T-bet both *in vivo* and *in vitro*. Treatment with HSF then inhibited T-bet expression in $CD8^+$ cells, as well as $PD\text{-}1^{Lo}$ and $PD\text{-}1^{Int}$ cell populations. Thus, HSF regulation of PD-1 is related to T-bet. However, we also found that Eomes was highly expressed in $PD\text{-}1^{Lo}$ and $PD\text{-}1^{Hi}$ cell populations. Moreover, HSF promoted Eomes expression in $CD8^+$ T cells, $PD\text{-}1^{Lo}$, $PD\text{-}1^{Int}$, and $PD\text{-}1^{Hi}$ cell populations. These findings indicate that HSF increases T cell function mainly related to promoting the expression of Eomes (**Figure 7**).

CONCLUSION

Our study demonstrated that HSF exerted anti-tumour effects mainly through effects on the immune system. Specifically, HSF reduced the expression of immune checkpoints through inhibiting T-bet in T cells. This then lowered Tex cell production in the tumor microenvironment. Additionally, HSF promoted Eomes expression to enhance T cell function. These finding provided a new insight into the effects of HSF on tumor immune responses, we recommend that future research investigate the ability of HSF to synergize its effects on immune checkpoint inhibitors.

DATA AVAILABILITY STATEMENT

The original contributions presented in the study are included in the article/Supplementary Material, further inquiries can be directed to the corresponding authors.

ETHICS STATEMENT

The animal study was reviewed and approved by Ethics Committee of Zhejiang Chinese Medical University.

AUTHOR CONTRIBUTIONS

HF and QS conceived and designed the research. QS, LJ (1st author), LJ (2nd author), XL, RW, XZ performed the experiments. HF and LJ (1st author) analyzed the data. HF and QS provided reagents and materials. HF and LJ (1st author) wrote the manuscript.

FUNDING

This project was sponsored in part by National Natural Science Foundation of China (81673645, 81873047, and 81573677), the Natural Science Foundation of Zhejiang province (LQ17H030006), Research Fund of Zhejiang Chinese Medical University (2020ZZ01), and Zhejiang Provincial Program for the Cultivation of High-level Innovative Health talents.

REFERENCES

Alfei, F., Kanev, K., Hofmann, M., Wu, M., Ghoneim, H. E., and Zehn, D. (2019). TOX reinforces the phenotype and longevity of exhausted T cells in chronic viral infection. *Nature* 571 (7764), 65–269. doi:10.1038/s41586-019-1326-9

Allen, B. M., Hiam, K. J., Burnett, C. E., Venida, A., Spitzer, R., Tenvooren, I., et al. (2020). Systemic dysfunction and plasticity of the immune macroenvironment in cancer models. *Nat. Med.* 26 (4), 1125–1134. doi:10.1038/s41591-020-0892-6

Beltra, J. C., Manne, S., Abdel-Hakeem, M. S., Giles, M., Giles, J. R., Chen, Z., et al. (2020). Developmental relationships of four exhausted CD8+ T cell subsets reveals underlying transcriptional and epigenetic landscape control mechanisms. *Immunity* 52 (5), 825–8e8. doi:10.1016/j.immuni.2020.04.014

Boudousquié, C., Danilo, M., Pousse, L., Jeevan-Raj, B., Angelov, G. S., Chennupati, V., et al. (2014). Differences in the transduction of canonical Wnt signals demarcate effector and memory CD8 T cells with distinct recall proliferation capacity. *J. Immunol.* 193 (6), 2784–2791. doi:10.4049/jimmunol.1400465

Chen, Z. J. Z., Ngiow, S. F., Manne, S., Cai, Z., Huang, A. C., and Wherry, E. J. (2019). TCF-1-Centered transcriptional network drives an effector versus exhausted CD8 T cell-fate decision. *Immunity* 51 (5), 840–855. doi:10.1016/j.immuni.2019.09.013

Chiu, D. K., Yuen, V. W., Cheu, J. W., Wei, L. L., Ting, V., Fehlings, M., et al. (2020). Hepatocellular carcinoma cells up-regulate PVRL1, stabilizing PVR and inhibiting the cytotoxic T-cell response via TIGIT to mediate tumor resistance to PD1 inhibitors in mice. *Gastroenterology* 159 (2), 609–623. doi:10.1053/j.gastro.2020.03.074

Doering, T. A., Crawford, A., Angelosanto, J. M., Paley, M. A., Ziegler, C. G., and Wherry, E. J. (2012). Network analysis reveals centrally connected genes and pathways involved in CD8+ T cell exhaustion versus memory. *Immunity* 37 (6), 1130–1144. doi:10.1016/j.immuni.2012.08.021

Farber, D. L., Yudanin, N. A., and Restifo, N. P. (2014). Human memory T cells: generation, compartmentalization and homeostasis. *Nat. Rev. Immunol.* 14 (1), 24–35. doi:10.1038/nri3567

Fu, H., Fu, W., Sun, M., Shou, Q., Zhai, Y., Cheng, H., et al. (2011). Kinetic cellular phenotypic profiling: prediction, identification, and analysis of bioactive natural products. *Anal. Chem.* 83 (17), 6518–6526. doi:10.1021/ac201670e

Fu, H., Jin, L., Shao, X., Li, Y., and Shou, Q. (2018). Hirsutella sinensis inhibits lewis lung cancer via tumor microenvironment effector t cells in mice. *Am. J. Chin. Med.* 46 (4), 1–12. doi:10.1142/S0192415X18500489

Jiang, Y., Li, Y., and Zhu, B. (2015). T-cell exhaustion in the tumor microenvironment. *Cell Death Dis.* 6 (6), e1792. doi:10.1038/cddis.2015.162

Khan, O., Giles, J. R., McDonald, S., Manne, S., Ngiow, S. F., Patel, K. P., et al. (2019). TOX transcriptionally and epigenetically programs CD8+ T cell exhaustion. *Nature* 571 (7764), 211–218. doi:10.1038/s41586-019-1325-x

Li, J., Cai, H., Sun, H., Qu, J., Zhao, B., Hu, X., et al. (2020). Extracts of Cordyceps sinensis inhibit breast cancer growth through promoting M1 macrophage polarization via NF-κB pathway activation. *J. Ethnopharmacol.* 260, 112969. doi:10.1016/j.jep.2020.112969

Liu, W. B., Xie, F., Sun, H. Q., Meng, M., and Zhu, Z. Y. (2017). Anti-tumor effect of polysaccharide from Hirsutella sinensis on human non-small cell lung cancer and nude mice through intrinsic mitochondrial pathway. *Int. J. Biol. Macromol.* 99, 258–264. doi:10.1016/j.ijbiomac.2017.02.071

Mann, T. H., and Kaech, S. M. (2019). Tick-TOX, it's time for T cell exhaustion. *Nat. Immunol.* 20 (9), 1092–1094. doi:10.1038/s41590-019-0478-y

Mclane, L. M., Abdel-Hakeem, M. S., and Wherry, E. J. (2019). CD8 T cell exhaustion during chronic viral infection and cancer. *Annu. Rev. Immunol.* 37 (1), 457–495. doi:10.1146/annurev-immunol-041015-055318

Paley, M. A., Kroy, D. C., Odorizzi, P. M., Johnnidis, J. B., Dolfi, D. V., and Wherry, E. J. (2012). Progenitor and terminal subsets of CD8+ T cells cooperate to contain chronic viral infection. *Science* 338 (6111), 1220–1225. doi:10.1126/science.1229620

Pauken, K. E., and Wherry, E. J. (2015a). SnapShot: T cell exhaustion. *Cell* 163 (4), 1038–e1. doi:10.1016/j.cell.2015.10.054

Pauken, K. E., and Wherry, E. J. (2015b). Overcoming t cell exhaustion in infection and cancer. *Trends Immunol.* 36 (4), 265–276. doi:10.1016/j.it.2015.02.008

Pearce, E. L., Mullen, A. C., Martins, G. A., Krawczyk, C. M., Hutchins, A. S., Hunter, C. A., et al. (2003). Control of effector CD8+ T cell function by the transcription factor Eomesodermin. *Science* 302 (5647), 1041–1043. doi:10.1126/science.1090148

Philip, M., and Schietinger, A. (2019). Heterogeneity and fate choice: T cell exhaustion in cancer and chronic infections. *Curr. Opin. Immunol.* 58, 98–103. doi:10.1016/j.coi.2019.04.014

Sen, D. R., Kaminski, J., Barnitz, R. A., Kurachi, M., Gerdemann, U., Yates, K. B., et al. (2016). The epigenetic landscape of T cell exhaustion. *Science* 354 (6316), 1165–1169. doi:10.1126/science.aae0491

Spitzer, M. H., Carmi, Y., Reticker-Flynn, N. E., Kwek, S. S., Madhireddy, D., Martins, M. M., et al. (2017). Systemic immunity is required for effective cancer immunotherapy. *Cell* 168 (3), 487–502.e15. doi:10.1016/j.cell.2016.12.022

Wherry, E. J., and Kurachi, M. (2015). Molecular and cellular insights into T cell exhaustion. *Nat. Rev. Immunol.* 15 (8), 486–499. doi:10.1038/nri3862

Wherry, E. J. (2011). T cell exhaustion. *Nat. Immunol.* 12 (6), 492–499. doi:10.1038/ni.2035

Yan, P., Shou, Q., and Fu, H. (2020). Applications of Cordyceps sinensis in cancer. *J. Altern. Complement. Integr. Med.* 6, 108. doi:10.4103/0975-9476.78183

Zhang, L., Lang, J., Jin, L., Jin, L., Cao, B., Shao, X., et al. (2020). Effect of Hirsutella sinensis fungus on the hypothalamic-pituitary-adrenal Axis in lewis rats with kidney-yang deficiency syndrome. *Evid. Based. Complement. Alternat. Med.* 2020, 5952612. doi:10.1155/2020/5952612

Conflict of Interest: The authors declare that the research was conducted in the absence of any commercial or financial relationships that could be construed as a potential conflict of interest.

frontiers in Pharmacology

ORIGINAL RESEARCH
published: 25 January 2021
doi: 10.3389/fphar.2020.598155

Synthesis, Characterization, Cellular Uptake, and *In Vitro* Anticancer Activity of Fullerenol-Doxorubicin Conjugates

Beihua Xu[1], Li Yuan[2,3], Ying Hu[4], Zhiyuan Xu[2], Jiang-Jiang Qin[1,2] and Xiang-Dong Cheng[2]**

[1]College of Pharmaceutical Sciences, Zhejiang Chinese Medical University, Hangzhou, China, [2]Institute of Cancer and Basic Medicine, Chinese Academy of Sciences, Cancer Hospital of the University of Chinese Academy of Sciences, Zhejiang Cancer Hospital, Hangzhou, China, [3]First Clinical Medical College, Zhejiang Chinese Medical University, Hangzhou, China, [4]School of Pharmaceutical Sciences, Zhejiang Pharmaceutical College, Ningbo, China

Doxorubicin (DOX) is one of the most commonly used chemotherapeutic agents for treating human cancer. However, its clinical use has been limited by DOX-induced cardiotoxicity as well as other side effects. In the present study, we designed and synthesized the fullerenol (FU)-DOX conjugates and folic acid (FA)-grafted FU-DOX conjugates for improving the selectivity and activity of DOX in cancer cells. We further characterized the physicochemical properties and examined the release kinetics, cellular uptake, and *in vitro* anticancer activities of FU-DOX and FA-FU-DOX. The results showed that FU-DOX and FA-FU-DOX had a mean diameter of <200 nm and a low polydispersity. Both FU-DOX and FA-FU-DOX exhibited pH sensitivity and their DOX release rates were higher at pH 5.9 vs. pH 7.4. The cellular uptake studies indicated that FU conjugation enhanced the intracellular accumulation of DOX in human hepatocellular carcinoma (HCC) cell lines (BEL-7402 and HepG2) and the immortalized normal human hepatocytes (L02). The conjugation of FA to FU-DOX further promoted the drug internalization in an FR-dependent manner and enhanced the cytotoxicity against HCC cells. In conclusion, the newly prepared FA-FU-DOX conjugates can optimize the safety and efficacy profile of DOX.

Keywords: fullerenol-doxorubicin conjugates, cancer, cellular uptake, microscopic imaging, targeted delivery

OPEN ACCESS

Edited by:
Qi Zeng,
Xidian University, China

Reviewed by:
Qixiang Ma,
Fudan University, China
Qingyu Shen,
Tsinghua University, China

****Correspondence:***
Jiang-Jiang Qin
jqin@zcmu.edu.cn,
Xiang-Dong Cheng
chengxd516@126.com

Specialty section:
This article was submitted to Pharmacology of Anti-Cancer Drugs, a section of the journal Frontiers in Pharmacology

Received: *23 August 2020*
Accepted: *28 September 2020*
Published: *25 January 2021*

Citation:
Xu B, Yuan L, Hu Y, Xu Z, Qin J-J and Cheng X-D (2020) Synthesis, Characterization, Cellular Uptake, and In Vitro Anticancer Activity of Fullerenol-Doxorubicin Conjugates. Front. Pharmacol. 11:598155. doi: 10.3389/fphar.2020.598155

INTRODUCTION

Doxorubicin (DOX, also named adriamycin), as a broad-spectrum anticancer drug, is widely used in leukemia, lymphomas, and solid tumors such as liver cancer, breast cancer, ovarian cancer, etc. (Kalyanaraman, 2020). However, the side effects of DOX, such as life-threatening cardiotoxicity, hepatotoxicity, and bone marrow suppression limit its clinical application (Gonçalves et al., 2020). The development of drug delivery system is considered as an effective and feasible strategy to enhance the efficacy of chemotherapeutic drugs and reduce its side effects (Raj et al., 2019; Ouyang et al., 2020). In recent years, numerous studies have shown that a variety of nanocarriers can improve the bioavailability and therapeutic efficacy of anticancer drugs while providing preferential accumulation at the target site (Tan et al., 2020). Among them, fullerenes and their derivatives are also attracting more attention for their unique physicochemical properties and biological activities (Kumar and Raza 2018).

Fullerene is a series of cage-like, spherical nano-molecules formed by carbon atoms, which have been found to have some excellent biological activities, such as antioxidant, antiviral, anticancer, and

immunomodulatory effects, etc. (Xu et al., 2011; Martinez et al., 2016; Hao et al., 2017; Xu et al., 2019). Besides, fullerenes have the ability to accumulate in the tumor mass; based on the enhanced permeability and retention (EPR) effect, they penetrate easily through the less-tight blood vessels nourishing cancer (Kepinska et al., 2018a; Kepinska et al., 2018b). In addition, fullerene and hydroxylated fullerene (fullerenol, FU) have also been reported to have the cardioprotective and hepatoprotective effects (Borović et al., 2014; Elshater et al., 2018; Petrovic et al., 2018). The administration of fullerene alone before DOX administration or complexed with DOX via non-covalent bonds could diminish DOX-induced acute toxicity in the heart or liver (Borović et al., 2014; Seke et al., 2016; Jacevic et al., 2019; Petrovic et al., 2018). More importantly, fullerene can act as a transporter for anticancer drugs, such as DOX (Grebinyk et al., 2019; Kazemzadeh and Mozafari, 2019). These biological properties of fullerenes and the potential ability to carry drugs make it attractive to be applied in the drug delivery system.

Tumor targeted drug delivery systems (TTDDSs) can selectively deliver cytotoxic substances to tumor tissues, thus minimizing the side effects of patients and improving the treatment index (Xiao et al., 2020). Folate receptor (FR) has attracted considerable attention in this field. Its expression is limited in normal cells but overexpressed in most tumor cells, such as liver cancer, lung cancer, breast cancer, and so on (Boss and Ametamey, 2020). More importantly, in the receptor-mediated internalization pathway, FR interacts with TTDDSs and rapidly recycles back to the cell surface for the maximum delivery of targeted therapeutics (Fernández et al., 2018). Researchers have grafted folic acid (FA) to the surface of various drug delivery systems, which has significantly increased the drug accumulation in tumors (Su et al., 2020; Tie et al., 2020).

Since cardiotoxicity and hepatotoxicity are the main reasons for restricting the application of DOX, FU with cardioprotective and hepatoprotective effects is increasingly being developed as a drug delivery system for DOX. Several recent studies have indicated that the non-covalent nanocomplex of DOX and fullerene or FU can significantly increase the cytotoxicity of DOX and reduce its side effects on the heart and liver (Seke et al., 2016; Petrovic et al., 2018; Maleki et al., 2020). However, other studies have shown that the loading of DOX onto FU nanoparticles with non-covalent bonds or the conjugated complex of DOX and FU with ester bonds might be unstable in the body and cannot deliver drugs efficiently (Chaudhuri et al., 2009). In the present study, DOX and FU conjugates (FU-DOX) were synthesized by using an acid-sensitive hydrazone bond and further modified by FA to obtain FA-FU-DOX conjugates for improving the tumor-targeting effects. Besides, the cellular uptake and cytotoxicity of FU-DOX and FA-FU-DOX were also examined.

MATERIALS AND METHODS

Materials

Doxorubicin hydrochloride (DOX, also named adriamycin, Shanghai Jizhi Biochemical Technology Co., Ltd.), fullerenol (FU, Suzhou Hengqiu Technology Co., Ltd.), folic acid (FA), N-hydroxysuccinimide (NHS), N1-((ethylimino)methylene)-N3,N3-dimethylpropane-1,3-diamine (EDC), oxalohydrazide, dimethyl sulfoxide (DMSO), acetic acid, ethanol, methanol, etc. were obtained commercially and used without further purification.

Synthesis of Folic Acid-Grafted Fullerenol-Doxorubicin Conjugates (FA-FU-DOX).

Preparation of Hydrazinated Fullerenol (FU-CONHNH2)

As shown in **Figure 1**, oxalohydrazide (100 mg) was added to a solution of fullerenol (100 mg, 87 μmol) in purified water (10 ml). The reaction mixture was stirred at 50°C for 5 days. Then, it was subjected to dialysis through a cellulose membrane (MW 1000) against deionized water for three times. After 2 days of lyophilization, a dark brown product FU-CONHNH2 was obtained.

Synthesis of Fullerenol-Doxorubicin Conjugates (FU-DOX)

Doxorubicin hydrochloride (30 mg, 50 μmol) and acetic acid (1 drop) as a catalyst were added to the solution of FU-CONHNH2 (70 mg, 50 μmol) in water (10 ml) (**Figure 1**). The reaction solution was stirred for 2 days in the dark at room temperature. When the thin-layer chromatography (TLC) showed little DOX left, the reaction mixture was poured into methanol (30 ml) to precipitate the products. The precipitation was filtrated and washed by methanol three times and dried under reduced pressure to give 58 mg dark red solid with 69% yield.

Preparation of Folic Acid Succinimidyl Ester (FA-NHS)

Folic acid (38 mg, 86 μmol) and DMSO (2 ml) were put into a round bottom flask and sonicated until completely dissolved (**Figure 1**). Then, NHS (11 mg, 95 μmol) and EDC (33 mg, 172 μmol) were added and the reaction mixture was stirred under nitrogen protection in dark at room temperature overnight. An orange-red solution was obtained, which was the activated folic acid (FA-NHS).

Synthesis of Folic Acid-Grafted Fullerenol-Doxorubicin Conjugates (FA-FU-DOX)

The prepared FA-NHS solution (19 mg, 43 μmol, 1 ml) was added into a solution of fullerenol-doxorubicin conjugates (85 mg, 43 μmol) in a mixed solvent of water and DMSO (1:1) (20 ml). The reaction solution was stirred in dark at room temperature for 8 h (**Figure 1**). The products were precipitated upon treatment with ethanol and filtered to give a brown solid with 64% yield.

Characterization of FA-FU-DOX

Nuclear Magnetic Resonance, Infrared Spectroscopy, and Differential Thermal Analysis

The NMR spectra were recorded on a Bruker advance 500 nuclear magnetic resonance (NMR) spectrometer, using tetramethylsilane (TMS) as an internal reference. D_2O was used as a solvent for fullerenol and deuterated DMSO was used as a solvent for FA,

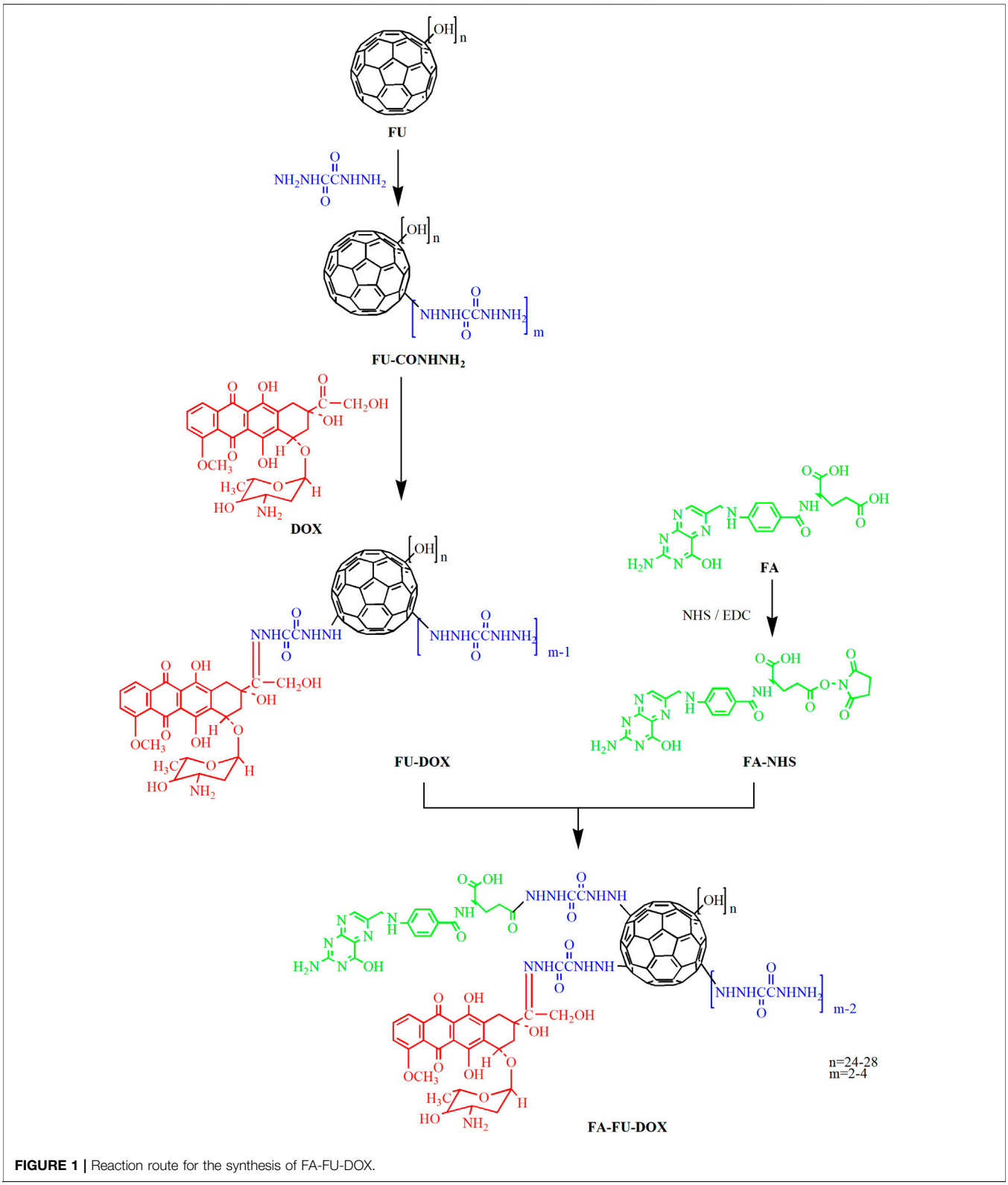

FIGURE 1 | Reaction route for the synthesis of FA-FU-DOX.

DOX, and FA-FU-DOX. The infrared (IR) spectra were recorded on a Fourier-transform infrared (FTIR) spectrometer (Thermo Fisher Nicolet iS50). KBr tablets of DOX and DOX derivatives were used in the IR instrument. The IR spectra were acquired after 16 scans with a scanning range of 400–4,000 cm^{-1}. Differential thermal analysis (DTA) was done in Mettler Toledo DSC. The detection conditions were 30–300°C, the heating rate was 15°C/min, and the N_2 flow was 100 ml/min.

Transmission Electron Microscope and Dynamic Light Scattering

The diameter and morphology of FU, FU-DOX, and FA-FU-DOX were obtained by a transmission electron microscope (TEM, H-7650, Hitachi, Japan). Dispersions of particles were dropped onto a carbon-coated copper grid, dried in air at room temperature, and imaged immediately. The size distribution of the FU-DOX and FA-FU-DOX complexes was determined by dynamic light scattering (DLS) using Zetasizer Nano ZS-90 (Malvern, United Kingdom). Data were recorded at 25°C with a detection angle of 173° (Voruganti et al., 2015).

Release Kinetic Studies of FU-DOX and FA-FU-DOX

Preparation of a Standardization Curve

To obtain a 100 mg/L stock solution of DOX, the accurately weighed DOX (5.0 mg) was put in a 50 ml volumetric flask, to which DMSO was added to dissolve and dilute to the set volume. To prepare the DOX series solutions with concentrations of 2, 5, 10, 20, and 40 mg/L, 0.2, 0.5, 1.0, 2.0, and 4.0 ml of the stock solutions were added into a 10 ml volumetric flask, diluted with DMSO to a constant volume, and recorded on a UV-2550 spectrophotometer (Shimadzu, Japan). The regression equation was $A = 0.022C - 0.027$ ($r = 0.999$), indicating that the peak area of DOX has a good linear relationship within the concentration of 0–40 mg/L region.

Drug Release Studies

Portions (2.0 mg) of FU-DOX or FA-FU-DOX were put into dialysis bags (MW 1000), which were placed into the releasing medium of phosphate buffer (30 ml) at a pH of 7.4 or 5.9, in vials respectively. The closed vials were then placed in the water bath and incubated at 37°C. The concentration of released DOX was determined by the UV spectrophotometer at predetermined time points. The rate of drug release was calculated by dividing the concentration of DOX (released from FU-DOX or FA-FU-DOX) at a certain time by the initial concentration of FU-DOX or FA-FU-DOX (Voruganti et al., 2015).

Cell Lines and Cell Culture

Human hepatocellular carcinoma (HCC) cell lines (BEL-7402 and HepG2) and the immortalized normal human hepatocytes (L02) were obtained from the Cell Bank of the Chinese Academy of Science (Shanghai, China). All cell lines were cultured in DMEM medium supplemented with 10% fetal bovine serum (FBS) and 1% penicillin/streptomycin as described previously (Wang et al., 2019).

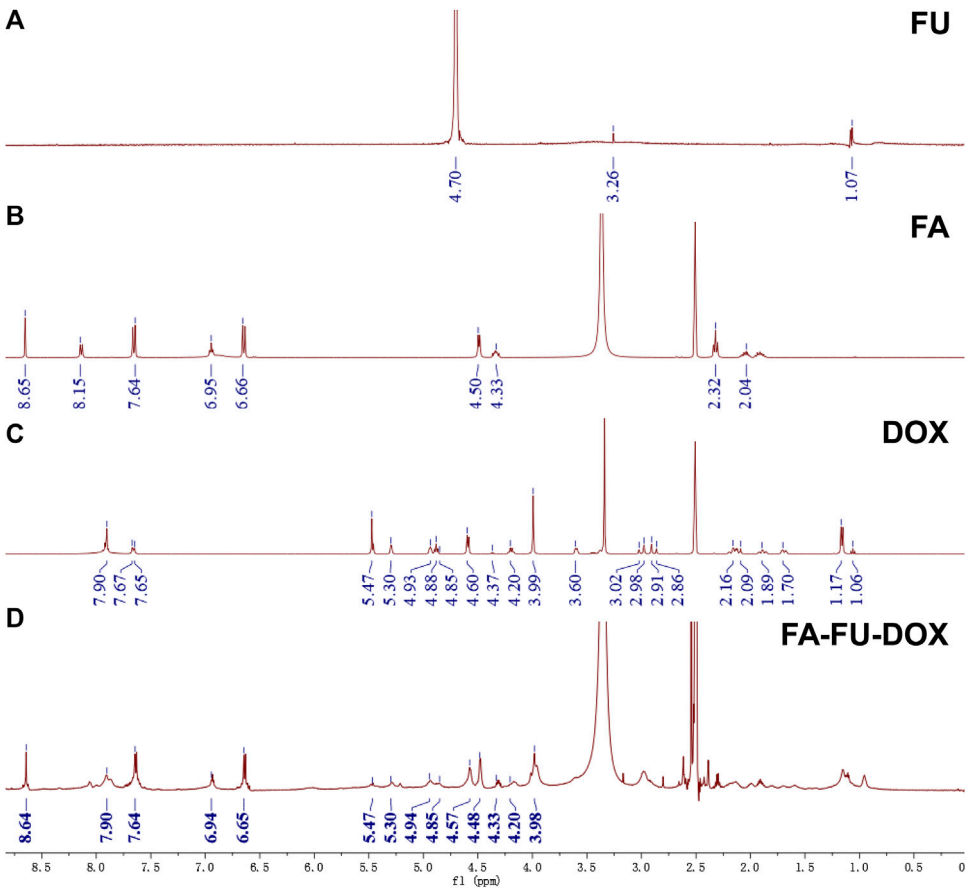

FIGURE 2 | The ^{1}H NMR spectra of **(A)** FU, **(B)** FA, **(C)** DOX, and **(D)** FA-FU-DOX.

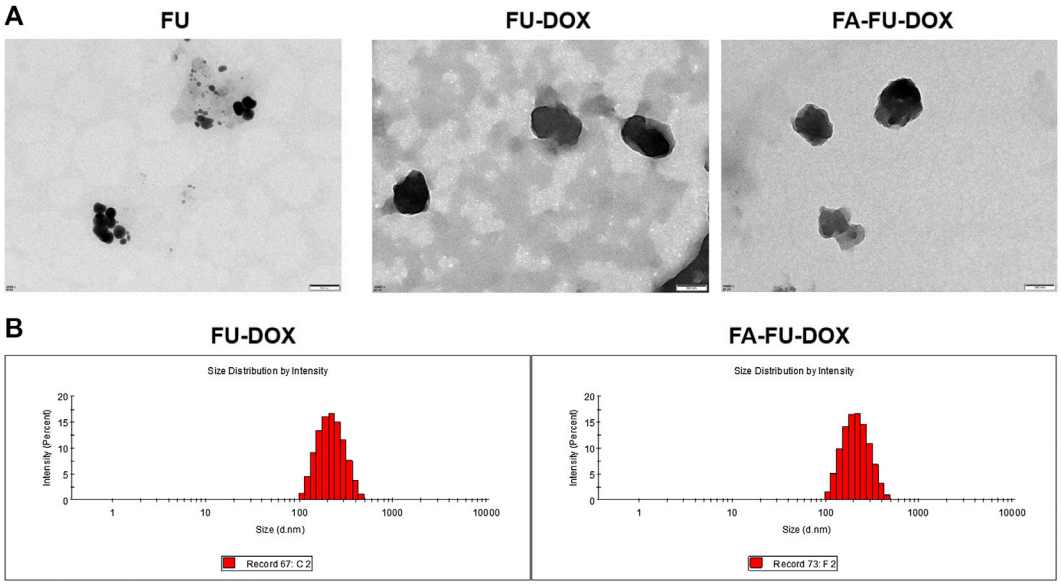

FIGURE 3 | The characterization of FU-DOX and FA-FU-DOX. **(A)** Transmission electron microscopy (TEM) images of FU, FU-DOX, and FA-FU-DOX. **(B)** Particle size distributions of FU-DOX and FA-FU-DOX.

Cellular Uptake Studies of DOX, FU-DOX, and FA-FU-DOX

Fluorescence Microscopic Imaging

The cellular uptake of DOX, FU-DOX, and FA-FU-DOX was examined by fluorescence microscopic imaging as reported previously (Qin et al., 2016). In detail, a piece of coverslip was put into each well of 6-well plates. Cells were seeded on the coverslips in 6-well plates at a cell density of 3×10^5 cells/well in 2 ml of culture medium. After 24 h of incubation, cells were treated with DOX, FU-DOX, or FA-FU-DOX at equivalent concentrations of 3 μM DOX. After 1, 2, and 4 h of incubation, the drug-containing medium was discarded. The cells were washed with PBS three times, fixed with 75% ice-cold ethanol for 30 min, and analyzed under a Fluorescence Microscope Axio Observer A1 (Zeiss, German).

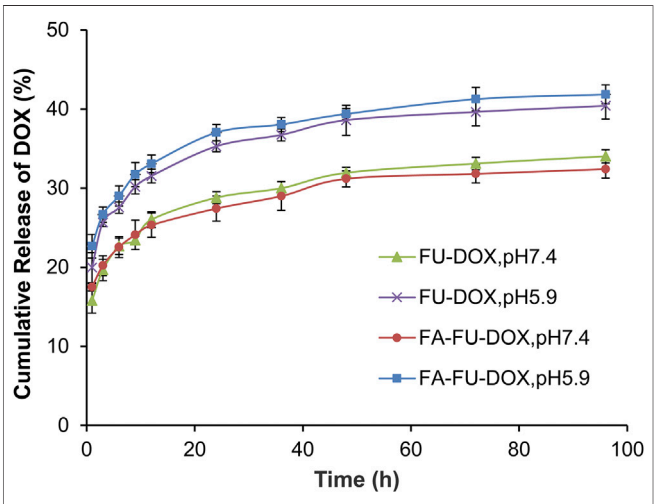

FIGURE 4 | The cumulative release kinetics of DOX from FU-DOX and FA-FU-DOX in PBS at a pH of 7.4 or 5.9 at 37°C.

Flow Cytometry Analysis

Cells were incubated in 6-well plates (3×10^5 cells/well) for 24 h and then treated with DOX, FU-DOX, or FA-FU-DOX at equivalent concentrations of 3 μM DOX for 1, 2, and 4 h. The treated cells were washed with PBS, harvested, measured by an FACS Calibur flow cytometer (BD, United States), and analyzed with the CytExpert software (Beckman Coulter, United States) (Wang et al., 2020b).

In Vitro Anticancer Activity Evaluation

The cell viability assay was performed as described previously (Wang et al., 2020a; Zhang et al., 2020). Briefly, cells were grown in 96-well plates (3×10^3 cells/well) for 24 h and incubated with DOX, FU-DOX, or FA-FU-DOX at equivalent concentrations for 72 h. Then, 10 μL of CCK-8 solution (Beyotime, CA) was added to each well. The cells were further incubated at 37°C for 2 h and examined by measuring absorption at 450 nm with an MK-3 microplate reader (Thermo Fisher Scientific, United States) (Li et al., 2013; Qin et al., 2013).

Statistical Analysis

All data were generated from three or more independent experiments and presented as means ± SD. The data were analyzed using Student's t-test by Prism software version 6 (Graph Pad Software Inc., United States) and the critical level of significance was set at $p < 0.05$.

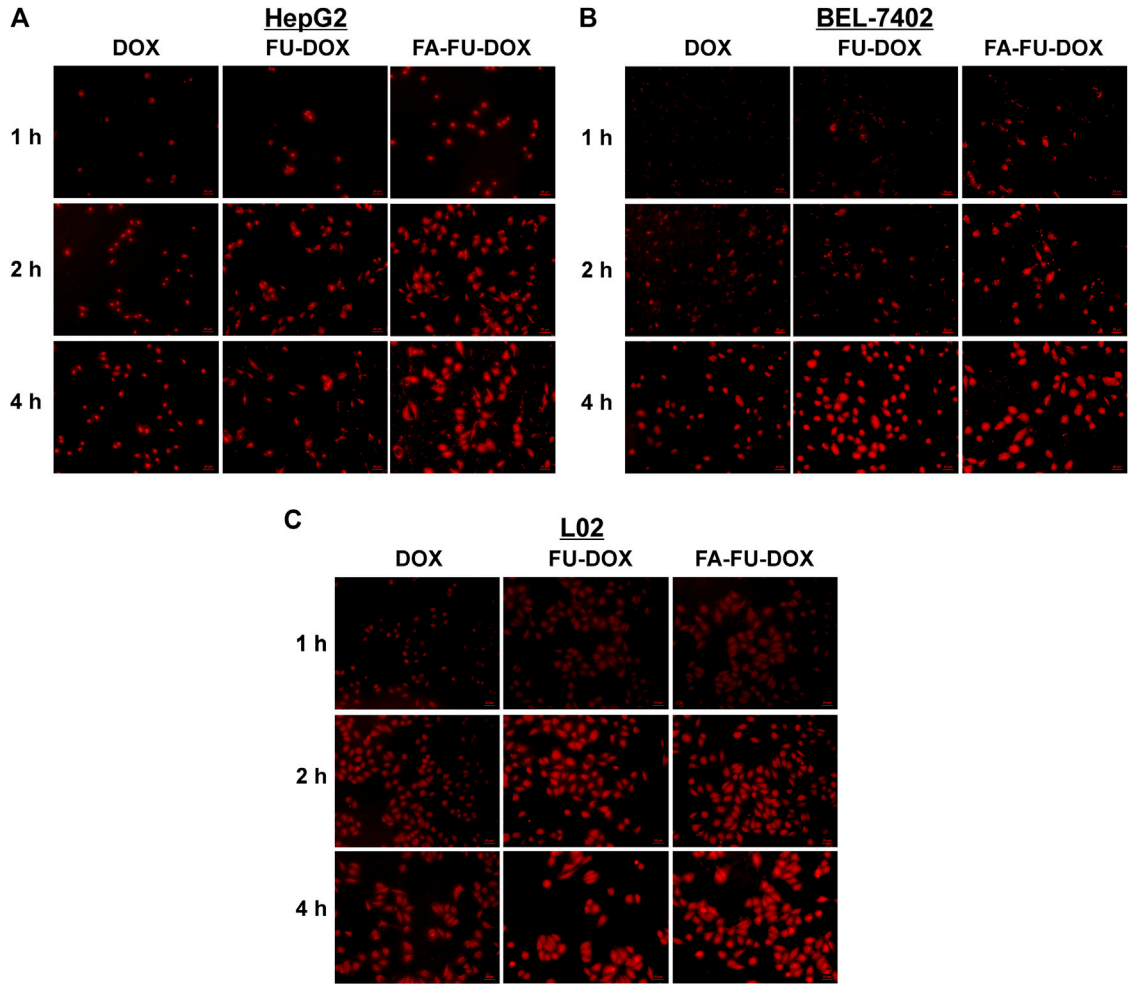

FIGURE 5 | Cellular uptake of FU-DOX and FA-FU-DOX. **(A)** HepG2, **(B)** BEL-7402, and **(C)** L02 cells were incubated with DOX, FU-DOX, or FA-FU-DOX for 1, 2, and 4 h, then the cellular uptake was monitored by a fluorescent microscopy (scale bar, 20 μm).

RESULTS

Preparation and Characterization of FA-FU-DOX

As shown in **Figure 1**, FA-FU-DOX was successfully synthesized and characterized using NMR spectroscopy. The NMR spectrum of FA-FU-DOX (**Figure 2**) showed signals at 8.64, 7.64, 6.94, 6.65, 4.48, and 4.33 ppm, representing H-carbon units of FA, and signals at 7.90, 5.47, 5.30, 4.94, 4.85, 4.57, 4.20, and 3.98 ppm, belonging to H-carbon units of DOX, which indicated that FA and DOX had been successfully linked to FU carrier. The formation of FA-FU-DOX was further validated by IR spectroscopy (**Supplementary Figure S1**). Except for the characteristic peaks belonging to DOX (1,615, 1,584, 1,283, 1,211, and 1,115 cm^{-1}), FA (1,512 and 1,407 cm^{-1}), and FU (1,380 and 1,081 cm^{-1}) in the IR spectrum of FA-FU-DOX, the absence of the carbonyl peak of DOX at 1730 cm^{-1} and the presence of the -C=N peak of the hydrazone bond at 1,638 cm^{-1} were observed, indicating the successful coupling of the carbonyl group of DOX with the amine group of FU-CONHNH2. The large endothermic peak at 67°C in the DSC spectrum of FA-FU-DOX also confirmed the formation of this conjugate (**Supplementary Figure S2**).

The TEM images of FU, FU-DOX, and FA-FU-DOX are shown in **Figure 3**. Compared to FU, FU-DOX and FA-FU-DOX were larger in diameters, indicating the coupling of DOX and/or FA with FU. DLS established that the mean diameters for FU-DOX and FA-FU-DOX conjugates were about 199 nm (PDI = 0.123) and 195 nm (PDI = 0.108), respectively. The diameters are suitable for efficient targeting in circulation.

Drug Release Study of FA-FU-DOX

The stabilities of FU-DOX and FA-FU-DOX were examined by evaluating the cumulative release of DOX at physiological (pH 7.4) and endolysosomal pH conditions (pH 5.9). As shown in **Figure 4**, after 96 h of incubation, the cumulative

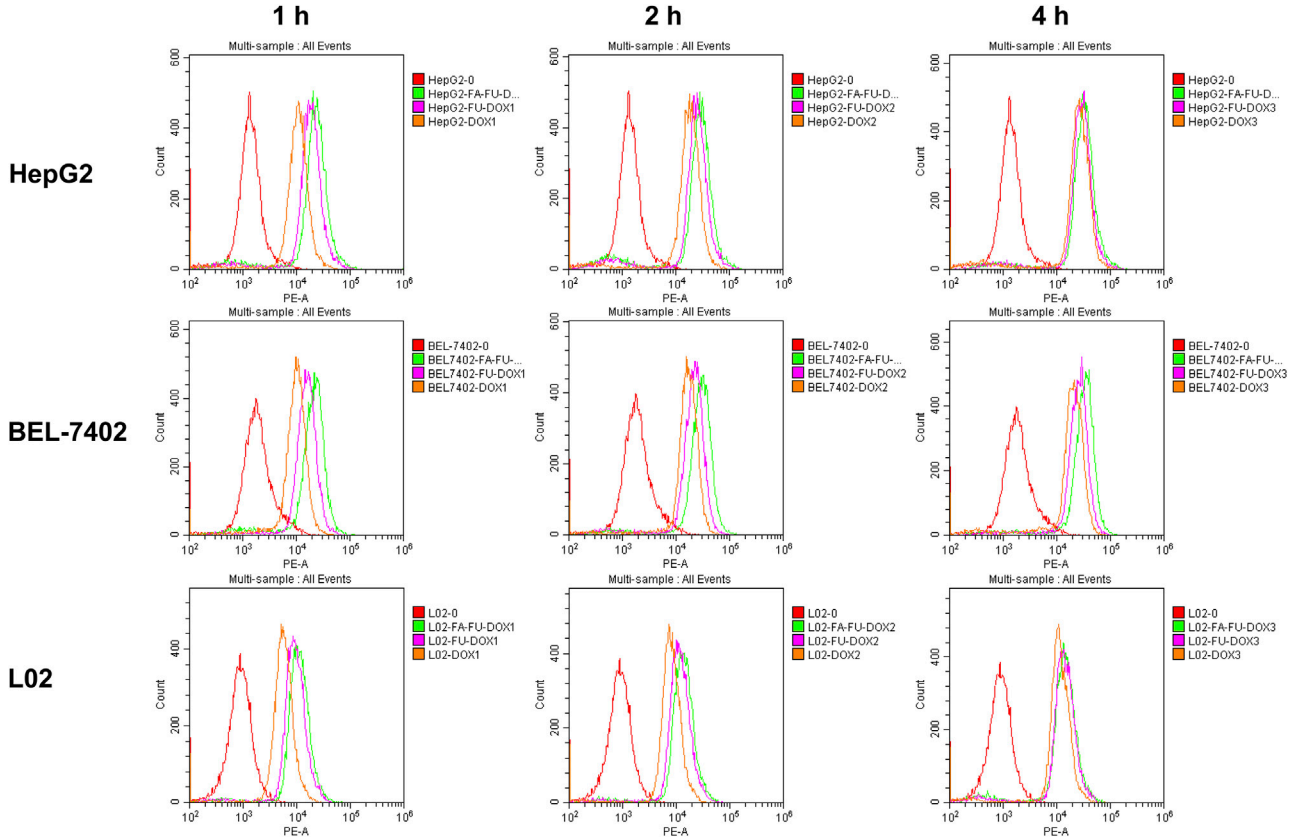

FIGURE 6 | Flow cytometry analyses of the intracellular accumulation of DOX, FU-DOX, and FA-FU-DOX in HepG2, BEL-7402, and L02 cells after 1-, 2-, or 4-h incubation.

release rates of DOX from FA-FU-DOX were found to be 32% (pH 7.4) and 42% (pH 5.9), respectively, while that from FU-DOX were 34% (pH 7.4) and 41% (pH 5.9), respectively. These results were consistent with the degradation characteristics of the hydrazone bond. The introduction of FA did not significantly alter the release kinetics. Both FU-DOX and FA-FU-DOX are expected to release DOX more rapidly in cancer cells after endocytosis than in circulation (Gao et al., 2017).

Cellular Uptake of FA-FU-DOX

The cellular uptake of DOX, FU-DOX, and FA-FU-DOX was investigated in the HCC cell lines BEL-7402 (FR-positive) (Dai et al., 2011) and HepG2 (FR-negative) (Gao et al., 2015) and the normal human hepatocytes L02 (FR-negative). As shown in **Figure 5**, the fluorescence microscopy images exhibited that DOX, FU-DOX, and FA-FU-DOX (shown as the red dots) were uptaken by all three cell lines in a time-dependent manner. The FU-DOX and FA-FU-DOX conjugates exhibited higher fluorescence intensity than free DOX, especially at 1 h incubation time, indicating a higher amount of cellular uptake than that for free DOX. It may be explained that the intracellular drug accumulation was efficiently promoted by the FU carrier at the experimental conditions (Grebinyk et al., 2019). Moreover, FA-FU-DOX showed the best cellular uptake in FR-positive BEL-7402 cells but it did not exhibit significant higher accumulation than FU-DOX in FR-negative HepG2 and L02 cells (**Figure 5**), which suggested that the attachment of FA to FU-DOX enhanced the uptake of the conjugates into FR-positive cells via an FR-mediated endocytic process. Similar results were also obtained by flow cytometry analyses, confirming the important roles of FA and FU in enhancing the cellular uptake of DOX (**Figure 6**).

In Vitro Anticancer Activity of FA-FU-DOX

We further compared the *in vitro* anticancer activities of DOX, FU-DOX, and FA-FU-DOX in HepG2, BEL-7402, and L02 cell lines. As shown in **Figure 7**, all cell lines were more sensitive to DOX than FU-DOX or FA-FU-DOX, which could be attributed to the slow release of DOX from FU-DOX and FA-FU-DOX after endocytosis. Importantly, DOX did not show any selective cytotoxicity against cancer cells but exhibited more potent inhibitory effects on the viability of normal human hepatocytes L02. However, FU-DOX and FA-FU-DOX showed significantly weaker cytotoxicities against L02 cells, especially at lower concentrations (32 and 64 nM), suggesting that the conjugations of FU and FA to DOX could improve the safety profile of DOX. Furthermore, FA-FU-DOX exhibited more potent cytotoxicity than FU-DOX in FR-positive BEL-7402

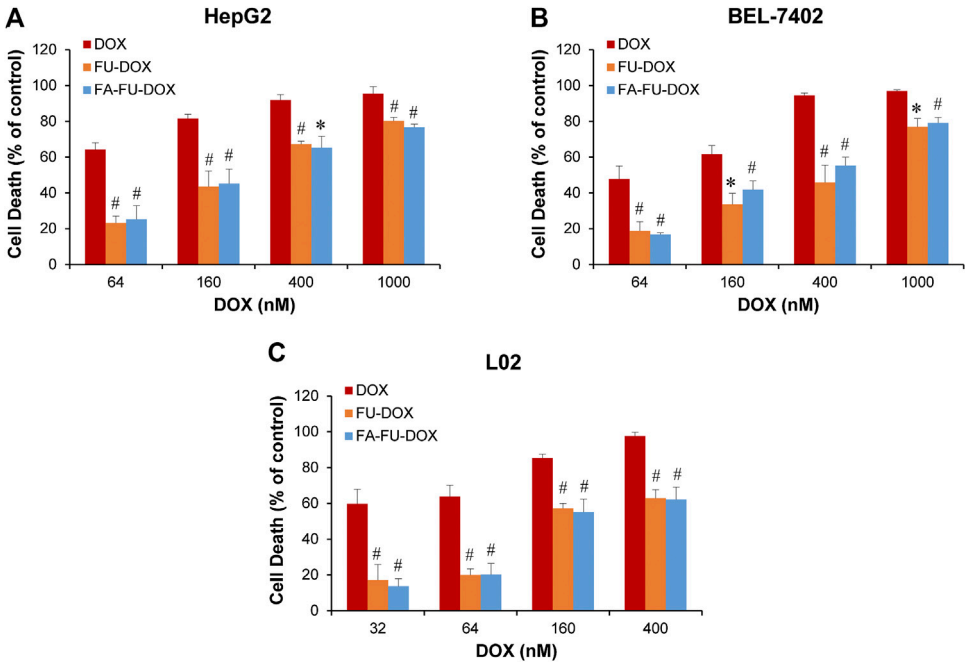

FIGURE 7 | *In vitro* cytotoxicity of DOX, FU-DOX, and FA-FU-DOX. **(A)** HepG2, **(B)** BEL-7402, and **(C)** L02 cells were exposed to various concentrations of DOX, FU-DOX, and FA-FU-DOX for 72 h for determination of cell death by CCK-8 assays. Data represent mean ± SD from three independent experiments (*$p < 0.05$ and $^{\#}p < 0.01$).

cells (at 160 and 400 nM), further supporting the inference of FA-mediated endocytosis and FU-mediated transportation.

CONCLUSION

In the present study, we designed, synthesized, and characterized the FA-FU-DOX conjugate as a new delivery system for the commonly used chemotherapeutic agent DOX. FA-FU-DOX has a diameter of around 190–200 nm, beneficial to the targeting of tumor tissues in the circulation. Our results have shown that the cumulative release rates of DOX from FU-DOX and FA-FU-DOX are similar at both physiological (pH 7.4) and endolysosomal pH conditions (pH 5.9), which is in line with the degradation features of the hydrazine group (Liu et al., 2014; Rezaian et al., 2018). We have also shown that FU-DOX and FA-FU-DOX have a higher release rate in an acidic environment, suggesting that DOX may release from these conjugates faster in the tumor microenvironment (acidic environment) (Seyfoori et al., 2019; Maleki et al., 2020).

Because FR is overexpressed in tumor tissues but restricted in normal tissues, it has been considered as a promising target for developing efficient TTDDSs. FA and methotrexate (MTX) through ethylenediamine have been attached to the surface of functionalized multi-walled carbon nanotubes by Karimi *et al.*, which improves the cancer cell-targeting ability of MTX and enhances its anticancer activity (Karimi et al., 2019). Moreover, the modification of nanomaterials with FA terminated-polyglycol as well as the subsequent loading with DOX improve the biocompatibility and selectivity against cancer cells, consequently improving its ability to eradicate tumors *in vivo* with negligible systemic toxicity (Wang et al., 2018). Besides, Yan *et al.* have used FA-modified multi-walled carbon nanotubes to deliver DOX to tumor sites, which not only enhanced the suppression of tumor growth but also decreased the side effects of DOX (Yan et al., 2018).

In this study, the cellular uptake and cytotoxicities of FU-DOX and FA-FU-DOX have been investigated in BEL-7402 (HCC, FR-positive), HepG2 (HCC, FR-negative), and L02 (normal, FR-negative) cells. It has been observed that the attachment of FA to FU-DOX increases the cellular uptake in FR-positive BEL-7402 cells in an FR-dependent manner. As expected, FA-FU-DOX has also exhibited more potent cytotoxicity than FU-DOX in BEL-7402 cells but not in FR-negative HepG2 and L02 cells. Besides, FU-DOX and FA-FU-DOX have shown relatively weak cytotoxicities against normal L02 cells. Taken together, the FA-FU-DOX conjugate has a better selectivity against cancer cells and a more promising safety profile.

In conclusion, our studies have demonstrated that the FA-FU-DOX conjugate has the potential to be developed as an effective approach for enhancing the efficacy and reducing the toxicity of chemotherapeutic drugs. Further investigations are warranted to examine the tumor-targeting efficacy and safety in clinically relevant animal models, especially liver cancer models.

DATA AVAILABILITY STATEMENT

The raw data supporting the conclusions of this article will be made available by the authors, without undue reservation.

AUTHOR CONTRIBUTIONS

BX, LY, YH, and ZX designed and conducted experiments, and wrote the manuscript. JJQ and XDC organized, conceived, and supervised the study. All authors read and approved the manuscript.

FUNDING

This work was supported by Traditional Chinese Medical Science and Technology Major Project of Zhejiang Province (2018ZY006), National Natural Science Foundation of China (81903842, 81573953), Program of Zhejiang Provincial TCM Sci-tech Plan (2020ZZ005, 2016ZZ012), Zhejiang Chinese Medical University Startup Funding (111100E014), Medical Science and Technology Project of Zhejiang Province (WKJ-ZJ-1728), Science and Technology Projects of Zhejiang Province (2019C03049), and Zhejiang Province Public Welfare Technology Application Research Project of China (LGF19H300007).

ACKNOWLEDGMENTS

We thank the specialists from the Public Platform of Medical Research Center, Academy of Chinese Medical Sciences, Zhejiang Chinese Medical University for their technical supports to this work.

SUPPLEMENTARY MATERIAL

The Supplementary Material for this article can be found online at: https://www.frontiersin.org/articles/10.3389/fphar.2020.598155/full#supplementary-material.

REFERENCES

Borović, M. L., Ičević, I., Kanački, Z., Žikić, D., Seke, M., Injac, R., et al. (2014). Effects of fullerenol C60(OH)24 nanoparticles on a single-dose doxorubicin-induced cardiotoxicity in pigs: an ultrastructural study. *Ultrastruct. Pathol.* 38 (2), 150–163. doi:10.3109/01913123.2013.822045

Boss, S. D., and Ametamey, S. M. (2020). Chaudhuri, S. D., and Ametamey, S. M. (2020). Development of folate receptor–targeted PET radiopharmaceuticals for tumor imaging-A bench-tobedside journey. *Cancers* 12 (6), 1508. doi:10.3390/cancers12061508

Chaudhuri, P., Paraskar, A., Soni, S., Mashelkar, R. A., and Sengupta, S. (2009). Fullerenol–cytotoxic conjugates for cancer chemotherapy. *ACS Nano.* 3 (9), 2505–2514. doi:10.1021/nn900318y

Dai, J., Zou, S., Pei, Y., Cheng, D., Ai, H., and Shuai, X. (2011). Polyethyleniminegrafted copolymer of poly(l-lysine) and poly(ethylene glycol) for gene delivery. *Biomaterials* 32 (6), 1694–1705. doi:10.1016/j.biomaterials.2010.10.044

Elshater, A.-E. A., Haridy, M. A. M., Salman, M. M. A., Fayyad, A. S., and Hammad, S. (2018). Fullerene C60 nanoparticles ameliorated cyclophosphamide-induced acute hepatotoxicity in rats. *Biomed. Pharmacother.* 97**,** 53–59. doi:10.1016/j.biopha.2017.10.134

Fernández, M., Javaid, F., and Chudasama, V. (2018). Advances in targeting the folate receptor in the treatment/imaging of cancers. *Chem. Sci.* 9 (4)**,** 790–810. doi:10.1039/c7sc04004k

Gao, W., Ye, G., Duan, X., Yang, X., and Yang, V. C. (2017). Transferrin receptor-targeted pH-sensitive micellar system for diminution of drug resistance and targetable delivery in multidrug-resistant breast cancer. *Ijn* Vol. 12**,** 1047–1064. doi:10.2147/IJN.S115215

Gao, Y., Li, Z., Xie, X., Wang, C., You, J., Mo, F., et al. (2015). Dendrimeric anticancer prodrugs for targeted delivery of ursolic acid to folate receptor-expressing cancer cells: synthesis and biological evaluation. *Eur. J. Pharmaceut. Sci.* 70**,** 55–63. doi:10.1016/j.ejps.2015.01.007

Gonçalves, M., Mignani, S., Rodrigues, J., and Tomás, H. (2020). A glance over doxorubicin based-nanotherapeutics: From proof-of-concept studies to solutions in the market. *J. Contr.ournal of Controlled Release* 317**,** 347–374. doi:10.1016/j.jconrel.2019.11.016

Grebinyk, A., Prylutska, S., Chepurna, O., Grebinyk, S., Prylutskyy, Y., Ritter, U., et al. (2019). Synergy of chemo- and photodynamic therapies with C60 fullerene-doxorubicin nanocomplex. *Nanomaterials* 9 (11), 1540. doi:10.3390/nano9111540

Hao, T., Li, J., Yao, F., Dong, D., Wang, Y., Yang, B., et al. (2017). Injectable fullerenol/alginate hydrogel for suppression of oxidative stress damage in brown adipose-derived stem cells and cardiac repair. *ACS Nano.* 11 (6), 5474–5488. doi:10.1021/acsnano.7b00221

Kalyanaraman, B. (2020). Teaching the basics of the mechanism of doxorubicin-induced cardiotoxicity: Have we been barking up the wrong tree? *Redox Biology* 29, 101394. doi:10.1016/j.redox.2019.101394

Karimi, A., Erfan, M., Mortazavi, S. A., Ghorbani-Bidkorbeh, F., Kobarfard, F., and Shirazi, F. H. (2019). Functionalisation of carbon nanotubes by methotrexate and study of synchronous photothermal effect of carbon nanotube and anticancer drug on cancer cell death. *IET Nanobiotechnol.* 13 (1)**,** 52–57. doi:10.1049/iet-nbt.2018.5085

Kazemzadeh, H., and Mozafari, M. (2019). Fullerene-based delivery systems. *Drug Discov. Today* 24 (3)**,** 898–905. doi:10.1016/j.drudis.2019.01.013

Kepinska, M., Kizek, R., and Milnerowicz, H. (2018a). Fullerene as a doxorubicin nanotransporter for targeted breast cancer therapy: capillary electrophoresis analysis. *Electrophoresis* 39 (18)**,** 2370–2379. doi:10.1002/elps.201800148

Kepinska, M., Kizek, R., and Milnerowicz, H. (2018b). Metallothionein and superoxide dismutase-antioxidative protein status in fllerene-doxorubicin delivery to MCF-7 human breast cancer cells. *Ijms* 19 (10), 3253. doi:10.3390/ijms19103253

Kumar, M., and Raza, K. (2018). C60-fullerenes as drug delivery carriers for anticancer agents: promises and hurdles. *Pnt* 5 (3)**,** 169–179. doi:10.2174/2211738505666170301142232

Li, X., Yang, X., Liu, Y., Gong, N., Yao, W., Chen, P., et al. (2013). Japonicone A suppresses growth of Burkitt lymphoma cells through its effect on NF- B. *Clin. Canc. Res.* 19 (11)**,** 2917–2928. doi:10.1158/1078-0432.ccr-12-3258

Maleki, R., Khoshoei, A., Ghasemy, E., and Rashidi, A. (2020). Molecular insight into the smart functionalized TMC-Fullerene nanocarrier in the pH-responsive adsorption and release of anti-cancer drugs. *J. Mol. Graph. Model.* 100**,** 107660. doi:10.1016/j.jmgm.2020.107660

Martinez, Z. S., Castro, E., Seong, C.-S., Cerón, M. R., Echegoyen, L., and Llano, M. (2016). Fullerene derivatives strongly inhibit HIV-1 replication by affecting virus maturation without impairing protease activity. *Antimicrob. Agents Chemother.* 60 (10)**,** 5731–5741. doi:10.1128/aac.00341-16

Ohulchanskyy, A., Prylutska, S., Grebinyk, S., Prylutskyy, Y., Ritter, U., Matyshevska, O., et al. (2019). Complexation with C60 fullerene increases doxorubicin efficiency against leukemic cells in vitro. *Nanoscale Res. Lett.* 14 (1)**,** 61. doi:10.1186/s11671-019-2894-1

Ouyang, C., Zhang, S., Xue, C., Yu, X., Xu, H., Wang, Z., et al. (2020). Precision-guided missile-like DNA nanostructure containing warhead and guidance control for aptamer-based targeted drug delivery into cancer cells *in vitro* and *in vivo*. *J. Am. Chem. Soc.* 142 (3)**,** 1265–1277. doi:10.1021/jacs.9b09782

Petrovic, D., Seke, M., Borovic, M. L., Jovic, D., Borisev, l., Srdjenovic, B., et al. (2018). Hepatoprotective effect of fullerenol/doxorubicin nanocomposite in

acute treatment of healthy rats. *Exp. Mol. Pathol.* 104 (3), 199–211. doi:10.1016/jyexmp.2018.04.005

Qin, J.-J., Jin, H.-Z., Huang, Y., Zhang, S.-D., Shan, L., Voruganti, S., et al. (2013). Selective cytotoxicity, inhibition of cell cycle progression, and induction of apoptosis in human breast cancer cells by sesquiterpenoids from Inula linearifolia Turcz. *Eur. J. Med. Chem.* 68, 473–481. doi:10.1016/j.ejmech.2013.07.018

Qin, J.-J., Wang, W., Sarkar, S., and Zhang, R. (2016). Oral delivery of anti-MDM2 inhibitor SP141-loaded FcRn-targeted nanoparticles to treat breast cancer and metastasis. *J. Contr. Release 237*, 101–114. doi:10.1016/j.jconrel.2016.07.008

Qin, L., Yu, M., Zhang, Y., Wang, C., and Lu, H. (2014). Hydrazide functionalized core-shell magnetic nanocomposites for highly specific enrichment of N-glycopeptides. *ACS Appl. Mater. Interfaces* 6 (10), 7823–7832. doi:10.1021/am501110e

Raj, S., Khurana, S., Choudhari, R., Kesari, K. K., Kamal, M. A., Garg, N., et al. (2019). Specific targeting cancer cells with nanoparticles and drug delivery in cancer therapy. *Semin. Canc. Biol.* doi:10.1016/j.semcancer.2019.11.002

Ruokolainen, M., Maleki, R., Dahri Dahroud, M., Alamdari, A., and Alimohammadi, M. (2018). pH-sensitive co-adsorption/release of doxorubicin and paclitaxel by carbon nanotube, fullerene, and graphene oxide in combination with N-isopropylacrylamide: a molecular dynamics study. *Biomolecules* 8 (4), 127. doi:10.3390/biom8040127

Seke, M., Petrovic, D., Djordjevic, A., Jovic, D., Borovic, M. L., Kanacki, Z., et al. (2016). Fullerenol/doxorubicin nanocomposite mitigates acute oxidative stress and modulates apoptosis in myocardial tissue. *Nanotechnology* 27 (48), 485101. doi:10.1088/0957-4484/27/48/485101

Seyfoori, A., Sarfarazijami, S., and Seyyed Ebrahimi, S. A. (2019). pH-responsive carbon nanotube-based hybrid nanogels as the smart anticancer drug carrier. *Artif. Cells, Nanomed. Biotechnol.* 47 (1), 1437–1443. doi:10.1080/21691401.2019.1596939

Su, M., Xie, J., Zeng, Q., Shu, M., Liu, J., and Jiang, Z. (2020). Enzymatic synthesis of PEGylated lactide-diester-diol copolyesters for highly efficient targeted anticancer drug delivery. *Mater. Sci. Eng. C* 115, 111125. doi:10.1016/j.msec.2020.111125

Tan, Y. Y., Yap, P. K., Xin Lim, G. L., Mehta, M., Chan, Y., Ng, S. W., et al. (2020). Perspectives and advancements in the design of nanomaterials for targeted cancer theranostics. *Chem. Biol. Interact.* 329, 109221. doi:10.1016/j.cbi.2020.109221

Tie, Y., Zheng, H., He, Z., Yang, J., Shao, B., Liu, L., et al. (2020). Targeting folate receptor β positive tumor-associated macrophages in lung cancer with a folate-modified liposomal complex. *Sig. Transduct. Target Ther.* 5 (1), 6. doi:10.1038/s41392-020-0115-0

Voruganti, S., Qin, J.-J., Sarkar, S., Nag, S., Walbi, I. A., Wang, S., et al. (2015). Oral nanodelivery of anticancer ginsenoside 25-OCH3-PPD, a natural inhibitor of the MDM2 oncogene: nanoparticle preparation, characterization,in vitroandin vivoanti-prostate cancer activity, and mechanisms of action. *Oncotarget* 6 (25), 21379–21394. doi:10.18632/oncotarget.4091

Wang, D., Meng, L., Fei, Z., Hou, C., Long, J., Zeng, L., et al. (2018). Multi-layered tumor-targeting photothermal-doxorubicin releasing nanotubes eradicate tumors in vivo with negligible systemic toxicity. *Nanoscale* 10 (18), 8536–8546. doi:10.1039/c8nr00663f

Wang, V., Djordjevic, A., Srdjenovic, B., Milic-Tores, V., Segrt, Z., Dragojevic-Simic, V., et al. (2017). Fullerenol nanoparticles prevents doxorubicin-induced acute hepatotoxicity in rats. *Exp. Mol. Pathol.* 102 (2), 360–369. doi:10.1016/j.yexmp.2017.03.005

Wang, W., Cheng, J.-W, Qin, J.-J., Hu, B., Li, X., Nijampatnam, B., et al. (2019). MDM2-NFAT1 dual inhibitor, MA242: effective against hepatocellular carcinoma, independent of p53. *Canc. Lett.* 459, 156–167. doi:10.1016/jcanlet.2019.114429

Wang, W., Yang, J., Liao, Y.-Y., Cheng, G., Chen, J., Cheng, X.-D., et al. (2020a). Cytotoxic nitrogenated azaphilones from the deep-sea-derived fungus chaetomium globosum MP4-S01-7. *J. Nat. Prod.* 83 (4), 1157–1166. doi:10.1021/acs.jnatprod.9b01165

Wang, W., Yang, J., Liao, Y.-Y., Cheng, G., Chen, J., Mo, S., et al. (2020b). Aspeterreurone A, a cytotoxic dihydrobenzofuran-phenyl acrylate hybrid from the deep-sea-derived fungus aspergillus terreus CC-S06-18. *J. Nat. Prod.* 83 (6), 1998–2003. doi:10.1021/acs.jnatprod.0c00189

Xiao, H., Guo, Y., Liu, H., Liu, Y., Wang, Y., Li, C., et al. (2020). Structure-based design of charge-conversional drug self-delivery systems for better targeted cancer therapy. *Biomaterials* 232, 119701. doi:10.1016/j.biomaterials.2019.119701

Xu, J., Wang, H., Hu, Y., Zhang, Y. S, Wen, L., Yin, F., et al. (2019). Inhibition of CaMKIIα activity enhances antitumor effect of fullerene C60 nanocrystals by suppression of autophagic degradation. *Adv. Sci.* 6 (8), 1801233. doi:10.1002/advs.201801233

Xu, Y., Zhu, J., Xiang, K., Li, Y., Sun, R., Ma, J., et al. (2011). Synthesis and immunomodulatory activity of [60]fullerene-tuftsin conjugates. *Biomaterials* 32 (36), 9940–9949. doi:10.1016/j.biomaterials.2011.09.022

Yan, Y., Wang, R., Hu, Y., Sun, R., Song, T., Shi, X., et al. (2018). Stacking of doxorubicin on folic acid-targeted multiwalled carbon nanotubes for in vivo chemotherapy of tumors. *Drug Deliv.* 25 (1), 1607–1616. doi:10.1080/10717544.2018.1501120

Zhang, J., Wang, W., Zhou, Y., Yang, J., Xu, J., Xu, Z., et al. (2020). Terphenyllin suppresses orthotopic pancreatic tumor growth and prevents metastasis in mice. *Front. Pharmacol.* 11, 457. doi:10.3389/fphar.2020.00457

Conflict of Interest: The authors declare that the research was conducted in the absence of any commercial or financial relationships that could be construed as a potential conflict of interest.

frontiers in Pharmacology

MINI REVIEW
published: 03 February 2021
doi: 10.3389/fphar.2021.630167

Coherent Raman Scattering Microscopy in Oncology Pharmacokinetic Research

Junjie Zeng[1], *Wenying Zhao*[1] *and Shuhua Yue*[1,2]*

[1]*Institute of Medical Photonics, Beijing Advanced Innovation Center for Biomedical Engineering, School of Biological Science and Medical Engineering, Beihang University, Beijing, China,* [2]*Wuhan National Laboratory for Optoelectronics, Huazhong University of Science and Technology, Wuhan, China*

The high attrition rates of anti-cancer drugs during clinical development remains a bottleneck problem in pharmaceutical industry. This is partially due to the lack of quantitative, selective, and rapid readouts of anti-cancer drug activity *in situ* with high resolution. Although fluorescence microscopy has been commonly used in oncology pharmacological research, fluorescent labels are often too large in size for small drug molecules, and thus may disturb the function or metabolism of these molecules. Such challenge can be overcome by coherent Raman scattering microscopy, which is capable of chemically selective, highly sensitive, high spatial resolution, and high-speed imaging, without the need of any labeling. Coherent Raman scattering microscopy has tremendously improved the understanding of pharmaceutical materials in the solid state, pharmacokinetics of anti-cancer drugs and nanocarriers *in vitro* and *in vivo*. This review focuses on the latest applications of coherent Raman scattering microscopy as a new emerging platform to facilitate oncology pharmacokinetic research.

Keywords: coherent Raman scattering microscopy, label-free, Raman tag, pharmacology, anti-cancer drug, drug metabolism, drug dissolution, drug distribution

OPEN ACCESS

Edited by:
Xueli Chen,
Xidian University, China

Reviewed by:
Yinxin Zhang,
Tianjin University, China
Wei Min,
Columbia University, United States

***Correspondence:**
Shuhua Yue
yue_shuhua@buaa.edu.cn

Specialty section:
This article was submitted to Pharmacology of Anti-Cancer Drugs, a section of the journal Frontiers in Pharmacology

Received: *16 November 2020*
Accepted: *04 January 2021*
Published: *03 February 2021*

Citation:
Zeng J, Zhao W and Yue S (2021) Coherent Raman Scattering Microscopy in Oncology Pharmacokinetic Research. Front. Pharmacol. 12:630167. doi: 10.3389/fphar.2021.630167

INTRODUCTION

Although tremendous efforts have been made to promote anti-cancer drug development (Falzone et al., 2018) (Nass et al., 2018), the high attrition rates of anti-cancer drugs during clinical development remains a bottleneck problem in pharmaceutical industry (Liu et al., 2017). Over the past decade, only 5% of clinically tested anti-cancer drugs have successfully obtained FDA approval (Hay et al., 2014). Considering that anti-cancer drug development is an expensive, time-consuming, and high-risk endeavor, it is necessary to develop novel strategies to identify promising drug candidates and remove ill-fated compounds earlier in the development pipeline.

Imaging has been widely used in anti-cancer drug assessment (Mouras et al., 2010). Due to cell heterogeneity in complex tumor microenvironment, it has become increasingly important to achieve quantitative, selective, and rapid imaging of anti-cancer drug activity *in situ* with high resolution (Vinegoni et al., 2015). Fluorescence microscopy has helped direct visualization of fluorescently labeled molecules, including proteins, antibodies and small molecules such as drugs or their metabolites. Intravital fluorescence microscopy was developed to study anti-cancer drug action *in vivo* at the single-cell level (Thurber et al., 2013), which has been extensively reviewed by Weissleder (Miller and Weissleder 2017).

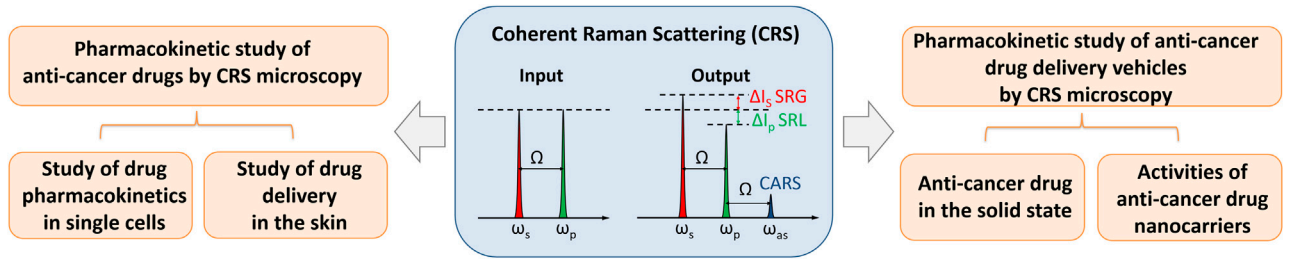

FIGURE 1 | Schematic showing coherent Raman scattering (CRS) microscopy and its application in oncology pharmacokinetics. When tuning the beating frequency (ω_p-ω_s) to match molecular vibration frequency Ω, multiple Raman transitions were excited simultaneously, including stimulated Raman gain (SRG), stimulated Raman loss (SRL), and coherent anti-Stokes Raman scattering (CARS). ω_p, ω_s, and ω_{as} denote the frequencies of the pump, Stokes, and anti-Stokes beam, respectively. CRS microscopy has shown great potential in the investigation of anti-cancer drug pharmacokinetics, anti-cancer drug stability and dissolution in the solid state, and activities of anti-cancer drug nanocarriers in single cells.

Although fluorescence microscopy has been commonly used in oncology pharmacological research, fluorescent labels are often large in size relative to small drug molecules, and thus may perturb the activity of these drug molecules. Thus, label-free optical microscopy that generates signals based on intrinsic molecular contrast would be desirable to study uptake, distribution, and metabolism of small drug molecules.

The efficacy of anti-cancer drugs also largely relies on drug delivery vehicles (e.g., tablets and nanocarriers) (Shi et al., 2017), which are formulated to enhance drug bioavailability, biocompatibility, and targeting to cancer tissues. Thorough understanding of the drug stability and activity within the final dosage form is required to optimize the dosing strategy and reduce toxic effects prior to regulatory approval. Encapsulation of fluorescent dyes has been commonly used to monitor nanocarriers, but this is limited by occasional loss and photobleaching of the dyes. Thus, it would be of great importance to develop label-free optical microscopy that can assess stability and dissolution of drugs in the solid state, and uptake, distribution, interaction, and excretion of anti-cancer drug nanocarriers in a biological environment.

Based on intrinsic contrasts from molecular vibrations, infrared absorption and Raman scattering offer attractive means for label-free chemical-selective imaging. Compared to infrared absorption, Raman scattering based imaging would have higher spatial resolution by use of visible/near-infrared light excitation. Moreover, different from infrared absorption, Raman scattering does not have background from water, which makes it much more suitable to study live biological systems. Despite that spontaneous Raman microscopy has been used in oncology pharmacokinetic research (Gala and Chauhan 2015), small cross section of Raman scattering makes it difficult to acquire strong enough signals for fast chemical imaging, which significantly hinders its application in dynamic readouts of anti-cancer drug activity *in situ*.

In order to enhance the Raman scattering signal, coherent Raman scattering (CRS) microscopy has been developed (Cheng and Xie 2012). When tuning the beating frequency to match a molecular vibration frequency, the CRS signal can be markedly boosted and so enables high-speed imaging, which is 10^4–10^6 times faster than spontaneous Raman microscopy (Cheng and Xie 2015) (**Figure 1**). Raman tags with distinct Raman peaks in cellular "silent region" have been shown to enhance molecular selectivity of CRS microscopy without perturbing biological activities (Wei et al., 2016). Owing to these unique advantages, CRS microscopy offer a powerful platform to study anti-cancer drug stability and activity within the final dosage form.

Here, we review the recent technical advances and applications of CRS microscopy in the study of anti-cancer drug pharmacokinetics at the single cell level, drug stability and dissolution in the solid state, and activities of anti-cancer drug nanocarriers in single cells (**Figure 1**). We then conclude with the discussion on the potential of CRS microscopy to promote oncology pharmacokinetic research.

CRS MICROSCOPY

In CRS microscopy, two ultra-short pulse excitation beams are used, denoted as pump (ω_p) and Stokes (ω_s) respectively. When the beating frequency ($\omega_p - \omega_s$) is in resonant with a molecular vibration frequency (Ω), the Raman scattering signal can be dramatically increased in coherent anti-Stokes Raman scattering (CARS) and stimulated Raman scattering (SRS) processes (Cheng and Xie 2012). The advantages of SRS over CARS lie in the fact that the SRS signal is completely free of non-resonant background, which makes SRS microscopy a highly sensitive method for biochemical imaging (Freudiger et al., 2008). In an effort to gain spectral information, hyperspectral CRS microscopy has been developed based on frame-by-frame wavelength scanning, which may take seconds to minutes to obtain an entire stack of images for reconstruction and leads to some spectral distortions. To avoid such distortion, multiplex CRS microscopy, where a CRS spectrum is instantaneously recorded at each pixel (microseconds per pixel), has been developed. These instrumental advancements and accompanied improvements in chemical map decomposing algorithms have been extensively reviewed in (Zhang et al., 2014; Cheng and Xie 2015; Fu 2017). Owing to the fast, label-free, and chemical-selective imaging capability, CRS microscopy has been widely used in biomedical research, as reviewed in (Min et al., 2011; Pezacki et al., 2011; Streets et al., 2014; Camp and

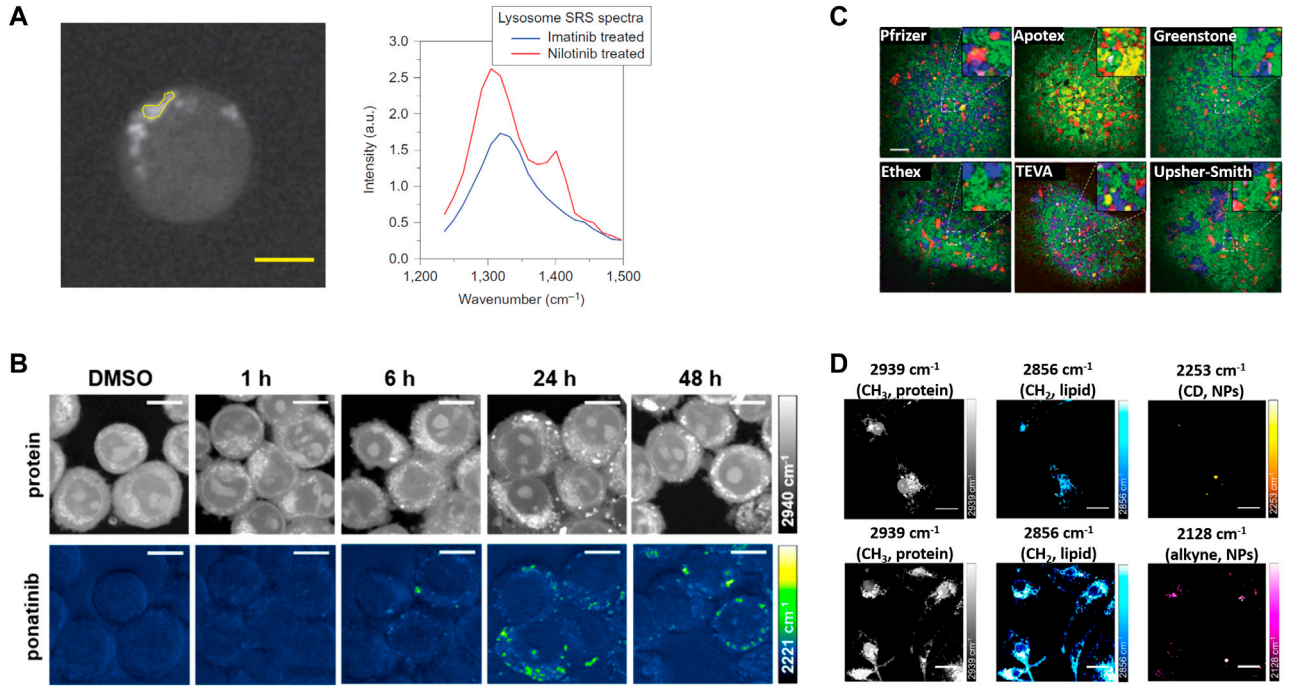

FIGURE 2 | The representative applications of coherent Raman scattering (CRS) microscopy in oncology pharmacokinetics. **(A)** Representative SRS images at 1305 cm^{-1} of BaF3/BCR-ABL1 cells treated with 20 mM nilotinib for 4 h. SRS spectra of selected ROI in the left image (yellow polygon). Reprinted with permission from Ref. (Fu et al., 2014). Copyright 2014 Nature Publishing Group. **(B)** SRS imaging of ponatinib uptake in $KCL22^{Pon-Res}$ cells. $KCL22^{Pon-Res}$ cells were treated with DMSO (0.0003%, v/v) or ponatinib (500 nM) for 1, 6, 24, or 48 h. SRS images acquired at 2940 cm^{-1} (CH_3, proteins), 2221 cm^{-1} (C≡C, ponatinib), Scale bars: 10 μm. Reprinted with permission from Ref. (Sepp et al., 2020). Copyright 2019 American Chemical Society. **(C)** Large area SRS imaging of tablets. Green, blue, red, yellow/orange, and magenta colors represent microcrystalline cellulose, dibasic calcium phosphate anhydrous, Amlodipine besylate (API), sodium starch glycolate, and magnesium stearate, respectively. In case of tablet from Apotex the yellow color corresponds to lactose monohydrate and corn starch. Inserts are four times magnified areas of the images indicated by dashed squares. Scale bar: 200 μm. Reprinted with permission from Ref. (Slipchenko et al., 2010). Copyright 2021 Royal Society of Chemistry **(D)** SRS imaging of nanoparticles (NPs) in microglia. Microglia were incubated with PLGA-CD NPs or PLGA-alkyne NPs. Scale bars: 20 μm. Reprinted with permission from Ref. (Vanden-Hehir et al., 2019a). Copyright © 2019 American Chemical Society.

Cicerone 2015; Schie et al., 2015; Winterhalder and Zumbusch 2015; Zhang et al., 2015; Yue and Cheng 2016; Zhang and Cheng 2018; Hill and Fu 2019; Hu et al., 2019).

The molecular selectivity and detection sensitivity of CRS microscopy can be further enhanced by small-sized Raman tags (e.g., deuterium, alkyne, and diyne), which show strong Raman peaks well separated from endogenous cellular signals without perturbing biological activities of small molecules. Based on this method, cellular uptake, distribution, and metabolism of small molecules can be monitored with high temporospatial resolution and high detection sensitivity (micromolar level) *in vitro* and *in vivo*, as reviewed in (Wei et al., 2016; Hu et al., 2019).

PHARMACOKINETIC STUDY OF ANTI-CANCER DRUGS BY CRS MICROSCOPY

Raman spectroscopy and microscopy can be used to investigate pharmacokinetics in living cells with high resolution and in a label-free manner. El-Mashtoly and co-workers have made tremendous efforts to push the study of pharmacokinetics via label-free molecular fingerprint (El-Mashtoly et al., 2014; El-Mashtoly et al., 2015; Aljakouch et al., 2018; Yosef et al., 2018; El-Mashtoly 2020). More recently, CRS microscopy has been increasingly employed for high-speed imaging of the uptake, distribution, and metabolism of anti-cancer drugs in single live cells *in vitro* and *in vivo* (Tipping et al., 2016). As discussed below, these studies show great impact on mechanistic understanding of the anti-cancer drug activity and may significantly accelerate the preclinical medicinal chemistry optimization pipelines.

Study of Drug Pharmacokinetics in Single Cells by CRS Microscopy

In 2014, Xie group, for the first time, demonstrated that hyperspectral SRS microscopy enabled label-free visualization and quantification of tyrosine-kinase inhibitors (imatinib and nilotinib) (**Figure 2A**), which are the front-line therapies for chronic myelogenous leukemia, inside living cells (Fu et al., 2014). Both tyrosine-kinase inhibitors were shown to enrich over 1,000-fold in lysosomes, probably due to low solubility. Moreover, this work unraveled a new mechanism by which chloroquine could increase the efficacy of tyrosine-kinase inhibitors, that is, lysosome-mediated drug-drug interaction.

Recently, Raman tagging strategies have been shown to enhance early stage drug discovery programmes. In 2014, Min group, for the first time, imaged the delivery pathways of alkyne-bearing terbinafine hydrochloride, a US Food and Drug Administration-approved antifungal drug, inside mouse ear skin tissue (Wei et al., 2014). Subsequently, Min group and collaborators used a Raman tag to determine the subcellular localization and mechanism of action of ferrostatins in suppressing ferroptosis, a form of nonapoptotic cell death (Gaschler et al., 2018). Min and coworkers further employed a Raman tag to study the intracellular enrichment and distribution of the anti-cancer antimycin-type depsipeptides in single live cells (Seidel et al., 2019). Hulme group demonstrated the feasibility of SRS microscopy to evaluate subcellular distribution of Phenyl-based Raman tag labeled anisomycin, and cellular response to the drug simultaneously (Tipping et al., 2017). Huang group reported hyperspectral SRS imaging of Diyne-based Raman tag labeled Triphenylphosphonium, a commonly used mitochondria-targeting agent, to track the dynamics of mitochondria in live cells (Bae et al., 2020). More recently, Hulme group took advantages of alkyne-based SRS imaging to assess label-free uptake and distribution of ponatinib, another tyrosine kinase inhibitor approved for chronic myeloid leukemia treatment, in cellular models of ponatinib resistance (Sepp et al., 2020) (**Figure 2B**). This study achieved at biologically relevant, nanomolar concentrations, allowing determination of changes in uptake and sequestration of ponatinib during the development of acquired drug resistance. Taken together, these works highlight the great potential of bioorthogonal chemical imaging (CRS microscopy of Raman tags) in anti-cancer drug pharmacokinetics research.

Study of Drug Delivery in the Skin by CRS Microscopy

The effective treatment of diseases of the skin remains an important unmet medical need, primarily because of poor drug delivery. To address this challenge, SRS microscopy has been used to visualize and characterize the diffusion of topically applied drugs into mammalian skins in real time. Ten years ago, Xie group developed video-rate SRS microscopy to study the penetration pathways of topically applied drugs in mice and humans non-invasively without any labeling (Saar et al., 2010). Their later study further revealed different rates of drug penetration via hair follicles as compared to the intercellular pathway across the stratum corneum (Saar et al., 2011). The high-speed three-dimensional imaging capability allowed SRS microscopy to provide mechanistic insight into the (trans) dermal drug delivery process. Similarly, Guy group studied diffusion of deuterated water, propylene glycol, and dimethyl sulfoxide in the human nail by SRS imaging of the O-D, -CD_2, and -CH_2 bond, respectively (Chiu et al., 2015). Taking advantage of alkyne-bearing drug, Min group imaged the delivery pathways of terbinafine hydrochloride, an antifungal skin drug, inside mouse ear tissue to a depth of about 100 μm (Wei et al., 2014). More recently, Evans group made use of deep learning-based computational methods to analyze SRS images, which help to quantify the flow and flux of small molecule drugs through the layers and structures of nude mouse ear skin (Feizpour et al., 2020; Pena et al., 2020). Although current *in vivo* pharmacokinetic studies by CRS microscopy are not directly related to anti-cancer treatment, the strategies demonstrated in these studies may open a new avenue for skin cancer pharmacokinetics *in vivo*.

Taken together, CRS microscopy provides unprecedented capabilities in dynamic visualization of drug activity in single cells and offer new insight into drug discovery and development.

PHARMACOKINETIC STUDY OF ANTI-CANCER DRUG DELIVERY VEHICLES BY CRS MICROSCOPY

Modern regulations demand thorough knowledge of drug stability and activity within the final dosage form (Yu et al., 2014). Thus, it is essential to assess drug delivery vehicles (e.g., tablets and nanocarrier) that are made to ensure the prolonged stability and bioavailability of the drug. The non-destructive and label-free features of Raman and infrared imaging make them desirable analytical tools to assess drug delivery vehicles, as reviewed in (Gowen et al., 2008; Gordon and McGoverin 2011). Owing to the advantage of high-speed imaging compared to spontaneous Raman microscopy, CRS microscopy has been increasingly used for pharmacokinetic study of anti-cancer drug delivery vehicles, in order to meet the quality by design demands in the modern pharmaceutical industry.

Anti-Cancer Drug Stability and Dissolution in the Solid State

Pharmaceutical tablets are composed of biologically active pharmaceutical ingredients (API) and inert excipients that ensure the pharmacological properties of the API. The therapeutic performance and stability of the final dosage form are affected by the spatial distribution and phase of API and excipients. Due to heterogeneous nature of solid drug formulations, it is essential to characterize the distribution and dissolution of drug formulations noninvasively at high temporospatial resolution. Below we will review the applications of CRS microscopy in assessment of API crystallization and polymorphism, chemical mapping of final dosage forms, and *in-situ* chemical imaging during dissolution.

Polymorphism refers to the ability of a molecule to crystallize into multiple crystal structures. In the development of an API, it is critical to identify polymorphic forms to ensure API stability, dissolution kinetics, and bioavailability. Cicerone group, for the first time, used broadband CARS microscopy with much higher speed and spatial resolution compared to spontaneous Raman imaging, allowing identification of three crystalline polymorphs and an unanticipated API phase within a tablet (Hartshorn et al., 2013). Slepkov group implemented spectral-focusing-CARS microscopy, with broadband hyperspectroscopy and rapid single vibrational frequency imaging, to discriminate

ibuprofen, common polymorphs of acetaminophen, and starchy binders on tablet samples (Porquez and Slepkov 2018).

Chemical mapping of final dosage forms is essential to validate a uniform distribution of ingredients within the tablet for reliable product performance. In 2010, Cheng group, for the first time, demonstrated SRS microscopy could map API (amlodipine besylate, a widely used drug for lowering the blood pressure) and a variety of excipients, including microcrystalline cellulose, dibasic calcium phosphate anhydrous, sodium starch glycolate, and magnesium stearate, with high chemical selectivity and high temporospatial resolution (Slipchenko et al., 2010) (**Figure 2C**). More recently, Rigneault group showed that few SRS images at selected wavenumbers could retrieve molecular maps of both API (clopidogrel and amibegron) polymorphs and excipients (polyethylene glycol, corn starch, and mannitol) over millimeter-size areas within compact tablets (Sarri et al., 2019).

Dissolution testing, which monitors API dissolution kinetics under conditions mimicking those *in vivo*, is an indispensable step in drug product development and quality control. As early as 2006, Cheng group and Park group demonstrated CARS microscopy could be used to examine distribution of anti-cancer drug paclitaxel based on its specific Raman peaks in polyethylene glycol (PEG) and poly (lactic-co-glycolic acid) (PLGA) films with high spatial resolution (Kang et al., 2006). This study further monitored the dynamic release of paclitaxel from a polymer matrix during dissolution *in situ*. Strachan group used CARS microscopy to monitor the dissolution of the model drug theophylline in lipid-based oral dosage forms, and found the drug tended to form the less soluble monohydrate during dissolution (Windbergs 2009). Their later study used hyperspectral CARS to monitor the solid-state change in oral dosage forms containing theophylline anhydrate during dissolution and found that theophylline anhydrate converted to theophylline monohydrate resulting in a reduction in the dissolution rate (Fussell et al., 2013).

More recently, SRS microscopy has been utilized for *in situ* chemical imaging of drug release and interaction with formulations. Fu group made use of SRS microscopy for chemical mapping of entecavir, a hepatitis B antiviral drug, embedded in a slow release poly (D,L-lactic acid) formulation. High spatial resolution of SRS microscopy allowed quantitative profiling of dissolution of single crystalline particles in implant formulations *in situ* (Francis et al., 2018). Their later work demonstrated chemical imaging of salt disproportionation reaction of pioglitazone hydrochloride (PIO-HCl) at a very low drug loading (1% w/w) by SRS microscopy (Figueroa et al., 2019). Huang group utilized Raman-tagged hyperspectral SRS microscopy to study dynamic interplay between antibiotics and biofilm, which is crucial for understanding of antibiotics resistance (Bae et al., 2019).

Furthermore, CRS microscopy can be integrated with other nonlinear optical (NLO) microscopy modalities, such as two- and three-photon fluorescence, second- and third-harmonic generation, on the same platform. Such multimodal NLO microscopy combined advantages of each phenomenon for imaging complex pharmaceutical systems. More details can be found in (Strachan et al., 2011; Novakovic et al., 2017; Schmitt 2017; Ojarinta et al., 2018).

Activities of Anti-Cancer Drug Nanocarriers in Single Cells

Nanocarriers are designed to enhance drug bioavailability, biocompatibility, and targeting to cancer tissues, which may lead to more effective and safer cancer treatment. The field of cancer nanomedicine has gained considerable technological success (Doane and Burda 2012; Wicki et al., 2015; Shi et al., 2017; Begines et al., 2020), but is currently facing several obstacles for clinical translation, especially little knowledge about nano-bio interactions (Shi et al., 2017). Raman microscopy has been utilized for noninvasive imaging of pharmaceutical nanocarriers (Chernenko et al., 2012; Chernenko et al., 2013; Vanden-Hehir et al., 2019b), and high chemical selectivity and high temporospatial resolution make CRS microscopy a more attractive way to study activities of anti-cancer drug nanocarriers in single cells and cellular response to the drugs.

As early as 2009, Yeo and Cheng groups used label-free CARS microscopy to reexamine cellular uptake of poly (lactic-co-glycolic acid) (PLGA) nanoparticles (NPs), and discussed the utility and limitations of PLGA NP as an intracellular drug delivery system (Xu et al., 2009). Garrett et al. presented CARS as a novel tool for label-free imaging of polymeric NPs in biological cells and tissues (Garrett et al., 2012a). Van den Mooter group showed the potential of CARS to investigate drug nano-/microcrystal–cell interactions in cell cultures and *ex vivo* in histological sections without labeling (Darville et al., 2015). Tolstik et al. used CARS for precise detection of the uptake of biodegradable non-toxic silicon NPs by cancer cells (Tolstik et al., 2016).

Recently, Wang group, for the first time, used hyperspectral SRS to investigate the subcellular distribution of NPs in the protozoan *Tetrahymena* thermophila, and found the two frequently studied nanoparticles, polyacrylate-coated alpha-Fe_2O_3 and TiO_2, had significant uptake competition and different subcellular distribution pattern (Huang et al., 2018). Hulme group synthesized alkyne-tagged PLGA to show direct visualization of nanoparticles *in vitro* within primary rat microglia and *ex vivo* cortical mouse brain tissue by SRS microscopy (Vanden-Hehir et al., 2019a) (**Figure 2D**).

Furthermore, multimodal NLO microscopy, which integrates CRS microscopy, two-photon fluorescence microscopy, and second harmonic generation, has shown great potential in investigation of cellular uptake and tissue distribution of drug nanocarriers. Garrett et al. utilized such label-free multimodal NLO microscopy to pinpoint polymeric NPs within the stomach, intestine, gall bladder and liver (Garrett et al., 2012b). Johnston et al. used CRS-based multimodal NLO microscopy to evaluate nanomaterial-cell interactions by visualizing the uptake of gold or titanium dioxide nanomaterials in live and fixed cell lines and biodistribution of nanomaterials in lung and liver tissues in rats (Johnston et al., 2015).

Taken together, in order to optimize the dosing and reduce unwanted toxic effects, it is advantageous of CRS microscopy in

label-free and non-invasive imaging drug nanocarrier activity at the single-cell level, which offers a deeper understanding of how nanocarriers interact with cells and tissues, as also reviewed in (Goodhead et al., 2015; Vanden-Hehir et al., 2019b).

CONCLUDING REMARKS

Given the time and overall costs required to bring novel therapeutics to patients, new technologies capable of providing earlier feedback and deeper understanding during the initial phases of drug development and validation are of great importance and urgent need. Owing to the capability of label-free, chemically selective, high temporospatial resolution, and highly sensitive imaging, CRS microscopy has remarkably improved the understanding of anti-cancer drug pharmacokinetics *in vitro* and *in vivo*. Advances in Raman tag design are expected to significantly enhance the detection sensitivity and selectivity, which may offer new opportunities for investigation of anti-cancer drugs that do not have distinctive Raman peaks. Advances in instrumental development, such as novel hyperspectral and multiplex CRS microscopy, are expected to promote high-speed simultaneous imaging of multiple drug molecules and drug vehicles. Furthermore, integration of multimodal NLO microscopy techniques is expected to shed new light on the understanding of how drug molecules and drug vehicles interact with cells within the complex tumor tissue environment.

AUTHOR CONTRIBUTIONS

JZ and WZ contributed to the systematic review of literatures and wrote the initial draft of the section about tablets. JZ also revised the manuscript according to reviewers' comments. SY wrote the manuscript, critically analyzed and revised the manuscript according to reviewers' comments.

FUNDING

This work is supported by National Natural Science Foundation of China (No. 91959120, No. 62027824 to SY), Beijing Natural Science Foundation (No. L172011 to SY), Open Project Program of Wuhan National Laboratory for Optoelectronics (No. 2018WNLOKF026 to SY), Fundamental Research Funds for the Central Universities (No. YWF-20-BJ-J-550 to SY), and "Excellent Hundred Talents" Program start-up fund from Beihang University (to SY).

REFERENCES

Aljakouch, K., Lechtonen, T., Yosef, H. K., Hammoud, M. K., Alsaidi, W., Kötting, C., et al. (2018). Raman microspectroscopic evidence for the metabolism of a tyrosine kinase inhibitor, neratinib, in cancer cells. *Angew. Chem. Int. Ed.* 57 (24), 7250–7254. doi:10.1002/anie.201803394

Bae, K., Zheng, W., Ma, Y., and Huang, Z. W. (2019). Real-time monitoring of pharmacokinetics of antibiotics in biofilms with Raman-tagged hyperspectral stimulated Raman scattering microscopy. *Theranostics* 9 (5), 1348–1357. doi:10.7150/thno.32043

Bae, K., Zheng, W., Ma, Y., and Huang, Z. W. (2020). Real-time monitoring of pharmacokinetics of mitochondria-targeting molecules in live cells with bioorthogonal hyperspectral stimulated Raman scattering microscopy. *Anal. Chem.* 92 (1), 740–748. doi:10.1021/acs.analchem.9b02838

Begines, B., Ortiz, T., Pérez-Aranda, M., Martínez, G., Merinero, M., Argüelles-Arias, F., et al. (2020). Polymeric nanoparticles for drug delivery: recent developments and future prospects. *Nanomaterials* 10 (7), 1403. doi:10.3390/nano10071403

Camp, C. H., and Cicerone, M. T. (2015). Chemically sensitive bioimaging with coherent Raman scattering. *Nat. Photon.* 9 (5), 295–305. doi:10.1038/nphoton.2015.60

Cheng, J. X., and Xie, X. S. (2015). Vibrational spectroscopic imaging of living systems: an emerging platform for biology and medicine. *Science* 350 (6264), 84. doi:10.1126/science.aaa8870

Chernenko, T., Buyukozturk, F., Miljkovic, M., Carrier, R., Diem, M., and Amiji, M. (2013). Label-free Raman microspectral analysis for comparison of cellular uptake and distribution between nontargeted and EGFR-targeted biodegradable polymeric nanoparticles. *Drug Deliv. Transl. Res.* 3 (6), 575–586. doi:10.1007/s13346-013-0178-3

Chernenko, T., Sawant, R. R., Miljkovic, M., Quintero, L., Diem, M., and Torchilin, V. (2012). Raman microscopy for noninvasive imaging of pharmaceutical nanocarriers: intracellular distribution of cationic liposomes of different composition. *Mol. Pharm.* 9 (4), 930–936. doi:10.1021/mp200519y

Chiu, W. S., Belsey, N. A., Garrett, N. L., Moger, J., Delgado-Charro, M. B., and Guy, R. H. (2015). Molecular diffusion in the human nail measured by stimulated Raman scattering microscopy. *Proc. Natl. Acad. Sci. U. S. A.* 112 (25), 7725–7730. doi:10.1073/pnas.1503791112

Darville, N., Saarinen, J., Isomäki, A., Khriachtchev, L., Cleeren, D., Patrick, S., et al. (2015). Multimodal non-linear optical imaging for the investigation of drug nano-/microcrystal–cell interactions. *Eur. J. Pharm. Biopharm.* 96, 338–348. doi:10.1016/j.ejpb.2015.09.003

Doane, T. L., and Burda, C. (2012). The unique role of nanoparticles in nanomedicine: imaging, drug delivery and therapy. *Chem. Soc. Rev.* 41 (7), 2885–2911. doi:10.1039/c2cs15260f

El-Mashtoly, S. F. (2020). Drug distribution in living cells via label-free molecular fingerprint. *J. Med. Chem.* 63 (7), 3472–3474. doi:10.1021/acs.jmedchem.0c00392

El-Mashtoly, S. F., Petersen, D., Yosef, H. K., Mosig, A., Reinacher-Schick, A., Kotting, C., et al. (2014). Label-free imaging of drug distribution and metabolism in colon cancer cells by Raman microscopy. *Analyst* 139 (5), 1155–1161. doi:10.1039/c3an01993d

El-Mashtoly, S. F., Yosef, H. K., Petersen, D., Mavarani, L., Maghnouj, A., Hahn, S., et al. (2015). Label-free Raman spectroscopic imaging monitors the integral physiologically relevant drug responses in cancer cells. *Anal. Chem.* 87 (14), 7297–7304. doi:10.1021/acs.analchem.5b01431

Falzone, L., Salomone, S., and Libra, M. (2018). Evolution of cancer pharmacological treatments at the turn of the third millennium. *Front. Pharmacol.* 9, 1300. doi:10.3389/fphar.2018.01300

Feizpour, A., Marstrand, T., Bastholm, L., Eirefelt, S., and Conor, L. E. (2020). Label-free quantification of pharmacokinetics in skin with stimulated Raman scattering microscopy and deep learning. *J. Invest. Dermatol.* S0022, 31884. doi:10.1016/j.jid.2020.06.027

Figueroa, B., Nguyen, T., Sotthivirat, S., Xu, W., Rhodes, T., Lamm, M. S., et al. (2019). Detecting and quantifying microscale chemical reactions in pharmaceutical tablets by stimulated Raman scattering microscopy. *Anal. Chem.* 91 (10), 6894–6901. doi:10.1021/acs.analchem.9b01269

Francis, A. T., Nguyen, T. T., Lamm, M. S., Teller, R., Forster, S. P., Xu, W., et al. (2018). *In Situ* stimulated Raman scattering (SRS) microscopy study of the dissolution of sustained-release implant formulation. *Mol. Pharm.* 15 (12), 5793–5801. doi:10.1021/acs.molpharmaceut.8b00965

Freudiger, C. W., Min, W., Saar, B. G., Lu, S., Holtom, G. R., He, C. W., et al. (2008). Label-free biomedical imaging with high sensitivity by stimulated Raman scattering microscopy. *Science* 322 (5909), 1857–1861. doi:10.1126/science.1165758

Fu, D. (2017). Quantitative chemical imaging with stimulated Raman scattering microscopy. *Curr. Opin. Chem. Biol.* 39, 24–31. doi:10.1016/j.cbpa.2017.05.002

Fu, D., Zhou, J., Zhu, W. S., Manley, P. W., Wang, Y. K., Hood, T., et al. (2014). Imaging the intracellular distribution of tyrosine kinase inhibitors in living cells with quantitative hyperspectral stimulated Raman scattering. *Nat. Chem.* 6 (7), 614–622. doi:10.1038/nchem.1961

Fussell, A., Garbacik, E., Herman, O., Peter, K., and Strachan, C. (2013). *In situ* dissolution analysis using coherent anti-Stokes Raman scattering (CARS) and hyperspectral CARS microscopy. *Eur. J. Pharm. Biopharm.* 85 (3), 1141–1147. doi:10.1016/j.ejpb.2013.08.012

Gala, U., and Chauhan, H. (2015). Principles and applications of Raman spectroscopy in pharmaceutical drug discovery and development. *Expet Opin. Drug Discov.* 10 (2), 187–206. doi:10.1517/17460441.2015.981522

Garrett, N. L., Lalatsa, A., Uchegbu, I., Schaetzlein, A., and Moger, J. (2012b). Exploring uptake mechanisms of oral nanomedicines using multimodal nonlinear optical microscopy. *J. Biophot.* 5 (5–6), 458–468. doi:10.1002/jbio.201200006

Garrett, N. L., Lalatsa, A., Begley, D., Mihoreanu, L., Uchegbu, I. F., Schoetzlein, A. G., et al. (2012a). Label-free imaging of polymeric nanomedicines using coherent anti-Stokes Raman scattering microscopy. *J. Raman Spectrosc.* 43 (5), 681–688. doi:10.1002/jrs.3170

Gaschler, M. M., Hu, F. H., Feng, H. Z., Linkermann, A., Min, W., and Stockwell, B. R. (2018). Determination of the subcellular localization and mechanism of action of ferrostatins in suppressing ferroptosis. *ACS Chem. Biol.* 13 (4), 1013–1020. doi:10.1021/acschembio.8b00199

Goodhead, R. M., Moger, J., Galloway, T. S., and Tyler, C. R. (2015). Tracing engineered nanomaterials in biological tissues using coherent anti-Stokes Raman scattering (CARS) microscopy—a critical review. *Nanotoxicology* 9 (7), 928–939. doi:10.3109/17435390.2014.991773

Gordon, K. C., and McGoverin, C. M. (2011). Raman mapping of pharmaceuticals. *Int. J. Pharm.* 417 (1–2), 151–162. doi:10.1016/j.ijpharm.2010.12.030

Gowen, A. A., O'Donnell, C. P., Cullen, P. J., and Bell, S. E. (2008). Recent applications of Chemical Imaging to pharmaceutical process monitoring and quality control. *Eur. J. Pharm. Biopharm.* 69 (1), 10–22. doi:10.1016/j.ejpb.2007.10.013

Hartshorn, C. M., Lee, Y. J., Camp, C. H., Jr., Liu, Z., Heddleston, J., Canfield, N., et al. (2013). Multicomponent chemical imaging of pharmaceutical solid dosage forms with broadband CARS microscopy. *Anal. Chem.* 85 (17), 8102–8111. doi:10.1021/ac400671p

Hay, M., Thomas, D. W., Craighead, J. L., Economides, C., and Rosenthal, J. (2014). Clinical development success rates for investigational drugs. *Nat. Biotechnol.* 32 (1), 2786. doi:10.1038/nbt.2786

Hill, A. H., and Fu, D. (2019). Cellular imaging using stimulated Raman scattering microscopy. *Anal. Chem.* 91 (15), 9333–9342. doi:10.1021/acs.analchem.9b02095

Hu, F. H., Shi, L. X., and Min, W. (2019). Biological imaging of chemical bonds by stimulated Raman scattering microscopy. *Nat. Methods* 16 (9), 830–842. doi:10.1038/s41592-019-0538-0

Huang, B., Yan, S., Xiao, L., Ji, R., Yang, L. Y., Miao, A. J., et al. (2018). Label-free imaging of nanoparticle uptake competition in single cells by hyperspectral stimulated Raman scattering. *Small* 14 (10), 10. doi:10.1002/smll.201703246

J.-X. Cheng and X. S. Xie (Editors) (2012). *Coherent Raman microscopy* (New York: Taylor & Francis Group).

Johnston, H. J., Mouras, R., Brown, D. M., Elfick, A., and Stone, V. (2015). Exploring the cellular and tissue uptake of nanomaterials in a range of biological samples using multimodal nonlinear optical microscopy. *Nanotechnology* 26 (50), 11. doi:10.1088/0957-4484/26/50/505102

Kang, E., Wang, H., Kwon, I. K., Robinson, J., Park, K., and Cheng, J.-X. (2006). *In Situ* visualization of paclitaxel distribution and release by coherent anti-Stokes Raman scattering microscopy. *Anal. Chem.* 78 (23), 8036–8043. doi:10.1021/ac061218s

Liu, Z., Delavan, B., Roberts, R., and Tong, W. (2017). Lessons learned from two decades of anticancer drugs. *Trends Pharmacol. Sci.* 38 (10), 852–872. doi:10.1016/j.tips.2017.06.005

Miller, M. A., and Weissleder, R. (2017). Imaging of anticancer drug action in single cells. *Nat. Rev. Canc.* 17 (7), 399–414. doi:10.1038/nrc.2017.41

Min, W., Freudiger, C. W., Lu, S., and Xie, X. S. (2011). Coherent nonlinear optical imaging: beyond fluorescence microscopy. *Annu. Rev. Phys. Chem.* 62, 507–530. doi:10.1146/annurev.physchem.012809.103512

Mouras, R., Rischitor, G., Downes, A., Salter, D., and Elfick, A. (2010). Nonlinear optical microscopy for drug delivery monitoring and cancer tissue imaging. *J. Raman Spectrosc.* 41 (8), 848–852. doi:10.1002/jrs.2622

Nass, S. J., Pentz, R., Hricak, H., Abernethy, A., Anderson, K., Wagner Gee, A., et al. (2018). Accelerating anticancer drug development — opportunities and trade-offs. *Nat. Rev. Clin. Oncol.* 15 (12), 777–786. doi:10.1038/s41571-018-0102-3

Novakovic, D., Saarinen, J., Rojalin, T., Antikainen, O., Fraser-Miller, S. J., Laaksonen, T., et al. (2017). Multimodal nonlinear optical imaging for sensitive detection of multiple pharmaceutical solid-state forms and surface transformations. *Anal. Chem.* 89 (21), 11460–11467. doi:10.1021/acs.analchem.7b02639

Ojarinta, R., Saarinen, J., Strachan, C. J., Korhonen, O., and Laitinen, R. (2018). Preparation and characterization of multi-component tablets containing co-amorphous salts: combining multimodal non-linear optical imaging with established analytical methods. *Eur. J. Pharm. Biopharm.* 132, 112–126. doi:10.1016/j.ejpb.2018.09.013

Pena, A.-M., Chen, X., Pence, I. J., Bornschlogl, T., Jeong, S., Gregoire, S., et al. (2020). Imaging and quantifying drug delivery in skin - Part 2: fluorescence and vibrational spectroscopic imaging methods. *Adv. Drug Deliv. Rev.* 153, 147–168. doi:10.1016/j.addr.2020.03.003

Pezacki, J. P., Blake, J. A., Danielson, D. C., Kennedy, D. C., Lyn, R. K., and Singaravelu, R. (2011). Chemical contrast for imaging living systems: molecular vibrations drive CARS microscopy. *Nat. Chem. Biol.* 7 (3), 137–145. doi:10.1038/nchembio.525

Porquez, J. G., and Slepkov, A. D. (2018). Application of spectral-focusing-CARS microscopy to pharmaceutical sample analysis. *AIP Adv.* 8 (9), 7. doi:10.1063/1.5027273

Saar, B. G., Contreras-Rojas, L. R., Xie, X. S., and Guy, R. H. (2011). Imaging drug delivery to skin with stimulated Raman scattering microscopy. *Mol. Pharm.* 8 (3), 969–975. doi:10.1021/mp200122w

Saar, B. G., Freudiger, C. W., Reichman, J., Stanley, C. M., Holtom, G. R., and Xie, X. S. (2010). Video-rate molecular imaging *in vivo* with stimulated Raman scattering. *Science* 330 (6009), 1368–1370. doi:10.1126/science.1197236

Sarri, B., Canonge, R., Audier, X., Lavastre, V., Penarier, G., Alie, J., et al. (2019). Discriminating polymorph distributions in pharmaceutical tablets using stimulated Raman scattering microscopy. *J. Raman Spectrosc.* 50 (12), 1896–1904. doi:10.1002/jrs.5743

Schie, I. W., Krafft, C., and Popp, J. (2015). Applications of coherent Raman scattering microscopies to clinical and biological studies. *Analyst* 140 (12), 3897–3909. doi:10.1039/c5an00178a

Schmitt, P. D. (2017). Recent advances in nonlinear optical analyses of pharmaceutical materials in the solid state. *Mol. Pharm.* 14 (3), 555–565. doi:10.1021/acs.molpharmaceut.6b00809

Seidel, E. R., Miao, Y. P., Porterfield, L., Cai, W. L., Zhu, X. J., Kim, S. O. O., et al. (2019). Structure-activity-distribution relationship study of anti-cancer antimycin-type depsipeptides. *Chem. Commun.* 55 (63), 9379–9382. doi:10.1039/c9cc03051d

Sepp, K., Lee, M., Marie, T., Bluntzer, J., Vignir Helgason, G., Hulme, A. N., et al. (2020). Utilizing stimulated Raman scattering microscopy to study intracellular distribution of label-free ponatinib in live cells. *J. Med. Chem.* 63, 2028–2034. doi:10.1021/acs.jmedchem.9b01546

Shi, J., Kantoff, P. W., Wooster, R., and Farokhzad, O. C. (2017). Cancer nanomedicine: progress, challenges and opportunities. *Nat. Rev. Canc.* 17 (1), 20–37. doi:10.1038/nrc.2016.108

Slipchenko, M. N., Chen, H., Ely, D. R., Jung, Y., Teresa Carvajal, M., and Cheng, J.-X. (2010). Vibrational imaging of tablets by epi-detected stimulated Raman scattering microscopy. *Analyst* 135 (10), 2613. doi:10.1039/c0an00252f

Strachan, C. J., Windbergs, M., and Offerhaus, H. L. (2011). Pharmaceutical applications of non-linear imaging. *Int. J. Pharm.* 417 (1–2), 163–172. doi:10.1016/j.ijpharm.2010.12.017

Streets, A. M., Li, A., Chen, T., and Huang, Y. (2014). Imaging without fluorescence: nonlinear optical microscopy for quantitative cellular imaging. *Anal. Chem.* 86 (17), 8506–8513. doi:10.1021/ac5013706

Thurber, G. M., Yang, K. S., Reiner, T., Kohler, R. H., Peter, S., Tim, M., et al. (2013). Single-cell and subcellular pharmacokinetic imaging allows insight into drug action *in vivo*. *Nat. Commun.* 4 (1). doi:10.1038/ncomms2506

Tipping, W. J., Lee, M., Serrels, A., Brunton, V. G., and Hulme, A. N. (2017). Imaging drug uptake by bioorthogonal stimulated Raman

scattering microscopy. *Chem. Sci.* 8 (8), 5606–5615. doi:10.1039/c7sc01837a

Tipping, W. J., Lee, M., Serrels, A., Brunton, V. G., and Hulme, A. N. (2016). Stimulated Raman scattering microscopy: an emerging tool for drug discovery. *Chem. Soc. Rev.* 45 (8), 2075–2089. doi:10.1039/c5cs00693g

Tolstik, E., Osminkina, L. A., Akimov, D., Gongalsky, M. B., Kudryavtsev, A. A., Timoshenko, V. Y., et al. (2016). Linear and non-linear optical imaging of cancer cells with silicon nanoparticles. *Int. J. Mol. Sci.* 17 (9), 1536. doi:10.3390/ijms17091536

Vanden-Hehir, S., Cairns, S. A., Lee, M., Zoupi, L., Shaver, M. P., Brunton, V. G., et al. (2019a). Alkyne-tagged PLGA allows direct visualization of nanoparticles in vitro and ex vivo by stimulated Raman scattering microscopy. *Biomacromolecules* 20 (10), 4008–4014. doi:10.1021/acs.biomac.9b01092

Vanden-Hehir, S., Tipping, W. J., Lee, M., Brunton, V. G., Williams, A., and Hulme, A. N. (2019b). Raman imaging of nanocarriers for drug delivery. *Nanomaterials*. 9 (3), 341. doi:10.3390/nano9030341

Vinegoni, C., Dubach, J. M., Thurber, G. M., Miller, M. A., Mazitschek, R., and Weissleder, R. (2015). Advances in measuring single-cell pharmacology *in vivo*. *Drug Discov. Today* 20 (9), 1087–1092. doi:10.1016/j.drudis.2015.05.011

Wei, L., Hu, F. H., Chen, Z. X., Shen, Y. H., Zhang, L. Y., and Min, W. (2016). Live-cell bioorthogonal chemical imaging: stimulated Raman scattering microscopy of vibrational probes. *Acc. Chem. Res.* 49 (8), 1494–1502. doi:10.1021/acs.accounts.6b00210

Wei, L., Hu, F. H., Shen, Y. H., Chen, Z. X., Yu, Y., Lin, C. C., et al. (2014). Live-cell imaging of alkyne-tagged small biomolecules by stimulated Raman scattering. *Nat. Methods* 11 (4), 410–412. doi:10.1038/nmeth.2878

Wicki, A., Witzigmann, D., Balasubramanian, V., and Huwyler, J. (2015). Nanomedicine in cancer therapy: challenges, opportunities, and clinical applications. *J. Contr. Release* 200, 138–157. doi:10.1016/j.jconrel.2014.12.030

Windbergs, M., Martin, J., Offerhaus, H. L., Herek, J. L., Peter, K., and Strachan, C. J. (2009). Chemical imaging of oral solid dosage forms and changes upon dissolution using coherent anti-Stokes Raman scattering microscopy. *Anal. Chem.* 81, 2085–2091. doi:10.1021/ac8020856

Winterhalder, M. J., and Zumbusch, A. (2015). Beyond the borders - biomedical applications of non-linear Raman microscopy. *Adv. Drug Deliv. Rev.* 89, 135–144. doi:10.1016/j.addr.2015.04.024

Xu, P. S., Gullotti, E., Tong, L., Highley, C. B., Errabelli, D. R., Hasan, T., et al. (2009). Intracellular drug delivery by poly(lactic-co-glycolic acid) nanoparticles, revisited. *Mol. Pharm.* 6 (1), 190–201. doi:10.1021/mp800137z

Yosef, H. K., Frick, T., Hammoud, M. K., Maghnouj, A., Hahn, S., Gerwert, K., et al. (2018). Exploring the efficacy and cellular uptake of sorafenib in colon cancer cells by Raman micro-spectroscopy. *Analyst* 143 (24), 6069–6078. doi:10.1039/c8an02029a

Yu, L. X., Amidon, G., Khan, M. A., Hoag, S. W., Polli, J., Raju, G. K., et al. (2014). Understanding pharmaceutical quality by design. *AAPS J.* 16 (4), 771–783. doi:10.1208/s12248-014-9598-3

Yue, S. H., and Cheng, J. X. (2016). Deciphering single cell metabolism by coherent Raman scattering microscopy. *Curr. Opin. Chem. Biol.* 33, 46–57. doi:10.1016/j.cbpa.2016.05.016

Zhang, C., and Cheng, J. X. (2018). Perspective: coherent Raman scattering microscopy, the future is bright. *APL Photonics* 3 (9), 16. doi:10.1063/1.5040101

Zhang, C., Zhang, D. L., and Cheng, J.-X. (2015). Coherent Raman scattering microscopy in biology and medicine. *Ann. Rev. Biomed. Eng.* 17, 415–445. doi:10.1146/annurev-bioeng-071114-040554

Zhang, D., Wang, P., Slipchenko, M. N., and Cheng, J. X. (2014). Fast vibrational imaging of single cells and tissues by stimulated Raman scattering microscopy. *Acc. Chem. Res.* 47 (8), 2282–2290. doi:10.1021/ar400331q

Conflict of Interest: The authors declare that the research was conducted in the absence of any commercial or financial relationships that could be construed as a potential conflict of interest.

frontiers in Pharmacology

SYSTEMATIC REVIEW
published: 27 April 2021
doi: 10.3389/fphar.2021.627693

Preclinical Advances in Theranostics for the Different Molecular Subtypes of Breast Cancer

Hanyi Fang[1,2,3], *Alessandra Cavaliere*[1], *Ziqi Li*[1,4], *Yiyun Huang*[1] and *Bernadette Marquez-Nostra*[1]*

[1]PET Center, Department of Radiology and Biomedical Imaging, School of Medicine, Yale University, New Haven, CT, United States, [2]Department of Nuclear Medicine, Union Hospital, Tongji Medical College, Huazhong University of Science and Technology, Wuhan, China, [3]Hubei Province Key Laboratory of Molecular Imaging, Wuhan, China, [4]Department of Nuclear Medicine, Tongji Hospital, Tongji Medical College, Huazhong University of Science and Technology, Wuhan, China

Breast cancer is the most common cancer in women worldwide. The heterogeneity of breast cancer and drug resistance to therapies make the diagnosis and treatment difficult. Molecular imaging methods with positron emission tomography (PET) and single-photon emission tomography (SPECT) provide useful tools to diagnose, predict, and monitor the response of therapy, contributing to precision medicine for breast cancer patients. Recently, many efforts have been made to find new targets for breast cancer therapy to overcome resistance to standard of care treatments, giving rise to new therapeutic agents to offer more options for patients with breast cancer. The combination of diagnostic and therapeutic strategies forms the foundation of theranostics. Some of these theranostic agents exhibit high potential to be translated to clinic. In this review, we highlight the most recent advances in theranostics of the different molecular subtypes of breast cancer in preclinical studies.

Keywords: theranostics (combined therapeutic and diagnostic technology), breast cancer subtypes, molecular imaging, targeted therapy, preclinical (*in-vivo*) studies, positron emission tomography, single-photon emission computed tomography

OPEN ACCESS

Edited by:
Hong Shan,
Sun Yat-Sen University, China

Reviewed by:
Zibo Li,
University of North Carolina at Chapel Hill, United States
Bo Yu,
The Fifth Affiliated Hospital of Sun Yat-Sen University, China

***Correspondence:**
Bernadette Marquez-Nostra
bernadette.marquez-nostra@yale.edu

Specialty section:
This article was submitted to Pharmacology of Anti-Cancer Drugs, a section of the journal Frontiers in Pharmacology

Received: *10 November 2020*
Accepted: *22 February 2021*
Published: *27 April 2021*

Citation:
Fang H, Cavaliere A, Li Z, Huang Y and Marquez-Nostra B (2021) Preclinical Advances in Theranostics for the Different Molecular Subtypes of Breast Cancer. Front. Pharmacol. 12:627693. doi: 10.3389/fphar.2021.627693

INTRODUCTION

The molecular subtypes of breast cancer are classified based on the status of estrogen receptor (ER), progesterone receptor (PR), and human epidermal growth factor receptor 2 (HER2). In addition to surgery, radiotherapy, and chemotherapy, the standard of care targeted treatments for breast cancer vary according to the molecular subtype of patient's tumor and stage of the disease. For ER-positive breast cancer, ER-targeting tamoxifen is the primary therapy for the non-metastastic luminal subtype of breast cancer (Masoud and Pagès, 2017). For HER2-positive breast cancer, monoclonal antibodies targeting this receptor, such as trastuzumab, have greatly improved the survival of breast cancer patients with non-metastatic disease (Waks and Winer, 2019). Finally, patients with advanced triple negative breast cancer are recently benefiting from immune therapy with the FDA-approval of the monoclonal antibody atezolizumab (Cyprian et al., 2019) or from the antibody drug conjugate, sacituzumab govitecan (Bardia et al., 2019).

However, patients with any breast cancer subtype can have intrinsic or acquired resistance to different therapeutics including chemotherapy, endocrine therapy, and targeted therapy (Chun et al., 2017). Further, tumor heterogeneity in the same patient presents a challenge for achieving complete and durable responses to targeted treatments (Steding, 2016; Blasco-Benito et al., 2018). To overcome resistance to standard of care treatments, many efforts have turned to combination therapies or addition of toxic payloads, such as

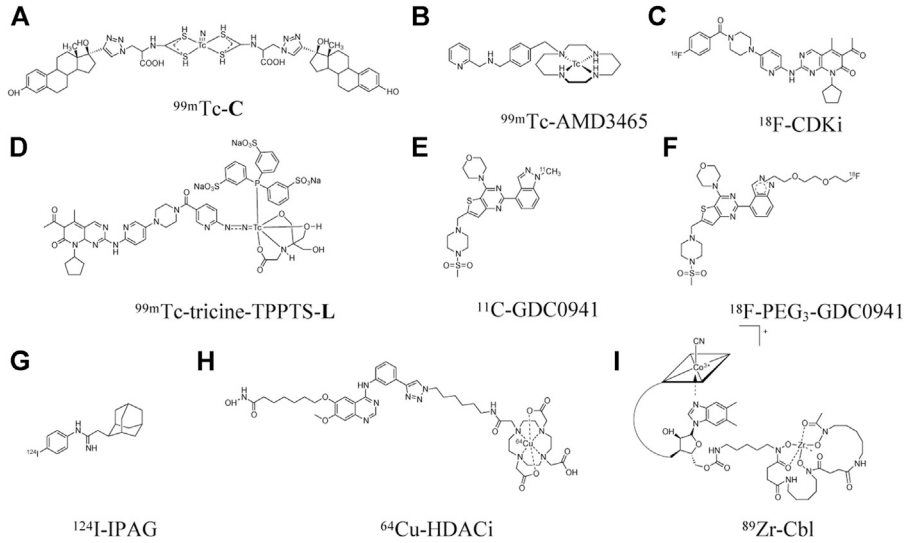

FIGURE 1 | Structures of radiolabeled small molecules for imaging of breast cancer.

ionizing radiation, for targeted radionuclide therapy (TRT) (Lopez and Banerji, 2017). Many investigations have also been devoted to find new therapeutic targets closely associated with breast cancer aggressiveness, invasion, metastasis, and recurrence, such the gastrin-releasing peptide receptors (GRPR) overexpressed on the surface of cancer cells, cyclin-dependent kinase 4 and 6 (CDK4/6), histone deacetylase (HDACs), and *MYC* proto-oncogene. The availability of new targeted treatments for these targets prompted the development of non-invasive imaging agents via positron emission tomography (PET) or single-photon emission tomography (SPECT) to help select patients most likely to benefit from these treatments. The combination of diagnostic imaging and therapy forms the foundation of theranostics.

Currently, the diagnosis of breast cancer still depends on biopsy followed by tissue analysis using immunohistochemistry (IHC) or fluorescence *in situ* hybridization (FISH) to define receptor status and guide treatments. However, tissue analysis results may not be accurate due to several limitations, such as sampling errors, tumor heterogeneity, and changes in receptor status over the course of treatment (de Vries et al., 2019). Thus, non-invasive imaging of therapeutic targets or distribution of therapeutic agents throughout the whole body via PET or SPECT with radiolabeled agents can serve as a complementary diagnostic technique to tissue-based analyses. The type of imaging agent for nuclear imaging is also diverse and includes small molecules, peptides, antibodies, affibodies, antisense oligonucleotides, bispecific scaffolds, and nanoparticles. **Figures 1**, **2** show the diverse set of probes described in this review.

Herein, we highlight recent advances in preclinical imaging and targeted therapy, the combination of which form the basis of theranostics, for the different molecular subtypes of breast cancer. **Table 1** lists the different imaging agents described in this review. We also draw attention to the different cell lines tested in preclinical

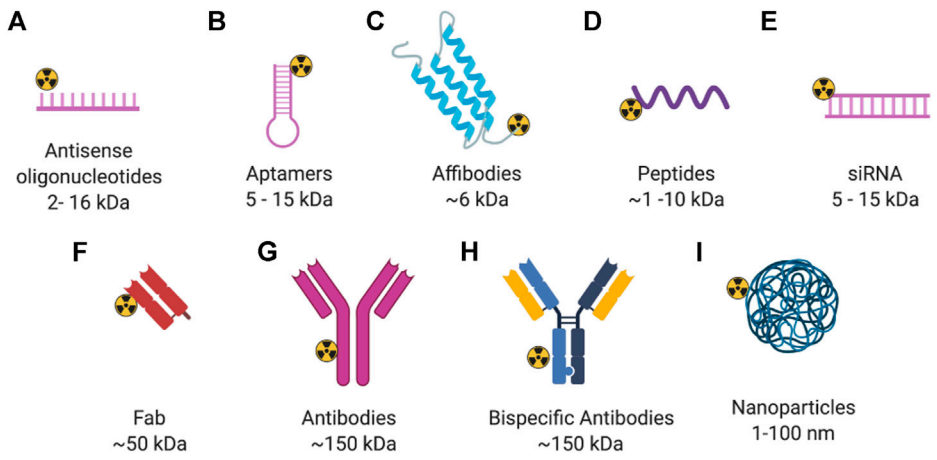

FIGURE 2 | General structure of radiolabeled biomolecules for imaging of breast cancer. Created with BioRender.com.

TABLE 1 | Summary of the preclinical imaging agents discussed in this review for the different subtypes of breast cancer.

Target	Agent	Type of structure	Tumor model	Imaging modality	References
Luminal-subtype					
ER	^{99m}Tc-DTPA-estradiol	Small molecule	MCF-7	SPECT	Xia et al. (2016)
	^{99m}Tc(V)-nitrido complex **C**	Small molecule	MCF-7	None	Tejería et al. (2019)
CXCR4	^{99m}Tc-AMD3465	Small molecule	MCF-7	SPECT/CT	Zhang et al. (2018)
GRPR	^{111}In-JMV4168	Peptide	T47D	SPECT/CT	Dalm et al. (2015)
CDK4/6	^{18}F-CDKi	Small molecule	MCF-7	PET/CT	Ramos et al. (2020)
	^{99m}Tc-labeled palbociclib analogs	Small molecule	MCF-7	SPECT/CT	Song et al. (2019)
	^{99m}Tc-tricine-TPPTS-L	Small molecule	MCF-7	SPECT/CT	Gan et al. (2020)
PI3K	^{11}C-pictilisib (GDC-0941)	Small molecule	MCF-7	PET	Han et al. (2019)
	^{18}F-PEG$_3$-GDC-0941	Small molecule	MCF-7	PET	Altine et al. (2019)
Sigma-1 receptor	^{124}I-IPAG	Small molecule	MCF-7	PET	Gangangari et al. (2020)
MDM2	^{99m}Tc-HYNIC-ASON	Antisense oligonucleotide	MCF-7	SPECT	Fu et al. (2010)
HER2-subtype					
HER2	^{18}F-aptamer	Aptamer	BT-474	PET	Kim et al. (2019)
HER3	^{111}In-HEHEHE-Z08698-NOTA	Affibody	BT-474	SPECT	Andersson et al. (2015)
GRPR	^{68}Ga-NOTA-PEG$_3$-RM26	Peptide	BT-474	PET/CT	Varasteh et al. (2014)
VPAC	^{68}Ga-NODAGA-peptide	Peptide	BT-474	PET/CT	Kumar et al. (2019)
Cobalamin (cbl)	^{89}Zr-cbl	Small molecule	MDA-MB-453	PET	Kuda-Wedagedara et al. (2017)
Triple-negative breast cancer					
EGFR	^{99m}Tc-PmFab-His6	Fab	MDA-MB-468	SPECT/CT	Ku et al. (2019a)
CMKLR1	^{68}Ga-DOTA-ADX-CG34	Peptide	DU4475	PET/MR	Erdmann et al. (2019)
HDAC	^{64}Cu-HDACi	Small molecule	MDA-MB-231	PET/CT	Meng et al. (2013)
MYC	^{89}Zr-transferrin	Protein	MDA-MB-231; MDA-MB-157	PET	Henry et al. (2018)
TF	^{64}Cu-NOTA-ALT-836-fab	Fab	MDA-MB-231	PET	Shi et al. (2015)
CXCR4	^{99m}Tc-HYNIC-siRNA1	siRNA	MDA-MB-231	SPECT	Fu et al. (2016)
MUC1	^{99m}Tc-S1-apMUC1	Nanoparticle-aptamer conjugate	MDA-MB-231	SPECT	Pascual et al. (2017)
Dual-receptor					
GRPR/FA	^{99m}Tc-BBN-FA	Bispecific peptide	T47D	SPECT/CT	Aranda-Lara et al. (2016a)
	^{177}Lu-BBN-FA	Bispecific peptide	T47D	SPECT/CT	Aranda-lara et al. (2016b)
GRPR/ NPY(Y_1)R	^{68}Ga-24	Bispecific peptide	T47D	PET/CT	Vall-Sagarra et al. (2018)
$\alpha_v\beta_3$/CD13	^{68}Ga-NGR-RGD	Bispecific peptide	MCF-7	PET/CT	Gai et al. (2020)
EGFR/HER2	^{64}Cu-NOTA-fab-PEG24-EGF	Bispecific fab	MDA-MB-231-H2N	PET/CT	Kwon et al. (2017)
T-cell/CEA	^{89}Zr-AMG211	Bispecific antibody	BT-474	PET	Waaijer et al. (2018)
EGFR/c-MET	[^{89}Zr]ZrDFO-amivantamab	Bispecific antibody	MDA-MB-468; MDA-MB-231; MDA-MB-453	PET/CT	Cavaliere et al. (2020)

studies, which represent each molecular subtype of breast cancer to help guide future investigations of novel theranostic agents.

PRECLINICAL IMAGING AGENTS FOR THE DIFFERENT SUBTYPES OF BREAST CANCER

Luminal Subtype

The luminal subtype of breast cancer accounts for about 70% of all breast cancer patients and encompasses molecular signatures that are ER and/or PR positive, and HER2 negative (Waks and Winer, 2019). As the luminal subtype is the most common subtype of breast cancer, many research efforts have been focused on cell surface receptors and intracellular targets for development of both molecular imaging and targeted therapy of luminal breast cancer. Summarized below are some of the most promising agents for PET and SPECT imaging of the luminal subtype of breast cancer.

Cell Surface Receptor

Approximately 70% of breast cancers express ER or PR, or both. Hence, endocrine therapy is the most important treatment for the

luminal subtype of breast cancer. Imaging of ER and PR can help determine the status of the tumor tissue, and thus predict prognosis and efficacy of endocrine therapy. A recent review highlighted the preclinical and clinical research progress within the last 5 years of ER imaging with ^{18}F-fluoroestradiol (^{18}F-FES) and PR imaging with ^{18}F-fluorofuranyl norprogesterone (^{18}F-FFNP) in breast cancer (Kumar et al., 2020). Here, we summarized some promising studies that showed imaging of other targets in breast cancer luminal subtype xenografts.

Typically, the MCF-7 and T47D xenograft models are used as high ER-expressing animal models while the MDA-MB-231 xenograft is used as a low ER-expressing model in many of the studies that we summarize herein (Dai et al., 2017). One SPECT imaging agent for ER is an estradiol analog labeled with ^{99m}Tc ($t_{1/2}$ = 6 h) using diethylenetriamine pentaacetate (DTPA) as the chelate to afford ^{99m}Tc-DTPA-estradiol (Xia et al., 2016). High tumor uptake was found in MCF-7 xenografts with 6.1 ± 0.38 %ID/g at 4 h post-injection (p.i.), and high tumor-to-blood (T/B) ratio of 2.8 ± 0.39. As expected, low tumor uptake was observed in the MDA-MB-231 xenografts. Nonetheless, high uptake that amounted to 50% ID/g at 4 h p. i. in the liver, which is a common site for metastasis of breast tumor (Ma et al., 2015), may limit the detection of metastatic lesions in this organ when ^{99m}Tc-DTPA-estradiol is translated to clinical studies. Another derivative of estradiol, ^{99m}Tc(V)-nitrido complex C (^{99m}Tc-C, **Figure 1**), was also developed for SPECT imaging of ER (Tejería et al., 2019). Uptake of ^{99m}Tc-C in the liver, at 1.1 ± 0.38% ID/g at 2 h p. i., was much lower than that of ^{99m}Tc-DTPA-estradiol. However, its tumor uptake was also very low (0.59 ± 0.12% ID/g), which resulted in a low T/B ratio of only 0.35 ± 0.19 at 1 h p. i., i.e., lower concentration in tumor tissue than blood. Differences in tumor uptake of these two estradiol-derived probes might be due to their different chemical structures that can affect pharmacokinetic properties and receptor-binding specificity. Hence, further optimization is still needed to improve ER targeting and pharmacokinetic properties and provide better contrast between metastatic lesions and surrounding normal tissue.

The chemokine receptor 4 (CXCR4), a seven-transmembrane G protein-coupled receptor (GPCR), is another promising target for theranostic development (Kircher et al., 2018). CXCR4 is expressed in 67% of breast cancer cells, with a level double of that in normal breast tissues (Salvucci et al., 2006). Several studies demonstrated that CXCR4 expression may have value in predicting breast cancer prognosis (Xu et al., 2015). For examples, breast cancer patients with high levels of CXCR4 were found to have more extensive metastasis to lymph nodes (Kato et al., 2003) and significantly reduced disease-free survival and overall survival (Zhang et al., 2014a). There are several CXCR4 inhibitors under clinical trials for the treatment of multiple myeloma, small cell lung cancer, and leukemia (Cooper et al., 2017; Salgia et al., 2017; Ghobrial et al., 2019), although none has been reported for breast cancer. AMD3465, a small molecule antagonist of CXCR4, was labeled with ^{99m}Tc to obtain ^{99m}Tc-AMD3465 (**Figure 1**) (Zhang et al., 2018). It showed a moderate tumor uptake of 2.1 ± 0.39% ID/g, but high T/B ratio of 9.4 at 1 h p. i. Specific binding of ^{99m}Tc-AMD3465 to CXCR4 was demonstrated by treatment with excess unlabeled AMD3465 which reduced tumor uptake by 36%.

Another example of a cell surface receptor is the gastrin-releasing peptide receptor (GRPR), which is a G-protein coupled receptor highly expressed in the pancreas and lowly expressed in the normal breast tissues (Baratto et al., 2020). In autoradiography studies, GRPR was reported to be expressed at high density (>2000 dpm/mg tissue) in 74% (50 of 68) of breast cancer tissues from patients (Reubi et al., 2002).

Evaluating radiotracers that bind to GRPR typically employ the T47D xenograft model, as this cell line express high levels of GRPR. Agonists and antagonists of GRPR have been adapted as SPECT imaging agents. ^{111}In-AMBA (^{111}In $t_{1/2}$ = 2.8 days) is a GRPR agonist that has been tested in an autoradiography study of 50 human breast cancer tissue specimens, with 96% (48/50) of them showing elevated GRPR levels (Dalm et al., 2015). A positive correlation was also found between ER status and GRPR expression. Those results were in agreement with previous studies, where a positive correlation between ER expression and GRPR binding affinity was detected in human breast cancer samples (Halmos et al., 1995). ^{111}In-JMV4168 (Peptides, **Figure 2**), a GRPR antagonist, was developed for SPECT/CT imaging (Dalm et al., 2015). Tumor uptake was about 5% ID/g in both subcutaneous and orthotopic tumors of T47D xenografts (**Figure 3**). Autoradiography showed high binding of ^{111}In-JMV4168 in T47D xenografts. In orthotopic tumor tissues, ^{111}In-JMV4168 bound with 2.2 ± 4% of added dose (%AD), whereas low binding was observed in the blocking group with 0.1% AD, confirming the specific binding of ^{111}In-JMV4168 to GRPR *ex vivo* (Dalm et al., 2015).

Intracellular Targets

Cell cycle dysregulation leads to uncontrolled progression to tumor (Schafer, 1998). The cell cycle consists of 4 phases: DNA replication (S), mitosis (M), and two gaps (G1 and G2)

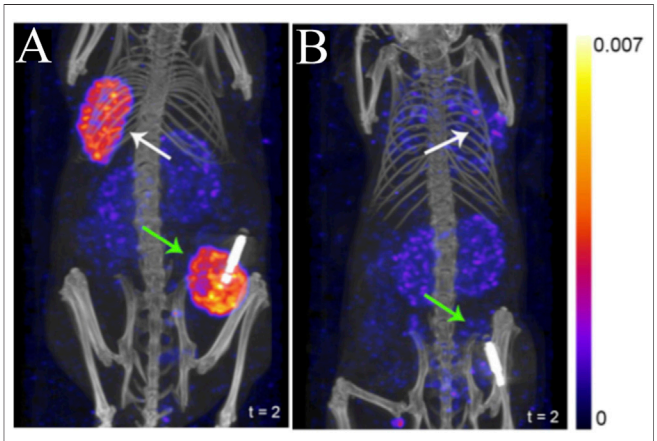

FIGURE 3 | SPECT/CT imaging using ^{111}In-JMV4168 in orthotopic (green arrows) and subcutaneous (white arrows) tumors of T47D **(A)** and MCF7 **(B)** xenografts at 4 h post-injection of ^{111}In-JMV4168 (Dalm et al., 2015). The general structure of ^{111}In-JMV4168 was shown in **Figure 2D**.

between the S and M phases. Cyclin-dependent kinases 4/6 (CDK4/6) are two kinases that control cell cycle from G1 to S phase (Lee et al., 2019). CDK4/6 overexpression occurs in many cancers, including breast cancer (O'Sullivan et al., 2019; VanArsdale et al., 2015). Palbociclib, a CDK4/6 inhibitor (CDKi), is in phase 3 clinical trials for the treatment of ER-positive advanced breast cancer (Finn et al., 2016). The use of radiolabeled CDKi for tumor imaging has gained increased attention as companion diagnostic imaging agents to these inhibitors. The palbociclib CDKi was labeled with ^{18}F ($t_{1/2}$ = 110 min) to obtain ^{18}F-CDKi (**Figure 1**), for PET imaging of MCF-7 xenografts (Ramos et al., 2020). Tumor uptake was high at about 4% ID/g at 2 h p. i for ^{18}F-CDKi, which translated into a high T/B ratio of about 5. The tumor uptake decreased to 0.3% ID/g at 2 h p. i. when mice were blocked with excess of palbociclib.

A series of ^{99m}Tc-labeled palbociclib analogs were also developed for SPECT imaging (Song et al., 2019). However, tumor uptake was moderate, and T/B ratios were low for the ligand series, accompanied by very high liver uptake of more than 50% ID/g. In this study, ^{99m}Tc-L2 showed the highest tumor uptake of 2.7 ± 0.26% ID/g but low T/B ratio of 0.42 at 2 h p. i. However, the highest radiotracer accumulation was observed in the liver of greater than 50% ID/g from ^{99m}Tc-L2 to L5, which might be due to their relatively high lipophilicity (Log P = 1.5). To reduce the liver uptake, the chelator was changed from an isocyano-group to an hydrazinonicotinamide (HYNIC) moiety, where tricine/TPPTS were used as co-ligands to afford a new ^{99m}Tc-labeled palbociclib complex, ^{99m}Tc-tricine-TPPTS-L (**Figure 1**) (Gan et al., 2020). The Log P of the ^{99m}Tc-tricine-TPPTS-L variant was −2.9 ± 0.1, which was much lower than that of ^{99m}Tc-L2 to L5, demonstrating that ^{99m}Tc-tricine-TPPTS-L was more hydrophilic. Tumor uptake of ^{99m}Tc-tricine-TPPTS-L was good, at 3.8 ± 1.3 and 2.7 ± 0.58% ID/g at 1 and 2 h p. i., respectively, albeit with low T/B ratio of about 0.4. The liver uptake was indeed much reduced to as low as 4.2 ± 0.33% ID/g at 2 h p. i. These studies showed that radiolabeled palbociclib analogs may have the potential to image CDK4/6 via PET or SPECT as a companion diagnostic agent to CDK4/6 inhibitors.

Another intracellular kinase that also regulates cell proliferation, survival, and migration is the phosphatidylinositol 3-kinase (PI3K) (Bader et al., 2005). Abnormal activation of PI3K/Akt/mTOR has been found in about 70% of breast cancer cases (Cancer-Genome-Atlas-Network, 2012). Pictilisib (GDC-0941), a PI3K inhibitor, is currently under phase Ib clinical trial in patients with advanced breast cancer and non-small cell lung cancer (Yamamoto et al., 2017; Schöffski et al., 2018). Pictilisib was labeled with ^{11}C ($t_{1/2}$ = 20 min) for PET imaging in pictilisib-sensitive MCF-7 xenograft models (Han et al., 2019). The tumor uptake of ^{11}C-pictilisib was 2.9 ± 0.07% ID/g with T/B ratio of 2.1 ± 0.34 at 1 h p. i. in these xenograft models, demonstrating excellent tumor penetration regardless of the short half-life of ^{11}C. In contrast, PET imaging with ^{11}C-pictilisib in pictilisib-resistant MDA-MB-231 xenograft models showed significantly decreased tumor uptake. However, uptake in the liver was the highest. To reduce liver uptake, a triethylene glycol di (*p*-toluenesulfonate) (TsO-PEG$_3$-OTs) modified agent, ^{18}F-PEG$_3$-GDC-0941, was developed (Altine et al., 2019). Its liver uptake was 4.7 ± 0.86 %ID/g at 1 h p. i., which is about 76% lower than that of ^{11}C-pictilisib. ^{18}F-PEG$_3$-GDC-0941 also showed high and specific tumor uptake, indicating that imaging PI3K could be a potential strategy for monitoring response to pictilisib treatment.

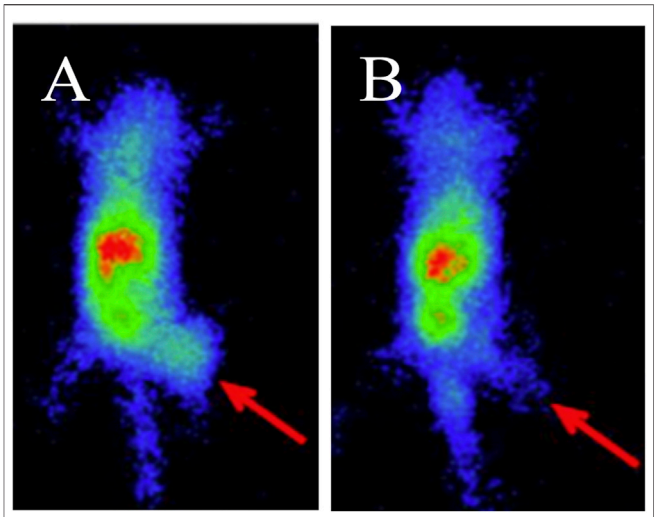

FIGURE 4 | SPECT Imaging of MDM2 expression in MCF-7 xenografts using ^{99m}Tc-HYNIC-antisense **(A)** and mismatch **(B)** probes at 4 h post-injection. Tumors are indicated by red arrows (Fu et al., 2010). The general structure of ^{99m}Tc-HYNIC-antisense was shown in **Figure 2A**.

Sigma-1 receptors (S1R) is a unique ligand-regulated membrane protein involved in modulating cellular protein and lipid homeostasis (Maher et al., 2018). S1R mRNA was found to be overexpressed in 64% of breast cancer tissues, and in several ER-positive breast cancer cell lines on the cell membrane and in the endoplasmic reticulum (Wang et al., 2004). The small molecule inhibitor of S1R 1-(4-Iodophenyl)-3-(2-adamantyl) guanidine (IPAG) was shown to decrease the expression of the programmed death receptor ligand 1 (PD-L1) and suppress PD-L1 interaction with its PD-1 receptor in T-cell, and in cell lines of PC3 prostate cancer and MDA-MB-231 triple negative breast cancer (Maher et al., 2018). IPAG was labeled with ^{124}I ($t_{1/2}$ = 4.18 days) (**Figure 1**) for PET imaging in MCF-7 xenografts (Gangangari et al., 2020). The tumor uptake of ^{124}I-IPAG was 1.1 ± 0.24 and 0.94 ± 0.22% ID/g at 24 and 48 h p. i., respectively, with extremely high T/B ratio of 22 ± 6.6 and 46 ± 10.0. With the specific targeting and the high T/B ratios, ^{124}I-IPAG holds great potential for imaging S1R in tumor and may be used to help to define the interaction between S1R and PD-L1 as a consequence of S1R-targeted or checkpoint inhibitor therapy.

Apart from protein targets, oncogenes are also attractive targets in breast cancer. Mouse double-minute 2 (MDM2), an oncogene, is regarded as the major negative regulator of the function of the p53 tumor suppressor, and found to be overexpressed in many malignant tumors, including breast cancer (Haupt et al., 2017). High expression of MDM2 with the consequent inactivating of p53 is associated with tumor development (Graat et al., 2007, Zhang et al., 2017). The

^{99m}Tc-labeled antisense oligonucleotides (ASONs) (Antisense oligonucleotides, **Figure 2**) has been used to visualize MDM2 mRNA expression in MCF-7 xenografts through SPECT imaging (**Figure 4**) (Fu et al., 2010). This antisense probe and its mismatched oligonucleotide control have similar biodistribution properties in normal organs with fast blood clearance. The tumor uptake of the probe was high and steady from 9.2 ± 1.4 to 8.1 ± 1.1% ID/g at 1 and 6 h p. i., respectively, with increasing T/B ratio of 1.24 at 1 h p. i. to 4.11 at 6 h p. i.. In contrast, tumor uptake of the mismatched oligonucleotide control was significantly lower. This study demonstrates the feasibility of specifically targeting MDM2 mRNA with ^{99m}Tc-HYNIC-ASON. With increasing evidence showing that antisense oligonucleotides contribute to breast cancer treatment (Yang et al., 2003), *in vivo* imaging with radiolabeled antisense oligonucleotides may provide a tool to monitor therapeutic response.

HER2 Subtype

The HER2 subtype of breast cancer is classified by amplification of the HER2 oncogene and overexpression of the HER2 transmembrane receptor tyrosine kinase (Ross et al., 2009). HER2 belongs to the epidermal growth factor receptor family, consisting of HER1/EGFR, HER3, and HER4 (Wang, 2017). HER2 is amplified in 15–20% of all breast cancers, and the HER2 subtype is associated with more aggressive growth and poor prognosis (Waks and Winer, 2019). One of the previous reviews has presented a comprehensive summary of recent advances in HER2-targeted imaging and therapy in nuclear medicine prior to 2018 (Massicano et al., 2018). Herein, we summarize new findings in preclinical studies from 2018 to 2020. We will also discuss imaging studies with other novel targets that evaluate xenograft models within the HER2 subtype. In these recent studies, the BT-474 xenograft model is typically used due to its overexpression of HER2, high tumorigenicity in standard immune compromised mice strains, and high sensitivity to HER2-targeted treatments.

HER2

Aptamers are single-stranded oligonucleotides that have unique three-dimensional shape to specifically and tightly bind to their protein targets (Ireson and Kelland, 2006). Currently, many therapeutic aptamers are under clinical investigation, including a nucleolin-targeted DNA aptamer for the treatment of renal cell carcinoma (Rosenberg et al., 2014) and several anti-VEGF aptamers for macular degeneration and angioma (Eyetech-Study-Group, 2002; Dahr et al., 2007). One recent study demonstrated that a HER2-targeted aptamer can differentiate both HER2-positive breast cancer cells and xenografted mice models from other subtypes of breast cancer through fluorescence imaging (Liu et al., 2018). SH-1194-35, a HER2-targeted DNA aptamer, was labeled with ^{18}F using click chemistry between the amine-terminal and an *N*-succinimidyl 4-^{18}F-fluorobenzoate (^{18}F-SFB) to form an amide linkage (Aptamer, **Figure 2**) (Kim et al., 2019). Tumor uptake of this ^{18}F-labeled HER2 aptamer in BT474 xenograft models was rather low at 0.62 ± 0.04% ID/g at 1 h p. i., but was higher than that in the HER2-negative MDA-MB-231 xenograft models. The highest uptake was observed in the intestines and kidneys. Although optimization is still needed to increase uptake in the tumor and reduce uptake in normal organs, the translational potential of aptamers to clinical studies opens a new direction for HER2-targeted therapy against breast cancer.

HER3

HER3 overexpression is a resistance mechanism to several anticancer therapies, including hormone therapy in breast cancer (Johnston et al., 2016). Imaging HER3 may help to explain the mechanism of resistance to standard of care treatments. This approach could also predict the HER3-targeted therapeutic efficacy of tyrosine kinase inhibitors neratinib and anti-HER3 antibody patritumab in advanced solid tumors, including breast cancer (Sergina et al., 2007; LoRusso et al., 2013; Mukai et al., 2016; Hyman et al., 2018). Andersson et al. developed a radiolabeled anti-HER3 affibody ^{111}In-HEHEHE-Z08698-NOTA (Affibody, **Figure 2**) which had extremely high binding affinity for HER3 (K_D of 5.4 ± 0.4 pM) (Andersson et al., 2015). The tumor uptake of ^{111}In-HEHEHE-Z08698-NOTA in the BT-474 xenograft models was 5.1 ± 0.4 and 3.7 ± 0.2 at 1 and 24 h p. i., respectively, and T/B ratio increased from 5.3 ± 0.4 to 15.5 ± 0.7 at these time points. These properties are desirable for clinical translation, given the feasibility of same-day imaging of HER3 expression.

Other Targets in HER2-Positive Models

GRPR

GRPR is also expressed in HER2-positive cells. GRPR belongs to the mammalian bombesin (BBN)-like peptide receptor family (Qu et al., 2018). BBN is a 14-amino acid peptide, originally found in the frog skin (Erspamer et al., 1970; Jensen et al., 2008). One of its mammalian homologs is a gastrin-releasing peptide (GRP) (Qu et al., 2018), which binds specifically to GRPR. RM26 (D-Phe-Gln-Trp-Ala-Val-Gly-His-Sta-Leu-NH2), an antagonist analog of BBN, was conjugated to different lengths of polyethylene glycol (PEG_x) and the NOTA chelator for radiolabeling with ^{68}Ga to obtain ^{68}Ga-NOTA-PEG_x-RM26 (Peptides, **Figure 2**) to optimize the radiotracer's targeting efficiency (Varasteh et al., 2014). ^{68}Ga-NOTA-PEG_3-RM26, with a three PEG unit linker, was found to have the lowest liver uptake of 0.7 ± 0.1% ID/g at 2 h p. i. Tumor uptake in the BT-474 xenograft models was 2.8 ± 0.4% ID/g with an extremely high T/B ratio of 42 ± 5 at 2 h p. i. Therefore, it appears that biological properties can be optimized by insertion of an appropriate length of the PEG spacer between the peptide and radiometal chelator. Since PEG has been widely used for modification of therapeutic peptides and proteins to reduce enzymatic degradation (Roberts et al., 2002), the above study presents a rational approach for optimizing the *in vivo* pharmacokinetic and binding properties of peptide probes.

VPAC

TP-3805 is an analog of the pituitary adenylate cyclase-activating peptide (PACAP), which has high affinity for the VPAC [combination of vasoactive intestinal peptide (VIP) and

PACAP] receptors (Thakur et al., 2013). These receptors are highly expressed in malignant breast cancer. TP-3805 was conjugated to either 1,4,7-triazacyclononane,1-glutaric acid-4,7-acetic acid (NODAGA) or 1,4,7,10-tetraazacyclododecane-1,4,7,10-tetraacetic acid (DOTA) chelate for radiolabeling with ^{68}Ga to obtain ^{68}Ga-NODAGA-peptide or ^{68}Ga-DOTA-peptide, respectively (Peptides, **Figure 2**). PET imaging with these radiotracers was performed to compare their *in vivo* stability and pharmacokinetic properties in breast cancer xenografts (Kumar et al., 2019). Tumor uptake of ^{68}Ga-NODAGA-peptide in the BT-474 xenograft models was 2.4 ± 0.3% ID/g at 1 h p. i., with tumor to muscle (T/M) ratio of 3.4 ± 0.3 whereas ^{68}Ga-DOTA-peptide showed similar tumor uptake but a lower T/M ratio of 1.9 ± 0.9 at 1 h p. i. Further, ^{68}Ga-NODAGA-peptide also showed more flexibility in radiolabeling, higher stability *in vitro*, and higher cell binding affinity than ^{68}Ga-DOTA-peptide. These differences may be due to differences in coordination chemistry. For example, Ga(III) uses all 11 of its coordination sites to form a complex with NODAGA, whereas two sites remain uncoordinated when DOTA is used as a chelator (Viola-Villegas and Doyle, 2009). Although the *in vivo* stability of both ^{68}Ga-NODAGA- and ^{68}Ga-DOTA-labeled TP-3805 needs improvement, this study suggests that changing the chelator is a strategy to optimize the pharmacologic properties of probes.

Cobalamin

Vitamin B_{12}, or cobalamin (Cbl), is an essential nutrient required to maintain cell growth and differentiation (Gherasim et al., 2013). Cbl is transported by binding to the transport protein transcobalamin, which is recognized by specific receptors such as CD320 (Quadros and Sequeira, 2013), which is highly expressed in several cancers, including breast cancer (Sysel et al., 2013). Cbl was radiolabeled with ^{89}Zr ($t_{1/2}$ = 78.4 h) and used for PET imaging (Kuda-Wedagedara et al., 2017). Tumor uptake of ^{89}Zr-Cbl (**Figure 1**) in HER2-positive MDA-MB-453 xenograft models was 3.8 ± 0.77% ID/g with T/B ratio of about 9.7 at 48 h p. i. In addition, clearance from blood was evident from 4 to 48 h with approximately 90% decrease in activity concentration by 48 h p. i. A drawback of this radiotracer is its high uptake in the kidney. This study demonstrates the feasibility of labeling vitamin B12 as a tracer and use it for breast cancer imaging.

In summary, HER2 remains an important target for theranostic development. Several other promising targets in the HER2 subtype of breast cancer such as HER3, GRPR, and vitamin B12 offer additional options for targeted therapy, with their respective companion diagnostic imaging agents readily available for assessing target engagement or monitoring response to treatment. Further investigations are still needed for optimization and validation of these nuclear imaging agents.

Triple-Negative Breast Cancer

Triple-negative breast cancer (TNBC) is characterized by the absence of ER and PR expression, or lack of HER2 overexpression (Waks and Winer, 2019). TNBC makes up approximately 15% of all breast cancers (Waks and Winer, 2019). The absence of these receptors has long limited the treatment of patients with TNBC to chemotherapy, with its accompanying serious adverse effects and drug resistance. Hence, patients with TNBC are faced with a grim prospect of poor prognosis, high rate of distant metastasis and short survival time (Bianchini et al., 2016; He et al., 2018). However, a new era in TNBC treatment has recently begun with the FDA-approval of drugs targeting PD-L1 (e.g., atezolizumab), and trophoblast antigen 2 (Trop-2) (e.g., sacituzumab govitecan) (Bardia et al., 2019; Cyprian et al., 2019). Development of new PET and SPECT imaging agents that inform on the status of new therapeutic targets could help guide treatment options for patients with TNBC. In the preclinical studies of new imaging probes described below, MDA-MB-231 and MDA-MB-468 xenograft models are typically used as animal models for TNBC.

EGFR

TNBC patients with higher expression of the epidermal growth factor receptor (EGFR) have shorter overall survival (Vallböhmer et al., 2005, Zhang et al., 2003). Panitumumab combined with chemotherapy showed promising results in a phase II clinical trial (Cowherd et al., 2015). Thus, imaging EGFR with a radiolabeled panitumumab Fab (PmFab) could afford a tool to monitor response to this combination treatment. The SPECT imaging agent ^{99m}Tc-PmFab-His$_6$ (Fab, **Figure 2**) was prepared by conjugating PmFab and the hexahistidine peptide (His_6) which serves as a chelate for ^{99m}Tc labeling (Ku et al., 2019a). Tumor uptake in MDA-MB-468 xenograft models was 15 ± 3.1% ID/g with T/B ratio of 12 ± 1.4 at 24 h p. i., indicating that ^{99m}Tc-PmFab-His$_6$ is a promising probe for imaging EGFR and may be used to monitor the response to EGFR-directed therapies.

Chemokine-like Receptor 1

Chemerin is known to be involved in angiogenesis, cancer-related inflammation, and insulin resistance (Perumalsamy et al., 2017). The chemokine-like receptor 1 (CMKLR1) is a chemotactic cellular receptor for chemerin (Pachynski et al., 2019). CMKLR1 and chemerin have recently been recognized as modulators of tumor proliferation (Shin and Pachynski, 2018). Increasing chemerin expression in the breast tumor microenvironment can suppress tumor growth (Pachynski et al., 2019). Further, high mRNA expression of CMKLR1 is associated with a longer relapse-free survival of breast cancer patients (Treeck et al., 2019). The first imaging of CMKLR1 *in vivo* was performed with a family of five novel CMKLR1 peptides derived from chemerin-9 and labeled with ^{68}Ga (Erdmann et al., 2019) (Peptides, **Figure 2**). One of the radiotracers, ^{68}Ga-DOTA-ADX-CG34, showed the highest tumor uptake with 6.2 ± 0.5% ID/g in CMKLR1-positive DU4475 (TNBC) xenograft models, while ^{68}Ga-DOTA-AHX-CG34 presented the highest T/B ratio of 5.9 ± 0.7 at 1 h p. i., and ^{68}Ga-DOTA-KCap-CG34 the lowest kidney and liver uptake. Since high CMKLR1 expression is associated with longer relapse-free survival, CMKLR1-targeted probes are promising prognostic tools for breast cancer.

Histone Deacetylases

Histone deacetylases (HDACs) are a class of enzymes that modulate transcription and therefore alter gene expression (Bolden et al., 2006; Falkenberg and Johnstone, 2014). Four HDAC inhibitors (HDACi),

namely romidepsin, panobinostat, vorinostat, and belinostat, have been approved by the Food and Drug Administration (FDA) for the treatment of T-cell lymphoma and multiple myelomas, while several other HDACi compounds are under clinical investigation (Singh et al., 2018). Therefore, imaging HDAC is needed for non-invasive assessment of its expression in the body and prediction of response to HDAC-targeted treatment. Preclinical studies have shown that HDACi is toxic to TNBC cells and decreases tumorigenesis *in vivo* (Tate et al., 2012). CUDC-101, a small molecule HDACi, is currently in phase I clinical trials for the treatment of advanced breast cancer (Shimizu et al., 2014). CUDC-101 was labeled with ^{64}Cu to obtain ^{64}Cu-HDACi (**Figure 1**) for PET imaging of TNBC xenografts (Meng et al., 2013). Tumor uptake of ^{64}Cu-HDACi in was 2.2 ± 0.18% ID/g, as well as high T/B ratio of 4.4 ± 0.88 at 24 h p. i. with moderate uptake in the liver and kidney (3.2 ± 1.3 and 1.9 ± 0.06% ID/g, respectively). Thus, ^{64}Cu-HDACi shows promise for clinical translation to monitor the response to HDACi treatment in breast cancer.

C-Myc Proto-Oncogene

The c-myc proto-oncogene (MYC) is known to play important roles in mRNA regulation, cell proliferation, cell metabolism, and cell death (Horiuchi et al., 2012; Stine et al., 2015). MYC expression is found in 87% of TNBC patients (164 of 187) and associated with poor survival (Bouchalova et al., 2015). There is also evidence that MYC overexpression contributes to drug resistance in patients with TNBC (Carey et al., 2018, Lee et al., 2017). However, directly targeting of the MYC gene remains a challenge, and alternate approaches have been developed (Horiuchi et al., 2014). It has been shown that upregulation of MYC leads to increased surface expression of transferrin receptor (TfR) (O'Donnell et al., 2006), hence ^{89}Zr-transferrin was developed as a potential probe for MYC status and tumor burden in several cancer models, such as prostate cancer and lymphoma (Holland et al., 2012; Doran et al., 2016). Recently, PET imaging with ^{89}Zr-transferrin in TNBC models has also been performed using MDA-MB-231 and MDA-MB-157 xenografts, showing similar accumulation of the radiotracer in both models with 4% ID/g at 48 h p. i. (Henry et al., 2018). In patient-derived xenograft models of TNBC PET imaging with ^{89}Zr-transferrin at 48 h p. i. delineated xenografted tumors from normal organs, indicating the potential of ^{89}Zr-transferrin as a probe for MYC to monitor response to treatments that modulate this oncogene.

Tissue Factor

Tissue factor (TF), also known as thrombokinase or CD142, has been confirmed to be overexpressed on TNBC cells (Callander et al., 1992). Importantly, a high level of TF also contributes to progression and poor survival in TNBC patients (Ruf et al., 2010; Ueno et al., 2000). ALT-836, a chimeric anti-human TF monoclonal antibody (mAb), has been used for the treatment of solid tumors that overexpress TF in a clinical trial (Clinical Trials.gov Identifier: NCT01325558). A radiolabeled antibody fragment, ^{64}Cu-NOTA-ALT-836-Fab (Fab, **Figure 2**), was developed and shown to have an uptake level of about 4% ID/g with T/B ratio of 2 at 24 h p. i. in MDA-MB-231 xenograft models (Shi et al., 2015). Therefore, targeting TF could be a potential way for imaging and therapy of TNBC.

CXCR4

Similar to its involvement in the luminal subtype, CXCR4 is also a potential target for theranostics of TNBC using RNA interference (RNAi) technology, a powerful tool in gene therapy research (Bottai et al., 2017). The delivery of small-interference RNA (siRNA) can affect the efficacy of RNAi therapy *in vivo* (Chen et al., 2018). A ^{99m}Tc-labeled siRNA was used to target CXCR4 in breast cancer xenografts for tracing the delivery of siRNAs *in vivo* (Fu et al., 2016). Due to its fast blood clearance, the tumor uptake of ^{99m}Tc-HYNIC-siRNA1 (siRNA, **Figure 2**) in MDA-MB-231 xenograft models increased from 4.5 ± 0.47 to 8.4 ± 1.1% ID/g at 1 and 6 h p. i., respectively, with corresponding increase in T/B ratio from 0.6 to 4.8. In comparison, tumor uptake of the siRNA control was lower, indicating specific targeting of ^{99m}Tc-HYNIC-siRNA1 to breast cancer. This probe may be a useful tool to predict the efficacy of RNAi gene therapy.

Mucin 1

Mucin 1 (MUC1) is a cell surface glycoprotein and expressed in over 90% of all breast cancers (Miller-Kleinhenz et al., 2015) and 94% of the TNBC subtype (Siroy et al., 2013). High expression of MUC1 has also been found to be associated with metastases and poor survival (Kim et al., 2020, McGuckin et al., 1995), and MUC1 has been reported to contribute to immune escape in TNBC, indicating that MUC1 is a potential immunotherapeutic target for TNBC (Maeda et al., 2018). Several clinical trials targeting MUC1 are ongoing in breast cancer patients (Apostolopoulos et al., 2006; Ibrahim et al., 2011, Tang et al., 2017). Therefore, MUC1 is recognized as a promising marker for theranostics of breast cancer and has been targeted for imaging agent development. One example is ^{99m}Tc-labeled mesoporous silica nanoparticles (MSNs), ^{99m}Tc-S1-apMUC1 (Nanoparticles, **Figure 2**), with the MSN functionalized with positively charged aminopropyl groups and gated with negatively charged MUC1 aptamer via electrostatic and hydrogen bonding interactions (Pascual et al., 2017). Tumor uptake of ^{99m}Tc-S1-apMUC1 was up to 20% ID/g with T/B ratio of about 7 at 2 h p. i. Notably, ^{99m}Tc-S1-apMUC1 uptake in the liver and spleen was as low as about 1% ID/g, suggesting that ^{99m}Tc-S1-apMUC1 nanoparticles bypassed elimination by the mononuclear phagocytic system (MPS). Its uptake in the lung was 15% ID/g, possibly due to the high-expression of MUC1 in this organ. High kidney uptake of about 20 %ID/g provides evidence of renal clearance. ^{99m}Tc-S1-apMUC1 SPECT imaging can be a useful tool to detect MUC1 expression and predict the prognosis of MUC1-targeted treatment.

DUAL-RECEPTOR TARGETED IMAGING OF BREAST CANCER

Recently, multiple antibodies, peptides, and nanoparticles have been developed to target two receptors simultaneously on the same cell or to elicit contact between two different cell types

(Ehlerding et al., 2018). Those dual-receptor targeting strategies have multiple advantages over the mono-targeted ones such as improved target specificity and biodistribution *in vivo* (Kontermann, 2012). Most importantly, bispecific constructs targeting receptors expressed on the same cancer cell have the potential to overcome resistance mechanisms associated with mono-targeted therapies. Certain bispecific constructs have been designed so that they bind two distinct cells such as T cells and cancer cells and can therefore re-direct immune cells to tumor cells to stimulate cytotoxic activity (Ehlerding et al., 2018; Labrijn et al., 2019). The concept of dual-receptor targeting is of particular interest in heterogeneous subtypes of breast cancer, where a mono-targeted approach might fail to treat lesions absent of its target, especially in metastatic disease (McGuire et al., 2015; Peart, 2017). In this section, we discuss the progress made in the preclinical development and evaluation of bispecific agents with regards to imaging of breast cancer, independent of its molecular subtypes.

GRPR/FA

Folate (FA) is a basic component of cell metabolism and DNA synthesis and repair. Folate receptor (FR) is a membrane-bound protein that binds and transports FA into cells (Frigerio et al., 2019) and its overexpression has been confirmed in all clinical breast cancer subtypes (Karuppaiah et al., 2020; Wang et al., 2020; Zhang et al., 2014b). As described above, overexpression of GRPR is also observed in 96% of all breast cancer tissues (Dalm et al., 2015). Therefore, an heterobivalent agent targeting GRPR and FR could improve breast cancer imaging. The radioconjugate ^{99m}Tc-BBN-FA (Peptides, **Figure 2**) has been synthesized to target the GRPR with the BBN portion and the FR with the FA portion for SPECT imaging in preclinical models of breast cancer (Aranda-Lara et al., 2016b). Tumor uptake of ^{99m}Tc-BBN-FA in T47D xenograft models was 5.4 ± 0.97% ID/g at 2 h p. i. and remained stable at 24 h p. i. with values of 2.5 ± 0.63% ID/g. Further, very fast blood clearance contributed to high T/B ratio of 124 at 24 h p. i. High uptake in the pancreas was observed due to the high GRPR expression in this organ. Tumor uptake of ^{99m}Tc-BBN-FA was higher than that of ^{99m}Tc-BBN or ^{99m}Tc-FA alone, demonstrating the advantage of the bispecific construct. BBN and FA were also labeled with ^{177}Lu ($t_{1/2}$ = 6.71 days) for SPECT imaging in T47D xenograft models (Aranda-Lara et al., 2016a). ^{177}Lu-BBN-FA (Peptides, **Figure 2**) showed similar excellent tumor uptake and biodistribution compared with the ^{99m}Tc-labeled variant. In addition, when administering 74 MBq of each radiotracer, ^{177}Lu-BBN-FA was shown to substantially enhance radiation absorbed dose in the tumor with up to 24 ± 2.1 Gy, as compared with those of the mono-targeted ^{177}Lu-BBN and ^{177}Lu-FA, which were lower by 47 and 67%, respectively. Clearly, the bispecific construct is also advantageous for therapy, as it can deliver greater radiation dose to the tumor. Taken together, these studies demonstrate that GRPR/FA dual-receptor targeted imaging perform better than its respective mono-specific variants and has potential for clinical translation for imaging and targeted radiotherapy of breast cancer.

GRPR/NPY(Y_1)R

A study conducted on human breast cancer patient tissues reported that 51% of them (32/63) showed an overexpression of GRPR together with another receptor called the neuropeptide Y receptor subtype 1 (NPY(Y_1)R) (Reubi et al., 2002). Thus, a series of ^{68}Ga-labeled heterobivalent peptidic ligands were synthesized to target both receptors with the goal of achieving increased binding to breast cancer cells over the mono-specific targeting agents (Vall-Sagarra et al., 2018). The best bispecific agent in this study was found to be the compound, ^{68}Ga-24 (Peptides, **Figure 2**), with tumor uptake of 3.1 ± 0.33% ID/g and T/B ratio of 2.7 ± 0.43 at 130 min p. i. in the T47D xenograft models. Conversely, tumor uptake of the GRPR or NPY(Y_1)R mono-specific targeted agents were lower, confirming the improved tumor uptake of the bispecific construct over the mono-targeted agents.

$\alpha_v\beta_3$/CD13

The integrin $\alpha_v\beta_3$ receptor and CD13 are two other receptors whose expression levels are correlated with neoangiogenesis, invasiveness, metastasis, and poor overall survival in breast cancer (Ranogajec et al., 2012; Rolli et al., 2003). The ligands RGD and NGR bind to $\alpha_v\beta_3$ and CD13, respectively, and have been used as anti-angiogenic drugs in radionuclide therapy (Debordeaux et al., 2018; Goodman and Picard, 2012). Hence, a bispecific agent derived from these mono-specific targeting agents, ^{68}Ga-NGR-RGD (Peptides, **Figure 2**), has recently been synthesized for PET imaging in breast cancer xenografts (Gai et al., 2020). Tumor uptake in the MCF-7 xenograft models was 1.0 ± 0.16% ID/g with T/B ratio of about 6. Further, tumor uptake of ^{68}Ga-NGR-RGD was significantly higher than that of ^{68}Ga-NGR and ^{68}Ga-RGD at 1 h p. i. More importantly, ^{68}Ga-NGR-RGD detected lung metastases in MCF-7 xenografts. This study represents another proof of concept for the increased tumor targeting ability of bispecific agents over the mono-specific constructs.

EGFR/HER2

As previously discussed, HER2 represents a common therapeutic target in the HER2 subtype of breast cancer. However, HER2-directed therapies such as trastuzumab can develop resistance through several mechanisms including heterodimerization of EGFR with HER2 (Dua et al., 2010). A ^{64}Cu-labeled bispecific antibody fragment, ^{64}Cu-NOTA-Fab-PEG$_{24}$-EGF (Fab, **Figure 2**), was thus developed to inhibit the EGFR and HER2 receptors simultaneously (Kwon et al., 2017). In order to increase the blood circulation time and potentially increase tumor uptake of the tracer, Kwon et al. linked the Fab of the trastuzumab to that of the EGF through a PEG$_{24}$ linker, conjugated the resulting construct to NOTA, and radiolabeled with ^{64}Cu to obtain ^{64}Cu-NOTA-Fab-PEG$_{24}$-EGF. In the MDA-MB-231/H2N xenograft model, which is characterized by low expression of HER2 and moderate expression of EGFR, the bispecific ^{64}Cu-NOTA-Fab-PEG$_{24}$-EGF showed much greater tumor uptake (4.9% ID/g at 48 h p. i.) than those of the radiolabeled Fab (against HER2) and EGF monomers (1.9% ID/g and 0.7% ID/g, respectively). The highest uptake of ^{64}Cu-NOTA-Fab-PEG$_{24}$-EGF in normal organs was observed in the kidney with 25 ± 4.2% ID/g. Further investigation is needed to evaluate the ability of PET imaging with ^{64}Cu-NOTA-Fab-PEG$_{24}$-EGF to predict treatment response (efficacy) in HER2-and EGFR-directed therapies.

T-Cell/CEA

Another bispecific agent is the AMG211, a T-cell engager antibody construct used in phase I trials for targeting carcinoembryonic antigen (CEA) (Kebenko et al., 2018; Pishvaian et al., 2016), an established therapeutic target in a number of solid tumors, including breast cancer (Tang et al., 2016, Wang et al., 2017). A PET companion diagnostic agent for AMG211 was recently developed by radiolabeling the antibody with ^{89}Zr to obtain ^{89}Zr-AMG211 (Antibodies, **Figure 2**) (Waaijer et al., 2018). Tumor uptake of ^{89}Zr-AMG211 in CEA-positive BT-474 xenograft models was 3.8 ± 1.1% ID/g with T/B ratio of about 10 at 24 h p. i., while uptake was significantly lower in the CEA-negative HL-60 xenograft models ($p < 0.01$). A major drawback of this imaging agent is its extremely high uptake in the kidneys (~150% ID/g).

EGFR/C-MET

Amivantamab is a new bispecific antibody with multiple mechanisms of action, including inhibition of the EGFR and the hepatocyte growth factor receptor (HGFR/c-MET) pathways (Moores et al., 2016). In a recent report it was radiolabeled with ^{89}Zr via a desferrioxamine chelate (DFO) to create a companion diagnostic imaging agent for this bispecific antibody (Cavaliere et al., 2020) (Bispecific antibodies, **Figure 2**). As overexpression of EGFR and c-MET was found in TNBC and associated with progression of the disease, the resulting [^{89}Zr]ZrDFO-amivantamab radioconjugate was evaluated in TNBC xenograft models (Cavaliere et al., 2020; Chae et al., 2016). Three xenografts were used, MDA-MB-468, MDA-MB-231, and MDA-MB-453, which are characterized by high, moderate, and negative co-expression of EGFR and c-MET, respectively (**Figure 5**). PET/CT imaging with [^{89}Zr]ZrDFO-amivantamab showed its ability to detect graded levels of EGFR and c-MET with standard uptake values (SUV_{mean}) of 6.0 ± 1.1, 4.2 ± 1.4, 1.5 ± 1.4 96 h p. i. in MDA-MB-468, MDA-MB-231, and MDA-MB-453, respectively (**Figure 5**) (Cavaliere et al., 2020). Further, tumor uptake of [^{89}Zr]ZrDFO-amivantamab was significantly higher than those of the radiolabeled single-arm parent antibodies [^{89}Zr]ZrDFO-α-EGFR or [^{89}Zr]ZrDFO-α-c-MET. This imaging agent has the potential to be clinically translated to provide a more quantitative assessment of the total expression of EGFR and c-MET for patient selection in clinical trials that evaluate the efficacy of amivantamab.

As more bispecific agents are being developed to overcome resistance and limitations associated with mono-targeted therapies, there is an increasing need for development of their companion diagnostic imaging agents. Molecular imaging has the potential to accelerate the development of novel bispecific constructs by predicting response and selecting patients most likely to benefit from these dual-targeted therapies.

PRECLINICAL TARGETED THERAPY AGENTS FOR BREAST CANCER

The two strategies to incorporate cytotoxic payloads into targeting agents are to conjugate non-specific cytotoxic drugs, and to attach radioisotopes that emit DNA-damaging energy. These targeting agents typically employ peptides and antibodies, as they can be chemically modified with the cytotoxic payloads while maintaining their pharmacokinetic properties and specific binding to target proteins on the surface of cancer cells. These vehicles may internalize in the cancer cell once bound to the target protein and deliver their cytotoxic payload.

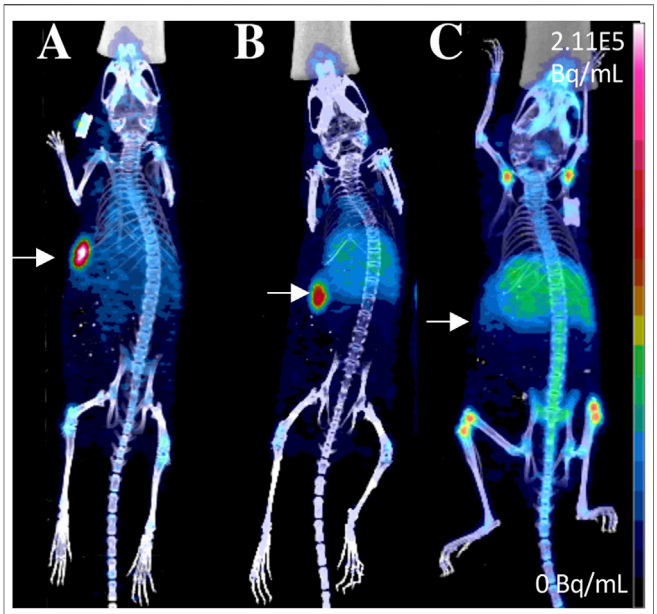

FIGURE 5 | PET/CT imaging of [^{89}Zr]ZrDFO-Amivantamab in MDA-MB-468 **(A)**, MDA-MB-231 **(B)** and MDA-MB-453 **(C)** xenografts of TNBC at 96 h p. i. Tumors are marked with arrows (Cavaliere et al., 2020). The general structure of [^{89}Zr]ZrDFO-Amivantamab was shown in **Figure 2H**.

Targeted Radionuclide Therapy

Targeted radionuclide therapy (TRT) combines the specificity of targeting molecules and the cytotoxicity of ionizing radiation as an approach to overcome resistance to other drugs (Gill et al., 2017). The diverse combinations of targeting molecules and radioisotopes provide flexible choices in the treatment of the different molecular subtypes of breast cancer for both primary and metastatic disease.

There are three types of radiation related to TRT: β-particles, α particles, and Auger electrons, which can irradiate volumes with multicellular, cellular, and subcellular dimensions, respectively (Gill et al., 2017). The β-emitters are considered ideal for targeting large tumors due to their long range path length of 0.05–12.0 mm in tissue, and the ability to induce formation of radical species that are damaging to DNA (Pouget et al., 2011). The α emitters, with a short-range path length of 20–100 μm, has a high linear energy transfer and are ideal for treating micrometastases and blood or bone marrow malignancies (Dahle et al., 2007). Finally, Auger electrons have the shortest range of 1–23 μm and are suitable for targeting single cells (Ku et al., 2019b).

Recently, ^{177}Lu and ^{111}In have attracted the most attention for TRT of breast cancer. ^{177}Lu is a low-energy β-emitter (0.497 MeV_{max}) with tissue penetration of up to 1.6 mm, which considerably lowers the dosimetry (i.e., radiation dose to organs and whole body) for patients (Massicano et al.,

TABLE 2 | Preclinical targeted therapy agents for the different subtypes of breast cancer. Those with additional imaging properties are checked in the theranostics column.

Target	Agent	Structure	Imaging and therapy	Models	References
HER2-positive					
HER2	^{89}Zr-AF-*Lx*-trastuzumab	Antibody conjugate	√	JIMT-1	Sijbrandi et al. (2017)
	^{111}In-NLS-trastuzumab	Antibody-peptide conjugate	—	MDA-MB-361	Costantini et al. (2010)
	^{111}In-trastuzumab-DOX-APTES-PEG-SPIONs	Nanoparticles, antibody and chemotherapeutics	√	SK-BR-3	Zolata et al. (2015)
HER2 and EGFR	^{177}Lu-AuNPs-trastuzumab-panitumumab	Nanoparticle-antibody conjugate	—	MDA-MB-231-H2N; MDA-MB-468; BT-474	Yook et al. (2020)
Triple negative					
EGFR	^{111}In-bn-DTPA-nimotuzumab	Antibody	—	MDA-MB-468	Chan et al. (2020)
PSMA	^{177}Lu-PSMA-617/^{68}Ga-PSMA-11	Small molecule	√	MDA-MB-231	Morgenroth et al. (2019)
Subtype independent					
GRPR	^{177}Lu-DOTA-DN(PTX)-BN	Nanoparticle-peptide conjugate loaded with chemotherapeutics	√	T47D	Gibbens-Bandala et al. (2019a)
	^{177}Lu-BN-PLGA(PTX)	Nanoparticle-peptide conjugate loaded with chemotherapeutics	√	MDA-MB-231	Gibbens-Bandala et al. (2019b)
FA	^{99m}Tc-PEG-PAMAM G4-FA-5FU	Nanoparticle-peptide conjugate loaded with chemotherapeutics	√	MCF-7	Narmani et al. (2017)
Nucleolin	^{111}In-BnDTPA-F3	Peptide	√	MDA-MB-231-H2N	Cornelissen et al. (2012)

2018). The long half-life of ^{177}Lu (6.71 days) also provides advantages in production and transportation to facilities that do not have the capability to produce this radioisotope. In contrast, ^{111}In is an Auger electron with low-energy (<30 keV) and a very short path length of less than 10 μm, and must be delivered to the tumor cell nucleus to achieve maximum cell-killing ability via DNA double-strand breaks (Valkema et al., 2002; Boswell and Brechbiel, 2005). The radiopharmaceuticals based on Auger electrons can be enhanced by increasing nuclear localization, either by attaching a peptide with an nuclear localization sequence (NLS) (Costantini et al., 2010), or co-administer with other pharmaceuticals capable of intensifying nuclear localization (Bailey et al., 2007). In this section, we review examples of new antibody drug conjugates and TRT in breast cancer, as listed in **Table 2**.

HER2-Positive Breast Cancer

Many kinds of HER2-directed agents have been labeled with different radionuclides and previously reviewed (Massicano et al., 2018). Here, we summarize recent strategies on the preclinical development of HER2-targeted therapy agents not discussed by Massicano et al.

Sijbrandi et al. used a novel strategy of conjugating an ethylenediamine platinum (*Lx*) to trastuzumab (Sijbrandi et al., 2017), with the expected effects of improved aqueous solubility for the *Lx*-payload complexes and the *Lx* able to coordinate to unique amino acids, including methionines, cysteines, and histidines, which is a valuable alternative to the currently used strategy of coupling to lysines and cysteines (Messori et al., 2014). In this study, auristatin F (AF) coordinated *Lx* was conjugated to trastuzumab and radiolabeled with ^{89}Zr to obtain the companion diagnostic agent, ^{89}Zr-AF-*Lx*-trastuzumab. The therapeutic efficacy of AF-*Lx*-trastuzumab was evaluated in HER2-positive and trastuzumab resistant JIMT-1 xenograft models. All tumors regressed completely with no regrowth observed until the end of the experiment at day 125, indicating that all xenografted tumors had complete response in mice treated with AF-*Lx*-trastuzumab. In contrast, only 25% of mice had complete response when treated with the ado-trastuzumab emtansine (T-DM1) control. The therapeutic efficacy of AF-*Lx*-trastuzumab demonstrates its superiority over the T-DM1 standard-of-care. While these results are promising, toxicity studies in higher species are needed before translation to clinical evaluation.

An ^{111}In-labeled trastuzumab was modified with the nuclear localization sequence (NLS) peptides (CGYGPKKKRKVGG) to obtain ^{111}In-NLS-trastuzumab (Costantini et al., 2010). Tumor growth was delayed in the HER2-positive MDA-MB-361 xenografts treated with a single dose of ^{111}In-NLS-trastuzumab (9.25 MBq, 4 mg/kg). On the contrary, ^{111}In-NLS-trastuzumab had no effect on tumor growth of the HER2-negative MDA-MB-231 xenografts. When two doses (9.25 MBq, 4 mg/kg) of ^{111}In-NLS-trastuzumab were administered two weeks apart, the survival time of MDA-MB-361 xenograft models was significantly prolonged and 50% of the tumors (3 of 6 mice) regressed completely. Based on these results, ^{111}In-NLS-trastuzumab achieved high targeted radiotherapeutic efficacy in HER2-positive tumors.

Nanotechnology represents a hot area in drug delivery research. Superparamagnetic iron oxide nanoparticles (SPIONs) with appropriate surface modification have been

widely used for biomedical applications. For example, SPIONs decorated with trastuzumab-doxorubicin (DOX) conjugate and labeled with ^{111}In were evaluated as a theranostic agent in HER2-positive SK-BR-3 xenograft models (Zolata et al., 2015). Tumor uptake of the ^{111}In-labeled SPIONs was 13 ± 0.76% ID/g with T/B ratio of 10 at 48 h p. i. After treatment with ^{111}In-labeled trastuzumab-DOX conjugated SPIONs, tumor volumes were reduced by 36% in 3 weeks, while the tumor volumes of the control group were 4-fold larger than those in the treated group. Therapeutic efficacy was increased due to appropriate surface modification on SPIONs to prolong circulation time, specific targeting by trastuzumab, controlled DOX release, and Auger electrons and gamma rays of the ^{111}In radionuclide.

Recent studies reported that trastuzumab resistance in HER2-positive cells might be due to activation of the EGFR pathway and hence increased EGFR protein expression. The heterodimers formed between EGFR and HER2 may circumvent the anti-tumor effects of HER2-targeted therapies. A bispecific agent ^{177}Lu-AuNPs-trastuzumab-panitumumab was developed to overcome resistance to trastuzumab by targeting both HER2 and EGFR simultaneously (Yook et al., 2020). This dual-receptor-targeted agent was specifically bound and internalized by breast cancer cells that expressed HER2, or EGFR, or both, and showed high absorbed radiation doses with 36–119 Gy in the cell nucleus treated with ^{177}Lu-AuNPs-trastuzumab-panitumumab. Although the study was conducted *in vitro*, this agent is promising for further evaluation *in vivo* in breast cancer xenografts.

Triple-Negative Breast Cancer

One potential strategy to overcome drug resistance in TNBC is to combine mAbs with therapeutic radionuclides. Nimotuzumab is a mAb that binds to EGFR and clinically used in several countries for the treatment of epithelial-derived tumors that overexpress EGFR (Mazorra et al., 2018). In one recent study, ^{111}In-Bn-DTPA-nimotuzumab (Antibodies, **Figure 2**) was prepared by conjugating nimotuzumab to benzyl isothiocyanate DTPA (Bn-DTPA) and radiolabeling with ^{111}In, and evaluated in MDA-MB-468 xenograft models (Chan et al., 2020). Therapeutic efficacy was demonstrated by its enhanced inhibition of tumor growth, where the tumor doubling ratio of MDA-MB-468 xenografts was about 2-fold longer than those treated with the unlabeled Bn-DTPA-nimotuzumab or saline. ^{111}In-Bn-DTPA-nimotuzumab may provide an alternative strategy for targeted treatment of TNBC. This approach might be beneficial to the basal-like subtype of TNBC, whose gene expression profiles suggest sensitivity to therapies that employ DNA damage mechanisms (Lehmann et al., 2011).

Prostate-specific membrane antigen (PSMA) is an established target for theranostics of prostate cancer, but a potential new target for breast cancer. A recent study reported that PSMA was expressed in tumor cells and tumor-associated neovasculature of primary breast cancer and distant metastases, while normal breast tissues expressed PSMA only in the glandular cells (Kasoha et al., 2017). One recent study evaluated the efficacy of radiolabeled PSMA-ligand in TNBC models (Morgenroth et al., 2019). High specific tumor uptake of ^{68}Ga-PSMA-11 was shown in MDA-MB-231 xenografts with T/B ratio of 43.3 ± 0.9 at 30 min p. i., while tumor uptake in the control MCF-7 xenografts was negligible, with T/B ratio of 1.1 ± 0.1 (**Figure 6**). The MDA-MB-231 cells showed a high pro-angiogenic potential on tube formation of endothelial huvec cells. ^{177}Lu-PSMA-617 strongly impaired the vitality and angiogenic potential of MDA-MB -231 medium-conditioned HUVEC cells. This study presented the rationale for PSMA-targeted therapy for TNBC.

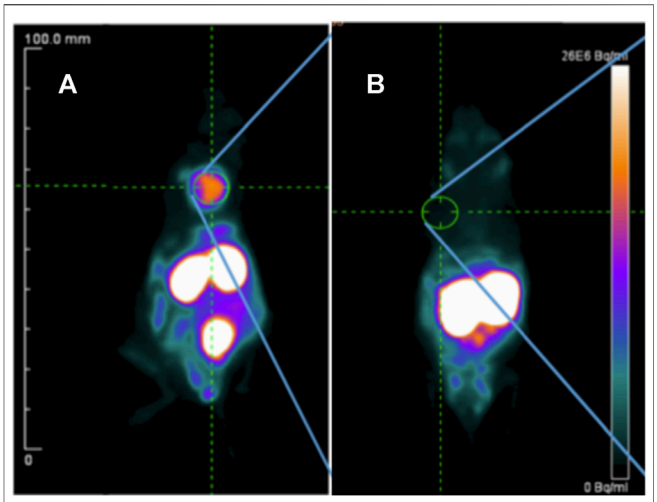

FIGURE 6 | PET imaging of ^{68}Ga-PSMA-11 in MDA-MB-231 **(A)** and MCF-7 **(B)** xenografts at 30 min post-injection (Morgenroth et al., 2019).

Subtype-Independent Therapy Agents

The peptide-receptor radionuclide therapy (PRRT) is an approach that uses radiolabeled peptides that bind to receptors on the surface of cancer cells for specific delivery of ionizing radiation. Since GRPR are overexpressed across all subtypes of breast cancer, PRRT of GRPR might have a more general application for breast cancer treatment. To increase the stability of the targeting peptide, nanoparticles have been increasingly used as drug delivery vehicles. A nanosystem based on the ^{177}Lu-labeled polyamidoamine (PAMAM) dendrimer (DN) loaded with paclitaxel (PTX) and functionalized on the surface with the DOTA-BBN peptide was designed for specific targeting to GRPR in T47D breast cancer xenografts (Gibbens-Bandala et al., 2019a). The ^{177}Lu-DOTA-DN(PTX)-BBN nanoconjugate had significant uptake and internalization in T47D cells, with an estimated absorbed radiation dose of 3.0 Gy/MBq at infinite time. Tumor uptake of ^{177}Lu-DOTA-DN(PTX)-BBN was about 35% ID/g at 120 h p. i., with a corresponding reduction in tumor volume by 16% (**Figure 7**). Another nanoparticle, poly lactic-co-glycolic acid (PLGA), was also evaluated for delivery of drugs and radiation (Gibbens-Bandala et al., 2019b). A PTX-loaded PLGA was conjugated to DOTA-BBN, labeled with ^{177}Lu, and tested in MDA-MB-231 xenografts. The ^{177}Lu-BBN-PLGA (PTX) treated group showed the lowest tumor proliferation and strongest inhibition of tumor growth among the other control groups. The average absorbed radiation dose in the tumor was 37 ±

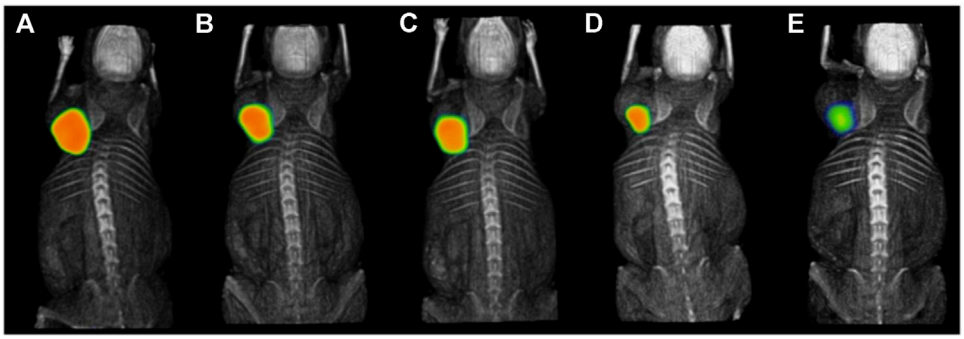

FIGURE 7 | Intratumoral administration of ^{177}Lu-DOTA-DN(PTX)-BN after 1.5 h **(A)**, 9 h **(B)**, 10 h **(C)**, 24 h **(D)**, and 120 h **(E)** in T47D xenograft model (Gibbens-Bandala et al., 2019a). The general structure of ^{177}Lu-DOTA-DN(PTX)-BN was shown in **Figure 2I**.

7.0 Gy. These two nanosystems both exhibited enhanced therapeutic efficacy due to β-radiation from ^{177}Lu and controlled release of PTX. Another example of ^{177}Lu-labeled nanosystem is a dendrimer conjugated to folate and BBN with gold nanoparticles in the dendritic cavity (Mendoza-Nava et al., 2017). The bispecific ^{177}Lu-DenAuNP-FA-BBN showed high absorbed radiation dose with 63 ± 4.2 Gy delivered to T47D cells. Further studies are needed to evaluate its therapeutic efficacy *in vivo*. Taken together, these strategies of using ^{177}Lu-labeled chemotherapeutic drug-loaded nanosystems with BBN peptides for combined targeted therapy have shown promise in their application to GRPR-positive breast cancers.

Besides the classic breast cancer targets, such as ER, PR, HER2, EGFR, and recently, GRPR, other targets such as FA and nucleolin have also shown some promise for theranostics of breast cancer. A drug delivery nanosystem based on ^{99m}Tc-labeled 5-fluorouracil (5-FU)-loaded and FA-functionalized PAMAM G4 dendrimer (^{99m}Tc-PEG-PAMAM G4-FA-5FU) was designed for chemotherapy delivery to FA-overexpressing tumors with ^{99m}Tc serving as the SPECT reporter for this treatment, and high tumor uptake of the agent in MCF-7 xenografts (Narmani et al., 2017).

An ^{111}In-labeled F3 peptide (Peptides, **Figure 2**), which is a fragment of the human high mobility group protein 2-binding nucleolin, was developed to investigate the Auger electron-targeted radiotherapy in HER2-positive breast cancer xenograft models (Cornelissen et al., 2012). Animal treated with ^{111}In-BnDTPA-F3 showed significantly slower tumor growth and longer survival time. SPECT imaging is feasible with this agent.

DISCUSSION AND PERSPECTIVES

In the era of precision medicine, theranostic agents are becoming increasingly important for selecting breast cancer patients most likely to benefit from targeted treatments through imaging and offering more options for effective treatments in this heterogenous disease. In this review, we highlight many imaging probes for novel targets with potential for translation to clinical studies. Among the different targets discussed for breast cancer imaging, the GRPR is the most promising novel target in our opinion. GRPR is reported to be overexpressed in 96% of breast cancer tissues across all molecular subtypes of breast cancer. The GRPR-targeted agents for both imaging and therapy achieved excellent tumor uptake, such as ^{111}In-JMV4168 for luminal-subtype imaging (Dalm et al., 2015), ^{68}Ga-NOTA-PEG$_3$-RM26 for HER2-subtype imaging (Varasteh et al., 2014), ^{99m}Tc-BN4 for TNBC imaging (De et al., 2019), ^{177}Lu-DOTA-DN(PTX)-BN for luminal-subtype therapy (Gibbens-Bandala et al., 2019a), and ^{177}Lu-BN-PLGA (PTX) for TNBC therapy (Gibbens-Bandala et al., 2019b). These independent studies indicate that GRPR is a highly promising target for theranostics of breast cancer.

Additionally, there are many targeted small molecule inhibitors under clinical trials for the treatment of breast cancer, such as the CDK4/6 inhibitor palbociclib (Song et al., 2019; Gan et al., 2020; Ramos et al., 2020), the PI3K/Akt/mTOR pathway inhibitor pictilisib (Altine et al., 2019; Han et al., 2019), the HDAC inhibitor CUDC-101 (Meng et al., 2013). The radiolabeled analogs of these small molecule inhibitors that we described in this review showed high tumor uptake in breast cancer xenografts. These agents may provide a non-invasive diagnostic imaging tool to monitor the responses to their therapeutic equivalents.

Recently, dual-receptor targeted strategies have attracted increasing attention in heterogeneous subtypes of breast cancer imaging within primary and metastatic lesions. One of the reasons for their success is that bispecific constructs targeting two receptors can help to overcome drug resistance associated with mono-targeted therapies (Thakur et al., 2018). Different bispecific imaging and/or theranostic agents have also been developed, notably the scaffolds targeting GRPR/FA and EGFR/c-MET with ^{99m}Tc/^{177}Lu-BBN-FA (Aranda-Lara et al., 2016a; Aranda-Lara et al., 2016b) and [^{89}Zr]ZrDFO-amivantamab (Cavaliere et al., 2020), respectively. These agents hold potential for clinical translation due to the high expression of targets in several molecular subtypes of breast cancer and the promise to overcome resistance to mono-targeted therapy due to their multiple mechanisms of action. Overall, a significant progress has been made in pursing novel targets for breast cancer imaging.

Although the studies mentioned above have shown promising results in rodent xenografts and in the setting of primary breast cancer, most of them did not focus on metastatic models. Of all the studies we reviewed, only ^{68}Ga-NGR-RGD was evaluated in a lung metastasis model of breast cancer (Gai et al., 2020). The most typical sites of metastatic breast cancer are regional lymph nodes, bone, liver, lung, and brain (Jin et al., 2018). Hence, a good imaging agent should reach these organs, but there are still many challenges to overcome. For instance, a high liver uptake, commonly seen in PET and SPECT imaging with tracers that are metabolized in the liver, such as ^{99m}Tc-DTPA-estradiol (Xia et al., 2016), ^{99m}Tc-labeled palbociclib analogs (^{99m}Tc-L2 to L5) (Song et al., 2019), and ^{11}C-pictilisib (Han et al., 2019), may be insensitive in detecting liver metastasis. Thus, future studies should make more efforts into evaluating imaging agents in the metastatic setting.

Crossing the blood-brain barrier (BBB) represents another dilemma for detecting brain metastasis. The BBB with its tight junctions limits the passage of large molecules from the blood to the brain (Deeken and Löscher, 2007). In addition, there are various efflux transporters expressed in the BBB, including P-glycoprotein and breast cancer resistance protein, which contribute to restrict the entry of potentially therapeutic agents (de Vries et al., 2007). A recent study reported that trastuzumab conjugated with melanotransferrin may help treat brain metastasis, and melanotransferrin may be a potential delivery vehicle to increase antibody transport across the BBB (Nounou et al., 2016).

A limitation of the preclinical studies we introduced above is that they all used animal xenograft models due to poor or no cross-reactivity to mouse antigens. While these animal models allow for a convenient method to determine specificity *in vivo* for human targets, they do not capture accurate biodistribution to normal organs, which pose challenges with using rodents for dosimetry estimates for clinical translation. Nevertheless, companion imaging agents such as those described in this review have the potential to predict and monitor response to treatment, especially for the diverse molecular subtypes in breast cancer. The preclinical studies described in this review showed promising results of targeted imaging in breast cancer xenografts. Validation in human studies warrants further investigation.

With regard to TRT, ^{177}Lu is a widely used radionuclide due to its relatively long-range in tissues (Massicano et al., 2018), which allows a cross-fire effect with the surrounding cells into the tumor. ^{111}In can exhibit high therapeutic efficacy after being delivered to the tumor cell nucleus to maximize the cell-killing ability with the methods of attaching nuclear localization sequence (NLS) peptides, such as ^{111}In-NLS-trastuzumab (Costantini et al., 2010), and co-administration with other pharmaceuticals including mAbs such as ^{111}In-Bn-DTPA-nimotuzumab (Chan et al., 2020).

Another useful tool for drug delivery is nanosystems, especially to deliver chemotherapeutic drugs, mAbs, or their combination, such as ^{111}In-trastuzumab-DOX-SPIONs (Zolata et al., 2015), ^{177}Lu-AuNPs-trastuzumab-panitumumab (Yook et al., 2020), and ^{177}Lu-DOTA-DN(PTX)-BBN (Gibbens-Bandala et al., 2019a). TRT combined with chemotherapy or antibodies have proven to be beneficial to breast cancer treatment. Although the tumor uptake and absorbed radiation dose might vary considerably between different patients, precision medicine for breast cancer patients may help to make TRT more effective and reduce normal tissue toxicity.

CONCLUSION

Targeted imaging and therapy using nuclear medicine methods show promise for precision medicine for patients with breast cancer. Molecular imaging can help with diagnosis, staging, guiding treatment, and predicting response to corresponding targeted therapy. Many studies discussed here have made great contributions in the investigation of new strategies and new agents for breast cancer imaging and therapy. A series of new targets have been found to be valuable for potentially overcoming resistance to standard of care treatments. These new investigations are inspiring in preclinical studies. We look forward to seeing more studies advance to clinical trials in the near future.

DATA AVAILABILITY STATEMENT

The original contributions presented in the study are included in the article/Supplementary Material, further inquiries can be directed to the corresponding author.

AUTHOR CONTRIBUTIONS

HF, AC, and ZL wrote and edited the manuscript. YH and BM-N edited the manuscript. All authors read and approved the final manuscript.

FUNDING

HF is supported by the China Scholarship Council (No. 201906160034).

REFERENCES

Altine, B., Gai, Y., Han, N., Jiang, Y., Ji, H., Fang, H., et al. (2019). Preclinical evaluation of a fluorine-18 (^{18}F)-Labeled phosphatidylinositol 3-kinase inhibitor for breast cancer imaging. *Mol. Pharmaceutics* 16 (11), 4563–4571. doi:10.1021/acs.molpharmaceut.9b00690

Andersson, K. G., Rosestedt, M., Varasteh, Z., Malm, M., Sandström, M., Tolmachev, V., et al. (2015). Comparative evaluation of ^{111}In-labeled NOTA-conjugated affibody molecules for visualization of HER3 expression in malignant tumors. *Oncol. Rep.* 34 (2), 1042–1048. doi:10.3892/or.2015.4046

Apostolopoulos, V., Pietersz, G. A., Tsibanis, A., Tsikkinis, A., Drakaki, H., Loveland, B. E., et al. (2006). Pilot phase III immunotherapy study in early-

stage breast cancer patients using oxidized mannan-MUC1 [ISRCTN71711835]. *Breast Cancer Res.* 8 (3), R27. doi:10.1186/bcr1505

Aranda-Lara, L., Ferro-Flores, G., Azorín-Vega, E., Ramírez, F. d. M., Jiménez-Mancilla, N., Ocampo-García, B., et al. (2016a). Synthesis and evaluation of Lys 1 (α,γ-Folate)Lys 3 (^{177}Lu-DOTA)-Bombesin(1-14) as a potential theranostic radiopharmaceutical for breast cancer. *Appl. Radiat. Isot.* 107, 214–219. doi:10.1016/j.apradiso.2015.10.030

Aranda-Lara, L., Ferro-Flores, G., Ramírez, F. d. M., Ocampo-García, B., Santos-Cuevas, C., Díaz-Nieto, L., et al. (2016b). Improved radiopharmaceutical based on ^{99m}Tc-Bombesin-folate for breast tumour imaging. *Nucl. Med. Commun.* 37 (4), 377–386. doi:10.1097/mnm.0000000000000460

Bader, A. G., Kang, S., Zhao, L., and Vogt, P. K. (2005). Oncogenic PI3K deregulates transcription and translation. *Nat. Rev. Cancer* 5 (12), 921–929. doi:10.1038/nrc1753

Bailey, K. E., Costantini, D. L., Cai, Z., Scollard, D. A., Chen, Z., Reilly, R. M., et al. (2007). Epidermal growth factor receptor inhibition modulates the nuclear localization and cytotoxicity of the Auger electron emitting radiopharmaceutical ^{111}In-DTPA human epidermal growth factor. *J. Nucl. Med.* 48 (9), 1562–1570. doi:10.2967/jnumed.107.044073

Baratto, L., Duan, H., Mäcke, H., and Iagaru, A. (2020). Imaging the distribution of gastrin-releasing peptide receptors in cancer. *J. Nucl. Med.* 61 (6), 792–798. doi:10.2967/jnumed.119.234971

Bardia, A., Mayer, I. A., Vahdat, L. T., Tolaney, S. M., Isakoff, S. J., Diamond, J. R., et al. (2019). Sacituzumab govitecan-hziy in refractory metastatic triple-negative breast cancer. *N. Engl. J. Med.* 380 (8), 741–751. doi:10.1056/NEJMoa1814213

Bianchini, G., Balko, J. M., Mayer, I. A., Sanders, M. E., and Gianni, L. (2016). Triple-negative breast cancer: challenges and opportunities of a heterogeneous disease. *Nat. Rev. Clin. Oncol.* 13 (11), 674–690. doi:10.1038/nrclinonc.2016.66

Blasco-Benito, S., Seijo-Vila, M., Caro-Villalobos, M., Tundidor, I., Andradas, C., García-Taboada, E., et al. (2018). Appraising the "entourage effect": antitumor action of a pure cannabinoid versus a botanical drug preparation in preclinical models of breast cancer. *Biochem. Pharmacol.* 157, 285–293. doi:10.1016/j.bcp.2018.06.025

Bolden, J. E., Peart, M. J., and Johnstone, R. W. (2006). Anticancer activities of histone deacetylase inhibitors. *Nat. Rev. Drug Discov.* 5 (9), 769–784. doi:10.1038/nrd2133

Boswell, C. A., and Brechbiel, M. W. (2005). Auger electrons: lethal, low energy, and coming soon to a tumor cell nucleus near you. *J. Nucl. Med.* 46 (12), 1946–1947.

Bottai, G., Truffi, M., Corsi, F., and Santarpia, L. (2017). Progress in nonviral gene therapy for breast cancer and what comes next? *Expert Opin. Biol. Ther.* 17 (5), 595–611. doi:10.1080/14712598.2017.1305351

Bouchalova, K., Svoboda, M., Kharaishvili, G., Vrbkova, J., Bouchal, J., Trojanec, R., et al. (2015). BCL2 is an independent predictor of outcome in basal-like triple-negative breast cancers treated with adjuvant anthracycline-based chemotherapy. *Tumor Biol.* 36 (6), 4243–4252. doi:10.1007/s13277-015-3061-7

Callander, N. S., Varki, N., and Vijaya Rao, L. M. (1992). Immunohistochemical identification of tissue factor in solid tumors. *Cancer* 70 (5), 1194–1201. doi:10.1002/1097-0142(19920901)70:5<1194::aid-cncr2820700528>3.0.co;2-e

Cancer-Genome-Atlas-Network (2012). Comprehensive molecular portraits of human breast tumours. *Nature* 490 (7418), 61–70. doi:10.1038/nature11412

Carey, J. P. W., Karakas, C., Bui, T., Chen, X., Vijayaraghavan, S., Zhao, Y., et al. (2018). Synthetic lethality of PARP inhibitors in combination with MYC blockade is independent of BRCA status in triple-negative breast cancer. *Cancer Res.* 78 (3), 742–757. doi:10.1158/0008-5472.CAN-17-1494

Cavaliere, A., Sun, S., Lee, S., Bodner, J., Li, Z., Huang, Y., et al. (2020). Development of [^{89}Zr]ZrDFO-amivantamab bispecific to EGFR and c-MET for PET imaging of triple-negative breast cancer. *Eur. J. Nucl. Med. Mol. Imaging* 48, 383. doi:10.1007/s00259-020-04978-6

Chae, Y. K., Gagliato, D. d. M., Pai, S. G., Carneiro, B., Mohindra, N., Giles, F. J., et al. (2016). The association between EGFR and cMET expression and phosphorylation and its prognostic implication in patients with breast cancer. *PLoS One* 11 (4), e0152585. doi:10.1371/journal.pone.0152585

Chan, C., Fonge, H., Lam, K., and Reilly, R. M. (2020). Effectiveness and normal tissue toxicity of Auger electron (AE) radioimmunotherapy (RIT) with [^{111}In]In-Bn-DTPA-nimotuzumab in mice with triple-negative or trastuzumab-resistant human breast cancer xenografts that overexpress EGFR. *Nucl. Med. Biol.* 80-81, 37–44. doi:10.1016/j.nucmedbio.2019.10.001

Chen, X., Mangala, L. S., Rodriguez-Aguayo, C., Kong, X., Lopez-Berestein, G., and Sood, A. K. (2018). RNA interference-based therapy and its delivery systems. *Cancer Metastasis Rev.* 37 (1), 107–124. doi:10.1007/s10555-017-9717-6

Chun, K.-H., Park, J. H., and Fan, S. (2017). Predicting and overcoming chemotherapeutic resistance in breast cancer. *Adv. Exp. Med. Biol.* 1026, 59–104. doi:10.1007/978-981-10-6020-5_4

Cooper, T. M., Sison, E. A. R., Baker, S. D., Li, L., Ahmed, A., Trippett, T., et al. (2017). A phase 1 study of the CXCR4 antagonist plerixafor in combination with high-dose cytarabine and etoposide in children with relapsed or refractory acute leukemias or myelodysplastic syndrome: a Pediatric Oncology Experimental Therapeutics Investigators' Co. *Pediatr. Blood Cancer* 64 (8), e26414. doi:10.1002/pbc.26414

Cornelissen, B., Waller, A., Target, C., Kersemans, V., Smart, S., and Vallis, K. A. (2012). ^{111}In-BnDTPA-F3: an Auger electron-emitting radiotherapeutic agent that targets nucleolin. *EJNMMI Res.* 2, 9. doi:10.1186/2191-219X-2-9

Costantini, D. L., McLarty, K., Lee, H., Done, S. J., Vallis, K. A., and Reilly, R. M. (2010). Antitumor effects and normal-tissue toxicity of ^{111}In-nuclear localization sequence-trastuzumab in athymic mice bearing HER-positive human breast cancer xenografts. *J. Nucl. Med.* 51 (7), 1084–1091. doi:10.2967/jnumed.109.072389

Cowherd, S., Miller, L. D., Melin, S. A., Akman, S., Isom, S., Cole, J., et al. (2015). A phase II clinical trial of weekly paclitaxel and carboplatin in combination with panitumumab in metastatic triple negative breast cancer. *Cancer Biol. Ther.* 16 (5), 678–683. doi:10.1080/15384047.2015.1026481

Cyprian, F. S., Akhtar, S., Gatalica, Z., and Vranic, S. (2019). Targeted immunotherapy with a checkpoint inhibitor in combination with chemotherapy: a new clinical paradigm in the treatment of triple-negative breast cancer. *Bosn J. Basic Med. Sci.* 19 (3), 227–233. doi:10.17305/bjbms.2019.4204

Dahle, J., Borrebæk, J., Jonasdottir, T. J., Hjelmerud, A. K., Melhus, K. B., Bruland, Ø. S., et al. (2007). Targeted cancer therapy with a novel low-dose rate α-emitting radioimmunoconjugate. *Blood* 110 (6), 2049–2056. doi:10.1182/blood-2007-01-066803

Dahr, S. S., Cusick, M., Rodriguez-Coleman, H., Srivastava, S. K., Thompson, D. J., Linehan, W. M., et al. (2007). Intravitreal anti-vascular endothelial growth factor therapy with pegaptanib for advanced von Hippel-Lindau disease of the retina. *Retina* 27 (2), 150–158. doi:10.1097/IAE.0b013e318030a290

Dai, X., Cheng, H., Bai, Z., and Li, J. (2017). Breast cancer cell line classification and its relevance with breast tumor subtyping. *J. Cancer* 8 (16), 3131–3141. doi:10.7150/jca.18457

Dalm, S. U., Martens, J. W. M., Sieuwerts, A. M., van Deurzen, C. H. M., Koelewijn, S. J., de Blois, E., et al. (2015). *In vitro* and *in vivo* application of radiolabeled gastrin-releasing peptide receptor ligands in breast cancer. *J. Nucl. Med.* 56 (5), 752–757. doi:10.2967/jnumed.114.153023

De, K., Mukherjee, D., Sinha, S., and Ganguly, S. (2019). HYNIC and DOMA conjugated radiolabeled bombesin analogs as receptor-targeted probes for scintigraphic detection of breast tumor. *EJNMMI Res.* 9 (1), 25. doi:10.1186/s13550-019-0493-x

de Vries, E. G. E., Kist de Ruijter, L., Lub-de Hooge, M. N., Dierckx, R. A., Elias, S. G., and Oosting, S. F. (2019). Integrating molecular nuclear imaging in clinical research to improve anticancer therapy. *Nat. Rev. Clin. Oncol.* 16 (4), 241–255. doi:10.1038/s41571-018-0123-y

de Vries, N. A., Zhao, J., Kroon, E., Buckle, T., Beijnen, J. H., and van Tellingen, O. (2007). P-glycoprotein and breast cancer resistance protein: two dominant transporters working together in limiting the brain penetration of topotecan. *Clin. Cancer Res.* 13 (21), 6440–6449. doi:10.1158/1078-0432.CCR-07-1335

Debordeaux, F., Chansel-Debordeaux, L., Pinaquy, J.-B., Fernandez, P., and Schulz, J. (2018). What about αvβ3 integrins in molecular imaging in oncology? *Nucl. Med. Biol.* 62-63, 31–46. doi:10.1016/j.nucmedbio.2018.04.006

Deeken, J. F., and Löscher, W. (2007). The blood-brain barrier and cancer: transporters, treatment, and Trojan horses. *Clin. Cancer Res.* 13 (6), 1663–1674. doi:10.1158/1078-0432.CCR-06-2854

Doran, M. G., Carnazza, K. E., Steckler, J. M., Spratt, D. E., Truillet, C., Wongvipat, J., et al. (2016). Applying ^{89}Zr-transferrin to study the pharmacology of inhibitors to BET bromodomain containing proteins. *Mol. Pharmaceutics* 13 (2), 683–688. doi:10.1021/acs.molpharmaceut.5b00882

Dua, R., Zhang, J., Nhonthachit, P., Penuel, E., Petropoulos, C., and Parry, G. (2010). EGFR over-expression and activation in high HER2, ER negative breast cancer cell line induces trastuzumab resistance. *Breast Cancer Res. Treat.* 122 (3), 685–697. doi:10.1007/s10549-009-0592-x

Ehlerding, E. B., Sun, L., Lan, X., Zeng, D., and Cai, W. (2018). Dual-targeted molecular imaging of cancer. *J. Nucl. Med.* 59 (3), 390–395. doi:10.2967/jnumed.117.199877

Erdmann, S., Niederstadt, L., Koziolek, E. J., Gómez, J. D. C., Prasad, S., Wagener, A., et al. (2019). CMKLR1-targeting peptide tracers for PET/MR imaging of breast cancer. *Theranostics* 9 (22), 6719–6733. doi:10.7150/thno.34857

Erspamer, V., Erspamer, G. F., and Inselvini, M. (1970). Some pharmacological actions of alytesin and bombesin. *J. Pharm. Pharmacol.* 22 (11), 875–876. doi:10.1111/j.2042-7158.1970.tb08465.x

Eyetech-Study-Group (2002). Preclinical and phase 1A clinical evaluation of an anti-VEGF pegylated aptamer (EYE001) for the treatment of exudative age-related macular degeneration. *Retina (Philadelphia, Pa)* 22 (2), 143–152. doi:10.1097/00006982-200204000-00002

Falkenberg, K. J., and Johnstone, R. W. (2014). Histone deacetylases and their inhibitors in cancer, neurological diseases and immune disorders. *Nat. Rev. Drug Discov.* 13 (9), 673–691. doi:10.1038/nrd4360

Finn, R. S., Martin, M., Rugo, H. S., Jones, S., Im, S.-A., Gelmon, K., et al. (2016). Palbociclib and letrozole in advanced breast cancer. *N. Engl. J. Med.* 375 (20), 1925–1936. doi:10.1056/NEJMoa1607303

Frigerio, B., Bizzoni, C., Jansen, G., Leamon, C. P., Peters, G. J., Low, P. S., et al. (2019). Folate receptors and transporters: biological role and diagnostic/therapeutic targets in cancer and other diseases. *J. Exp. Clin. Cancer Res.* 38 (1), 125. doi:10.1186/s13046-019-1123-1

Fu, P., Shen, B., Zhao, C., and Tian, G. (2010). Molecular imaging of MDM2 messenger RNA with ^{99m}Tc-labeled antisense oligonucleotides in experimental human breast cancer xenografts. *J. Nucl. Med.* 51 (11), 1805–1812. doi:10.2967/jnumed.110.077982

Fu, P., Tian, L., Cao, X., Li, L., Xu, P., and Zhao, C. (2016). Imaging CXCR4 expression with ^{99m}Tc-radiolabeled small-interference RNA in experimental human breast cancer xenografts. *Mol. Imaging Biol.* 18 (3), 353–359. doi:10.1007/s11307-015-0899-4

Gai, Y., Jiang, Y., Long, Y., Sun, L., Liu, Q., Qin, C., et al. (2020). Evaluation of an integrin αvβ3 and aminopeptidase N dual-receptor targeting tracer for breast cancer imaging. *Mol. Pharmaceutics* 17 (1), 349–358. doi:10.1021/acs.molpharmaceut.9b01134

Gan, Q., Song, X., Zhang, X., and Zhang, J. (2020). Preparation and evaluation of ^{99m}Tc-labeled HYNIC-palbociclib analogs for cyclin-dependent kinase 4/6-positive tumor imaging. *Eur. J. Med. Chem.* 188, 112032. doi:10.1016/j.ejmech.2019.112032

Gangangari, K. K., Váradi, A., Majumdar, S., Larson, S. M., Pasternak, G. W., and Pillarsetty, N. K. (2020). Imaging sigma-1 receptor (S1R) expression using iodine-124-labeled 1-(4-Iodophenyl)-3-(2-adamantyl)guanidine ([^{124}I]IPAG). *Mol. Imaging Biol.* 22 (2), 358–366. doi:10.1007/s11307-019-01369-8

Gherasim, C., Lofgren, M., and Banerjee, R. (2013). Navigating the B12 road: assimilation, delivery, and disorders of cobalamin. *J. Biol. Chem.* 288 (19), 13186–13193. doi:10.1074/jbc.R113.458810

Ghobrial, I. M., Liu, C. J., Zavidij, O., Azab, A. K., Baz, R., Laubach, J. P., et al. (2019). Phase I/II trial of the CXCR4 inhibitor plerixafor in combination with bortezomib as a chemosensitization strategy in relapsed/refractory multiple myeloma. *Am. J. Hematol.* 94 (11), 1244–1253. doi:10.1002/ajh.25627

Gibbens-Bandala, B., Morales-Avila, E., Ferro-Flores, G., Santos-Cuevas, C., Luna-Gutiérrez, M., Ramírez-Nava, G., et al. (2019a). Synthesis and evaluation of ^{177}Lu-DOTA-DN(PTX)-BN for selective and concomitant radio and drug-therapeutic effect on breast cancer cells. *Polymers* 11 (10), 1572. doi:10.3390/polym11101572

Gibbens-Bandala, B., Morales-Avila, E., Ferro-Flores, G., Santos-Cuevas, C., Meléndez-Alafort, L., Trujillo-Nolasco, M., et al. (2019b). ^{177}Lu-Bombesin-PLGA (paclitaxel): a targeted controlled-release nanomedicine for bimodal therapy of breast cancerLu-Bombesin-PLGA (paclitaxel): a targeted controlled-release nanomedicine for bimodal therapy of breast cancer. *Mater. Sci. Eng. C* 105, 110043. doi:10.1016/j.msec.2019.110043

Gill, M. R., Falzone, N., Du, Y., and Vallis, K. A. (2017). Targeted radionuclide therapy in combined-modality regimens. *Lancet Oncol.* 18 (7), e414–e423. doi:10.1016/S1470-2045(17)30379-0

Goodman, S. L., and Picard, M. (2012). Integrins as therapeutic targets. *Trends Pharmacol. Sci.* 33 (7), 405–412. doi:10.1016/j.tips.2012.04.002

Graat, H. C. A., Carette, J. E., Schagen, F. H. E., Vassilev, L. T., Gerritsen, W. R., Kaspers, G. J. L., et al. (2007). Enhanced tumor cell kill by combined treatment with a small-molecule antagonist of mouse double minute 2 and adenoviruses encoding p53. *Mol. Cancer Ther.* 6 (5), 1552–1561. doi:10.1158/1535-7163.MCT-06-0631

Halmos, G., Wittliff, J. L., and Schally, A. V. (1995). Characterization of bombesin/gastrin-releasing peptide receptors in human breast cancer and their relationship to steroid receptor expression. *Cancer Res.* 55 (2), 280–287.

Han, N., Jiang, Y., Gai, Y., Liu, Q., Yuan, L., Wang, Y., et al. (2019). ^{11}C-Labeled pictilisib (GDC-0941) as a molecular tracer targeting phosphatidylinositol 3-kinase (PI3K) for breast cancer imaging. *Contrast Media Mol. Imaging* 2019, 1. doi:10.1155/2019/17601842019

Haupt, S., Vijayakumaran, R., Miranda, P. J., Burgess, A., Lim, E., and Haupt, Y. (2017). The role of MDM2 and MDM4 in breast cancer development and prevention. *J. Mol. Cel Biol* 9 (1), 53–61. doi:10.1093/jmcb/mjx007

He, M. Y., Rancoule, C., Rehailia-Blanchard, A., Espenel, S., Trone, J.-C., Bernichon, E., et al. (2018). Radiotherapy in triple-negative breast cancer: current situation and upcoming strategies. *Crit. Rev. Oncology/Hematology* 131, 96–101. doi:10.1016/j.critrevonc.2018.09.004

Henry, K. E., Dilling, T. R., Abdel-Atti, D., Edwards, K. J., Evans, M. J., and Lewis, J. S. (2018). Noninvasive ^{89}Zr-transferrin PET shows improved tumor targeting compared with ^{18}F-FDG PET in MYC-overexpressing human triple-negative breast cancer. *J. Nucl. Med.* 59 (1), 51–57. doi:10.2967/jnumed.117.192286

Holland, J. P., Evans, M. J., Rice, S. L., Wongvipat, J., Sawyers, C. L., and Lewis, J. S. (2012). Annotating MYC status with ^{89}Zr-transferrin imaging. *Nat. Med.* 18 (10), 1586–1591. doi:10.1038/nm.2935

Horiuchi, D., Anderton, B., and Goga, A. (2014). Taking on challenging targets: making MYC druggable. *Am. Soc. Clin. Oncol. Educ. Book*, e497–e502. doi:10.14694/EdBook_AM.2014.34.e497

Horiuchi, D., Kusdra, L., Huskey, N. E., Chandriani, S., Lenburg, M. E., Gonzalez-Angulo, A. M., et al. (2012). MYC pathway activation in triple-negative breast cancer is synthetic lethal with CDK inhibition. *J. Exp. Med.* 209 (4), 679–696. doi:10.1084/jem.20111512

Hyman, D. M., Piha-Paul, S. A., Won, H., Rodon, J., Saura, C., Shapiro, G. I., et al. (2018). HER kinase inhibition in patients with HER2- and HER3-mutant cancers. *Nature* 554 (7691), 189–194. doi:10.1038/nature25475

Ibrahim, N. K., Yariz, K. O., Bondarenko, I., Manikhas, A., Semiglazov, V., Alyasova, A., et al. (2011). Randomized phase II trial of letrozole plus anti-MUC1 antibody AS1402 in hormone receptor-positive locally advanced or metastatic breast cancer. *Clin. Cancer Res.* 17 (21), 6822–6830. doi:10.1158/1078-0432.CCR-11-1151

Ireson, C. R., and Kelland, L. R. (2006). Discovery and development of anticancer aptamers. *Mol. Cancer Ther.* 5 (12), 2957–2962. doi:10.1158/1535-7163.MCT-06-0172

Jensen, R. T., Battey, J. F., Spindel, E. R., and Benya, R. V. (2008). International Union of Pharmacology. LXVIII. Mammalian bombesin receptors: nomenclature, distribution, pharmacology, signaling, and functions in normal and disease states. *Pharmacol. Rev.* 60 (1), 1–42. doi:10.1124/pr.107.07108

Jin, L., Han, B., Siegel, E., Cui, Y., Giuliano, A., and Cui, X. (2018). Breast cancer lung metastasis: molecular biology and therapeutic implications. *Cancer Biol. Ther.* 19 (10), 858–868. doi:10.1080/15384047.2018.1456599

Johnston, S., Basik, M., Hegg, R., Lausoontornsiri, W., Grzeda, L., Clemons, M., et al. (2016). Inhibition of EGFR, HER2, and HER3 signaling with AZD8931 in combination with anastrozole as an anticancer approach: phase II randomized study in women with endocrine-therapy-naïve advanced breast cancer. *Breast Cancer Res. Treat.* 160 (1), 91–99. doi:10.1007/s10549-016-3979-5

Karuppaiah, A., Rajan, R., Hariharan, S., Balasubramaniam, D. K., Gregory, M., and Sankar, V. (2020). Synthesis and characterization of folic acid conjugated Gemcitabine tethered silver nanoparticles (FA-GEM-AgNPs) for targeted delivery. *Cpd* 26 (26), 3141–3146. doi:10.2174/1381612826666200316143239

Kasoha, M., Unger, C., Solomayer, E.-F., Bohle, R. M., Zaharia, C., Khreich, F., et al. (2017). Prostate-specific membrane antigen (PSMA) expression in breast cancer and its metastases. *Clin. Exp. Metastasis* 34 (8), 479–490. doi:10.1007/s10585-018-9878-x

Kato, M., Kitayama, J., Kazama, S., and Nagawa, H. (2003). Expression pattern of CXC chemokine receptor-4 is correlated with lymph node metastasis in human

invasive ductal carcinoma. *Breast Cancer Res.* 5 (5), R144–R150. doi:10.1186/bcr627

Kebenko, M., Goebeler, M.-E., Wolf, M., Hasenburg, A., Seggewiss-Bernhardt, R., Ritter, B., et al. (2018). A multicenter phase 1 study of solitomab (MT110, AMG 110), a bispecific EpCAM/CD3 T-cell engager (BiTE) antibody construct, in patients with refractory solid tumors. *Oncoimmunology* 7 (8), e1450710. doi:10.1080/2162402X.2018.1450710

Kim, H. J., Park, J. Y., Lee, T. S., Song, I. H., Cho, Y. L., Chae, J. R., et al. (2019). PET imaging of HER2 expression with an ^{18}F-fluoride labeled aptamer. *PLoS One* 14 (1), e0211047. doi:10.1371/journal.pone.0211047

Kim, M. J., Choi, J. R., Tae, N., Wi, T. M., Kim, K. M., Kim, D. H., et al. (2020). Novel antibodies targeting MUC1-C showed anti-metastasis and growth-inhibitory effects on human breast cancer cells. *Ijms* 21 (9), 3258. doi:10.3390/ijms21093258

Kircher, M., Herhaus, P., Schottelius, M., Buck, A. K., Werner, R. A., Wester, H.-J., et al. (2018). CXCR4-directed theranostics in oncology and inflammation. *Ann. Nucl. Med.* 32 (8), 503–511. doi:10.1007/s12149-018-1290-8

Kontermann, R. (2012). Dual targeting strategies with bispecific antibodies. *MAbs* 4 (2), 182–197. doi:10.4161/mabs.4.2.19000

Ku, A., Chan, C., Aghevlian, S., Cai, Z., Cescon, D., Bratman, S. V., et al. (2019a). MicroSPECT/CT imaging of cell-line and patient-derived EGFR-positive tumor xenografts in mice with panitumumab Fab modified with hexahistidine peptides to enable labeling with ^{99m}Tc(I) tricarbonyl complex. *Mol. Pharmaceutics* 16 (8), 3559–3568. doi:10.1021/acs.molpharmaceut.9b00422

Ku, A., Facca, V. J., Cai, Z., and Reilly, R. M. (2019b). Auger electrons for cancer therapy - a review. *EJNMMI Radiopharm. Chem.* 4 (1), 27. doi:10.1186/s41181-019-0075-2

Kuda-Wedagedara, A. N. W., Workinger, J. L., Nexo, E., Doyle, R. P., and Viola-Villegas, N. (2017). ^{89}Zr-Cobalamin PET tracer: synthesis, cellular uptake, and use for tumor imaging. *ACS Omega* 2 (10), 6314–6320. doi:10.1021/acsomega.7b01180

Kumar, M., Salem, K., Tevaarwerk, A. J., Strigel, R. M., and Fowler, A. M. (2020). Recent advances in imaging steroid hormone receptors in breast cancer. *J. Nucl. Med.* 61 (2), 172–176. doi:10.2967/jnumed.119.228858

Kumar, P., Tripathi, S. K., Chen, C. P., Wickstrom, E., and Thakur, M. L. (2019). Evaluating Ga-68 peptide conjugates for targeting VPAC receptors: stability and pharmacokinetics. *Mol. Imaging Biol.* 21 (1), 130–139. doi:10.1007/s11307-018-1207-x

Kwon, L. Y., Scollard, D. A., and Reilly, R. M. (2017). ^{64}Cu-Labeled trastuzumab fab-PEG24-EGF radioimmunoconjugates bispecific for HER2 and EGFR: pharmacokinetics, biodistribution, and tumor imaging by PET in comparison to monospecific agents. *Mol. Pharmaceutics* 14 (2), 492–501. doi:10.1021/acs.molpharmaceut.6b00963

Labrijn, A. F., Janmaat, M. L., Reichert, J. M., and Parren, P. W. H. I. (2019). Bispecific antibodies: a mechanistic review of the pipeline. *Nat. Rev. Drug Discov.* 18 (8), 585–608. doi:10.1038/s41573-019-0028-1

Lee, K.-m., Giltnane, J. M., Balko, J. M., Schwarz, L. J., Guerrero-Zotano, A. L., Hutchinson, K. E., et al. (2017). MYC and MCL1 cooperatively promote chemotherapy-resistant breast cancer stem cells via regulation of mitochondrial oxidative phosphorylation. *Cel Metab.* 26 (4), 633–647. doi:10.1016/j.cmet.2017.09.009

Lee, Y., Lahens, N. F., Zhang, S., Bedont, J., Field, J. M., and Sehgal, A. (2019). G1/S cell cycle regulators mediate effects of circadian dysregulation on tumor growth and provide targets for timed anticancer treatment. *Plos Biol.* 17 (4), e3000228. doi:10.1371/journal.pbio.3000228

Lehmann, B. D., Bauer, J. A., Chen, X., Sanders, M. E., Chakravarthy, A. B., Shyr, Y., et al. (2011). Identification of human triple-negative breast cancer subtypes and preclinical models for selection of targeted therapies. *J. Clin. Invest.* 121 (7), 2750–2767. doi:10.1172/JCI45014

Liu, M., Wang, Z., Tan, T., Chen, Z., Mou, X., Yu, X., et al. (2018). An aptamer-based probe for molecular subtyping of breast cancer. *Theranostics* 8 (20), 5772–5783. doi:10.7150/thno.28949

Lopez, J. S., and Banerji, U. (2017). Combine and conquer: challenges for targeted therapy combinations in early phase trials. *Nat. Rev. Clin. Oncol.* 14 (1), 57–66. doi:10.1038/nrclinonc.2016.96

LoRusso, P., Jänne, P. A., Oliveira, M., Rizvi, N., Malburg, L., Keedy, V., et al. (2013). Phase I study of U3-1287, a fully human anti-HER3 monoclonal antibody, in patients with advanced solid tumors. *Clin. Cancer Res.* 19 (11), 3078–3087. doi:10.1158/1078-0432.CCR-12-3051

Ma, R., Feng, Y., Lin, S., Chen, J., Lin, H., Liang, X., et al. (2015). Mechanisms involved in breast cancer liver metastasis. *J. Transl Med.* 13, 64. doi:10.1186/s12967-015-0425-0

Maeda, T., Hiraki, M., Jin, C., Rajabi, H., Tagde, A., Alam, M., et al. (2018). MUC1-C induces PD-L1 and immune evasion in triple-negative breast cancer. *Cancer Res.* 78 (1), 205–215. doi:10.1158/0008-5472.CAN-17-1636

Maher, C. M., Thomas, J. D., Haas, D. A., Longen, C. G., Oyer, H. M., Tong, J. Y., et al. (2018). Small-molecule Sigma1 modulator induces autophagic degradation of PD-L1. *Mol. Cancer Res.* 16 (2), 243–255. doi:10.1158/1541-7786.MCR-17-0166

Masoud, V., and Pagès, G. (2017). Targeted therapies in breast cancer: new challenges to fight against resistance. *Wjco* 8 (2), 120–134. doi:10.5306/wjco.v8.i2.120

Massicano, A. V. F., Marquez-Nostra, B. V., and Lapi, S. E. (2018). Targeting HER2 in nuclear medicine for imaging and therapy. *Mol. Imaging* 17, 153601211774538. doi:10.1177/1536012117745386

Mazorra, Z., Chao, L., Lavastida, A., Sanchez, B., Ramos, M., Iznaga, N., et al. (2018). Nimotuzumab: beyond the EGFR signaling cascade inhibition. *Semin. Oncol.* 45 (1-2), 18–26. doi:10.1053/j.seminoncol.2018.04.008

McGuckin, M., Walsh, M. D., Hohn, B. G., Ward, B. G., and Wright, R. G. (1995). Prognostic significance of muc1 epithelial mucin expression in breast cancer*1. *Hum. Pathol.* 26 (4), 432–439. doi:10.1016/0046-8177(95)90146-9

McGuire, A., Brown, J. A. L., and Kerin, M. J. (2015). Metastatic breast cancer: the potential of miRNA for diagnosis and treatment monitoring. *Cancer Metastasis Rev.* 34 (1), 145–155. doi:10.1007/s10555-015-9551-7

Mendoza-Nava, H., Ferro-Flores, G., Ramírez, F. d. M., Ocampo-García, B., Santos-Cuevas, C., Azorín-Vega, E., et al. (2017). Fluorescent, plasmonic, and radiotherapeutic properties of the ^{177}Lu-Dendrimer-AuNP-Folate-Bombesin nanoprobe located inside cancer cells. *Mol. Imaging* 16, 153601211770476. doi:10.1177/1536012117704768

Meng, Q., Li, F., Jiang, S., and Li, Z. (2013). Novel 64Cu-labeled CUDC-101 for *in Vivo* PET imaging of histone deacetylases. *ACS Med. Chem. Lett.* 4 (9), 858–862. doi:10.1021/ml400191z

Messori, L., Marzo, T., Michelucci, E., Russo Krauss, I., Navarro-Ranninger, C., Quiroga, A. G., et al. (2014). Interactions between anticancer trans-platinum compounds and proteins: crystal structures and ESI-MS spectra of two protein adducts of trans-(dimethylamino)(methylamino)dichloridoplatinum(II). *Inorg. Chem.* 53 (15), 7806–7808. doi:10.1021/ic5012583

Miller-Kleinhenz, J. M., Bozeman, E. N., and Yang, L. (2015). Targeted nanoparticles for image-guided treatment of triple-negative breast cancer: clinical significance and technological advances. *WIREs Nanomed Nanobiotechnol* 7 (6), 797–816. doi:10.1002/wnan.1343

Moores, S. L., Chiu, M. L., Bushey, B. S., Chevalier, K., Luistro, L., Dorn, K., et al. (2016). A novel bispecific antibody targeting EGFR and cMet is effective against EGFR inhibitor-resistant lung tumors. *Cancer Res.* 76 (13), 3942–3953. doi:10.1158/0008-5472.can-15-2833

Morgenroth, A., Tinkir, E., Vogg, A. T. J., Sankaranarayanan, R. A., Baazaoui, F., and Mottaghy, F. M. (2019). Targeting of prostate-specific membrane antigen for radio-ligand therapy of triple-negative breast cancer. *Breast Cancer Res.* 21 (1), 116. doi:10.1186/s13058-019-1205-1

Mukai, H., Saeki, T., Aogi, K., Naito, Y., Matsubara, N., Shigekawa, T., et al. (2016). Patritumab plus trastuzumab and paclitaxel in human epidermal growth factor receptor 2-overexpressing metastatic breast cancer. *Cancer Sci.* 107 (10), 1465–1470. doi:10.1111/cas.13017

Narmani, A., Yavari, K., and Mohammadnejad, J. (2017). Imaging, biodistribution and *in vitro* study of smart ^{99m}Tc-PAMAM G4 dendrimer as novel nano-complex. *Colloids Surf. B: Biointerfaces* 159, 232–240. doi:10.1016/j.colsurfb.2017.07.089

Nounou, M. I., Adkins, C. E., Rubinchik, E., Terrell-Hall, T. B., Afroz, M., Vitalis, T., et al. (2016). Anti-cancer antibody trastuzumab-melanotransferrin conjugate (BT2111) for the treatment of metastatic HER2+ breast cancer tumors in the brain: an in-vivo study. *Pharm. Res.* 33 (12), 2930–2942. doi:10.1007/s11095-016-2015-0

O'Donnell, K. A., Yu, D., Zeller, K. I., Kim, J.-w., Racke, F., Thomas-Tikhonenko, A., et al. (2006). Activation of transferrin receptor 1 by c-Myc enhances cellular

proliferation and tumorigenesis. *Mcb* 26 (6), 2373–2386. doi:10.1128/MCB.26.6.2373-2386.2006

O'Sullivan, C. C., Suman, V. J., and Goetz, M. P. (2019). The emerging role of CDK4/6i in HER2-positive breast cancer. *Ther. Adv. Med. Oncol.* 11, 1758835919887665. doi:10.1177/1758835919887665

Pachynski, R. K., Wang, P., Salazar, N., Zheng, Y., Nease, L., Rosalez, J., et al. (2019). Chemerin suppresses breast cancer growth by recruiting immune effector cells into the tumor microenvironment. *Front. Immunol.* 10, 983. doi:10.3389/fimmu.2019.00983

Pascual, L., Cerqueira-Coutinho, C., García-Fernández, A., de Luis, B., Bernardes, E. S., Albernaz, M. S., et al. (2017). MUC1 aptamer-capped mesoporous silica nanoparticles for controlled drug delivery and radio-imaging applications. *Nanomedicine: Nanotechnology, Biol. Med.* 13 (8), 2495–2505. doi:10.1016/j.nano.2017.08.006

Peart, O. (2017). Metastatic breast cancer. *Radiol. Technol.* 88 (5), 519M–539M.

Perumalsamy, S., Aqilah Mohd Zin, N. A., Widodo, R. T., Wan Ahmad, W. A., Vethakkan, S. R. D. B., and Huri, H. Z. (2017). Chemokine like receptor-1 (CMKLR-1) receptor: a potential therapeutic target in management of chemerin induced type 2 diabetes mellitus and cancer. *Cpd* 23 (25), 3689–3698. doi:10.2174/1381612823666170616081256

Pishvaian, M., Morse, M. A., McDevitt, J., Norton, J. D., Ren, S., Robbie, G. J., et al. (2016). Phase 1 dose escalation study of MEDI-565, a bispecific T-cell engager that targets human carcinoembryonic antigen, in patients with advanced gastrointestinal adenocarcinomas. *Clin. Colorectal Cancer* 15 (4), 345–351. doi:10.1016/j.clcc.2016.07.009

Pouget, J.-P., Navarro-Teulon, I., Bardiès, M., Chouin, N., Cartron, G., Pèlegrin, A., et al. (2011). Clinical radioimmunotherapy-the role of radiobiology. *Nat. Rev. Clin. Oncol.* 8 (12), 720–734. doi:10.1038/nrclinonc.2011.160

Qu, X., Wang, H., and Liu, R. (2018). Recent insights into biological functions of mammalian bombesin-like peptides and their receptors. *Curr. Opin. Endocrinol. Diabetes Obes.* 25 (1), 36–41. doi:10.1097/MED.0000000000000375

Quadros, E. V., and Sequeira, J. M. (2013). Cellular uptake of cobalamin: transcobalamin and the TCblR/CD320 receptor. *Biochimie* 95 (5), 1008–1018. doi:10.1016/j.biochi.2013.02.004

Ramos, N., Baquero-Buitrago, J., Ben Youss Gironda, Z., Wadghiri, Y. Z., Reiner, T., Boada, F. E., et al. (2020). Noninvasive PET imaging of CDK4/6 activation in breast cancer. *J. Nucl. Med.* 61 (3), 437–442. doi:10.2967/jnumed.119.232603

Ranogajec, I., Jakić-Razumović, J., Puzović, V., and Gabrilovac, J. (2012). Prognostic value of matrix metalloproteinase-2 (MMP-2), matrix metalloproteinase-9 (MMP-9) and aminopeptidase N/CD13 in breast cancer patients. *Med. Oncol.* 29 (2), 561–569. doi:10.1007/s12032-011-9984-y

Reubi, J., Gugger, M., and Waser, B. (2002). Co-expressed peptide receptors in breast cancer as a molecular basis for *in vivo* multireceptor tumour targeting. *Eur. J. Nucl. Med.* 29 (7), 855–862. doi:10.1007/s00259-002-0794-5

Roberts, M. J., Bentley, M. D., and Harris, J. M. (2002). Chemistry for peptide and protein PEGylation. *Adv. Drug Deliv. Rev.* 54 (4), 459–476. doi:10.1016/s0169-409x(02)00022-4

Rolli, M., Fransvea, E., Pilch, J., Saven, A., and Felding-Habermann, B. (2003). Activated integrin v 3 cooperates with metalloproteinase MMP-9 in regulating migration of metastatic breast cancer cells. *Proc. Natl. Acad. Sci.* 100 (16), 9482–9487. doi:10.1073/pnas.1633689100

Rosenberg, J. E., Bambury, R. M., Van Allen, E. M., Drabkin, H. A., Lara, P. N., Jr., Harzstark, A. L., et al. (2014). A phase II trial of AS1411 (a novel nucleolin-targeted DNA aptamer) in metastatic renal cell carcinoma. *Invest. New Drugs* 32 (1), 178–187. doi:10.1007/s10637-013-0045-6

Ross, J. S., Slodkowska, E. A., Symmans, W. F., Pusztai, L., Ravdin, P. M., and Hortobagyi, G. N. (2009). The HER-2 receptor and breast cancer: ten years of targeted anti-HER-2 therapy and personalized medicine. *Oncol.* 14 (4), 320–368. doi:10.1634/theoncologist.2008-0230

Ruf, W., Yokota, N., and Schaffner, F. (2010). Tissue factor in cancer progression and angiogenesis. *Thromb. Res.* 125 (Suppl. 2), S36–S38. doi:10.1016/S0049-3848(10)70010-4

Salgia, R., Weaver, R. W., McCleod, M., Stille, J. R., Yan, S. B., Roberson, S., et al. (2017). Prognostic and predictive value of circulating tumor cells and CXCR4 expression as biomarkers for a CXCR4 peptide antagonist in combination with carboplatin-etoposide in small cell lung cancer: exploratory analysis of a phase II study. *Invest. New Drugs* 35 (3), 334–344. doi:10.1007/s10637-017-0446-z

Salvucci, O., Bouchard, A., Baccarelli, A., Deschenes, J., Sauter, G., Simon, R., et al. (2006). The role of CXCR4 receptor expression in breast cancer: a large tissue microarray study. *Breast Cancer Res. Treat.* 97 (3), 275–283. doi:10.1007/s10549-005-9121-8

Schafer, K. A. (1998). The cell cycle: a review. *Vet. Pathol.* 35 (6), 461–478. doi:10.1177/030098589803500601

Schöffski, P., Cresta, S., Mayer, I. A., Wildiers, H., Damian, S., Gendreau, S., et al. (2018). A phase Ib study of pictilisib (GDC-0941) in combination with paclitaxel, with and without bevacizumab or trastuzumab, and with letrozole in advanced breast cancer. *Breast Cancer Res.* 20 (1), 109. doi:10.1186/s13058-018-1015-x

Sergina, N. V., Rausch, M., Wang, D., Blair, J., Hann, B., Shokat, K. M., et al. (2007). Escape from HER-family tyrosine kinase inhibitor therapy by the kinase-inactive HER3. *Nature* 445 (7126), 437–441. doi:10.1038/nature05474

Shi, S., Hong, H., Orbay, H., Graves, S. A., Yang, Y., Ohman, J. D., et al. (2015). ImmunoPET of tissue factor expression in triple-negative breast cancer with a radiolabeled antibody Fab fragment. *Eur. J. Nucl. Med. Mol. Imaging* 42 (8), 1295–1303. doi:10.1007/s00259-015-3038-1

Shimizu, T., LoRusso, P. M., Papadopoulos, K. P., Patnaik, A., Beeram, M., Smith, L. S., et al. (2014). Phase I first-in-human study of CUDC-101, a multitargeted inhibitor of HDACs, EGFR, and HER2 in patients with advanced solid tumors. *Clin. Cancer Res.* 20 (19), 5032–5040. doi:10.1158/1078-0432.CCR-14-0570

Shin, W. J., and Pachynski, R. K. (2018). Chemerin modulation of tumor growth: potential clinical applications in cancer. *Discov. Med.* 26 (141), 31–37.

Sijbrandi, N. J., Merkul, E., Muns, J. A., Waalboer, D. C. J., Adamzek, K., Bolijn, M., et al. (2017). A novel platinum(II)-Based bifunctional ADC linker benchmarked using 89Zr-desferal and auristatin F-conjugated trastuzumab. *Cancer Res.* 77 (2), 257–267. doi:10.1158/0008-5472.CAN-16-1900

Singh, A., Bishayee, A., and Pandey, A. (2018). Targeting histone deacetylases with natural and synthetic agents: an emerging anticancer strategy. *Nutrients* 10 (6), 731. doi:10.3390/nu10060731

Siroy, A., Abdul-Karim, F. W., Miedler, J., Fong, N., Fu, P., Gilmore, H., et al. (2013). MUC1 is expressed at high frequency in early-stage basal-like triple-negative breast cancer. *Hum. Pathol.* 44 (10), 2159–2166. doi:10.1016/j.humpath.2013.04.010

Song, X., Gan, Q., Zhang, X., and Zhang, J. (2019). Synthesis and biological evaluation of novel ^{99m}Tc-labeled palbociclib derivatives targeting cyclin-dependent kinase 4/6 (CDK4/6) as potential cancer imaging agents. *Mol. Pharmaceutics* 16 (10), 4213–4222. doi:10.1021/acs.molpharmaceut.9b00540

Steding, C. E. (2016). Creating chemotherapeutic-resistant breast cancer cell lines: advances and future perspectives. *Future Oncol.* 12 (12), 1517–1527. doi:10.2217/fon-2016-0059

Stine, Z. E., Walton, Z. E., Altman, B. J., Hsieh, A. L., and Dang, C. V. (2015). MYC, metabolism, and cancer. *Cancer Discov.* 5 (10), 1024–1039. doi:10.1158/2159-8290.CD-15-0507

Sysel, A. M., Valli, V. E., Nagle, R. B., and Bauer, J. A. (2013). Immunohistochemical quantification of the vitamin B12 transport protein (TCII), cell surface receptor (TCII-R) and Ki-67 in human tumor xenografts. *Anticancer Res.* 33 (10), 4203–4212.

Tang, S., Zhou, F., Sun, Y., Wei, L., Zhu, S., Yang, R., et al. (2016). CEA in breast ductal secretions as a promising biomarker for the diagnosis of breast cancer: a systematic review and meta-analysis. *Breast Cancer* 23 (6), 813–819. doi:10.1007/s12282-016-0680-9

Tang, Y., Cui, X., Xiao, H., Qi, S., Hu, X., Yu, Q., et al. (2017). Binding of circulating anti-MUC1 antibody and serum MUC1 antigen in stage IV breast cancer. *Mol. Med. Rep.* 15 (5), 2659–2664. doi:10.3892/mmr.2017.6323

Tate, C. R., Rhodes, L. V., Segar, H. C., Driver, J. L., Pounder, F. N., Burow, M. E., et al. (2012). Targeting triple-negative breast cancer cells with the histone deacetylase inhibitor panobinostat. *Breast Cancer Res.* 14 (3), R79. doi:10.1186/bcr3192

Tejería, E., Giglio, J., Fernández, L., and Rey, A. (2019). Development and evaluation of a ^{99m}Tc(V)-nitrido complex derived from estradiol for breast cancer imaging. *Appl. Radiat. Isot.* 154, 108854. doi:10.1016/j.apradiso.2019.108854

Thakur, A., Huang, M., and Lum, L. G. (2018). Bispecific antibody based therapeutics: strengths and challenges. *Blood Rev.* 32 (4), 339–347. doi:10.1016/j.blre.2018.02.004

Thakur, M. L., Zhang, K., Berger, A., Cavanaugh, B., Kim, S., Channappa, C., et al. (2013). VPAC1 receptors for imaging breast cancer: a feasibility study. *J. Nucl. Med.* 54 (7), 1019–1025. doi:10.2967/jnumed.112.114876

Treeck, O., Buechler, C., and Ortmann, O. (2019). Chemerin and cancer. *Ijms* 20 (15), 3750. doi:10.3390/ijms20153750

Ueno, T., Toi, M., Koike, M., Nakamura, S., and Tominaga, T. (2000). Tissue factor expression in breast cancer tissues: its correlation with prognosis and plasma concentration. *Br. J. Cancer* 83 (2), 164–170. doi:10.1054/bjoc.2000.1272

Valkema, R., de Jong, M., Bakker, W. H., Breeman, W. A. P., Kooij, P. P. M., Lugtenburg, P. J., et al. (2002). Phase I study of peptide receptor radionuclide therapy with [^{111}In-DTPA]octreotide: the rotterdam experience. *Semin. Nucl. Med.* 32 (2), 110–122. doi:10.1053/snuc/2002.31025

Vall-Sagarra, A., Litau, S., Decristoforo, C., Wängler, B., Schirrmacher, R., Fricker, G., et al. (2018). Design, synthesis, in vitro, and initial in vivo evaluation of heterobivalent peptidic ligands targeting both NPY(Y1)- and GRP-receptors-an improvement for breast cancer imaging?. *Pharmaceuticals* 11 (3), 65. doi:10.3390/ph11030065

Vallböhmer, D., Zhang, W., Gordon, M., Yang, D. Y., Yun, J., Press, O. A., et al. (2005). Molecular determinants of cetuximab efficacy. *Jco* 23 (15), 3536–3544. doi:10.1200/JCO.2005.09.100

VanArsdale, T., Boshoff, C., Arndt, K. T., and Abraham, R. T. (2015). Molecular pathways: targeting the cyclin D-CDK4/6 *Axis* for cancer treatment. *Clin. Cancer Res.* 21 (13), 2905–2910. doi:10.1158/1078-0432.CCR-14-0816

Varasteh, Z., Rosenström, U., Velikyan, I., Mitran, B., Altai, M., Honarvar, H., et al. (2014). The effect of mini-PEG-based spacer length on binding and pharmacokinetic properties of a ^{68}Ga-labeled NOTA-conjugated antagonistic analog of bombesin. *Molecules* 19 (7), 10455–10472. doi:10.3390/molecules190710455

Viola-Villegas, N., and Doyle, R. P. (2009). The coordination chemistry of 1,4,7,10-tetraazacyclododecane-N,N′,N″,N‴-tetraacetic acid (H4DOTA): structural overview and analyses on structure-stability relationships. *Coord. Chem. Rev.* 253 (13-14), 1906–1925. doi:10.1016/j.ccr.2009.03.013

Waaijer, S. J. H., Warnders, F. J., Stienen, S., Friedrich, M., Sternjak, A., Cheung, H. K., et al. (2018). Molecular imaging of radiolabeled bispecific T-cell engager ^{89}Zr-AMG211 targeting CEA-positive tumors. *Clin. Cancer Res.* 24 (20), 4988–4996. doi:10.1158/1078-0432.Ccr-18-0786

Waks, A. G., and Winer, E. P. (2019). Breast cancer treatment. *JAMA* 321 (3), 288–300. doi:10.1001/jama.2018.19323

Wang, B., Guo, C., Liu, Y., Han, G., Li, Y., Zhang, Y., et al. (2020). Novel nano-pomegranates based on astragalus polysaccharides for targeting ERα-positive breast cancer and multidrug resistance. *Drug Deliv.* 27 (1), 607–621. doi:10.1080/10717544.2020.1754529

Wang, B., Rouzier, R., Albarracin, C. T., Sahin, A., Wagner, P., Yang, Y., et al. (2004). Expression of sigma 1 receptor in human breast cancer. *Breast Cancer Res. Treat.* 87 (3), 205–214. doi:10.1007/s10549-004-6590-0

Wang, W., Xu, X., Tian, B., Wang, Y., Du, L., Sun, T., et al. (2017). The diagnostic value of serum tumor markers CEA, CA19-9, CA125, CA15-3, and TPS in metastatic breast cancer. *Clinica Chim. Acta* 470, 51–55. doi:10.1016/j.cca.2017.04.023

Wang, Z. (2017). ErbB receptors and cancer. *Methods Mol. Biol.* 1652, 3–35. doi:10.1007/978-1-4939-7219-7_1

Xia, X., Feng, H., Li, C., Qin, C., Song, Y., Zhang, Y., et al. (2016). ^{99m}Tc-labeled estradiol as an estrogen receptor probe: preparation and preclinical evaluation. *Nucl. Med. Biol.* 43 (1), 89–96. doi:10.1016/j.nucmedbio.2015.09.006

Xu, C., Zhao, H., Chen, H., and Yao, Q. (2015). CXCR4 in breast cancer: oncogenic role and therapeutic targeting. *Drug Des. Devel Ther.* 9, 4953–4964. doi:10.2147/DDDT.S84932

Yamamoto, N., Fujiwara, Y., Tamura, K., Kondo, S., Iwasa, S., Tanabe, Y., et al. (2017). Phase Ia/Ib study of the pan-class I PI3K inhibitor pictilisib (GDC-0941) administered as a single agent in Japanese patients with solid tumors and in combination in Japanese patients with non-squamous non-small cell lung cancer. *Invest. New Drugs* 35 (1), 37–46. doi:10.1007/s10637-016-0382-3

Yang, S. P., Song, S. T., and Song, H. F. (2003). Advancements of antisense oligonucleotides in treatment of breast cancer. *Acta Pharmacol. Sin* 24 (4), 289–295.

Yook, S., Cai, Z., Jeong, J. J., Lu, Y., Winnik, M. A., Pignol, J.-P., et al. (2020). Dual-receptor-targeted (DRT) radiation nanomedicine labeled with ^{177}Lu is more potent for killing human breast cancer cells that coexpress HER2 and EGFR than single-receptor-targeted (SRT) radiation nanomedicines. *Mol. Pharmaceutics* 17 (4), 1226–1236. doi:10.1021/acs.molpharmaceut.9b01259

Zhang, C.-X., Zhang, Q., Xie, Y.-Y., He, X.-Y., Xiang, C., Hou, X.-S., et al. (2017). Mouse double minute 2 actively suppresses p53 activity in oocytes during mouse folliculogenesis. *Am. J. Pathol.* 187 (2), 339–351. doi:10.1016/j.ajpath.2016.09.023

Zhang, J. Y., Mai, G. F., Zheng, H., Luo, R. C., Song, H. Z., Miao, J. X., et al. (2003). [Association between the survival time and high-expression of EGFR and HER-2 in breast cancer]. *Di Yi Jun Yi Da Xue Xue Bao* 23 (10), 1090–1092.

Zhang, X., You, L., Chen, S., Gao, M., Guo, Z., Du, J., et al. (2018). Development of a novel ^{99m}Tc-labeled small molecular antagonist for CXCR4 positive tumor imaging. *J. Label Compd. Radiopharm.* 61 (5), 438–446. doi:10.1002/jlcr.3608

Zhang, Z., Ni, C., Chen, W., Wu, P., Wang, Z., Yin, J., et al. (2014a). Expression of CXCR4 and breast cancer prognosis: a systematic review and meta-analysis. *BMC Cancer* 14, 49. doi:10.1186/1471-2407-14-49

Zhang, Z., Wang, J., Tacha, D. E., Li, P., Bremer, R. E., Chen, H., et al. (2014b). Folate receptor α associated with triple-negative breast cancer and poor prognosis. *Arch. Pathol. Lab. Med.* 138 (7), 890–895. doi:10.5858/arpa.2013-0309-OA

Zolata, H., Abbasi Davani, F., and Afarideh, H. (2015). Synthesis, characterization and theranostic evaluation of Indium-111 labeled multifunctional superparamagnetic iron oxide nanoparticles. *Nucl. Med. Biol.* 42 (2), 164–170. doi:10.1016/j.nucmedbio.2014.09.007

Conflict of Interest: The authors declare that the research was conducted in the absence of any commercial or financial relationships that could be construed as a potential conflict of interest.

Advantages of publishing in Frontiers

OPEN ACCESS
Articles are free to read for greatest visibility and readership

FAST PUBLICATION
Around 90 days from submission to decision

HIGH QUALITY PEER-REVIEW
Rigorous, collaborative, and constructive peer-review

TRANSPARENT PEER-REVIEW
Editors and reviewers acknowledged by name on published articles

Frontiers
Avenue du Tribunal-Fédéral 34
1005 Lausanne | Switzerland

Visit us: www.frontiersin.org
Contact us: frontiersin.org/about/contact

REPRODUCIBILITY OF RESEARCH
Support open data and methods to enhance research reproducibility

DIGITAL PUBLISHING
Articles designed for optimal readership across devices

FOLLOW US
@frontiersin

IMPACT METRICS
Advanced article metrics track visibility across digital media

EXTENSIVE PROMOTION
Marketing and promotion of impactful research

LOOP RESEARCH NETWORK
Our network increases your article's readership